Drug discovery for rare neurological disorders using human cellular models

Inaugural-Dissertation

zur Erlangung des Doktorgrades
der Mathematisch-Naturwissenschaftlichen Fakultät
der Heinrich-Heine-Universität Düsseldorf

vorgelegt von
Annika Wittich
aus Hamburg

Düsseldorf, Dezember 2025

Aus dem Fraunhofer-Institut für Translationale Medizin und Pharmakologie ITMP Hamburg

in Assoziation mit der Heinrich-Heine-Universität Düsseldorf

Gedruckt mit der Genehmigung der
Mathematisch-Naturwissenschaftlichen Fakultät der
Heinrich-Heine-Universität Düsseldorf

Berichterstatter:

1. Prof. Dr. Alessandro Prigione

2. Prof. Dr. Erdem Gültekin Tamgüney

Tag der mündlichen Prüfung: 09.04.2026

Disclaimer

The language in the thesis has been improved using Grammarly.

Table of contents

Summary 1

Zusammenfassung 2

1. Introduction 3

1.1 Neurological disorders 3

1.2 Parkinson's disease 4

1.3 Rare diseases 5

1.3.1 Multiple sulfatase deficiency 6

1.3.2 Leigh syndrome 7

1.4 Mitochondria 8

1.4.1 Oxidative phosphorylation 9

1.4.2 Mitochondria in neurodegenerative diseases 12

1.5 Research models for neurological diseases 13

1.6 Drug development 15

1.7 High-throughput screening 17

2. Aim and organization of the thesis 18

3. Results 18

3.1 High-content screening of mitochondrial polarization in neural cells derived from human pluripotent stem cells 20

3.1.1 Contribution 20

3.1.2 Graphical summary 20

3.1.3 Summary 21

3.2 Pluripotent stem-cell-based screening uncovers sildenafil as a mitochondrial disease therapy 22

3.2.1 Contribution 22

3.2.2 Graphical summary 23

3.2.3 Summary 23

3.3 Morphological profiling reveals neuroprotection via mitochondrial uncoupling in human dopaminergic neurons 24

3.3.1 Contribution 24

3.3.2 Graphical summary 24

3.3.3 Summary 25

3.4 Human organoids: Fit for drug discovery? 26

3.4.1 Contribution 26

3.4.2 Graphical summary 26
3.4.3 Summary 27
3.5 Accelerating Leigh syndrome drug discovery through deep learning screening in brain organoids 28
3.5.1 Contribution 28
3.5.2 Graphical summary 29
3.5.3 Summary 29
3.6 Cortical organoid-derived models of the melanoma brain metastatic niche enable prioritization of cancer-targeting drugs 30
3.6.1 Contribution 30
3.6.2 Graphical summary 31
3.6.3 Summary 31
3.7 High-throughput screen identifies repurposing candidates for Multiple sulfatase deficiency 32
3.7.1 Contribution 32
3.7.2 Graphical summary 32
3.7.3 Summary 33
4. Discussion 34
4.1 Choosing the right model for drug discovery in rare neurological diseases 34
4.2 Sildenafil as a treatment for neurological diseases 36
4.3 Mitochondrial uncoupling in neurodegenerative diseases 39
4.4 Clinical potential of newly identified compounds for MSD 41
5. Conclusion and perspectives 43
6. Acknowledgements 44
7. References 45
8. Eidesstattliche Erklärung 66
9. Appendix I 67
10. Appendix II 88
11. Appendix III 156
12. Appendix IV 175
13. Appendix V 197
14. Appendix VI 223
15. Appendix VII 251

Abbreviations

2D	Two-dimensional
3D	Three-dimensional
AAV	Adeno-associated virus
AD	Alzheimer's disease
ADME-T	Absorption, Distribution, Metabolism, Excretion and Toxicity
ADP	Adenosine diphosphate
ALS	Amyotrophic lateral sclerosis
AMPK	Adenosine monophosphate-activated protein kinase
ARSA	Arylsulfatase A
ATP	Adenosine triphosphate
BBB	Blood-brain barrier
Cas9	CRISPR-associated protein 9
CCCP	Carbonyl cyanide m-chlorophenyl hydrazone
cGMP	Cyclic guanosine monophosphate
CNS	Central nervous system
CoQ	Coenzyme Q10
COX	Cytochrome c oxidase
CP	Cell Painting
CRISPR	Clustered regularly interspaced short palindromic repeats
Cyt c	Cytochrome c
DALY	Disability-adjusted life-years
DETFs	Differentially expressed transcription factors
DL	Deep learning
DNP	2-azido-4-nitrophenol
DRP1	Dynamin-related protein 1
e^-	Electron
ED	Erectile dysfunction
EMA	European Medicines Agency
ER	Endoplasmic reticulum
ETC	Electron transport chain
FCCP	Carbonyl cyanide-p-trifluoromethoxyphenyl-hydrazone
FDA	Food and Drug Administration
FGE	Formylglycine-generating enzyme
GTP	Guanosine triphosphate
H^+	Proton
hCOs	Cortical organoids
HCS	High-content screening
HD	Huntington's disease
HFEA	The Human Fertilisation and Embryology Authority
HTS	High-throughput screening
ICC	Immunocytochemistry

iPSC	Induced pluripotent stem cells
KO	Knockout
LRRK2	Leucine-rich repeat kinase 2
LS	Leigh syndrome
MAP2	Microtubule-associated protein 2
MBMs	Melanoma brain metastasis
mDA	Midbrain dopaminergic neuron
MelDCCs	Melanoma disseminated cancer cells
MFN1	Mitofusin 1
MFN2	Mitofusin 2
MILS	Maternally inherited Leigh syndrome
MMP/ΔΨ	Mitochondrial membrane potential
MRT	Mitochondrial replacement therapies
MSD	Multiple sulfatase deficiency
mtDNA	Mitochondrial DNA
NADH	Nicotinamide adenine dinucleotide
NAMs	New Approach Methodologies
nDNA	Nuclear DNA
NO	Nitric oxide
NPCs	Neuronal precursor cells
ODD	Orphan Drug Designation
OPA1	Optic atrophy 1
OXPHOS	Oxidative phosphorylation
PD	Parkinson's disease
PDE	Phosphodiesterases
PDE5	Phosphodiesterase 5
PDE5i	Phosphodiesterase 5 inhibitor
PINK1	PTEN-induced kinase 1
PPARγ	Peroxisome proliferator-activated receptor gamma
PRKG1	cGMP-dependent protein kinase 1
PRKN	Parkin RBR E3 ubiquitin protein ligase
PSCs	Pluripotent stem cells
ROS	Reactive oxygen species
Sc-RNA	Single-cell ribonucleic acid
smNPCS	Small molecule neuronal precursor cells
SNT	Spindle nuclear transfer
SUMF1	Sulfatase-modifying factor 1
SV40	Simian virus 40
TALE	Transcription activator-like effector
TMRM	Tetramethylrhodamine methyl ester
U.S.	United States
UK	United Kingdom
αSyn	α-Synuclein

Summary

Rare diseases, though individually uncommon, collectively affect many people. The burden of rare neurological conditions is steadily rising, increasing the need for effective treatments. High failure rates in drug discovery and the infrequent translation of findings from biomedical research and preclinical studies into clinical practice are common challenges. Additionally, limited transport across the blood-brain barrier (BBB) complicates drug development and delivery to the brain. Predictive preclinical models could help integrate drug discovery and clinical development trials. Human induced pluripotent stem cell (iPSC)-derived *in vitro* models are able to mimic key features of human disease-relevant tissues, such as the brain. They enable the generation of human cell types that are otherwise limited in accessibility, offering potential for more relevant models in rare neurological disease research and drug development. This study aimed to develop scalable, reliable iPSC-based *in vitro* platforms to identify and validate drugs for rare neurological disorders.

Within this work, human cellular models were used to identify therapeutic candidates targeting Leigh syndrome (LS), Parkinson's disease (PD), melanoma brain metastasis (MBMs), and Multiple sulfatase deficiency (MSD). The drug repurposing screen identified phosphodiesterase 5 inhibitors as a promising compound class, with sildenafil discovered as a novel treatment strategy for LS, capable of crossing the BBB, and now advancing into clinical trials. Additionally, screening activities revealed tyrphostins as uncoupler of mitochondrial membrane potential. This mitochondrial uncoupling by tyrphostin A9 has been shown to be beneficial in neuronal models of PD by reducing alpha-synuclein accumulation and reactive oxygen species levels. Using deep learning and yeast LS models, azole derivatives were identified, and the two most active, talarozole and sertaconazole, were validated in complex 3D brain organoids from iPSCs of an LS patient. These compounds proved effective in normalizing neuromorphogenesis and lactate levels. Moreover, a 3D co-culture model using iPSC-derived brain organoids with melanoma and disseminated cancer cells was employed to validate seven hit compounds that were previously identified through a 2D screen with melanoma and cancer cells, revealing selinexor as effectively eliminating cancer cells without neurotoxicity. A drug repurposing screen involving 5,632 compounds in MSD patient fibroblasts identified six novel drug candidates that more effectively enhanced ARSA activity, which is reduced in MSD patients than previous retinoids such as tazarotene and bexarotene, without inducing toxicity.

In conclusion, this work highlights an effective strategy of combining 2D and 3D human cellular *in vitro* models and demonstrates how they can support drug discovery for rare neurological diseases, paving the way for new treatment options for affected patients.

Zusammenfassung

Seltene Krankheiten treten mit einer geringen Prävalenz auf, doch die Gesamtzahl der Betroffenen ist groß. Mit sich ständig verbessernden molekularen Methoden steigt die Zahl der gesicherten Diagnosen und damit der Bedarf an wirksamen Therapien. Die Entwicklung neuer Medikamente für neurologische Erkrankungen steht vor Herausforderungen wie einem hohen Scheitern bei klinischer Testung, geringer Translation biomedizinischer Forschung und dem limitierten Transport vieler Substanzen durch die Blut-Hirn-Schranke (BHS). Prädiktive präklinische humane Modelle könnten die Arzneimittelforschung verbessern. *In vitro* Modelle aus menschlichen induzierten pluripotenten Stammzellen (iPS) ermöglichen die Nachbildung menschlicher Gehirnzellen und erleichtern den Zugang zu relevanten Zelltypen für Forschung und Entwicklung.
Ziel dieser Arbeit war die Entwicklung und Anwendung skalierbarer Plattformen auf Basis humaner (iPS-)Zellmodelle, um neue Wirkstoffe für seltene neurologische Erkrankungen wie das Leigh-Syndrom (LS), Parkinson (Parkinson disease, PD), Melanom-Hirnmetastasen und Multiplen Sulfatase-Mangel (Multiple sulfatase deficiency, MSD) zu identifizieren. Für LS wurden Phosphodiesterase-5-Inhibitoren, darunter Sildenafil, als neue Behandlungsstrategie entdeckt. Sildenafil verbesserte krankheitsspezifische Merkmale in neuronalen *in vitro* Modellen, normalisierte das mitochondriale Membranpotenzial und zeigte in iPS-abgeleiteten Modellen der BHS, dass es diese überwinden kann. Sildenafil wurde bereits erfolgreich bei LS-Patienten angewendet und wird nun klinisch weiter erprobt. Darüber hinaus wurde gezeigt, dass Tyrphostine als Entkoppler des mitochondrialen Membranpotentials wirken. Tyrphostin A9 reduzierte in einem iPS-PD-Modell Alpha-Synuclein-Ablagerungen und reaktive Sauerstoffspezies. Deep Learning und Hefe-LS-Modelle identifizierten Azolderivate als Hitsubstanzen. Die aktivsten, Talarozol und Sertaconazol, normalisierten in iPS-abgeleiteten 3D-Hirnorganoiden die Neuromorphogenese und den Laktatspiegel. Ein 3D-Co-Kulturmodell mit Hirnorganoiden und Melanomzellen validierte sieben zuvor identifizierte Wirkstoffe. Selinexor eliminierte Krebszellen wirksam ohne Neurotoxizität. Ein Hochdurchsatz-Screen von 5.632 Substanzen an MSD-Fibroblasten identifizierte sechs neue Kandidaten, die die reduzierte ARSA-Aktivität stärker als zuvor gefundene Retinoide steigerten, ohne Toxizität zu verursachen.
Zusammenfassend zeigt diese Arbeit, dass kombinierte 2D- und 3D (iPS) *in vitro* Modelle die Medikamentenentwicklung für seltene neurologische Erkrankungen effektiv unterstützen und neue therapeutische Ansätze ermöglichen können.

1. Introduction

1.1 Neurological disorders

Neurological disorders are conditions that impact the central and peripheral nervous systems, including the brain, spinal cord, and peripheral nerves. These disorders can result from structural, biochemical, or electrical abnormalities in nerve cells (Farooqui and Farooqui, 2016), and they account for about 6.3% of the global disease burden. In the past 30 years, disability-adjusted life-years (DALYs; the total of years of life lost and years lived with disability) for neurological disorders have risen by 15% (Feigin et al., 2020). Although the prevalence of neurological disorders varies across regions and populations (Thakur et al., 2016), these figures emphasize the need for effective treatment and rehabilitation options. Neurological disorders can be sub-grouped into neurotraumatic diseases (stroke, traumatic brain injury, and spinal cord injury), neuropsychiatric diseases (depression, autism, schizophrenia, and hyperactivity disorders), and neurodegenerative diseases (Alzheimer's, Parkinson's, and Huntington's disease) (Farooqui and Farooqui, 2016). Neuropsychiatric and neurodegenerative diseases can be caused by inherited genetic abnormalities, an abnormal immune system, and environmental factors (Migliore and Coppedè, 2002).

Neurotraumatic diseases are often defined as abrupt injuries to the brain or spinal cord, resulting from mechanical damage to neural tissue (Ali et al., 2024). Neuropsychiatric diseases are characterized by psychiatric symptoms that cause cognitive impairment, including dementia, amnestic syndrome, and personality-behavioral changes (Miyoshi, Morimura, and Maeda, 2010). Environmental factors, including diet, substance abuse, and educational background, are recognized as risk factors that can influence the development and progression of neuropsychiatric diseases (Meyer-Lindenberg and Tost, 2012). However, it is also widely accepted that gene malfunction plays a significant role in these diseases.

Neurodegenerative diseases are characterized by the progressive loss of nerve cells, such as neurons, glia cells, and respective networks. They can be classified based on primary clinical features, the anatomical distribution of neurodegeneration, or principal molecular abnormalities (Pathak et al., 2022). Neurodegenerative diseases can occur in both familial and sporadic forms. While familial variants play a significant role in protein misfolding and aggregation, most cases of neurodegenerative diseases are sporadic, indicating that other factors, such as age, diet, and lifestyle, may also contribute to their development (Farooqui, 2022).

1.2 Parkinson's disease

Parkinson's disease (PD) is the second most common neurodegenerative disorder, after Alzheimer's disease (AD), albeit the familial inherited forms are considered rare (Matilla-Dueñas et al., 2017). PD was first described by James Parkinson in his "Essay on the shaking palsy" in 1817 (J. Parkinson, 1817). The clinical manifestations of this neurodegenerative disease include resting tremor, muscular rigidity, bradykinesia (slowness of movement), and postural instability (Jankovic, 2008), which are caused by the death of dopaminergic neurons in specific brain regions, particularly the substantia nigra. The rare familial PD is often caused by variants in a specific gene, while sporadic PD is linked to variants of genes that may influence the risk of developing the disease (Tang et al., 2017).
A relatively specific pathological feature of neuronal degeneration in PD is an intracellular inclusion body, known as the Lewy body, which is found in cells of affected brain regions. Lewy bodies contain the protein α-synuclein (αSyn), which forms filaments that trap organelles such as mitochondria and lysosomes (Duffy and Tennyson, 1965). Variants in the *SNCA* gene, which codes for αSyn, were the first genetic defects identified as causing PD (Polymeropoulos et al., 1997). Both rare and common genetic variants of *SNCA* contribute to disease risk, onset, and progression (Blauwendraat, Nalls, and Singleton, 2020). In addition to these rare variants of *SNCA*, duplications and triplications of the entire gene have been reported (Ikeuchi et al., 2008; Konno et al., 2016). Both pathological variants in *SNCA* and overexpression of αSyn are sufficient to enhance the formation of insoluble αSyn fibrils and promote the degeneration of dopaminergic neurons (Tofaris, 2022).
Other rare genes associated with PD are *PINK1* (*PTEN Induced Kinase 1*), *PRKN* (*Parkin RBR E3 Ubiquitin Protein Ligase*) and *LRRK2* (*Leucine Rich Repeat Kinase 2*). *PINK1* encodes a kinase that senses mitochondrial damage and recruits Parkin, an E3 ubiquitin ligase encoded by the *PRKN* gene, to the outer mitochondrial membrane, initiating mitophagy by tagging dysfunctional mitochondria for degradation. Variants in *PINK1* or *PRKN* can lead to the accumulation of damaged mitochondria, which may contribute to the progression of PD by impairing neuronal function (Quinn et al., 2020). *LRRK2* encodes a large multidomain protein that contains a leucine-rich repeat (LRR) domain and a kinase domain (Taymans et al., 2023). Biochemical analysis revealed that many PD-associated variants led to an increase in LRRK2 autophosphorylation activity (West et al., 2005). Hyperactivation of LRRK2 disrupts vesicular trafficking and inhibits autophagy, while increasing sensitivity to oxidative stress and αSyn toxicity (Coukos and Krainc, 2024).
The treatment options for PD are continually evolving, with new therapeutic approaches emerging (Alotaibi, Alfayez, and Alkhudhair, 2024). Targeting dopamine deficiency as the key hallmark of the disease, by application of levodopa or dopamine receptor agonists, remains the most common treatment option (Goldenberg, 2008). There are also surgical approaches approved for PD, including ablative surgery (destroys the tissues in the brain that cause, e.g., tremors) and deep brain stimulation (electric stimulation of brain areas

that cause tremors and slowness) (Sharma, Patel, and Miocinovic, 2020). Recently, cell therapy, primarily neural transplantation, has emerged as another surgical approach. Bemdaneprocel (NCT06944522) is the most clinically advanced investigational cell therapy, where human embryonic stem cell-derived dopaminergic neuron precursors are implanted into the brain of a person with PD, and showed promising results in a phase I study, demonstrating safety and graft survival (Tabar et al., 2025).

1.3 Rare diseases

A rare disease is a condition that affects a relatively small number of individuals. However, the cumulative impact of rare diseases creates a significant global health challenge. Around 7,000 unique rare diseases have been identified, with an estimated 46-263 million people worldwide living with at least one such condition at any given time (Nguengang Wakap et al., 2020). This number continues to grow, mainly due to technological advances that allow for earlier and more accurate diagnoses (Chaudhary and Kumar, 2025). Definitions of what qualifies as a rare disease differ across regions. In the United States, the 1983 Orphan Drug Act defines a rare disease as one affecting fewer than 200,000 people, while the European Union considers a disease rare if it impacts fewer than 1 in 2,000 individuals (Richter et al., 2015). Although there is no worldwide agreement on the definition of "rare," an average global prevalence of about 1 in 2,500 people has been found (Ferreira, 2019). The development of treatments for rare diseases has historically faced obstacles due to their limited market potential compared to drugs for more common conditions (The Lancet Global Health, 2024). The U.S. Orphan Drug Act of 1983 paved the way for the approval of hundreds of so-called orphan drugs in the United States, and similar legislation in the European Union in 1999 aimed to promote innovation in rare disease therapies (Saltonstall, Ross, and Kim, 2024). Nearly half of rare diseases are neurological, and 90% of rare childhood disorders have major neurological impacts (The Lancet Neurology, 2022), including neurological regression, seizures, and ataxia, as seen in Rett syndrome (Gold et al., 2024), lysosomal storage disorders such as Batten disease (Ziółkowska et al., 2025), Multiple sulfatase deficiency (Schlotawa et al., 2019), and Leigh syndrome (Baertling et al., 2014), emphasizing the need to develop new treatments targeting the nervous system.

Unlike many common neurological disorders, where environmental factors contribute to disease onset, rare neurological disorders are mainly caused by genetic variants (Miyoshi et al., 2010). These conditions often show both neurological and psychiatric signs, such as changes in neuronal and synaptic architecture, disruptions in the balance between excitatory and inhibitory neuronal activity, and abnormalities in calcium regulation (Peall, Owen, and Hall, 2024). Rare neurological disorders display a wide variety of signs and symptoms, making diagnosis difficult. Especially, conditions with infantile or early

childhood onset have overlapping symptoms, like muscular hypotonia or developmental delay, which can lead to late diagnosis (Flotte and Gessler, 2022).
This work focuses mainly on three different rare neurological diseases: Multiple sulfatase deficiency, Leigh syndrome, and PD with triplication of the *SNCA* gene.

1.3.1 Multiple sulfatase deficiency

Multiple sulfatase deficiency (MSD) is a rare lysosomal storage disorder with an estimated prevalence of 1 in 1.4 million individuals. MSD was first identified in 1965 as a distinct form of metachromatic leukodystrophy, a disorder caused by variants in the *ARSA* gene encoding Arylsulfatase A (Austin, Armstrong, and Shearer, 1965). Unlike metachromatic leukodystrophy, MSD affects all sulfatases and results from variants in the *SUMF1* (*sulfatase-modifying factor 1*) gene. Two research groups independently identified *SUMF1* variants as the cause of MSD in 2003 (Cosma et al., 2003; Dierks et al., 2003). *SUMF1* encodes the formylglycine-generating enzyme (FGE), which is localized in the endoplasmic reticulum (ER). FGE plays a critical role in the post-translational activation of all 17 human sulfatases. These enzymes are highly conserved across eukaryotic and prokaryotic species, underscoring their essential function (Hanson, Best, and Wong, 2004). Sulfatases remove sulfate groups from a substrate, such as sulfolipids, glycosaminoglycans, and steroid hormones, each with high substrate specificity (Mashima and Nakanishi, 2022). Sulfatases contain a unique aldehyde residue in their active site(s), formylglycine (FGly), which FGE installs post-translationally by oxidizing a cysteine to Cα-formylglycine (Appel et al., 2019). Variants in the *SUMF1* gene decrease FGE activity, either through catalytic inactivity or protein instability (Dierks et al., 2005; Schlotawa et al., 2011). This impairs the post-translational activation of all 17 human sulfatases. Most sulfatases are located in the lysosome, so their dysfunction leads to lysosomal accumulation of glycosaminoglycans and sulfatides. Others are found in the ER, Golgi apparatus, or on the cell surface (Schlotawa, Adang, et al., 2020).
Clinical manifestations of MSD are multisystemic and highly variable, but common symptoms include neurological decline, cardiac involvement, hearing impairment, and airway obstruction (Schlotawa et al., 2019). Typically, patients experience normal early development, followed by a progressive decline in cognitive and motor functions. Disease severity is classified into neonatal, late infantile, and juvenile subtypes, based on disease onset and progression (Eto et al., 1987). The average life expectancy for MSD patients is about 13 years (Schlotawa, Preiskorn, et al., 2020). Currently, there is no cure for MSD, and only symptomatic treatments are available.

1.3.2 Leigh syndrome

Leigh syndrome (LS) is a severe and rare genetic neurological disease with an estimated incidence of 1 in 32,000 (Darin et al., 2001). It was first described by Denis Archibald Leigh in 1951 as subacute necrotizing encephalomyelopathy, characterized by degeneration of the central nervous system (CNS), including the thalamus, brainstem, and posterior columns of the spinal cord (Leigh, 1951). The symptoms of LS typically appear in infancy or early childhood, often following a metabolic crisis. However, cases with late onset have also been reported (Poole et al., 2019). LS is clinically and genetically heterogeneous, resulting in a wide range of phenotypes, including loss of motor skills, appetite issues, vomiting, seizures, as well as general weakness, decreased muscle tone, and lactic acidosis, which can lead to dysfunction in the heart, liver, gastrointestinal tract, and kidneys (Hong et al., 2020; Magro, Laterza, and Tosto, 2025). Due to this diversity and variability in symptom presentation, LS is classified as a syndrome. The underlying causes of LS are defects in mitochondrial energy production, arising from deficiencies in enzymes of the mitochondrial respiratory chain (Rahman et al., 1996). LS was first associated with mitochondrial dysfunction in 1965, when lactic acidosis was observed in two patients with progressive ataxia, mental decline, and degenerative changes of the CNS (Worsley et al., 1965). In 1989, cytochrome c oxidase (COX) deficiency was identified as one cause of LS (DiMauro et al., 1987). To date, more than 100 genes have been identified as causative for the LS spectrum (McCormick et al., 2023). All genes associated with LS encode proteins that are part of the mitochondrial oxidative phosphorylation system (OXPHOS), which also classifies LS as a mitochondrial disease (Holt et al., 1990; Magro et al., 2025). The pathogenic gene variants can be located on either nuclear DNA (nDNA) or mitochondrial DNA (mtDNA). Notably, mitochondria are inherited exclusively from the mother, not following Mendelian patterns of inheritance. LS caused by variants in mtDNA is therefore also known as maternally inherited LS (MILS) (Ciafaloni et al., 1993). The loss of mitochondrial protein function leads to decreased energy production, which in turn causes various symptoms, including psychomotor regression and acute metabolic crises.

To date, there is no cure for LS patients, and therapy mainly focuses on alleviating symptoms. Currently available treatments include supplements such as coenzyme Q10, vitamins (e.g., riboflavin and biotin), pyruvate, dichloroacetate, and a ketogenic diet (Magro et al., 2025). Ketogenic diets are thought to increase fatty acid β-oxidation, providing an alternative source of acetyl-CoA for energy production when oxidative phosphorylation is compromised (Banka et al., 2014). Supplements primarily work through their antioxidant properties to scavenge ROS, thereby preventing cellular death (Kozlov, Javadov, and Sommer, 2024).

Despite the use of supplements in clinical intervention, promising therapeutic approaches are currently in preclinical development. One such approach is gene therapy using adeno-associated virus (AAV) vectors, which enable targeted delivery of functional copies of

nuclear-encoded mitochondrial genes to improve mitochondrial function in patients' cells. AAVs are nonpathogenic, can transduce both dividing and nondividing cells, and have the capacity of their capsids to undergo modifications at the residue level. These modifications enable precise tuning of cellular tropism, transduction efficiency, and immunological characteristics of the vector (Li and Samulski, 2020). Currently, AAV9 is the most widely used vector in gene therapy clinical trials targeting the CNS because of its ability to cross the BBB (Foust et al., 2009; Kuzmin et al., 2021). However, systemic administration (intravenously or intrathecally) for CNS targeting often lacks specificity and efficiency, resulting in significant transduction of off-target tissues and increasing the risk of toxicity (Hinderer et al., 2018; Mullard, 2021). Studies on AAV-based interventions have shown promise in murine preclinical models, especially in addressing defects related to complex I deficiencies, the most common cause of LS (Reynaud-Dulaurier et al., 2020). However, AAV-based gene therapy is only applicable for variants on nDNA, and obstacles remain in crossing the BBB and maintaining long-term expression (Hanaford, Cho, and Nakai, 2022).

One strategy for preventing MILS is spindle nuclear transfer (SNT), where the mother's nucleus is transferred into a donor egg with healthy mitochondria (Zhang et al., 2017). Nonetheless, ethical issues, limited long-term safety data, and legal restrictions limit its use.

The challenges associated with currently available or preclinical therapies highlight the need for a safe, effective, and broad-use therapy. Small molecules are a compound class with low molecular weight, able to modulate biochemical processes, often with good tissue permeability properties, flexible administration, and a broad target range (Southey and Brunavs, 2023). The identification of an approved small molecule drug that can be repurposed for LS could thereby accelerate clinical translation and offer therapeutic options to LS patients.

1.4 Mitochondria

The underlying cause of LS is a loss of energy caused by defective mitochondria. Mitochondria are double-membrane organelles commonly known as the "powerhouses" of the cell. They are found in nearly all eukaryotic cells and contain circular genomes (Borst, 1977) consisting of 16,569 base pairs (Anderson et al., 1981). These genomes encode 13 genes as well as their own tRNAs and rRNAs, in order to allow mitochondria to produce some of their own proteins independently (Moura, Oliveira, and Urbano, 2025). In 1967, it was proposed that mitochondria originated from endosymbiotic bacteria (Sagan, 1967), a theory later supported by phylogenetic studies (Bonen et al., 1977; Schwartz and Dayhoff, 1978). Their main function is to convert energy from fuel molecules into adenosine triphosphate (ATP) through aerobic respiration. Most ATP is produced via OXPHOS, the

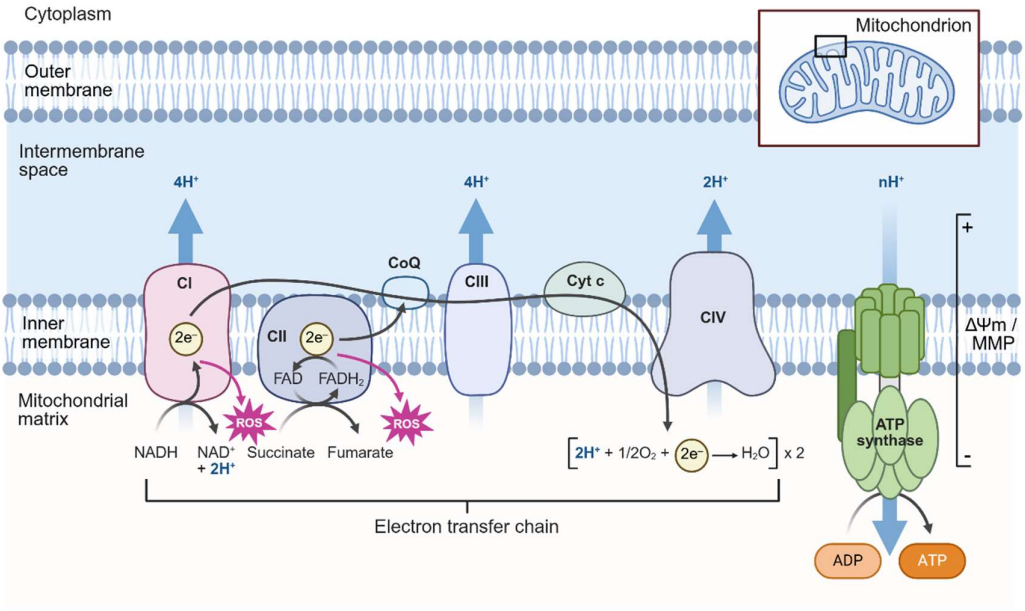
final stage of aerobic respiration. The number of mitochondria varies among cell types, ranging from two in oocytes to around 2 million in neuronal cells (Moura, Oliveira, and Urbano, 2025). The number of mtDNA copies generally depends on the energy demands of a cell (Nissanka and Moraes, 2020). Energy-demanding cells, such as neurons and cardiomyocytes, tend to have higher mtDNA copy numbers, while less active cells usually have fewer copies (Brunetti et al., 2021).

An essential characteristic of mitochondria is their ability to change shape through continuous cycles of membrane fission (division) and fusion, which support mitochondrial function and allow adaptations to metabolic changes or cellular stress (Tábara, Segawa, and Prudent, 2025). Mitochondrial dynamics are primarily regulated by four large GTPases, enzymes that bind to the nucleotide guanosine triphosphate (GTP): Dynamin-related protein 1 (DRP1) controls mitochondrial division, while mitofusins 1 and 2 (MFN1 and MFN2) and optic atrophy 1 (OPA1) mediate fusion, respectively (Tábara et al., 2025). An imbalance in mitochondrial dynamics can impair mitochondrial function, disrupt cellular processes, and contribute to various diseases, including neurodegenerative disorders, metabolic diseases, cardiovascular diseases, and cancers (Chen, Zhao, and Li, 2023). Besides the dynamic morphology of mitochondria, cells can specifically remove defective or surplus mitochondria through autophagy, also known as “mitophagy" (Scott and Klionsky, 1998; Youle and Narendra, 2011). Usually, mitophagy is initiated by oxidative stress and serves as a cellular defense system to eliminate damaged mitochondria that generate high levels of reactive oxygen species (ROS) (Schofield and Schafer, 2021). As an important quality control process, mitophagy is essential for maintaining the proper quantity and normal function of mitochondria (Pickles, Vigié, and Youle, 2018). It also promotes cells survival by removing damaged mitochondria since the release of cytochrome c into the cytosol during mitochondrial damage is linked to the initiation of programmed cell death via apoptosis (Cai, Yang, and Jones, 1998).

1.4.1 Oxidative phosphorylation

Mitochondria produce ATP through a distinctive process called OXPHOS. The OXPHOS system consists of five protein complexes located in the inner mitochondrial membrane: complex I (NADH dehydrogenase), complex II (succinate dehydrogenase), complex III (cytochrome bc1 oxidoreductase), complex IV (cytochrome c oxidase), and complex V (ATP synthase). It also includes two mobile electron carriers: ubiquinone and soluble cytochrome c (Kadenbach, 2012). Complexes I through IV form the electron transport chain (ETC), which uses electrons from reduced nicotinamide adenine dinucleotide (NADH) and succinate from the Krebs cycle to generate a proton gradient (ΔpH) across the inner mitochondrial membrane (Lehninger, 1961). This creates an electrical potential difference across the membrane due to charge separation, making the matrix negative relative to the intermembrane space. This electrical gradient is also called the mitochondrial membrane

potential (ΔΨ or MMP) (Bagkos, Koufopoulos, and Piperi, 2014; Zorova et al., 2018). Complexes I, III, and IV pump protons into the intermembrane space, while complex II transfers electrons to ubiquinone without pumping protons. In the final step of OXPHOS, complex V synthesizes ATP from adenosine diphosphate (ADP) using the energy of the proton gradient (Mitchell, 1961; Vercellino and Sazanov, 2022). The ETC consists of 92 structural proteins that form the four enzyme complexes and complex V of OXPHOS (Koopman et al., 2012). Most of these proteins are encoded by nDNA, but 13 subunits are encoded by mtDNA: NADH dehydrogenase subunits (MT-ND1-ND6 and ND4L), cytochrome b (MT-CYB), cytochrome c oxidase subunits (COX1-3), and ATP synthase subunits (ATP8 and ATP6) (Larsson and Clayton, 1995). Besides energy production, mitochondria create ROS, maintain calcium balance, and mediate apoptotic cell death (Roger, Muñoz-Gómez, and Kamikawa, 2017). ROS are produced when electrons leak from complexes I and III, causing oxidative stress in cells (Murphy, 2009; Dröse and Brandt, 2012). ROS and calcium are essential second messengers involved in cellular signaling. However, excessive ROS production that surpasses the cell's antioxidant defenses can damage macromolecules (Kozlov et al., 2024).



	Complex I	Complex II	Complex III	Complex IV	Complex V
mtDNA-encoded subunits genes	*MT-ND1, MT-ND2, MT-ND3, MT-ND4, MT-ND4L, MT-ND5, MT-ND6*		*MT-CYB*	*MT-COX1, MT-COX2, MT-COX3*	*MT-ATP6, MT-ATP8*
nDNA-encoded subunits genes	*NDUFS1, NDUFS2, NDUFS3, NDUFS4, NDUFS5, NDUFS6, NDUFS7, NDUFS8, NDUFA3, NDUFA5, NDUFA6, NDUFA7, NDUFA8, NDUFA9, NDUFA10, NDUFA11, NDUFA12, NDUFA13, NDUFAB1, NDUFV1, NDUFV2, NDUFV3, NDUFB1, NDUFB2, NDUFB3, NDUFB4, NDUFB5, NDUFB6, NDUFB7, NDUFB8, NDUFB9, NDUFB10, NDUFB11, NDUFC1, NDUFC2*	*SDHA, SDHB, SDHC, SDHD*	*UQCRB, UQCRC1, CYC1, UQCRC2, UQCRFS1, UQCRH, UQCRQ, UQCR10, UQCR11*	*COX4, COX5A, COX5B, COX6A, COX6B, COX6C, COX7A, COX7B, COX7C, COX8*	*ATP5A1, ATP5B, ATP5C1, ATP5D, ATP5E, ATP5F1, ATP5G1, ATP5G2, ATP5G3, ATP5H, ATPI, ATP5O, ATP5J, ATP5J2, ATP5L, ATP5L2*
nDNA-encoded assembly factor genes	*NDUFAF1, NDUFAF2, NDUFAF3, NDUFAF4, NDUFAF5, NDUFAF6, NDUFAF7, TIMMDC1,ESCIT, NUBPL,C8orf38, C20orf7, ACAD9, FOXRED1*	*SDHAF1, SDHAF2, SDHAF3, SDHAF4*	*BCS1L, LYRM7, UQCC1, UQCC2, UQCC3, TTC19, PTCD2*	*COA1, COA3, COA4, COA5, COA6, COA7, COX10,COX11, COX14, COX15, COX16, COX17, COX18, COX19, COX20, PET117, PET100, CEP89, OXA1L, APOPT1, NDUFA4 FASTKD2, LRPPRC, SCO1, SCO2, SURF1, TACO1*	*ATPAF1, ATPAF2, TMEM70*

Figure 1: Scheme of the OXPHOS system. Complexes I-V (CI-IV) transfer electrons (e^-), generated by reduced nicotinamide adenine dinucleotide (NADH) and succinate, through the respiratory chain, facilitated by the reduction of the cofactors coenzyme Q10 (CoQ) and cytochrome c (Cyt c). Electron transfer is linked to the transfer of protons (H^+) across the inner mitochondrial membrane. This process generates a proton motive force, along with an electrical gradient known as the mitochondrial membrane potential (MMP or ΔΨ), which is utilized by ATP synthase to produce ATP. Characterization of OXPHOS complexes has identified the constitutive subunits that are either mtDNA-encoded or nuclear-encoded. Many of the nuclear-encoded proteins are involved in complex assembly, biogenesis, or ancillary functions (Alston et al., 2017). Created with BioRender.com.

1.4.2 Mitochondria in neurodegenerative diseases

The oxidative imbalance, along with mitochondrial dysfunction, plays a major role in neurodegenerative diseases like LS and PD (Farooqui and Farooqui, 2016). Since each mitochondrion contains its own genome with varying copy numbers, wildtype and mtDNA with genetic variants can coexist within a cell (Taylor, 2001). This means patients with mtDNA variants may display different symptoms depending on the inherited pathogenic mitochondrial load. This phenomenon, called heteroplasmy, also contributes to the complexity and diversity of phenotypes seen in MILS. It has been reported that a phenotypic threshold, defined by the percentage of mtDNA with variants, must be exceeded to cause decreased OXPHOS function and disease manifestation within an organ system (Rossignol et al., 2003). This threshold can vary depending on the genetic variant, cell type, and tissue, and can range from 60% to 90% mutant mtDNA for a phenotype to appear (Holt et al., 1990). For example, low mutant loads (between 50-60%) can lead to NARP (neuropathy, ataxia, and retinitis pigmentosa), while higher mutant loads (>90%) typically produce the full LS phenotype (Bakare, Lesnefsky, and Iyer, 2021). Mitochondrial heteroplasmy can also vary over time due to replicative segregation, causing changes in the amount of mtDNA variants among cells, tissues, or generations. This variation can influence the variability in penetrance and the age at which symptoms appear (Wallace and Chalkia, 2013). In neurodegenerative disorders, common features include mitochondrial dysfunction and oxidative stress (Norat et al., 2020). In PD, alterations in mitochondrial structure and dynamics, caused by variants in genes such as *PARKIN*, *PINK1*, and *DJ1*, are linked to increased ROS production, abnormal intracellular calcium levels, and decreased mitochondrial ATP production (Nicoletti et al., 2021). Mitochondria with a deficit of Parkin showed reduced activity of complexes I and IV of the respiratory chain, higher levels of ROS, and greater vulnerability to complex I inhibitors (Whitworth et al., 2005). Pathogenic variants in mtDNA have also been linked to PD (Sena-dos-Santos et al., 2024) and AD (Hutchin and Cortopassi, 1995), making mitochondria an intriguing focus for studying neurological diseases in general.

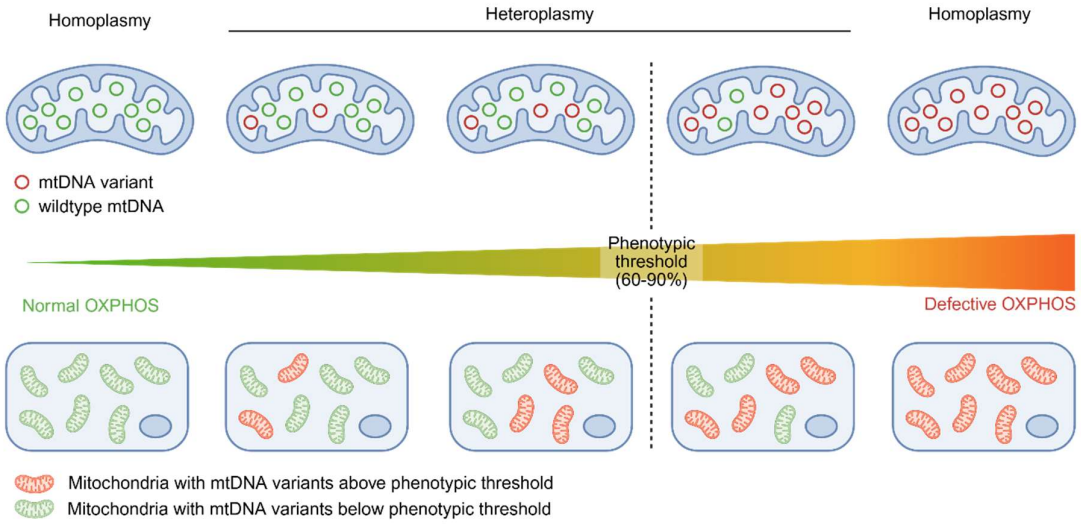


Figure 2: Schematic representation of the mitochondrial phenotypic threshold. Healthy (functional) mitochondria and mitochondrial DNA (mtDNA) are illustrated in green, while dysfunctional mitochondria and mtDNA with pathogenic variants are shown in red. When a population of mtDNA variants is below a cell-specific phenotypic threshold, it ensures normal overall OXPHOS activity and, therefore, an asymptomatic status. Conversely, when the population of diseased mitochondria exceeds the phenotypic threshold tolerated by a cell within an organ system, it results in defective OXPHOS, giving rise to a symptomatic status (Li et al., 2021; Mutti, Silva-Pinheiro, and Minczuk, 2022). Created with BioRender.com.

1.5 Research models for neurological diseases

Enhancing clinical success in drug discovery begins with selecting and establishing the right disease model. Modeling neurological diseases involves many challenges due to the complexity and heterogeneity of human pathophysiology. There is an essential need for physiological disease models for neurological conditions to enhance understanding of disease onset and progression and, notably, to support drug development through compound testing. *Saccharomyces cerevisiae* (yeast) has long been recognized as a relevant and powerful model to study human diseases. In 1996, after the yeast genome had been completed sequenced, 30-40% of the known human disease-associated genes were shown to share significant sequence identity with yeast genes (Bassett, Boguski, and Hieter, 1996). Furthermore, gene editing utilizing CRISPR/Cas9 represents a relatively straightforward methodology in yeast (Akhmetov et al., 2018; Kapoor, Choudhary, and Kasana, 2025), and the replacement of yeast genes with their human orthologs enables functional genetic analysis (Kachroo et al., 2015). Additionally, yeast is an advantageous model to investigate mitochondrial diseases because its high fermentation capacity enables its survival in the presence of variants impairing oxidative phosphorylation (Lasserre et al., 2015). This remarkable property among eukaryotes has considerably eased the identification and understanding of the primary effects of many pathogenic variants

responsible for human mitochondrial diseases, for example, in LS (Kucharczyk et al., 2013; Schwimmer et al., 2006). Small non-mammalian animals such as *Drosophila melanogaster* (fruit fly) or *Danio rerio* (zebrafish) are valuable models for studying neurological diseases. Fruit flies have been successfully used to study diseases like LS, Huntington's disease (HD), PD, and AD (Bolus et al., 2020). Notably, the importance of mitochondria to PD was discovered in flies (Clark et al., 2006; Park et al., 2006). Despite their advantages of a fast life cycle and a large number of offspring, fruit flies are accessible to genetic engineering to create a variety of mutants (Jeibmann and Paulus, 2009); (Venken, Simpson, and Bellen, 2011). Zebrafish offer unique capabilities for modeling neurological diseases, with irreplaceable features, such as transparency during embryonic development, easy breeding, high genetic similarity to humans, and straightforward gene manipulation (Liu et al., 2023), which make them a valuable research tool (Meng et al., 2025). Zebrafish has contributed to research aiming to understand the pathogenesis of neurodegenerative diseases such as PD, AD, HD and Amyotrophic lateral sclerosis (ALS) (Chia et al., 2022).

Mice are genetically even closer to humans and have therefore been used extensively to study human diseases. There are various mouse models for different neurological diseases, such as AD (Onos et al., 2016) and PD (Blesa et al., 2012), which recapitulate the essential features of each disease. For LS, the most widely used model is the *Ndufs4* knockout (KO) mouse (Van De Wal et al., 2025), first developed in 2008 (Kruse et al., 2008). Mouse models significantly advanced our understanding of the molecular basis of disease progression. However, their translational impact remains limited, as human neurodegenerative diseases exhibit substantial heterogeneity across both pathological and clinical dimensions (Chesselet and Carmichael, 2012). For example, some genetically engineered mice with LS-causing variants led to aberrant phenotypes compared to patients, such as increased longevity (Dell'Agnello et al., 2007).

Cytoplasmic hybrids (cybrids) are created by fusing mitochondria-deficient cell lines with cell lines that contain mitochondria, by inactivating mtDNA with replication inhibitors, such as DNA intercalating dye ethidium bromide (3,8-diamino-5-ethyl-6-phenyl phenanthridinium bromide) (Sazonova et al., 2018). Since the nuclear background of different cybrid lines can be kept constant, this technique allows investigators to study the influence of mtDNA on cell function (Wilkins, Carl, and Swerdlow, 2014). Cybrids are used as cellular models for studying mitochondrial dysfunction and its association with a variety of human diseases, such as AD (Trimmer et al., 2004), sporadic PD (Trimmer and Bennett, 2009) and LS (D'Aurelio et al., 2010; Trounce, Neill, and Wallace, 1994).

Primary fibroblasts are easily obtained from a minimally invasive skin biopsy. However, these cells are subject to telomere-controlled senescence, which limits the number of passages as telomeres shorten with each cell division (Harley, Futcher, and Greider, 1990). The large T antigen of simian virus 40 (SV40) is a protein that inhibits the p53 and retinoblastoma family of tumor suppressors (Ahuja, Sáenz-Robles, and Pipas, 2005), thereby promoting cell proliferation (Engeland, 2022). When the SV40 large T gene is introduced

into the primary cell via a viral vector, its expression results in escape from replicative senescence and the immortalization of the culture of infected cells (Madelaire et al., 2022). This enables the study of diseases in a cellular model by preserving the disease-causing variants, e.g., for MSD (Cosma et al., 2003).

In 2006, the development of induced pluripotent stem cells (iPSC) technology by Shinya Yamanaka and Kazutoshi Takahashi opened new possibilities for disease modeling by using mouse fibroblasts (Takahashi and Yamanaka, 2006). A year later, they also demonstrated the generalizability of this approach by reprogramming human fibroblasts into indefinitely propagating, pluripotent stem cells using four transcription factors (OCT4, SOX2, CMYC, and KLF4) (Takahashi et al., 2007). These cells can then be differentiated into any cell type of interest while retaining their specific genetic background, for both nDNA and mtDNA (Lorenz et al., 2017). This enables the study of human cells, such as cardiomyocytes (Zhang et al., 2009), neuronal precursor cells (NPCs) and neurons (Chambers et al., 2009), and even co-culture systems that include neurons, microglia, and astrocytes (Abud et al., 2017; Ryan, Jordan-Sciutto, and Anderson 2020), where access is otherwise very limited. Recently, the complexity of iPSC-derived disease models has increased, and protocols have been established for various tissues where differentiated cells self-organize into three-dimensional (3D) models (Sinha et al., 2025). These so-called “organoids” are *in vitro* tissues designed to replicate the structural, functional, and biological complexity of an organ, making them valuable for modeling human diseases, drug development, and toxicity assessments (Tang et al., 2022; Yang et al., 2023).

1.6 Drug development

Drug development involves the identification, development, and marketing of new therapeutics. It is a lengthy and costly process that typically takes 10-15 years and costs between 1-2 billion dollars (Hinkson, Madej, and Stahlberg, 2020). This process can be divided into six stages: (1) basic research, where the underlying cause of a disease is studied; (2) drug discovery, which involves the search for active compounds; (3) preclinical development, in which drug candidate’s efficacy and toxicity are validated by using various *in vitro* and *in vivo* models; (4) clinical research, including Phase I, Phase II, and Phase III studies in humans; (5) review by regulatory agencies, such as the Food and Drug Administration (FDA), European Medicines Agency (EMA), or others; and finally (6) drug approval (Singh et al., 2023). During drug discovery, different test systems can be used, including genetic, cellular, and *in vivo* experimental models, focusing on one or a few quantitative measurable readouts (Hughes et al., 2011; Zhou and Zhong, 2017).

Drug repurposing has been proposed as a strategy to accelerate therapeutics development by using already approved drugs for alternative indications, since preclinical and clinical data, including ADME-T (absorption, distribution, metabolism, excretion and

toxicity) and safety in humans, are already available. It also provides the potential to discover treatments for rare diseases, which are often neglected by pharmaceutical companies. However, the joint application process for orphan drug submissions in the United States and the European Union in 2007 (Mariz et al., 2016), along with the financial incentives provided by the Orphan Drug Act of 1983 through its Orphan Drug Designation (ODD) Program, in conjunction with significant scientific advances over the past 40 years, have resulted in the approval of hundreds of drugs for rare diseases (Fermaglich and Miller, 2023). Another important aspect of developing treatments for neurological diseases is that they must be able to cross the blood-brain barrier (BBB) in order to reach the CNS and engage with their respective targets (Rosenberg, 2012). This, along with the complexity of neurological diseases, is also one reason why treatment options for patients remain limited to date.

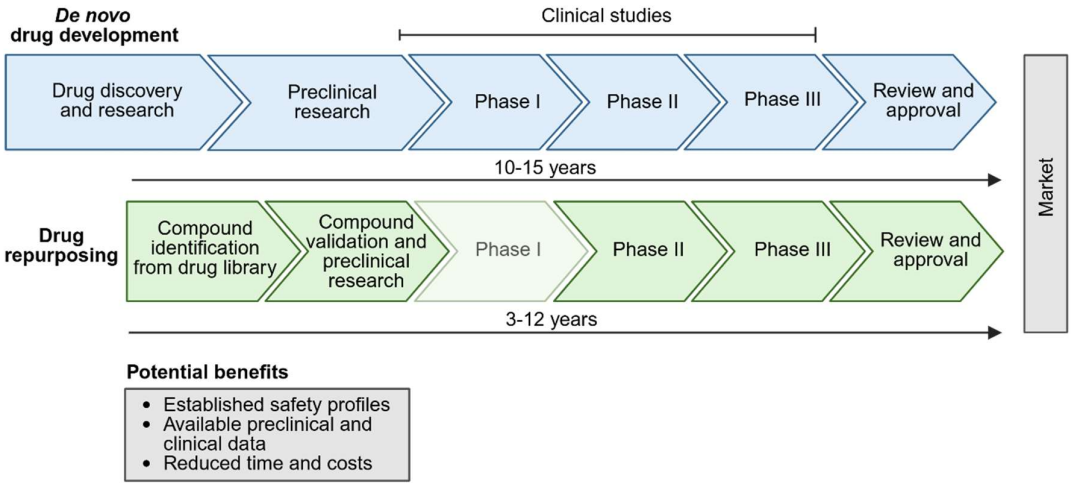


Figure 3: Schematic representation of the de novo drug development process compared to the drug repurposing approach. Drug repurposing is an alternative strategy to de novo drug development, where an already approved or investigational drug is tested for a new use outside the scope of the original medical indication (Scherman and Fetro, 2020). Since the tested drugs have already proven to be safe in preclinical models or humans, they increase success rates, lower development costs, shorten time to market, and therefore decrease overall development risk compared to traditional drug development strategies (Roessler et al., 2021). Often, the only step left towards market access is to confirm efficacy for the new indication in Phase II and Phase III clinical studies (Recino et al., 2025). Created with BioRender.com.

1.7 High-throughput screening

Drug discovery involves the identification of disease modulating agents, enabling the development of new therapeutic interventions. One entry point for drug discovery is high-throughput screening (HTS), in which thousands of compounds are tested simultaneously in a miniaturized assay using multi-well plates (Bleicher et al., 2003; Broach and Thorner, 1996). Ultimately, this method saves time and costs. The assay, which refers to the experimental test system with a measurable endpoint, needs to be scalable (Corbett and Duncan, 2019). There are various detection modalities used in screening applications, each designed to identify and measure a biological, chemical, or physical phenomenon. Commonly used modalities include absorbance, fluorescence, and luminescence (Wildey et al., 2017). Lab automation systems are often employed to increase speed, reduce pipetting errors, and enhance reproducibility (Holland and Davies, 2020). To ensure quality, the Z' factor is frequently used in HTS screens as a parameter to assess assay suitability, indicating the separation between the control distributions. It captures both the dynamic range and data variation related to signal measurements (Zhang, Chung, and Oldenburg, 1999). After establishing an HTS-compatible assay, the primary screen can be conducted, during which tested compounds are evaluated and so-called "hits" are identified when they exceed a certain threshold of the desired effect size. These hits need to be validated through a confirmatory assay, which involves retesting the hits in replicates and in secondary or orthogonal assays that differ from the primary screening assay (Broach and Thorner, 1996). This process is followed by synthesizing analogs (hit expansion) to study structure-activity relationships. Ultimately, one or a few lead compounds that show activity, selectivity, and low toxicity can be selected. These lead compounds undergo further optimization in a later stage of drug discovery called lead optimization, where rational medicinal chemistry strategies are used to improve their efficacy and safety profiles. One lead compound with verified ADME-T properties is ultimately chosen as a drug candidate for preclinical and clinical development (Bleicher et al., 2003).

Subtypes of HTS screens include high content screening (HCS), which assesses multiple parameters using an image-based approach. HCS is a multidisciplinary, multistep process used to understand how compounds affect biological processes at the cellular level (Soleilhac, Nadon, and Lafanechere, 2010). Recently, Cell Painting (CP) has emerged as an HCS method. It is a technique in which cell organelles are simultaneously stained with different fluorescent dyes, capturing thousands of morphological features such as shape, texture, size, intensity, and spatial relationships among organelles to predict the mechanism of action of a perturbing substance (Bray et al., 2016).

2. Aim and organization of the thesis

This work aimed to apply patient-derived advanced cellular models for drug discovery targeting rare neurological diseases such as LS, PD, and MSD by developing screening and analysis strategies, including automation technologies. Among these, iPSC-derived organoids were used to validate hit compounds identified from screening methods in the context of LS and brain metastasis. Specifically, screening assays were developed, miniaturized, and scaled up to enable HTS, support the characterization of hit compounds, and ultimately facilitate their development into clinically applied drugs. Eventually, the drug candidate sildenafil advanced to clinical use and was designated as an orphan medicine for treating LS. This thesis is based on seven manuscripts, of which six are published and one is in preparation. To guide the reader, each chapter begins with the author's contribution statements followed by a graphical and written summary. The subsequent sections highlight the main findings and their context in transitioning from two-dimensional (2D) to 3D screening platforms, along with their application to rare neurological diseases.

3. Results

The result section presents publications and manuscripts of the following studies:

1. Annika Zink[*], Undine Haferkamp[*], **Annika Wittich**, Mathias Beller, Ole Pless[§], and Alessandro Prigione[§]. High-content screening of mitochondrial polarization in neural cells derived from human pluripotent stem cells. *STAR Protocols* 3(3):101602 (2022). https://doi.org/10.1016/j.xpro.2022.101602

2. Annika Zink[*], Dao-Fu Dai[*], **Annika Wittich**[*], Marie-Thérèse Henke[*], Giulia Pedrotti[*], Sonja Heiduschka[*], Guillem S. Aguilar, Tancredi Massimo Pentimalli, Christian Brueser, Sofia Notopoulou, Abdul Rahim Umar, Aleksandra Zhaivoron, Laura Petersilie, Caleb Jerred, Jesper Bergmans, Lois Anton Neu, Fabian Schumacher, Jan Keller-Findeisen, Agnieszka Rybak-Wolf, Daniel Stach, Jeanette Reinshagen, Undine Haferkamp, Kim Krieg, Andrea Zaliani, Liliya Euro, Alessia Di Donfrancesco, Chiara Santanatoglia, Enrica Cappellozza, Marta Suarez Cubero, Mario Pavez-Giani, Oleh Bakumenko, David Meierhofer, Alan Foley, Susanne Morales-Gonzalez, Isabella Tolle, Diran Herebian, Daniele Bonesso, Giulia Cecchetto, Sakurako Nagumo Wong, Monica Moresco, Alessandra Maresca, Ilaria Decimo, Francesco De Sanctis, Annalisa Adamo, Merel J.W. Adjobo-Hermans, Roberto Duchi, Maria Barandalla, Marco Scaglia, Andrea Perota, Cesare Galli, Burkhard Kleuser, Lukas Cyganek, Chris Mühlhausen, Lars Schlotawa, Valeria Tiranti, Ertan Mayatepek, Ildiko Szabo, Chiara La Morgia, Thomas Klopstock, Valerio Carelli, Felix Distelmaier, Andrea Rossi, Nikolaus Rajewsky, Ghanim Ullah, Stefan Jakobs, Christine R. Rose, Spyros Petrakis, Frank Edenhofer, Werner

J.H. Koopmann, Pawel Lisowski, Anu Suomalainen, Dario Brunetti§, Antonio del Sol§, Emanuela Bottani§, Ole Pless§, Markus Schuelke§, and Alessandro Prigione§. Pluripotent stem-cell-based screening uncovers sildenafil as a mitochondrial disease therapy. *Cell* 189(6):1656-1679.e42 (2026). https://doi.org/10.1016/j.cell.2026.02.008

3. Vyron Gorgogietas*, Amélie Weiss*, Loïc Cousin, David Hoffmann, Karen Schmitt, Arnaud Ogier, Peter A. Barbuti, Bruno F.R. Santos, Ibrahim Boussaad, **Annika Wittich**, Andrea Zaliani, Ole Pless, Rejko Krüger, Peter Sommer§, and Johannes H. Wilbertz§. Morphological profiling reveals neuroprotection via mitochondrial uncoupling in human dopaminergic neurons. *Scientific Reports* 15(1):29507 (2025). https://doi.org/10.1038/s41598-025-14735-0

4. **Annika Wittich***, Kim Krieg, Philip Gribbon, Jakob Metzger, Alessandro Prigione, and Ole Pless§. Human organoids: Fit for drug discovery? *Stem Cell Reports* 21:102898 (2026). https://doi.org/10.1016/j.stemcr.2026.102898

5. Carmen Menacho*, Satoshi Okawa*, Iris Álvarez-Merz, **Annika Wittich**, Mikel Muñoz Oreja, Pawel LisowskiMario López Martín, Tancredi Massimo Pentimalli, Shiri Zakin, Mathuravani Thevandavakkam, Caleb Jerred, Selene Lickfett, Laura Petersilie, Agnieszka Rybak-Wolf, Annette Seibt, Diran Herebian, Gizem Inak, Susanne Brodesser, Andrea Zaliani, Barbara Mlody, Justin Donnelly, Kasey Woleben, Francesc Xavier Soriano, Jose C. Fernandez-Checa, Natascia Ventura, Sidney Cambridge, Ertan Mayatepek, Antonella Spinazzola, Markus Schuelke, Nikolaus Rajewsky, Andrea Rossi, Alex Peralvarez-Marin, Felix Distelmaier, Ethan Perlstein, Ian J. Holt, Emma Puighermanal, Ole Pless, Christine R. Rose, Antonio Del Sol§, and Alessandro Prigione§. Accelerating Leigh syndrome drug discovery through deep learning screening in brain organoids. *Nature Communications*, 17(1):3570 (2026). https://doi.org/10.1038/s41467-026-71391-2

6. Kim Krieg*, Silvia Materna-Reichelt, Tobias Naber, Fatima-Zahra Rachad, Pia Kauven, Arjen Weller, Undine Haferkamp, **Annika Wittich**, Andrea Zaliani, Marcel S. Woo, Mark Walkenhorst, Malte Siegmund, Jann Harberts, Robert Zierold, Robert Blick, Christian Conze, Patricia Muschong, Dominik Miltner, Manuel A. Friese, Mario Mezler, Heiko Siegmund, Katja Evert, Susanne Krasemann, Nataša Stojanović Gužvić, Christoph Klein, Melanie Werner-Klein, Joachim Wegener, and Ole Pless§. Cortical organoid-derived models of the melanoma brain metastatic niche enable prioritization of cancer-targeting drugs. *Cell Reports Methods* 5:101236 (2025). https://doi.org/10.1016/j.crmeth.2025.101236

7. **Annika Wittich**, Alisa DeGrave, Jeanette Reinshagen, Lina Schmidt, Ole Pless, and Lars Schlotawa. High-throughput drug repurposing screen identifies candidates targeting Multiple sulfatase deficiency. *In preparation*.

3.1 High-content screening of mitochondrial polarization in neural cells derived from human pluripotent stem cells

This section presents the following publication (see Appendix I):

Annika Zink*, Undine Haferkamp*, **Annika Wittich**, Mathias Beller, Ole Pless§, and Alessandro Prigione§. High-content screening of mitochondrial polarization in neural cells derived from human pluripotent stem cells. *STAR Protocols* 3(3):101602 (2022). https://doi.org/10.1016/j.xpro.2022.101602

3.1.1 Contribution

Methodology: Assay optimization and miniaturization; Investigation: contributed to Figures 1C, 1E, 2; Writing - Review and editing: Writing parts of the manuscript and reviewing the manuscript.

3.1.2 Graphical summary

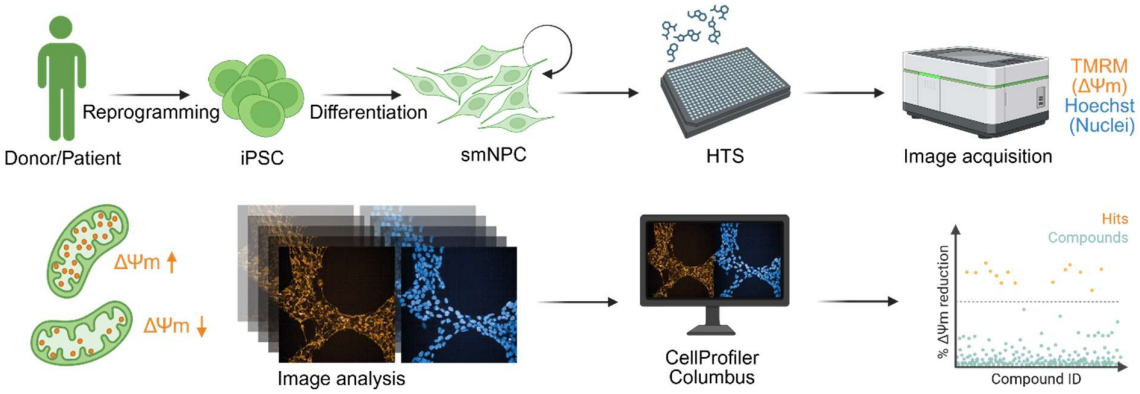


Figure 4: Graphical summary of "High-content screening of mitochondrial polarization in neural cells derived from human pluripotent stem cells", Zink, Haferkamp et al., *STAR Protocols*, 2022. iPSCs: induced pluripotent stem cells; smNPC: small molecule neuronal precursor cell; HTS: high-throughput screening; TMRM: Tetramethylrhodamine methyl ester. Created with BioRender.com.

3.1.3 Summary

HCS is an image-based variant of HTS, that aims at unravelling complex cellular phenotypes by analyzing multiple parameters of whole cells or their components. HTS and HCS both require a well-established and reproducible experimental pipeline, including data management strategies and analysis tools, that are capable of extracting meaningful results. In this section, we showcase an approach of how NPCs derived from iPSCs can be utilized for an HCS assay with a focus on mitochondria. This strategy has the potential to accelerate the drug discovery process for diseases that display a mitochondrial phenotype, e.g., LS or PD.

The published protocol "High-content screening of mitochondrial polarization in neural cells derived from human pluripotent stem cells" presents an HCS method to measure ΔΨm in human iPSC-derived NPCs using Tetramethylrhodamine methyl ester (TMRM) dye in live-cell imaging. Due to its positive charge, TMRM accumulates proportionally to the negatively charged mitochondrial matrix in mitochondria of living cells. Quantifying the fluorescent intensity of the TMRM signal thereby enables the assessment of mitochondrial polarization.

Here, we explain the culture preparation steps using NPCs, derived from human iPSCs, staining procedures, and imaging acquisition using the Operetta CLS high-throughput microscope. We developed and compared two independent data analysis workflows utilizing both open-source (CellProfiler) and proprietary (Columbus) software. Both produce similar and precise results for ΔΨm quantification. The method enables high-throughput assessment of mitochondrial (de)polarization, useful for drug screening and phenotyping of disease models, with user guidance on quality control, troubleshooting, and assay optimization. This method paper laid the groundwork for the high-throughput screen based on patient-derived NPCs from a patient with LS (see Appendix II), which aimed to identify mild uncouplers of mitochondrial membrane potential, as described in detail in the next chapter.

3.2 Pluripotent stem-cell-based screening uncovers sildenafil as a mitochondrial disease therapy

This section presents the following publication (see Appendix II):

Annika Zink*, Dao-Fu Dai*, **Annika Wittich***, Marie-Thérèse Henke*, Giulia Pedrotti*, Sonja Heiduschka*, Guillem S. Aguilar, Tancredi Massimo Pentimalli, Christian Brueser, Sofia Notopoulou, Abdul Rahim Umar, Aleksandra Zhaivoron, Laura Petersilie, Caleb Jerred, Jesper Bergmans, Lois Anton Neu, Fabian Schumacher, Jan Keller-Findeisen, Agnieszka Rybak-Wolf, Daniel Stach, Jeanette Reinshagen, Undine Haferkamp, Kim Krieg, Andrea Zaliani, Liliya Euro, Alessia Di Donfrancesco, Chiara Santanatoglia, Enrica Cappellozza, Marta Suarez Cubero, Mario Pavez-Giani, Oleh Bakumenko, David Meierhofer, Alan Foley, Susanne Morales-Gonzalez, Isabella Tolle, Diran Herebian, Daniele Bonesso, Giulia Cecchetto, Sakurako Nagumo Wong, Monica Moresco, Alessandra Maresca, Ilaria Decimo, Francesco De Sanctis, Annalisa Adamo, Merel J.W. Adjobo-Hermans, Roberto Duchi, Maria Barandalla, Marco Scaglia, Andrea Perota, Cesare Galli, Burkhard Kleuser, Lukas Cyganek, Chris Mühlhausen, Lars Schlotawa, Valeria Tiranti, Ertan Mayatepek, Ildiko Szabo, Chiara La Morgia, Thomas Klopstock, Valerio Carelli, Felix Distelmaier, Andrea Rossi, Nikolaus Rajewsky, Ghanim Ullah, Stefan Jakobs, Christine R. Rose, Spyros Petrakis, Frank Edenhofer, Werner J.H. Koopmann, Pawel Lisowski, Anu Suomalainen, Dario Brunetti§, Antonio del Sol§, Emanuela Bottani§, Ole Pless§, Markus Schuelke§, and Alessandro Prigione§. Pluripotent stem-cell-based screening uncovers sildenafil as a mitochondrial disease therapy. *Cell* 189(6):1656-1679.e42 (2026). https://doi.org/10.1016/j.cell.2026.02.008

3.2.1 Contribution

Methodology: Development and design of experiments; Investigation: Contributed to Figures 1A-D, 1J, 4K, 6A-C, S2A-I, S3A-F, S3H, S3I, S3K; Visualization: Reviewing of Figures; Writing - Review and editing: Writing methods related to mentioned Figures and reviewing of the manuscript.

3.2.2 Graphical summary

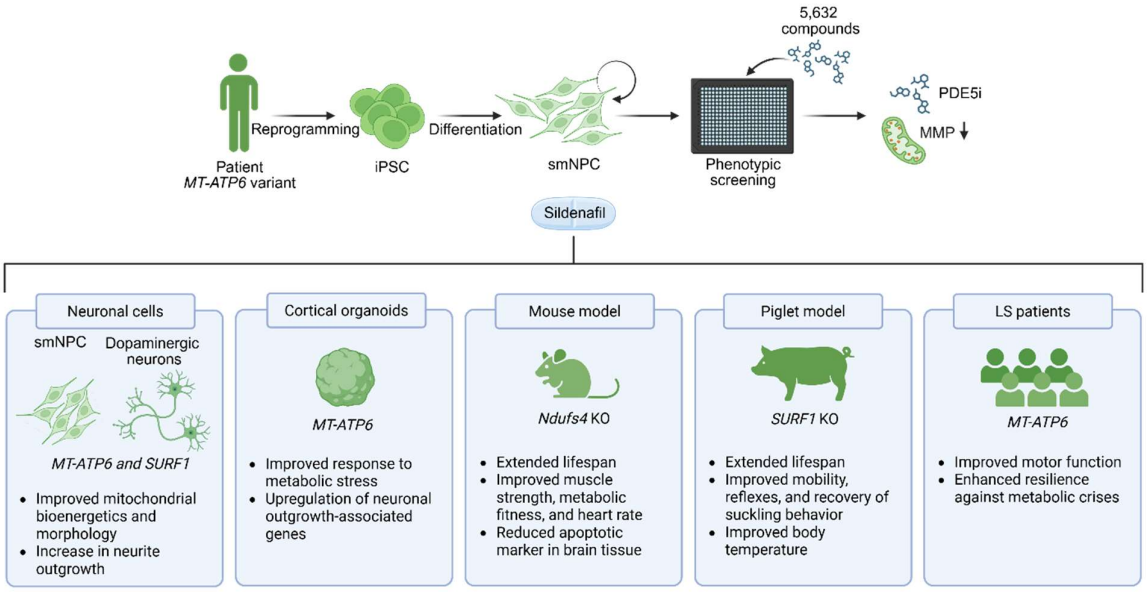


Figure 5: Graphical summary of "Pluripotent stem-cell-based screening uncovers sildenafil as a mitochondrial disease therapy", Zink, Dai, Wittich, Henke, Pedrotti, Heiduschka et al., *Cell*, 2026. iPSCs: induced pluripotent stem cells; smNPC: small molecule neuronal precursor cell; PDE5i: phosphodiesterase 5 inhibitor; MMP: mitochondrial membrane potential; LS: Leigh syndrome. Created with BioRender.com.

3.2.3 Summary

The established robust screening workflow that was introduced in chapter 3.1 enabled HTS screening of a drug repurposing collection using iPSC-derived NPCs from a LS patient. To date, there is no cure for LS and only limited symptomatic treatment options are available. The HTS approach aimed to accelerate drug discovery for LS by screening a drug repurposing collection of 5,632 well-annotated compounds. In the hit population, we identified phosphodiesterase 5 inhibitors (PDE5i) as leads capable of normalizing mitochondrial membrane potential in LS NPCs. Due to its safety profile in children and adults, we prioritized sildenafil among the PDE5i. Sildenafil was shown to restore key signaling pathways involved in nervous system development, promote neurite outgrowth in iPSC-derived LS neurons, and normalize aberrant calcium responses in iPSC-derived LS brain organoids under metabolic stress. Sildenafil extended lifespan in a mouse and pig model of LS and rescued both metabolic and neurological phenotypes. Furthermore, sildenafil demonstrated acceptable blood-brain barrier permeability, as shown in an iPSC-derived model using LS iPSCs. Notably, chronic compassionate off-label treatment with sildenafil in six LS patients was well tolerated and associated with improved motor function and increased resilience to metabolic crises. These findings underscore the promise of iPSC-based drug discovery for rare, currently untreatable disorders and support sildenafil as a potential therapeutic candidate for LS.

3.3 Morphological profiling reveals neuroprotection via mitochondrial uncoupling in human dopaminergic neurons

This section presents the following publication (see Appendix III):

Vyron Gorgogietas*, Amélie Weiss*, Loïc Cousin, David Hoffmann, Karen Schmitt, Arnaud Ogier, Peter A. Barbuti, Bruno F.R. Santos, Ibrahim Boussaad, **Annika Wittich**, Andrea Zaliani, Ole Pless, Rejko Krüger, Peter Sommer§, and Johannes H. Wilbertz§. Morphological profiling reveals neuroprotection via mitochondrial uncoupling in human dopaminergic neurons. *Scientific Reports* 15(1):29507 (2025).
https://doi.org/10.1038/s41598-025-14735-0

3.3.1 Contribution

Validation: Conducting preliminary studies to validate tyrphostin's analog effects on MMP; Resources: Providing tyrphostin analogs; Writing - Review and editing: Reviewing the manuscript draft.

3.3.2 Graphical summary

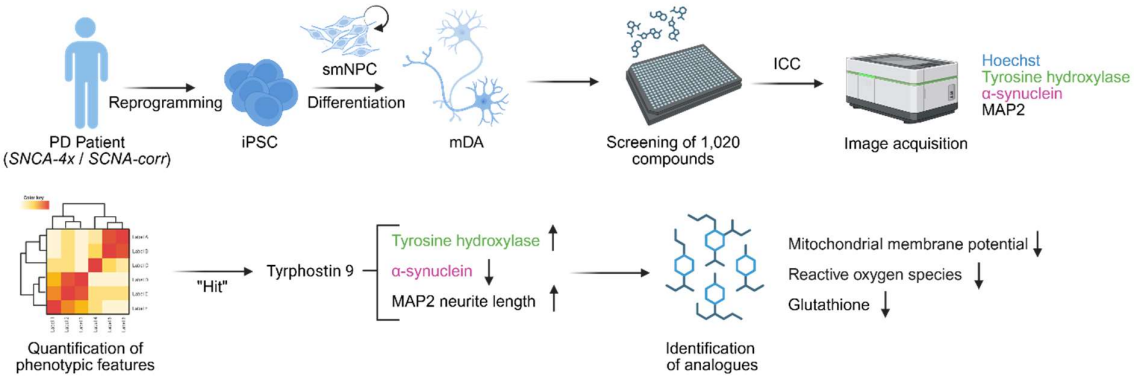


Figure 6: Graphical summary of "Morphological profiling reveals neuroprotection via mitochondrial uncoupling in human dopaminergic neurons", Gorgogietas, Weiss et al., *Scientific Reports*, 2025. PD: Parkinson disease; iPSC: induced pluripotent stem cell; smNPC: small molecule neuronal precursor cell; mDA: midbrain dopaminergic neuron; ICC: Immunocytochemistry; MAP2: Microtubule-associated protein 2. Created with BioRender.com.

3.3.3 Summary

While we searched for mild modulators of the MMP in the context of LS (see Chapter 3.2), we identified strong, non-toxic uncouplers of the mitochondrial respiratory chain in the HTS, with tyrphostin A9 and tyrphostin AG879 being the most active hits. tyrphostin A9 also emerged as a frontrunner in a phenotypic HTS assay using iPSC-derived dopaminergic neurons from a PD patient, capable of reducing the increase of ROS and αSyn protein signatures of diseased cells. Therefore, we nominated four structural analogues for further profiling and for testing the general effectiveness of tyrphostins in ameliorating PD-specific phenotypes.

PD is increasingly recognized as a complex disorder with diverse genotypic, phenotypic, and neuropathological manifestations. Grouping patients based on their genetic profiles has emerged as a critical approach, with significant progress in identifying genes associated with PD, including rare monogenic forms, such as the *SNCA* gene. These monogenic forms have been instrumental in research, as patient-derived cell models exhibit disease-specific cellular phenotypes that in part mirror those observed in patients. In this publication, patient-derived iPSCs with a triplication in the *SNCA* gene (*SNCA*-4x) and isogenic controls (*SNCA*-corr) were differentiated into midbrain dopaminergic (mDA) neurons. A library of 1,020 small molecules was screened, including FDA-approved drugs and compounds targeting PD-relevant processes. In this phenotypic approach, compounds were evaluated based on their ability to shift *SNCA*-4x profiles towards *SNCA*-corr profiles. Tyrphostin A9 was identified as a potent compound that rescued *SNCA*-4x morphological profiles in a dose-dependent manner. It also reduced αSyn levels, increased Tyrosine Hydroxylase intensity, decreased MMP and ROS levels. To establish a structure-function relationship of tyrphostin A9 in mDA neurons, structural analogues such as AG879 and AG1024 were identified and tested, demonstrating similar effects, including mitochondrial uncoupling, ROS reduction, and decreased αSyn protein levels. These findings suggest that shared structural features are critical for tyrphostins' function in the context of PD. Overall, the study demonstrates that screening small molecules in a PD-relevant human model system using a multi-phenotypical readout can lead to the identification of modulators of multiple disease-relevant phenotypes.

3.4 Human organoids: Fit for drug discovery?

This section presents the following publication (see Appendix IV):

Annika Wittich*, Kim Krieg, Philip Gribbon, Jakob Metzger, Alessandro Prigione, and Ole Pless§. Human organoids: Fit for drug discovery? *Stem Cell Reports* 21:102898 (2026). https://doi.org/10.1016/j.stemcr.2026.102898

3.4.1 Contribution

Conceptualization: Developing the concept of the review article; Visualization: Preparation of Figures; Writing - original draft: Writing the manuscript draft.

3.4.2 Graphical summary

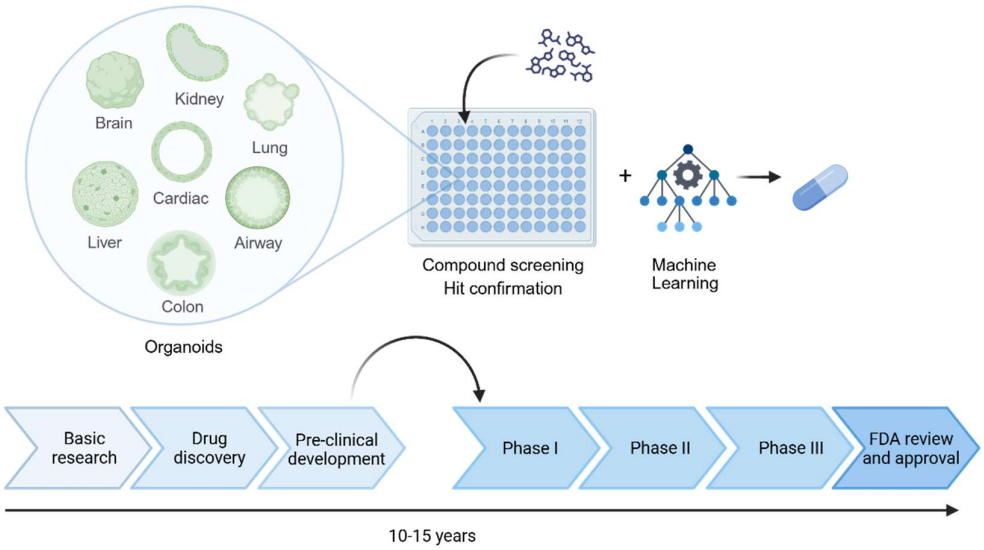


Figure 7: Graphical summary of "Human organoids: Fit for drug discovery?", Wittich et al., *Stem Cell Reports*, 2026. Created with BioRender.com.

3.4.3 Summary

Previous sections focused mainly on 2D drug screening models for neurological disorders. Recently, research has shifted toward even more physiologically relevant systems, necessitating an evaluation of current 3D screening models and key assay implementation requirements. The following review provides an overview of organoid screening technologies and outlines key considerations for integrating them into drug discovery pipelines.
Organoids are lineage-specific, self-organized 3D *in vitro* tissues that aim to recapitulate the structural, functional, and biological complexity of an organ. Derived from pluripotent stem cells (PSCs), they contain multiple cell types found in the human body and exhibit organized tissue architecture, making them valuable for human disease modeling, drug discovery, and toxicity assessments. As new approach methodologies (NAMs), organoids have the potential to reduce or replace animal models by enabling the study of cellular responses to pharmacological interventions within a human-relevant physiological context. However, questions remain about whether organoids can be reliably used in drug discovery applications. This manuscript reviews the current landscape of compound screening approaches based on PSC-derived organoids. It discusses readouts and analysis techniques, including machine-learning algorithms, and evaluates their added value for current drug discovery efforts. Challenges such as developing high-throughput assays capable of reliably capturing the models' complexity are highlighted, along with the need for standardized protocols. Establishing feasible and validated methods will ultimately allow the routine use of organoids in pharmaceutical development and help reduce attrition rates in clinical candidate discovery.

3.5 Accelerating Leigh syndrome drug discovery through deep learning screening in brain organoids

This section presents the following publication (see Appendix V):

Carmen Menacho*, Satoshi Okawa*, Iris Álvarez-Merz, **Annika Wittich**, Mikel Muñoz Oreja, Pawel LisowskiMario López Martín, Tancredi Massimo Pentimalli, Shiri Zakin, Mathuravani Thevandavakkam, Caleb Jerred, Selene Lickfett, Laura Petersilie, Agnieszka Rybak-Wolf, Annette Seibt, Diran Herebian, Gizem Inak, Susanne Brodesser, Andrea Zaliani, Barbara Mlody, Justin Donnelly, Kasey Woleben, Francesc Xavier Soriano, Jose C. Fernandez-Checa, Natascia Ventura, Sidney Cambridge, Ertan Mayatepek, Antonella Spinazzola, Markus Schuelke, Nikolaus Rajewsky, Andrea Rossi, Alex Peralvarez-Marin, Felix Distelmaier, Ethan Perlstein, Ian J. Holt, Emma Puighermanal, Ole Pless, Christine R. Rose, Antonio Del Sol§, and Alessandro Prigione§. Accelerating Leigh syndrome drug discovery through deep learning screening in brain organoids. *Nature Communications* 17(1):3570 (2026). https://doi.org/10.1038/s41467-026-71391-2

3.5.1 Contribution

Formal analysis: Analysis of immunostained midbrain organoid imaging data (related to Figures 3h, 4d); Writing - Review and editing: Revision of the manuscript draft.

3.5.2 Graphical summary

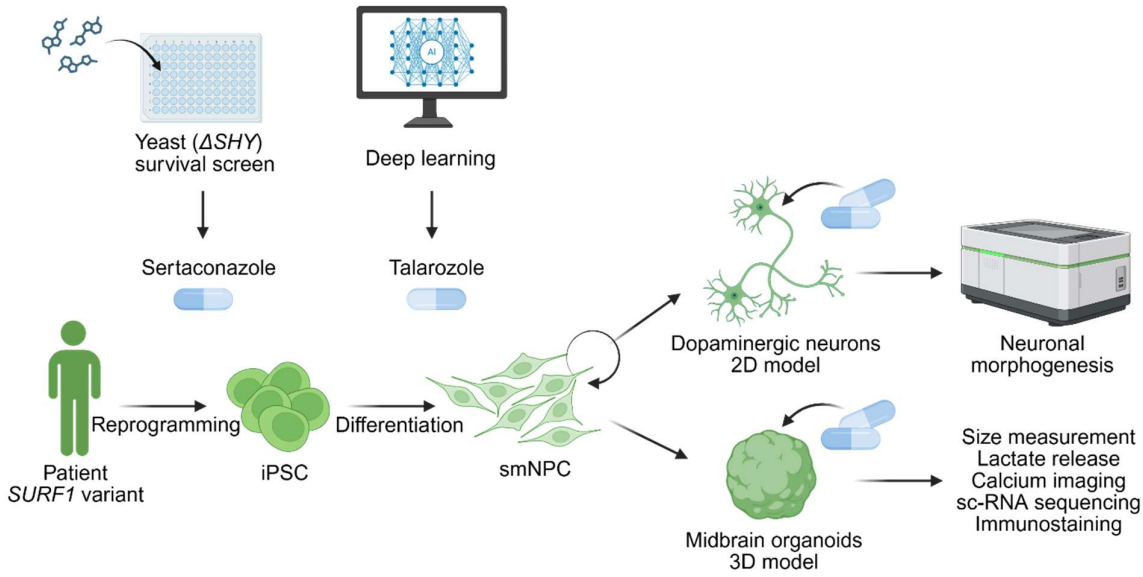


Figure 8: Graphical summary of "Accelerating Leigh syndrome drug discovery through deep learning screening in brain organoids", Menacho, Okawa et al., *Nature Communications*, 2026. iPSC: induced pluripotent stem cell; smNPC: small molecule neuronal precursor cell; sc-RNA: single cell ribonucleic acid. Created with BioRender.com.

3.5.3 Summary

This study combined experimental and computational approaches to explore neuromorphogenesis defects and mitochondrial dysfunction in 2D and 3D models of LS, which carry a mutation in the *SURF1* gene. Initially, published scRNAseq datasets of isogenic Leigh cortical organoids were analyzed to identify neuronal populations with impaired neuromorphogenesis in LS. Differentially expressed transcription factors (DETFs) across neuronal types were found and used, along with a cell type-specific drug perturbation transcriptomics database, to develop a deep learning (DL) strategy aimed at discovering drugs that can induce cellular conversion to neurons. This approach led to the identification of 34 compounds. Simultaneously, a rescue screen in Leigh yeast cultures tested a library of 2,250 repurposing drugs, revealing four azole-containing compounds as the most effective rescuers. Altogether, nine compounds (five from DL screen and four from the yeast screen) were selected given their safety profile in humans and validated in a 2D neuronal LS model. Talarozole and sertaconazole increased neuronal numbers and neurite length. The two azoles were then additionally validated in 3D LS midbrain organoids, where talarozole promoted dopaminergic neuron development and restored neurite organization and lactate levels.

3.6 Cortical organoid-derived models of the melanoma brain metastatic niche enable prioritization of cancer-targeting drugs

This section presents the following publication (see Appendix VI):

Kim Krieg*, Silvia Materna-Reichelt, Tobias Naber, Fatima-Zahra Rachad, Pia Kauven, Arjen Weller, Undine Haferkamp, **Annika Wittich**, Andrea Zaliani, Marcel S. Woo, Mark Walkenhorst, Malte Siegmund, Jann Harberts, Robert Zierold, Robert Blick, Christian Conze, Patricia Muschong, Dominik Miltner, Manuel A. Friese, Mario Mezler, Heiko Siegmund, Katja Evert, Susanne Krasemann, Nataša Stojanović Gužvić, Christoph Klein, Melanie Werner-Klein, Joachim Wegener, and Ole Pless§. Cortical organoid-derived models of the melanoma brain metastatic niche enable prioritization of cancer-targeting drugs. *Cell Reports Methods* 5:101236 (2025).
https://doi.org/10.1016/j.crmeth.2025.101236

3.6.1 Contribution

Validation: Conducting experiments for neurotoxicity data of identified hit compounds (related to Figure 4E); Writing - Review and editing: Reviewing the manuscript draft.

3.6.2 Graphical summary

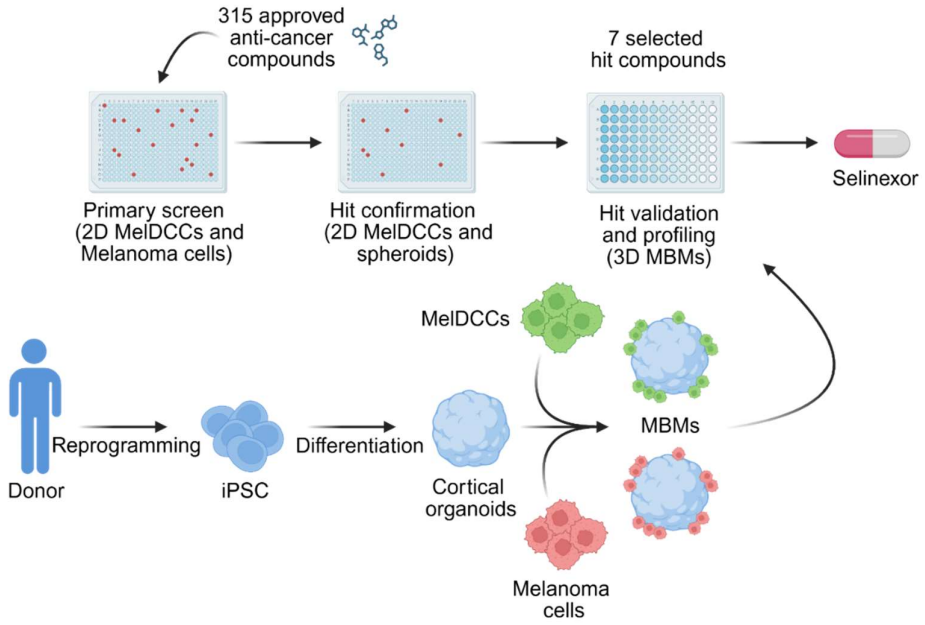


Figure 9: Graphical summary of "Cortical organoid-derived models of the melanoma brain metastatic niche enable prioritization of cancer-targeting drugs", Krieg et al., *Cell Reports Methods*, 2025. MelDCCs: melanoma disseminated cancer cells; MBMs: melanoma brain metastasis; iPSC: induced pluripotent stem cell. Created with BioRender.com.

3.6.3 Summary

This study is another example of the application of 3D iPSC-derived models for drug screening addressing neurological disease. Here, melanoma brain metastasis (MBMs) were modelled using human iPSC-derived cortical organoids (hCOs), which were co-cultured with melanoma cells, creating a physiologically relevant model that mimics tumor colonization and metastasis. Melanoma is the most lethal form of skin cancer. It's spread to the brain, especially in advanced cases, worsens patient outcomes and highlights the need for accurate *in vitro* models to study MBMs. A key challenge is the brain microenvironment and the BBB, which limits drug delivery to the CNS. This study introduces a reproducible iPSC-derived MBM model that aids in identifying potential treatments. The model was validated using gene expression profiles, imaging, ultrastructural analysis, and electrophysiology, demonstrating cortical features and tumor growth similar to those of patient MBMs. Unique gene signatures associated with metastasis and epithelial-to-mesenchymal transition, as well as astrocyte-like cells in the metastatic region were identified. The 3D MBM model facilitated drug screening of seven hit compounds identified from an anti-cancer library tested on 2D melanoma cells and tumoroids, leading to the discovery of selinexor, a potent MBM inhibitor that crosses the BBB with low neurotoxicity. This organoid-based system thus represents a significant advance for studying brain metastasis biology and potentially accelerates the development of targeted therapies.

3.7 High-throughput screen identifies repurposing candidates for Multiple sulfatase deficiency

This section presents the following manuscript, which is currently in preparation (see Appendix VII):

Annika Wittich, Alisa DeGrave, Jeanette Reinshagen, Lina Schmidt, Ole Pless, and Lars Schlotawa. High-throughput drug repurposing screen identifies candidates targeting Multiple sulfatase deficiency. *In preparation*

3.7.1 Contribution

Methodology: Assay development and high-throughput screening, hit confirmation and hit profiling assays; Investigation: Performed all the experiments; Visualization: Preparation of Figures; Writing - original draft: Writing the manuscript draft.

3.7.2 Graphical summary

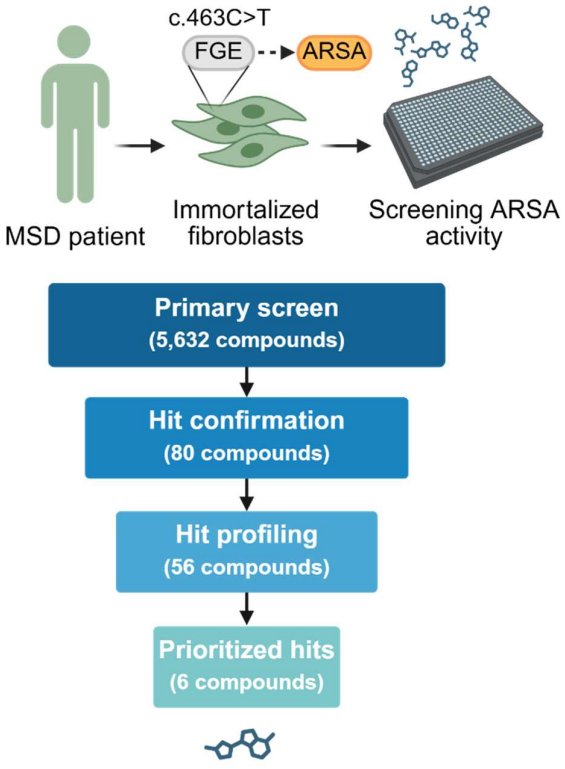


Figure 10: Graphical summary of "High-throughput screen identifies repurposing candidates for Multiple sulfatase deficiency", which is currently in preparation. MSD: Multiple sulfatase deficiency; FGE: Formylglycine-generating enzyme; ARSA: Arylsulfatase A. Created with BioRender.com.

3.7.3 Summary

In the previous chapters, the main focus was on phenotypic primary screening for rare neurological disorders. In this chapter, we describe the development of a cell-based enzymatic HTS assay that identified six hit compounds capable of restoring arylsulfatase A (ARSA) function in the lysosomal storage disorder MSD using patient-derived fibroblasts as the experimental model.

MSD is an ultra-rare monogenic disease caused by a deficiency in multiple sulfatase enzymes and is currently incurable. The leading cause of this multisystemic disease are variants in the *SUMF1* gene, which encodes the formylglycine-generating enzyme (FGE). FGE is an essential protein for the activation of all human sulfatases, including ARSA, that break down glycosaminoglycans and sulfatides in the cell. Variants in *SUMF1* can lead to inactive forms of FGE and thereby loss of sulfatase activity. Sulfatase dysfunction leads to the accumulation of toxic substances in the lysosome, which subsequently leads to cell death and severe neurological and physical symptoms. We developed a high-throughput screening assay using patient-derived fibroblasts, immortalized with SV40 large T antigen, to identify therapeutic candidates that restore ARSA activity as a downstream effect of enhanced FGE activity. Again, we screened the highly annotated small molecule repurposing library containing 5,632 compounds, including (pre-)clinical, marketed, and withdrawn drugs. We identified 80 compounds that significantly increased ARSA activity, validated 56 after hit confirmation and profiling in the primary assay and selected 6 top candidates based on potency, toxicity, predicted targets, and blood-brain barrier permeability. Our findings highlight repurposable compounds with the potential to restore sulfatase activity by increasing FGE activity in patients with MSD.

4. Discussion

The identification of treatment opportunities for rare neurological diseases is of significant importance given the limited available therapeutic options. Drug discovery thereby enables the identification of active compounds that subsequently advance into preclinical development and clinical trials. This work demonstrates how advanced human-derived disease models have been used in modern phenotypic and target-based drug discovery efforts, particularly in the context of rare neurodegenerative diseases such as PD, LS, and MSD. In the first publication, we established a scalable and reproducible HCS using NPCs from one LS patient. This HCS workflow allowed us to discover PDE5i as a potential small molecule compound class. We demonstrated the efficacy and safety of the PDE5i sildenafil in 2D and 3D LS disease models as a novel treatment strategy for LS, which is now progressing into clinical trials. The screening of 5,632 repurposable compounds additionally identified tyrphostins as a class of compounds capable of reducing elevated MMP levels. Further exploration showed that mitochondrial uncoupling by tyrphostin A9 is beneficial in iPSC-derived neuronal models of PD by reducing αsyn accumulation and ROS levels. Furthermore, talarozole and sertaconazole were identified using DL and yeast LS models, and validated in complex 3D brain organoids derived from iPSCs of an LS patient, demonstrating effectiveness in normalizing neuromorphogenesis and lactate levels. The application of a 3D co-culture model using iPSC-derived brain organoids with melanoma and disseminated cancer cells enabled the validation of seven compounds identified via 2D screening with melanoma and cancer cells, including Selinexor, which was found to be an effective drug that eliminated cancer cells without neurotoxicity. Finally, the drug repurposing screen with 5,632 compounds on MSD patient fibroblasts identified six new drug candidates that increased ARSA activity better than earlier identified retinoids, tazarotene and bexarotene, without causing toxicity.

4.1 Choosing the right model for drug discovery in rare neurological diseases

Choosing the right model for drug discovery in rare neurological diseases is essential, as these conditions often involve complex, cell-type-specific mechanisms that are difficult to capture in a single system. In drug discovery, balancing biological relevance and practicality is vital. One method for creating models of neurological diseases suitable for drug discovery is the use of iPSCs. For rare neurological diseases, patient materials are limited, making them hard to obtain. iPSCs enable upscaling of cell material and the creation of disease-relevant 2D or 3D cellular models containing patient-specific nuclear or mitochondrial variants (Tolle, Tiranti, and Prigione, 2023). The disease models used here

include iPSC-derived 2D models, such as NPCs (Zink et al., 2026), mDANs (Gorgogietas et al., 2025; Menacho et al., 2026), 3D cortical or midbrain organoids (Krieg et al., 2025; Menacho et al., 2026), and immortalized fibroblasts from patients (Appendix VII). Additionally, the here-presented review article "Human organoids: Fit for drug discovery?" summarizes the advantages and limitations of organoids in drug discovery (Appendix IV). In rare diseases, such models have played a crucial role in revealing disease mechanisms, such as for LS, including changes in calcium regulation (Galera-Monge et al., 2020; Lorenz et al., 2017), defects in neuronal, and impaired cortical development in 3D brain organoids (Inak et al., 2021; Romero-Morales et al., 2022). Patient-derived iPSC models can faithfully reproduce human neuronal phenotypes, while animal models provide the whole-organism context and long-term physiological insights (Barré-Sinoussi and Montagutelli, 2015; Chang and Grieder, 2024).

An important aspect of neurological diseases is the need for treatments to cross the BBB and to reach the CNS. The unique barrier properties of the BBB complicate drug development and brain delivery, leading to high failure rates in CNS target drug discovery (Morofuji and Nakagawa, 2020; Pardridge, 2005). In the studies by Zink et al., 2026 and Krieg et al., 2025, iPSC-derived BBB models were established to predict whether the identified leads, sildenafil for LS and selinexor for MBM, can cross the human BBB to reach the brain. This early *in vitro* testing of compounds using a model that mimics the biophysical barrier of the human and patients' BBB is essential for drug development and to prevent compounds from failing in later clinical testing.

Despite significant progress in disease modeling, most current *in vitro* models used to study neurological diseases still lack microglia, the brain's resident immune cells, creating a notable gap in understanding disease mechanisms. Other than neurons, astrocytes and oligodendrocytes differentiating from the neuroectoderm, microglia originate from the mesoderm in early embryogenesis and migrate into the developing brain (Ginhoux et al., 2010; Monier et al., 2007). Without microglia, the neuroinflammation process cannot be accurately investigated, a key process in many neurodegenerative and neurodevelopmental disorders. This limitation also impacts cancer research, where microglia and related myeloid cells play vital roles in tumor initiation, progression, and response to therapy (Sevenich, 2018). As a result, models that exclude microglia provide an incomplete picture of both normal brain function and disease-related inflammatory interactions. Although microglia were absent in the here-presented disease models, applying iPSC technology and patient-derived cells allowed for the identification of clear biomarkers and cellular phenotypes, followed by the nomination of compounds capable of reversing them.

The most effective strategy often combines multiple complementary models, e.g., 2D cells and 3D organoids, enabling the validation of mechanistic insights across biological levels and enhancing the chances that early therapeutic results will lead to meaningful clinical progress. A feasible approach is to increase the model's complexity at each step of drug

discovery to more precisely predict compound responses and enable higher-throughput screening at earlier stages.

4.2 Sildenafil as a treatment for neurological diseases

In the here-presented manuscript "Pluripotent stem cell-based drug discovery uncovers sildenafil as a treatment for mitochondrial disease" (Zink et al., 2026), sildenafil proved beneficial in LS *in vitro* and *in vivo* disease models, and improved clinical outcomes in six LS patients as part of off-label use. In 2017, the PDE5i avanafil was identified in a smaller-scale drug screen, already highlighting the potential of this drug class in the context of LS (Lorenz et al., 2017). Moreover, the high-throughput screen identified the PDE5i's vardenafil hydrochloride and T-0156 as hits, able to reduce the elevated MMP levels in a dose-dependent manner in NPCs with variants in the *MT-ATP6* gene without loss of viability. Among the first PDE5i that were identified were caffeine and theophylline (Sutherland and Rall, 1958). Those have been shown to inhibit almost all known phosphodiesterases (PDEs), although they are relatively weak in potency. However, these early observations provided the biochemical basis for the development of more specific and potent PDE inhibitors, such as sildenafil, targeting specifically PDE5 (Francis and Corbin, 2004).
Sildenafil was discovered by Pfizer in 1989 and was originally intended to dilate coronary arteries and prevent anginal pain. It entered clinical trials in 1991 but showed no efficacy for the treatment of angina (Goldstein et al., 2019). However, the clinical trials revealed that penile erection is a common side effect in the studied men's cohort. After showing effectiveness and safety, sildenafil was approved for oral treatment of erectile dysfunction (ED) under the brand name Viagra® by both the FDA and the EMA in 1998 (Goldstein et al., 1998), making sildenafil a drug that had already been repurposed once. In the context of ED, sildenafil blocks the degradation of cyclic guanosine monophosphate (cGMP) by inhibiting PDE5, thereby elevating the cGMP signal initiated by nitric oxide (NO) release in response to sexual stimulation, ultimately leading to smooth muscle relaxation and increased blood flow to the corpus cavernosum (Boolell et al., 1996). Following the approval of sildenafil for the treatment of ED, considerations began to shift towards other potential indications for this medication (Ghofrani, Osterloh, and Grimminger, 2006).
In the context of AD, sildenafil also received attention since the NO/cGMP pathway is significantly impaired (Domek-Łopacińska and Strosznajder, 2010; Puzzo et al., 2005), leading to reduced levels of cGMP (Sanders, 2020). Sildenafil showed effectiveness in improving cognitive function, enhancing mitochondrial biogenesis, reducing amyloid beta accumulation, and decreasing neuroinflammation in preclinical AD models (Sanders, 2020). Similar to the *in vivo* studies of *SURF1* KO piglets, where a higher dose of sildenafil led to microhemorrhages (Zink et al., 2026), the therapeutic effects of sildenafil for AD showed strong dose-dependencies, with low doses showing promise in improving brain

perfusion, mitochondrial health, and neurogenesis, while higher doses may activate non-beneficial pathways (Sanders, 2020). Furthermore, sildenafil reduced cognitive decline in murine models of HD (Puerta et al., 2010; Saavedra et al., 2013) and enhanced both motor and cognitive performance in patients diagnosed with HD (Achenbach, Faissner, and Saft, 2022).

It has been observed that PDE5 gene expression is upregulated in lungs suffering from pulmonary hypertension (Sanchez et al., 1998). A study showed that oral treatment with sildenafil selectively reduced pulmonary pressure and pulmonary vascular resistance in adults with pulmonary arterial hypertension (Galiè et al., 2005). Importantly, sildenafil was evaluated in children as a treatment for pulmonary hypertension and was reported to be well tolerated, safe, and have an acceptable side effect profile (Cohen et al., 2019). In 2023, the FDA approved sildenafil for pediatric use of pulmonary hypertension under the brand name Revatio® (U.S. Food and Drug Administration, 2023).

Given sildenafil's safety profile and approval for pediatric use, it is considered a potential treatment for LS patients, who typically develop the disease early in life (Hong et al., 2020). In the here-presented study of Zink et al., 2026 sildenafil was active despite LS being a heterogeneous disease. Sildenafil demonstrated effectiveness in *in vitro* models of *MT-ATP6* and *SURF1* variants as well as in *in vivo* models of LS-causing variants *SURF1* and *Ndufs4*, highlighting its potential as a general treatment for LS. In addition to its neurological impact, sildenafil modulated bioenergetic processes and improved the metabolic fitness of LS mice and LS pigs. The enhanced bioenergetics and normalization of MMP demonstrated in *in vitro* models of LS may be linked to sildenafil's regulation of calcium homeostasis. Pre-treatment of LS brain organoids with sildenafil reduced their aberrant calcium response to metabolic stress, highlighting sildenafil's potential in counteracting metabolic crises, which is also observed in LS patients treated with sildenafil (Zink et al., 2026). This is also in line with previously reported findings that PDE5i improved calcium defects in LS NPCs (Lorenz et al., 2017). cGMP-dependent protein kinase 1 (PRKG1) has been proposed as a regulator of energy homeostasis (Kaun and Sokolowski, 2009) and may also be involved in neuronal calcium signaling (Paupardin-Tritsch et al., 1986), thereby positioning PRKG1 as a potential downstream target for sildenafil. Sildenafil did not restore MMP in LS neural cells when PRKG1 was inhibited, underscoring the role of PRKG1 as a sildenafil-related target. Sildenafil may enhance PRKG1 activity, as reduced PRKG1 protein levels were not fully normalized in LS models. Although there is substantial evidence that PRKG1 plays a key role, further investigation into how sildenafil modulates PRKG1's function is necessary to fully understand its mechanism of action related to this target protein.

Despite the small molecule sildenafil, cannabidiol has also been tested in the context of LS. Cannabidiol is a small molecule derived from the cannabis plant, which showed efficacy in LS *Ndufs4* KO mouse model, by enhancing social and motor function, extension of lifespan, and improved cellular function in fibroblasts from LS patients. They found

peroxisome proliferator-activated receptor gamma (PPARγ) as a key nuclear receptor mediating cannabidiol's beneficial effects. The results show evidence for cannabidiol as a potential therapy, by targeting a different pathway than sildenafil. An ODD was obtained for the treatment of LS (EU/3/23/2800).

Other therapeutic options for LS patients are currently very limited and primarily focus on treating clinical symptoms. Current treatments include supplements such as coenzyme Q10 and its derivatives, vitamins, pyruvate, dichloroacetate, and a ketogenic diet (Magro et al., 2025). However, those showed minimal effects and are target-unspecific, aiming to improve mitochondrial function (Baertling et al., 2014).

Mitochondrial replacement therapies (MRT), such as pronuclear or spindle nuclear transfer, are preventive approaches for families with known mtDNA variants, aiming to prevent vertical transmission of these variants (Wolf, Mitalipov, and Mitalipov, 2015). During pronuclear transfer, the cytoplasm of a fertilized egg containing defective mitochondria is replaced with cytoplasm from a donor zygote containing unaffected mitochondria, producing a reconstructed embryo (Hyslop, 2018). SNT is a process that involves transferring the donor nucleus into an unfertilized oocyte from a healthy donor with unaffected mitochondria after the donor's nucleus has been removed (Magro et al., 2025). The Human Fertilisation and Embryology Authority (HFEA) Regulations 2015 were established to permit mitochondrial donation treatments. These regulations aimed to modernize the United Kingdom (UK) fertility laws and offer new options for parents wanting to prevent serious inherited mitochondrial disorders (Human Fertilisation and Embryology Authority, 2015). Mitochondria transfer-based therapies have been shown to improve morbidity and mortality of the *Ndufs4* KO mouse model of LS (Nakai et al., 2024). A human study proved that oocytes reconstituted by SNT are capable of producing a healthy live birth (Zhang et al., 2017). To date, eight children have been born in the UK, receiving mitochondrial replacement therapy, with no or low levels of mtDNA heteroplasmy in blood (McFarland et al., 2025). However, ethical concerns, e.g., about the creation of multiple embryos needed, hinder the wider use of this approach outside the UK, and MRTs are not a treatment option for patients with LS.

Another alternative therapeutic modality that holds great potential for treating rare diseases is gene therapy. AAV is a well-characterized gene replacement vector, aiming to deliver functional copies of nuclear-encoded genes, and its safety profile and ability to transduce quiescent cells nominate it as a potential gene therapy vehicle for different mitochondrial diseases (Hanaford et al., 2022). Studies have demonstrated its potential in preclinical models of LS, such as *Ndufs4* KO mice (Di Meo et al., 2017) and *Surf1* KO mice (Ling et al., 2021, 2025). The EMA issued an ODD for gene replacement therapy using the AAV9/hSURF1 vector in patients with LS with variants in *SURF1* (EU/3/21/2531).

However, AAV-based gene therapy targeting mtDNA poses an additional challenge because AAVs naturally deliver their genomes to the nucleus and cannot cross the mitochondrial double membrane, limiting AAV-based gene therapies to LS caused by nuclear

variants (Hanaford et al., 2022). Mitochondria also lack the pathways needed to express and process AAV-delivered DNA, making targeted editing of mitochondrial genomes with nuclear-delivered tools ineffective. Despite this, recent breakthroughs have transformed the field of mtDNA engineering. Mitochondrial genome editing uses a combination of DNA-targeting domains, such as zinc-finger or transcription activator-like effector (TALE) domains, which ensure specific binding to the desired mtDNA sequence, and an mtDNA-manipulating domain connected to the targeting domain, which facilitates degradation or base editing around the DNA-binding site. However, they still lack specificity, and studies are needed to elucidate safety. Moreover, challenges remain, such as optimizing tissue-specific targeting, crossing the BBB, maintaining sustained expression without adverse immune responses, and limited therapy accessibility, along with high costs.
Small molecules, like sildenafil are therefore advantageous, as they are more likely to cross the BBB, as also demonstrated applying sildenafil in iPSC-derived models of the BBB (Zink et al., 2026) and not cause immune reactions. While sildenafil would not be a curative treatment for LS patients, it would provide an accessible, relatively inexpensive, and potentially long-term treatment option. Sildenafil has proven safety, importantly also in children, and has been shown to ameliorate LS-disease signatures. Sildenafil has obtained an ODD for its use in the treatment of LS (EU/3/23/2831). The next step is to determine the efficacy of sildenafil in children and adults with LS through a controlled, randomized, double-blind clinical trial.

4.3 Mitochondrial uncoupling in neurodegenerative diseases

The drug repurposing HTS screen, involving 5,632 compounds aimed at identifying mitochondrial uncouplers targeting LS caused by variants in the *MT-ATP6* gene, has not only led to the discovery of sildenafil, but also tyrphostin A9 and tyrphostin A879. Tyrphostins are defined as a class of inhibitors that target tyrosine phosphorylation, affecting both receptor and non-receptor tyrosine kinases (Cismowski, 2017). Their structures derive from the natural product erbstatin, a non-selective kinase inhibitor. Several tyrphostins have been developed as cancer treatments, including imatinib, gefitinib, erlotinib, and sunitinib (Cismowski, 2017). Previously, tyrphostins have also been described as protonophores and mitochondrial uncouplers (Sagara et al., 2002; Soltoff, 2004). Protonophores are compounds capable of electrogenic transport of protons across membranes. Classical protonophores that uncouple the mitochondrial membrane potential include 2-azido-4-nitrophenol (DNP), carbonyl cyanide m-chlorophenyl hydrazone (CCCP), and carbonyl cyanide-p-trifluoromethoxyphenyl-hydrazone (FCCP), as they can transfer protons across the lipid part of the mitochondrial membrane (Kotova and Antonenko, 2022). Mitochondrial uncoupling has been previously described as a neuroprotective strategy for neurodegenerative diseases (Geisler et al., 2017; Kumar et al., 2022; Zorov et al., 2021).

In the context of AD, it has been shown that low concentrations of 2,4-dinitrophenol (DNP) increase neuronal cAMP and tau levels, promote neurite outgrowth and neuronal differentiation, and inhibit the oligomerization and neurotoxicity of amyloid beta (Sebollela et al., 2009; Wasilewska-Sampaio et al., 2007). Moreover, it has been shown that tyrphostin A9 treatment could stimulate neurite outgrowth in SH-SY5Y neuroblastoma cells and protect primary substantia nigra neuronal cultures from the substantia nigra from neurotoxin MPP+ induced damage (Dai et al., 2022).

In the here-presented study "Morphological profiling reveals neuroprotection via mitochondrial uncoupling in human dopaminergic neurons" (Gorgogietas et al., 2025), tyrphostin A9 was independently identified as a mitochondrial uncoupler that shifts *SNCA*-4x profiles toward *SNCA*-corr-like phenotypes, as assessed in iPSC-derived mDANs using morphological profiling. For hit profiling, additional tyrphostin A9 analogues were assessed in the same assays to evaluate structure-activity relationships. Despite tyrphostin A9's ability to lower the MMP, it also reduces ROS and αSyn levels in the PD-causing variant *SNCA*-4x. Tyrphostin A879 and its analogue, tyrphostin A1024, showed similar activities but with smaller effect sizes. However, tyrphostin A9 also decreased neuronal activity for a short period after administration, followed by a phase of recovery. The proposed mechanism of action in the context of αSyn degradation involves a lysosome-associated pathway. Autophagy might also be further induced by tyrphostins through mitochondrial uncoupling, leading to decreased ATP levels and adenosine monophosphate-activated protein kinase (AMPK) phosphorylation and may help prevent αSyn misfolding and facilitate its degradation (Gorgogietas et al., 2025). There is evidence that when the MMP becomes depolarized, PINK1 accumulates on the outer mitochondrial membrane and phosphorylates ubiquitin at serine-65 (Malpartida et al., 2021). This phosphorylated ubiquitin recruits cytosolic, autoinhibited parkin. PINK1 activates parkin, leading to mitophagy and lysosomal degradation of the damaged mitochondrion (Swatek et al., 2019).

In LS, sildenafil was shown to mildly depolarize mitochondria in NPCs with an *MT-ATP6* mitochondrial variant (Zink et al., 2026). However, the observed sildenafil-induced MMP normalization may not be due to a direct mitochondrial uncoupling effect. NPCs with variants of the nuclear gene *SURF1* exhibit a depolarized MMP compared to isogenic controls, due to reduced proton pump activity of complex IV. Nevertheless, sildenafil still ameliorates the MMP in NPCs with a *SURF1* variant. This indicates that MMP reduction in *MT-ATP6* variants is not the cause but rather a consequence of sildenafil's mechanism of action. This emphasizes that phenotypic observations are valuable for drug discovery, but the underlying mechanisms of action are more complex and require extensive target deconvolution studies. Phenotypic studies need to be complemented with functional studies and/or multi-omics (e.g., transcriptomics, proteomics, metabolomics, or genetic expression profiling).

Unlike sildenafil, tyrphostin A9 and AG879 are not approved drugs and probably will not be because of the high potential risks when clinically applied. Along with a strong

reduction of MMP, mitochondrial ATP synthetic activity is reduced, leading to a possible energy crisis in the cell and a switch to less efficient glycolysis for ATP synthesis. Therefore, it is necessary to carefully regulate uncoupler concentrations to hit the therapeutic window and to prevent levels that would lead to a mismatch between energy needs and ATP generation in the cell (Zorov et al., 2021).
Taken together, mild mitochondrial uncoupling reduces ROS, as shown by treatment with lower doses of tyrphostin A9, tyrphostin A879, and tyrphostin A1024. However, it is not clear whether tyrphostins have a specific target in the context of PD and LS mitochondrial uncoupling activity, or whether this effect is due to their protonophoric activity.
However, tyrphostin A9 serves as an example of a compound that modulates disease phenotypes in different contexts through a shared compound effect (reduction of MMP) and, along with sildenafil, demonstrates that (mild) mitochondrial uncoupling indeed has a beneficial impact in neurodegenerative diseases like PD and LS.

4.4 Clinical potential of newly identified compounds for MSD

To date, treatment for MSD patients involves a multidisciplinary, expert-driven approach to control and alleviate organ-specific symptoms, along with personalized palliative care, helping to restore, maintain, and improve the quality of life for individuals with MSD (Ahrens-Nicklas et al., 2018). The screening of 5,632 repurposable compounds in immortalized fibroblasts from an MSD patient identified six compounds that significantly and reproducibly increased ARSA activity in a biochemical assay without reducing cell viability. Some of the compounds are already approved for other disease indications or are in advanced stages of clinical development. Therefore, clinical data are available, helping to develop these drugs as treatments for MSD. However, to further advance drug development, it is necessary to conduct safety and efficacy assessments in more complex disease models, such as iPSC-derived 2D cells and organoids from MSD patients. It needs to be investigated whether those compounds are efficacious in neurons and astrocytes, and whether they can reach the CNS, which is mainly responsible for the clinical symptoms of MSD patients (Ahrens-Nicklas et al., 2018), at sufficiently high concentrations to activate sulfatases effectively. In contrast to bexarotene, where treatment of a healthy individual using standard concentrations revealed a low penetrance of the drug into the CNS (Ghosal et al, 2016), a good BBB permeability is described for compound #45. This should be experimentally confirmed using, e.g., iPSC-derived BBB models (Appelt-Menzel et al., 2020). Moreover, the effect on the activities of other sulfatases should be investigated, since the data presented here only focuses on ARSA activity. Future studies could also test the compounds in the context of metachromatic leukodystrophy, where variants in the gene encoding ARSA are causative (Austin et al., 1965), and patients could potentially benefit from future investigations. Additionally, more genetic variants should be tested, as the

data shown here only reflect one *SUMF1* variant. Importantly, the mechanism of action should be elucidated using multi-omics approaches, including transcriptomics and proteomics, comparing untreated cells with treated cells and with cells from an unaffected donor. This could elucidate whether compounds work by increasing transcriptional levels of *SUMF1*, the protein half-life of FGE or similar. The compounds may act via a different mechanism of action and target compared to tazarotene and bexarotene, offering another potential therapy, which is important, since some patients are non-responders (Boessen et al., 2012; Khaleva et al., 2023). Thereby, new compounds could be an alternative to tazarotene and bexarotene and would provide a relatively inexpensive and accessible therapy for patients with MSD. In summary, the newly identified compounds are promising candidates, but more safety and efficacy data are needed to advance them towards clinical application.

5. Conclusion and perspectives

The application of human cellular disease models for drug discovery laid the foundation for the work presented here, demonstrating how patient-derived systems uncovered disease-relevant mechanisms and unveiled potential treatments using small molecules. This approach led to the identification of sildenafil, talarozole, and sertaconazole for LS, tyrphostin A9 for PD, selinexor for MBM, and six drug candidates targeting MSD.

A major bottleneck for studying neurological diseases has been the limited access to patient material. Neurological diseases caused by mtDNA variants are challenging to model due to the limited ability to engineer mitochondrial DNA. This has hindered the development of targeted therapies for conditions like LS. With the emergence of the human iPSC-derived technology in 2007, disease modeling entered a new era. iPSC-derived disease models demonstrated the potential to deepen mechanistic understanding of human disease mechanisms, with the possibility of widely replacing animal testing and creating more precise, effective treatments for clinical use. Phenotypic screening of a repurposing library containing 5,632 small molecules identified PDE5 inhibitors and tyrphostins in iPSC-derived NPCs from an LS patient. For the first time, sildenafil has been shown to normalize mitochondrial function, promote neuronal outgrowth, and be beneficial in *in vivo* models of LS. Since PRKG1 function is likely altered after sildenafil administration, a new mechanism of action in the context of LS was proposed here. Tyrphostins A9 and A879 reduced ROS and αSyn levels in mDANs from a PD patient with *SNCA* triplication. Azole-containing compounds were identified through a deep-learning strategy combined with a rescue screen in Leigh yeast cultures. Talarozole and sertaconazole were confirmed in 2D and 3D models of LS with a *SURF1* variant. Both compounds enhanced dopaminergic neuron development and restored neurite organization and lactate levels.

To address the need for therapies that cross the BBB and to predict drug permeability, we developed BBB models using hiPSC-derived cells to evaluate the likelihood of sildenafil and selinexor reaching the CNS. We demonstrated that both lead compounds can cross the BBB at an acceptable rate.

Looking ahead, several challenges and opportunities remain for advancing the identified compounds towards clinical use. Safety studies and long-term evaluations are essential to fully understand their therapeutic potential and tolerability. Sildenafil must demonstrate both efficacy and safety in a clinical trial to receive approval as a treatment for LS. Similarly, ongoing development and adoption of advanced human disease models will be crucial for accelerating drug discovery while reducing reliance on animal studies.

6. Acknowledgements

I would like to thank all the people who guided and supported me throughout the last years and during my PhD.
First, I thank my supervisor at the Heinrich Heine University, Prof. Dr. Alessandro Prigione, for his continuous scientific advice, feedback, and support. I am also very grateful for the support and advice of Prof. Dr. Erdem Gültekin Tamgüney, my second supervisor at the Heinrich Heine University Düsseldorf. My greatest gratitude goes to Dr. Ole Pless, not just for his scientific support, expertise, and encouragement, but also for his guidance, trust, constant feedback, and motivation. I thank you for all your support over the past years.
I am also grateful to Prof. Dr. Carsten Clausen and Dr. Philip Gribbon for the opportunity to join Fraunhofer ITMP, as well as for providing opportunities to learn and for my personal growth.
I am especially thankful for the chance to collaborate with many excellent scientists from various research institutions. My thanks go to Prof. Dr. Lars Schlotawa and Dr. Alisa DeGrave from Fraunhofer ITMP in Göttingen for their close collaboration and active scientific exchange during the ScreenMSD project, as well as to Dr. Christian Brüser and Jan Keller-Findeisen, who contributed their expertise to the superresolution microscopy part of the CureMILS project and were always welcoming. Many thanks also to Prof. Dr. Felix Distelmaier and his team for analyzing samples via mass spectrometry. In particular, I want to thank Dr. Annika Zink from the University Hospital in Düsseldorf, who not only supported me scientifically but also became a friend.
A special thanks goes to all my colleagues at Fraunhofer ITMP who helped with technical questions, supported me in the laboratory, and throughout my PhD. I want to mention Markus Wolf, Dr. Bernhard Ellinger, Gesa Witt, Jeanette Reinshagen, Dr. Johanna Huchting, and Dr. Maria Kuzikov. Special thanks to Dr. Leonie von Berlin, who proofread my thesis. Thank you all for your support and for creating a positive work environment. My deepest gratitude is to my partner in crime, Kim Krieg, who always supported me and offered sound advice. I sincerely thank the Stem Cell Team, Dr. Undine Haferkamp, Daniel Stach, Fatima-Zahra Rachad, and Dr. Arjen Weller, for their outstanding support and for making hours in the stem cell laboratory enjoyable.
Lastly, I want to thank my family and friends for their constant support and encouragement. Especially, I thank my parents, Angelika and Hans, along with Mareike and Lukas, for their endless love and support.

7. References

Abud, Edsel M., Ricardo N. Ramirez, Eric S. Martinez, Luke M. Healy, Cecilia H. H. Nguyen, Sean A. Newman, Andriy V. Yeromin, Vanessa M. Scarfone, Samuel E. Marsh, Cristhian Fimbres, Chad A. Caraway, Gianna M. Fote, Abdullah M. Madany, Anshu Agrawal, Rakez Kayed, Karen H. Gylys, Michael D. Cahalan, Brian J. Cummings, Jack P. Antel, Ali Mortazavi, Monica J. Carson, Wayne W. Poon, and Mathew Blurton-Jones. 2017. "iPSC-Derived Human Microglia-like Cells to Study Neurological Diseases." *Neuron* 94(2):278-293.e9. doi:10.1016/j.neuron.2017.03.042.

Achenbach, Jannis, Simon Faissner, and Carsten Saft. 2022. "Resurrection of Sildenafil: Potential for Huntington's Disease, Too?" *Journal of Neurology* 269(9):5144–50. doi:10.1007/s00415-022-11196-7.

Ahrens-Nicklas, Rebecca, Lars Schlotawa, Andrea Ballabio, Nicola Brunetti-Pierri, Mauricio De Castro, Thomas Dierks, Florian Eichler, Can Ficicioglu, Alan Finglas, Jutta Gaertner, Brian Kirmse, Joerg Klepper, Marcus Lee, Amber Olsen, Giancarlo Parenti, Arastoo Vossough, Adeline Vanderver, and Laura A. Adang. 2018. "Complex Care of Individuals with Multiple Sulfatase Deficiency: Clinical Cases and Consensus Statement." *Molecular Genetics and Metabolism* 123(3):337–46. doi:10.1016/j.ymgme.2018.01.005.

Ahuja, Deepika, M. Teresa Sáenz-Robles, and James M. Pipas. 2005. "SV40 Large T Antigen Targets Multiple Cellular Pathways to Elicit Cellular Transformation." *Oncogene* 24(52):7729–45. doi:10.1038/sj.onc.1209046.

Akhmetov, Azat, Jon Laurent, Jimmy Gollihar, Elizabeth Gardner, Riddhiman Garge, Andrew Ellington, Aashiq Kachroo, and Edward Marcotte. 2018. "Single-Step Precision Genome Editing in Yeast Using CRISPR-Cas9." *BIO-PROTOCOL* 8(6). doi:10.21769/BioProtoc.2765.

Ali, Hossam Tharwat, Idris Sula, Abrar AbuHamdia, Sewar A. Elejla, Ahmed Elrefaey, Hiba Hamdar, and Mohamed Elfil. 2024. "Nervous System Response to Neurotrauma: A Narrative Review of Cerebrovascular and Cellular Changes After Neurotrauma." *Journal of Molecular Neuroscience* 74(1):22. doi:10.1007/s12031-024-02193-8.

Alotaibi, Shabab, Lujain Alfayez, and Mohammed Alkhudhair. 2024. "Parkinson's Disease: Current Treatment Modalities and Emerging Therapies." *Cureus*. doi:10.7759/cureus.75647.

Alston, Charlotte L., Mariana C. Rocha, Nichola Z. Lax, Doug M. Turnbull, and Robert W. Taylor. 2017. "The Genetics and Pathology of Mitochondrial Disease." *The Journal of Pathology* 241(2):236–50. doi:10.1002/path.4809.

Appel, Mason J., Katlyn K. Meier, Julien Lafrance-Vanasse, Hyeongtaek Lim, Chi-Lin Tsai, Britt Hedman, Keith O. Hodgson, John A. Tainer, Edward I. Solomon, and Carolyn R. Bertozzi. 2019. "Formylglycine-Generating Enzyme Binds Substrate Directly at a Mononuclear Cu(I) Center to Initiate O_2 Activation." *Proceedings of the National Academy of Sciences* 116(12):5370–75. doi:10.1073/pnas.1818274116.

Appelt-Menzel, Antje, Sabrina Oerter, Sanjana Mathew, Undine Haferkamp, Carla Hartmann, Matthias Jung, Winfried Neuhaus, and Ole Pless. 2020. "Human iPSC-Derived Blood-Brain Barrier Models: Valuable Tools for Preclinical Drug Discovery and Development?" *Current Protocols in Stem Cell Biology* 55(1):e122. doi:10.1002/cpsc.122.

Austin, Armstrong, and Shearer. 1965. "Metachromatic Form of Diffuse Cerebral Sclerosis: V. The Nature and Significance of Low Sulfatase Activity: A Controlled Study of Brain, Liver and Kidney in Four Patients With Metachromatic Leukodystrophy (MLD)." *Archives of Neurology* 13(6):593. doi:10.1001/archneur.1965.00470060029003.

Baertling, F., R. J. Rodenburg, J. Schaper, J. A. Smeitink, W. J. H. Koopman, E. Mayatepek, E. Morava, and F. Distelmaier. 2014. "A Guide to Diagnosis and Treatment of Leigh Syndrome." *Journal of Neurology, Neurosurgery & Psychiatry* 85(3):257–65. doi:10.1136/jnnp-2012-304426.

Bagkos, Georgios, Kostas Koufopoulos, and Christina Piperi. 2014. "A New Model for Mitochondrial Membrane Potential Production and Storage." *Medical Hypotheses* 83(2):175–81. doi:10.1016/j.mehy.2014.05.001.

Bakare, Ajibola B., Edward J. Lesnefsky, and Shilpa Iyer. 2021. "Leigh Syndrome: A Tale of Two Genomes." *Frontiers in Physiology* 12:693734. doi:10.3389/fphys.2021.693734.

Banka, Siddharth, Christian De Goede, Wyatt W. Yue, Andrew A. M. Morris, Beate Von Bremen, Kate E. Chandler, René G. Feichtinger, Claire Hart, Nasaim Khan, Verena Lunzer, Lavinija Mataković, Thorsten Marquardt, Christine Makowski, Holger Prokisch, Otfried Debus, Kazuto Nosaka, Hemant Sonwalkar, Franz A. Zimmermann, Wolfgang Sperl, and Johannes A. Mayr. 2014. "Expanding the Clinical and Molecular Spectrum of Thiamine Pyrophosphokinase Deficiency: A Treatable Neurological Disorder Caused by TPK1 Mutations." *Molecular Genetics and Metabolism* 113(4):301–6. doi:10.1016/j.ymgme.2014.09.010.

Barré-Sinoussi, Françoise, and Xavier Montagutelli. 2015. "Animal Models Are Essential to Biological Research: Issues and Perspectives." *Future Science OA* 1(4):FSO63. doi:10.4155/fso.15.63.

Bassett, Douglas E., Mark S. Boguski, and Philip Hieter. 1996. "Yeast Genes and Human Disease." *Nature* 379(6566):589–90. doi:10.1038/379589a0.

Blauwendraat, Cornelis, Mike A. Nalls, and Andrew B. Singleton. 2020. "The Genetic Architecture of Parkinson's Disease." *The Lancet Neurology* 19(2):170–78. doi:10.1016/S1474-4422(19)30287-X.

Bleicher, Konrad H., Hans-Joachim Böhm, Klaus Müller, and Alexander I. Alanine. 2003. "Hit and Lead Generation: Beyond High-Throughput Screening." *Nature Reviews Drug Discovery* 2(5):369–78. doi:10.1038/nrd1086.

Blesa, Javier, Sudarshan Phani, Vernice Jackson-Lewis, and Serge Przedborski. 2012. "Classic and New Animal Models of Parkinson's Disease." *Journal of Biomedicine and Biotechnology* 2012:1–10. doi:10.1155/2012/845618.

Boessen, Ruud, Rolf H. H. Groenwold, Mirjam J. Knol, Diederick E. Grobbee, and Kit C. B. Roes. 2012. "Classifying Responders and Non-Responders; Does It Help When There Is Evidence of Differentially Responding Patient Groups?" *Journal of Psychiatric Research* 46(9):1169–73. doi:10.1016/j.jpsychires.2012.05.005.

Bolus, Harris, Kassi Crocker, Grace Boekhoff-Falk, and Stanislava Chtarbanova. 2020. "Modeling Neurodegenerative Disorders in Drosophila Melanogaster." *International Journal of Molecular Sciences* 21(9):3055. doi:10.3390/ijms21093055.

Boolell, M., M. J. Allen, S. A. Ballard, S. Gepi-Attee, G. J. Muirhead, A. M. Naylor, I. H. Osterloh, and C. Gingell. 1996. "Sildenafil: An Orally Active Type 5 Cyclic GMP-Specific Phosphodiesterase Inhibitor for the Treatment of Penile Erectile Dysfunction." *International Journal of Impotence Research* 8(2):47–52.

Bray, Mark-Anthony, Shantanu Singh, Han Han, Chadwick T. Davis, Blake Borgeson, Cathy Hartland, Maria Kost-Alimova, Sigrun M. Gustafsdottir, Christopher C. Gibson, and Anne E. Carpenter. 2016. "Cell Painting, a High-Content Image-Based Assay for Morphological Profiling Using Multiplexed Fluorescent Dyes." *Nature Protocols* 11(9):1757–74. doi:10.1038/nprot.2016.105.

Broach, James R., and Jeremy Thorner. 1996. "High-Throughput Screening for Drug Discovery." *Nature* 384.

Cai, Jiyang, Jie Yang, and DeanP. Jones. 1998. "Mitochondrial Control of Apoptosis: The Role of Cytochrome c." *Biochimica et Biophysica Acta (BBA) - Bioenergetics* 1366(1–2):139–49. doi:10.1016/S0005-2728(98)00109-1.

Chambers, Stuart M., Christopher A. Fasano, Eirini P. Papapetrou, Mark Tomishima, Michel Sadelain, and Lorenz Studer. 2009. "Highly Efficient Neural Conversion of Human ES and iPS Cells by Dual Inhibition of SMAD Signaling." *Nature Biotechnology* 27(3):275–80. doi:10.1038/nbt.1529.

Chang, Michael C. J., and Franziska B. Grieder. 2024. "The Continued Importance of Animals in Biomedical Research." *Lab Animal* 53(11):295–97. doi:10.1038/s41684-024-01458-4.

Chaudhary, Aryan, and Vidyapati Kumar. 2025. "Rare Diseases: A Comprehensive Literature Review and Future Directions." *Journal of Rare Diseases* 4(1):33. doi:10.1007/s44162-025-00099-6.

Chen, Wen, Huakan Zhao, and Yongsheng Li. 2023. "Mitochondrial Dynamics in Health and Disease: Mechanisms and Potential Targets." *Signal Transduction and Targeted Therapy* 8(1):333. doi:10.1038/s41392-023-01547-9.

Chesselet, Marie-Francoise, and S. Thomas Carmichael. 2012. "Animal Models of Neurological Disorders." *Neurotherapeutics* 9(2):241–44. doi:10.1007/s13311-012-0118-9.

Chia, Kelda, Anna Klingseisen, Dirk Sieger, and Josef Priller. 2022. "Zebrafish as a Model Organism for Neurodegenerative Disease." *Frontiers in Molecular Neuroscience* 15:940484. doi:10.3389/fnmol.2022.940484.

Ciafaloni, Emma, Filippo M. Santorelli, Sara Shanske, Thierry Deonna, Eliane Roulel, Charles Janzer, Graziano Pescia, and Salvatore DiMauro. 1993. "Maternally Inherited Leigh Syndrome." *The Journal of Pediatrics* 122(3):419–22. doi:10.1016/S0022-3476(05)83431-6.

Cismowski, M. J. 2017. "AG953 ☆." P. B9780128012383975263 in *Reference Module in Biomedical Sciences*. Elsevier.

Clark, Ira E., Mark W. Dodson, Changan Jiang, Joseph H. Cao, Jun R. Huh, Jae Hong Seol, Soon Ji Yoo, Bruce A. Hay, and Ming Guo. 2006. "Drosophila Pink1 Is Required for Mitochondrial Function and Interacts Genetically with Parkin." *Nature* 441(7097):1162–66. doi:10.1038/nature04779.

Cohen, Jennifer L., Shannon N. Nees, Gerson A. Valencia, Erika B. Rosenzweig, and Usha S. Krishnan. 2019. "Sildenafil Use in Children with Pulmonary Hypertension." *The Journal of Pediatrics* 205:29-34.e1. doi:10.1016/j.jpeds.2018.09.067.

Corbett, James L., and Stephen A. Duncan. 2019. "iPSC-Derived Hepatocytes as a Platform for Disease Modeling and Drug Discovery." *Frontiers in Medicine* 6:265. doi:10.3389/fmed.2019.00265.

Cosma, Maria Pia, Stefano Pepe, Ida Annunziata, Robert F. Newbold, Markus Grompe, Giancarlo Parenti, and Andrea Ballabio. 2003. "The Multiple Sulfatase Deficiency Gene Encodes an Essential and Limiting Factor for the Activity of Sulfatases." *Cell* 113(4):445–56. doi:10.1016/S0092-8674(03)00348-9.

Coukos, Robert, and Dimitri Krainc. 2024. "Key Genes and Convergent Pathogenic Mechanisms in Parkinson Disease." *Nature Reviews Neuroscience* 25(6):393–413. doi:10.1038/s41583-024-00812-2.

Dai, Xiaodong, Yongmei Wang, Yuexin Li, Yongping Zhong, Min Pei, Jing Long, Xingchen Dong, Yi-Li Chen, Qi Wang, Guifeng Wang, Bruce G. Gold, Arthur A. Vandenbark, Kim A. Neve, Halina Offner, and Chunhe Wang. 2022. "Tyrphostin A9 Protects Axons in Experimental Autoimmune Encephalomyelitis through Activation of ERKs." *Life Sciences* 294:120383. doi:10.1016/j.lfs.2022.120383.

Darin, Niklas, Anders Oldfors, Ali-Reza Moslemi, Elisabeth Holme, and Már Tulinius. 2001. "The Incidence of Mitochondrial Encephalomyopathies in Childhood: Clinical Features and Morphological, Biochemical, and DNA Abnormalities." *Annals of Neurology* 49(3):377–83. doi:10.1002/ana.75.

D'Aurelio, M., C. Vives-Bauza, M. M. Davidson, and G. Manfredi. 2010. "Mitochondrial DNA Background Modifies the Bioenergetics of NARP/MILS ATP6 Mutant Cells." *Human Molecular Genetics* 19(2):374–86. doi:10.1093/hmg/ddp503.

Dell'Agnello, Carlotta, Sara Leo, Alessandro Agostino, György Szabadkai, Cecilia Tiveron, Alessandra Zulian, Alessandro Prelle, Pierre Roubertoux, Rosario Rizzuto, and

Massimo Zeviani. 2007. “Increased Longevity and Refractoriness to Ca2+-Dependent Neurodegeneration in Surf1 Knockout Mice.” *Human Molecular Genetics* 16(4):431–44. doi:10.1093/hmg/ddl477.

Di Meo, I., S. Marchet, C. Lamperti, M. Zeviani, and C. Viscomi. 2017. “AAV9-Based Gene Therapy Partially Ameliorates the Clinical Phenotype of a Mouse Model of Leigh Syndrome.” *Gene Therapy* 24(10):661–67. doi:10.1038/gt.2017.53.

Dierks, Thomas, Achim Dickmanns, Andrea Preusser-Kunze, Bernhard Schmidt, Malaiyalam Mariappan, Kurt Von Figura, Ralf Ficner, and Markus Georg Rudolph. 2005. “Molecular Basis for Multiple Sulfatase Deficiency and Mechanism for Formylglycine Generation of the Human Formylglycine-Generating Enzyme.” *Cell* 121(4):541–52. doi:10.1016/j.cell.2005.03.001.

Dierks, Thomas, Bernhard Schmidt, Ljudmila V. Borissenko, Jianhe Peng, Andrea Preusser, Malaiyalam Mariappan, and Kurt Von Figura. 2003. “Multiple Sulfatase Deficiency Is Caused by Mutations in the Gene Encoding the Human Cα-Formylglycine Generating Enzyme.” *Cell* 113(4):435–44. doi:10.1016/S0092-8674(03)00347-7.

DiMauro, Salvatore, Serenella Servidei, Massimo Zeviani, Maja DiRocco, Darryl C. DeVivo, Stefano DiDonato, Graziella Uziel, Kenneth Berry, George Hoganson, Stanley D. Johnsen, and Peter C. Johnson. 1987. “Cytochrome *c* Oxidase Deficiency in Leigh Syndrome.” *Annals of Neurology* 22(4):498–506. doi:10.1002/ana.410220409.

Domek-Łopacińska, Katarzyna Urszula, and Joanna B. Strosznajder. 2010. “Cyclic GMP and Nitric Oxide Synthase in Aging and Alzheimer’s Disease.” *Molecular Neurobiology* 41(2–3):129–37. doi:10.1007/s12035-010-8104-x.

Duffy, Philip E., and Virginia M. Tennyson. 1965. “PHASE AND ELECTRON MICROSCOPIC OBSERVATIONS OF LEWY BODIES AND MELANIN GRANULES IN THE SUBSTANTIA NIGRA AND LOCUS CAERULEUS IN PARKINSON’S DISEASE:” *Journal of Neuropathology and Experimental Neurology* 24(3):398–414. doi:10.1097/00005072-196507000-00003.

Engeland, Kurt. 2022. “Cell Cycle Regulation: P53-P21-RB Signaling.” *Cell Death & Differentiation* 29(5):946–60. doi:10.1038/s41418-022-00988-z.

Eto, Y., I. Gomibuchi, F. Umezawa, and T. Tsuda. 1987. “Pathochemistry, Pathogenesis and Enzyme Replacement inMultiple-Sulfatase Deficiency.” *Enzyme* 38(1–4):273–79. doi:10.1159/000469216.

Farooqui, Akhlaq A. 2022. “Contribution of Neuroinflammation, Resolution, and Neuroprotection in Neurodegenerative Diseases.” Pp. 121–60 in *Neuroinflammation, Resolution, and Neuroprotection in the Brain*. Elsevier.

Farooqui, T., and A. A. Farooqui. 2016. “Perspective and Directions for Future Research on Trace Amines and Neurological Disorders.” Pp. 369–86 in *Trace Amines and Neurological Disorders*. Elsevier.

Feigin, Valery L., Theo Vos, Emma Nichols, Mayowa O. Owolabi, William M. Carroll, Martin Dichgans, Günther Deuschl, Priya Parmar, Michael Brainin, and Christopher

Murray. 2020. “The Global Burden of Neurological Disorders: Translating Evidence into Policy.” *The Lancet Neurology* 19(3):255–65. doi:10.1016/S1474-4422(19)30411-9.

Fermaglich, Lewis J., and Kathleen L. Miller. 2023. “A Comprehensive Study of the Rare Diseases and Conditions Targeted by Orphan Drug Designations and Approvals over the Forty Years of the Orphan Drug Act.” *Orphanet Journal of Rare Diseases* 18(1):163. doi:10.1186/s13023-023-02790-7.

Ferreira, Carlos R. 2019. “The Burden of Rare Diseases.” *American Journal of Medical Genetics Part A* 179(6):885–92. doi:10.1002/ajmg.a.61124.

Flotte, Terence R., and Dominic J. Gessler. 2022. “Gene Therapy for Rare Neurological Disorders.” *Clinical Pharmacology & Therapeutics* 111(4):743–57. doi:10.1002/cpt.2543.

Foust, Kevin D., Emily Nurre, Chrystal L. Montgomery, Anna Hernandez, Curtis M. Chan, and Brian K. Kaspar. 2009. “Intravascular AAV9 Preferentially Targets Neonatal Neurons and Adult Astrocytes.” *Nature Biotechnology* 27(1):59–65. doi:10.1038/nbt.1515.

Francis, Sharron H., and Jackie D. Corbin. 2004. “Sildenafil, Pharmacology of a Highly Selective PDE5 Inhibitor.” Pp. 15–33 in *Sildenafil*, edited by U. Dunzendorfer. Basel: Birkhäuser Basel.

Galera-Monge, Teresa, Francisco Zurita-Díaz, Isaac Canals, Marita Grønning Hansen, Laura Rufián-Vázquez, Johannes K. Ehinger, Eskil Elmér, Miguel A. Martin, Rafael Garesse, Henrik Ahlenius, and M. Esther Gallardo. 2020. “Mitochondrial Dysfunction and Calcium Dysregulation in Leigh Syndrome Induced Pluripotent Stem Cell Derived Neurons.” *International Journal of Molecular Sciences* 21(9):3191. doi:10.3390/ijms21093191.

Galiè, Nazzareno, Hossein A. Ghofrani, Adam Torbicki, Robyn J. Barst, Lewis J. Rubin, David Badesch, Thomas Fleming, Tamiza Parpia, Gary Burgess, Angelo Branzi, Friedrich Grimminger, Marcin Kurzyna, and Gérald Simonneau. 2005. “Sildenafil Citrate Therapy for Pulmonary Arterial Hypertension.” *New England Journal of Medicine* 353(20):2148–57. doi:10.1056/NEJMoa050010.

Geisler, John G., Krisztina Marosi, Joshua Halpern, and Mark P. Mattson. 2017. “DNP, Mitochondrial Uncoupling, and Neuroprotection: A Little Dab’ll Do Ya.” *Alzheimer’s & Dementia* 13(5):582–91. doi:10.1016/j.jalz.2016.08.001.

Ghofrani, Hossein A., Ian H. Osterloh, and Friedrich Grimminger. 2006. “Sildenafil: From Angina to Erectile Dysfunction to Pulmonary Hypertension and Beyond.” *Nature Reviews Drug Discovery* 5(8):689–702. doi:10.1038/nrd2030.

Ginhoux, Florent, Melanie Greter, Marylene Leboeuf, Sayan Nandi, Peter See, Solen Gokhan, Mark F. Mehler, Simon J. Conway, Lai Guan Ng, E. Richard Stanley, Igor M. Samokhvalov, and Miriam Merad. 2010. “Fate Mapping Analysis Reveals That Adult Microglia Derive from Primitive Macrophages.” *Science* 330(6005):841–45. doi:10.1126/science.1194637.

Gold, Wendy A., Alan K. Percy, Jeffrey L. Neul, Stuart R. Cobb, Lucas Pozzo-Miller, Jasmeen K. Issar, Bruria Ben-Zeev, Aglaia Vignoli, and Walter E. Kaufmann. 2024. "Rett Syndrome." *Nature Reviews Disease Primers* 10(1):84. doi:10.1038/s41572-024-00568-0.

Goldenberg, Marvin M. 2008. "Medical Management of Parkinson's Disease." *P & T: A Peer-Reviewed Journal for Formulary Management* 33(10):590–606.

Goldstein, Irwin, Arthur L. Burnett, Raymond C. Rosen, Peter W. Park, and Vera J. Stecher. 2019. "The Serendipitous Story of Sildenafil: An Unexpected Oral Therapy for Erectile Dysfunction." *Sexual Medicine Reviews* 7(1):115–28. doi:10.1016/j.sxmr.2018.06.005.

Goldstein, Irwin, Tom F. Lue, Harin Padma-Nathan, Raymond C. Rosen, William D. Steers, and Pierre A. Wicker. 1998. "Oral Sildenafil in the Treatment of Erectile Dysfunction." *New England Journal of Medicine* 338(20):1397–1404. doi:10.1056/NEJM199805143382001.

Gorgogietas, Vyron, Amélie Weiss, Loïc Cousin, David Hoffmann, Karen Schmitt, Arnaud Ogier, Peter A. Barbuti, Bruno F. R. Santos, Ibrahim Boussaad, Annika Wittich, Andrea Zaliani, Ole Pless, Rejko Krüger, Peter Sommer, and Johannes H. Wilbertz. 2025. "Morphological Profiling Reveals Neuroprotection via Mitochondrial Uncoupling in Human Dopaminergic Neurons." *Scientific Reports* 15(1):29507. doi:10.1038/s41598-025-14735-0.

Hanaford, Allison R., Yoon-Jae Cho, and Hiroyuki Nakai. 2022. "AAV-Vector Based Gene Therapy for Mitochondrial Disease: Progress and Future Perspectives." *Orphanet Journal of Rare Diseases* 17(1):217. doi:10.1186/s13023-022-02324-7.

Hanson, Sarah R., Michael D. Best, and Chi-Huey Wong. 2004. "Sulfatases: Structure, Mechanism, Biological Activity, Inhibition, and Synthetic Utility." *Angewandte Chemie International Edition* 43(43):5736–63. doi:10.1002/anie.200300632.

Harley, Calvin B., A. Bruce Futcher, and Carol W. Greider. 1990. "Telomeres Shorten during Ageing of Human Fibroblasts." *Nature* 345(6274):458–60. doi:10.1038/345458a0.

Hinderer, Christian, Nathan Katz, Elizabeth L. Buza, Cecilia Dyer, Tamara Goode, Peter Bell, Laura K. Richman, and James M. Wilson. 2018. "Severe Toxicity in Nonhuman Primates and Piglets Following High-Dose Intravenous Administration of an Adeno-Associated Virus Vector Expressing Human SMN." *Human Gene Therapy* 29(3):285–98. doi:10.1089/hum.2018.015.

Hinkson, Izumi V., Benjamin Madej, and Eric A. Stahlberg. 2020. "Accelerating Therapeutics for Opportunities in Medicine: A Paradigm Shift in Drug Discovery." *Frontiers in Pharmacology* 11:770. doi:10.3389/fphar.2020.00770.

Holland, Ian, and Jamie A. Davies. 2020. "Automation in the Life Science Research Laboratory." *Frontiers in Bioengineering and Biotechnology* 8:571777. doi:10.3389/fbioe.2020.571777.

Holt, I. J., A. E. Harding, R. K. Petty, and J. A. Morgan-Hughes. 1990. "A New Mitochondrial Disease Associated with Mitochondrial DNA Heteroplasmy." *American Journal of Human Genetics* 46(3):428–33.

Hong, Chan-Mi, Ji-Hoon Na, Soyoung Park, and Young-Mock Lee. 2020. "Clinical Characteristics of Early-Onset and Late-Onset Leigh Syndrome." *Frontiers in Neurology* 11:267. doi:10.3389/fneur.2020.00267.

Hughes, Jp, S. Rees, Sb Kalindjian, and Kl Philpott. 2011. "Principles of Early Drug Discovery." *British Journal of Pharmacology* 162(6):1239–49. doi:10.1111/j.1476-5381.2010.01127.x.

Human Fertilisation and Embryology Authority (HFEA). 2015. "Explanatory Memorandum to the Human Fertilisation and Embryology (Mitochondrial Donation) Regulations 2015."

Hutchin, T., and G. Cortopassi. 1995. "A Mitochondrial DNA Clone Is Associated with Increased Risk for Alzheimer Disease." *Proceedings of the National Academy of Sciences* 92(15):6892–95. doi:10.1073/pnas.92.15.6892.

Hyslop, Louise. 2018. "Pronuclear Transfer in Human Oocytes." Pp. 31–36 in *Mouse Oocyte Development*. Vol. 1818, *Methods in Molecular Biology*, edited by M.-H. Verlhac and M.-E. Terret. New York, NY: Springer New York.

Ikeuchi, Takeshi, Akiyoshi Kakita, Atsushi Shiga, Kensaku Kasuga, Hiryoyuki Kaneko, Chun-Feng Tan, Jiro Idezuka, Koichi Wakabayashi, Osamu Onodera, Takeshi Iwatsubo, Masatoyo Nishizawa, Hitoshi Takahashi, and Atsushi Ishikawa. 2008. "Patients Homozygous and Heterozygous for SNCA Duplication in a Family With Parkinsonism and Dementia." *Archives of Neurology* 65(4):514. doi:10.1001/archneur.65.4.514.

Inak, Gizem, Agnieszka Rybak-Wolf, Pawel Lisowski, Tancredi M. Pentimalli, René Jüttner, Petar Glažar, Karan Uppal, Emanuela Bottani, Dario Brunetti, Christopher Secker, Annika Zink, David Meierhofer, Marie-Thérèse Henke, Monishita Dey, Ummi Ciptasari, Barbara Mlody, Tobias Hahn, Maria Berruezo-Llacuna, Nikos Karaiskos, Michela Di Virgilio, Johannes A. Mayr, Saskia B. Wortmann, Josef Priller, Michael Gotthardt, Dean P. Jones, Ertan Mayatepek, Werner Stenzel, Sebastian Diecke, Ralf Kühn, Erich E. Wanker, Nikolaus Rajewsky, Markus Schuelke, and Alessandro Prigione. 2021. "Defective Metabolic Programming Impairs Early Neuronal Morphogenesis in Neural Cultures and an Organoid Model of Leigh Syndrome." *Nature Communications* 12(1):1929. doi:10.1038/s41467-021-22117-z.

J. Parkinson. 1817. "An Essay on the Shaking Palsy."

Jeibmann, Astrid, and Werner Paulus. 2009. "Drosophila Melanogaster as a Model Organism of Brain Diseases." *International Journal of Molecular Sciences* 10(2):407–40. doi:10.3390/ijms10020407.

Kachroo, Aashiq H., Jon M. Laurent, Christopher M. Yellman, Austin G. Meyer, Claus O. Wilke, and Edward M. Marcotte. 2015. "Systematic Humanization of Yeast Genes

Reveals Conserved Functions and Genetic Modularity." *Science* 348(6237):921–25. doi:10.1126/science.aaa0769.

Kadenbach, Bernhard. 2012. "Introduction to Mitochondrial Oxidative Phosphorylation." Pp. 1–11 in *Mitochondrial Oxidative Phosphorylation*. Vol. 748, *Advances in Experimental Medicine and Biology*, edited by B. Kadenbach. New York, NY: Springer New York.

Kapoor, Sumedha Arora, Poonam Choudhary, and Ramesh Chand Kasana. 2025. "Exploring CRISPR/Cas9-Mediated Gene Editing Advances in Conventional and Non-Conventional Yeast Species." *Applied Biochemistry and Biotechnology*. doi:10.1007/s12010-025-05382-2.

Kaun, Karla R., and Marla B. Sokolowski. 2009. "cGMP-Dependent Protein Kinase: Linking Foraging to Energy Homeostasis" edited by A. Hilliker. *Genome* 52(1):1–7. doi:10.1139/G08-090.

Khaleva, Ekaterina, Anna Rattu, Chris Brightling, Andrew Bush, Arnaud Bourdin, Apostolos Bossios, Kian Fan Chung, Rekha Chaudhuri, Courtney Coleman, Ratko Djukanovic, Sven-Erik Dahlén, Andrew Exley, Louise Fleming, Stephen J. Fowler, Atul Gupta, Eckard Hamelmann, Gerard H. Koppelman, Erik Melén, Vera Mahler, Paul Seddon, Florian Singer, Celeste Porsbjerg, Valeria Ramiconi, Franca Rusconi, Valentyna Yasinska, and Graham Roberts. 2023. "Definitions of Non-Response and Response to Biological Therapy for Severe Asthma: A Systematic Review." *ERJ Open Research* 9(3):00444–02022. doi:10.1183/23120541.00444-2022.

Konno, Takuya, Owen A. Ross, Andreas Puschmann, Dennis W. Dickson, and Zbigniew K. Wszolek. 2016. "Autosomal Dominant Parkinson's Disease Caused by SNCA Duplications." *Parkinsonism & Related Disorders* 22:S1–6. doi:10.1016/j.parkreldis.2015.09.007.

Kotova, E. A., and Y. N. Antonenko. 2022. "Fifty Years of Research on Protonophores: Mitochondrial Uncoupling As a Basis for Therapeutic Action." *Acta Naturae* 14(1):4–13. doi:10.32607/actanaturae.11610.

Kozlov, Andrey V., Sabzali Javadov, and Natascha Sommer. 2024. "Cellular ROS and Antioxidants: Physiological and Pathological Role." *Antioxidants (Basel, Switzerland)* 13(5):602. doi:10.3390/antiox13050602.

Krieg, Kim, Silvia Materna-Reichelt, Tobias Naber, Fatima-Zahra Rachad, Pia Kauven, Arjen Weller, Undine Haferkamp, Annika Wittich, Andrea Zaliani, Marcel S. Woo, Mark Walkenhorst, Malte Siegmund, Jann Harberts, Robert Zierold, Robert Blick, Christian Conze, Patricia Muschong, Dominik Miltner, Manuel A. Friese, Mario Mezler, Heiko Siegmund, Katja Evert, Susanne Krasemann, Nataša Stojanović Gužvić, Christoph A. Klein, Melanie Werner-Klein, Joachim Wegener, and Ole Pless. 2025. "Cortical Organoid-Derived Models of the Melanoma Brain Metastatic Niche Enable Prioritization of Cancer-Targeting Drugs." *Cell Reports Methods* 101236. doi:10.1016/j.crmeth.2025.101236.

Kruse, Shane E., William C. Watt, David J. Marcinek, Raj P. Kapur, Kenneth A. Schenkman, and Richard D. Palmiter. 2008. "Mice with Mitochondrial Complex I Deficiency

Develop a Fatal Encephalomyopathy." *Cell Metabolism* 7(4):312–20. doi:10.1016/j.cmet.2008.02.004.

Kucharczyk, Roza, Marie-France Giraud, Daniel Brèthes, Monica Wysocka-Kapcinska, Nahia Ezkurdia, Bénédicte Salin, Jean Velours, Nadine Camougrand, Francis Haraux, and Jean-Paul Di Rago. 2013. "Defining the Pathogenesis of Human mtDNA Mutations Using a Yeast Model: The Case of T8851C." *The International Journal of Biochemistry & Cell Biology* 45(1):130–40. doi:10.1016/j.biocel.2012.07.001.

Kumar, Rahul, Amruthanjali T, Siva Singothu, Shashi Bala Singh, and Vasundhra Bhandari. 2022. "Uncoupling Proteins as a Therapeutic Target for the Development of New Era Drugs against Neurodegenerative Disorder." *Biomedicine & Pharmacotherapy* 147:112656. doi:10.1016/j.biopha.2022.112656.

Kuzmin, Dmitry A., Maria V. Shutova, Natalie R. Johnston, Owen P. Smith, Vasily V. Fedorin, Yury S. Kukushkin, Johannes C. M. Van Der Loo, and Elaine C. Johnstone. 2021. "The Clinical Landscape for AAV Gene Therapies." *Nature Reviews Drug Discovery* 20(3):173–74. doi:10.1038/d41573-021-00017-7.

Lasserre, Jean-Paul, Alain Dautant, Raeka S. Aiyar, Roza Kucharczyk, Annie Glatigny, Déborah Tribouillard-Tanvier, Joanna Rytka, Marc Blondel, Natalia Skoczen, Pascal Reynier, Laras Pitayu, Agnès Rötig, Agnès Delahodde, Lars M. Steinmetz, Geneviève Dujardin, Vincent Procaccio, and Jean-Paul Di Rago. 2015. "Yeast as a System for Modeling Mitochondrial Disease Mechanisms and Discovering Therapies." *Disease Models & Mechanisms* 8(6):509–26. doi:10.1242/dmm.020438.

Lehninger. 1961. "How Cells Transform Energy." 205(3):62–73.

Leigh, D. 1951. "SUBACUTE NECROTIZING ENCEPHALOMYELOPATHY IN AN INFANT." *Journal of Neurology, Neurosurgery & Psychiatry* 14(3):216–21. doi:10.1136/jnnp.14.3.216.

Li, Chengwen, and R. Jude Samulski. 2020. "Engineering Adeno-Associated Virus Vectors for Gene Therapy." *Nature Reviews Genetics* 21(4):255–72. doi:10.1038/s41576-019-0205-4.

Li, Haorong, Martine Uittenbogaard, Ling Hao, and Anne Chiaramello. 2021. "Clinical Insights into Mitochondrial Neurodevelopmental and Neurodegenerative Disorders: Their Biosignatures from Mass Spectrometry-Based Metabolomics." *Metabolites* 11(4):233. doi:10.3390/metabo11040233.

Ling, Qinglan, Matthew Rioux, Harrison Higgs, Yuhui Hu, Scarlett E. Dwyer, and Steven J. Gray. 2025. "Improved AAV9-Based Gene Therapy Design for SURF1-Related Leigh Syndrome with Minimal Toxicity." *Molecular Therapy Methods & Clinical Development* 33(3):101554. doi:10.1016/j.omtm.2025.101554.

Ling, Qinglan, Matthew Rioux, Yuhui Hu, MinJae Lee, and Steven J. Gray. 2021. "Adeno-Associated Viral Vector Serotype 9-Based Gene Replacement Therapy for SURF1-Related Leigh Syndrome." *Molecular Therapy - Methods & Clinical Development* 23:158–68. doi:10.1016/j.omtm.2021.09.001.

Liu, Lei, Yanjun Li, Guo Chen, and Quan Chen. 2023. "Crosstalk between Mitochondrial Biogenesis and Mitophagy to Maintain Mitochondrial Homeostasis." *Journal of Biomedical Science* 30(1):86. doi:10.1186/s12929-023-00975-7.

Lorenz, Carmen, Pierre Lesimple, Raul Bukowiecki, Annika Zink, Gizem Inak, Barbara Mlody, Manvendra Singh, Marcus Semtner, Nancy Mah, Karine Auré, Megan Leong, Oleksandr Zabiegalov, Ekaterini-Maria Lyras, Vanessa Pfiffer, Beatrix Fauler, Jenny Eichhorst, Burkhard Wiesner, Norbert Huebner, Josef Priller, Thorsten Mielke, David Meierhofer, Zsuzsanna Izsvák, Jochen C. Meier, Frédéric Bouillaud, James Adjaye, Markus Schuelke, Erich E. Wanker, Anne Lombès, and Alessandro Prigione. 2017. "Human iPSC-Derived Neural Progenitors Are an Effective Drug Discovery Model for Neurological mtDNA Disorders." *Cell Stem Cell* 20(5):659-674.e9. doi:10.1016/j.stem.2016.12.013.

Madelaire, Carla B., Amy C. Klink, William J. Israelsen, and Allyson G. Hindle. 2022. "Fibroblasts as an Experimental Model System for the Study of Comparative Physiology." *Comparative Biochemistry and Physiology Part B: Biochemistry and Molecular Biology* 260:110735. doi:10.1016/j.cbpb.2022.110735.

Magro, Giuseppe, Vincenzo Laterza, and Federico Tosto. 2025. "Leigh Syndrome: A Comprehensive Review of the Disease and Present and Future Treatments." *Biomedicines* 13(3):733. doi:10.3390/biomedicines13030733.

Malpartida, Ana Belen, Matthew Williamson, Derek P. Narendra, Richard Wade-Martins, and Brent J. Ryan. 2021. "Mitochondrial Dysfunction and Mitophagy in Parkinson's Disease: From Mechanism to Therapy." *Trends in Biochemical Sciences* 46(4):329–43. doi:10.1016/j.tibs.2020.11.007.

Mariz, Segundo, James H. Reese, Kerstin Westermark, Lesley Greene, Takahiro Goto, Tatsuro Hoshino, Jordi Llinares-Garcia, and Bruno Sepodes. 2016. "Worldwide Collaboration for Orphan Drug Designation." *Nature Reviews Drug Discovery* 15(6):440–41. doi:10.1038/nrd.2016.80.

Mashima, Ryuichi, and Mahito Nakanishi. 2022. "Mammalian Sulfatases: Biochemistry, Disease Manifestation, and Therapy." *International Journal of Molecular Sciences* 23(15):8153. doi:10.3390/ijms23158153.

Matilla-Dueñas, Antoni, Marc Corral-Juan, Agustí Rodríguez-Palmero Seuma, Dolores Vilas, Lourdes Ispierto, Sara Morais, Jorge Sequeiros, Isabel Alonso, Víctor Volpini, Carmen Serrano-Munuera, Guillem Pintos-Morell, Ramiro Álvarez, and Ivelisse Sánchez. 2017. "Rare Neurodegenerative Diseases: Clinical and Genetic Update." Pp. 443–96 in *Rare Diseases Epidemiology: Update and Overview*. Vol. 1031, *Advances in Experimental Medicine and Biology*, edited by M. Posada De La Paz, D. Taruscio, and S. C. Groft. Cham: Springer International Publishing.

McCormick, Elizabeth M., Kierstin Keller, Julie P. Taylor, Alison J. Coffey, Lishuang Shen, Danuta Krotoski, Brian Harding, NICHD ClinGen U24 Mitochondrial Disease Gene Curation Expert Panel, Xiaowu Gai, Marni J. Falk, Zarazuela Zolkipli-Cunningham, and Shamima Rahman. 2023. "Expert Panel Curation of 113 Primary Mitochondrial Disease Genes for the Leigh Syndrome Spectrum." *Annals of Neurology* 94(4):696–712. doi:10.1002/ana.26716.

McFarland, Robert, Louise A. Hyslop, Catherine Feeney, Rekha N. Pillai, Emma L. Blakely, Eilis Moody, Matthew Prior, Anita Devlin, Robert W. Taylor, Mary Herbert, Meenakshi Choudhary, Jane A. Stewart, and Douglass M. Turnbull. 2025. "Mitochondrial Donation in a Reproductive Care Pathway for mtDNA Disease." *New England Journal of Medicine* 393(5):461–68. doi:10.1056/NEJMoa2503658.

Menacho, Carmen, Satoshi Okawa, Iris Álvarez-Merz, Annika Wittich, Mikel Muñoz-Oreja, Pawel Lisowski, Mario López Martín, Tancredi Massimo Pentimalli, Shiri Zakin, Mathuravani Thevandavakkam, Caleb Jerred, Selene Lickfett, Laura Petersilie, Agnieszka Rybak-Wolf, Annette Seibt, Diran Herebian, Gizem Inak, Susanne Brodesser, Andrea Zaliani, Barbara Mlody, Justin Donnelly, Kasey Woleben, Francesc Xavier Soriano, Jose C. Fernandez-Checa, Natascia Ventura, Sidney Cambridge, Ertan Mayatepek, Antonella Spinazzola, Markus Schuelke, Nikolaus Rajewsky, Andrea Rossi, Alex Peralvarez-Marin, Felix Distelmaier, Ethan Perlstein, Ian J. Holt, Emma Puighermanal, Ole Pless, Christine R. Rose, Antonio Del Sol, and Alessandro Prigione. 2026. "Accelerating Leigh Syndrome Drug Discovery through Deep Learning Screening in Brain Organoids." *Nature Communications* 17(1):3570. doi:10.1038/s41467-026-71391-2.

Meng, Xin, Lan Yang, Zi Liao, Feiyue Sun, Meng Su, and Zhigang Mei. 2025. "Modeling Central Nervous System Disorders in Zebrafish: Novel Insights into Pathophysiology and Therapeutic Discovery." *Neurobiology of Disease* 216:107123. doi:10.1016/j.nbd.2025.107123.

Meyer-Lindenberg, Andreas, and Heike Tost. 2012. "Neural Mechanisms of Social Risk for Psychiatric Disorders." *Nature Neuroscience* 15(5):663–68. doi:10.1038/nn.3083.

Migliore, Lucia, and Fabio Coppedè. 2002. "Genetic and Environmental Factors in Cancer and Neurodegenerative Diseases." *Mutation Research/Reviews in Mutation Research* 512(2–3):135–53. doi:10.1016/S1383-5742(02)00046-7.

Miyoshi, Koho, Yasushi Morimura, and Kiyoshi Maeda, eds. 2010. *Neuropsychiatric Disorders*. Tokyo: Springer Japan.

Monier, Anne, Homa Adle-Biassette, Anne-Lise Delezoide, Philippe Evrard, Pierre Gressens, and Catherine Verney. 2007. "Entry and Distribution of Microglial Cells in Human Embryonic and Fetal Cerebral Cortex:" *Journal of Neuropathology and Experimental Neurology* 66(5):372–82. doi:10.1097/nen.0b013e3180517b46.

Morofuji, Yoichi, and Shinsuke Nakagawa. 2020. "Drug Development for Central Nervous System Diseases Using In Vitro Blood-Brain Barrier Models and Drug Repositioning." *Current Pharmaceutical Design* 26(13):1466–85. doi:10.2174/1381612826666200224112534.

Moura, João P., Paulo J. Oliveira, and Ana M. Urbano. 2025. "Mitochondria: An Overview of Their Origin, Genome, Architecture, and Dynamics." *Biochimica et Biophysica Acta (BBA) - Molecular Basis of Disease* 1871(5):167803. doi:10.1016/j.bbadis.2025.167803.

Mullard, Asher. 2021. “Gene Therapy Community Grapples with Toxicity Issues, as Pipeline Matures.” *Nature Reviews Drug Discovery* 20(11):804–5. doi:10.1038/d41573-021-00164-x.

Mutti, Christian, Pedro Silva-Pinheiro, and Michal Minczuk. 2022. “Fixing the Powerhouse: Genetic Engineering of Mitochondrial DNA.” *The Biochemist* 44(4):9–13. doi:10.1042/bio_2022_120.

Nakai, Ritsuko, Stella Varnum, Rachael L. Field, Henyun Shi, Rocky Giwa, Wentong Jia, Samantha J. Krysa, Eva F. Cohen, Nicholas Borcherding, Russell P. Saneto, Rick C. Tsai, Masashi Suganuma, Hisashi Ohta, Takafumi Yokota, and Jonathan R. Brestoff. 2024. “Mitochondria Transfer-Based Therapies Reduce the Morbidity and Mortality of Leigh Syndrome.” *Nature Metabolism* 6(10):1886–96. doi:10.1038/s42255-024-01125-5.

Nguengang Wakap, Stéphanie, Deborah M. Lambert, Annie Olry, Charlotte Rodwell, Charlotte Gueydan, Valérie Lanneau, Daniel Murphy, Yann Le Cam, and Ana Rath. 2020. “Estimating Cumulative Point Prevalence of Rare Diseases: Analysis of the Orphanet Database.” *European Journal of Human Genetics* 28(2):165–73. doi:10.1038/s41431-019-0508-0.

Nicoletti, Valentina, Giovanni Palermo, Eleonora Del Prete, Michelangelo Mancuso, and Roberto Ceravolo. 2021. “Understanding the Multiple Role of Mitochondria in Parkinson’s Disease and Related Disorders: Lesson From Genetics and Protein–Interaction Network.” *Frontiers in Cell and Developmental Biology* 9:636506. doi:10.3389/fcell.2021.636506.

Norat, Pedro, Sauson Soldozy, Jennifer D. Sokolowski, Catherine M. Gorick, Jeyan S. Kumar, Youngrok Chae, Kaan Yağmurlu, Francesco Prada, Melanie Walker, Michael R. Levitt, Richard J. Price, Petr Tvrdik, and M. Yashar S. Kalani. 2020. “Mitochondrial Dysfunction in Neurological Disorders: Exploring Mitochondrial Transplantation.” *Npj Regenerative Medicine* 5(1):22. doi:10.1038/s41536-020-00107-x.

Onos, Kristen D., Stacey J. Sukoff Rizzo, Gareth R. Howell, and Michael Sasner. 2016. “Toward More Predictive Genetic Mouse Models of Alzheimer’s Disease.” *Brain Research Bulletin* 122:1–11. doi:10.1016/j.brainresbull.2015.12.003.

P. Mitchell. 1961. “Coupling of Phosphorylation to Electron and Hydrogen Transfer by a Chemi-Osmotic Type of Mechanism.” (191(4784), 144-148.).

Pardridge, William M. 2005. “The Blood-Brain Barrier: Bottleneck in Brain Drug Development.” *NeuroRX* 2(1):3–14. doi:10.1602/neurorx.2.1.3.

Park, Jeehye, Sung Bae Lee, Sungkyu Lee, Yongsung Kim, Saera Song, Sunhong Kim, Eunkyung Bae, Jaeseob Kim, Minho Shong, Jin-Man Kim, and Jongkyeong Chung. 2006. “Mitochondrial Dysfunction in Drosophila PINK1 Mutants Is Complemented by Parkin.” *Nature* 441(7097):1157–61. doi:10.1038/nature04788.

Pathak, Nishit, Sunil Kumar Vimal, Ishi Tandon, Lokesh Agrawal, Cao Hongyi, and Sanjib Bhattacharyya. 2022. “Neurodegenerative Disorders of Alzheimer, Parkinsonism, Amyotrophic Lateral Sclerosis and Multiple Sclerosis: An Early Diagnostic

Approach for Precision Treatment." *Metabolic Brain Disease* 37(1):67–104. doi:10.1007/s11011-021-00800-w.

Paupardin-Tritsch, Danièle, Constance Hammond, Hersch M. Gerschenfeld, Angus C. Nairn, and P. Greengard. 1986. "cGMP-Dependent Protein Kinase Enhances Ca2+ Current and Potentiates the Serotonin-Induced Ca2+ Current Increase in Snail Neurones." *Nature* 323(6091):812–14. doi:10.1038/323812a0.

Peall, Kathryn J., Michael J. Owen, and Jeremy Hall. 2024. "Rare Genetic Brain Disorders with Overlapping Neurological and Psychiatric Phenotypes." *Nature Reviews Neurology* 20(1):7–21. doi:10.1038/s41582-023-00896-x.

Pickles, Sarah, Pierre Vigié, and Richard J. Youle. 2018. "Mitophagy and Quality Control Mechanisms in Mitochondrial Maintenance." *Current Biology* 28(4):R170–85. doi:10.1016/j.cub.2018.01.004.

Polymeropoulos, Mihael H., Christian Lavedan, Elisabeth Leroy, Susan E. Ide, Anindya Dehejia, Amalia Dutra, Brian Pike, Holly Root, Jeffrey Rubenstein, Rebecca Boyer, Edward S. Stenroos, Settara Chandrasekharappa, Aglaia Athanassiadou, Theodore Papapetropoulos, William G. Johnson, Alice M. Lazzarini, Roger C. Duvoisin, Giuseppe Di Iorio, Lawrence I. Golbe, and Robert L. Nussbaum. 1997. "Mutation in the α-Synuclein Gene Identified in Families with Parkinson's Disease." *Science* 276(5321):2045–47. doi:10.1126/science.276.5321.2045.

Poole, Olivia V., Chris M. Everett, Sonia Gandhi, Silvia Marino, Enrico Bugiardini, Cathy Woodward, Amanda Lam, Ros Quinlivan, Michael G. Hanna, and Robert D. S. Pitceathly. 2019. "Adult-Onset Leigh Syndrome Linked to the Novel Stop Codon Mutation m.6579G>A in MT-CO1." *Mitochondrion* 47:294–97. doi:10.1016/j.mito.2019.02.004.

Puerta, Elena, Isabel Hervias, Lucía Barros-Miñones, Joaquin Jordan, Ana Ricobaraza, Mar Cuadrado-Tejedor, Ana García-Osta, and Norberto Aguirre. 2010. "Sildenafil Protects against 3-Nitropropionic Acid Neurotoxicity through the Modulation of Calpain, CREB, and BDNF." *Neurobiology of Disease* 38(2):237–45. doi:10.1016/j.nbd.2010.01.013.

Puzzo, Daniela, Ottavio Vitolo, Fabrizio Trinchese, Joel P. Jacob, Agostino Palmeri, and Ottavio Arancio. 2005. "Amyloid-β Peptide Inhibits Activation of the Nitric Oxide/cGMP/cAMP-Responsive Element-Binding Protein Pathway during Hippocampal Synaptic Plasticity." *The Journal of Neuroscience* 25(29):6887–97. doi:10.1523/JNEUROSCI.5291-04.2005.

Quinn, Peter M. J., Paula I. Moreira, António Francisco Ambrósio, and C. Henrique Alves. 2020. "PINK1/PARKIN Signalling in Neurodegeneration and Neuroinflammation." *Acta Neuropathologica Communications* 8(1):189. doi:10.1186/s40478-020-01062-w.

Rahman, S., R. B. Blok, H. -H. M. Dahl, D. M. Danks, D. M. Kirby, C. W. Chow, J. Christodoulou, and D. R. Thorburn. 1996. "Leigh Syndrome: Clinical Features and Biochemical and DNA Abnormalities." *Annals of Neurology* 39(3):343–51. doi:10.1002/ana.410390311.

Recino, Asha, Melissa L. D. Rayner, Jennifer L. Rohn, Oscar Della Pasqua, Asha Recino, Melissa L. D. Rayner, Jennifer L. Rohn, Brian Carter, Anna Cupani, Annegret Dahlmann-Noor, Thomas Foltynie, Jennifer Furman, Stephen Hobbiger, Eleonora Lugarà, Sara E. Mole, Mine Orlu, James B. Phillips, Paolo Spingardi, and Oscar Della Pasqua. 2025. "Therapeutic Innovation in Drug Repurposing: Challenges and Opportunities." *Drug Discovery Today* 30(7):104390. doi:10.1016/j.drudis.2025.104390.

Reynaud-Dulaurier, Robin, Giorgia Benegiamo, Elena Marrocco, Racha Al-Tannir, Enrico Maria Surace, Johan Auwerx, and Michael Decressac. 2020. "Gene Replacement Therapy Provides Benefit in an Adult Mouse Model of Leigh Syndrome." *Brain* 143(6):1686–96. doi:10.1093/brain/awaa105.

Richter, Trevor, Sandra Nestler-Parr, Robert Babela, Zeba M. Khan, Theresa Tesoro, Elizabeth Molsen, and Dyfrig A. Hughes. 2015. "Rare Disease Terminology and Definitions—A Systematic Global Review: Report of the ISPOR Rare Disease Special Interest Group." *Value in Health* 18(6):906–14. doi:10.1016/j.jval.2015.05.008.

Roessler, Helen I., Nine V. A. M. Knoers, Mieke M. Van Haelst, and Gijs Van Haaften. 2021. "Drug Repurposing for Rare Diseases." *Trends in Pharmacological Sciences* 42(4):255–67. doi:10.1016/j.tips.2021.01.003.

Romero-Morales, Alejandra I., Gabriella L. Robertson, Anuj Rastogi, Megan L. Rasmussen, Hoor Temuri, Gregory Scott McElroy, Ram Prosad Chakrabarty, Lawrence Hsu, Paula M. Almonacid, Bryan A. Millis, Navdeep S. Chandel, Jean-Philippe Cartailler, and Vivian Gama. 2022. "Human iPSC-Derived Cerebral Organoids Model Features of Leigh Syndrome and Reveal Abnormal Corticogenesis." *Development* 149(20):dev199914. doi:10.1242/dev.199914.

Rosenberg, Gary A. 2012. "Neurological Diseases in Relation to the Blood–Brain Barrier." *Journal of Cerebral Blood Flow & Metabolism* 32(7):1139–51. doi:10.1038/jcbfm.2011.197.

Rossignol, Rodrigue, Benjamin Faustin, Christophe Rocher, Monique Malgat, Jean-Pierre Mazat, and Thierry Letellier. 2003. "Mitochondrial Threshold Effects." *Biochemical Journal* 370(3):751–62. doi:10.1042/bj20021594.

Ryan, Sean K., Kelly L. Jordan-Sciutto, and Stewart A. Anderson. 2020. "Protocol for Tri-Culture of hiPSC-Derived Neurons, Astrocytes, and Microglia." *STAR Protocols* 1(3):100190. doi:10.1016/j.xpro.2020.100190.

Saavedra, Ana, Albert Giralt, Helena Arumí, Jordi Alberch, and Esther Pérez-Navarro. 2013. "Regulation of Hippocampal cGMP Levels as a Candidate to Treat Cognitive Deficits in Huntington's Disease" edited by P. Gonzalez-Alegre. *PLoS ONE* 8(9):e73664. doi:10.1371/journal.pone.0073664.

Sagara, Yutaka, Kumiko Ishige, Cindy Tsai, and Pamela Maher. 2002. "Tyrphostins Protect Neuronal Cells from Oxidative Stress." *Journal of Biological Chemistry* 277(39):36204–15. doi:10.1074/jbc.M203895200.

Saltonstall, Peter, Heidi Ross, and Paul T. Kim. 2024. "The Orphan Drug Act at 40: Legislative Triumph and the Challenges of Success." *The Milbank Quarterly* 102(1):83–96. doi:10.1111/1468-0009.12680.

Sanchez, Lucienne S., Suzanne M. De La Monte, Galina Filippov, Rosemary C. Jones, Warren M. Zapol, and Kenneth D. Bloch. 1998. "Cyclic-GMP-Binding, Cyclic-GMP-Specific Phosphodiesterase (PDE5) Gene Expression Is Regulated during Rat Pulmonary Development." *Pediatric Research* 43(2):163–68. doi:10.1203/00006450-199802000-00002.

Sanders, Owen. 2020. "Sildenafil for the Treatment of Alzheimer's Disease: A Systematic Review." *Journal of Alzheimer's Disease Reports* 4(1):91–106. doi:10.3233/ADR-200166.

Sazonova, Margarita A., Vasily V. Sinyov, Anastasia I. Ryzhkova, Elena V. Galitsyna, Alexandra A. Melnichenko, Anton Y. Postnov, Alexander N. Orekhov, and Igor A. Sobenin. 2018. "Cybrid Models of Pathological Cell Processes in Different Diseases" edited by K. V. Ramana. *Oxidative Medicine and Cellular Longevity* 2018(1):4647214. doi:10.1155/2018/4647214.

Scherman, Daniel, and Christine Fetro. 2020. "Drug Repositioning for Rare Diseases: Knowledge-Based Success Stories." *Therapies* 75(2):161–67. doi:10.1016/j.therap.2020.02.007.

Schlotawa, Lars, Laura A. Adang, Karthikeyan Radhakrishnan, and Rebecca C. Ahrens-Nicklas. 2020. "Multiple Sulfatase Deficiency: A Disease Comprising Mucopolysaccharidosis, Sphingolipidosis, and More Caused by a Defect in Posttranslational Modification." *International Journal of Molecular Sciences* 21(10):3448. doi:10.3390/ijms21103448.

Schlotawa, Lars, Laura Adang, Mauricio De Castro, and Rebecca Ahrens-Nicklas. 2019. "Multiple Sulfatase Deficiency." in *GeneReviews*®, edited by M. P. Adam, J. Feldman, G. M. Mirzaa, R. A. Pagon, S. E. Wallace, and A. Amemiya. Seattle (WA): University of Washington, Seattle.

Schlotawa, Lars, Eva Charlotte Ennemann, Karthikeyan Radhakrishnan, Bernhard Schmidt, Anupam Chakrapani, Hans-Jürgen Christen, Hugo Moser, Beat Steinmann, Thomas Dierks, and Jutta Gärtner. 2011. "SUMF1 Mutations Affecting Stability and Activity of Formylglycine Generating Enzyme Predict Clinical Outcome in Multiple Sulfatase Deficiency." *European Journal of Human Genetics* 19(3):253–61. doi:10.1038/ejhg.2010.219.

Schlotawa, Lars, Joana Preiskorn, Rebecca Ahrens-Nicklas, Stina Schiller, Laura A. Adang, Jutta Gärtner, and Tim Friede. 2020. "A Systematic Review and Meta-analysis of Published Cases Reveals the Natural Disease History in Multiple Sulfatase Deficiency." *Journal of Inherited Metabolic Disease* 43(6):1288–97. doi:10.1002/jimd.12282.

Schwimmer, Christine, Malgorzata Rak, Linnka Lefebvre-Legendre, Stéphane Duvezin-Caubet, Guillaume Plane, and Jean-Paul Di Rago. 2006. "Yeast Models of Human

Mitochondrial Diseases: From Molecular Mechanisms to Drug Screening." *Biotechnology Journal* 1(3):270–81. doi:10.1002/biot.200500053.

Sebollela, Adriano, Léo Freitas-Corrêa, Fábio F. Oliveira, Camila T. Mendes, Ana Paula Wasilewska-Sampaio, Juliana Camacho-Pereira, Antonio Galina, Helena Brentani, Fabio Passetti, Fernanda G. De Felice, Emmanuel Dias-Neto, and Sérgio T. Ferreira. 2009. "Expression Profile of Rat Hippocampal Neurons Treated with the Neuroprotective Compound 2,4-Dinitrophenol: Up-Regulation of cAMP Signaling Genes." *Neurotoxicity Research* 18(2):112–23. doi:10.1007/s12640-009-9133-y.

Sena-dos-Santos, Camille, Dafne Dalledone Moura, Matheus Caetano Epifane-de-Assunção, Ândrea Ribeiro-dos-Santos, and Bruno Lopes Santos-Lobato. 2024. "Mitochondrial DNA Variants, Haplogroups and Risk of Parkinson's Disease: A Systematic Review and Meta-Analysis." *Parkinsonism & Related Disorders* 125:107044. doi:10.1016/j.parkreldis.2024.107044.

Sevenich, Lisa. 2018. "Brain-Resident Microglia and Blood-Borne Macrophages Orchestrate Central Nervous System Inflammation in Neurodegenerative Disorders and Brain Cancer." *Frontiers in Immunology* 9:697. doi:10.3389/fimmu.2018.00697.

Sharma, Vibhash D., Margi Patel, and Svjetlana Miocinovic. 2020. "Surgical Treatment of Parkinson's Disease: Devices and Lesion Approaches." *Neurotherapeutics* 17(4):1525–38. doi:10.1007/s13311-020-00939-x.

Singh, Natesh, Philippe Vayer, Shivalika Tanwar, Jean-Luc Poyet, Katya Tsaioun, and Bruno O. Villoutreix. 2023. "Drug Discovery and Development: Introduction to the General Public and Patient Groups." *Frontiers in Drug Discovery* 3:1201419. doi:10.3389/fddsv.2023.1201419.

Sinha, Aprajita, Maheshree Maibam, Ronit Jain, Kalash Aggarwal, Asish Kumar Sahu, Pawan Gupta, Sayan Paul, Bharti Bisht, and Manash K. Paul. 2025. "Organoid: Biomedical Application, Biobanking, and Pathways to Translation." *Heliyon* 11(10):e43028. doi:10.1016/j.heliyon.2025.e43028.

Soleilhac, Emmanuelle, Robert Nadon, and Laurence Lafanechere. 2010. "High-Content Screening for the Discovery of Pharmacological Compounds: Advantages, Challenges and Potential Benefits of Recent Technological Developments." *Expert Opinion on Drug Discovery* 5(2):135–44. doi:10.1517/17460440903544456.

Soltoff, Stephen P. 2004. "Evidence That Tyrphostins AG10 and AG18 Are Mitochondrial Uncouplers That Alter Phosphorylation-Dependent Cell Signaling." *Journal of Biological Chemistry* 279(12):10910–18. doi:10.1074/jbc.M305396200.

Southey, Michelle W. Y., and Michael Brunavs. 2023. "Introduction to Small Molecule Drug Discovery and Preclinical Development." *Frontiers in Drug Discovery* 3:1314077. doi:10.3389/fddsv.2023.1314077.

Sutherland, Earl W., and T. W. Rall. 1958. "FRACTIONATION AND CHARACTERIZATION OF A CYCLIC ADENINE RIBONUCLEOTIDE FORMED BY TISSUE PARTICLES." *Journal of Biological Chemistry* 232(2):1077–91. doi:10.1016/S0021-9258(19)77423-7.

Swatek, Kirby N., Joanne L. Usher, Anja F. Kueck, Christina Gladkova, Tycho E. T. Mevissen, Jonathan N. Pruneda, Tim Skern, and David Komander. 2019. "Insights into Ubiquitin Chain Architecture Using Ub-Clipping." *Nature* 572(7770):533–37. doi:10.1038/s41586-019-1482-y.

Tabar, V., H. Sarva, A. M. Lozano, A. Fasano, S. K. Kalia, K. K. H. Yu, C. Brennan, Y. Ma, S. Peng, D. Eidelberg, M. Tomishima, S. Irion, W. Stemple, N. Abid, A. Lampron, L. Studer, and C. Henchcliffe. 2025. "Phase I Trial of hES Cell-Derived Dopaminergic Neurons for Parkinson's Disease." *Nature* 641(8064):978–83. doi:10.1038/s41586-025-08845-y.

Tábara, Luis-Carlos, Mayuko Segawa, and Julien Prudent. 2025. "Molecular Mechanisms of Mitochondrial Dynamics." *Nature Reviews Molecular Cell Biology* 26(2):123–46. doi:10.1038/s41580-024-00785-1.

Takahashi, Kazutoshi, Koji Tanabe, Mari Ohnuki, Megumi Narita, Tomoko Ichisaka, Kiichiro Tomoda, and Shinya Yamanaka. 2007. "Induction of Pluripotent Stem Cells from Adult Human Fibroblasts by Defined Factors." *Cell* 131(5):861–72. doi:10.1016/j.cell.2007.11.019.

Takahashi, Kazutoshi, and Shinya Yamanaka. 2006. "Induction of Pluripotent Stem Cells from Mouse Embryonic and Adult Fibroblast Cultures by Defined Factors." *Cell* 126(4):663–76. doi:10.1016/j.cell.2006.07.024.

Tang, Xiao-Yan, Shanshan Wu, Da Wang, Chu Chu, Yuan Hong, Mengdan Tao, Hao Hu, Min Xu, Xing Guo, and Yan Liu. 2022. "Human Organoids in Basic Research and Clinical Applications." *Signal Transduction and Targeted Therapy* 7(1):168. doi:10.1038/s41392-022-01024-9.

Tang, Yan, Xue Xiao, Hua Xie, Chang-min Wan, Li Meng, Zhen-hua Liu, Wei-hua Liao, Beisha Tang, and Ji-feng Guo. 2017. "Altered Functional Brain Connectomes between Sporadic and Familial Parkinson's Patients." *Frontiers in Neuroanatomy* 11:99. doi:10.3389/fnana.2017.00099.

Taylor, R. W. 2001. "The Determination of Complete Human Mitochondrial DNA Sequences in Single Cells: Implications for the Study of Somatic Mitochondrial DNA Point Mutations." *Nucleic Acids Research* 29(15):74e–774. doi:10.1093/nar/29.15.e74.

Taymans, Jean-Marc, Matt Fell, Tim Greenamyre, Warren D. Hirst, Adamantios Mamais, Shalini Padmanabhan, Inga Peter, Hardy Rideout, and Avner Thaler. 2023. "Perspective on the Current State of the LRRK2 Field." *Npj Parkinson's Disease* 9(1):104. doi:10.1038/s41531-023-00544-7.

Thakur, Kiran T., Emiliano Albanese, Panteleimon Giannakopoulos, Nathalie Jette, Mattias Linde, Martin J. Prince, Timothy J. Steiner, and Tarun Dua. 2016. "Neurological Disorders." in *Mental, Neurological, and Substance Use Disorders: Disease Control Priorities, Third Edition (Volume 4)*, edited by V. Patel, D. Chisholm, T. Dua, R. Laxminarayan, and M. E. Medina-Mora. Washington (DC): The International Bank for Reconstruction and Development / The World Bank.

The Lancet Global Health. 2024. “The Landscape for Rare Diseases in 2024.” *The Lancet Global Health* 12(3):e341. doi:10.1016/S2214-109X(24)00056-1.

The Lancet Neurology. 2022. “Rare Diseases: Maintaining Momentum.” *The Lancet Neurology* 21(3):203. doi:10.1016/S1474-4422(22)00046-1.

Tofaris, George K. 2022. “Initiation and Progression of α-Synuclein Pathology in Parkinson’s Disease.” *Cellular and Molecular Life Sciences* 79(4):210. doi:10.1007/s00018-022-04240-2.

Tolle, Isabella, Valeria Tiranti, and Alessandro Prigione. 2023. “Modeling Mitochondrial DNA Diseases: From Base Editing to Pluripotent Stem-cell-derived Organoids.” *EMBO Reports* 24(4):e55678. doi:10.15252/embr.202255678.

Trimmer, Patricia A., and James P. Bennett. 2009. “The Cybrid Model of Sporadic Parkinson’s Disease.” *Experimental Neurology* 218(2):320–25. doi:10.1016/j.expneurol.2009.03.016.

Trimmer, Patricia A., Paula M. Keeney, M. Kate Borland, Frederic A. Simon, Jatanna Almeida, Russell H. Swerdlow, Janice P. Parks, W. Davis Parker, and James P. Bennett. 2004. “Mitochondrial Abnormalities in Cybrid Cell Models of Sporadic Alzheimer’s Disease Worsen with Passage in Culture.” *Neurobiology of Disease* 15(1):29–39. doi:10.1016/j.nbd.2003.09.011.

Trounce, I., S. Neill, and D. C. Wallace. 1994. “Cytoplasmic Transfer of the mtDNA Nt 8993 T-->G (ATP6) Point Mutation Associated with Leigh Syndrome into mtDNA-Less Cells Demonstrates Cosegregation with a Decrease in State III Respiration and ADP/O Ratio.” *Proceedings of the National Academy of Sciences* 91(18):8334–38. doi:10.1073/pnas.91.18.8334.

U.S. Food and Drug Administration. 2023. “Approval Letter NDA 021845/S-025.” https://www.accessdata.fda.gov/drugsatfda_docs/nda/2023/021845Orig1s025.pdf

Van De Wal, Melissa A. E., Cenna Doornbos, Janne M. Bibbe, Judith R. Homberg, Clara Van Karnebeek, Martijn A. Huynen, Jaap Keijer, Evert M. Van Schothorst, Peter A. C. ’T Hoen, Mirian C. H. Janssen, Merel J. W. Adjobo-Hermans, Mariusz R. Wieckowski, and Werner J. H. Koopman. 2025. “Ndufs4 Knockout Mice with Isolated Complex I Deficiency Engage a Futile Adaptive Brain Response.” *Biochimica et Biophysica Acta (BBA) - Proteins and Proteomics* 1873(1):141055. doi:10.1016/j.bbapap.2024.141055.

Venken, Koen J. T., Julie H. Simpson, and Hugo J. Bellen. 2011. “Genetic Manipulation of Genes and Cells in the Nervous System of the Fruit Fly.” *Neuron* 72(2):202–30. doi:10.1016/j.neuron.2011.09.021.

Vercellino, Irene, and Leonid A. Sazanov. 2022. “The Assembly, Regulation and Function of the Mitochondrial Respiratory Chain.” *Nature Reviews Molecular Cell Biology* 23(2):141–61. doi:10.1038/s41580-021-00415-0.

Wallace, D. C., and D. Chalkia. 2013. “Mitochondrial DNA Genetics and the Heteroplasmy Conundrum in Evolution and Disease.” *Cold Spring Harbor Perspectives in Biology* 5(11):a021220–a021220. doi:10.1101/cshperspect.a021220.

Wasilewska-Sampaio, A. P. Barbosa, C.A. Gomes, and T. Ferreira. 2007. “Cyclic AMP Enhancers and Aβ Oligomerization Blockers as Potential Therapeutic Agents in Alzheimers Disease.” *Current Alzheimer Research* 4(3):263–71. doi:10.2174/156720507781077287.

West, Andrew B., Darren J. Moore, Saskia Biskup, Artem Bugayenko, Wanli W. Smith, Christopher A. Ross, Valina L. Dawson, and Ted M. Dawson. 2005. “Parkinson’s Disease-Associated Mutations in Leucine-Rich Repeat Kinase 2 Augment Kinase Activity.” *Proceedings of the National Academy of Sciences* 102(46):16842–47. doi:10.1073/pnas.0507360102.

Whitworth, Alexander J., Dorothy A. Theodore, Jessica C. Greene, Helen Beneš, Paul D. Wes, and Leo J. Pallanck. 2005. “Increased Glutathione *S* -Transferase Activity Rescues Dopaminergic Neuron Loss in a *Drosophila* Model of Parkinson’s Disease.” *Proceedings of the National Academy of Sciences* 102(22):8024–29. doi:10.1073/pnas.0501078102.

Wildey, Mary Jo, Anders Haunso, Matthew Tudor, Maria Webb, and Jonathan H. Connick. 2017. “High-Throughput Screening.” Pp. 149–95 in *Annual Reports in Medicinal Chemistry*. Vol. 50. Elsevier.

Wilkins, Heather M., Steven M. Carl, and Russell H. Swerdlow. 2014. “Cytoplasmic Hybrid (Cybrid) Cell Lines as a Practical Model for Mitochondriopathies.” *Redox Biology* 2:619–31. doi:10.1016/j.redox.2014.03.006.

Wolf, Don P., Nargiz Mitalipov, and Shoukhrat Mitalipov. 2015. “Mitochondrial Replacement Therapy in Reproductive Medicine.” *Trends in Molecular Medicine* 21(2):68–76. doi:10.1016/j.molmed.2014.12.001.

Worsley, H. E., R. W. Brookfield, J. S. Elwood, R. L. Noble, and W. H. Taylor. 1965. “Lactic Acidosis with Necrotizing Encephalopathy in Two Sibs.” *Archives of Disease in Childhood* 40(213):492–501. doi:10.1136/adc.40.213.492.

Yang, Siqi, Haijie Hu, Hengchung Kung, Ruiqi Zou, Yushi Dai, Yafei Hu, Tiantian Wang, Tianrun Lv, Jun Yu, and Fuyu Li. 2023. “Organoids: The Current Status and Biomedical Applications.” *MedComm* 4(3):e274. doi:10.1002/mco2.274.

Zhang, Jianhua, Gisela F. Wilson, Andrew G. Soerens, Chad H. Koonce, Junying Yu, Sean P. Palecek, James A. Thomson, and Timothy J. Kamp. 2009. “Functional Cardiomyocytes Derived From Human Induced Pluripotent Stem Cells.” *Circulation Research* 104(4). doi:10.1161/CIRCRESAHA.108.192237.

Zhang, Ji-Hu, Thomas D. Y. Chung, and Kevin R. Oldenburg. 1999. “A Simple Statistical Parameter for Use in Evaluation and Validation of High Throughput Screening Assays.” *SLAS Discovery* 4(2):67–73. doi:10.1177/108705719900400206.

Zhang, John, Hui Liu, Shiyu Luo, Zhuo Lu, Alejandro Chávez-Badiola, Zitao Liu, Mingxue Yang, Zaher Merhi, Sherman J. Silber, Santiago Munné, Michalis Konstantinidis, Dagan Wells, Jian J. Tang, and Taosheng Huang. 2017. "Live Birth Derived from Oocyte Spindle Transfer to Prevent Mitochondrial Disease." *Reproductive BioMedicine Online* 34(4):361–68. doi:10.1016/j.rbmo.2017.01.013.

Zhou, Shu-Feng, and Wei-Zhu Zhong. 2017. "Drug Design and Discovery: Principles and Applications." *Molecules* 22(2):279. doi:10.3390/molecules22020279.

Zink, Annika, Dao-Fu Dai, Annika Wittich, Marie-Thérèse Henke, Giulia Pedrotti, Sonja Heiduschka, Guillem Santamaria, Tancredi Massimo Pentimalli, Christian Brueser, Sofia Notopoulou, Abdul Rahim Umar, Aleksandra Zhaivoron, Laura Petersilie, Caleb Jerred, Jesper Bergmans, Louis Anton Neu, Fabian Schumacher, Jan Keller-Findeisen, Agnieszka Rybak-Wolf, Daniel Stach, Jeanette Reinshagen, Undine Haferkamp, Kim Krieg, Andrea Zaliani, Liliya Euro, Alessia Di Donfrancesco, Chiara Santanatoglia, Enrica Cappellozza, Marta Suarez Cubero, Mario Pavez-Giani, Oleh Bakumenko, David Meierhofer, Alan Foley, Susanne Morales-Gonzalez, Isabella Tolle, Diran Herebian, Daniele Bonesso, Giulia Cecchetto, Sakurako Nagumo Wong, Monica Moresco, Alessandra Maresca, Ilaria Decimo, Francesco De Sanctis, Annalisa Adamo, Merel J. W. Adjobo-Hermans, Roberto Duchi, Maria Barandalla, Marco Scaglia, Andrea Perota, Cesare Galli, Burkhard Kleuser, Lukas Cyganek, Chris Mühlhausen, Lars Schlotawa, Valeria Tiranti, Ertan Mayatepek, Ildiko Szabo, Chiara La Morgia, Thomas Klopstock, Valerio Carelli, Felix Distelmaier, Andrea Rossi, Nikolaus Rajewsky, Ghanim Ullah, Stefan Jakobs, Christine R. Rose, Spyros Petrakis, Frank Edenhofer, Werner J. H. Koopman, Pawel Lisowski, Anu Suomalainen, Dario Brunetti, Antonio Del Sol, Emanuela Bottani, Ole Pless, Markus Schuelke, and Alessandro Prigione. 2026. "Pluripotent Stem-Cell-Based Screening Uncovers Sildenafil as a Mitochondrial Disease Therapy." *Cell* 189(6):1656-1679.e42. doi:10.1016/j.cell.2026.02.008.

Ziółkowska, Ewa A., Keigo Takahashi, Patricia I. Dickson, Marco Sardiello, Mark S. Sands, and Jonathan D. Cooper. 2025. "Neuronal Ceroid Lipofuscinosis: Underlying Mechanisms and Emerging Therapeutic Targets." *Nature Reviews Neurology* 21(11):606–22. doi:10.1038/s41582-025-01132-4.

Zorov, Dmitry B., Nadezda V. Andrianova, Valentina A. Babenko, Irina B. Pevzner, Vasily A. Popkov, Savva D. Zorov, Ljubava D. Zorova, Egor Yu. Plotnikov, Gennady T. Sukhikh, and Denis N. Silachev. 2021. "Neuroprotective Potential of Mild Uncoupling in Mitochondria. Pros and Cons." *Brain Sciences* 11(8):1050. doi:10.3390/brainsci11081050.

Zorova, Ljubava D., Vasily A. Popkov, Egor Y. Plotnikov, Denis N. Silachev, Irina B. Pevzner, Stanislovas S. Jankauskas, Valentina A. Babenko, Savva D. Zorov, Anastasia V. Balakireva, Magdalena Juhaszova, Steven J. Sollott, and Dmitry B. Zorov. 2018. "Mitochondrial Membrane Potential." *Analytical Biochemistry* 552:50–59. doi:10.1016/j.ab.2017.07.009.

8. Eidesstattliche Erklärung

Ich versichere an Eides statt, dass die Dissertation von mir selbständig und ohne unzulässige fremde Hilfe unter Beachtung der „Grundsätze zur Sicherung guter wissenschaftlicher Praxis an der Heinrich-Heine-Universität Düsseldorf“ erstellt worden ist.

Die Dissertation wurde weder an einer anderen Fakultät vorgelegt noch wurden zuvor andere Promotionsversuche unternommen.

_____ _____

Ort, Datum Unterschrift

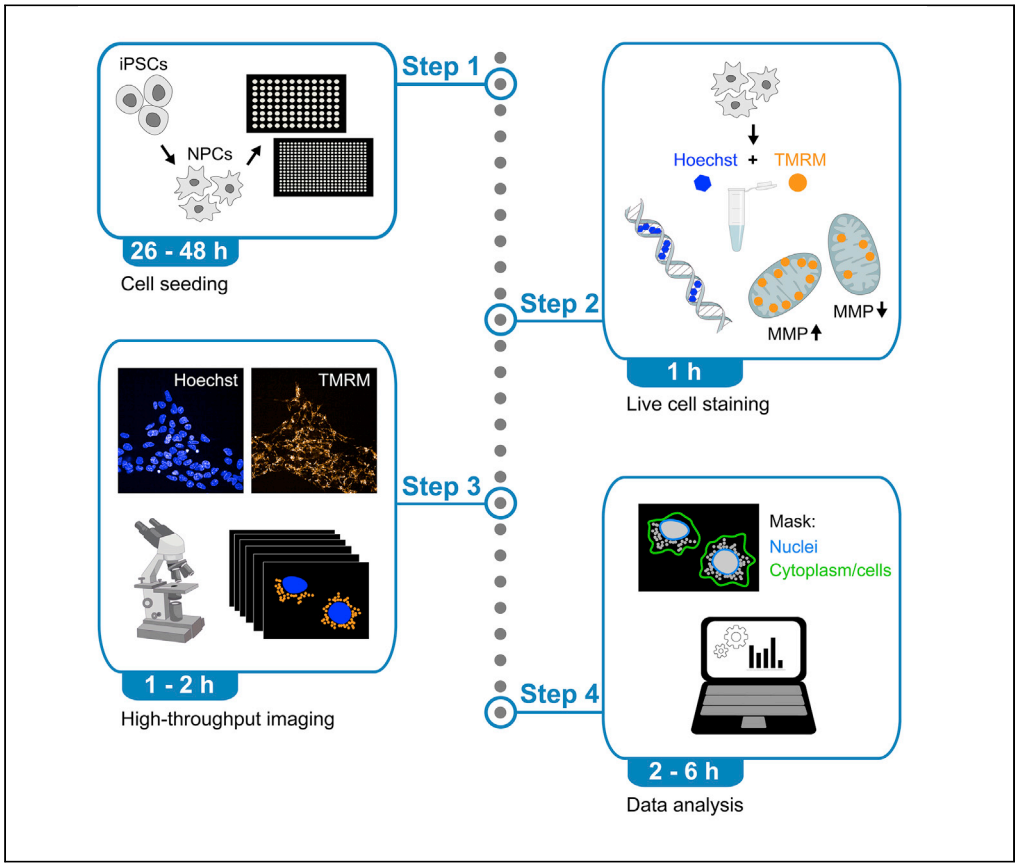
9. Appendix I

STAR Protocols

CellPress
OPEN ACCESS

Protocol

High-content screening of mitochondrial polarization in neural cells derived from human pluripotent stem cells



We present a high-content screening (HCS) protocol for quantifying mitochondrial activity in live neural cells from human induced pluripotent stem cells (iPSCs). The assessment is based on mitochondrial membrane potential, which is influenced by the efficiency of mitochondrial bioenergetics. We describe how to perform the analysis using both an HCS platform and the open-source software CellProfiler. The protocol can identify the mitochondrial fitness of human neurons and may be used to carry out high-throughput compound screenings in patient-derived neural cells.

Publisher's note: Undertaking any experimental protocol requires adherence to local institutional guidelines for laboratory safety and ethics.

Annika Zink, Undine Haferkamp, Annika Wittich, Mathias Beller, Ole Pless, Alessandro Prigione

alessandro.prigione@hhu.de

Highlights

High-content screening (HCS) of live neural cells derived from human iPSCs

Assessment of mitochondrial activity based on mitochondrial membrane potential (MMP)

Quantification using automated microscopic image analysis

Data analysis using both an HCS system and the open-source software CellProfiler

Zink et al., STAR Protocols 3, 101602
September 16, 2022 © 2022 The Author(s).
https://doi.org/10.1016/j.xpro.2022.101602

STAR Protocols

CellPress
OPEN ACCESS

Protocol

High-content screening of mitochondrial polarization in neural cells derived from human pluripotent stem cells

Annika Zink,[1,4,6] Undine Haferkamp,[2,4] Annika Wittich,[2] Mathias Beller,[3] Ole Pless,[2,5] and Alessandro Prigione[1,5,7,*]

[1]Department of General Pediatrics, Neonatology and Pediatric Cardiology, Medical Faculty, Heinrich Heine University, 40225 Düsseldorf, Germany

[2]Fraunhofer Institute for Translational Medicine and Pharmacology ITMP, ScreeningPort, 22525 Hamburg, Germany

[3]Institute for Mathematical Modeling of Biological Systems, Heinrich Heine University, 40225 Düsseldorf, Germany

[4]These authors contributed equally

[5]These authors contributed equally

[6]Technical contact: annika.zink@med.uni-duesseldorf.de

[7]Lead contact

*Correspondence: alessandro.prigione@hhu.de
https://doi.org/10.1016/j.xpro.2022.101602

SUMMARY

We present a high-content screening (HCS) protocol for quantifying mitochondrial activity in live neural cells from human induced pluripotent stem cells (iPSCs). The assessment is based on mitochondrial membrane potential, which is influenced by the efficiency of mitochondrial bioenergetics. We describe how to perform the analysis using both an HCS platform and the open-source software CellProfiler. The protocol can identify the mitochondrial fitness of human neurons and may be used to carry out high-throughput compound screenings in patient-derived neural cells.

For complete details on the use and execution of this protocol, please refer to Lorenz et al. (2017) and Zink et al. (2020).

BEFORE YOU BEGIN

The protocol described here can be applied to various neural cell types differentiated from human induced pluripotent stem cells (iPSCs). Before starting differentiation, it is important to carefully monitor the genetic integrity of the iPSC lines to be used. This aspect is crucial to ensure that no unwanted abnormalities might have occurred during iPSC culture (Rossi et al., 2022). Proper health of iPSC lines should be ensured by growing cells with appropriate medium and coating material. In our hands, it is helpful to grow iPSCs in incubators with low oxygen concentration (5%). It is also crucial to always monitor the absence of mycoplasma contamination.

With respect to differentiated neural cells, we focus here on neural progenitor cells (NPCs). In fact, NPCs are easier to expand than differentiated neurons, and at the same time already rely on mitochondrial respiration (Lorenz et al., 2017). Homogenous NPC cultures can be obtained from iPSCs in about 4–6 weeks using previously published protocols (Reinhardt et al., 2013; Zink et al., 2021). NPCs generated using this protocol express typical NPC markers including NESTIN, DACH1, SOX2, and PAX6, and the proliferation marker Ki-67. These NPCs retain their multipotent identity over multiple passages (>30), have the potential to form both neural tube and neural crest lineages, and can be effectively differentiated into motor neurons and dopaminergic neurons (Reinhardt et al., 2013). Beside NPCs, it is possible to apply the protocol described here also to other types of neural cells derived from human iPSCs. For example, we successfully employed the HCS protocol to screen for drugs affecting mitochondrial polarization in dopaminergic neurons from iPSCs derived from

This is an open access article under the CC BY-NC-ND license (http://creativecommons.org/licenses/by-nc-nd/4.0/).

controls and patients (Zink et al., 2020). For this protocol we used NPCs generated from a published human iPSC line (Wang et al., 2018). This protocol can be used in combination with the quantification of neuronal morphology described in Lickfett et al., 2022.

Institutional permissions

Studies with control iPSCs were performed in accordance with the approval by the Ethic Committee of the Medical Faculty of Heinrich Heine University (study number: 2020-967_2).

Preparation of cell culture materials and buffers

Timing: 1 h

⚠ CRITICAL: Adhere to the necessary precautions when working with human samples. They should be handled in a biological safety cabinet. When experimenting with human iPSC lines, comply with relevant local institutional and government regulations.

Prepare cell culture media according to the information provided in the tables below or use media following other standard protocols.

NPC basal medium (sm−)

Medium	Component	Amount	Stock con.	Final conc.
Basal medium for NPCs (sm-)	DMEM/F12	240 mL	1 ×	0.5 ×
	Neurobasal	240 mL	1 ×	0.5 ×
	N2	2.5 mL	100 ×	0.5 ×
	B27 w/o Vitamin A	5 mL	50 ×	0.5 ×
	Glutamine	5 mL	200 mM	2 mM
	MycoZap	1 mL	500 ×	1 ×
	[Pen/Strep*]	[5 mL]	[100 ×]	[1 ×]

Note: sm- basal medium can be stored for two weeks at 2°C–8°C.

NPC growth medium (sm+)

Medium	Component	Amount	Stock con.	Final conc.
Growth medium for NPCs (sm+)	sm-	10 mL	1 ×	1 ×
	CHIR99021 (Glycogen synthase kinase (GSK)-3 inhibitor)	5 µL	6 mM	3 µM
	Purmorphamine	7.69 µL	0.65 mM	500 nM
	Vitamin C	7.5 µL	200 mM	150 µM

Note: sm+ growth medium can be stored for one week at 2°C–8°C.

NPC basal medium (sm−) for live-cell imaging

Medium	Component	Amount	Stock concentration	Final concentration
Phenol red-free basal medium for live-cell imaging of NPCs	DMEM/F12 without phenol red	240 mL	1 ×	0.5 ×
	Neurobasal without phenol red	240 mL	1 ×	0.5 ×
	N2	2.5 mL	100 ×	0.5 ×
	B27 w/o Vitamin A	5 mL	50 ×	0.5 ×
	Glutamine	5 mL	200 mM	2 mM
	MycoZap	1 mL	500 ×	1 ×
	[Pen/Strep*]	[5 mL]	[100 ×]	[1 ×]

Note: Phenol red-free basal medium can be stored for two weeks at 2°C–8°C.

NPC growth medium (sm+) for live-cell imaging				
Medium	Component	Amount	Stock concentration	Final concentration
Phenol red-free growth medium for live-cell imaging of NPCs	Sm- without phenol red	10 mL	1 ×	1 ×
	CHIR99021	5 µL	6 mM	3 µM
	Purmorphamine	7.69 µL	0.65 mM	500 nM
	Vitamin C	7.5 µL	200 mM	150 µM

Note: Phenol red-free growth medium can be stored for one week at 2°C–8°C.

Note: All media should be sterile-filtered and prepared under sterile conditions. Before usage, pre-warm the media to room temperature (20°C–25°C).

**Note:* We supplement our cell culture media with MycoZap Plus-CL antibiotics to minimize the loss of valuable cells due to contamination (including mycoplasma). The use of MycoZap-Plus-CL replaces Penicillin and Streptomycin (Pen/Strep) but can still be used in parallel. At the same time, it is essential to always work under clean and sterile conditions, and to perform routine tests to monitor the absence of mycoplasma in the cultures. For mycoplasma testing, we use PCR analysis of cell supernatants or the test kit Venor®GeM OneStep from MB Minerva Biolabs (Cat. No. 11-8100).

KEY RESOURCES TABLE

REAGENT or RESOURCE	SOURCE	IDENTIFIER
Chemicals, peptides, and recombinant proteins		
Accutase™ Cell Dissociation Reagent	Gibco	A1110501
Antimycin A, 25 mM	Sigma-Aldrich	A8674
B27 w/o Vitamin A	Gibco	12587010
CHIR99021	Sigma-Aldrich	SML1046
DMEM/F-12	Gibco	31330038
FCCP, 25 mM	Sigma-Aldrich	C2920
Geltrex	Gibco	A1413201
Glutamine	Gibco	25030149
Hoechst 33342	Life Technologies	H3570
Matrigel, Growth Factor Reduced	BD Biosciences	356231
MycoZap	Lonza	VZA-2012
N2	Gibco	17502-048
Neurobasal	Gibco	21103-049
Purmorphamine	Sigma-Aldrich	540220
TMRE	Invitrogen/Molecular Probes	T-669
TMRM	Invitrogen/Molecular Probes	T-668
Vitamin C	Sigma-Aldrich	A4034
Software and algorithms		
CellProfiler 4.2.1	Broad Institute	www.cellprofiler.org
Columbus 2.9.0	PerkinElmer	n/a
GraphPad Prism 5.01	GraphPad Software	https://www.graphpad.com/
Critical commercial assays		
Venor®GeM OneStep	MB Minerva Biolabs	11-8100

(*Continued on next page*)

Continued		
REAGENT or RESOURCE	SOURCE	IDENTIFIER
Other		
384-well Cell Culture Microplate, PS, F-Bottom, black TC, μCLEAR, 384-well black, clear bottom	Greiner Bio-One	781091
96-well Cell Culture Microplate, PS, F-Bottom, black TC, μCLEAR, 96-well black, clear bottom	Greiner Bio-One	655090
Operetta CLS™	PerkinElmer	https://www.perkinelmer.com/de/category/operetta-cls-high-content-analysis-system
PhenoPlate 384-well, black, optically clear flat-bottom, tissue-culture treated, lids	PerkinElmer	6057302
Neubauer hemocytometer	VWR	6310696
Deposited data		
Pipeline and raw images	GitHub	https://github.com/StemCellMetab/Mitochondrial-membrane-potential (https://doi.org/10.5281/zenodo.6794537)
Experimental models: Cell lines		
Human: NPCs from iPSC line HMGUi001-A	Wang et al.	https://hpscreg.eu/cell-line/HMGUi001-A

MATERIALS AND EQUIPMENT

High-content imaging system

For HCS, we here describe the use of the Operetta CLS High-Content Analysis System (Manufacturer PerkinElmer, https://www.perkinelmer.com/de/Product/operetta-cls-system-hh16000000) controlled by the software Harmony™ (PerkinElmer). Following image acquisition, data analysis can be performed using different approaches. Here, we describe two different pipelines. The first one is based on the open-source software CellProfiler (www.cellprofiler.org). The use of such external software may be ideal for laboratories that do not have access to expensive HCS software and are faced with limited computational possibilities. The second pipeline is based on the image data storage and analysis system Columbus™ (PerkinElmer). This system is more user-friendly, and therefore the establishment of new analysis routines requires less time investment. In order to compare the two pipelines, we show here results obtained by running the same datasets using the two approaches (Figure 1). The comparable results confirm the reproducibility of the HCS protocol, and demonstrate how the protocol outcome should not be influenced by the type of software used for data analysis.

Automated imaging of mitochondrial membrane potential		
Cellular target	Channel	Dye/antibody
Nucleus	1	Hoechst 33342 (Invitrogen)
Mitochondrial membrane potential ($\Delta\Psi m$)	2	TMRM (Invitrogen/Molecular Probes T-668)

STEP-BY-STEP METHOD DETAILS

Cell seeding on the assay plate for HCS

Timing: 26–48 h

In this step, the seeding of the cells on the assay plate is described.

1. Preparation of HCS plates (~2–24 h).
   a. Coat a black wall, clear F-bottom 96- or 384-well plate with appropriate coating solution. We recommend using Geltrex (1:100 dilution).

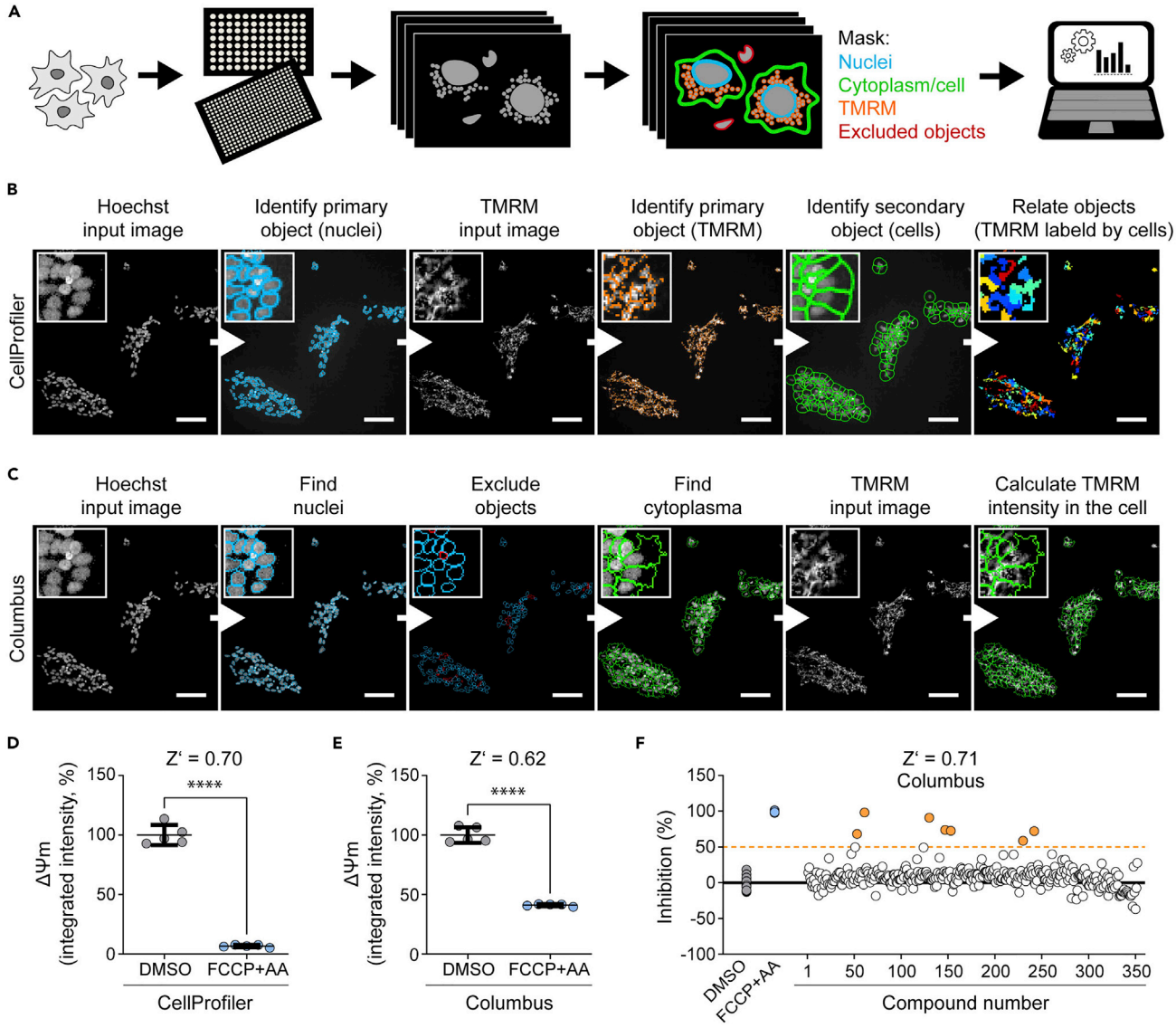


Figure 1. High-content screening (HCS) of mitochondrial membrane potential (ΔΨm) in iPSC-derived neural progenitor cells (NPCs)

(A) Schematic of the HCS protocol steps, including the mask established for the detection of ΔΨm in live-cells.

(B) Flow of imaging analysis using CellProfiler software. Scale bar: 100 μm.

(C) Flow of imaging analysis using Columbus software. Scale bar: 100 μm.

(D) ΔΨm intensity evaluated using the CellProfiler image analysis pipeline. Robustness of the HCS protocol was calculated based on Z′ score (for effective high-throughput assays, values should be between 0.5 and 1). Mean ± standard deviation (SD), unpaired Student's t-test, ****p<0.0001.

(E) ΔΨm intensity evaluated using the Columbus image analysis pipeline. Mean ± SD, unpaired Student's t-test, ****p < 0.0001.

(F) Compound screening performed in NPCs differentiated from human iPSCs based on the HCS protocol described here. Blue dots indicate the positive control samples treated with FCCP and antimycin A (AA). These drugs are known to decrease ΔΨm and their values are considered as 100% inhibition of ΔΨm. Orange dots indicate screened compounds that can lead to 50%–100% inhibition of ΔΨm.

⚠ CRITICAL: The use of transparent clear bottom microplates is essential for this assay. To determine the appropriate microplate type to be used, it is helpful to check beforehand which microplates are already calibrated with the correct dimensions in the instrument. Further helpful information on specific requirements and plate considerations can be found here: https://www.perkinelmer.com/de/lab-products-and-services/application-support-knowledgebase/microplates/high-content-screening-plates.html.

Alternatives: Other coating reagents may also be used. Instead of Geltrex, it is also possible to use Matrigel (200 μg/mL). However, Matrigel is not a defined material, so it may be possible to observe batch-related variability. We obtained comparable results also using poly-l-ornithine (50 μg/mL on glass; 20 μg/mL on polystyrene) plus laminin (10 μg/mL on glass; 5 μg/mL on polystyrene).

Note: Follow manufacturer's guidelines for coating with Matrigel (https://www.corning.com/worldwide/en/products/life-sciences/products/surfaces/matrigel-matrix.html).

2. Seeding of iPSC-derived neural cells (~ 24 h).
   a. Split the cells using 0.5 mL Accutase for 6-well plates for 5 min at room temperature (RT) (20°C–25°C).
   b. Dilute the Accutase to reduce its activity by adding at least double amount of culture media.
   c. Transfer the cells into a 15 mL falcon tube.
   d. Centrifuge for 3 min at 120 × *g*, remove the supernatant, and resuspend the cells in culture media.
   e. Count the cells using a hemocytometer or cell counter.
   f. Pipette 100 μL cell suspension containing 30,000–50,000 cells per well of a 96-well plate.
   g. Place the plate in a tissue culture incubator for 24 h.

⚠ CRITICAL: Optimal seeding density might need to be adapted according to the cell type used. Very dense cultures make HCS image analysis difficult, as the individual cell identification becomes more challenging. When using NPCs, we recommend using 30,000–50,000 cells per well of 96-well plates (90,000–150,000 cells*cm^{-2}) and 13,000–16,000 cells per well for 384-well plates (130,000–150,000 cells*cm^{-2}) (Zink et al., 2020).

Note: The described NPCs retain their multipotent identity over multiple passages and can therefore be used in a wide passage range. We generally use NPCs in the range of 10–25 passages.

Staining procedure for monitoring mitochondrial membrane potential

Timing: 1 h

To detect changes in $\Delta\Psi$m in live cells, iPSC-derived neural cells are stained with the potentiometric fluorescent dye tetramethylrhodamine methyl ester (TMRM). This dye is a lipophilic cation that accumulates across plasma membranes and within the mitochondrial matrix in an inverse proportion to the mitochondrial membrane potential according to the Nernst equation. TMRM accumulation in the mitochondria is dependent on both the plasma membrane potential and the mitochondrial membrane potential. Based on the surface-to-volume ratio, equilibration of TMRM across the mitochondrial membrane occurs more rapidly than across the plasma membrane (Nicholls, 2006). At high concentration, TMRM forms non-fluorescent aggregates within the mitochondrial matrix. Therefore, high concentration of TMRM should be avoided, and the dye should be used in non-quenching mode, which is considered to be the case for concentrations below 30 nM (Ward et al., 2007). The incorporation of the dye indicates active mitochondria and does not affect mitochondrial function. Several papers describe the use of TMRM to analyze $\Delta\Psi$m with slight differences in the staining method (Zimmermann et al., 2008; Perry et al., 2011; Nicholls, 2018). In our protocol, iPSC-derived NPCs are stained with 10 nM TMRM for 30 min, and then washed before imaging. In our hands, this is the most robust approach, as during imaging the $\Delta\Psi$m signal remains relatively stable for 30 min (Figure 2). For imaging experiments exceeding 30 min, we recommend to not wash out TMRM before the analysis but instead to dilute the TMRM concentration by adding more media to each well. This approach may allow the TMRM dye to remain in equilibrium for a longer time window (Iannetti et al., 2016). Lastly, given the influence of plasma membrane potential on TMRM accumulation,

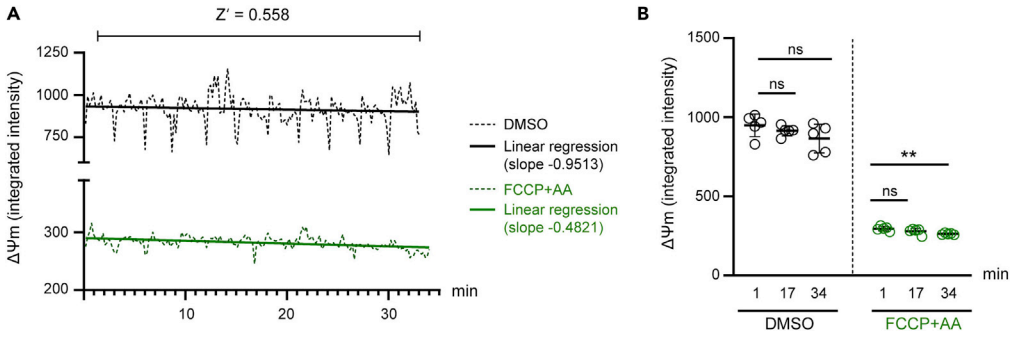


Figure 2. Kinetic assessment of ΔΨm

(A) Continuous monitoring of the ΔΨm over time and assessment of the robustness of the assay (Z′ score) in NPCs treated with DMSO or with FCCP and antimycin A (AA). iPSC-derived NPCs were stained with 10 nM TMRM (in non-quenching mode) for 30 min followed by a washing step and HCS-based quantification of ΔΨm.

(B) Quantification of ΔΨm intensity based on the TMRM signal in iPSC-derived NPCs treated with DMSO or with FCCP and antimycin A (AA) at dedicated time points. Mean ± SD, unpaired Student's t-test, **p < 0.01.

we advise to not use TMRM in case there might be indications that the plasma membrane potential is changing during the specific experimental set-up. In these cases, alternative strategies to TMRM should be applied (Nicholls, 2018).

3. Prepare TMRM stocks.
   a. Prepare a stock solution of TMRM at a concentration of 25 mM in dimethylsulfoxide (DMSO).

   Alternatives: Instead of TMRM, it is also possible to use TMRE (Invitrogen/Molecular Probes T-669).

   Note: Protect TMRM solution from light, and store sealed at −20°C. Prepare further dilutions in media fresh before each experiment.

4. Prepare staining solution.
   a. Add 10 nM TMRM and 1 μg/mL Hoechst 33342 dye to the culture media.

   ⚠ CRITICAL: The concentration of TMRM should be adjusted depending on the neural cell type used. For iPSC-derived NPCs, we carried out dose-dependent experiments and determined 10 nM as the lowest concentration of TMRM showing a reliable signal for HCS.

5. For control wells, prepare the staining solution containing ΔΨm modulators: FCCP and antimycin A (collectively defined as F+AA).
   a. Add 10 nM TMRM, 1 μg/mL Hoechst 33342 dye, 10 μM FCCP and 10 μM antimycin A to the culture media.

   Note: FCCP and antimycin A lead to ΔΨm depolarization and therefore serve as internal controls for the HCS assay. FCCP and antimycin A are dissolved in DMSO as 25 mM stock solutions. Adjust FCCP and antimycin A concentrations depending on the neural cell type used if needed.

   Alternatives: In addition to F+AA, other mitochondrial inhibitors and modulators may be included to support ΔΨm quantification (Nicholls, 2018). For example, rotenone can be used to lower ΔΨm by inhibiting mitochondrial complex I, oligomycin to increase ΔΨm and prevent reversal of ATP synthase that may lead to unwanted usage of cytosolic ATP,

and cyclosporine A to mitigate the opening of the mitochondrial permeability transition pore (mPTP).

6. Include DMSO controls accordingly.

⚠ CRITICAL: Wear protective clothing, gloves, and eye/face protection when handling DMSO or solutions containing DMSO. DMSO irritates the skin and eyes. Dispose DMSO in accordance with applicable regional, national, and local laws and regulations.

Optional: For high-throughput compound screenings, we recommend to add the compounds to the iPSC-derived neural cells prior to the staining, and then incubate the drugs for 1–24 h. The incubation time depends on the respective compounds and may need to be experimentally validated and adjusted accordingly. Following appropriate incubation, neural cells can be stained by adding 2 × TMRM and Hoechst (in medium) directly to the cells (without aspiration of the old medium) to obtain a final TMRM concentration of 10 nM and 1 μg/mL Hoechst 33342. After addition of the staining solution, continue with step 9.

7. Aspirate the medium and wash once with PBS without $MgCl_2$/$CaCl_2$.
8. Incubate the iPSC-derived neural cells with 50 μL live-cell staining solution for 96-well plates and 30 μL for 384-well plates (with and without $\Delta\Psi$m modulators) and incubate for 30 min at 37°C, 5% CO_2.
9. Turn on the HCS imaging platform. If possible, set the temperature to 37°C and the CO_2 level to 5%. If CO_2 control is not available, ensure that the imaging media contains an alternative pH buffer such as HEPES.
10. After the incubation time, remove the live-cell staining solution and gently wash 1–2 times with pre-warmed (RT) PBS without $MgCl_2$/$CaCl_2$.
11. Add 100 μL for 96-well plates and 30 μL for 384-well plates of phenol red-free cell culture media appropriate for your cell type of use (e.g., for NPCs see media list above).

⚠ CRITICAL: In our hands, the TMRM signal is relatively stable for 30 min when washed out and kept without temperature control (Figure 2). In case of time-dependent variability or lack of comparable and robust TMRM signal intensity across the plate, we recommend to perform image acquisition without complete washing of TMRM and to dilute the concentration of the dye by adding imaging medium (Iannetti et al., 2016) (see also troubleshooting problem 4).

12. Proceed to step 13 (HCS imaging) immediately for HCS.

HCS imaging

Timing: 1–2 h (depending on image acquisition settings)

This step describes the image acquisition using the Operetta CLS High Content Analysis System (PerkinElmer).

13. Place the plate in the HCS imaging platform.
14. Define the plate type (e.g., 96- or 384-well plate based on step 1.a).
    a. Check manufacturer comments on plate usage.
15. Select the appropriate light source and filter: for instance, detection at wavelength ranges from 365–465 nm for Hoechst 33342 and 550–610 nm for Alexa Fluor 568 / TMRM.

Alternatives: Instead of Alexa 568, comparable results can be obtained using Cy3.

16. Choose operational mode non-confocal (wide-field fluorescence).
17. Select the objective.
    a. See the notes section for advice on which objective to use.

Note: For live-cell imaging, always apply the control of temperature and CO_2 if possible.

Alternatives: It is possible to select confocal as operational mode. For measuring TMRM intensity, the non-confocal wide-field fluorescence mode is sufficient. However, for other HCS experiments (for example to assess detailed mitochondrial structure) confocal imaging may be crucial.

Note: For image acquisition of an entire 96- or 384-well plate, we recommend using the 20 × objective, as it reduces the image acquisition time. In our hands, the 20 × objective (air or water immersion) provides most robust results.

18. Determine microscope settings, exposure time, and Z-set-off for additional Z-positions. We suggest binning of 2 × 2, which reduces noise and the image size and increases acquisition speed, even if it lowers the digital resolution.
    a. Select a well containing iPSC-derived neural cells and take a snapshot. Find focus height using the Z-stack. The Z-stack heights may need to be optimized. Start at negative values and go up to positive until cells are in focus. Set the appropriate focus height for each channel individually.
    b. Evaluate brightness and set exposure times for each channel individually.

⚠ CRITICAL: Set up the image acquisition based on a well containing control cells. However, check the settings also in the wells treated with $\Delta\Psi$m modulators (or test compounds) in order to cover the dynamic range of the experiments and avoid over- or underexposure. Different drugs may cause big changes in $\Delta\Psi$m and TMRM fluorescence. Hence, imaging should be tuned to avoid signal saturation and take into account the expected dynamic range of the experimental set up.

19. Choose a different well to confirm or adjust settings and exclude plate-tilting.

Note: Accidental tilting of the plate could lead to out-of-focus images on one side of the plate. Ensure that the plate is placed correctly in the plate holder.

20. Define the plate layout.
    a. Select scan area and number of fields.
    b. Determine the appropriate number of fields needed to represent the well (e.g., 8 fields in a single well of a 96-well plate).
21. Start the run.

Note: Maximal excitation for TMRM may vary depending on the concentration of the dye in the mitochondria and the solvents used.

Note: Choosing "all fields" in plate layout definition will prolong the time of measurement.

Note: Avoid using the outer rows and outer columns of any given HCS plate due to edge effects (e.g., thermal evaporation and differences near the plate edge). The outer rows and outer columns should not be left blank but should be filled with buffer solution or PBS (at least the same volume as the wells containing cells, e.g., 100 µL for 96-well plates).

HCS analysis of the mitochondrial membrane potential using open-source software (CellProfiler)

Timing: ~2–6 h (depending on the computer capacity and the number of images to be processed)

This step describes the HCS image analysis for the quantification of $\Delta\Psi m$ in iPSC-derived neural cells based on the open-source software CellProfiler (Figures 1A, 1B and 1D), which is also suitable to quantify images from high-throughput experiments. The image processing time is based on the number of images acquired per field and the computing capacity. In our hands, 4–8 images (fields of view) per well are sufficient to generate robust data. When using the Operetta CLS, 16-bit images are generated with a pixel resolution of 2160 × 2160 resulting in 8–10 GB imaging data per 96-well plate (no outer row image acquisition).

The pipelines and examples images that can be used to try out our HCS protocol can all be downloaded here: https://github.com/StemCellMetab/Mitochondrial-membrane-potential. We also included a video showing all the steps of the CellProfiler analysis pipeline.

22. Install CellProfiler (https://cellprofiler.org/releases) and download the analysis pipeline (CellProfiler-Pipeline_MMP_20×.cpproj), and pipelines for illumination correction (CorrectIlluminationCalculate.cpproj, ApplyIllumCorr_DNA.cppoj, AplyIllumCorr_TMRM.cpproj) from GitHub (https://github.com/StemCellMetab/Mitochondrial-membrane-potential).
23. Open the "CorrectIlluminationCalculate" pipeline.

Note: For measuring intensity, correction of the illumination variation can be important. Due to the optics of the microscope, or imperfection in the slide or sensor bias, the intensity within a fluorescence image can vary by more than two-fold across the field of view. By applying the "CorrectIlluminationCalculate" and "CorrectIlluminationApply" modules, it is possible to compensate for non-uniformities in illumination. If correction of the illumination is not needed, move on to step 39.

24. Add the images to be analyzed by dragging and dropping them into CellProfiler.
25. Go to "Metadata".
    a. Enter the extraction method and metadata source. To set an expression to enable CellProfiler to interpret metadata from a file name or folder click on the magnifying glass. Adjust the regular expression ("Regex"). For further help on defining the regular expression syntax click on the "?" next to the magnifying glass.
    b. Click "Submit".
    c. Click "Update" to extract and display the metadata in the CellProfiler window.
26. Go to "NamesAndTypes".
    a. Type in a name to assign to the images.
27. Go to "CorrectIlluminationCalculate" and adjust the following steps.
    a. Select the input name (based on the name given in "NamesAndTypes").
    b. Name the output image (e.g., IllumNameOfTheExperiment).
    c. Adjust the smoothing filter size if necessary.
        i. In the example pipeline, the filter method is set to '*automatic*'. Should this setting not lead to sufficient illumination correction, try the method '*Object size*' and enter the approximate diameter of a typical object in pixels. Use the 'start test mode' to step through the pipeline and visually check the outcome, and increase or decrease the diameter if necessary.

Note: For more help on the "CorrectIlluminationPipeline" use the "?" button for detailed explanations or visit the CellProfiler homepage (https://cellprofiler.org/previous-examples#illumination-correction).

28. Go to "SaveImages".
    a. Select the image to save (from "CorrectIlluminationCalculate").
    b. Enter the single file name.
    c. Define the output file location.
29. Click "Start Test Mode" to check for errors in the pipeline.
    a. Errors are marked with a red "x".
    b. Click "Analyze Images" to start the pre-processing of the images using the "CorrectIlluminationCalculate" module.
    c. The representative image is stored at the destination set in step 28c.

Note: The module "CorrectIlluminationCalculate" is used to create the illumination function, which is an image that is representative of the overall pattern of uneven illumination in the image set.

30. Open the "ApplyIllumCalculate_DNA" pipeline (https://github.com/StemCellMetab/Mitochondrial-membrane-potential).
31. Add the images to be analyzed by dragging and dropping them into CellProfiler.
32. Go to "Metadata".
    a. Enter the extraction method and metadata source as under step 25.
    b. Click "Submit".
    c. Click "Update" to extract and display the metadata in the CellProfiler window.
33. Go to "NamesAndTypes".
    a. Type in a name to assign to the images.
    b. Select the single image location.
    c. Choose the single image to add to all image sets. This image has been generated in the "CorrectIlluminationCalculate" step.
34. Go to "CorrectIlluminationApply" and adjust the following steps.
    a. Select the input image.
        i. Image to be corrected (from "NamesAndTypes").
    b. Name the output image (e.g., CorrNameOfTheExperiment).
    c. Select the Illumination correction function.
        i. Image that will be used to perform the correction and has been generated in the "CorrectIlluminationCalculate" step.
35. Go to "SaveImages".
    a. Set the type of image to save to "image".
    b. Select the image to save (entry done for "CorrectIlluminationApply").
    c. Select the image name for file prefix.
    d. Enter the text to append to the image name.
    e. Define the output file location.
36. Click "Start Test Mode" to check for errors in the pipeline.
37. Click "Analyze Images" to start the pre-processing of the images using the "CorrectIllumination Apply" module.
    a. The images generated are saved in the defined file location and are ready to be analyzed using the CellProfiler analysis pipeline.
38. Repeat steps 30–37 using the "ApplyIllumCalculate_TMRM" pipeline (https://github.com/StemCellMetab/Mitochondrial-membrane-potential).

Note: The illumination pattern may differ between experiments. For example, different staining reagents for a batch of images or changes in the settings in the optical path of the microscope will change the illumination pattern. This means that the illumination function has to be performed for each set of imaging or sample preparation condition separately.

Note: For small image sets, the workflow for creating and applying the illumination correction can be integrated into the CellProfiler analysis pipeline. For large image sets, it is advisable to first create and save the illumination functions using one CellProfiler pipeline, and then retrieve and apply the illumination functions using the CellProfiler analysis pipeline as described in this protocol.

39. For image analysis of $\Delta\Psi$m using CellProfiler, open the CellProfiler analysis pipeline (CellProfiler-Pipeline_MMP_20x.cpproj: https://github.com/StemCellMetab/Mitochondrial-membrane-potential).
40. Add the pre-processed images (or raw images if illumination correction has not been applied) generated in step 37 by dragging and dropping them into CellProfiler.
41. Go to "Metadata".
    a. Enter the extraction method and metadata source as under step 25.
42. Go to "NameAndTypes" and adjust the settings.
    a. In the default settings of the downloaded pipeline channel 1 is set as DNA (Hoechst staining for nuclei) and channel 2 is set as TMRM (TMRM staining for $\Delta\Psi$m).
43. Set the default input and output folders.
    a. Select the "File" dropdown menu and select "Preferences". Select "Browse" next to the "Default Output Folder" and "Default Input Folder".
    b. Enter a filename for saving.
44. Go to the "ExportToSpreadsheet" module.
    a. Enter a name at "filename prefix".
45. Testing and adjusting the pipeline.
    a. Click on "Start Test Mode".
    b. A green checkmark will display next to the modules that have no errors. A red "x" will display next to the modules that have an error. The "ExportToSpreadsheet" module always has a red "x" during the test mode.
    c. Use the "Step" button to step through each module. Visually check the images and adjust each module according to your cells and image intensity. The applied analysis algorithm and a short description of the building blocks can be found in the following table (see also Figure 1B for a graphical visualization of the pipeline):

CellProfiler image analysis pipeline

Building block	Specification/details
Images	The image module is used to compile the images for analysis.
Metadata	The Metadata module allows to extract information describing your images (i.e., metadata).
NamesAndTypes	The NamesAndTypes module allows to assign a meaningful name to each image by which other modules will refer to it.
IdentifyPrimaryObjects	The nuclei are identified based on Hoechst staining. Nuclei at the border of the image are removed as well as objects not matching the size and intensity criteria (threshold).
IdentifyPrimaryObjects	The TMRM staining is identified. Objects not matching the size and intensity criteria (threshold) are excluded.
IdentifySecondaryObjects	Cell edges are defined based on the previously selected nuclei, here defined as "Cell".
RelateObjects	TMRM objects (child object) are associated with the previously defined Cell objects (parent object). This enables to calculate mean measurement values for TMRM associated to the Cell.
MeasureImageAreaOccupied	The area occupied by previously identified objects is measured (DNA, Cells and TMRM).
MeasureObjectIntensity	TMRM intensity is calculated in relation to the cell. Additional intensity parameters can be chosen (e.g., intensity of the nuclei).

(*Continued on next page*)

Continued

Building block	Specification/details
MeasureObjectSizeShape	Additional output parameter for size and shape of the objects can be chosen.
ExportToSpreadsheet	Output results and storage location are defined.

Note: The "IdentifyPrimaryObjects" and "IdentifySecondaryObjects" modules might need to be adjusted according to the cell type and intensity of the dyes. The first parameters to optimize are the typical size of objects limits and the threshold method and values.

46. Start analysis.
    a. Ensure to exit the test mode (click "Exit Test Mode") and click the "Analyze Images" button.
    b. CellProfiler will analyze the image sets and will export the results to a spreadsheet on the selected drive and folder. The pipeline will also save a spreadsheet containing the used settings (filename prefixExperiment). For opening in Excel, choose "," as delimiter, "." as decimal separator, and "(space)" as thousands separator.

Note: The time necessary to complete analysis depends on the computer used. For the analysis of large datasets, a fast computer with sufficient RAM (32 GB recommended) would help to speed up the analysis.

Note: The number of *workers* can be adjusted in the preferences of CellProfiler (File - Preferences - Maximum number of workers). This allows machines with many computational cores to use their resources efficiently.

Note: Representative graphs for the quantification of $\Delta\Psi$m can be created in Microsoft Excel or statistics analysis software such as GraphPad Prism.

HCS analysis of the mitochondrial membrane potential using commercial software (Columbus)

Timing: ~2–6 h (depending on the computer capacity and the number of images to be processed)

This step describes the HCS image analysis for the quantification of $\Delta\Psi$m in iPSC-derived neural cells based on the custom image data storage and analysis system Columbus™ (PerkinElmer) (Figures 1A, 1C, 1E). The image analysis pipeline and exemplary images for trial analysis can be downloaded here: https://github.com/StemCellMetab/Mitochondrial-membrane-potential.

47. For data migration from the Operetta CLS High-Content Analysis System to Columbus export TIF files and image-related metadata from the Harmony software and import data to Columbus.
    a. Open "Settings" and then "Data Management", and "Export Data" in the Harmony software.
    b. Specify "Columbus Export (Index and Images)".
    c. Select data and measurements to be exported and specify "Export Path".
    d. Start the export from Harmony by clicking "Start".
    e. Open the Columbus software and move to the "Import" screen. The "Columbus Helper Required" window will appear. Download the connection file and connect the Columbus Helper App. If the Columbus Helper App is not installed yet follow the instructions for installation.
    f. Specify the "Import Type: Operetta IDX/TIF" and "Source Folder". Optional: Specify "Import Mode" and "Screen Name".
    g. Start the import to Columbus by clicking "Start".

Note: Alternatively, the "Columbus Transfer" function can be used to reduce time and to automate the data migration process. For "Columbus Transfer", a network connection between Columbus and the Operetta CLS High-Content Analysis System is required.

48. For image analysis of ΔΨm quantification using Columbus, open the Columbus software.
49. Move to "Image Analysis" screen.
    a. Select the measurement you want to analyze from the Data Tree on the left.
    b. Select one single image (e.g., well and field) as representative image.
    c. The selected image is displayed in the Image View section.
50. Load existing image analysis pipeline for ΔΨm quantification.
    a. Click "Load Analysis from Disk".
    b. "Choose File" and open the *.aas file analysis script file (https://github.com/StemCellMetab/Mitochondrial-membrane-potential).
    c. Click "Open" and "OK".

Note: As an alternative, the image analysis pipeline can be set up by the user using the building blocks implemented in the Columbus software. The applied analysis algorithm and a short description of the building blocks can be found in the following table (see also Figure 1C for a graphical visualization of the pipeline):

Columbus image analysis pipeline

Building block	Specification/details
Input Image	Selected input image is displayed.
Find Nuclei	Nuclei are detected based on Hoechst signal. Output population: I
Calculate Intensity Properties	Intensities of nuclei are calculated.
Calculate Morphology Properties	Area and roundness of nuclei are calculated.
Select Population	Nuclei at the border of the image are removed. Output population: II
Select Population (2)	Additional nuclei are excluded based on individual area, roundness, and intensity parameters. Output population: III
Find Cytoplasm	Cell cytoplasms are defined based on previously selected nuclei (Output population: III).
Calculate Intensity Properties (2)	ΔΨm intensity is calculated based on TMRM channel within the previously defined cell regions.
Define Results	Output results are defined. "Population III" is used to select "Number of Objects" (nuclei) and the mean "ΔΨm intensity" in the cell as results.
Sequence Comment	Comment section for the script.

51. Adjust and test the settings.
    a. The mask/segmentation of defined objects is displayed in the Image View. The illustration of the mask (Regions, Overlays) can be adjusted as preferred. Intermediate results for the selected building block are displayed in the Table View section.
    b. If required, adjust the filters and input parameters of the building blocks to optimize the segmentation of objects. Define the final readout parameters of the analysis in the last building block "Define Results".
    c. Once you have achieved good results, select a few other image fields to test and optimize the analysis with these images.

Note: In particular, the building blocks "Find Nuclei", "Find Cytoplasm", and "Select Population" typically require adjustment of the filter methods and parameters according to imaging settings, the cell type and density used, and the intensity of the dyes.

52. Save the analysis to the database or the file system as an *.aas file.
53. Start Analysis.
    a. Move to "Batch Analysis" screen.
    b. Select one or multiple measurements in the Data Tree (right click "Select").
    c. Click "..." to load the saved analysis script file. Alternatively, you can select the analysis script directly from the database in the Data Tree via left mouse click.
    d. Click the green arrow to start the batch analysis. A background job is started to analyze all selected measurements using the selected script file.
    e. Use the Job Status screen to view the progress of the analysis.
    f. The results are written to the database.

Note: Make sure that the used channels for the selected measurements and the channel names are the same, and correspond to the names defined in the analysis.

54. Export of results.
    a. Move to "Export" screen.
    b. Connect to Columbus Helper.
    c. Select your measurement from the Data Tree.
55. Specify export options.
56. Choose a destination export folder on your server.
    a. Tick the type of file for the export (for the results choose "Results" as *.txt File).
    b. Click the green arrow to start the export.
57. The results can be found as a Text Document in previously defined folder.

Note: To import or export files, you must connect Columbus to the Columbus Helper App. If the Columbus Helper App is not installed, follow the instructions for installation.

Note: Representative graphs for the quantification of $\Delta\Psi$m can be created in Microsoft Excel or statistics analysis software such as GraphPad Prism.

EXPECTED OUTCOMES

The protocol described here enables the monitoring and quantification of mitochondrial activity based on $\Delta\Psi$m in human iPSC-derived neural cells. Previous protocols have been generated for assessing $\Delta\Psi$m in live cells using HCS (Iannetti et al., 2016). Our protocol is specifically designed for neural cells obtained from human iPSCs. When applied to patient-derived iPSC lines or genetically modified iPSCs, this protocol could lead to identify disease-specific or mutation-specific defects in neural mitochondrial activity. Such defects can be scored as "phenotypes" to perform phenotypic compound screenings using the HCS pipeline that we provide here. We previously applied this approach to identify compounds capable of counteracting $\Delta\Psi$m defects in neural cells derived from patients affected by Maternally Inherited Leigh Syndrome (MILS) carrying mutations in the mitochondrial gene *MT-ATP6* (Lorenz et al., 2017). Our HCS protocol can be used also in combination with another HCS assay that quantifies neurite outgrowth (Lickfett et al., STAR Protocols, 2022). We previously used the combination of these two protocols to screen for modulators of human neurotoxicity that can affect $\Delta\Psi$m and neurite count in different ways (Zink et al., 2020).

LIMITATIONS

This HCS protocol is essentially an endpoint measurement for high-throughput assessment of changes in mitochondrial membrane potential ($\Delta\Psi$m), which is an important parameter regulating mitochondrial bioenergetics and cellular physiology. For detailed kinetic experiments aimed at addressing dynamic changes of $\Delta\Psi$m, important modifications should be applied, since the TMRM signal may vary if the cells are assessed for periods longer than 30 min (Figure 2). In these cases, changes in the washing step may be beneficial (see troubleshooting problem 4). Automated

dispensing of reagents for example by liquid handling might also be considered to reduce the variability of the assay.

The protocol reliably quantifies changes in the existing baseline rate of dye loss from the mitochondria, but it is not effective in monitoring transient changes of $\Delta\Psi m$. In order to address this and to increase the identification of modifiers that could lead to increased $\Delta\Psi m$, we recommend to include positive modulators of $\Delta\Psi m$ (e.g., oligomycin) and to be aware of the strict time sensitivity of the assay (see troubleshooting problem 7).

Since our protocol measures the functional mitochondrial state of live neural cells, it is possible that external conditions may influence the results. For example, changes in environment (temperature, CO_2, or humidity), improper coating of the plates, or mechanical forces may induce cellular stress or detachment leading to changes in the $\Delta\Psi m$ signal. This could lead to inconsistent results. In order to avoid this, particular care needs to be applied to the handling of the neural cells and the HCS plates. A reference sample can be included in each plate to serve as internal control in order to prevent low quality data caused by inter-plate variability (Bray and Carpenter, 2004).

Our HCS protocol is based on non-confocal wide-field fluorescence mode, and is therefore not suitable for assessing detailed structures (e.g., mitochondrial morphology). In fact, we only use variations in the Z-axis for optimal cell focus. It is possible to adapt the HCS pipeline to confocal mode and include multiple Z-stacks images for the same field of view. However, this approach generates multiple measurements of the same cells, and this needs to be taken into account during data analysis and processing. In order to correctly assign multiple images to the same cells, it is possible to run a maximal intensity projection on all Z-stacks to generate a pseudo 2D image. This approach should eliminate out-of-focus pixels and could produce acceptable images for analysis.

Lastly, there are challenges associated with data storage. This protocol is based on images that can take up a conspicuous hard drive space, and may require additional computational power for analysis and long-term storage. As an example, we commonly generate 16-bit images with a pixel resolution of 2160 × 2160. For a single 96-well plate, we obtain approximately 8–10 GB of data.

TROUBLESHOOTING

Problem 1

iPSC-derived neural cells detach after washing steps (e.g., step 7).

Potential solution

- Try different coating reagents and/or increase the concentration of the coating.
- Reduce number of washing steps. One way to reduce washing steps is to add the staining solution directly to the cells in equal volume as 2 × to obtain a final concentration of 10 nM for TMRM and 1 μg/mL for Hoechst.
- Seed more cells to compensate for cell loss during staining.

Problem 2

Cells are out-of-focus (steps 17–19).

Potential solution

- Try different Z-positions.
- Optimize the seeding conditions. Ideally, cells should grow as single cells.
- Check if the plate type used is suitable for the device and whether the optical quality is sufficient (e.g., evenness).
- Check that the plate is correctly positioned and is not tilted.

- Make sure that the wells contain enough medium so that the liquid level does not affect the autofocus of the instrument.

Problem 3

iPSC-derived neural cells are not correctly visualized and analyzed (step 45).

Potential solution

- Determine the optimal cell density in a pilot experiment. Cells should be dense enough to ensure survival, but also sufficiently sparse for the pipeline to work properly. In general, always analyze more than 1,000 cells per individual well (see also step 2).

Problem 4

The TMRM signal is variable across the plate and within different wells of the same cell line (steps 10–20).

Potential solution

- Instead of washing off the TMRM, add imaging medium in each well in order to dilute the TMRM concentration. This approach has been suggested to maintain the TMRM signal in equilibrium for longer time (Iannetti et al., 2016). Alternatively, it is also possible to not wash the cells, and leave the TMRM concentration as it is during the imaging step (Nicholls, 2018).
- The presence of light-induced oxidative stress may compromise cell viability. Extensive exposure to light may induce reactive oxygen species (ROS), which in turn also influences the TMRM signal. Reduce the images acquired from one well. This will reduce the time of exposure to light. Also, ensure that cell viability is maintained by monitoring the Hoechst signal.
- Check for photobleaching. By reducing the energy of the excitation beam and the irradiation time of the fluorophore, an attempt can be made to minimize the effect of photobleaching.
- Check for quenching effect. Use low concentrations of TMRM (<30 nM is considered for non-quenching mode) in order to avoid auto-quenching of mitochondrial TMRM. In this case, the fluorescence signal of TMRM can be directly correlated to $\Delta\Psi$m across the inner mitochondrial membrane. A loss of $\Delta\Psi$m may cause TMRM to leak from mitochondria resulting in a loss of fluorescence intensity. Ensure that the TMRM signal is due to changes in the $\Delta\Psi$m, e.g., by using a probe specific to the plasma membrane potential such as $DiBAC_2$ (Ward et al., 2007).

Problem 5

The HCS pipeline for $\Delta\Psi$m quantification does not generate stable results using CellProfiler (steps 39–46).

Potential solution

- The pipeline indicates when analysis for a given position fails. This is usually because primary objects, the Hoechst signal, or the TMRM signal are not properly detected. This can be solved by adjusting the "IdentifyPrimaryObjects" modules. Adjust the typical diameter of the objects (Nuclei and TMRM). To determine the average diameter of the objects, open an exemplary image and measure the distances using the "measure length" tool ("Tools" in the display window menu bar). Use the pixel intensity tool to estimate the pixel intensity and adjust the lower and upper bounds of the threshold accordingly. Adjust the method to distinguish clumped objects (decide between intensity or shape).
- The pipeline might stop with a memory error if the RAM was limiting. Try to restart the analysis running on fewer CPU cores (can be adjusted in CellProfiler settings).

Problem 6

The HCS pipeline for ΔΨm quantification does not generate stable results using Columbus (steps 48–57).

Potential solution

- Many nuclei are sorted out that actually look healthy. This is usually because the filter properties for nuclei exclusion do not fit with the cell type used. This can be solved by adjusting these filter properties within the building block "Select Population (2)". Define the minimal and maximal values for Hoechst intensity (Intensity Nucleus) and for the area (Nucleus area). Also, the Nucleus Roundness filter can be adjusted.
- ΔΨm quantification shows strongly fluctuating values. The reason for this could be an insufficient definition of the cell area. This could be solved by adjusting the methods used under the building block "Find Cytoplasm". Choose from method A-F and adjust the common/individual thresholds to improve cell segmentation.

Problem 7

iPSC-derived neural cells in the HCS plate treated with FCCP and antimycin A appear unhealthy, or the treatment does not lead to depolarization (i.e., to a decrease of the TMRM signal) (step 6).

Potential solution

- Optimize the FCCP and antimycin A concentration. Perform a dose-response curve to determine the most suitable concentration to induce depolarization, but without inducing cell death.

  Optional: Include oligomycin to prevent ATP synthase reversal.

RESOURCE AVAILABILITY

Lead contact

Further information and requests for resources should be directed to and will be fulfilled by the lead contact, Prof. Dr. Alessandro Prigione (alessandro.prigione@hhu.de).

Materials availability

This study did not generate new unique materials.

Data and code availability

The pipelines for ΔΨm analysis and example images have been deposited to GitHub: https://github.com/StemCellMetab/Mitochondrial-membrane-potential [https://doi.org/10.5281/zenodo.6794537].

ACKNOWLEDGMENTS

A.P. acknowledges support from the Deutsche Forschungsgemeinschaft (DFG) (#PR1527/5-1 and PR1527/6-1), the European Joint Programme for Rare Diseases (EJPRD) and German Federal Ministry of Education and Research (BMBF) (#01GM2002A), the United Mitochondrial Disease Foundation (UMDF), People Against Leigh Syndrome (PALS), Fondation Maladies Rares and Association AMMi, and the University Hospital Düsseldorf (Forschungskommission UKD). O.P. acknowledges funding from the European Joint Programme for Rare Diseases (EJPRD). M.B. acknowledges support from the Deutsche Forschungsgemeinschaft (DFG) (INST 208/760-1FUGG).

AUTHOR CONTRIBUTIONS

Conceptualization, A.Z. and A.P.; methodology, A.Z., U.H., A.W., O.P., and M.B.; investigation, A.Z., U.H., and A.W.; writing – original draft, A.Z.; writing – review and editing, A.Z., U.H., A.W.,

O.P., and A.P.; funding acquisition, A.P., O.P., and M.B.; resources, M.B., O.P., and A.P.; supervision, A.P. and O.P.

DECLARATION OF INTERESTS

The authors declare no competing interests.

REFERENCES

Bray, M.-A., Carpenter, A., and Imaging Platform, Broad Institute of MIT and Harvard. (2004). Advanced assay development guidelines for image-based high content screening and analysis. In Assay Guidance Manual, S. Markossian, A. Grossman, K. Brimacombe, M. Arkin, D. Auld, C.P. Austin, J. Baell, T.D.Y. Chung, N.P. Coussens, and J.L. Dahlin, et al., eds. (Eli Lilly & Company and the National Center for Advancing Translational Sciences). http://www.ncbi.nlm.nih.gov/books/NBK126174/.

Iannetti, E.F., Smeitink, J.A.M., Beyrath, J., Willems, P.H.G.M., and Koopman, W.J.H. (2016). Multiplexed high-content analysis of mitochondrial morphofunction using live-cell microscopy. Nat. Protoc. *11*, 1693–1710. https://doi.org/10.1038/nprot.2016.094.

Lickfett, S., Menacho, A., Zink, A., Telugu, N.S., Beller, M., Diecke, S., Cambridge, S., and Prigione, A. (2022). High-content analysis of neuronal morphology in human iPSC-derived neurons. STAR Protocols.

Lorenz, C., Lesimple, P., Bukowiecki, R., Zink, A., Inak, G., Mlody, B., Singh, M., Semtner, M., Mah, N., Auré, K., et al. (2017). Human iPSC-derived neural progenitors are an effective drug discovery model for neurological mtDNA disorders. Cell Stem Cell *20*, 659–674.e9. https://doi.org/10.1016/j.stem.2016.12.013.

Nicholls, D.G. (2006). Simultaneous monitoring of ionophore- and inhibitor-mediated plasma and mitochondrial membrane potential changes in cultured neurons. J. Biol. Chem. *281*, 14864–14874. https://doi.org/10.1074/jbc.M510916200.

Nicholls, D.G. (2018). Fluorescence measurement of mitochondrial membrane potential changes in cultured cells. In Mitochondrial Bioenergetics: Methods and Protocols Methods in Molecular Biology, C.M. Palmeira and A.J. Moreno, eds. (Springer), pp. 121–135. https://doi.org/10.1007/978-1-4939-7831-1_7.

Perry, S.W., Norman, J.P., Barbieri, J., Brown, E.B., and Gelbard, H.A. (2011). Mitochondrial membrane potential probes and the proton gradient: a practical usage guide. Biotechniques *50*, 98–115. https://doi.org/10.2144/000113610.

Reinhardt, P., Glatza, M., Hemmer, K., Tsytsyura, Y., Thiel, C.S., Höing, S., Moritz, S., Parga, J.A., Wagner, L., Bruder, J.M., et al. (2013). Derivation and expansion using only small molecules of human neural progenitors for neurodegenerative disease modeling. PLoS One *8*, e59252. https://doi.org/10.1371/journal.pone.0059252.

Rossi, A., Lickfett, S., Martins, S., and Prigione, A. (2022). A call for consensus guidelines on monitoring the integrity of nuclear and mitochondrial genomes in human pluripotent stem cells. Stem Cell Rep. *17*, 707–710. https://doi.org/10.1016/j.stemcr.2022.01.019.

Wang, X., Sterr, M., Burtscher, I., Chen, S., Hieronimus, A., Machicao, F., Staiger, H., Häring, H.U., Lederer, G., Meitinger, T., et al. (2018). Genome-wide analysis of PDX1 target genes in human pancreatic progenitors. Mol. Metab. *9*, 57–68. https://doi.org/10.1016/j.molmet.2018.01.011.

Ward, M.W., Huber, H.J., Weisová, P., Düssmann, H., Nicholls, D.G., and Prehn, J.H.M. (2007). Mitochondrial and plasma membrane potential of cultured cerebellar neurons during glutamate-induced necrosis, apoptosis, and tolerance. J. Neurosci. *27*, 8238–8249. https://doi.org/10.1523/JNEUROSCI.1984-07.2007.

Zimmermann, S., Zarse, K., Schulz, T.J., Siems, K., Müller-Kuhrt, L., Birringer, M., and Ristow, M. (2008). A cell-based high-throughput assay system reveals modulation of oxidative and nonoxidative glucose metabolism due to commonly used organic solvents. Horm. Metab. Res. *40*, 29–37. https://doi.org/10.1055/s-2007-1004542.

Zink, A., Conrad, J., Telugu, N.S., Diecke, S., Heinz, A., Wanker, E., Priller, J., and Prigione, A. (2020). Assessment of ethanol-induced toxicity on iPSC-derived human neurons using a novel high-throughput mitochondrial neuronal health (MNH) assay. Front. Cell Dev. Biol. *8*, 590540. https://doi.org/10.3389/fcell.2020.590540.

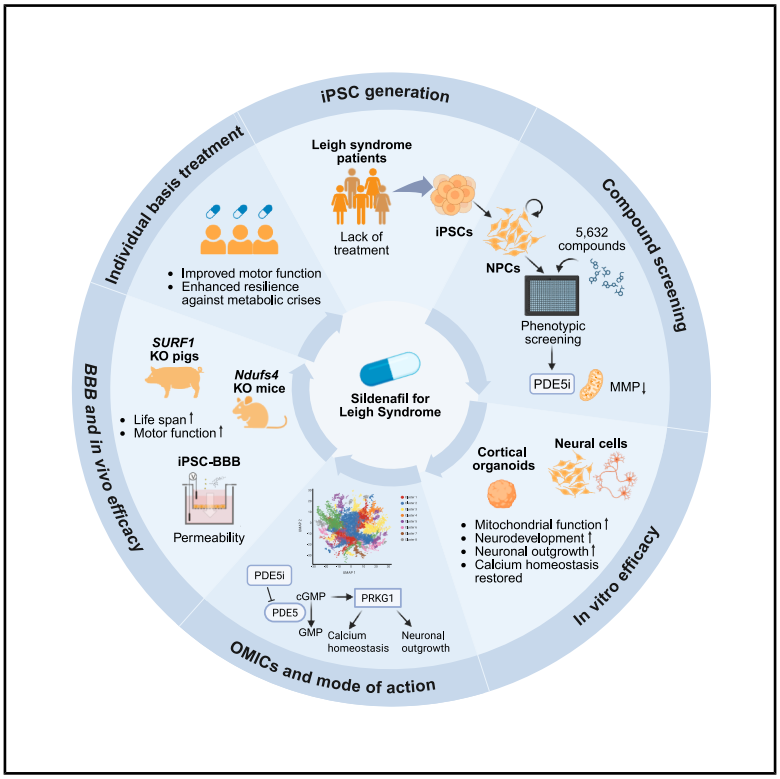
Zink, A., Lisowski, P., and Prigione, A. (2021). Generation of human iPSC-derived neural progenitor cells (NPCs) as drug discovery model for neurological and mitochondrial disorders. Bio. Protoc. *11*, e3939.

10. Appendix II

Cell

Pluripotent stem-cell-based screening uncovers sildenafil as a mitochondrial disease therapy

Graphical abstract



Highlights

- Repurposable drug screen in Leigh syndrome neural cells identifies PDE5 inhibitors
- PDE5 inhibitor sildenafil rescues the neurodevelopmental disease signature *in vitro*
- PDE5 inhibitor sildenafil extends the lifespan of Leigh syndrome animal models *in vivo*
- Sildenafil treatment on an individual basis clinically improves symptoms in six LS patients

Authors

Annika Zink, Dao-Fu Dai, Annika Wittich, ..., Ole Pless, Markus Schuelke, Alessandro Prigione

Correspondence

ddai4@jh.edu (D.-F.D.), dario.brunetti@unimi.it (D.B.), antonio.delsol@uni.lu (A.d.S.), emanuela.bottani@univr.it (E.B.), ole.pless@itmp.fraunhofer.de (O.P.), markus.schuelke@charite.de (M.S.), alessandro.prigione@hhu.de (A.P.)

In brief

Leigh syndrome is a severe and untreatable mitochondrial disease. Using patient-derived models in 2D and 3D, Zink and colleagues identify the PDE5 inhibitor sildenafil as a repurposable drug candidate, leading to lifespan extension in mammalian models and clinical improvement in six individuals with Leigh syndrome.

Zink et al., 2026, Cell *189*, 1656–1679
March 19, 2026 © 2026 The Author(s). Published by Elsevier Inc.
https://doi.org/10.1016/j.cell.2026.02.008

CellPress

CellPress
OPEN ACCESS

Cell

Article

Pluripotent stem-cell-based screening uncovers sildenafil as a mitochondrial disease therapy

Annika Zink,[1,51] Dao-Fu Dai,[2,51,52,*] Annika Wittich,[3,51] Marie-Thérèse Henke,[4,5,51] Giulia Pedrotti,[6,51] Sonja Heiduschka,[1,7,51] Guillem Santamaria,[8] Tancredi Massimo Pentimalli,[9,10] Christian Brueser,[11] Sofia Notopoulou,[12] Abdul Rahim Umar,[13] Aleksandra Zhaivoron,[14] Laura Petersilie,[15] Caleb Jerred,[1,7] Jesper Bergmans,[16,17] Louis Anton Neu,[15] Fabian Schumacher,[18] Jan Keller-Findeisen,[11] Agnieszka Rybak-Wolf,[9] Daniel Stach,[3] Jeanette Reinshagen,[3] Undine Haferkamp,[3] Kim Krieg,[3] Andrea Zaliani,[3] Liliya Euro,[14] Alessia Di Donfrancesco,[19] Chiara Santanatoglia,[6] Enrica Cappellozza,[6] Marta Suarez Cubero,[20] Mario Pavez-Giani,[21,22] Oleh Bakumenko,[11] David Meierhofer,[23]

(Author list continued on next page)

[1]Department of General Pediatrics, Neonatology and Pediatric Cardiology, Medical Faculty, University Hospital Düsseldorf, Heinrich-Heine-Düsseldorf, 40225 Düsseldorf, Germany
[2]Department of Pathology, Johns Hopkins University School of Medicine, Baltimore, MD 21218, USA
[3]Fraunhofer Institute for Translational Medicine and Pharmacology ITMP, Discovery Research ScreeningPort, 22525 Hamburg, Germany
[4]Charité - Universitätsmedizin Berlin, corporate member of Freie Universität Berlin and Humboldt-Universität zu Berlin, Department of Neuropediatrics, 10117 Berlin, Germany
[5]Charité - Universitätsmedizin Berlin, corporate member of Freie Universität Berlin and Humboldt-Universität zu Berlin, NeuroCure Clinical Research Center, 10117 Berlin, Germany
[6]Department of Diagnostics and Public Health, University of Verona, 37134 Verona, Italy
[7]Faculty of Mathematics and Natural Sciences, Heinrich Heine University, 40225 Düsseldorf, Germany
[8]Computational Biology Group, Luxembourg Centre for Systems Biomedicine, University of Luxembourg, 4366 Esch-sur-Alzette, Luxembourg
[9]Berlin Institute for Medical Systems Biology (BIMSB), Max Delbrück Center for Molecular Medicine in the Helmholtz Association (MDC), 10115 Berlin, Germany
[10]Charité – Universitätsmedizin Berlin, 10117 Berlin, Germany
[11]Fraunhofer Institute for Translational Medicine and Pharmacology ITMP, Translational Neuroinflammation and Automated Microscopy, 37037 Göttingen, Germany
[12]Institute of Applied Biosciences (INAB), Centre For Research and Technology Hellas (CERTH), 57001 Thessaloniki, Greece
[13]Department of Physics, University of South Florida, Tampa, FL 33620, USA
[14]Stem Cells and Metabolism Program, Faculty of Medicine, University of Helsinki, 00014 Helsinki, Finland
[15]Institute of Neurobiology, Heinrich Heine University, 40225 Düsseldorf, Germany
[16]Radboud Center for Mitochondrial Medicine, Radboud University Medical Center, 6500 HB Nijmegen, the Netherlands

(Affiliations continued on next page)

SUMMARY

Mitochondrial disease encompasses inherited disorders affecting mitochondrial function. A severe and untreatable form of mitochondrial disease is Leigh syndrome (LS), causing psychomotor regression and metabolic crises. To accelerate drug discovery for LS, we screen a library of 5,632 repurposable compounds in neural cells from LS-patient-derived induced pluripotent stem cells (iPSCs). We identify phosphodiesterase type 5 (PDE5) inhibitors as leads and prioritize sildenafil for its clinical safety. Sildenafil corrects mitochondrial membrane potential defects, restores neurodevelopmental pathways, and normalizes calcium responses in LS brain organoids. In small and large mammalian models of LS, sildenafil extends lifespan and ameliorates disease phenotypes. Off-label treatment on an individual basis with sildenafil in six LS patients improves their motor function and resistance to metabolic crises. Collectively, the findings highlight the potential of iPSC-driven drug discovery and position sildenafil as a promising drug candidate for mitochondrial disease.

INTRODUCTION

Mitochondrial disease encompasses rare genetic conditions caused by dysfunction in the cell's energy-producing organelles.[1] A severe form of mitochondrial disease is Leigh syndrome (LS, OMIM #256000), which is characterized by neurodevelopmental regression and muscle weakness, with early death following metabolic crises.[2,3] LS can result from pathogenic variants in more than 100 genes in nuclear DNA or mitochondrial DNA (mtDNA) involved in oxidative phosphorylation (OXPHOS),[4]

 © 2026 The Author(s). Published by Elsevier Inc.
This is an open access article under the CC BY license (http://creativecommons.org/licenses/by/4.0/).

CellPress
OPEN ACCESS

Alan Foley,[8] Susanne Morales-Gonzalez,[4] Isabella Tolle,[1] Diran Herebian,[1] Daniele Bonesso,[24] Giulia Cecchetto,[1] Sakurako Nagumo Wong,[9] Monica Moresco,[25] Alessandra Maresca,[25] Ilaria Decimo,[6] Francesco De Sanctis,[26] Annalisa Adamo,[26] Merel J.W. Adjobo-Hermans,[16,27] Roberto Duchi,[28] Maria Barandalla,[28] Marco Scaglia,[28] Andrea Perota,[28] Cesare Galli,[28] Burkhard Kleuser,[18] Lukas Cyganek,[11,21,37] Chris Mühlhausen,[29] Lars Schlotawa,[11,29,30] Valeria Tiranti,[19] Ertan Mayatepek,[1] Ildiko Szabo,[24] Chiara La Morgia,[25,31] Thomas Klopstock,[32,33,34] Valerio Carelli,[25,31] Felix Distelmaier,[1] Andrea Rossi,[35] Nikolaus Rajewsky,[9,36,37,38,39] Ghanim Ullah,[13] Stefan Jakobs,[11,30,40,41] Christine R. Rose,[15] Spyros Petrakis,[12] Frank Edenhofer,[20] Werner J.H. Koopman,[16,17,42] Pawel Lisowski,[9,43,44] Anu Suomalainen,[14,45,46] Dario Brunetti,[19,47,52,*] Antonio del Sol,[8,48,49,52,*] Emanuela Bottani,[6,52,*] Ole Pless,[3,52,*] Markus Schuelke,[4,5,50,52,*] and Alessandro Prigione[1,52,53,*]

[17]Department of Pediatrics, Amalia Children's Hospital, Radboud University Medical Center, 6525 GA Nijmegen, the Netherlands
[18]Institute of Pharmacy, Freie Universität Berlin, 14195 Berlin, Germany
[19]Fondazione IRCCS Istituto Neurologico Carlo Besta, 20126 Milan, Italy
[20]Department of Molecular Biology & CMBI, Genomics, Stem Cell & Regenerative Medicine Group, University of Innsbruck, 6020 Innsbruck, Austria
[21]Stem Cell Unit, Clinic for Cardiology and Pneumology, University Medical Center Göttingen, 37075 Göttingen, Germany
[22]Experimental Cardiology Institute, Medical Clinic I/Cardiology and Angiology, Justus Liebig University of Giessen, 35392 Giessen, Germany
[23]Max Planck Institute for Molecular Genetics, 14195 Berlin, Germany
[24]Department of Biology, University of Padova, 35121 Padova, Italy
[25]IRCCS Istituto delle Scienze Neurologiche di Bologna, Programma di Neurogenetica, 40139 Bologna, Italy
[26]Department of Medicine, Section of Immunology, University of Verona Hospital Trust, 37134 Verona, Italy
[27]Department of Medical BioSciences, Radboud Center for Mitochondrial Medicine, Radboud University Medical Center, 6525 GA Nijmegen, the Netherlands
[28]Avantea, 26100 Cremona, Italy
[29]Department of Pediatrics and Adolescent Medicine, University Medical Center, Georg-August-University, 37075 Göttingen, Germany
[30]German Center for Child and Adolescent Health (DZKJ), Section CNS Development and Neurological Disease, partner site Göttingen, Robert-Koch-Str. 40, 37075 Göttingen, Germany
[31]Department of Biomedical and Neuromotor Sciences (DIBINEM), University of Bologna, 40127 Bologna, Italy
[32]Friedrich-Baur-Institute, Department of Neurology, LMU University Hospital, Ludwig-Maximilians-Universität München, 80336 Munich, Germany
[33]Munich Cluster for Systems Neurology (SyNergy), 81377 Munich, Germany
[34]German Center for Neurodegenerative Diseases (DZNE), 81377 Munich, Germany
[35]Genome Engineering and Model Development lab (GEMD), IUF-Leibniz Research Institute for Environmental Medicine, 40223 Düsseldorf, Germany
[36]NeuroCure Cluster of Excellence, 10117 Berlin, Germany
[37]German Center for Cardiovascular Research (DZHK), partner site Lower Saxony and Berlin, 10785 Berlin, Germany
[38]National Center for Tumor Diseases (NCT), German Cancer Consortium (DKTK), 13125 Berlin, Germany
[39]German Center for Neurodegenerative Diseases (DZNE), 10117 Berlin, Germany
[40]Department of NanoBiophotonics, Max Planck Institute for Multidisciplinary Sciences, 37077 Göttingen, Germany
[41]Department of Neurology, University Medical Center Göttingen, 37075 Göttingen, Germany
[42]Human and Animal Physiology, Wageningen University, 6708 WD Wageningen, the Netherlands
[43]Neuropsychiatry and Laboratory of Molecular Psychiatry, Department of Psychiatry and Neurosciences, Charité - Universitätsmedizin Berlin, 10117 Berlin, Germany
[44]Department of Molecular Biology, Institute of Genetics and Animal Biotechnology, Polish Academy of Sciences, 05-552 Jastrzebiec n/Warsaw, Poland
[45]HiLife, University of Helsinki, 0004 Helsinki, Finland
[46]HUS Diagnostics, Helsinki University Hospital, 00290 Helsinki, Finland
[47]Department of Clinical Sciences and Community Health, Dipartimento di Eccellenza 2023-2027, University of Milan, 20122 Milan, Italy
[48]IKERBASQUE, Basque Foundation for Science, 48009 Bilbao, Spain
[49]CIC bioGUNE-BRTA (Basque Research and Technology Alliance), Bizkaia Technology Park, 48160 Derio, Spain
[50]German Center for Child and Adolescent Health (DZKJ), Section CNS Development and Neurological Disease, partner site Berlin, 13353 Berlin, Germany
[51]These authors contributed equally
[52]Senior author
[53]Lead contact
*Correspondence: ddai4@jh.edu (D.-F.D.), dario.brunetti@unimi.it (D.B.), antonio.delsol@uni.lu (A.d.S.), emanuela.bottani@univr.it (E.B.), ole.pless@itmp.fraunhofer.de (O.P.), markus.schuelke@charite.de (M.S.), alessandro.prigione@hhu.de (A.P.)
https://doi.org/10.1016/j.cell.2026.02.008

including complex V (CV) gene *MT-ATP6* (mitochondrially encoded ATP synthase subunit 6),[5] complex IV (CIV) assembly factor gene *SURF1* (SURFEIT1),[6] and complex I gene *NDUFS4* (nicotinamide adenine dinucleotide [NAD] + hydrogen [NADH] dehydrogenase [ubiquinone] iron-sulfur protein 4).[7]

Currently, there are no treatments for LS.[8] One obstacle to therapy discovery is the paucity of model systems.[9] The difficulties in mtDNA editing have hindered the establishment of models for mtDNA defects.[10] A pig model of LS due to *SURF1* knockout (KO) showed neurodevelopmental defects

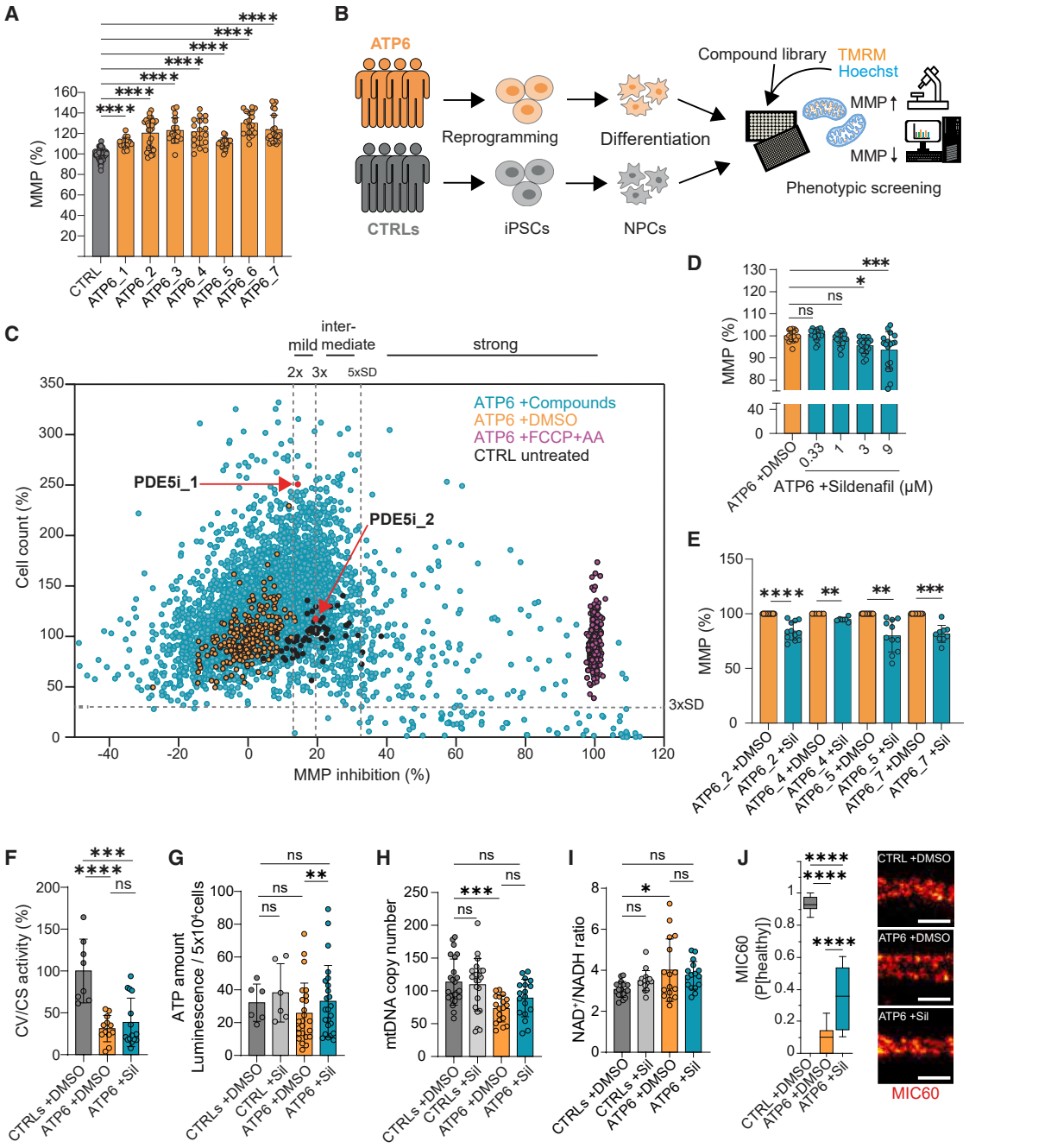


Figure 1. Compound screen in LS NPCs leads to identifying the PDE5i sildenafil

(A) HCA MMP quantification in LS NPCs (ATP6_1, ATP6_2, ATP6_3, ATP6_4, ATP6_5, ATP6_6, and ATP6_7) and control NPCs (CTRL_1). Dots: mean value/well, $n = 3$–5 independent experiments. ****$p < 0.0001$; ordinary one-way ANOVA with Dunnett's multiple comparisons.

(B) Screening approach.

(C) Compound screen in LS NPCs (ATP6_2) based on MMP depolarization (TMRM) vs. cell count (Hoechst). Control NPCs: CTRL_1; PDE5i_1: T-0156, PDE5i_2: vardenafil hydrochloride.

(D) HCA MMP quantification in LS NPCs (ATP6_2) treated with sildenafil compared with DMSO. Dots: mean value/well, $n = 4$ independent experiments; *$p < 0.05$, ***$p < 0.001$, ns, not significant; ordinary one-way ANOVA with Dunnett's multiple comparisons.

(E) Cytofluorimetry MMP quantification in LS NPCs treated with sildenafil (Sil) compared with DMSO. Dots: individual values, $n = 3$ independent experiments. **$p < 0.01$, ***$p < 0.001$, ****$p < 0.0001$; two-tailed paired t test.

(F) CV activity normalized to citrate synthase (CS) activity in LS NPCs (ATP6_2, ATP6_4, ATP6_5, and ATP6_7) compared with control NPCs (CTRL_1 and CTRL_3). Dots: pool of 10–15 million cells, $n = 3$ independent experiments. ***$p < 0.001$, ****$p < 0.0001$; one-way ANOVA with Tukey's multiple comparisons.

(legend continued on next page)

and early lethality,[11] but *Surf1* KO mice failed to replicate LS phenotypes.[12,13] The most widely used model of LS is the homozygous *Ndufs4* KO mouse, characterized by progressive encephalopathy, growth retardation, and premature death.[14,15] This model has been used to propose therapeutic interventions, including antioxidants,[16–18] rapamycin,[19] interferon-gamma-targeting therapies,[20] cannabidiol,[21] or hypoxia.[22,23] Only a few of these strategies have been tested in LS individuals, and no successful results have been obtained.

New approach methodologies (NAMs) with LS patient-derived induced pluripotent stem cells (iPSCs)[24] have been instrumental in uncovering pathological mechanisms. These include neuronal outgrowth defects,[25] altered calcium homeostasis,[26,27] and glutamate toxicity in neuronal cultures,[28] as well as impaired cortical development and neuromorphogenesis in brain organoids.[25,29,30] Despite these advances, large-scale drug screens in iPSC models of mitochondrial disease have yet to be performed.

We previously demonstrated that iPSC-derived neural precursor cells (NPCs) are an effective drug discovery platform for mtDNA diseases.[27] LS NPCs carrying a *MT-ATP6* variant exhibited abnormal mitochondrial membrane potential (MMP), a feature that can be exploited for high-throughput screens.[31] Here, we leveraged this MMP phenotype to screen a library of 5,632 repurposable drug candidates in LS NPCs. We identified phosphodiesterase type 5 (PDE5) inhibitors as lead compounds and prioritized sildenafil for its safety profile.[32] Sildenafil rescued the neurodevelopmental disease signature, promoted neuronal outgrowth, and normalized calcium homeostasis in human LS models. *In vivo*, sildenafil extended the lifespan of *Ndufs4* KO mice and *SURF1* KO pigs. Mechanistically, sildenafil's action appeared to be mediated through cyclic GMP (cGMP)-dependent protein kinase 1 (PRKG1). Off-label treatment on an individual basis with sildenafil in six patients with LS carrying *MT-ATP6* variants improved muscle strength and resistance to metabolic crises. The data implicate sildenafil as a repurposable drug for mitochondrial disorders.

RESULTS

Repurposable drug screen in LS NPCs identifies PDE5i

To determine whether MMP hyperpolarization observed in LS NPCs carrying the m.9185T>C variant in the *MT-ATP6* gene[27] represented a robust phenotype, we generated NPCs from 7 LS patients carrying different *MT-ATP6* variants (3 m.9185T>C, 1 m.8993T>C, 2 m.8993T>G, and one m.9176T>G) (Figure S1A).[27,33–36] For controls, we used NPCs from 8 healthy individuals, including 2 patients' mothers carrying *MT-ATP6* variants at low heteroplasmy (<2%) (Figure S10H). LS NPCs expressed NPC markers similarly to control NPCs (Figures S1E and S1F) and retained mtDNA heteroplasmy of parental iPSCs (Figure S10H). LS NPCs showed defective bioenergetics (Figure S1C), disrupted MT-ATP6 protein expression (Figure S1B) and CV assembly structure (Figures S4A and S4B), and MMP hyperpolarization (Figure 1A).

We applied a well-curated library of 5,632 repurposable molecules[37] to modulate the MMP of LS NPCs. We used live-cell high-content analysis (HCA) based on tetramethylrhodamine methyl ester (TMRM) intensity[31] (Figures 1B, S2A, and S2B). Compounds were applied with 0.05% maximal concentration of DMSO, which was not toxic in LS NPCs (Figure S2C). We included MMP values from one control NPC line for baseline MMP after having confirmed that various control NPC lines displayed comparable MMP (Figure S2D). We established the Z′ factor[38] to be ∼0.68–0.85 across plates (Figures S2E–S2G) and identified 5 μM as the optimal screening concentration achieving an ∼5% hit rate with low toxicity (Figure S2H) and high reproducibility (Figure S2I).

We classified compounds based on their depolarizing effect in LS NPCs (MMP inhibition) relative to the standard deviation (SD) of DMSO-treated LS NPCs (SD = 6.51%). We identified 767 mild uncouplers (13.0%–19.5% inhibition, >2 SD), 520 intermediate uncouplers (19.5%–32.5% inhibition, >3 SD), and 187 strong uncouplers (>5 SD) (Figure 1C). We excluded toxic compounds based on cell count (cut-off: 29.86%). We focused on mild uncouplers that depolarized the MMP of LS NPCs to values similar to control NPCs (Figure 1C). Among those, we identified two PDE5 inhibitors (PDE5i), T-0156 and vardenafil hydrochloride, which showed dose-dependent MMP depolarization in LS NPCs without loss of viability (Figures S3A–S3D).

As our previous proof-of-concept screen in LS NPCs highlighted the PDE5i avanafil,[27] we prioritized PDE5i employed in pediatric settings. Sildenafil emerged as a strong candidate, given its safety profile in children treated for pulmonary arterial hypertension (PAH) or lymphatic malformations.[39–42] Sildenafil led to dose-dependent MMP depolarization in LS NPCs (Figure 1D) without toxicity (Figures S3E–S3G) and with a half-maximal inhibitory concentration (IC_{50}) of ∼3 μM at 16 h (Figure S3H). MMP normalization occurred similarly in LS NPCs carrying different *MT-ATP6* variants with overall MMP depolarization of ∼16% (Figure 1E). Sildenafil did not modify the MMP in control NPCs (Figures S3I and S3J).

Bioenergetically, sildenafil did not lead to a measurable improvement in CV activity (Figure 1F) or in CV assembly structure[43,44] (Figure S4C). The protein levels of known mitochondrial modulators were also not significantly impacted (Figures S4D and S4E). Nonetheless, sildenafil increased intracellular ATP in

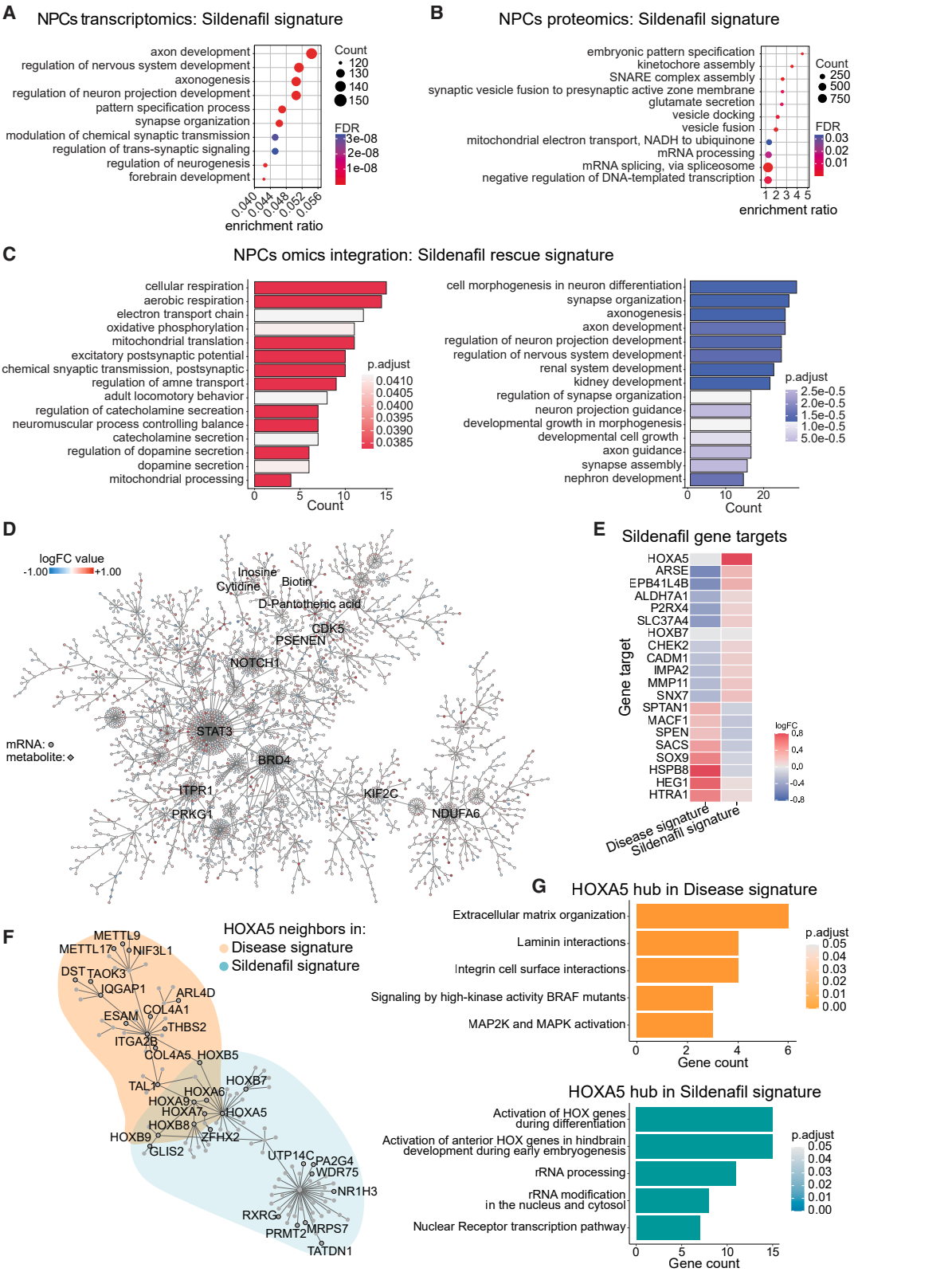
(G) ATP content in control NPCs (CTRL_1 and CTRL_3) and LS NPCs (ATP6_2, ATP6_4, ATP6_5, and ATP6_7). Dots: biological replicates, $n = 3$ independent experiments. $^{**}p < 0.01$; mixed-effects model (equivalent to repeated-measures ANOVA) with multiple comparisons.

(H) mtDNA copy number in control NPCs (CTRL_1, $n = 5$–6; CTRL_2, $n = 6$; CTRL_3, $n = 6$; CTRL_4, $n = 6$) and LS NPCs (ATP6_2, $n = 6$; ATP6_4, $n = 6$; ATP6_7 $n = 6$). Dots: biological replicates, $n = 3$ independent experiments. $^{***}p < 0.001$; one-way ANOVA with Tukey's multiple comparisons.

(I) NAD^+/NADH ratio in control NPCs (CTRL_1, CTRL_2, CTRL_3, and CTRL_4) and LS NPCs (ATP6_2, ATP6_4, ATP6_5, and ATP6_7). Dots: individual values, $n = 3$ independent experiments. $^{*}p < 0.05$; unpaired two-tailed t test.

(J) Left, probability of MIC60 staining pattern of LS NPCs (ATP6_2) to be similar to that of control NPCs (CTRL_1). $n = 3$ independent experiments, comprising a total of 4,000 images. $^{****}p < 0.0001$; Kruskal-Wallis with Dunn's multiple comparisons. Right, representative STED images. Scale bar: 500 nm.

See also Figures S1–S4.



(legend on next page)

LS NPCs (Figure 1G) and restored mtDNA copy number (Figure 1H). The NAD^+/NADH ratio was also normalized (Figures 1I and S1D). Because *MT-ATP6* defects may disrupt mitochondrial cristae,[45] we analyzed the cristae junction regulator MIC60 with stimulated emission depletion (STED) microscopy.[46] We inspected the MIC60 labeling pattern of 4,000 STED images with a machine-learning approach by training a neural network classifier to distinguish control NPCs (P[healthy]-score = 1) from LS NPCs (P[healthy]-score = 0). Using images not used for training, we detected altered MIC60 localization in LS NPCs that were partially reversed by sildenafil (Figures 1J and S3K). Manual quantification of approximately 300 STED images yielded similar results (Figure S3L) and highlighted a peripheral MIC60 distribution pattern in LS NPCs that was restored by sildenafil (Figures S3M and S3N). Hence, sildenafil improved mitochondrial phenotypes in LS neural cells.

The PDE5i sildenafil ameliorates the LS disease signature by modulating neuronal development pathways

To investigate the mechanism of action of sildenafil, we performed multi-omics in 4 LS NPC lines (1 for each *MT-ATP6* variant: m.9185T>C, m.8993T>C, m.8993T>G, and m.9176T>G) and 4 healthy control NPC lines. The omics design identified (1) the disease signature by comparing DMSO-treated LS NPCs to DMSO-treated control NPCs and (2) the sildenafil signature by comparing sildenafil-treated LS NPCs to DMSO-treated LS NPCs (Figure S1G).

The disease signature included biological processes (BPs) related to nervous system and axon development and cellular components (CCs) implicated in the mitochondrial inner membrane and neuronal cell body in transcriptomics (Figures S5A and S5B), and mitochondrial translation and mitochondrial membrane in proteomics (Figures S5F, S5G, and S5I). The sildenafil signature affected similar pathways, including axon and nervous system development (Figure 2A) and mitochondrial inner membrane and neuronal cell body in transcriptomics (Figure S5C) and electron transport chain (ETC) in proteomics (Figures 2B and S5H). Genes restored by sildenafil (Figures S5D and S5E) included neuron-specific calcium sensor *CABP1*[47] (Table S1) and neurodevelopment-associated genes *HOXA5*[48,49] and *DBX1*[50] (Figure S5E; Table S1). Restored proteins included BAG4, protecting against ATP depletion-induced cell death,[51] downregulated in LS NPCs (Table S1) and upregulated after treatment (Figure S5J). No significant transcriptional changes were observed in sildenafil-treated control NPCs (Figure S5K).

Metabolomics identified metabolites important for brain energy metabolism, including creatine[52,53] and cysteine,[54] that were altered by the disease (Figure S4F) and normalized by sildenafil (Figure S4G; Table S1). Creatinine, a non-enzymatic breakdown product of creatine, was not normalized, possibly reflecting an increased use of creatine. The disease and sildenafil signatures also impacted the glutathione metabolism pathway (Figures S6A and S6B).

Multi-omics integration[55] revealed 796 molecules shared between the integrated signatures for disease and sildenafil, with 724 exhibiting opposite regulation. Hence, sildenafil reversed 33.5% of dysregulated molecules (724 over 2,160). The integrated signatures impacted signaling pathways (e.g., Notch and WNT) and axon guidance (Figures S6C and S6D). Reversed BPs included one group related to mitochondrial respiration and one related to morphogenesis and axon development (Figure 2C). The multi-omics map of the sildenafil rescue signature (including only transcriptomics and metabolomics, as proteomics did not show sufficiently significant changes) highlighted a network comprising metabolites (e.g., biotin and pantothenic acid) and genes related to ETC (e.g., *NDUFA6*) and development (e.g., *NOTCH1*, *BRD4*, and *STAT3*) (Figure 2D).

We identified 20 putative sildenafil targets whose gene expression was altered in LS NPCs compared with control NPCs and restored in LS NPCs treated with sildenafil (Figure 2E). The top responsive gene was *HOXA5* (logFC_diseased = −0.02, logFC_treated = +5.2). The *HOXA5* hub was involved in extracellular matrix organization in LS NPCs but became associated with differentiation and neurodevelopment upon treatment (Figures 2F and 2G). The *HOXA5* network may thus be dysregulated in LS, and its modulation by sildenafil might contribute to healthy neurodevelopment. Another key responder was *PRKG1*, a master regulator and downstream target of PDE5,[56] which was highlighted by the multi-omics map of the sildenafil rescue signature (Figure 2D). To monitor the expression of putative sildenafil-responsive genes, we treated LS NPCs grown in physiologically low glucose with 1 or 10 μM sildenafil for 6 and 24 h (Figures S6E and S6F). The treatments modulated the expression of sildenafil targets over time, including proliferation-related genes *BRD4*, *STAT3*, and *NOTCH1*[57,58]; synapsis-associated *NRG1*[59]; neuroinflammation-associated *P2RX4*[60]; and glucose metabolism-related *SLC37A4*.[61]

LS brain organoids show neurodevelopmental defects and highlight the impact of sildenafil on progenitor populations

We used cortical brain organoids to explore the impact of sildenafil on human neurodevelopment. In agreement with previous studies in LS brain organoids,[25,29,30] *MT-ATP6* variants impaired neurogenic zone formation (Figure 3A) and altered the ratio of early neurons to neural progenitors (Figure 3B). Two different protocols for generating cortical brain organoids showed

Figure 2. Neurodevelopmental impact of sildenafil revealed by multi-omics

(A) Top ten biological processes (BPs) in sildenafil-treated LS NPCs based on transcriptomics (FDR, false discovery rate).

(B) Top ten BPs in sildenafil-treated LS NPCs based on proteomics.

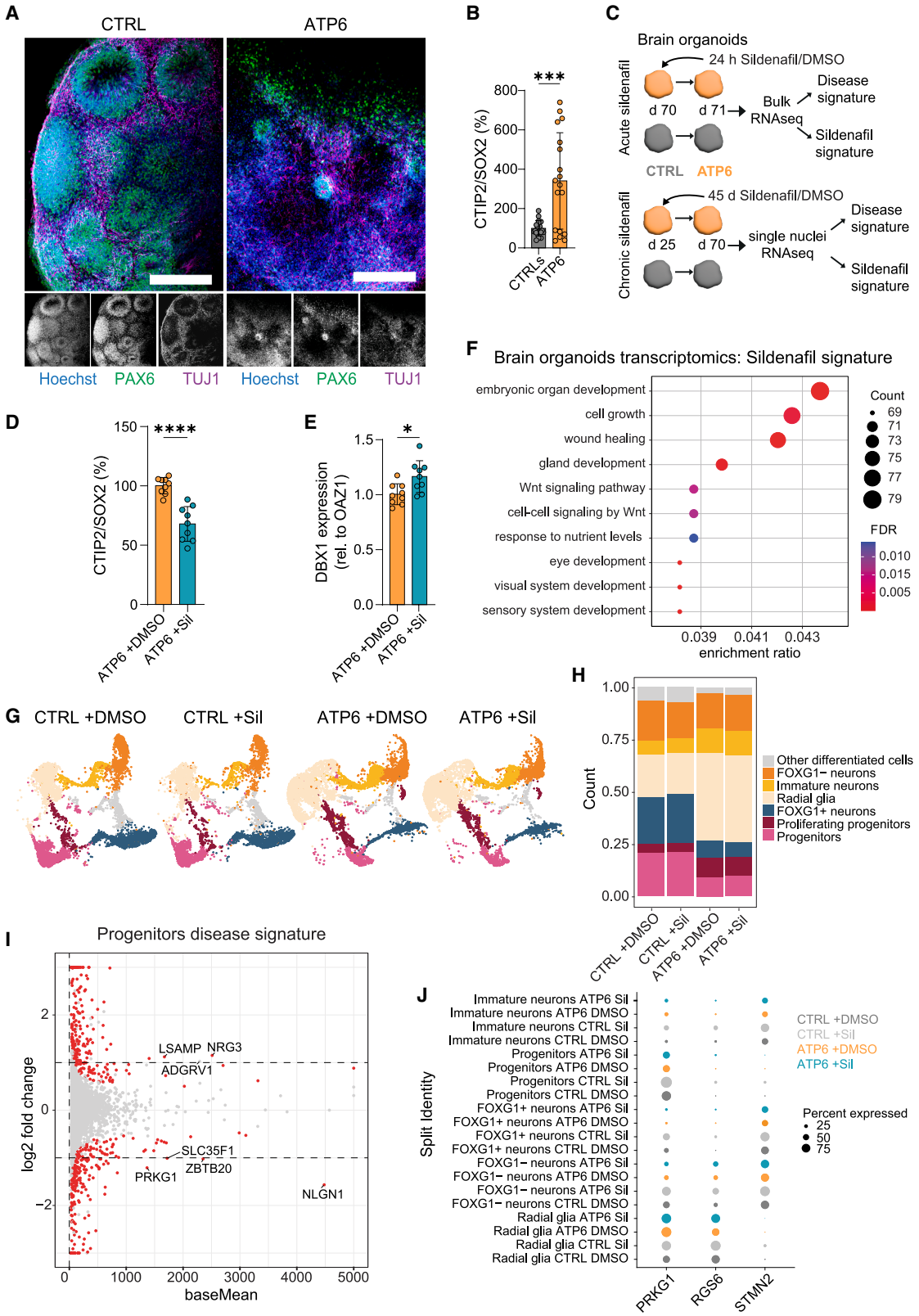
(C) BPs of 724 molecules reversed by sildenafil with logarithmic fold change (logFC) > 0 based on multi-omics integration.

(D) Multi-omics network of sildenafil signature in LS NPCs. Dot size: centrality in the network; dot color: logFC value.

(E) Putative sildenafil-responsive genes based on transcriptomics.

(F and G) Network analysis for *HOXA5* hub and associated pathways.

See also Figures S4–S6 and Table S1.



(legend on next page)

defective growth rates (Figure S7A). One protocol[62] showed size defects in LS organoids after 50 days in culture (Figure S7B); another protocol,[63] allowing initial homogeneous organoid shape, resulted in earlier growth defects in LS organoids that became less pronounced over time (Figure S7B). The results suggest that *MT-ATP6* variants might affect neural progenitor development.

We treated LS brain organoids with sildenafil for either 24 h (acute paradigm) or 45 days (chronic paradigm) (Figure 3C). *MT-ATP6* variants disrupted BPs related to synapses and neuronal projections (Figure S7E) and CCs related to neuronal cell bodies and synapses (Figure S7F). The acute sildenafil signature modulated pathways related to embryonic development and Wingless-related integration site (WNT) signaling (Figure 3F) and corrected gene defects (Figures S7C and S7D), including *WDR45B*, which was downregulated in LS brain organoids (Table S1) and upregulated by sildenafil (Figure S7D), and whose variants are associated with neurodevelopmental disorders.[64] Sildenafil also rescued the ratio of early neurons to neural progenitors (Figure 3D) and upregulated *DBX1* (Figure 3E).

To dissect the cell populations affected by *MT-ATP6* variants and chronic sildenafil, we performed single-nucleus RNA sequencing (snRNA-seq) (Figure 3C). Unsupervised clustering highlighted 9 clusters (Figure S8A): clusters 0 and 3 for radial glia, clusters 4 and 8 for progenitors, cluster 6 for proliferating progenitors, cluster 5 for immature neurons, cluster 2 for FOXG1-positive neurons, cluster 1 for FOXG1-negative neurons, and cluster 7 for other cell types (Figure S8B). This annotation revealed that *MT-ATP6* variants impaired neuronal commitment, with alterations in radial glia, progenitors, and FOXG1-positive neurons (Figures 3G and 3H). The disease signature involved the downregulation in the progenitor population of *PRKG1* and *NLGN1*, a regulator for synapse development[65] (Figure 3I), and the downregulation in the neuronal population of genes impacting neurite outgrowth, such as *STMN2*[66] (Figure S8D; Table S1). The sildenafil signature upregulated neuronal outgrowth-associated genes, such as *RGS6*[67] (Figures S8C and S8D; Table S1). The effect of sildenafil was mostly evident in radial glia and progenitors (Figure S8C; Table S1). Whereas *STMN2* was mainly present in FOXG1-positive neurons and immature neurons, *RGS6* was found mainly in radial glia, and *PRKG1* in radial glia and progenitors (Figures 3J and S8D). The glycolytic signature, suggested to be an indicator of brain organoid stress,[68] was not altered, indicating that neither *MT-ATP6* variants nor sildenafil posed additional stress (Figure S8E). Altogether, LS disrupted brain organoid development by impairing early neuronal organization of radial glia and progenitor populations, and sildenafil specifically affected those populations.

Sildenafil improves calcium homeostasis and neurite outgrowth in LS neural models

We examined the functional consequences of sildenafil in LS neural cells. Given the reported calcium dysregulation[26,27] and the known deterioration of LS patients upon metabolic decompensation,[3] we induced acute metabolic stress in LS brain organoids to monitor their intracellular calcium response. We dissected brain organoids on days 70–74 to prepare cortical brain organoid slices (cBOSs),[69] which we grew until day 129 and then treated with sildenafil for 24 h before applying acute metabolic stress (2 min of glucose deprivation and inhibition of glycolysis [GLY] and OXPHOS) (Figure 4A). The calcium response to metabolic stress was more pronounced and premature in LS cBOS compared with control cBOS, suggesting increased susceptibility to metabolic imbalance (Figures 4B and 4C). Pre-treatment with sildenafil in LS cBOS reduced their calcium load after metabolic stress and also their peak calcium amplitude (Figures 4B and 4C). Hence, sildenafil might prevent excessive decompensation in LS neuronal cells under acute metabolic stress.

To investigate the interplay between calcium and bioenergetics in treated LS neural cells, we applied a mathematical model[70] that coupled cytosolic calcium dynamics with mitochondrial function, incorporating F_1F_0 ATPase activity (F1F0), GLY, the adenine nucleotide translocator (ANT), NADH production via the aspartate-glutamate carrier (AGC), and NADH oxidation in ETC (o). Based on our previous calcium modeling,[71–73] we integrated additional fluxes through the plasma membrane calcium ATPase (PMCA), the sarcoplasmic/endoplasmic reticulum calcium ATPase (SERCA), and IP_3 receptors (IP3Rs) (Table S2). Following global sensitivity analysis[70] (Figure S9A), the model recapitulated the pattern of calcium traces measured in LS cBOS (Figure S9B). Combining a high rate of F1F0 with a low rate of IP3R (Figure S9C) reproduced the reduction of calcium peak in sildenafil-treated LS cBOS under stress (Figures 4B and 4C) and key features observed in sildenafil-treated LS NPCs, including MMP reduction (Figures 1D and 1E), slight NADH reduction (Figure S1D), and ATP increase (Figure 1G). Other combinations failed to recapitulate sildenafil effects (Figures S9D and S9E). The modeling thus suggested that

Figure 3. Sildenafil affects progenitor populations in LS brain organoids

(A) Representative images of day 35 brain organoids from controls (CTRL_2) and LS (ATP6_7). Scale bar: 200 μm.

(B) Differentiation ratio in day 70 brain organoids from controls (CTRL_1 and CTRL_2) and LS (ATP6_4 and ATP6_7). Five organoids per line per independent experiment ($n = 3$). ***$p < 0.001$; unpaired two-tailed *t* test.

(C) Brain organoid experiments to assess acute (10 μM for 24 h) and chronic (10 μM for 45 days) sildenafil treatment signatures.

(D) Differentiation ratio in day 70 brain organoids from LS (ATP6_4). Ten organoids per line per independent experiment ($n = 3$). ****$p < 0.0001$; unpaired two-tailed *t* test.

(E) qPCR analysis of *DBX1* in day 70 LS brain organoids (ATP6_4). Ten organoids per line per independent experiment ($n = 3$). *$p < 0.05$; unpaired two-tailed *t* test.

(F) Top-ten BPs of acute sildenafil signature based on transcriptomics.

(G and H) Population distribution and related quantification in chronic sildenafil-treated brain organoids.

(I) Disease signature in the progenitor population of brain organoids.

(J) Expression patterns of *PRKG1*, *RGS6*, and *STMN2* across distinct populations of brain organoids.

See also Figures S7 and S8 and Table S1.

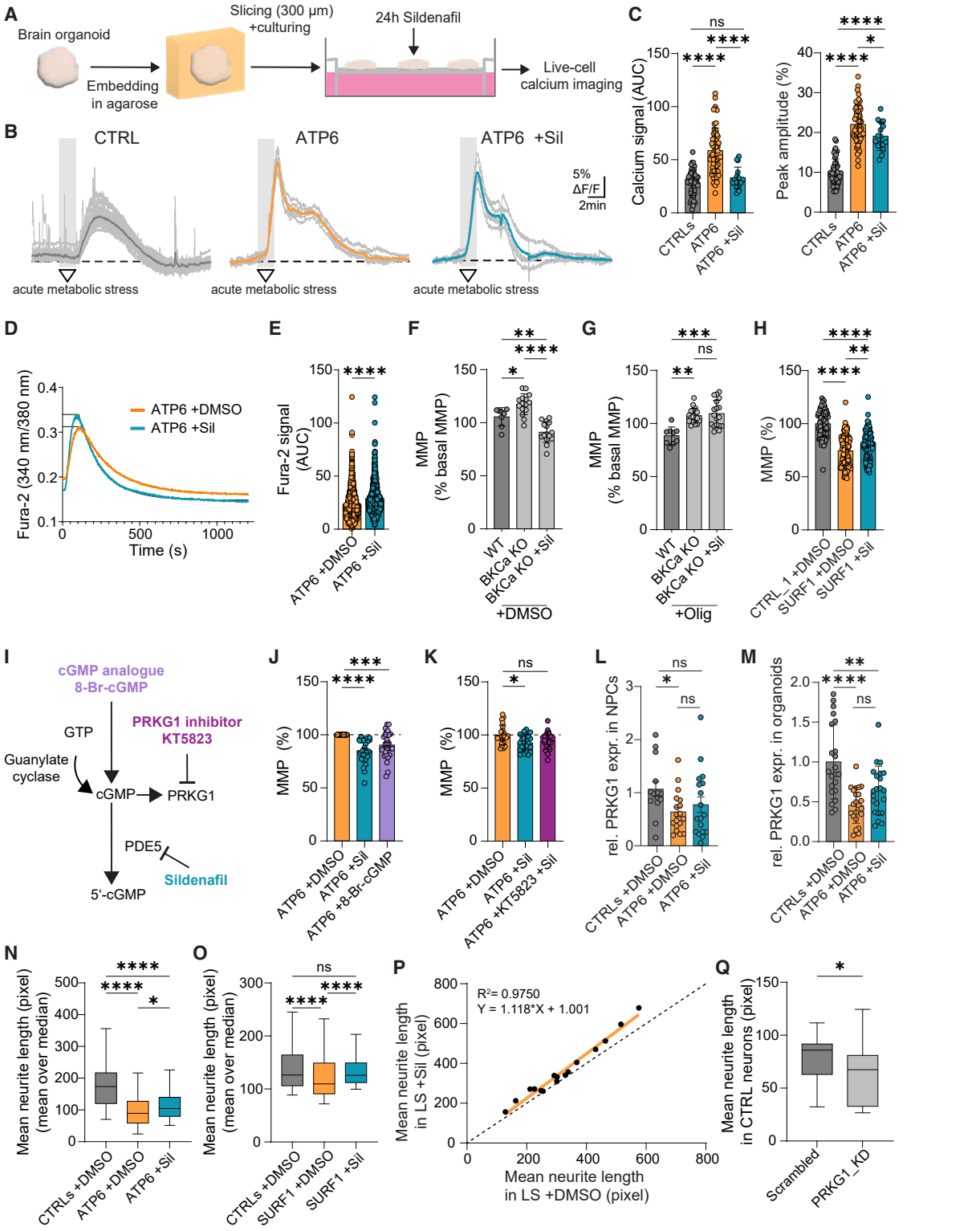


Figure 4. Sildenafil ameliorates calcium homeostasis and neurite outgrowth

(A) cBOS generation for live-cell calcium imaging.

(B) Representative calcium traces of cBOS from control (CTRL_2) and LS (ATP6_7). Gray lines: individual cells; colored lines: average traces.

(legend continued on next page)

sildenafil's action may be mimicked by increasing CV activity together with decreasing calcium release from the endoplasmic reticulum (ER), in turn improving cellular bioenergetics.

We analyzed ER calcium with the SERCA inhibitor thapsigargin. In the absence of extracellular calcium, pre-treatment with sildenafil in LS NPCs increased the thapsigargin-induced cytoplasmic calcium signal (Figures 4D and 4E), possibly indicating higher ER calcium storage or modulation of mitochondrial calcium homeostasis.[74,75] A faster decline of calcium in sildenafil-treated cells (Figure 4D) could imply reduced calcium release from the ER through IP3R, as suggested by the model, or enhanced cytosolic calcium efflux to the extracellular space through the sodium-calcium exchanger (NCX) or the PMCA because of increased cytosolic ATP levels by sildenafil or augmented uptake into mitochondria. To indirectly address mitochondrial calcium, we investigated big-conductance calcium-activated potassium (BKCa) channels, which are localized in the plasma and mitochondrial membrane[76] and have been implicated in sildenafil's action.[77,78] As previously shown,[79] human BKCa KO cells[80] displayed increased MMP compared with wild type (WT) (Figures 4F and 4G). Sildenafil normalized MMP when BKCa KO cells were incubated in DMSO (Figure 4F) but not when they were acutely exposed to the CV inhibitor oligomycin (Figure 4G). The results suggest that BKCa channels may contribute to the action of sildenafil on MMP when cells lack a functional CV and that residual CV activity is necessary for the restorative effect of sildenafil, as indicated by the model.

These findings raised the possibility that MMP normalization by sildenafil may not be due to direct mitochondrial uncoupling. To test this, we employed NPCs carrying a variant in the nuclear gene *SURF1*[25] (Figure S10H). The MMP of *SURF1* mutant NPCs was depolarized compared with that of isogenic control NPCs (Figure 4H). Nonetheless, sildenafil still restored MMP (Figure 4H). Hence, sildenafil might also be beneficial in other forms of LS where MMP is depolarized.

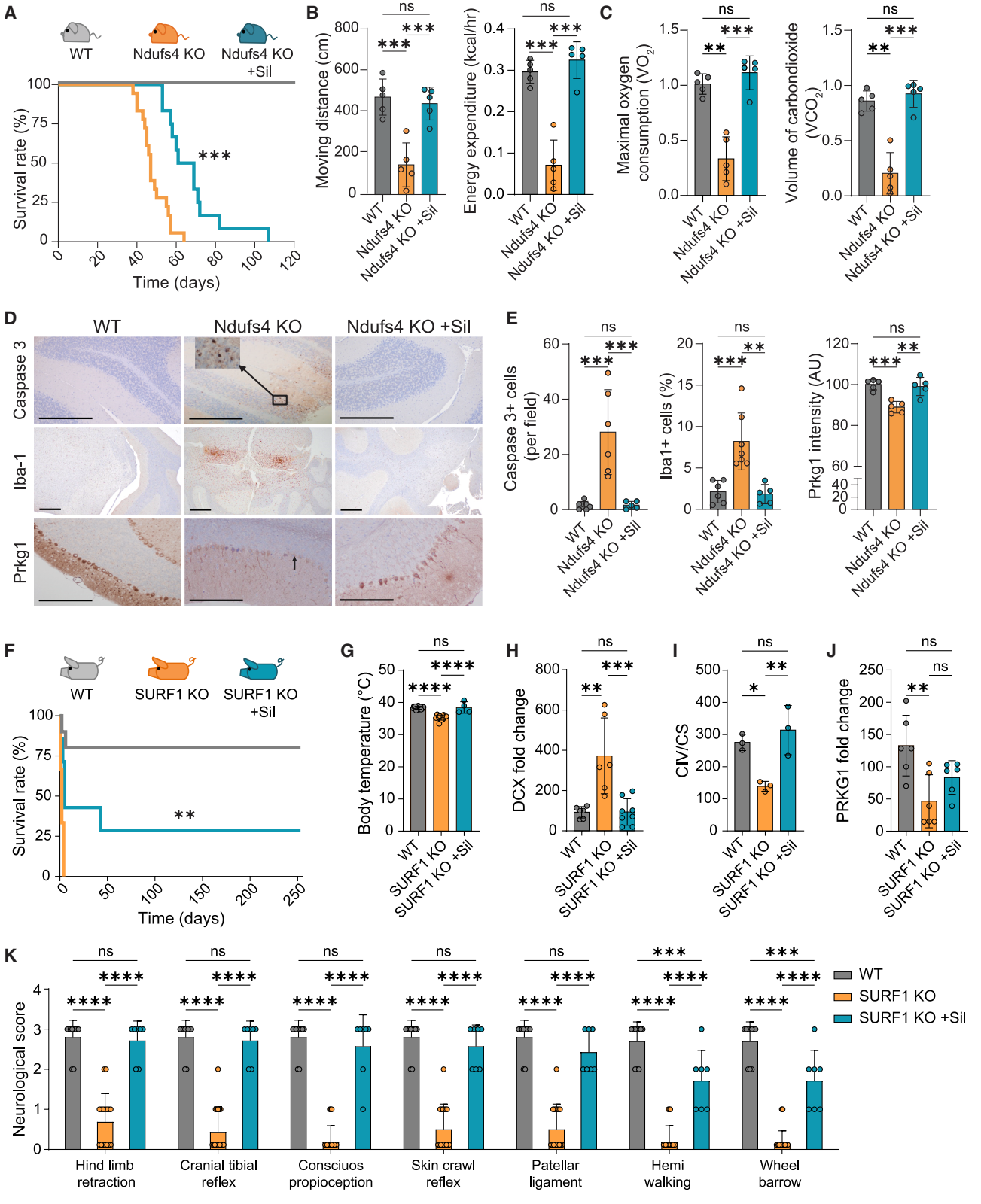
We applied chemical manipulation of the PDE5 pathway to prove its involvement in the MMP rescue of LS NPCs (Figure 4I). The cGMP analog 8-Br-cGMP recapitulated the MMP amelioration seen with sildenafil (Figure 4J). Inhibition of the downstream target PRKG1 with KT5823 blunted the effect of sildenafil on MMP normalization (Figure 4K). Indeed, PRKG1 levels were reduced in *MT-ATP6* mutant NPCs (Figures 4L and S10A), *MT-ATP6* mutant brain organoids (Figure 4M), and *SURF1* mutant neurons and brain organoids (Figure S10B).

We quantified the effect of sildenafil on neuronal outgrowth[81] of dopaminergic neurons (Figure S10C). In agreement with previous findings,[25,30] *MT-ATP6* mutant neurons and *SURF1* mutant neurons exhibited reduced neurite length (Figures 4N, 4O, and S10D). Sildenafil promoted neurite outgrowth in LS neurons (Figures 4N, 4O, and S10D). This improvement was specific to LS neurons (carrying *MT-ATP6*, *SURF1*, or *NDUFS4* variants) (Figure 4P) and was not observed in control neurons (Figure S10E). PRKG1 signal was reduced in LS neurons (Figure S10F), and PRKG1 knockdown in control neurons recapitulated the neurite growth defects seen in LS neurons (Figure 4Q). Because PRKG1 is involved in both calcium homeostasis and neurite outgrowth,[82–86] its dysregulation in LS might underscore its role as a therapeutic target that could contribute to the sildenafil response (Figure S10G).

Sildenafil extends the lifespan of LS animals and crosses the human BBB

To address the therapeutic potential of sildenafil *in vivo*, we employed the germline *Ndufs4* KO mouse.[14,15] Sildenafil was added to the drinking water of the animals starting on day 25. The treatment extended the lifespan of *Ndufs4* KO mice (Figure 5A) and alleviated muscle weakness and ataxia by partially correcting defective energy expenditure (Figure 5B). Upon placing LS mice in metabolic chambers (Figure S11A), we observed improved oxygen consumption and carbon dioxide production with sildenafil (Figure 5C), possibly indicating enhanced

(C) Area under the curve (AUC) and peak intracellular calcium in cBOS from controls (CTRL_1, $n = 10$; CTRL_2, $n = 40$) and LS (ATP6_7, $n = 58$; ATP6_7 +Sil, $n = 16$). Dots: individual cells. $^{*}p < 0.05$, $^{****}p < 0.0001$; two-tailed Mann-Whitney U test.
(D and E) Mean calcium trace and AUC quantification of intracellular calcium in LS NPCs (ATP6_2, ATP6_4, ATP6_5, and ATP6_7). Dots: individual cells, n = at least 3 independent experiments per line. $^{****}p < 0.001$; unpaired two-tailed t test.
(F and G) HCA MMP quantification in WT and BKCa KO cells after DMSO (F) or oligomycin (G). $n = 3$ independent replicates. $^{*}p < 0.05$, $^{**}p < 0.01$, $^{****}p < 0.001$, $^{****}p < 0.0001$; one-way ANOVA with Tukey's multiple comparisons test (F) and Kruskal-Wallis with Dunn's multiple comparisons (G).
(H) HCA MMP quantification in *SURF1* mutant NPCs (SURF1_1) and isogenic control NPCs (CTRL_1). Dots: mean value/image, $n = 3$ independent experiments. $^{**}p < 0.01$, $^{****}p < 0.0001$; ordinary one-way ANOVA with Holm-Šídák's multiple comparisons.
(I) PDE5-PRKG1 pathway and modulations.
(J) Cytofluorimetry MMP quantification in LS NPCs (ATP6_2, ATP6_4, ATP6_5, and ATP6_7). Dots: individual values, $n = 7$ independent experiments. $^{***}p < 0.001$, $^{****}p < 0.0001$; one-way ANOVA with Tukey's multiple comparisons.
(K) HCA MMP quantification in LS NPCs (ATP6_2). Dots: mean value/image, $n = 3$ independent experiments. $^{*}p < 0.05$; one-way ANOVA with Dunnett's T3 multiple comparisons.
(L) PRKG1 protein expression in control NPCs (CTRL_1, CTRL_2, CTRL_3, CTRL_4, and CTRL_5) and LS NPCs (ATP6_2, ATP6_4, ATP6_5, and ATP6_7) from immunoblots (Figure S10A), $n = 5$ independent experiments. $^{*}p < 0.05$; unpaired two-tailed t test.
(M) qPCR analysis of *PRKG1* in day 70 brain organoids from controls (CTRL_1 and CTRL_2) and LS (ATP6_4 and ATP6_7). Five organoids per line per independent experiment ($n = 3$). $^{**}p < 0.01^{****}$, $p < 0.0001$; two-tailed Mann-Whitney U test.
(N and O) Neurite outgrowth in neurons from *MT-ATP6* variants (ATP6_2, $n = 2$; ATP6_4, $n = 1$) and controls (CTRL_1, $n = 2$; CTRL_2, $n = 2$; and CTRL_3, $n = 1$), and from *SURF1* variant (SURF1_1, $n = 3$) and isogenic control (CTRL_1, $n = 3$). $^{*}p < 0.05$, $^{****}p < 0.0001$; Kruskal-Wallis with Dunn's multiple comparisons.
(P) Linear regression (sildenafil over DMSO) of mean neurite length in LS neurons (ATP6_2, $n = 3$; ATP6_4, $n = 1$; ATP6_7, $n = 3$; SURF1_1 $n = 3$; NDUFS4_1, $n = 3$; NDUFS4_2, $n = 3$). Dots: individual experiments. Black dotted line: hypothetical linear regression with no effect (y = x or slope = 1).
(Q) Neurite outgrowth in control neurons (CTRL_1), $n = 3$ independent experiments. $^{*}p < 0.05$; unpaired two-tailed t test.
See also Figures S9 and S10 and Table S2.



(legend on next page)

metabolic fitness. Cardiac bradyarrhythmia and dysfunction were also ameliorated (Figure S11B).

Consistent with previous observations,[14,87,88] LS mice showed cleaved caspase-3 staining in the cerebellum and brain stem regions associated with increased Iba1 staining,[89] suggestive of cell death and microglial activation (Figures 5D and 5E). The number of cells positive for caspase-3 or Iba1 decreased in sildenafil-treated LS mice (Figures 5D and 5E). The loss of Purkinje cells of the cerebellum was also ameliorated (Figures S11C and S11D). The expression of Prkg1, which is particularly evident in normal cerebellar Purkinje neurons,[15] was reduced in LS mice and rescued by sildenafil (Figures 5D and 5E).

Next, we employed *SURF1* KO pigs, which exhibit severe neurodevelopmental impairment.[11] *SURF1* KO piglets were treated immediately at birth ($n = 3$ animals with 2.1 mg/kg/day, $n = 4$ animals with 0.5 mg/kg/day). Sildenafil improved animal responsiveness, mobility, and suckling behavior, leading to lifespan extension once the unstable perinatal phase was overcome (Figure 5F). Some LS pigs survived beyond day 261 despite reduced body weight (98 kg vs. 140–170 kg in age-matched controls). Sildenafil increased the body temperature of LS pigs, suggesting an effect on systemic metabolism (Figures 5G and S11F). The expression of NPC-associated doublecortin (DCX) was normalized by sildenafil (Figures 5H and S11G), indicating neurodevelopmental amelioration. CIV activity was also restored (Figure 5I). Reduced PRKG1 levels in the basal ganglia of LS pigs increased with treatment in most animals (Figures 5J and S11G). By adapting the Newcastle Pediatric Mitochondrial Disease Scale (NPMDS), we observed improvement in multiple domains of neuromotor integrity (Figures 5K and S11E). Collectively, the *in vivo* data highlighted the potential clinical effectiveness of sildenafil and underscored PRKG1 as one of its mechanistic targets.

In some LS pigs treated with high sildenafil doses, we noticed microhemorrhages (Figure S11H). We further assessed toxicity using LS iPSC-derived cardiomyocytes (Figure S12A). Only high concentrations of sildenafil (>50 μM) appeared to be cardiotoxic (Figures S12B–S12D), as 10 μM sildenafil did not affect cell viability in LS cardiomyocytes (Figures S12B–S12D) and did not alter their glycolytic rate (Figure S12E). The findings are in agreement with the higher mortality rate seen in children with PAH treated with high sildenafil doses.[40]

We then probed the blood-brain barrier (BBB) permeability of sildenafil using an iPSC-based model[90] (Figure 6A). Similar to control brain capillary endothelial cells (BCECs), LS BCECs showed correct morphology and marker expression (Figure 6B) as well as monolayer integrity and transendothelial electrical resistance (TEER) (Figures S12F and S12G). The permeability of sildenafil and sildenafil citrate (the active pharmacological substance applied orally in clinical applications) in LS BCECs was similar to that of control BCECs (Figure 6C). The results are consistent with permeability values of sildenafil reported in other settings[91] and imply that sildenafil can effectively cross the BBB in LS.

Sildenafil treatment on an individual basis improved clinical outcome in six LS patients

Because sildenafil can be used safely in pediatric conditions,[39–42] we initiated off-label treatment on an individual basis with sildenafil in six LS patients carrying *MT-ATP6* variants (Tables 1 and S3). All patients showed cranial magnetic resonance imaging (cMRI) signs consistent with LS lesions (Figures 6E and S12H). From patient 1, we also obtained iPSCs (line ATP6_7), which were used to generate NPCs and brain organoids (Figure S10H). When selecting the sildenafil dosage, we referred to the trial STARTS-1 (Sildenafil in Treatment-Naive Children, Aged 1 to 17 Years, With Pulmonary Arterial Hypertension)[41] and the trial STARTS-2[40] in children with PAH. Given the potential toxic effects of high dosages, we only considered low (0.66–1.49 mg/kg/day) or medium dosages (1.50–3.00 mg/kg/day). Two patients/guardians opted for low dosages and four for medium dosages. Mass spectrometry quantification of total sildenafil concentration in the plasma[91] showed a plasma concentration of ∼1 μM (Figure 6D), which is close to the IC_{50} value of 3 μM that was found effective for normalizing MMP in LS NPCs (Figure S3H).

To monitor the occurrence of adverse reactions, we asked patients/guardians to respond to a questionnaire on side effects after 6 months of sildenafil use (Table S4). In patient 3, sildenafil had to be discontinued due to a rash, even though the frequent episodes of sudden muscle weakness were resolved during sildenafil medication and returned once the drug was discontinued (Tables 1 and S4). In all the other cases, sildenafil was well

Figure 5. Sildenafil extends the lifespan of small and large mammalian models of LS

(A) Kaplan-Meier survival curve of treated ($n = 18$) and sildenafil-treated *Ndufs4* KO mice ($n = 12$). ***$p < 0.001$; log-rank (Mantel-Cox) test.

(B and C) Functional parameters in a metabolic chamber with 42- to 45-day-old *Ndufs4* KO mice ($n = 15$, 5 independent experiments). **$p < 0.01$, ***$p < 0.001$; ANOVA post hoc analysis.

(D and E) Representative immunohistochemistry and quantification in 50-day-old *Ndufs4* KO mice. **$p < 0.01$, ***$p < 0.001$; ANOVA post hoc analysis. Scale bar: 500 μm.

(F) Kaplan-Meier survival curve of WT pigs ($n = 10$), untreated *SURF1* KO pigs ($n = 16$), and sildenafil-treated *SURF1* KO pigs ($n = 3$ with 2.1 mg/kg/day, $n = 4$ with 0.5 mg/kg/day). **$p < 0.01$; log-rank (Mantel-Cox) test.

(G) Body temperature in *SURF1* KO pigs. ****$p < 0.0001$; one-way ANOVA with Tukey's multiple comparisons.

(H) DCX protein expression in basal ganglia of *SURF1* KO pigs from immunoblots (Figure S11G). $n = 3$ replicates per sample. ***$p < 0.001$, **$p < 0.01$; one-way ANOVA with Tukey's multiple comparisons.

(I) CIV activity normalized to citrate synthase (CS) activity in basal ganglia of *SURF1* KO pigs. $n = 3$ replicates per sample. **$p < 0.01$, *$p < 0.05$; one-way ANOVA with Tukey's multiple comparisons.

(J) PRKG1 protein expression in basal ganglia of *SURF1* KO pigs from immunoblots (Figure S11G). $n = 3$ replicates per sample. **$p < 0.01$; one-way ANOVA with Tukey's multiple comparisons.

(K) Neurological score in *SURF1* KO pigs. ****$p < 0.0001$, ***$p < 0.001$; two-way ANOVA with Tukey's multiple comparisons.

See also Figure S11.

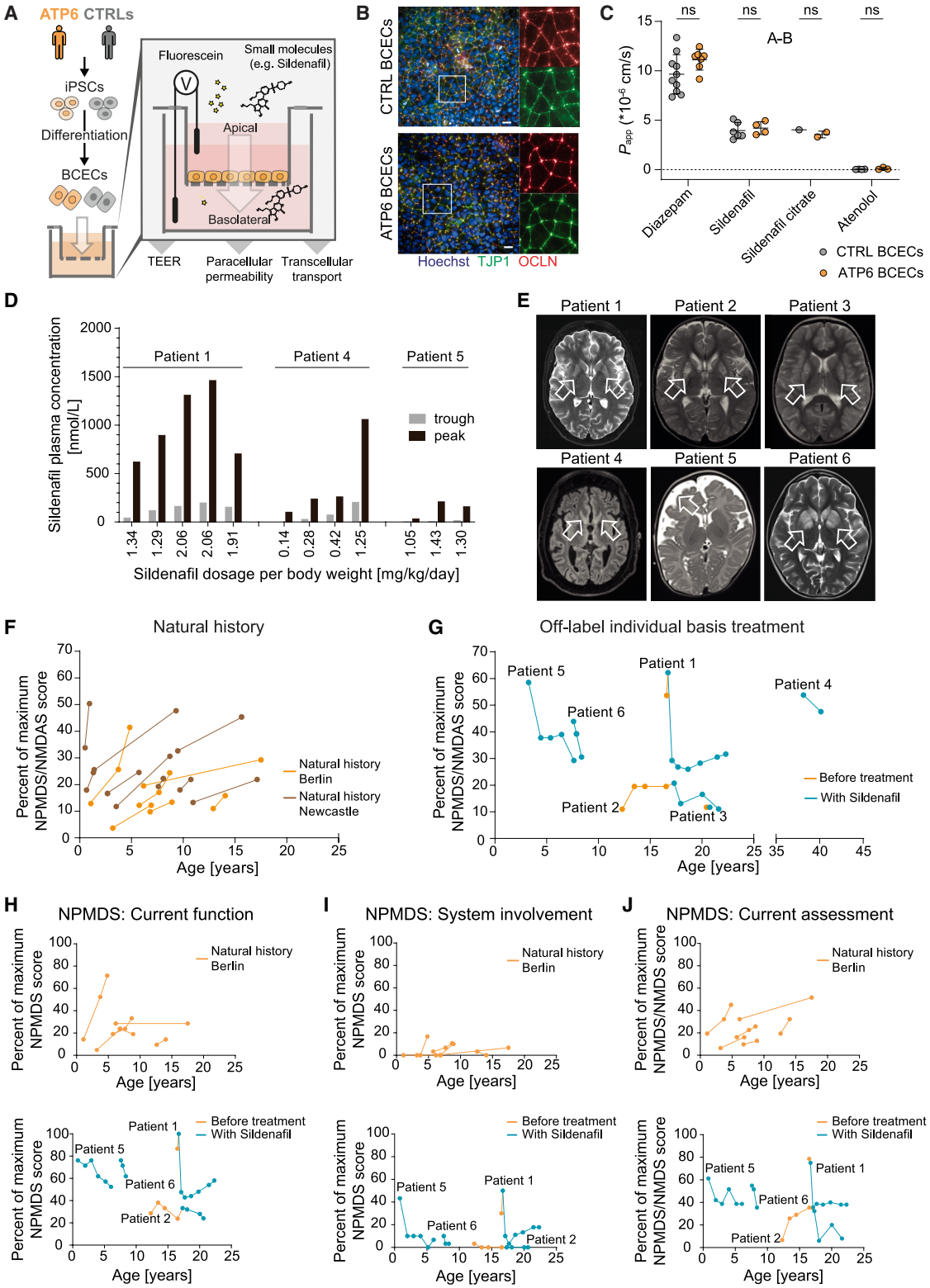


Figure 6. Sildenafil crosses the BBB and improves clinical features in six LS patients with *MT-ATP6* variants

(A) iPSC-derived BBB model.

(B) Representative immunostaining of BCECs from controls (CTRL_8) and LS (ATP6_2). Scale bar: 20 μm.

(legend continued on next page)

tolerated (Table S4), leading to improvement in motor function and development (Tables 1 and S3). Patient 5 showed protection from metabolic crises that had occurred nearly monthly before sildenafil treatment, while mild improvements in cognitive abilities were reported for patients 4 and 6 (Tables 1 and S3).

We assessed disease progression using the NPMDS[92] or the Newcastle Mitochondrial Disease Adult Scale (NMDAS).[93] These rating scales cover multiple aspects of mitochondrial disease, including clinical assessments and quality of life. The total score describes the overall severity of disease burden and typically increases over time.[92,93] The rise of NPMDS/NMDAS was evident in LS patients with *MT-ATP6* variants previously described in a cohort in Newcastle[94] (Δ8.8 percent points per year [SD = 11.4]) (Figure 6F) and in our cohort in Berlin[95] (Δ3.4 percent points per year [SD = 2.2]) (Figure 6F). Remarkably, NPMDS/NMDAS scores of the six sildenafil-treated patients decreased or showed reduced rates of increase over time (Figure 6G). The effect was evident across all dimensions of NPMDS (Figures 6H–6J). In patients 1, 5, and 6, sildenafil was started during a metabolic crisis, which resolved rapidly and led to a rapid drop in NMDAS/NPMDS. The subsequent NPMDS/NMDAS increase seen in patient 1 may be due to natural progression of the disease or reduced compliance. Overall, chronic treatment on an individual basis with sildenafil showed clinical improvements in LS patients carrying *MT-ATP6* variants.

DISCUSSION

Sildenafil is a well-studied molecule in clinical applications.[32] In addition to its use in adult men with erectile dysfunction,[96] sildenafil can treat PAH and rare lymphatic malformations in children.[39–42] Recent studies suggest that it might be a repurposable candidate for nervous system disorders.[97] Sildenafil use was associated with reduced risk of developing Alzheimer's disease (AD) and promoted neuronal outgrowth in AD iPSC-derived neurons.[98,99] Sildenafil lowered cognitive decline in mouse models of Huntington's disease (HD)[100,101] and increased motor and cognitive performance in HD individuals.[102] It also alleviated neuropathological signs in animal models of multiple sclerosis[103] and ischemic stroke.[104] In this study, we found that sildenafil might slow down the neurological decline of the severe mitochondrial brain disease LS. Sildenafil increased the lifespan of two mammalian models of LS. One treated pig remained clinically stable for over 6 months, an unprecedented health span and lifespan extension in this model. In treated LS individuals, the reduction of the upward sloping trend in the NPMDS/NMDAS score over time possibly implies that sildenafil modified the disease trajectory.

Sildenafil releases cGMP, which has a wide range of functions, likely resulting in a poly-pharmacological mode of action.[32] Sildenafil showed enhanced neurogenesis in mice,[105,106] as cGMP and PRKG1 modulated neurotransmitter release, neuronal survival, and neurite formation.[82–85] Mice deficient for Prkg1 exhibit impaired axon guidance and connectivity.[86] Consistently, we found that the signature of sildenafil primarily involved the regulation of neurodevelopment, and it acted specifically on progenitors and radial glia populations. LS neural cells showed reduced PRKG1 levels, and knockdown of PRKG1 in healthy neurons recapitulated the branching defects seen in patient cells. In mouse brain, *Prkg1* is known to be highly expressed in Purkinje cells, where its selective depletion results in motor learning defects.[107] Here, we found that treatment with sildenafil increased Prkg1 levels in LS mice and some LS pigs, potentially promoting neuronal morphogenesis and connectivity.

In addition to its neurological impact, sildenafil might induce mitochondrial biogenesis and oxygen consumption,[108,109] as PRKG1 may represent a regulator of energy homeostasis.[110] This is supported by our findings showing that PRKG1 inhibition blunted MMP normalization by sildenafil. Sildenafil also reversed changes in mitochondrial cristae junction distributions that may reflect cristae morphology defects caused by *MT-ATP6* variants.[45] We postulate that the bioenergetic improvement and MMP normalization by sildenafil may be related to its action on calcium homeostasis. Modulation of BKCa channels has been implicated in the sildenafil effect in other disease contexts[77,78] and neuronal calcium signaling can be mediated by PRKG1.[111,112] However, because PRKG1 protein levels were not fully normalized in all LS models, it is possible that sildenafil might enhance PRKG1 enzymatic activity rather than its protein abundance.[56] In fact, continuous application of the cGMP analog 8-Br-cGMP can reduce PRKG1 expression.[113] Further dissection of this pathway is required.

Whether the restorative effects of sildenafil seen in LS are linked to its vasodilatory mechanisms[32] remains to be studied. The increase in blood flow and oxygen delivery to muscle and brain tissue may potentially contribute to beneficial metabolic effects. Sildenafil led to vascular and metabolic improvements in individuals with AD[114] and in subjects with vascular cognitive impairment.[115] The effect of sildenafil on the vasculature[32] and the beneficial consequences of hypoxia seen in animal models of LS[22,23] might indicate that modulation of brain vascularization and associated oxygenation[116] could represent important therapeutic targets in LS.

Our findings underscore the power of conducting drug discovery studies driven by iPSC models. Similar strategies could

(C) Permeability coefficient (*p*app) in the apical-basolateral (AB) media of control BCECs (CTRL_8) and LS BCECs (ATP6_2), n = 1–5 independent experiments; two-way ANOVA.
(D) Quantification of sildenafil in the plasma of three LS patients treated with sildenafil.
(E) Exemplary cMRI taken during the diagnosis of the six LS patients who were subsequently treated with sildenafil. In patients 1–4 and 6, the arrows point towards T_2-hyperintense pathological basal ganglia lesions in the *Putamen* and *Globus pallidus* and in the *Nucleus caudatus* (patient 4); in patient 5, the arrow points towards frontal brain atrophy with an enlargement of the external cerebrospinal fluid spaces.
(F and G) NMDAS/NPMDS plotted as percentage of the maximum reachable score for the respective age group. Left: cohort in Newcastle (brown lines) and in Berlin (orange lines). Right: six LS patients treated with sildenafil.
(H–J) Different dimensions of NPMDS in untreated and sildenafil-treated LS patients.
See also Figure S12.

Table 1. Clinical characteristics and response to sildenafil treatment on an individual basis in six LS patients carrying *MT-ATP6* variants

Patient [sex assigned at birth]	Variant [mtDNA haplogroup] (heteroplasmy)	mtDNA variant on the protein level	Phenotype [manifestation age]	[HPO number] symptoms	cMRI features [at age in years]	Initiation of sildenafil treatment [years] (dosage)	Effect of sildenafil treatment
1 [male]	m.9176T>G [K1b2a3] (99.4%)	MT-ATP6 p.L217R	LEIGH [2 years]	[HPO:1250] epilepsy, [HPO:1260] dysarthria, [HPO:1270] motor developmental delay, [HPO:1639] cardiomyopathy, [HPO:2093] respiratory insufficiency, [HPO:3477] demyelinating neuropathy, [HPO:6789] encephlopathy, [HPO:7240] ataxia	increased T_2-signal intensities at the *Putamen*, *Nucleus caudatus* on both sides and at the perisylvian gray matter [16.5 years]	December 2018 ongoing [16 years] (2.0 mg/kg/day)	Improvements: independent breathing (tracheostoma could be closed), motor abilities (can sit, walk with support, maneuver wheel-chair), seizures stopped, independent eating and swallowing, cardiomyopathy improved; No change: neuropathy, dysarthria
2 [male]	m.8993T>G [U5a1b3] (87.7%)	MT-ATP6 p.L156R	LEIGH [2.5 years]	[HPO:1270] motor developmental delay, [HPO:2381] transient aphasia, [HPO:4911] metabolic crises, [HPO:7021] pain insensitivity, [HPO:7240] ataxia	increased T_2- and FLAIR-signal intensities at the *Putamen* and *Nucleus caudatus* on both sides [2.2 years]	October 2019 ongoing [15 years] (1.2 mg/kg/day)	Improvements: no metabolic crises during febrile illness, improvement of exercise tolerance (free walking distance improved from 500 to >5,000 m), no daytime sleepiness, ataxia improved, SARA score improved from 15.5 to 11 points; No change: mild intellectual disability
3 [female]	m.9185T>C [T2b] (100.0%)	MT-ATP6 p.L220P	LEIGH [5 years]	[HPO:0544] horizontal ophthalmoplegia, [HPO:1256] mild intellectual disability, [HPO:1270] motor developmental delay, [HPO:2355] loss of ambulation, [HPO:3477] axonal neuropathy, [HPO:3752] episodic muscle weakness	increased T_2-signal intensities at the *Putamen* on both sides [5 years], which had spontaneously disappeared by the age of 14 years	May 2019 until November 2021 [21 years] (2.9 mg/kg/day)	Improvements: reduction of episodes of muscle weakness, improvement of exercise intolerance; No change: neuropathy; Comments: after stopping sildenafil due to a delayed drug reaction (skin rash), the disease symptoms reappeared

(*Continued on next page*)

Table 1. ***Continued***

Patient [sex assigned at birth]	Variant [mtDNA haplogroup] (heteroplasmy)	mtDNA variant on the protein level	Phenotype [manifestation age]	[HPO number] symptoms	cMRI features [at age in years]	Initiation of sildenafil treatment [years] (dosage)	Effect of sildenafil treatment
4 [male]	m.8993T>G [R0a1a] (96.7%)	MT-ATP6 p.L156R	LEIGH [2–3 years]	[HPO:0365] deafness, [HPO:1249] intellectual developmental delay, [HPO:1270] motor developmental delay, [HPO:2123] myoclonic seizures, [HPO:2421] loss of head control, [HPO:3546] exercise intolerance, [HPO:7240] ataxia	increased FLAIR-signal intensities at the *Nuclei caudati* on both sides and enlargement of the internal and external CSF spaces due to diffuse brain atrophy [35 years]	May 2022 ongoing [38 years] (1.5 mg/kg/day)	Improvements: increased muscle strength (keeping his head position, ability to sit and walk), dysphagia, hyposthenia, slight improvement of in cognitive abilities; No change: deafness, ataxia; Comments: while the patient had to discontinue sildenafil for the time of an operation, the symptoms reoccurred after a short time and disappeared again after reinitiation of sildenafil
5 [male]	m.8570T>C[H4] (98.5%)	MT-ATP6 p.L15P, MT-ATP8 p.X68Q+26AS*	NARP [2 months]	[HPO:1639] hypertrophic cardiomyopathy, [HPO:1903] anemia, [HPO:2015] dysphagia, [HPO:4911] multiple metabolic crises, [HPO:8947] floppy infant	delayed myelination, frontal brain atrophy; increased T_2-signal intensities in the brain stem affecting the *Fasciculus longitudinalis* and the *Substantia nigra* on both sides [2.2 years]	September 2019 ongoing [9 months] (1.5 mg/kg/day)	Improvements: dysphagia, did not have a metabolic crisis after initiation of sildenafil therapy (before nearly one crisis every month with ICU admission), cardiomyopathy stable**;** No change: intellectual disability, delayed motor and cognitive development

(*Continued on next page*)

Table 1. *Continued*

Patient [sex assigned at birth]	Variant [mtDNA haplogroup] (heteroplasmy)	mtDNA variant on the protein level	Phenotype [manifestation age]	[HPO number] symptoms	cMRI features [at age in years]	Initiation of sildenafil treatment [years] (dosage)	Effect of sildenafil treatment
6 [female]	m.8993T>C [T2a1a] (100.0%)	MT-ATP6 p.L156R	LEIGH [7 years]	[HPO:1258] spastic paraplegia, [HPO:1268] intellectual decline, [HPO:1290] muscular hypotonia, [HPO:1332] dystonia, [HPO:2015] dysphagia, [HPO:2371] loss of speech, [HPO:2421] loss of head control, [HPO:4911] metabolic crisis, [HPO:6789] encephalopathy	increased T_2-signal intensities at the *Putamen*, *Pallidum*, and *Nucleus caudatus* on both sides and within the cortical gray matter [7.5 years]	June 2024 ongoing [7 years] (1.8 mg/kg/day)	Improvements: sitting with support and standing with assistance, consciousness normalized, normal language perception, slow improvement of muscle tone and movement disorder; No change: still wheelchair-dependent due to profound dystonia

NARP, neuropathy, ataxia, and retinitis pigmentosa; HPO, Human Phenotype Ontology; cMRI, cranial magnetic resonance imaging; FLAIR, fluid-attenuated inversion recovery; CSF, cerebrospinal fluid; SARA, scale for the assessment and rating of ataxia.See also Tables S3 and S4.

be applied to other neurological diseases for which effective model systems are lacking. Considering that mitochondria play a crucial role in cellular health and brain function and homeostasis,[117–119] understanding the potential effects of PDE5i in mitochondrial diseases may also have important implications in the context of common aging-related neurological disorders.

Limitations of the study

We reported clinical effects observed in a small cohort of mitochondrial disease patients. It is imperative that the safety and efficacy of sildenafil in patients with LS be assessed in a larger, double-blind, randomized, placebo-controlled trial. High sildenafil dosages were associated with toxicity in LS cardiomyocytes and microhemorrhages in newborn LS pigs. Although the doses that we used in LS patients have been found safe for neonatal encephalopathy,[120,121] particular precautions should be taken in infants due to the low sildenafil clearance in postnatal age that leads to longer half-lives in neonates compared with adults.[122] Sildenafil dosage should therefore be carefully monitored in treated children. Other more potent PDE5i, such as vardenafil (IC_{50} = 0.091 ± 0.031 nM) and tadalafil (IC_{50} = 1.8 ± 0.4 nM),[123] could be considered as alternatives to sildenafil in patients with mitochondrial disorders.[124]

The predictions of the mathematical model and the role of mitochondrial calcium fluxes, including the mitochondrial calcium uniporter and other ion channels that could be directly modified by cGMP or PRKG1, warrant further investigation to elucidate the effects of sildenafil in neural cells. We identified here putative sildenafil-responsive genes, but additional work is needed to dissect their biological role in LS. Besides experiments in pigs, which were carried out only in male animals, both sexes were investigated in all other experiments in mice and iPSCs, as well as in treatments on an individual basis. Nonetheless, we did not assess the influence of sex or gender on disease phenotypes and treatment outcomes. Future studies are required to address these aspects in the context of sildenafil treatment in mitochondrial diseases.

RESOURCE AVAILABILITY

Lead contact

Further information and requests for resources and reagents should be directed to and will be fulfilled by the lead contact, Alessandro Prigione (alessandro.prigione@hhu.de).

Information requests regarding Leigh syndrome patients and their treatment should be directed to the lead clinical scientist, Markus Schuelke (markus.schuelke@charite.de).

Materials availability

There are restrictions on the availability of patient-derived iPSCs used in this study due to our ethical approval, which does not support sharing with third parties without a specific amendment and does not allow performing genomic studies, in order to respect the European privacy protection law.

Data and code availability

- Raw and processed RNA-seq data are deposited in the NCBI Gene Expression Omnibus (GEO) or Sequence Read Archive (SRA): bulk RNA-seq NPC dataset at GEO: GSE292178; bulk RNA-seq brain organoids dataset at SRA BioProject: https://www.ncbi.nlm.nih.gov/bioproject/?term=PRJNA1248577; and snRNA-seq brain organoids dataset at GEO: GSE293573.

- The proteomics NPC dataset is deposited in the ProteomeXchange Consortium via the PRIDE partner repository[125] at PRIDE: PXD059519.
- The metabolomics NPC dataset is deposited in the MassIVE repository at MassIVE: https://www.omicsdi.org/dataset/massive/MSV000097182.
- Codes to reproduce our snRNA-seq results are available at: https://github.com/tpentim/Leigh_Sildenafil_Organoids.
- All original code is available in this paper's STAR Methods.
- Any additional information required to reanalyze the data reported in this paper is available from the lead contact upon request.

ACKNOWLEDGMENTS

We are grateful for technical support from Dr. Francesca Griggio, Samantha Solito, and Dr. Giulia Finotti (University of Verona); Leonardo Caporali (Carelli lab); Noemi Cannizzaro (Bottani lab); and Dr. Alessia Adelizzi, Dr. Chiara Guarona, and Dr. Martina Greco (Brunetti lab). We acknowledge financial support from the European Joint Programme for Rare Diseases (EJPRD) (CureMILS to A. Prigione, O.P., W.J.H.K., A.D.-S., P.L., E.B., A.S., and F.E.); the Bundesministerium für Forschung, Technologie und Raumfahrt (BMFTR) (01GM2002A to A. Prigione, 01GM2002B to O.P., mitoNET 01GM1906A and GENOMIT 01GM1920A to T.K., and the German Center for Child and Adolescent Health to M. Schuelke); the European Commission's Horizon Europe Programme (SIMPATHIC 101080249 to A. Prigione, M. Schuelke, and W.J.H.K.); the Deutsche Forschungsgemeinschaft (DFG) (PR1527/13-1, PR1527/14-1, and PR1527/15-1 to A. Prigione; RO5380/1-1 to A.R.; and FOR 2795 "Synapses under Stress" Ro2327/13-2 to C.R.R. and PR1527/6-1 to A. Prigione); AFM-Téléthon (SildeMITO 28545 to A. Prigione, M. Schuelke, V.C., V.T., and A.R.; 25179 to A.R.; and 29044 to A. Prigione); the German Excellence Strategy (EXC-2049-390688087) through the NeuroCure Consortium at Charité-Universitätsmedizin Berlin (to M. Schuelke); the SPARK program at the Berlin Institute of Health (BIH) (to A. Prigione and M. Schuelke); Telethon Italy (GMR23T2021 to I.S.); the Austrian Science Fund (FWF) (10.55776/I5184 and 10.55776/F78 to F.E.); the United Mitochondrial Disease Foundation (UMDF) and the Leigh Syndrome International Consortium (LSIC) (to A. Prigione and D.-F.D.); the foundations People Against Leigh Syndrome (PALS), Mito Foundation, Foundation Maladies Rares and Association (AMMi), Cure Mito and Cure ATP6, and Mitocon Italy (to A. Prigione); MitoHelp and the Eva Luise Köhler Foundation (to A. Prigione and M. Schuelke); KIAT 2410008128 and NIH DK133118 (to D.-F.D.); North Rhine-Westphalia and the European Union (IN-SU-3-001 to A.R.); the European Union (FETPROACT-2018-2020 HERMES 824164 to I.D.); the National Recovery and Resilience Plan (NRRP) (Mission 4, Component 2, Investment 1.1, Call for Tender No. 104 on February 2, 2022, by the Italian Ministry of University and Research, funded by the European Union – NextGeneration EU, project CUP B53D23018710001, Grant Assignment Decree no. 1110, adopted on July 20, 2023, by MUR) (to E.B.); Fondazione Telethon (GSA23F002 to E.B.; GMR23T2152 to D. Brunetti); the Italian Foundation A.M.Me.C. (to E.B.); Fondazione Regionale per la Ricerca Biomedica (Regione Lombardia-FRRB) (1740526 to D. Brunetti); the Italian Ministry of Health (RRC to D. Brunetti); RO5380/1-1, RO5380/10-1, and RO5380/13-1 (to A.R.); Leibniz Competition (SAW) Cooperative Excellence Project (K642/2024 to A.R.); and VHL Betroffene Familien e.V. (to A.R.). S.H. was supported by the Jürgen Manchot Stiftung. V.T., C.L.M., V.C., and M. Schuelke are members of the European Reference Network for Rare Neuromuscular Diseases (ERN EURO-NMD). Part of the work was performed at the Center for the Study of Mitochondrial Pediatric Diseases, funded by the Mariani Foundation, Italy, at Fondazione IRCCS Istituto Neurologico "Carlo Besta." During this study, A.S. was funded by the Research Council of Finland, the Jane and Aatos Erkko Foundation, the PolG Foundation, and the Sigrid Jusélius Foundation. We acknowledge the Center for Advanced Imaging (CAi) at HHU for providing access to the Revvity Operetta CLS. The graphical abstract was created with BioRender: https://BioRender.com/hi5ov9y.

AUTHOR CONTRIBUTIONS

Conceptualization, A. Prigione, M. Schuelke, O.P., D.-F.D., E.B., W.J.H.K., A.d.S., A.S., P.L., and F.E.; methodology, A. Zink, A.W., M.-T.H., G.P., S.H., C.J., L.P., M.S.C., J.B., C.B., L.E., A.D.D., F.S., D.M., A.R.-W., U.H., K.K., I.T., D. Brunetti, D. Bonesso, D.H., G.C., S.N.W., D.-F.D., C.M., L.S., T.K., M. Scaglia, J.K.-F., D.S., J.R., C.S., E.C., M.P.-G., S.M.-G., C.L.-M., F.D., I.D., F.D.S., A.A., R.D., M.B., M. Scaglia, C.G., L.A.N., and A. Perota; formal analysis, G.S., T.M.P., S.N., A.F., A.R.U., M. Schuelke, A. Zhaivoron, A. Zaliani, O.B., D.M., M.M., and A.M.; resources, E.M., V.C., V.T., A.R., N.R., P.L., B.K., I.D., and S.J.; writing – original draft, A. Prigione; writing – review & editing, A. Prigione, O.P., M. Schuelke, D.-F.D., E.B., and C.R.R.; supervision, A. Prigione, O.P., C.R.R., I.S., M.J.W.A.-H., E.M., S.J., G.U., S.P., W.J.H.K., A.S., F.E., E.B., M. Schuelke, L.C., V.C., S.J., A.d.S., and D. Brunetti; visualization, A. Zink, A.W., O.P., A. Prigione, M.-T.H., G.P., S.H., and M. Schuelke; funding acquisition, A. Prigione, D. Brunetti, A.d.S., O.P., W.J.H.K., P.L., A.S., F.E., E.B., M. Schuelke, and C.R.R.

DECLARATION OF INTERESTS

A. Prigione and M. Schuelke filed patent applications for sildenafil in the treatment of CIV and CV defects and obtained Orphan Drug Designation (ODD) for sildenafil in Leigh syndrome from the Committee for Orphan Medicinal Products (COMP) of the European Medicines Agency (EMA) (EU/3/23/2831). A.S. and L.E. are co-founders of NADMED Ltd.

STAR★METHODS

Detailed methods are provided in the online version of this paper and include the following:

- KEY RESOURCES TABLE
- EXPERIMENTAL MODEL AND STUDY PARTICIPANT DETAILS
  - Induced pluripotent stem cells (iPSCs)
  - Animals
  - Cell lines
  - Human participants
- METHOD DETAILS
  - Neural precursor cells (NPCs) and differentiated neurons
  - Cortical brain organoids
  - Assessment of mitochondrial membrane potential (MMP)
  - Compound screening
  - Bioenergetic assessment
  - Quantification of NAD metabolites
  - Quantification of mtDNA copy number
  - Analysis of mitochondrial nanostructure
  - Bulk RNA sequencing
  - Single-nucleus RNA sequencing
  - Proteomics analysis
  - Targeted metabolomics profiling
  - Multi-omics integration
  - Calcium imaging in cortical brain organoid slices (cBOS)
  - Calcium imaging in NPCs
  - Neurite outgrowth quantification
  - Experiments with *Ndufs4* KO mice
  - Experiments with *SURF1* KO pigs
  - Quantification of sildenafil concentration in patient plasma
  - Genotyping and heteroplasmy quantification
  - Cranial magnetic resonance imaging (cMRI)
  - Toxicity assays
  - Immunostaining
  - Immunoblot analysis
  - Mitochondrial complex assembly
  - Quantitative polymerase chain reaction (qPCR)
  - Human blood-brain barrier (BBB) model
  - iPSC-derived cardiomyocyte (iPSC-CMs)
  - Computational modeling of calcium and bioenergetics
- QUANTIFICATION AND STATISTICAL ANALYSIS

SUPPLEMENTAL INFORMATION

Supplemental information can be found online at https://doi.org/10.1016/j.cell.2026.02.008.

Received: April 14, 2025
Revised: August 19, 2025
Accepted: February 6, 2026
Published: March 11, 2026

REFERENCES

1. Gorman, G.S., Chinnery, P.F., DiMauro, S., Hirano, M., Koga, Y., McFarland, R., Suomalainen, A., Thorburn, D.R., Zeviani, M., and Turnbull, D.M. (2016). Mitochondrial diseases. Nat. Rev. Dis. Primers *2*, 16080. https://doi.org/10.1038/nrdp.2016.80.
2. Leigh, D. (1951). Subacute necrotizing encephalomyelopathy in an infant. J. Neurol. Neurosurg. Psychiatry *14*, 216–221. https://doi.org/10.1136/jnnp.14.3.216.
3. Baertling, F., Rodenburg, R.J., Schaper, J., Smeitink, J.A., Koopman, W.J.H., Mayatepek, E., Morava, E., and Distelmaier, F. (2014). A guide to diagnosis and treatment of Leigh syndrome. J. Neurol. Neurosurg. Psychiatry *85*, 257–265. https://doi.org/10.1136/jnnp-2012-304426.
4. McCormick, E.M., Keller, K., Taylor, J.P., Coffey, A.J., Shen, L., Krotoski, D., Harding, B., NICHD ClinGen U24 Mitochondrial Disease Gene Curation Expert Panel, Gai, X., Falk, M.J., et al. (2023). Expert Panel Curation of 113 Primary Mitochondrial Disease Genes for the Leigh Syndrome Spectrum. Ann. Neurol. *94*, 696–712. https://doi.org/10.1002/ana.26716.
5. Thorburn, D.R., Rahman, J., and Rahman, S. (1993). Mitochondrial DNA-Associated Leigh Syndrome and NARP. In GeneReviews®, M.P. Adam, D.B. Everman, G.M. Mirzaa, R.A. Pagon, S.E. Wallace, L.J.H. Bean, K.W. Gripp, and A. Amemiya, eds. (University of Washington).
6. Tiranti, V., Hoertnagel, K., Carrozzo, R., Galimberti, C., Munaro, M., Granatiero, M., Zelante, L., Gasparini, P., Marzella, R., Rocchi, M., et al. (1998). Mutations of SURF-1 in Leigh disease associated with cytochrome c oxidase deficiency. Am. J. Hum. Genet. *63*, 1609–1621. https://doi.org/10.1086/302150.
7. Petruzzella, V., Vergari, R., Puzziferri, I., Boffoli, D., Lamantea, E., Zeviani, M., and Papa, S. (2001). A nonsense mutation in the NDUFS4 gene encoding the 18 kDa (AQDQ) subunit of complex I abolishes assembly and activity of the complex in a patient with Leigh-like syndrome. Hum. Mol. Genet. *10*, 529–535. https://doi.org/10.1093/hmg/10.5.529.
8. Weissig, V. (2020). Drug Development for the Therapy of Mitochondrial Diseases. Trends Mol. Med. *26*, 40–57. https://doi.org/10.1016/j.molmed.2019.09.002.
9. Henke, M.T., Prigione, A., and Schuelke, M. (2024). Disease models of Leigh syndrome: From yeast to organoids. J. Inherit. Metab. Dis. *47*, 1292–1321. https://doi.org/10.1002/jimd.12804.
10. Gammage, P.A., Moraes, C.T., and Minczuk, M. (2018). Mitochondrial Genome Engineering: The Revolution May Not Be CRISPR-Ized. Trends Genet. *34*, 101–110. https://doi.org/10.1016/j.tig.2017.11.001.
11. Quadalti, C., Brunetti, D., Lagutina, I., Duchi, R., Perota, A., Lazzari, G., Cerutti, R., Di Meo, I., Johnson, M., Bottani, E., et al. (2018). SURF1 knockout cloned pigs: Early onset of a severe lethal phenotype. Biochim. Biophys. Acta Mol. Basis Dis. *1864*, 2131–2142. https://doi.org/10.1016/j.bbadis.2018.03.021.
12. Dell'agnello, C., Leo, S., Agostino, A., Szabadkai, G., Tiveron, C., Zulian, A., Prelle, A., Roubertoux, P., Rizzuto, R., and Zeviani, M. (2007). Increased longevity and refractoriness to Ca(2+)-dependent neurodegeneration in Surf1 knockout mice. Hum. Mol. Genet. *16*, 431–444. https://doi.org/10.1093/hmg/ddl477.
13. Kovářová, N., Pecina, P., Nůsková, H., Vrbacký, M., Zeviani, M., Mráček, T., Viscomi, C., and Houštěk, J. (2016). Tissue- and species-specific differences in cytochrome c oxidase assembly induced by SURF1 defects. Biochim. Biophys. Acta *1862*, 705–715. https://doi.org/10.1016/j.bbadis.2016.01.007.
14. Quintana, A., Kruse, S.E., Kapur, R.P., Sanz, E., and Palmiter, R.D. (2010). Complex I deficiency due to loss of Ndufs4 in the brain results in progressive encephalopathy resembling Leigh syndrome. Proc. Natl. Acad. Sci. USA *107*, 10996–11001. https://doi.org/10.1073/pnas.1006214107.
15. van de Wal, M.A.E., Adjobo-Hermans, M.J.W., Keijer, J., Schirris, T.J.J., Homberg, J.R., Wieckowski, M.R., Grefte, S., van Schothorst, E.M., van Karnebeek, C., Quintana, A., et al. (2022). Ndufs4 knockout mouse models of Leigh syndrome: pathophysiology and intervention. Brain *145*, 45–63. https://doi.org/10.1093/brain/awab426.
16. Martinelli, D., Catteruccia, M., Piemonte, F., Pastore, A., Tozzi, G., Dionisi-Vici, C., Pontrelli, G., Corsetti, T., Livadiotti, S., Kheifets, V., et al. (2012). EPI-743 reverses the progression of the pediatric mitochondrial disease–genetically defined Leigh Syndrome. Mol. Genet. Metab. *107*, 383–388. https://doi.org/10.1016/j.ymgme.2012.09.007.
17. Kayser, E.B., Mulholland, M., Olkhova, E.A., Chen, Y., Coulson, H., Cairns, O., Truong, V., James, K., Johnson, B.M., Hanaford, A., et al. (2025). Evaluating the efficacy of vatiquinone in preclinical models of Leigh syndrome and GPX4 deficiency. Orphanet J. Rare Dis. *20*, 65. https://doi.org/10.1186/s13023-025-03582-x.
18. de Haas, R., Das, D., Garanto, A., Renkema, H.G., Greupink, R., van den Broek, P., Pertijs, J., Collin, R.W.J., Willems, P., Beyrath, J., et al. (2017). Therapeutic effects of the mitochondrial ROS-redox modulator KH176 in a mammalian model of Leigh Disease. Sci. Rep. *7*, 11733. https://doi.org/10.1038/s41598-017-09417-5.
19. Johnson, S.C., Yanos, M.E., Kayser, E.B., Quintana, A., Sangesland, M., Castanza, A., Uhde, L., Hui, J., Wall, V.Z., Gagnidze, A., et al. (2013). mTOR inhibition alleviates mitochondrial disease in a mouse model of Leigh syndrome. Science *342*, 1524–1528. https://doi.org/10.1126/science.1244360.
20. Hanaford, A.R., Khanna, A., James, K., Truong, V., Liao, R., Chen, Y., Mulholland, M., Kayser, E.B., Watanabe, K., Hsieh, E.S., et al. (2024). Interferon-gamma contributes to disease progression in the Ndufs4(-/-) model of Leigh syndrome. Neuropathol. Appl. Neurobiol. *50*, e12977. https://doi.org/10.1111/nan.12977.
21. Puighermanal, E., Luna-Sánchez, M., Gella, A., van der Walt, G., Urpi, A., Royo, M., Tena-Morraja, P., Appiah, I., de Donato, M.H., Menardy, F., et al. (2024). Cannabidiol ameliorates mitochondrial disease via PPARgamma activation in preclinical models. Nat. Commun. *15*, 7730. https://doi.org/10.1038/s41467-024-51884-8.
22. Jain, I.H., Zazzeron, L., Goli, R., Alexa, K., Schatzman-Bone, S., Dhillon, H., Goldberger, O., Peng, J., Shalem, O., Sanjana, N.E., et al. (2016). Hypoxia as a therapy for mitochondrial disease. Science *352*, 54–61. https://doi.org/10.1126/science.aad9642.
23. Blume, S.Y., Garg, A., Martí-Mateos, Y., Midha, A.D., Chew, B.T.L., Lin, B., Yu, C., Dick, R., Lee, P.S., Situ, E., et al. (2025). HypoxyStat, a small-molecule form of hypoxia therapy that increases oxygen-hemoglobin affinity. Cell *188*, 1580–1588.e11. https://doi.org/10.1016/j.cell.2025.01.029.
24. Tolle, I., Tiranti, V., and Prigione, A. (2023). Modeling mitochondrial DNA diseases: from base editing to pluripotent stem-cell-derived organoids. EMBO Rep. *24*, e55678. https://doi.org/10.15252/embr.202255678.
25. Inak, G., Rybak-Wolf, A., Lisowski, P., Pentimalli, T.M., Jüttner, R., Glažar, P., Uppal, K., Bottani, E., Brunetti, D., Secker, C., et al. (2021). Defective metabolic programming impairs early neuronal morphogenesis in neural cultures and an organoid model of Leigh syndrome. Nat. Commun. *12*, 1929. https://doi.org/10.1038/s41467-021-22117-z.
26. Galera-Monge, T., Zurita-Díaz, F., Canals, I., Hansen, M.G., Rufián-Vázquez, L., Ehinger, J.K., Elmér, E., Martin, M.A., Garesse, R., Ahlenius, H., et al. (2020). Mitochondrial Dysfunction and Calcium Dysregulation in Leigh Syndrome Induced Pluripotent Stem Cell Derived Neurons. Int. J. Mol. Sci. *21*, 3191. https://doi.org/10.3390/ijms21093191.
27. Lorenz, C., Lesimple, P., Bukowiecki, R., Zink, A., Inak, G., Mlody, B., Singh, M., Semtner, M., Mah, N., Auré, K., et al. (2017). Human iPSC-Derived Neural Progenitors Are an Effective Drug Discovery Model for Neurological mtDNA Disorders. Cell Stem Cell *20*, 659–674.e9. https://doi.org/10.1016/j.stem.2016.12.013.

28. Zheng, X., Boyer, L., Jin, M., Kim, Y., Fan, W., Bardy, C., Berggren, T., Evans, R.M., Gage, F.H., and Hunter, T. (2016). Alleviation of neuronal energy deficiency by mTOR inhibition as a treatment for mitochondria-related neurodegeneration. eLife *5*, e13378. https://doi.org/10.7554/eLife.13378.

29. Romero-Morales, A.I., Robertson, G.L., Rastogi, A., Rasmussen, M.L., Temuri, H., McElroy, G.S., Chakrabarty, R.P., Hsu, L., Almonacid, P.M., Millis, B.A., et al. (2022). Human iPSC-derived cerebral organoids model features of Leigh syndrome and reveal abnormal corticogenesis. Development *149*, dev199914. https://doi.org/10.1242/dev.199914.

30. Menacho, C., Okawa, S., Álvarez-Merz, I., Wittich, A., Muñoz-Oreja, M., Lisowski, P., Pentimalli, T.M., Rybak-Wolf, A., Inak, G., Zakin, S., et al. (2024). Deep learning-driven neuromorphogenesis screenings identify repurposable drugs for mitochondrial disease. Preprint at bioRxiv. https://doi.org/10.1101/2024.07.08.602501.

31. Zink, A., Haferkamp, U., Wittich, A., Beller, M., Pless, O., and Prigione, A. (2022). High-content screening of mitochondrial polarization in neural cells derived from human pluripotent stem cells. Star Protoc. *3*, 101602. https://doi.org/10.1016/j.xpro.2022.101602.

32. Ghofrani, H.A., Osterloh, I.H., and Grimminger, F. (2006). Sildenafil: from angina to erectile dysfunction to pulmonary hypertension and beyond. Nat. Rev. Drug Discov. *5*, 689–702. https://doi.org/10.1038/nrd2030.

33. Henke, M.T., Zink, A., Diecke, S., Prigione, A., and Schuelke, M. (2023). Generation of two mother-child pairs of iPSCs from maternally inherited Leigh syndrome patients with m.8993 T > G and m.9176 T > G MT-ATP6 mutations. Stem Cell Res. *67*, 103030. https://doi.org/10.1016/j.scr.2023.103030.

34. Lorenz, C., Zink, A., Henke, M.T., Staege, S., Mlody, B., Bünning, M., Wanker, E., Diecke, S., Schuelke, M., and Prigione, A. (2022). Generation of four iPSC lines from four patients with Leigh syndrome carrying homoplasmic mutations m.8993T > G or m.8993T > C in the mitochondrial gene MT-ATP6. Stem Cell Res. *61*, 102742. https://doi.org/10.1016/j.scr.2022.102742.

35. Steiner, T., Zink, A., Henke, M.T., Cecchetto, G., Buenning, M., Rossi, A., Schuelke, M., and Prigione, A. (2022). RNA-based generation of iPSCs from a boy carrying the mutation m.9185 T>C in the mitochondrial gene MT-ATP6 and from his healthy mother. Stem Cell Res. *64*, 102920. https://doi.org/10.1016/j.scr.2022.102920.

36. Haschke, A.M., Diecke, S., and Schuelke, M. (2024). Characterization of two iPSC lines from patients with maternally inherited leigh (MILS) and neuropathy, ataxia, and retinitis pigmentosa (NARP) syndrome carrying the MT-ATP6 m.8993 T>G mutation at different degrees of heteroplasmy. Stem Cell Res. *81*, 103547. https://doi.org/10.1016/j.scr.2024.103547.

37. Corsello, S.M., Bittker, J.A., Liu, Z., Gould, J., McCarren, P., Hirschman, J.E., Johnston, S.E., Vrcic, A., Wong, B., Khan, M., et al. (2017). The Drug Repurposing Hub: a next-generation drug library and information resource. Nat. Med. *23*, 405–408. https://doi.org/10.1038/nm.4306.

38. Zhang, J.H., Chung, T.D., and Oldenburg, K.R. (1999). A Simple Statistical Parameter for Use in Evaluation and Validation of High Throughput Screening Assays. J. Biomol. Screen. *4*, 67–73. https://doi.org/10.1177/108705719900400206.

39. Sun, L., Wang, C., Zhou, Y., Sun, W., and Wang, C. (2021). Clinical Efficacy and Safety of Different Doses of Sildenafil in the Treatment of Persistent Pulmonary Hypertension of the Newborn: A Network Meta-analysis. Front. Pharmacol. *12*, 697287. https://doi.org/10.3389/fphar.2021.697287.

40. Barst, R.J., Beghetti, M., Pulido, T., Layton, G., Konourina, I., Zhang, M., and Ivy, D.D.; STARTS-2 Investigators (2014). STARTS-2: long-term survival with oral sildenafil monotherapy in treatment-naive pediatric pulmonary arterial hypertension. Circulation *129*, 1914–1923. https://doi.org/10.1161/CIRCULATIONAHA.113.005698.

41. Barst, R.J., Ivy, D.D., Gaitan, G., Szatmari, A., Rudzinski, A., Garcia, A.E., Sastry, B.K., Pulido, T., Layton, G.R., Serdarevic-Pehar, M., et al. (2012). A randomized, double-blind, placebo-controlled, dose-ranging study of oral sildenafil citrate in treatment-naive children with pulmonary arterial hypertension. Circulation *125*, 324–334. https://doi.org/10.1161/CIRCULATIONAHA.110.016667.

42. Danial, C., Tichy, A.L., Tariq, U., Swetman, G.L., Khuu, P., Leung, T.H., Benjamin, L., Teng, J., Vasanawala, S.S., and Lane, A.T. (2014). An open-label study to evaluate sildenafil for the treatment of lymphatic malformations. J. Am. Acad. Dermatol. *70*, 1050–1057. https://doi.org/10.1016/j.jaad.2014.02.005.

43. Bugiardini, E., Bottani, E., Marchet, S., Poole, O.V., Beninca, C., Horga, A., Woodward, C., Lam, A., Hargreaves, I., Chalasani, A., et al. (2020). Expanding the molecular and phenotypic spectrum of truncating MT-ATP6 mutations. Neurol. Genet. *6*, e381. https://doi.org/10.1212/NXG.0000000000000381.

44. Carrozzo, R., Wittig, I., Santorelli, F.M., Bertini, E., Hofmann, S., Brandt, U., and Schägger, H. (2006). Subcomplexes of human ATP synthase mark mitochondrial biosynthesis disorders. Ann. Neurol. *59*, 265–275. https://doi.org/10.1002/ana.20729.

45. Kenvin, S., Torregrosa-Muñumer, R., Reidelbach, M., Pennonen, J., Turkia, J.J., Rannila, E., Kvist, J., Sainio, M.T., Huber, N., Herukka, S.K., et al. (2022). Threshold of heteroplasmic truncating MT-ATP6 mutation in reprogramming, Notch hyperactivation and motor neuron metabolism. Hum. Mol. Genet. *31*, 958–974. https://doi.org/10.1093/hmg/ddab299.

46. Stephan, T., Brüser, C., Deckers, M., Steyer, A.M., Balzarotti, F., Barbot, M., Behr, T.S., Heim, G., Hübner, W., Ilgen, P., et al. (2020). MICOS assembly controls mitochondrial inner membrane remodeling and crista junction redistribution to mediate cristae formation. EMBO J. *39*, e104105. https://doi.org/10.15252/embj.2019104105.

47. Li, C., Enomoto, M., Rossi, A.M., Seo, M.D., Rahman, T., Stathopulos, P.B., Taylor, C.W., Ikura, M., and Ames, J.B. (2013). CaBP1, a neuronal Ca2+ sensor protein, inhibits inositol trisphosphate receptors by clamping intersubunit interactions. Proc. Natl. Acad. Sci. USA *110*, 8507–8512. https://doi.org/10.1073/pnas.1220847110.

48. Jeannotte, L., Gotti, F., and Landry-Truchon, K. (2016). Hoxa5: A Key Player in Development and Disease. J. Dev. Biol. *4*, 13. https://doi.org/10.3390/jdb4020013.

49. Philippidou, P., Walsh, C.M., Aubin, J., Jeannotte, L., and Dasen, J.S. (2012). Sustained Hox5 gene activity is required for respiratory motor neuron development. Nat. Neurosci. *15*, 1636–1644. https://doi.org/10.1038/nn.3242.

50. Inamata, Y., and Shirasaki, R. (2014). Dbx1 triggers crucial molecular programs required for midline crossing by midbrain commissural axons. Development *141*, 1260–1271. https://doi.org/10.1242/dev.102327.

51. Eichholtz-Wirth, H., Fritz, E., and Wolz, L. (2003). Overexpression of the 'silencer of death domain', SODD/BAG-4, modulates both TNFR1- and CD95-dependent cell death pathways. Cancer Lett. *194*, 81–89. https://doi.org/10.1016/s0304-3835(03)00009-0.

52. Kreider, R.B., and Stout, J.R. (2021). Creatine in Health and Disease. Nutrients *13*, 447. https://doi.org/10.3390/nu13020447.

53. Wyss, M., and Kaddurah-Daouk, R. (2000). Creatine and creatinine metabolism. Physiol. Rev. *80*, 1107–1213. https://doi.org/10.1152/physrev.2000.80.3.1107.

54. Paul, B.D., Sbodio, J.I., and Snyder, S.H. (2018). Cysteine Metabolism in Neuronal Redox Homeostasis. Trends Pharmacol. Sci. *39*, 513–524. https://doi.org/10.1016/j.tips.2018.02.007.

55. Lisowski, P., Lickfett, S., Rybak-Wolf, A., Menacho, C., Le, S., Pentimalli, T.M., Notopoulou, S., Dykstra, W., Oehler, D., López-Calcerrada, S., et al. (2024). Mutant huntingtin impairs neurodevelopment in human brain organoids through CHCHD2-mediated neurometabolic failure. Nat. Commun. *15*, 7027. https://doi.org/10.1038/s41467-024-51216-w.

56. Francis, S.H., Busch, J.L., Corbin, J.D., and Sibley, D. (2010). cGMP-dependent protein kinases and cGMP phosphodiesterases in nitric oxide and cGMP action. Pharmacol. Rev. *62*, 525–563. https://doi.org/10.1124/pr.110.002907.

57. Andrieu, G., Tran, A.H., Strissel, K.J., and Denis, G.V. (2016). BRD4 Regulates Breast Cancer Dissemination through Jagged1/Notch1 Signaling. Cancer Res. *76*, 6555–6567. https://doi.org/10.1158/0008-5472.CAN-16-0559.

58. Xu, F., Lu, S., Jia, X., and Zhou, Y. (2023). Bromodomain protein 4 mediates the roles of TGFβ1-induced Stat3 signaling in mouse liver fibrogenesis. Toxicol. Lett. *385*, 42–50. https://doi.org/10.1016/j.toxlet.2023.08.009.

59. Shi, L., and Bergson, C.M. (2020). Neuregulin 1: an intriguing therapeutic target for neurodevelopmental disorders. Transl. Psychiatry *10*, 190. https://doi.org/10.1038/s41398-020-00868-5.

60. Sophocleous, R.A., Ooi, L., and Sluyter, R. (2022). The P2X4 Receptor: Cellular and Molecular Characteristics of a Promising Neuroinflammatory Target. Int. J. Mol. Sci. *23*, 5739. https://doi.org/10.3390/ijms23105739.

61. Chou, J.Y., and Mansfield, B.C. (2014). The SLC37 family of sugar-phosphate/phosphate exchangers. Curr. Top. Membr. *73*, 357–382. https://doi.org/10.1016/B978-0-12-800223-0.00010-4.

62. Le, S., Petersilie, L., Inak, G., Menacho-Pando, C., Kafitz, K.W., Rybak-Wolf, A., Rajewsky, N., Rose, C.R., and Prigione, A. (2021). Generation of Human Brain Organoids for Mitochondrial Disease Modeling. J. Vis. Exp. *172*, e62756. https://doi.org/10.3791/62756.

63. Miura, Y., Li, M.Y., Birey, F., Ikeda, K., Revah, O., Thete, M.V., Park, J.Y., Puno, A., Lee, S.H., Porteus, M.H., et al. (2020). Generation of human striatal organoids and cortico-striatal assembloids from human pluripotent stem cells. Nat. Biotechnol. *38*, 1421–1430. https://doi.org/10.1038/s41587-020-00763-w.

64. Cong, Y., So, V., Tijssen, M.A.J., Verbeek, D.S., Reggiori, F., and Mauthe, M. (2021). WDR45, one gene associated with multiple neurodevelopmental disorders. Autophagy *17*, 3908–3923. https://doi.org/10.1080/15548627.2021.1899669.

65. Craig, A.M., and Kang, Y. (2007). Neurexin-neuroligin signaling in synapse development. Curr. Opin. Neurobiol. *17*, 43–52. https://doi.org/10.1016/j.conb.2007.01.011.

66. Klim, J.R., Williams, L.A., Limone, F., Guerra San Juan, I., Davis-Dusenbery, B.N., Mordes, D.A., Burberry, A., Steinbaugh, M.J., Gamage, K.K., Kirchner, R., et al. (2019). ALS-implicated protein TDP-43 sustains levels of STMN2, a mediator of motor neuron growth and repair. Nat. Neurosci. *22*, 167–179. https://doi.org/10.1038/s41593-018-0300-4.

67. Liu, Z., Chatterjee, T.K., and Fisher, R.A. (2002). RGS6 interacts with SCG10 and promotes neuronal differentiation. Role of the G gamma subunit-like (GGL) domain of RGS6. J. Biol. Chem. *277*, 37832–37839. https://doi.org/10.1074/jbc.M205908200.

68. He, Z., Dony, L., Fleck, J.S., Szałata, A., Li, K.X., Slišković, I., Lin, H.C., Santel, M., Atamian, A., Quadrato, G., et al. (2024). An integrated transcriptomic cell atlas of human neural organoids. Nature *635*, 690–698. https://doi.org/10.1038/s41586-024-08172-8.

69. Petersilie, L., Heiduschka, S., Nelson, J.S.E., Neu, L.A., Le, S., Anand, R., Kafitz, K.W., Prigione, A., and Rose, C.R. (2024). Cortical brain organoid slices (cBOS) for the study of human neural cells in minimal networks. iScience *27*, 109415. https://doi.org/10.1016/j.isci.2024.109415.

70. Wacquier, B., Combettes, L., Van Nhieu, G.T., and Dupont, G. (2016). Interplay Between Intracellular Ca(2+) Oscillations and Ca(2+)-stimulated Mitochondrial Metabolism. Sci. Rep. *6*, 19316. https://doi.org/10.1038/srep19316.

71. Toglia, P., Cheung, K.H., Mak, D.O.D., and Ullah, G. (2016). Impaired mitochondrial function due to familial Alzheimer's disease-causing presenilins mutants via Ca(2+) disruptions. Cell Calcium *59*, 240–250. https://doi.org/10.1016/j.ceca.2016.02.013.

72. Toglia, P., and Ullah, G. (2016). The gain-of-function enhancement of IP3-receptor channel gating by familial Alzheimer's disease-linked presenilin mutants increases the open probability of mitochondrial permeability transition pore. Cell Calcium *60*, 13–24. https://doi.org/10.1016/j.ceca.2016.05.002.

73. Pensalfini, A., Umar, A.R., Glabe, C., Parker, I., Ullah, G., and Demuro, A. (2022). Intracellular Injection of Brain Extracts from Alzheimer's Disease Patients Triggers Unregulated Ca^{2+} Release from Intracellular Stores That Hinders Cellular Bioenergetics. Cells *11*, 3630. https://doi.org/10.3390/cells11223630.

74. D'Angelo, D., Sánchez-Vázquez, V.H., Cartes-Saavedra, B., Vecellio Reane, D., Cupo, R.R., Delgado de la Herran, H., Ghirardo, G., Shorter, J., Wevers, R.A., Wortmann, S.B., et al. (2025). Dependence of mitochondrial calcium signalling and dynamics on the disaggregase, CLPB. Nat. Commun. *16*, 2810. https://doi.org/10.1038/s41467-025-57641-9.

75. Waldeck-Weiermair, M., Deak, A.T., Groschner, L.N., Alam, M.R., Jean-Quartier, C., Malli, R., and Graier, W.F. (2013). Molecularly distinct routes of mitochondrial Ca2+ uptake are activated depending on the activity of the sarco/endoplasmic reticulum Ca2+ ATPase (SERCA). J. Biol. Chem. *288*, 15367–15379. https://doi.org/10.1074/jbc.M113.462259.

76. Szabo, I., and Szewczyk, A. (2023). Mitochondrial Ion Channels. Annu. Rev. Biophys. *52*, 229–254. https://doi.org/10.1146/annurev-biophys-092622-094853.

77. Behmenburg, F., Dorsch, M., Huhn, R., Mally, D., Heinen, A., Hollmann, M.W., and Berger, M.M. (2015). Impact of Mitochondrial Ca2+-Sensitive Potassium (mBKCa) Channels in Sildenafil-Induced Cardioprotection in Rats. PLoS One *10*, e0144737. https://doi.org/10.1371/journal.pone.0144737.

78. Prieto, D., Rivera, L., Benedito, S., Recio, P., Villalba, N., Hernández, M., and García-Sacristán, A. (2006). Ca2+-activated K+ (KCa) channels are involved in the relaxations elicited by sildenafil in penile resistance arteries. Eur. J. Pharmacol. *531*, 232–237. https://doi.org/10.1016/j.ejphar.2005.12.033.

79. Checchetto, V., Leanza, L., De Stefani, D., Rizzuto, R., Gulbins, E., and Szabo, I. (2021). Mitochondrial K^+ channels and their implications for disease mechanisms. Pharmacol. Ther. *227*, 107874. https://doi.org/10.1016/j.pharmthera.2021.107874.

80. Kulawiak, B., Żochowska, M., Bednarczyk, P., Galuba, A., Stroud, D.A., and Szewczyk, A. (2023). Loss of the large conductance calcium-activated potassium channel causes an increase in mitochondrial reactive oxygen species in glioblastoma cells. Pflugers Arch. *475*, 1045–1060. https://doi.org/10.1007/s00424-023-02833-9.

81. Lickfett, S., Menacho, C., Zink, A., Telugu, N.S., Beller, M., Diecke, S., Cambridge, S., and Prigione, A. (2022). High-content analysis of neuronal morphology in human iPSC-derived neurons. Star Protoc. *3*, 101567. https://doi.org/10.1016/j.xpro.2022.101567.

82. Shelly, M., Lim, B.K., Cancedda, L., Heilshorn, S.C., Gao, H., and Poo, M.M. (2010). Local and long-range reciprocal regulation of cAMP and cGMP in axon/dendrite formation. Science *327*, 547–552. https://doi.org/10.1126/science.1179735.

83. Zhao, Z., Wang, Z., Gu, Y., Feil, R., Hofmann, F., and Ma, L. (2009). Regulate axon branching by the cyclic GMP pathway via inhibition of glycogen synthase kinase 3 in dorsal root ganglion sensory neurons. J. Neurosci. *29*, 1350–1360. https://doi.org/10.1523/JNEUROSCI.3770-08.2009.

84. Fiscus, R.R. (2002). Involvement of cyclic GMP and protein kinase G in the regulation of apoptosis and survival in neural cells. Neurosignals. *11*, 175–190. https://doi.org/10.1159/000065431.

85. Barnstable, C.J., Wei, J.Y., and Han, M.H. (2004). Modulation of synaptic function by cGMP and cGMP-gated cation channels. Neurochem. Int. *45*, 875–884. https://doi.org/10.1016/j.neuint.2004.03.018.

86. Schmidt, H., Werner, M., Heppenstall, P.A., Henning, M., Moré, M.I., Kühbandner, S., Lewin, G.R., Hofmann, F., Feil, R., and Rathjen, F.G. (2002). cGMP-mediated signaling via cGKIalpha is required for the guidance and connectivity of sensory axons. J. Cell Biol. *159*, 489–498. https://doi.org/10.1083/jcb.200207058.

87. Yoon, J.Y., Daneshgar, N., Chu, Y., Chen, B., Hefti, M., Vikram, A., Irani, K., Song, L.S., Brenner, C., Abel, E.D., et al. (2022). Metabolic rescue ameliorates mitochondrial encephalo-cardiomyopathy in murine and

human iPSC models of Leigh syndrome. Clin. Transl. Med. *12*, e954. https://doi.org/10.1002/ctm2.954.

88. Aguilar, K., Comes, G., Canal, C., Quintana, A., Sanz, E., and Hidalgo, J. (2022). Microglial response promotes neurodegeneration in the Ndufs4 KO mouse model of Leigh syndrome. Glia *70*, 2032–2044. https://doi.org/10.1002/glia.24234.

89. Daneshgar, N., Leidinger, M.R., Le, S., Hefti, M., Prigione, A., and Dai, D.F. (2022). Activated microglia and neuroinflammation as a pathogenic mechanism in Leigh syndrome. Front. Neurosci. *16*, 1068498. https://doi.org/10.3389/fnins.2022.1068498.

90. Appelt-Menzel, A., Oerter, S., Mathew, S., Haferkamp, U., Hartmann, C., Jung, M., Neuhaus, W., and Pless, O. (2020). Human iPSC-Derived Blood-Brain Barrier Models: Valuable Tools for Preclinical Drug Discovery and Development? Curr. Protoc. Stem Cell Biol. *55*, e122. https://doi.org/10.1002/cpsc.122.

91. Gómez-Vallejo, V., Ugarte, A., García-Barroso, C., Cuadrado-Tejedor, M., Szczupak, B., Dopeso-Reyes, I.G., Lanciego, J.L., García-Osta, A., Llop, J., Oyarzabal, J., et al. (2016). Pharmacokinetic investigation of sildenafil using positron emission tomography and determination of its effect on cerebrospinal fluid cGMP levels. J. Neurochem. *136*, 403–415. https://doi.org/10.1111/jnc.13454.

92. Phoenix, C., Schaefer, A.M., Elson, J.L., Morava, E., Bugiani, M., Uziel, G., Smeitink, J.A., Turnbull, D.M., and McFarland, R. (2006). A scale to monitor progression and treatment of mitochondrial disease in children. Neuromuscul. Disord. *16*, 814–820. https://doi.org/10.1016/j.nmd.2006.08.006.

93. Schaefer, A.M., Phoenix, C., Elson, J.L., McFarland, R., Chinnery, P.F., and Turnbull, D.M. (2006). Mitochondrial disease in adults: a scale to monitor progression and treatment. Neurology *66*, 1932–1934. https://doi.org/10.1212/01.wnl.0000219759.72195.41.

94. Lim, A.Z., Ng, Y.S., Blain, A., Jiminez-Moreno, C., Alston, C.L., Nesbitt, V., Simmons, L., Santra, S., Wassmer, E., Blakely, E.L., et al. (2022). Natural History of Leigh Syndrome: A Study of Disease Burden and Progression. Ann. Neurol. *91*, 117–130. https://doi.org/10.1002/ana.26260.

95. Carli, S., Levarlet, A., Diodato, D., Bertini, E.S., Martinelli, D., Malandrini, A., Lopergolo, D., Gallus, G.N., Ganetzky, R.D., La Morgia, C., et al. (2025). Natural History of Patients With Mitochondrial ATPase Deficiency Due to Pathogenic Variants of MT-ATP6 and MT-ATP8. Neurology *104*, e213462. https://doi.org/10.1212/WNL.0000000000213462.

96. Giuliano, F., Jackson, G., Montorsi, F., Martin-Morales, A., and Raillard, P. (2010). Safety of sildenafil citrate: review of 67 double-blind placebo-controlled trials and the postmarketing safety database. Int. J. Clin. Pract. *64*, 240–255. https://doi.org/10.1111/j.1742-1241.2009.02254.x.

97. Xiong, Y., and Wintermark, P. (2022). The Role of Sildenafil in Treating Brain Injuries in Adults and Neonates. Front. Cell. Neurosci. *16*, 879649. https://doi.org/10.3389/fncel.2022.879649.

98. Fang, J., Zhang, P., Zhou, Y., Chiang, C.W., Tan, J., Hou, Y., Stauffer, S., Li, L., Pieper, A.A., Cummings, J., et al. (2021). Endophenotype-based in silico network medicine discovery combined with insurance record data mining identifies sildenafil as a candidate drug for Alzheimer's disease. Nat Aging *1*, 1175–1188. https://doi.org/10.1038/s43587-021-00138-z.

99. Sanders, O., and Rajagopal, L. (2020). Phosphodiesterase Inhibitors for Alzheimer's Disease: A Systematic Review of Clinical Trials and Epidemiology with a Mechanistic Rationale. J. Alzheimers. Dis. Rep. *4*, 185–215. https://doi.org/10.3233/ADR-200191.

100. Saavedra, A., Giralt, A., Arumí, H., Alberch, J., and Pérez-Navarro, E. (2013). Regulation of hippocampal cGMP levels as a candidate to treat cognitive deficits in Huntington's disease. PLoS One *8*, e73664. https://doi.org/10.1371/journal.pone.0073664.

101. Puerta, E., Hervias, I., Barros-Miñones, L., Jordan, J., Ricobaraza, A., Cuadrado-Tejedor, M., García-Osta, A., and Aguirre, N. (2010). Sildenafil protects against 3-nitropropionic acid neurotoxicity through the modulation of calpain, CREB, and BDNF. Neurobiol. Dis. *38*, 237–245. https://doi.org/10.1016/j.nbd.2010.01.013.

102. Achenbach, J., Faissner, S., and Saft, C. (2022). Resurrection of sildenafil: potential for Huntington's Disease, too? J. Neurol. *269*, 5144–5150. https://doi.org/10.1007/s00415-022-11196-7.

103. Duarte-Silva, E., Meiry da Rocha Araújo, S., Oliveira, W.H., Lós, D.B., Bonfanti, A.P., Peron, G., de Lima Thomaz, L., Verinaud, L., and Peixoto, C.A. (2021). Sildenafil Alleviates Murine Experimental Autoimmune Encephalomyelitis by Triggering Autophagy in the Spinal Cord. Front. Immunol. *12*, 671511. https://doi.org/10.3389/fimmu.2021.671511.

104. Ölmestig, J.N.E., Marlet, I.R., Hainsworth, A.H., and Kruuse, C. (2017). Phosphodiesterase 5 inhibition as a therapeutic target for ischemic stroke: A systematic review of preclinical studies. Cell. Signal. *38*, 39–48. https://doi.org/10.1016/j.cellsig.2017.06.015.

105. Zhang, R.L., Chopp, M., Roberts, C., Wei, M., Wang, X., Liu, X., Lu, M., and Zhang, Z.G. (2012). Sildenafil enhances neurogenesis and oligodendrogenesis in ischemic brain of middle-aged mouse. PLoS One *7*, e48141. https://doi.org/10.1371/journal.pone.0048141.

106. Feil, R., Hofmann, F., and Kleppisch, T. (2005). Function of cGMP-dependent protein kinases in the nervous system. Rev. Neurosci. *16*, 23–41. https://doi.org/10.1515/revneuro.2005.16.1.23.

107. Feil, R., Hartmann, J., Luo, C., Wolfsgruber, W., Schilling, K., Feil, S., Barski, J.J., Meyer, M., Konnerth, A., De Zeeuw, C.I., et al. (2003). Impairment of LTD and cerebellar learning by Purkinje cell-specific ablation of cGMP-dependent protein kinase I. J. Cell Biol. *163*, 295–302. https://doi.org/10.1083/jcb.200306148.

108. Corum, D.G., Jenkins, D.P., Heslop, J.A., Tallent, L.M., Beeson, G.C., Barth, J.L., Schnellmann, R.G., and Muise-Helmericks, R.C. (2020). PDE5 inhibition rescues mitochondrial dysfunction and angiogenic responses induced by Akt3 inhibition by promotion of PRC expression. J. Biol. Chem. *295*, 18091–18104. https://doi.org/10.1074/jbc.RA120.013716.

109. Zhu, G., Ueda, K., Hashimoto, M., Zhang, M., Sasaki, M., Kariya, T., Sasaki, H., Kaludercic, N., Lee, D.I., Bedja, D., et al. (2022). The mitochondrial regulator PGC1alpha is induced by cGMP-PKG signaling and mediates the protective effects of phosphodiesterase 5 inhibition in heart failure. FEBS Lett. *596*, 17–28. https://doi.org/10.1002/1873-3468.14228.

110. Kaun, K.R., and Sokolowski, M.B. (2009). cGMP-dependent protein kinase: linking foraging to energy homeostasis. Genome *52*, 1–7. https://doi.org/10.1139/G08-090.

111. Paupardin-Tritsch, D., Hammond, C., Gerschenfeld, H.M., Nairn, A.C., and Greengard, P. (1986). cGMP-dependent protein kinase enhances Ca2+ current and potentiates the serotonin-induced Ca2+ current increase in snail neurones. Nature *323*, 812–814. https://doi.org/10.1038/323812a0.

112. Dason, J.S., Allen, A.M., Vasquez, O.E., and Sokolowski, M.B. (2019). Distinct functions of a cGMP-dependent protein kinase in nerve terminal growth and synaptic vesicle cycling. J. Cell Sci. *132*, jcs227165. https://doi.org/10.1242/jcs.227165.

113. Soff, G.A., Cornwell, T.L., Cundiff, D.L., Gately, S., and Lincoln, T.M. (1997). Smooth muscle cell expression of type I cyclic GMP-dependent protein kinase is suppressed by continuous exposure to nitrovasodilators, theophylline, cyclic GMP, and cyclic AMP. J. Clin. Investig. *100*, 2580–2587. https://doi.org/10.1172/JCI119801.

114. Sheng, M., Lu, H., Liu, P., Li, Y., Ravi, H., Peng, S.L., Diaz-Arrastia, R., Devous, M.D., and Womack, K.B. (2017). Sildenafil Improves Vascular and Metabolic Function in Patients with Alzheimer's Disease. J. Alzheimers Dis. *60*, 1351–1364. https://doi.org/10.3233/JAD-161006.

115. Webb, A.J.S., Birks, J.S., Feakins, K.A., Lawson, A., Dawson, J., Rothman, A.M.K., Werring, D.J., Llwyd, O., Stewart, C.R., and Thomas, J. (2024). Cerebrovascular Effects of Sildenafil in Small Vessel Disease: The OxHARP Trial. Circ. Res. *135*, 320–331. https://doi.org/10.1161/CIRCRESAHA.124.324327.

116. Baik, A.H., and Jain, I.H. (2020). Turning the Oxygen Dial: Balancing the Highs and Lows. Trends Cell Biol. *30*, 516–536. https://doi.org/10.1016/j.tcb.2020.04.005.

117. Cunnane, S.C., Trushina, E., Morland, C., Prigione, A., Casadesus, G., Andrews, Z.B., Beal, M.F., Bergersen, L.H., Brinton, R.D., de la Monte, S., et al. (2020). Brain energy rescue: an emerging therapeutic concept for neurodegenerative disorders of ageing. Nat. Rev. Drug Discov. *19*, 609–633. https://doi.org/10.1038/s41573-020-0072-x.

118. Suomalainen, A., and Nunnari, J. (2024). Mitochondria at the crossroads of health and disease. Cell *187*, 2601–2627. https://doi.org/10.1016/j.cell.2024.04.037.

119. Iwata, R., Casimir, P., Erkol, E., Boubakar, L., Planque, M., Gallego López, I.M., Ditkowska, M., Gaspariunaite, V., Beckers, S., Remans, D., et al. (2023). Mitochondria metabolism sets the species-specific tempo of neuronal development. Science *379*, eabn4705. https://doi.org/10.1126/science.abn4705.

120. Wintermark, P., Lapointe, A., Steinhorn, R., Rampakakis, E., Burhenne, J., Meid, A.D., Bajraktari-Sylejmani, G., Khairy, M., Altit, G., Adamo, M.T., et al. (2024). Feasibility and Safety of Sildenafil to Repair Brain Injury Secondary to Birth Asphyxia (SANE-01): A Randomized, Double-blind, Placebo-controlled Phase Ib Clinical Trial. J. Pediatr. *266*, 113879. https://doi.org/10.1016/j.jpeds.2023.113879.

121. Wintermark, P., Lapointe, A., Altit, G., Steinhorn, R., Rampakakis, E., Meid, A.D., Burhenne, J., Bajraktari-Sylejmani, G., Khairy, M., Adamo, M.T., et al. (2025). Testing Higher Doses of Sildenafil to Repair Brain Injury Secondary to Birth Asphyxia: An Open-Label Dose-Finding Phase 1b Clinical Trial-Sildenafil Administration to Treat Neonatal Encephalopathy-Study 02. J. Pediatr. *285*, 114701. https://doi.org/10.1016/j.jpeds.2025.114701.

122. Mukherjee, A., Dombi, T., Wittke, B., and Lalonde, R. (2009). Population pharmacokinetics of sildenafil in term neonates: evidence of rapid maturation of metabolic clearance in the early postnatal period. Clin. Pharmacol. Ther. *85*, 56–63. https://doi.org/10.1038/clpt.2008.177.

123. Blount, M.A., Beasley, A., Zoraghi, R., Sekhar, K.R., Bessay, E.P., Francis, S.H., and Corbin, J.D. (2004). Binding of tritiated sildenafil, tadalafil, or vardenafil to the phosphodiesterase-5 catalytic site displays potency, specificity, heterogeneity, and cGMP stimulation. Mol. Pharmacol. *66*, 144–152. https://doi.org/10.1124/mol.66.1.144.

124. Preston, G., Jacob, N., Elsharkawi, I., Morava, E., and Kozicz, T. (2025). Phosphodiesterase type 5 inhibition as a therapeutic strategy in primary mitochondrial disease: Evidence from patient fibroblasts and clinical observations. Mol. Genet. Metab. *146*, 109197. https://doi.org/10.1016/j.ymgme.2025.109197.

125. Perez-Riverol, Y., Bai, J., Bandla, C., García-Seisdedos, D., Hewapathirana, S., Kamatchinathan, S., Kundu, D.J., Prakash, A., Frericks-Zipper, A., Eisenacher, M., et al. (2022). The PRIDE database resources in 2022: a hub for mass spectrometry-based proteomics evidences. Nucleic Acids Res. *50*, D543–D552. https://doi.org/10.1093/nar/gkab1038.

126. Pantazis, C.B., Yang, A., Lara, E., McDonough, J.A., Blauwendraat, C., Peng, L., Oguro, H., Kanaujiya, J., Zou, J., Sebesta, D., et al. (2022). A reference human induced pluripotent stem cell line for large-scale collaborative studies. Cell Stem Cell *29*, 1685–1702.e22. https://doi.org/10.1016/j.stem.2022.11.004.

127. Lee, J.H., Park, I.H., Gao, Y., Li, J.B., Li, Z., Daley, G.Q., Zhang, K., and Church, G.M. (2009). A robust approach to identifying tissue-specific gene expression regulatory variants using personalized human induced pluripotent stem cells. PLoS Genet. *5*, e1000718. https://doi.org/10.1371/journal.pgen.1000718.

128. Wang, X., Sterr, M., Burtscher, I., Chen, S., Hieronimus, A., Machicao, F., Staiger, H., Häring, H.U., Lederer, G., Meitinger, T., et al. (2018). Genome-wide analysis of PDX1 target genes in human pancreatic progenitors. Mol. Metab. *9*, 57–68. https://doi.org/10.1016/j.molmet.2018.01.011.

129. Rössler, U., Hennig, A.F., Stelzer, N., Bose, S., Kopp, J., Søe, K., Cyganek, L., Zifarelli, G., Ali, S., von der Hagen, M., et al. (2021). Efficient generation of osteoclasts from human induced pluripotent stem cells and functional investigations of lethal CLCN7-related osteopetrosis. J. Bone Miner. Res. *36*, 1621–1635. https://doi.org/10.1002/jbmr.4322.

130. Binder, S., Ramachandran, H., Hildebrandt, B., Dobner, J., and Rossi, A. (2024). Prime-Editing of human ACTB in induced pluripotent stem cells to model human ACTB Loss-of-Function diseases and compensatory mechanisms. Stem Cell Res. *75*, 103304. https://doi.org/10.1016/j.scr.2024.103304.

131. Yu, J., Vodyanik, M.A., Smuga-Otto, K., Antosiewicz-Bourget, J., Frane, J.L., Tian, S., Nie, J., Jonsdottir, G.A., Ruotti, V., Stewart, R., et al. (2007). Induced pluripotent stem cell lines derived from human somatic cells. Science *318*, 1917–1920. https://doi.org/10.1126/science.1151526.

132. Kruse, S.E., Watt, W.C., Marcinek, D.J., Kapur, R.P., Schenkman, K.A., and Palmiter, R.D. (2008). Mice with mitochondrial complex I deficiency develop a fatal encephalomyopathy. Cell Metab. *7*, 312–320. https://doi.org/10.1016/j.cmet.2008.02.004.

133. Reinhardt, P., Glatza, M., Hemmer, K., Tsytsyura, Y., Thiel, C.S., Höing, S., Moritz, S., Parga, J.A., Wagner, L., Bruder, J.M., et al. (2013). Derivation and expansion using only small molecules of human neural progenitors for neurodegenerative disease modeling. PLoS One *8*, e59252. https://doi.org/10.1371/journal.pone.0059252.

134. Velasco, S., Kedaigle, A.J., Simmons, S.K., Nash, A., Rocha, M., Quadrato, G., Paulsen, B., Nguyen, L., Adiconis, X., Regev, A., et al. (2019). Individual brain organoids reproducibly form cell diversity of the human cerebral cortex. Nature *570*, 523–527. https://doi.org/10.1038/s41586-019-1289-x.

135. Spinazzi, M., Casarin, A., Pertegato, V., Salviati, L., and Angelini, C. (2012). Assessment of mitochondrial respiratory chain enzymatic activities on tissues and cultured cells. Nat. Protoc. *7*, 1235–1246. https://doi.org/10.1038/nprot.2012.058.

136. Pfaffl, M.W. (2001). A new mathematical model for relative quantification in real-time RT-PCR. Nucleic Acids Res. *29*, e45. https://doi.org/10.1093/nar/29.9.e45.

137. Love, M.I., Huber, W., and Anders, S. (2014). Moderated estimation of fold change and dispersion for RNA-seq data with DESeq2. Genome Biol. *15*, 550. https://doi.org/10.1186/s13059-014-0550-8.

138. Yoon, S.J., Elahi, L.S., Paşca, A.M., Marton, R.M., Gordon, A., Revah, O., Miura, Y., Walczak, E.M., Holdgate, G.M., Fan, H.C., et al. (2019). Reliability of human cortical organoid generation. Nat. Methods *16*, 75–78. https://doi.org/10.1038/s41592-018-0255-0.

139. Hao, Y., Stuart, T., Kowalski, M.H., Choudhary, S., Hoffman, P., Hartman, A., Srivastava, A., Molla, G., Madad, S., Fernandez-Granda, C., et al. (2024). Dictionary learning for integrative, multimodal and scalable single-cell analysis. Nat. Biotechnol. *42*, 293–304. https://doi.org/10.1038/s41587-023-01767-y.

140. Hafemeister, C., and Satija, R. (2019). Normalization and variance stabilization of single-cell RNA-seq data using regularized negative binomial regression. Genome Biol. *20*, 296. https://doi.org/10.1186/s13059-019-1874-1.

141. Rybak-Wolf, A., Wyler, E., Pentimalli, T.M., Legnini, I., Oliveras Martinez, A., Glažar, P., Loewa, A., Kim, S.J., Kaufer, B.B., Woehler, A., et al. (2023). Modelling viral encephalitis caused by herpes simplex virus 1 infection in cerebral organoids. Nat. Microbiol. *8*, 1252–1266. https://doi.org/10.1038/s41564-023-01405-y.

142. Aibar, S., González-Blas, C.B., Moerman, T., Huynh-Thu, V.A., Imrichova, H., Hulselmans, G., Rambow, F., Marine, J.C., Geurts, P., Aerts, J., et al. (2017). SCENIC: single-cell regulatory network inference and clustering. Nat. Methods *14*, 1083–1086. https://doi.org/10.1038/nmeth.4463.

143. Liberzon, A., Birger, C., Thorvaldsdóttir, H., Ghandi, M., Mesirov, J.P., and Tamayo, P. (2015). The Molecular Signatures Database (MSigDB) hallmark gene set collection. Cell Syst. *1*, 417–425. https://doi.org/10.1016/j.cels.2015.12.004.

144. Petersilie, L., Kafitz, K.W., Neu, L.A., Heiduschka, S., Le, S., Prigione, A., and Rose, C.R. (2024). Protocol for the generation of cultured cortical brain organoid slices. Star Protoc. *5*, 103212. https://doi.org/10.1016/j.xpro.2024.103212.

145. Xia, W., Veeragandham, P., Cao, Y., Xu, Y., Rhyne, T.E., Qian, J., Hung, C.W., Zhao, P., Jones, Y., Gao, H., et al. (2024). Obesity causes mitochondrial fragmentation and dysfunction in white adipocytes due to RalA activation. Nat. Metab. *6*, 273–289. https://doi.org/10.1038/s42255-024-00978-0.

146. Picardi, E., and Pesole, G. (2012). Mitochondrial genomes gleaned from human whole-exome sequencing. Nat. Methods *9*, 523–524. https://doi.org/10.1038/nmeth.2029.

147. Rubino, F., Piredda, R., Calabrese, F.M., Simone, D., Lang, M., Calabrese, C., Petruzzella, V., Tommaseo-Ponzetta, M., Gasparre, G., and Attimonelli, M. (2012). HmtDB, a genomic resource for mitochondrion-based human variability studies. Nucleic Acids Res. *40*, D1150–D1159. https://doi.org/10.1093/nar/gkr1086.

148. Robinson, J.T., Thorvaldsdóttir, H., Winckler, W., Guttman, M., Lander, E.S., Getz, G., and Mesirov, J.P. (2011). Integrative genomics viewer. Nat. Biotechnol. *29*, 24–26. https://doi.org/10.1038/nbt.1754.

149. Krasemann, S., Haferkamp, U., Pfefferle, S., Woo, M.S., Heinrich, F., Schweizer, M., Appelt-Menzel, A., Cubukova, A., Barenberg, J., Leu, J., et al. (2022). The blood-brain barrier is dysregulated in COVID-19 and serves as a CNS entry route for SARS-CoV-2. Stem Cell Rep. *17*, 307–320. https://doi.org/10.1016/j.stemcr.2021.12.011.

150. Haferkamp, U., Hartmann, C., Abid, C.L., Brachner, A., Höchner, A., Gerhartl, A., Harwardt, B., Leckzik, S., Leu, J., Metzger, M., et al. (2023). Human isogenic cells of the neurovascular unit exert transcriptomic cell type-specific effects on a blood-brain barrier in vitro model of late-onset Alzheimer disease. Fluids Barriers CNS *20*, 78. https://doi.org/10.1186/s12987-023-00471-y.

151. Appelt-Menzel, A., Cubukova, A., Günther, K., Edenhofer, F., Piontek, J., Krause, G., Stüber, T., Walles, H., Neuhaus, W., and Metzger, M. (2017). Establishment of a Human Blood-Brain Barrier Co-culture Model Mimicking the Neurovascular Unit Using Induced Pluri- and Multipotent Stem Cells. Stem Cell Rep. *8*, 894–906. https://doi.org/10.1016/j.stemcr.2017.02.021.

152. Lippmann, E.S., Al-Ahmad, A., Azarin, S.M., Palecek, S.P., and Shusta, E.V. (2014). A retinoic acid-enhanced, multicellular human blood-brain barrier model derived from stem cell sources. Sci. Rep. *4*, 4160. https://doi.org/10.1038/srep04160.

153. Kleinsorge, M., and Cyganek, L. (2020). Subtype-Directed Differentiation of Human iPSCs into Atrial and Ventricular Cardiomyocytes. Star Protoc. *1*, 100026. https://doi.org/10.1016/j.xpro.2020.100026.

154. Cyganek, L., Tiburcy, M., Sekeres, K., Gerstenberg, K., Bohnenberger, H., Lenz, C., Henze, S., Stauske, M., Salinas, G., Zimmermann, W.H., et al. (2018). Deep phenotyping of human induced pluripotent stem cell-derived atrial and ventricular cardiomyocytes. JCI Insight *3*, e99941. https://doi.org/10.1172/jci.insight.99941.

155. Pavez-Giani, M.G., Sánchez-Aguilera, P.I., Bomer, N., Miyamoto, S., Booij, H.G., Giraldo, P., Oberdorf-Maass, S.U., Nijholt, K.T., Yurista, S.R., Milting, H., et al. (2021). ATPase Inhibitory Factor-1 Disrupts Mitochondrial Ca^{2+} Handling and Promotes Pathological Cardiac Hypertrophy through CaMKIIδ. Int. J. Mol. Sci. *22*, 4427. https://doi.org/10.3390/ijms22094427.

156. Bertram, R., Gram Pedersen, M., Luciani, D.S., and Sherman, A. (2006). A simplified model for mitochondrial ATP production. J. Theor. Biol. *243*, 575–586. https://doi.org/10.1016/j.jtbi.2006.07.019.

157. Magnus, G., and Keizer, J. (1998). Model of beta-cell mitochondrial calcium handling and electrical activity. II. Mitochondrial variables. Am. J. Physiol. *274*, C1174–C1184. https://doi.org/10.1152/ajpcell.1998.274.4.C1174.

158. Fall, C.P., and Keizer, J.E. (2001). Mitochondrial modulation of intracellular Ca(2+) signaling. J. Theor. Biol. *210*, 151–165. https://doi.org/10.1006/jtbi.2000.2292.

159. Cortassa, S., Aon, M.A., Marbán, E., Winslow, R.L., and O'Rourke, B. (2003). An integrated model of cardiac mitochondrial energy metabolism and calcium dynamics. Biophys. J. *84*, 2734–2755. https://doi.org/10.1016/S0006-3495(03)75079-6.

160. Tran Van Nhieu, G., Kai Liu, B., Zhang, J., Pierre, F., Prigent, S., Sansonetti, P., Erneux, C., Kuk Kim, J., Suh, P.G., Dupont, G., et al. (2013). Actin-based confinement of calcium responses during Shigella invasion. Nat. Commun. *4*, 1567. https://doi.org/10.1038/ncomms2561.

161. Contreras, L., Gomez-Puertas, P., Iijima, M., Kobayashi, K., Saheki, T., and Satrústegui, J. (2007). Ca2+ Activation kinetics of the two aspartate-glutamate mitochondrial carriers, aralar and citrin: role in the heart malate-aspartate NADH shuttle. J. Biol. Chem. *282*, 7098–7106. https://doi.org/10.1074/jbc.M610491200.

162. Lytton, J., Westlin, M., Burk, S.E., Shull, G.E., and MacLennan, D.H. (1992). Functional comparisons between isoforms of the sarcoplasmic or endoplasmic reticulum family of calcium pumps. J. Biol. Chem. *267*, 14483–14489. https://doi.org/10.1016/S0021-9258(19)49738-X.

163. Maravall, M., Mainen, Z.F., Sabatini, B.L., and Svoboda, K. (2000). Estimating intracellular calcium concentrations and buffering without wavelength ratioing. Biophys. J. *78*, 2655–2667. https://doi.org/10.1016/S0006-3495(00)76809-3.

164. Csordás, G., Golenár, T., Seifert, E.L., Kamer, K.J., Sancak, Y., Perocchi, F., Moffat, C., Weaver, D., Perez, S.F., Bogorad, R., et al. (2013). MICU1 controls both the threshold and cooperative activation of the mitochondrial Ca^{2+} uniporter. Cell Metab. *17*, 976–987. https://doi.org/10.1016/j.cmet.2013.04.020.

165. Jansen, M.J.W. (1999). Analysis of variance designs for model output. Comput. Phys. Commun. *117*, 35–43. https://doi.org/10.1016/S0010-4655(98)00154-4.

166. Saltelli, A., Annoni, P., Azzini, I., Campolongo, F., Ratto, M., and Tarantola, S. (2010). Variance based sensitivity analysis of model output. Design and estimator for the total sensitivity index. Comput. Phys. Commun. *181*, 259–270. https://doi.org/10.1016/j.cpc.2009.09.018.

167. Sobol′, I.M. (2001). Global sensitivity indices for nonlinear mathematical models and their Monte Carlo estimates. Math. Comput. Simul. *55*, 271–280. https://doi.org/10.1016/S0378-4754(00)00270-6.

STAR★METHODS

KEY RESOURCES TABLE

REAGENT or RESOURCE	SOURCE	IDENTIFIER
Antibodies		
Purified anti-Pax-6 antibody, rabbit polyclonal IgG	BioLegend	Cat#901301; RRID: AB_2565003
Anti-β-Tubulin III antibody, mouse monoclonal, clone 2G10 (TUJ1)	Sigma-Aldrich	Cat#T8578; RRID: AB_1841228
PRKG1 polyclonal antibody, rabbit polyclonal IgG	Proteintech	Cat#21646-1-AP; RRID: AB_2878897
Anti-Nestin antibody, mouse monoclonal IgG1, clone 10C2	Merck/ Sigma-Aldrich	Cat#MAB5326; RRID: AB_2251134
Occludin Antibody, mouse monoclonal IgG1, cloneOC-3F10	Invitrogen	Cat#33-1500; RRID: AB_2533101
ZO-1 antibody, rabbit polyclonal IgG (TJP1)	Proteintech	Cat#21773-1-AP; RRID: AB_10733242
Cleaved Caspase-3 (Asp175) antibody, rabbit polyclonal	Cell Signaling Technology	Cat#9661; RRID: AB_2341188
Anti-Iba1 antibody, mouse monoclonal IgG1, cloneEPR16589	Abcam	Cat#Ab283319; RRID: AB_2924797
ATP6 antibody, rabbit polyclonal IgG	Immunological Science	Cat#AB-83828
Anti-GAPDH antibody, mouse monoclonal IgG1, clone6C5	Abcam	Cat#Ab8245; RRID: AB_2107448
Anti-β-actin antibody, mouse monoclonal IgG1	Abcam	Cat#ab8226; RRID: AB_30637
PRKG1 antibody, rabbit polyclonal IgG	Cell Signaling Technology	Cat#3248; RRID: AB_2067450
mTOR-Ser2448 antibody, rabbit polyclonal	Cell Signaling Technology	Cat#2971; RRID: AB_330970
Phospho-AMPKa-Thr174 antibody, rabbit monoclonal	Cell Signaling Technology	Cat#2535; RRID: AB_331250
Phospho-PGC1a-Ser571 antibody, rabbit polyclonal IgG	Biotechne	Cat#AF6650; RRID: AB_10890391
Phospho-4EBP-1 antibody, rabbit monoclonal IgG	Cell Signaling Technology	Cat#2855; RRID: AB_560835
PGC1a antibody, rabbit polyclonalIgG	Novus Bio	Cat#NBP1-04676; RRID: AB_1522118
AMPKa antibody, rabbit polyclonal IgG	Cell Signaling Technology	Cat#2532; RRID: AB_330331
4EBP-1 antibody, rabbit monoclonal	Cell Signaling Technology	Cat#9644; RRID: AB_2097841
Anti-GAPDH antibody, rabbit monoclonal IgG	Abcam	Cat#ab181602; RRID: AB_2630358
Donkey anti-Rabbit IgG (H+L) Highly Cross-Adsorbed Secondary Antibody, Alexa Fluor488	Invitrogen	Cat#A-21206; RRID: AB_2535792
Donkey anti-mouse IgG Antibody, Cy3 conjugate	Millipore	Cat#AP192C; RRID:AB_92642
Donkey anti-rabbit IgG (H+L) Highly Cross-Absorbed Secondary Antibody, Alexa Fluor647	Invitrogen	Cat# A32795; RRID:AB_2762835
Goat anti-Mouse IgG (H+L) Cross-Adsorbed Secondary Antibody, Alexa Fluor633	Invitrogen	Cat#A-21050
Goat Anti-Mouse IgG (H + L)-HRP Conjugate	BioRad	Cat#1706516; RRID: AB_2921252
Anti-Rabbit IgG (H+L), HRP Conjugate	Promega	Cat#W4018
Anti-Mitofilin antibody (MIC60), monoclonal IgG, clone EPR8749	Abcam	Cat#Ab137057; RRID: AB_3676556

(*Continued on next page*)

Continued

REAGENT or RESOURCE	SOURCE	IDENTIFIER
Anti-ACTN2 antibody (alpha-actinin), mouse monoclonal, clone EA-53	Sigma-Aldrich	Cat#A7811; RRID: AB_476766
Anti-ATP5B antibody, rabbit polyclonal	Sigma-Aldrich	Cat#HPA001528; RRID: AB_1078242
NDUFA9 antibody, mouse monoclonal IgG, clone 20C11B11B11	Invitrogen	Cat#459100; RRID: AB_10376187
Anti-SDHB, mouse monoclonal IgG2a, clone 21A11EA7	Abcam	Cat#ab14714; RRID: AB_301432
Anti-UQCRSF1/RISP antibody, mouse monoclonal IgG2b, clone 5A5	Abcam	Cat#ab14746; RRID: AB_301445
Doublecortin antibody (DCX), rabbit	Cell Signaling Technology	Cat#4604; RRID: AB_561007
Chemicals, peptides, and recombinant proteins		
StemMACSiPS-Brew XF, human	Miltenyi Biotec	Cat#130-104-368
mTeSRPlus	STEMCELL Technologies	Cat#100-0276
KnockOut-DMEM	Gibco	Cat#10829-018
KnockOutserum replacement (SR)	Gibco	Cat#10828-028
DMEM/F/12	Gibco	Cat#31330038
DMEM glucose-free	Gibco	Cat#11966025
Glasgow-MEM	Gibco	Cat#11710035
Neurobasal A-Medium glucose-free	Gibco	Cat#A2477501
Neurobasal	Gibco	Cat#21103-049
Non-essential amino acids (MEM-NEAA) 100X	Gibco	Cat#11140-050
Sodium pyruvate	Gibco	Cat#11360070
B-27 with Vitamin A (50×)	Gibco	Cat#17504044
B-27 without Vitamin A (50×)	Gibco	Cat#12587010
N2 Supplement (100×)	Gibco	Cat#17502-048
DPBS, no calcium, no magnesium	Gibco	Cat#14190144
Accutase	Thermo Fisher Scientific; Sigma-Aldrich	Cat#A1110501; Cat#A6964-100ML
UltraPure0.5 M EDTA	Invitrogen	Cat#11568896
ROCK inhibitor Y-27632	Enzo Life Sciences	Cat#ALX-270-333-M005
MycoZap Plus-CL	Lonza	Cat#VZA-2012
Penicillin/Streptomycin	Gibco	Cat#15140122
GlutaMAX	Gibco	Cat#35050061
L-glutamine	Gibco	Cat#25030081
FBS	Gibco	Cat#10270106
Matrigel, Growth Factor Reduced	Corning	Cat#356231
GeltrexReduced-Growth Factor Basement-Membrane Matrix, LDEV-free, stem-cell qualified	Gibco	Cat#A1413302
Chemically Defined Lipid Concentrate	Gibco	Cat#11905031
Anti-Adherence Rinsing Solution	STEMCELL Technologies	Cat#07010
Purmorphamin	Sigma-Aldrich; Miltenyi Biotec	Cat#540220; Cat#130-104-465
CHIR 99021	Sigma-Aldrich	Cat#SML1046
Dorsomorphin	Sigma-Aldrich	Cat#P5499
SB431542	Miltenyi Biotec	Cat#130-105-336
GDNF	R&D System	Cat#212-GD-010
BDNF	MACS Miltenyi	Cat#130-096-811
EGF	R&D System	Cat#236-EG-200
FGF2	R&D System	Cat#3718-FB-100

(*Continued on next page*)

Continued

REAGENT or RESOURCE	SOURCE	IDENTIFIER
Dibutyryl-cAMP	StemCell Technologies	Cat#73886
Recombinant Human NT-3	Peprotech / Biozol	Cat#450-03
FGF8-a	R&D systems	Cat#4745-F8-050
TGF-beta 3	STEMCELL Technologies	Cat#78156
(+)-sodium L-ascorbate (Vitamin C)	Sigma-Aldrich	Cat#A4034
cis-4,7,10,13,16,19-Docosahexaenoic acid methyl ester (DHA)	Sigma-Aldrich	Cat#D2534
WNT antagonist IWR1	EMD Millipore Corp	Cat#681669
Heparin	Merck	Cat#375095
ß-mercaptoethanol	Gibco	Cat#31350010
DMSO	Sigma-Aldrich	Cat#D2650-100ML
SuperSignal West Pico PLUS Chemiluminescent Substrate	Thermo Fisher Scientific	Cat#34580
16% Paraformaldehyde (PFA)	Thermo Fisher Scientific	Cat#28906
Hoechst 33342	Invitrogen	Cat#H3570
Donkey serum (DNS)	Merck Millipore	Cat#S30
Triton X-100	Sigma-Aldrich	Cat#93443; Cat#93426
Tween 20	Sigma-Aldrich	Cat#P1504
abberior STAR 635 (STAR RED)	Abberior	Cat#ST635-1002
DAPI	Sigma-Aldrich	Cat#D9542
MitoProbeTMRM Assay Kit for Flow Cytometry	Invitrogen	Cat#M20036
Tetramethylrhodamine methyl ester (TMRM)	Invitrogen	Cat#T668
Incucyte dye red	Sartorius	Cat#4717
Calcein AM Viability Dye	Invitrogen	Cat#C1430
MitoSpyOrange	BioLegend	Cat#424803
d_3-Sildenafil	CDN isotopes	Cat#D-6366
HpaII	NEB	Cat#R0171
StuI	NEB	Cat#R0187
XbaI	NEB	Cat#R0145
FCCP	Biozol	Cat#SEL-S8276
Antimycin A	Sigma-Aldrich	Cat#A8674
Oligomycin	Sigma-Aldrich	Cat#O4876-5MG
CCCP	Sigma-Aldrich	Cat#555602
Propidium iodide	Invitrogen	Cat#P1304MP
Sildenafil citrate	Sigma-Aldrich	Cat#SML3033
KT5823	Biomol	Cat#LKT-K7602.100
8-Br-cGMP	Sigma-Aldrich	Cat#203820
Sildenafil	Selleckchem	Cat#S468402 and S468403
Mowiol with 0.1% 1,4-Diazabicyclo[2.2.2]octan (DABCO)	Carl Roth	Cat#0713.1
LB Agar	Sigma-Aldrich	Cat#L2897
SuperFrost Plus glass slides	VWR	Cat#631-0447
Pro-Long Glass Antifade Mountant	Invitrogen	Cat#P36984
oligo d(T)18 primers	Thermo Fisher Scientific	Cat#SO132
dNTP mix	Thermo Fisher Scientific	Cat#10319879
Rnase OUT Recombinant Ribonuclease Inhibitor	Invitrogen	Cat#10777-019
M-MLV Reverse Transcriptase (200 U/µL)	Invitrogen	Cat#28025021

(*Continued on next page*)

Continued

REAGENT or RESOURCE	SOURCE	IDENTIFIER
Human Endothelial-SFM	Gibco	Cat#11111044
hFGF	Peprotech	Cat#100-18B
Retinoic acid	STEMCELL Technologies	Cat#72262
Collagen IV	Sigma-Aldrich	Cat#c5533-5MG
Fibronectin	Gibco/Thermo Fisher Scientific	Cat#33016015
Transwell membranes	Greiner	Cat#662641
Sodium fluorescein	Sigma-Aldrich	Cat#F6377-100G
Diazepam	Sigma-Aldrich	Cat#D0899-100MG
Atenolol	Sigma-Aldrich	Cat#A7655-1G
LysC	Roche	Cat#11420429001
Low melting temperature agarose	Gibco	Cat#5517UB
Hank's Balanced Salt Solution (HBSS)	Sigma-Aldrich	Cat#H9394
Oregon Green 488 BAPTA-1 AM	Invitrogen	Cat#O6807
Deoxy-D-glucose	Apollo Scientific; Sigma-Aldrich	Cat#OR3900T; Cat#D8375-1g
RNase H	Epicentre/ LGC Biosearch Technologies	Cat#E0038-5D1
Acetonitrile	Biosolve, ULC/MS-CC/SFC	Cat#001204101BS
Fura-2 AM	Thermo Fisher Scientific	Cat#F1221
Thapsigargin	Thermo Fisher Scientific	Cat#T7459
Trypsin	Sigma-Aldrich/ Merck	Cat#T4799
$CaCl_2$	Sigma-Aldrich/ Merck	Cat#C7902
Altrenogest	MSD Animal Health	Regumate
PGF2-alpha ($PGF_{2\alpha}$)	Fatro S.P.A.	Prosolvin®
Critical commercial assays		
CellTiter-GloLuminescent Cell Viability assay	Promega	Cat#G7571
Rnase-Free Dnase Set (50) (250)	Qiagen	Cat#79254
RNeasy Mini Kit (50)	Qiagen	Cat#74104
Nucleo-Spin Tissue kit	Macherey-Nagel	Cat#740952.50
SYBR Green PCR Master Mix	Applied Biosystems	Cat#4364344
Bicinchoninic Acid (BCA) protein assay kit	Thermo Fisher Scientific	Cat#23252
NucleoSpin RNA Plus kit	Macherey-Nagel	Cat#740984.50
RNA Cleanup XP beads	Agencourt/Beckman coulter	Cat#A66514
TURBO DNase rigorous treatment	Invitrogen	Cat#AM1907
TruSeq Stranded Total LT Sample Prep Kit	Illumina	RS-122-2201, RS-122-2202
Chromium Single Cell 3′ (vNext) Reagent Kit	10X Genomics	Cat#PN-1000268 (16 rxns) or PN-1000269 (4 rxns)
ViaLight Plus Kit	Lonza	Cat#LT07-221
CyQUANT Cell Proliferation Assay	Invitrogen	Cat#C7026
jetPRIME transfection	Polyplus	Cat#101000027
Deposited data		
Bulk RNAses NPCs dataset	This paper	https://www.ncbi.nlm.nih.gov/geo/query/acc.cgi?acc=GSE292178; GEO: GSE292178
Bulk RNAseq organoids dataset	This paper	https://www.ncbi.nlm.nih.gov/bioproject/?term=PRJNA1248577SRA; BioProject ID: PRJNA1248577
Codes	This paper	https://github.com/tpentim/Leigh_Sildenafil_Organoids
snRNAseq organoids dataset	This paper	https://www.ncbi.nlm.nih.gov/geo/query/acc.cgi?acc=GSE293573; GEO: GSE293573

(*Continued on next page*)

Continued

REAGENT or RESOURCE	SOURCE	IDENTIFIER
Proteomics NPCs dataset	This paper	https://www.ebi.ac.uk/pride/archive/projects/PXD059519; ProteomeXchange: PXD059519
Metabolomics NPCs dataset	This paper	https://massive.ucsd.edu/ProteoSAFe/dataset.jsp?task=ee42368caf914a948db5983afe2460e4; MassIVE: MSV000097182
Experimental models: Cell lines		
Human iPSCs: HMGUi001-A	Helmholtz Zentrum München (HMGU)	PMID: 29396371
Human iPSCs: HHUUKDi009-A	Heinrich-Heine-Universität Düsseldorf (HHUUKD)	PMID: 28132834
Human iPSCs: CRMi003-A	RUCDR Infinite Biologics	PMID: 36459969
Human iPSCs: BIHi269-B	Berlin Institute of Health (BIH)	PMID: 36669241
Human iPSCs: HVRDi004-B	Synthego	PMID: 19911041
Human iPSCs: IUFi004-A	Cell Applications	PMID: 38217996
Human iPSCs: BIHi266-A	Berlin Institute of Health (BIH)	PMID: 36669241
Human iPSCs: WISCi004-B	WiCell	PMID: 18029452
Human iPSCs: UMGi014-C	University Medical Center Goettingen (UMG)	PMID: 33905594
Human iPSCs: HHUi001-A	Universitätsklinikum Düsseldorf (HHU)	PMID: 28132834
Human iPSCs: HHUi002-A	Universitätsklinikum Düsseldorf (HHU)	PMID: 28132834
Human iPSCs: HHUi003-C	Universitätsklinikum Düsseldorf (HHU)	PMID: 36137325
Human iPSCs: MDCi008-A	Max Delbrück Center Berlin Buch (MDC)	PMID: 35279592
Human iPSCs: MDCi009-A	Max Delbrück Center Berlin Buch (MDC)	PMID: 35279592
Human iPSCs: MDCi010-A	Max Delbrück Center Berlin Buch (MDC)	PMID: 35279592
Human iPSCs: BIHi267-B	Berlin Institute of Health (BIH)	PMID: 36669241
Human iPSCs: HMGUi001-A-64	Max Delbrück Center Berlin Buch (MDC)	PMID: 33771987
Human iPSCs: HVRDi004-B-6	Max Delbrück Center Berlin Buch (MDC)	PMID: 36741056
Human iPSCs: HVRDi004-B-7	Max Delbrück Center Berlin Buch (MDC)	PMID: 36741056
Experimental models: Organisms/strains		
Germline *Ndufs4* KO, C57/BL6/J background	University of Washington	PMID: 20534480
SURF1 KO pig, Large White background	Avantea	PMID: 29601977
Oligonucleotides		
See Table S5 for oligonucleotides	N/A	N/A
Software and algorithms		
CellProfiler	https://cellprofiler.org/	v.4.2.5.; RRID: SCR_007358
GraphPad Prism	GraphPad Software	v.5.01; RRID: SCR_007358
Adobe Illustrator	Adobe	v.29.6; RRID: SCR_010279
Cell Ranger	10x Genomics	v.7.10; RRID: SCR_017344
Ultivo triple-quadrupole mass spectrometer	Agilent Technologies; https://www.agilent.com/en/product/liquid-chromatography-mass-spectrometry-lc-ms/lc-ms-instruments/ultivo-lcms	N/A
MassHunter Software	Agilent Technologies	N/A; RRID: SCR_015040
MToolBox	https://github.com/mitoNGS/MToolBox[126]	v.1; RRID: SCR_012112
ImageJ	Fiji[127]; http://imagej.org	v1.53q and v1.54g; RRID: SCR_003070
IGV viewer	IGV; https://igv.org	v2.163; RRID: SCR_011793
CELLCYTE Studio	Cytena	N/A; RRID: SCR_021911
ZEN Microscopy Software	Zeiss	v.3.2RRID: SCR_013672
ND-1000 software	Thermo Fisher Scientific	v3.8.1; RRID: SCR_016517

(*Continued on next page*)

Continued

REAGENT or RESOURCE	SOURCE	IDENTIFIER
CFX96 software	Bio-Rad	N/A; RRID: SCR_018064
Image Lab software	Bio-Rad	v.6.1; RRID: SCR_014210
GeneMapper ID	Applied Biosystems	v.3.2.1; RRID: SCR_021103
Xcalibur software	Thermo Fischer Scientific	N/A; RRID: SCR_014593
TraceFinder 5.1 software	Thermo Fischer Scientific	N/A; RRID: SCR_023045
Columbus software	Revvity	v.2.9.0
FlowJo software	FlowJo	v.7.6; RRID: SCR_008520
OriginPro Software	OriginLab Corporation	N/A; RRID: SCR_014212
nfcore/rnaseq	https://zenodo.org/records/7998767	v.3.12.0
Trim Galore!	Babraham Bioinformatics; https://zenodo.org/records/7598955	v.0.6.10; RRID: SCR_011847
STAR aligner	https://github.com/alexdobin/star/releases	v. 2.7.10a; RRID: SCR_004463
Salmon	https://github.com/COMBINE-lab/salmon/releases	v.1.10.1; RRID: SCR_017036
DESeq2 package	https://github.com/thelovelab/DESeq2	v. 1.40.2 and v.7.5.1; RRID: SCR_015687
ClusterProfiler	DOI: 10.18129/B9.bioc.clusterProfiler	v4.8.3 and v4.10.0; RRID: SCR_016884
org.Hs.eg.db	DOI: 10.18129/B9.bioc.org.Hs.eg.db	v.3.18.0; RRID: SCR_024739
ggplot2	https://github.com/tidyverse/ggplot2/releases/tag/v3.5.1	v.3.5.1; RRID: SCR_014601
R	The R Project for Statistical Computing	v. 4.4.1; RRID: SCR_001905
Seurat	https://satijalab.org/seurat/ version: https://github.com/satijalab/seurat/releases	v. 5.1.0; RRID: SCR_016341
AUCell package	DOI: 10.18129/B9.bioc.AUCell	v. 1.26.0; RRID: SCR_021327
MsigDB package	https://data.broadinstitute.org/gsea-msigdb/msigdb/release/7.5.1/	v 7.5.1; RRID: SCR_022870
dplyr	https://cran.r-project.org/web/packages/dplyr/index.html	v. 1.1.4; RRID: SCR_016708
Dia-NN	https://github.com/vdemichev/DiaNN/releases/tag/1.8.1	v1.8.1; RRID: SCR_022865
OmicsNet platform	https://www.omicsnet.ca/	v.2.0
CytoNCA plugin	Cytoscape	v.3.10.2
KEGG database	GenomeNet	Release 112.0; RRID: SCR_001120
Vevo 2700 analysis software	FUJIFILM VisualSonics	v.1.5; RRID: SCR_015816
NIS-Elements Advanced Research	Nikon	v.3.2; RRID: SCR_027181
EZ-C1 Silver	Nikon	v.3.91
MATLAB 2023b	MathWorks; https://de.mathworks.com/products/new_products/release2023b.html	RRID:SCR_001622
IncuCyte Live-Cell Analysis System	Sartorius	RRID: SCR_023147
Other		
CytoSmart Cell Counter	Greiner Bio-One	Cat#6749
Orbital Shaker Heidolph Unimax 1010	Heidolph	Cat#543-12310-00
Operetta CLS	Revvity	Cat#HH16000020; RRID: SCR_018810
96-well Cell Culture Microplate, PS, F-Bottom, black TC, μCLEAR, 96-well black, clear bottom	Greiner Bio-One	Cat#655090
96-well Cell Culture Microplate, SCREENSTAR	Greiner Bio-One	Cat#655866
μ-Plate 96 Well Square	Ibidi	Cat#89626
DMS1000 microscope	Leica Microsystems	DMS1000
Eclipse Ts2	Nikon	Inverted Microscope; RRID: SCR_025716

(*Continued on next page*)

Continued

REAGENT or RESOURCE	SOURCE	IDENTIFIER
ZEISS Axio Observer Apotome 3	Zeiss	ZEISS Apotome 3: Optical sectioning in widefield fluorescence microscopy
ZEISS Axio Observer 7 inverted microscope	Zeiss	Inverted Microscope; RRID:SCR_023694
Magnification changer	Zeiss	Tuelens Optovar
Wavelength switcher	Sutter Instruments	Sutter Lambda DG5
Vibratome Microm HM 650 V	Thermo Fisher Scientific	Cat#920120
Multimode plate reader	Revvity	EnSight
CELLCYTE X	Cytena	CELLCYTE X™ - Live Cell Imager And Analyzer | CYTENA; RRID: SCR_021911
INFINITY platform	Abberior Instruments	INFINITY - @abberior.rocks
Promethion	Sable Systems International	Promethion Core Metabolic and Behavioral Phenotyping Systems
Infinite M1000 Pro	TECAN	Tecan | Thermo Fisher Scientific - DE; RRID: SCR_024561
Confocal laser scanning microscope C1	Nikon Mikroskope Solutions	Nikon's Digital Eclipse C1 Microscope System Delivers High Resolution Confocal Images at Sensible Price | News | Nikon Instruments Inc.
Mastercycler X50s	Eppendorf	6311000010; RRID: SCR_027059
CFX96Real-Time System qPCR machine	Bio-Rad	CFX96 Touch Real-Time PCR Detection System | Bio-Rad; RRID: SCR_018064
ChemiDoc MP Imaging system	Bio-Rad	ChemiDoc MP Imaging System | Bio-Rad; RRID: SCR_019037
Low-attachment U-bottom 96-well plates	Corning	Cat#3474
AggreWell	STEMCELL Technologies	Cat#34815
NovaSeq 6000 system	Illumina	NovaSeq 6000 System | Powerful sequencing with scalable throughput; RRID: SCR_016387
Dionex Ultimate 3000	Thermo Fisher Scientific	UltiMate 3000 HPLC and UHPLC Systems; RRID: SCR_019840
timsTOF SCP mass spectrometer	Bruker Daltonics	timsTOF SCP | Bruker; RRID: SCR_026542
SeQuant ZIC-pHILIC	Merck	Cat#1.50462
LSR-Fortessa X-20	Becton, Dickinson	LSRFortessa™ X-20 | Benchtop Flow Cytometer
384-well black-wall, clear-bottom plates	Revvity	Cat#6007460
Multidrop liquid dispenser	Thermo Fisher Scientific	https://www.thermofisher.com/de/de/home/life-science/lab-equipment/microplate-instruments/multidrop-dispensers.html
Rotating incubator	Thermo Electron	Cytomat
Echo 550	Beckman Coulter (Labcyte)	RRID: SCR_027476
Janus MDT	Revvity	Cat#YJLM001
Victor Multiple Plate Reader Spectrophotometer	Revvity	Cat#HH35000500
Millicell-CM inserts	Merck (MilliporeSigma in the USA)	https://www.sigmaaldrich.com
Eclipse FN-1	Nikon	ECLIPSE FN1 | Upright Microscopes | Microscope Products | Nikon Instruments Inc.
Eclipse 90i Upright Microscope	Nikon	RRID: SCR_020335
FLASH 4.0 LT camera	Hamamatsu Photonics	RRID: SCR_021971
NanoDrop 2000 Spectrophotometer	Thermo Fisher Scientific	RRID: SCR_018042
Nanodrop 1000 Spectrophotometer	peQlab	RRID: SCR_016517
Aurora Ultimate column	IonOpticks,	N/A
H-ESI source probe	Thermo Fisher Scientific	N/A

(*Continued on next page*)

Continued

REAGENT or RESOURCE	SOURCE	IDENTIFIER
In-house standard library	Merck	MSMLS-1EA library
1290 Infinity II HPLC	Agilent Technologies	https://www.agilent.com/en/product/liquid-chromatography/hplc-systems/gpc-sec-solutions/1290-infinity-ii-gpc-sec-system; RRID: SCR_019375
HPLC column	Agilent Technologies	Poroshell 120 EC-C18 column
3,500 Series Genetic Analyzer	Applied Biosystems	RRID: SCR_021901
Seahorse XFe24 Analyzer	Agilent Technologies	RRID: SCR_019539
IncuCyte	Sartorius	RRID: SCR_023147
Thermal camera	Dongguan Xintai Instrument Co., Ltd,	Cat#HT-18
Chemiluminescent Western Blot imager	Azure byosystem	Aerogene 300Q; RRID: SCR_026671

EXPERIMENTAL MODEL AND STUDY PARTICIPANT DETAILS

Induced pluripotent stem cells (iPSCs)

MT-ATP6 mutant iPSC lines were previously derived from three patients with m.9185T>C variant (ATP61_1: HHUi001-A; ATP6_2: HHUi002-A; ATP6_3: HHUi003-C), one patient with m.8993T>C variant (ATP6_4: MDCi008-A), two patients with m.8993T>G variant (ATP6_5: MDCi009-A; ATP6_6: MDCi010-A), and one patient with m.9176T>G variant (ATP6_7: BIHi267-B) (Figure S10H).[27,33–35] Genotyping of the lines was carried out by Sanger sequencing (Figure S1A). *SURF1* mutant iPSC isogenic lines (SURF1_1: HMGUi001-A-64) and *NDUFS4* mutant iPSC isogenic lines (NDUFS4_1: HVRDi004-B-6; NDUFS4_2: HVRDi004-B-7) were previously derived (Figure S10H).[25,89] Among healthy control iPSCs (Figure S10H), CTRL_1, (HMGUi001-A), CTRL_2 (HHUUKDi009-A), CTRL_4 (BIHi269-B), CTRL_7 (BIHi266-A), and CTRL_9 (UMGi014-C) were previously described,[27,33,128,129] CTRL_3 (CRMi003-A)[126] was purchased from RUCDR Infinite Biologics, CTRL_5 (HVRDi004-B, PGP1)[127] was purchased from Synthego, CTRL_6 (IUFi004-A, iPS12)[130] was purchased from Cell Applications, and CTRL_8 (WISCi004-B)[131] was purchased from WiCell. We cultured all iPSC lines on Matrigel (Corning)-coated plates using StemMACS iPS-Brew XF medium, supplemented with MycoZap (Lonza). CTRL_8 and ATP6_2 iPSCs were cultured in mTeSR Plus Medium (STEMCELL Technologies) prior to BCEC differentiation. Information on sex and age of the individuals from which the iPSCs were derived is provided in Figure S10H. We cultivated all iPSCs in a humidified atmosphere of 5 % CO_2 at 37 °C and 5 % oxygen. iPSCs were split at 70-80 % confluence with 0.5 μM EDTA (Invitrogen) in 1 x PBA (Gibco). We added 10 μM ROCK inhibitor (Enzo Biochem Inc) after splitting to promote survival. Cultures were routinely monitored for mycoplasma contamination by PCR using nine primers to amplify the six most common mycoplasma strains (Table S5). The positive control and internal contro were kindly provided by Dr. Cord Uphoff (DZMS, Germany). We monitored the identity of iPSCs using STR analysis, which was performed by the Forensic Department of the University Hospital Düsseldorf (Dr. Petra Böhme); 21 microsatellite loci were amplified using PCR and tagged products were analyzed using GeneMapper ID v.3.2.1 (Applied Biosystems). The use of iPSCs in pseudoanonymized manner was approved by the local ethic committees of Charité-Universitätsmedizin Berlin (EA2/131/13 and EA2/107/14) and Heinrich Heine University Düsseldorf (Study number 2020-967_5).

Animals

Germline *Ndufs4* KO mice were obtained from the University of Washington.[132] All mice were on the C57/BL6/J background and were fed the regular diet from Harlan Teklad.[132] Sildenafil citrate treatment was initiated soon after weaning and genotyping, between day 25-30 of age. Treatment studies were carried out in 16 female mice and 14 male mice. Mouse experiments were approved by the Institutional Animal Care and Use Committee (IACUC) of Johns Hopkins University, USA (M023M236).

Domestic pigs of large white background were used to study *SURF1* KO. Male KO animals were compared to sex and age-matched WT animals. 7 *SURF1* KO male animals were treated with sildenafil citrate starting immediately after birth. On the first day after birth, pigs were fed reconstituted milk (NeoPig Rescue, Provimi, 10-12 ml every hour) via gastric tube. By the second day, WT piglets and almost all sildenafil-treated *SURF1* KO piglets began drinking milk independently from an automatic feeder connected to the incubator. At day 30 after birth, pigs were transferred to the breeding cages and gradually switched from reconstituted milk to pelleted feed. Experiments in pigs were carried out according to the ARRIVE guidelines and approved by the Local Ethics Committee of Avantea, in accordance with the Italian Law (D.Lgs 26/2014) and EU directive 2010/63/EU regulating animal experimentation and approved by relevant authorities (Ministry of Health project # 367/2022-PR).

Cell lines

Big-conductance calcium-activated potassium (BKCa) KO human U87 glioblastoma lines with stably deletion of the *KCNMA1* gene, encoding for BKCa,[80] were kindly provided by Prof. Adam Szewczyk (Nencki Institute, Warsaw). WT and BKCa KO glioblastoma (U-87 MG) cells were grown in DMEM medium (Thermo Fisher Scientific) with 10 % fetal bovine serum (FBS) (Gibco) 100 U/ml penicillin and 100 μg/ml streptomycin (Gibco) in a humidified atmosphere of 5 % CO_2 at 37 °C.[80]

Human participants

The off-label individual basis treatment with sildenafil citrate (Revatio®) in LS patients carrying *MT-ATP6* variants was registered on ClinicalTrials.gov (ID: NCT06967831). The treatment was performed as ‘‘individual basis treatment", also known as ‘‘named-patient basis (NPB) therapy’’, which refers to pre-authorization access to unauthorized medicines requested by doctors for specific patients with serious unmet needs. In this treatment, the physicians carry an individual responsibility and there is no requirement of formal approval by EMA or a local IRB. This process is governed by national legislation within each EU Member State, under Article 5(1) of Directive 2001/83/EC. Patients were of Caucasian ethnicity and included both male and female individuals (according to sex assigned at birth). Details of patient features and clinical outcomes are reported in Tables 1, S3, and S4. We obtained written informed consent to use patient material and health data from the patients and their guardians according to the Declaration of Helsinki.

METHOD DETAILS

Neural precursor cells (NPCs) and differentiated neurons

We obtained NPCs from iPSCs using our previously published protocol.[133] Briefly, we detached iPSCs from Matrigel-coated plates using Accutase (Sigma-Aldrich) and transferred the collected cells into low-attachment 6-well plates where they were kept for two days in: KnockOut-DMEM (Thermo Fisher Scientific), KnockOut-SR (Thermo Fisher Scientific), non-essential amino acids (NEAA) (Thermo Fisher Scientific), plus 1 mM pyruvate (Thermo Fisher Scientific) 2 mM L-glutamine (Thermo Fisher Scientific), 1 x MycoZap Plus-CL (Lonza) with the addition of 0.5 μM purmorphamine (PMA) (Merck Millipore), 3 μM CHIR 99021 (Cayman Chemical), 10 μM SB-431542 (Selleckchem), and 1 μM dorsomorphin (Sigma-Aldrich). From day 2 to day 4, the media was switched to: Neurobasal:DMEM/F12 (Thermo Fisher Scientific) [1:1], 0.5 x N2, 0.5 x B27 without vitamin A, 1 x MycoZap Plus-CL, with the addition of 0.5 μM purmorphamine (PMA) (Merck Millipore), 3 μM CHIR 99021 (Cayman Chemical), 10 μM SB-431542 (Selleckchem), and 1 μM dorsomorphin (Sigma-Aldrich). On day 6, we transferred the suspended cells onto Matrigel-coated well plates using: the same media without SB-431542 and dorsomorphin, but with the addition of 150 μM ascorbic acid (Sigma-Aldrich). We maintained NPCs on this media and used them for experiments between passage 7 and passage 30.

Differentiation into neuronal cultures containing dopaminergic neurons was performed as previously described.[25] Briefly, starting from NPCs at low confluence (10-30 %), we switched to media containing Neurobasal:DMEM/F12 (1:1), 0.5 x N2, 0.5 x B27 with vitamin A, 1 x MycoZap Plus-CL, with the addition of 200 mM vitamin C, 100 ng/ml FGF8 (R&D Systems) and 1 mM PMA. After 8 days, we used the media Neurobasal:DMEM/F12 (1:1), 0.5 x N2, 0.5 x B27 with vitamin A, 1 x MycoZap Plus-CL, supplemented with 200 mM vitamin C, 0.5 mM PMA, 500 mM cAMP (STEMCELL Technologies), 10 ng/mL BDNF (MACS Miltenyi), 10 ng/ml GDNF (MACS Miltenyi) and 1ng/mL TGF-beta 3 (MACS Miltenyi). After ten days, the medium was changed to Neurobasal:DMEM/F12 (1:1), 0.5 x N2, 0.5 x B27 with vitamin A, 1 x MycoZap Plus-CL, supplemented with 200 mM vitamin C, 500 mM cAMP, 10 ng/ml BDNF, 10 ng/ml GDNF, and 1 ng/ml TGF-beta 3.

Cortical brain organoids

Cortical brain organoids were generated following two protocols (Figure S7A). The first protocol was based on our modifications[62] of a previous publication.[134] Briefly, on day 0, iPSCs at 80 % confluence were seeded into low-attachment U-bottom 96-well plates (Corning) to induce neurosphere formation. iPSCs were washed with DPBS (Gibco) and detached with Accutase (Gibco) for 5 min at 37 °C. Cell pellets were resuspended in cortical differentiation medium I (CDMI) consisting of Glasgow-MEM, 20 % Knockout Serum Replacement, MEM-NEAA, sodium pyruvate, 2-mercaptoethanol and penicillin-streptomycin (all from Gibco). After cell counting, the suspension was diluted with CDMI to a final cell concentration of 90,000 cells per ml and supplemented with 20 μM ROCK inhibitor (Enzo), 5 μM TGF-β inhibitor SB431542 (Cayman Chemical Company) and 3 μM WNT antagonist IWR1 (EMD Millipore Corp). The supplemented seeding suspension was distributed to low attachment U-bottom 96-well plates by adding 100 μl per well and incubated at 37 °C and 5 % CO_2. On day 3, the sides of the 96-well plates were carefully tapped to detach dead cells, and then 100 μl of CDMI supplemented with 20 μM ROCK inhibitor, 3 μM IWR1 and 5 μM SB431542. On days 6, 9, 12 and 15, 80 μl of the supernatant medium were removed from each well and replaced with 100 μl of CDMI supplemented with 3 μM IWR1 and 5 μM SB431542 per well. On day 18, the developing organoids were transferred to 100 mm petri dishes filled with cortical differentiation medium II (CDMII) consisting of DMEM/ F12, 1 % GlutaMAX, 1 % N2 supplement, 1 % chemically defined lipid concentrate and penicillin-streptomycin (Gibco). The petri dishes were placed on an orbital shaker at 70 rpm at 37 °C and 5 % CO_2. CDMII was changed every second day. On day 35, CDMII was replaced with cortical differentiation medium III (CDMIII) that in addition contains 10 % FBS (Gibco) and heparin (Merck). CDMIII was changed every two to four days, depending on the colour of the medium. From day 70 on, organoids were kept in cortical differentiation medium IV (CDMIV) that additionally was supplemented with 1 % B27 with vitamin A.

The second protocol was based on a different publication.[63] For this, AggreWell plates (STEMCELL Technologies) were prepared by incubation with Anti-Adherence Rinsing Solution (STEMCELL Technologies) for 15 min. iPSCs were detached from the 6-well plates using Accutase as described above. The cell suspension was pelleted at 200 x g for 4 min and resuspended in iPS Brew (Miltenyi Biotec) with 10 μM ROCK inhibitor. Cells were counted with CytoSmart Cell Counter (Greiner Bio-One) and 2.75 million cells were seeded in 1.5 ml per AggreWell. AggreWell plates were centrifuged at 100 x g for 3 min and left at 37 °C and 5 % CO_2 for 24 h. On day 1, spheroids were transferred to a petri dish using a cut P1000 tip and placed on a shaker. Medium was changed to embryonic stem (ES) medium composed of KO-DMEM, 20% Knockout Serum Replacement, MEM-NEAA, sodium pyruvate, GlutaMAX, penicillin-streptomycin (all from Gibco), and MycoZAP Plus-CL (Lonza), and supplemented with 10 μM SB431542 and 2.5 μM dorsomorphin (Sigma). Until day 6, ES medium was changed daily. Neurospheres were fed with Neural Differentiation Medium (NDM) consisting of Neurobasal A medium (Gibco), GlutaMAX, penicillin-streptomycin, MycoZAP and 2 % B27 without vitamin A (Gibco). From day 6-15, medium was changed daily and supplemented with 20 ng/ml EGF (R&D Systems) and 20 ng/ml FGF2 (R&D Systems). From day 16-21, medium was changed every second day, and from day 22-45, NDM medium was supplemented with 20 ng/ml BDNF (MACS Miltenyi), 20 ng/ml NT-3 (Peprotech), 200 μM (+)-sodium L-ascorbate (Sigma-Aldrich), 50 μM dibutyryl cAMP (STEMCELL Technologies), and 10 μM DHA (Sigma Aldrich), and changed every other day. For long-term maturation after day 46, NDM medium was prepared with 2 % B27 with vitamin A, and organoids were fed according to their needs. Images of brain organoids were acquired using the Eclipse Ts2 light microscope (Nikon), and at later growth stages, when the organoids were larger, using a DMS1000 microscope (Leica). The size of the organoids was determined by area calculation using ImageJ.

Assessment of mitochondrial membrane potential (MMP)

For MMP quantification, we applied a high-content analysis (HCA)-based live-cell detection assay that we previously established.[31] Briefly, we seeded NPCs onto black-wall, clear-bottom 96-well plates (SCREENSTAR, Greiner) pre-coated with Geltrex (Thermo Fisher Scientific) at a density of 1.5 x 10^5 cells/cm^2, and incubated them in NPC medium overnight at 37 °C, 5 % CO_2. The next day, NPCs were treated with either dimethylsulfoxide (DMSO) or sildenafil dilution series in 100 μl and incubated for 16 h at 37°C, 5% CO_2. On the day of the assay, we live-stained NPCs with 10 nM tetramethylrhodamine methyl ester (TMRM) (Invitrogen) and 1 μg/μl Hoechst 33342 (Thermo Fisher Scientific) in NPC medium for 30 min at 37 °C and 5 % CO_2. After 30 min incubation, cells were washed with 100 μl NPC medium without phenol red. NPCs were kept in 100 μl medium (w/o phenol red) for the duration of the assay. For confirming MMP depolarizing effect, we used the mitochondrial uncoupler carbonyl cyanide-p-trifluoromethoxyphenylhydrazone (FCCP) in combination with the mitochondrial complex III inhibitor antimycin A (AA).[31] Imaging was performed with an Operetta CLS high content imaging system (Revvity) with 20 x water objective in confocal mode. Imaging time did not exceed 30 min. TMRM and Hoechst 33342 intensity within the cells was calculated using Columbus software (Revvity, version 2.9.0). To assess the effect of KT5823 on MMP in presence and absence of sildenafil, NPCs were seeded, incubated as described above, and pre-treated for 1 h with either DMSO alone or 1 μM KT5823 dissolved in DMSO. After the incubation time, 10 μM sildenafil dissolved in DMSO was added on top and incubated for 16 h at 37°C, 5% CO_2. The final DMSO concentration was adjusted to 0.3 % for each condition. On the day of the assay, NPCs were live-stained and imaged. TMRM and Hoechst 33342 intensity within the cells was analyzed with CellProfiler (version 4.2.5). MMP values are presented as the TMRM intensity in a mutant or treated sample over the TMRM intensity in the control sample (%).

For MMP assessment using cytofluorimetry, we used LSR-Fortessa X-20 (Becton Dickinson) to monitor the fluorescence of TMRM (Invitrogen) following treatment with either 10 μM sildenafil, 10 μM 8-Br-cGMP (Sigma-Aldrich), or DMSO. Cells were harvested and resuspended in culture medium at approximately 1x10^6 cells/ml. The uncoupling agent carbonyl cyanide 3- chlorophenylhydrazone (CCCP, 50 μM final concentration) was added to the sample and incubated for 5 min at 37°C, 5% CO_2 to depolarize mitochondria. TMRM probe (20 nM final concentration) was added and incubated for 30 min at 37 °C and 5 % CO_2. After incubation, cells were washed once in 1 ml of culture medium, then resuspended in 300 μl of DPBS and analyzed on the flow cytometer. The TMRM-emitted fluorescence was detected by emission filters appropriate for R- phycoerythrin "PE" (585 nm ± 42 nm). An appropriate gating strategy was applied to select only live and single cells. Data were analyzed with FlowJo software (version 7.6); the median fluorescence intensity (MFI) for each sample was calculated and normalized on the relative unstained sample. TMRM intensity was quantified in at least 20,000 cells per sample; at least three biological replicates were analyzed. Statistical analysis was performed by one-way Anova. $p<0.05$ was considered statistically significant. MMP values are presented as the TMRM intensity in a mutant or treated sample over the TMRM intensity in the control sample (%).

For evaluating the MMP impact due to modulating BKCa channel, on day one, WT cells and BKCa KO cells were plated at a concentration to reach a 60 % confluence on day three. On day two, the cells were treated with 10 μM sildenafil or DMSO for 16 h. On day three, the cells were stained for 30 min at 37 °C with a staining solution containing HBSS 1 x (Gibco), 7 nM TMRM, 2 μM cyclosporin H, and 1:2,500 Hoechst. During the acquisition of the TMRM signal using the Operetta HTS system (PerkinElmer), cells were kept at 37 °C with 5 % CO_2 inside Operetta with the imaging solution containing HBSS 1 x (Gibco), 5 nM TMRM and 2 μM cyclosporin H. Measurement was performed for 111 minutes. Basal respiration was assessed by obtaining the mean TMRM values of the first 3 measurements. Values were then expressed as percentage of basal respiration. After 25 min, we injected either DMSO or oligomycin (2 μM), and the signal was recorded for further 50 min (4 measuring time points). Finally, FCCP (1 μM) was added to dissipate the membrane potential. The signal remaining following FCCP addition (two measuring points) was subtracted from TMRM signals of the basal and oligomycin-treated cells.

Compound screening

LS NPCs (ATP6_2) were seeded at a density of 1.5 x 10^5 cells/cm^2 onto Geltrex-coated 384-well black-wall, clear-bottom plates (Revvity) in 30 μl NPC medium using a Multidrop liquid dispenser (Thermo Fisher Scientific), which was calibrated prior to each usage. Using the MMP effect of FCCP in combination AA,[31] we established the Z' factor[38] of our assay to be about 0.68 - 0.85 across all screening plates. Assay plates with cells were placed into a rotating incubator (Thermo Electron, Cytomat) at 37 °C and 5 % CO_2 for 24 h. Cells were treated with 5 μM (0.05 % DMSO) of 5,632 different compounds from a drug repurposing library.[37] Compounds were transferred to 384-well assay plates using an Echo 550 (Beckman Coulter (Labcyte). Columns 23 and 24 contained controls on each plate. In row 23, a combination of 5 μM FCCP (Biozol) and antimycin A (Sigma Aldrich/Merck) was used as positive control to achieve complete mitochondrial depolarization. Row 24 contained 0.05 % DMSO as negative control. After incubation of 16 h, cells were live-stained for 30 min at 37 °C and 5 % CO_2 with a final concentration of 10 nM TMRM and 1 μg/μl Hoechst in 30 μl/well. Cells were then automated washed twice with 30 μl NPC medium (w/o phenol red) using the Janus MDT (Revvity). Images were directly acquired using an Operetta CLS high content imaging system with 20 x objective in confocal mode. Imaging time did not exceed 30 min. TMRM intensity within the cells and nuclei count was calculated using a customized Columbus software script and downstream data processing was performed with Activity Base (IDBS). 3 x DMSO standard deviation (SD) was set as the threshold for MMP depolarization to calculate and compare hit rates using different compound concentrations. To quantify the effects of compounds on depolarizing the hyperpolarized MMP of LS NPCs (ATP6_2), we normalized the percentage of MMP depolarization (TMRM signal) and the percentage of cell count (Hoechst signal) after treatment for 16 h with 5 μM of each compound in LS NPCs with respect to LS NPCs treated for 16 h with either 5 μM FCCP+AA or DMSO only. To achieve this normalization, we used the formula z = (y – min(x)) / (max(x) – min(x)) * 100, where z is the final normalized value, y is the value of interest in the dataset, min(x) is the mean value of DMSO-treated LS NPCs, and max(x) is the mean value of FCCP+AA-treated LS NPCs. We next scored the normalized values (z) based on their ability to depolarize the MMP (inhibition) and classified the compounds in mild, intermediate, and strong uncouplers.

Bioenergetic assessment

For biochemical activity of complex V, approximately 1 x 10^7 NPCs were suspended in 0.5 ml of 10 mM ice-cold hypotonic Tris buffer (pH 7.6) and homogenized with glass/glass Dounce homogenizer with a tight pestle by 10 strokes. 200 μl of 1.5 M sucrose was added and then samples were centrifuged at 600 g for 10 min at 4 °C. Supernatants were collected and centrifuge at 14,000 g for 10 min at 4 °C. Mitochondrial pellets were suspended in 0.2 ml of 10 mM ice-cold hypotonic Tris buffer (pH 7.6) and subjected to three freeze-thaw cycles. Protein concentration was quantified with the Bicinchoninic Acid (BCA) protein assay Kit (Thermo Fisher Scientific). Complex V activity (ATP hydrolysis) was measured at 340 nm cleared from oligomycin-insensitive ATPase activities as described[43] and normalized to citrate synthase activity.[135]

For ATP content analysis, NPCs were grown in NPC medium and then switched to DMEM glucose-free (Gibco) and Neurobasal A-Medium glucose-free (Gibco) 1:1 medium supplemented with 1 mM sodium pyruvate, 1 % B27, 0.5 % N2, 1 % Pen/Strep, 1 % L-glutamine and 0.01 % MycoZap Plus-CL with 5 mM galactose as a carbon source to measure OXPHOS-derived ATP content, and then treated with DMSO or 10 μM sildenafil for 16 h. Luminescence-based ATP levels were detected in cellular suspension (5 x 10^3 cells) with ViaLight™ Plus Kit (Lonza). ATP levels were determined by luminometry using Victor Multiple Plate Reader Spectrophotometer (Revvity). For normalization purposes, we employed the DNA quantification with CyQUANT Cell Proliferation Assay (Invitrogen). Results were then expressed as luminescence A.U. relative to control lines cultured in galactose.

For live-cell assessment of cellular bioenergetics, we employed Seahorse XF96 and XFe24 extracellular flux analyzer, as previously described.[25] Briefly, the day before the assay, 100,000 cells (for XF96) or 120,000 (for XFe24) were plated into each Matrigel-coated well of the XF96 well plates and incubated overnight at 37 °C with 5 % CO_2. On the day of the assay, the growth medium was removed and replaced with glucose-based unbuffered media. The cells were incubated at 37 °C for 60 min to allow media temperature and pH to reach equilibrium before starting the measurement of mitochondrial respiration (oxygen consumption rate, OCR). After baseline records, we subsequently injected oligomycin (1 μM), FCCP (1 μM), and rotenone/antimycin A (1 μM each). Normalization to DNA content in each well of the plate was performed using the CyQUANT Cell Proliferation Assay kit.

Quantification of NAD metabolites

Quantitative analyses of NAD^+, NADH, $NADP^+$, and NADPH were carried out as a service in NADMED laboratory (Helsinki, Finland) from same homogenates submitted for metabolomics analysis. We used four LS NPC lines (ATP6_2, ATP6_4, ATP6_5 and ATP6_7.) and four healthy control NPC lines (CTRL_1, CTRL_2, CTRL_3 and CTRL_4) either treated for 16 h with either 0.1 % of DMSO or with 10 μM sildenafil resuspended in 0.1 % DMSO. NPCs were washed on the plate with DPBS buffer to remove protein of the culture media followed by the addition of cold extraction solvent acetonitrile:methanol:MilliQ; 40:40:20 to quench cellular metabolism. Obtained sample homogenates were shipped on dry ice to the measurement facility. Before analysis the homogenates were equilibrated to room temperature and centrifuged at 20,000 x g for 10 min at 4 °C to remove proteins. Next, NAD^+, NADH, $NADP^+$, and NADPH were measured individually from every cell extract using modified cyclic enzymatic reactions with colorimetric detection. For normalization of the results, protein content was measured using the pellets obtained after centrifugation of the homogenate.

Quantification of mtDNA copy number

NPCs were switched to DMEM glucose-free (Gibco) and Neurobasal A-Medium glucose-free (Gibco) 1:1 medium supplemented with 1 mM sodium pyruvate, 1 % B27, 0.5 % N2, 1 % Pen/Strep, 1 % L-glutamine and 0.01 % MycoZap Plus-CL with low glucose (4.6 mM), and then treated with DMSO or 1 μM sildenafil for 16 h. Cells were grown to confluency in a 6-well plate format. Medium was aspirated and cells were washed twice with DPBS. Quickly, cells were scraped in 1 ml DPBS. Cell suspension was collected into a 1.5 ml tube and centrifuged at 8,000 x g for 5 min at 4 °C. Supernatant was aspirated. Cell pellets were frozen in liquid nitrogen and stored at -80 °C. gDNA was isolated using the NucleoSpin Tissue Kit (Macherery-Nagel). DNA concentration was measured with the NanoDrop 2000 and diluted to 50 ng/μl. qPCR was performed using the Power SYBR Green PCR Master Mix (Applied Biosystems) for the genes *MT-ND1* and *NDUVF1* in technical triplicates, including no-template control. Ct values were corrected based on the primer efficiency.[136] The mtDNA/gDNA ratio was calculated with the corrected CT values using the formula: (*MT-ND1*/*NDUFV1*) * 2.

Analysis of mitochondrial nanostructure

To examine the impact of sildenafil on the mitochondrial nanostructure, we immunolabeled LS NPCs (ATP6_2) and control NPCs (CTRL_1) treated with 1 μM sildenafil for 24 h for MIC60, a core protein of the mitochondrial contact site and cristae organizing system (MICOS). For immunolabelling of MIC60, cells were fixed with prewarmed (37 °C) 4 % formaldehyde in DPBS (137 mM NaCl, 2.68 mM KCl and 10 mM Na2HPO4, pH 7.4) for 5 min at RT. Fixed cells were extracted with 0.5 % (v/v) Triton X-100 in DPBS, blocked with 5 % (w/v) BSA in DPBS. Afterwards, cells were incubated with diluted primary antibodies against MIC60 (Abcam) in 5 % (w/v) BSA in DPBS for 1 h at RT. After washing with DPBS, the primary antibodies were detected with secondary goat anti-rabbit antibodies labelled with Abberior STAR RED (Abberior). After washing with DPBS, the cells were mounted in Mowiol with 0.1 % 1,4-Diazabicyclo[2.2.2]octan (DABCO). Confocal and stimulated emission depletion (STED) microscopy were performed using an INFINITY platform (Abberior Instruments). The objective was an UPLXAPO60xO, NA: 1.42, oil objective (Olympus). For STED super-resolution microscopy, Abberior STAR RED was excited at 640 nm and depleted with 775 nm. The fluorescence was collected between 650 nm and 720 nm. Images were recorded with a pixel size of 20 nm and a dwell time of 30 μs per pixel.

To detect structural differences between LS NPCs and control NPCs, we captured approximately 4,000 STED images and trained a neural network classifier on multiple biological replicates to distinguish control NPCs (P[healthy]-score = 1) from LS NPCs (P[healthy]-score = 0). A deep residual neuronal network (ResNet34) was trained with STED data of DMSO-treated LS NPCs (ATP6_2) and control NPCs (CTRL_1) in a supervised setting to distinguish between both conditions. For the training, STED images were percentile normalized and divided into 512 x 512 pixel-sized regions (patches). Every patch was assigned to the class ‘‘healthy’’ when it originated from control NPCs and to the class ‘‘ill’’ when it originated from LS NPCs. Using a mean intensity threshold, patches without a sufficient fluorescence signal were allocated to a third class (‘‘low information’’). The final training dataset consisted of equal numbers of patches from three different biological replicates and included in total 75,000 patches of the ‘‘healthy, ‘‘ill’’ and ‘‘low information’’ classes in a 0.4:0.4:0.2 ratio. The performance throughout the trainings process was monitored with a validation set of 11,000 patches. For every patch, the model predicts logits values corresponding to the three classes, that are then transformed with softmax function to receive a per class probability. The per-class accuracy computed from a confusion matrix was used as mean validation metric after each epoch and as an indicator for the best checkpoint. The final evaluation of the neuronal network after the training was carried out with a test set of 140,000 patches with a 0.4:0.4:0.2 ratio. The trained model was used to assign a P[healthy] score from zero to one to single STED images. For each STED image with a size of 2,048 x 2,048 pixels, 49 partially overlapping patches of 512 x 512 pixels were extracted and evaluated with the model. Patches with insufficient fluorescence signal were assigned to the ‘‘low information’’ class and excluded from the evaluation. For the remaining patches a P[healthy]-score was predicted. The P[healthy]-score of the single patches were averaged to assign a P(healthy)-scores to each STED image of 2,048 x 2,048 pixels. STED images which had a proportion of ‘‘low information’’ patches above 90 % were excluded. After training, the classifier could reliably differentiate the two conditions on images that were not used for the training, indicating alterations of the MIC60 fluorescence signal in LS NPCs. To gain further insights, we reviewed a subset of images individually. Confocal microscopy revealed a tubular mitochondrial network in both NPC cultures, with no evident phenotypic alterations in LS NPCs. STED imaging showed a largely uniform distribution of MIC60 clusters along mitochondrial tubules in control NPCs, whereas in LS NPCs, MIC60 appeared to accumulate at the sides of mitochondrial tubules. To investigate this phenotype, we manually analyzed the MIC60 pattern across the mitochondrial tubules in approximately 300 images. A semi-automated MATLAB-based analysis was employed to assess the MIC60 distribution in LS NPCs (ATP6_2) and control NPCs (CTRL_1). After blinding, individual elongated mitochondria were manually analyzed. The mitochondrial centerline was determined by marking discrete points along the mid-axis, which were then fitted to a Bézier curve to approximate the mitochondrial central axis. The fluorescence intensity profile across the mitochondrial transverse axis was measured every 10 nm at a length of 600 nm with its center at the Bézier curve. The profiles were averaged for all selected isolated mitochondrial fragments in a single STED image. A homogeneous MIC60 distribution results in a fluorescence intensity profile with a broad plateau at the central maximum along the transversal mitochondrial axis. MIC60 accumulation at the outer edge of the mitochondria creates a central intensity dip. LS NPCs revealed a clear dip in the distribution of fluorescence intensity. The altered distribution of MIC60 was expressed as a center-to-maximum fluorescence intensity ratio across the transversal mitochondrial axis.

Bulk RNA sequencing

For bulk transcriptomics of NPCs, we used four *MT-ATP6* mutant NPC lines (ATP6_2, ATP6_4, ATP6_5 and ATP6_7.) and four healthy control NPC lines (CTRL_1, CTRL_2, CTRL_3 and CTRL_4) either treated for 16 h with 0.1 % of DMSO alone or with 10 μM sildenafil resuspended in 0.1 % DMSO. We used n=3 biological replicates per condition. Total RNA was isolated from pelleted NPCs using the NucleoSpin RNA Plus kit (Macherey Nagel) and eluted in 30 μl RNase-free H_2O. RNA concentration was measured with NanoDrop 2000. For quality check, 300 ng RNA was run on a 2 % TBE gel.

For time-course bulk transcriptomics of NPCs grown in low glucose media, LS NPCs (ATP6_2, ATP6_4, and ATP6_7.) were switched to DMEM glucose-free (Gibco) and Neurobasal A-Medium glucose-free (Gibco) 1:1 medium supplemented with 1 mM sodium pyruvate, 1 % B27, 0.5 % N2, 1 % Pen/Strep, 1 % L-glutamine and 0.01 % MycoZap Plus-CL with low glucose (4.6 mM), and then treated for 6 or 24 h with 0.1 % DMSO alone, 1 μM sildenafil resuspended in 0.1 % DMSO, or 10 μM sildenafil resuspended in 0.1 % DMSO. We used n=3 biological replicates per condition. Total RNA was isolated from pelleted NPCs using the NucleoSpin RNA Plus kit (Macherey Nagel) and eluted in 30 μl RNase-free H_2O. RNA concentration was measured with NanoDrop 2000. For quality check, 300 ng RNA was run on a 2 %TBE gel. Differential expression analysis between the two timepoints was performed using DESeq2 (Wald test, Benjamini-Hochberg p-value adjustment). The values depicted in the boxplots (expression, y axis) in Figures S6E and S6F are variance-stabilized counts obtained with DESeq2's vst(), which normalized for sequencing depth and applies a transformation that is approximately log2 for large counts but reduces variance for low counts.

For bulk transcriptomics of brain organoids, total RNA was isolated from day 70 cortical brain organoids generated using the first protocol.[62,134] We used five pelleted organoids per sample with n=3 biological replicates per condition, grown under normal conditions (CTRL_1, CTRL_2, ATP6_4 and ATP6_7), or treated with 10 μM sildenafil for 24 h (ATP6_4 and ATP6_7). Total RNA was isolated using the RNeasy Mini Kit by Qiagen. RNA concentration as well as purity was measured at the Nanodrop Spectrophotometer ND1000 (peQlab) using ND-1000 software (V3.8.1). Total RNA was mixed with 1 μg of a DNA oligonucleotide pool comprising 50-nt long oligonucleotide mix covering the reverse complement of the entire length of each rRNA (28S rRNA, 18S rRNA, 16S rRNA, 5.8S rRNA, 5S rRNA, 12S rRNA), incubated with 1U of RNase H (Hybridase Thermostable RNase H, Epicentre), purified using RNA Cleanup XP beads (Agencourt), DNase treated using TURBO DNase rigorous treatment protocol (Thermo Fisher Scientific) and purified again with RNA Cleanup XP beads. rRNA-depleted RNA samples were further fragmented and processed into strand-specific cDNA libraries using TruSeq Stranded Total LT Sample Prep Kit (Illumina) and sequenced using the NovaSeq 6000 system with stranded technology, generating paired-end reads of 150 bp. Raw RNA sequencing data were processed to generate FASTQ files using Illumina bcl2fastq. Briefly, base calling was performed using Real-Time Analysis (RTA) software, and adapter sequences were trimmed. The resulting BCL files were converted to FASTQ format, followed by quality control assessment using FastQC before downstream analysis. The preprocessing of the FASTQ raw sequencing files was performed with nfcore/rnaseq (version 3.12.0) pipeline. Briefly, reads were trimmed with Trim Galore! (version 0.6.10) and mapped to the human genome (GRCh38 assembly) using STAR (version 2.7.10a) aligner.

For both NPCs and brain organoids samples, we performed different comparisons: i) LS with DMSO vs. controls with DMSO (disease signature), ii) LS + sildenafil vs. LS + DMSO (sildenafil signature), iii) controls + sildenafil vs. controls + DMSO (negative control test). Transcript counts were determined using Salmon (version 1.10.1). DESeq2 (version 1.40.2)[137] was used to identify differentially expressed genes in the NPC samples or in brain organoid samples (Table S1) (Benjamini-Hochberg-adjusted p-value 0.05). Gene Ontology (GO) enrichment analysis was performed to identify biological processes (BP) and cellular components (CC) using the enrichGO function within ClusterProfiler (4.8.3), using the annotations of org.Hs.eg.db (version 3.18.0). Visualizations were generated with ggplot2 (version 3.5.1).

Single-nucleus RNA sequencing

For single-nucleus RNA sequencing (snRNAseq), we used day 72 brain organoids generated with the second protocol[138] from control iPSCs (CTRL1) and LS iPSCs (ATP6_7). Brain organoids were treated with either DMSO or 10 μM sildenafil resuspended in DMSO for 45 days from day 27 to day 72. We used 15 pelleted organoids per sample (n=8 samples) with n=2 biological replicates per condition (n=120 cortical brain organoids in total). snRNA-seq was performed using the 10X Genomics Chromium system, following the manufacturer's protocol. Nuclei were isolated using mechanical dissociation with gradient centrifugation and stained with DAPI to assess nuclear integrity. Barcoding and cDNA amplification were carried out using the Chromium Single Cell 3' (vNext) Reagent Kit. Libraries were prepared and sequenced on the Illumina NovaSeq 6000, generating paired-end reads of 100 bp. Data processing, including demultiplexing, alignment to the reference genome (GRCh38-2020-A), and gene quantification, was performed using Cell Ranger (v7.2.0) from 10x Genomics with default parameters. To generate digital gene expression (DGE) matrices for each sample. DGEs were further processed in R (v. 4.4.1) using Seurat (v. 5.1.0).[139] Filtered DGEs were imported using the function "Read10x" and only genes detected in at least 5 cells were kept for downstream analyses. Similarly, cells with less than 200 genes and 3,000 unique transcripts or more than 0.5 % mitochondrial transcripts were discarded. After merging all samples in a single Seurat object, we performed gene expression normalization and scaling for each sample independently using SCTransform.[140] We performed unbiased clustering and dimensionality reduction using the first 20 principal components on all samples together. Clusters were manually annotated in 7 cell types analyzing their marker genes (Table S1). To identify differential genes induced by *MT-ATP6* variants and sildenafil treatment in a robust and reproducible way, we performed a pseudo-bulk analysis using the DESeq2 package[140] (v. 7.5.1), as described previously.[141] Pseudo-bulk analysis was used to determine differentially expressed genes within the individual populations (Table S1). For each population, we generated a pseudo-bulk expression profile for each organoid by summing the expression of 250

randomly selected cells. We filtered genes with less than 50 counts in at least 2 samples, normalized expression values by library size, estimated negative binomial dispersions. We performed different comparisons: i) LS + DMSO vs. controls + DMSO (disease signature), ii) LS + sildenafil vs. LS + DMSO (sildenafil signature), iii) controls + sildenafil vs. controls + DMSO (negative control test). For all comparisons, we identified differentially expressed genes and adjusted p value was calculated using Bonferroni correction for multiple testing correction. To estimate glycolytic pathway activity in single cells, we leveraged the AUCell package (v. 1.26.0)[142] and the 'Glycolysis' gene set in the 'Hallmark' database accessed from the MsigDB package (v 7.5.1).[143] Plots were generated with ggplot2 (v. 3.5.1) and piping using dplyr (v. 1.1.4) and visualized with uniform manifold approximation and projection (UMAP).

Proteomics analysis

We carried out proteomics using mass spectrometry (MS) for four *MT-ATP6* mutant NPC lines (ATP6_2, ATP6_4, ATP6_5, and ATP6_7) and four healthy control NPC lines (CTRL_1, CTRL_2, CTRL_3, and CTRL_4) with n=3 biological replicates per condition that were treated with either DMSO or 10 μM sildenafil in DMSO for 16 h. Cells were washed three times with ice-cold DPBS, detached using a cell scraper, transferred to pre-chilled 1.5 ml tubes and centrifuged at 1,000-3,000 rpm for 10 min at 4 °C. Subsequently, the supernatant was removed, and intact cells were snap-frozen. Cells were lysed under denaturing conditions in 300 μl of a buffer containing 3 M guanidinium chloride (GdmCl), 10 mM Tris(2-carboxyethyl)phosphine (TCEP), 40 mM chloroacetamide, and 100 mM Tris-HCl pH 8.5. Lysates were denatured at 95 °C for 10 min shaking at 1,000 rpm in a thermal shaker and sonicated in a water bath for 10 min. The protein concentration of each sample was measured with a BCA protein assay kit (23252, Thermo Fisher Scientific). 500 ng protein was used per sample and diluted with a dilution buffer containing 10 % acetonitrile and 25 mM Tris-HCl, pH 8.0, to reach a 1 M GdmCl concentration. Then, proteins were digested with LysC (Roche; enzyme to protein ratio 1:50, MS-grade) shaking at 800 rpm at 37 °C for 3.5 hours. The digestion mixture was diluted again with the same dilution buffer to reach 0.5 M GdmCl, followed by tryptic digestion (Roche, enzyme to protein ratio 1:50, MS-grade) and incubation at 37 °C overnight in a thermal shaker at 800 rpm. Peptides were acidified with formic acid to a final concentration of 2 %. LC-MS/MS was performed by nanoflow reversed-phase liquid chromatography (Dionex Ultimate 3000, Thermo Fisher Scientific) coupled online to a timsTOF SCP mass spectrometer (Bruker Daltonics) using the data-independent acquisition (DIA) method with parallel accumulation serial fragmentation (PASEF). Briefly, LC separation was performed using the Aurora Ultimate column (25 cm x 75 μm ID, C18, 1.7 μm beads, IonOpticks, Victoria, Australia). 150 ng of each desalted digest was applied to the column and peptides were eluted using a gradient of 3.8 to 38 % solvent B in solvent A over 60 min (total run time) at a flow rate of 400 nl per minute. Solvent A was 0.1 % formic acid and solvent B was 79.9 % acetonitrile, 20 % H_2O, and 0.1% formic acid. The "match between run" feature was used and the mass search range was set to m/z 400 to 1,000. MS data were processed with Dia-NN (v1.8.1) and searched against an in silico predicted human spectral library (Table S1).

Targeted metabolomics profiling

We carried out metabolomics using MS of four *MT-ATP6* mutant NPC lines (ATP6_2, ATP6_4, ATP6_5 and ATP6_7) and four healthy control N PC lines (CTRL_1, CTRL_2, CTRL_3 and CTRL_4) using n=4 replicates per condition that were treated with either 0.1 % DMSO or 10 μM sildenafil in 0.1 % DMSO for 16 h. NPCs were washed 1 x with DPBS, detached in 600 μl ice-cold extraction buffer (methanol, acetonitrile and Milli-Q water at a ratio of 40:40:20) using a cell scraper, transferred into an ice-cold 1.5 ml tube, and stored at -80 °C until use. Metabolites were extracted from cells with 500 μl of cold extraction solvent (Acetonitrile:Methanol:MilliQ; 40:40:20, Thermo Fischer Scientific). Subsequently, samples were processed with three cycles of sonication (60 s) and vortexing (120 s) followed by centrifugation at 14,000 rpm at 4 °C for 5 min. Next, the samples were centrifuged, the supernatants transferred to evaporation tube and evaporated to dry under nitrogen stream. Samples were reconstituted in 40 μl extraction buffer (Acetonitrile:Methanol:MilliQ; 40:40:20) and transferred to LC-MS vials. 2 μl of the samples were analyzed with Thermo Vanquish UHPLC coupled with Q-Exactive Orbitrap mass spectrometer equipped with a heated electrospray ionization (H-ESI) source probe (Thermo Fischer Scientific). A SeQuant ZIC-pHILIC (2.1 × 100 mm, 5 μm particle) column (Merck) was used for chromatographic separation. The gradient elution was carried out with a flow rate of 0.1 ml/min and mobile phase gradient with 20 mM ammonium hydrogen carbonate, adjusted to pH 9.4 with ammonium solution (25 %) as mobile phase A and acetonitrile as mobile phase B, 0-2 min 80 % B, 2-17 min 80-20 % B, 17-24 min 80 % B. The column oven and auto-sampler temperatures were set to 40 ± 3 °C and 5 ± 3 °C, respectively. Following setting were used for MS: full scan range: 55-825 m/z, polarity switching; resolution of 35,000, the spray voltages: 4250 V for positive and 3250 V for negative mode; the sheath gas: 25 arbitrary units (AU); the auxiliary gas: 15 AU; sweep gas flow 0; capillary temperature: 275 °C; S-lens RF level: 50.0. Instrument control was operated with the Xcalibur software (Thermo Fischer Scientific). The metabolite annotation and integration were done with the TraceFinder 5.1 software (Thermo Fischer Scientific) using confirmed retention times by in-house standard library (MSMLS-1EA, Merck) and their m/z. The data quality was monitored throughout the run using pooled QC sample prepared by pooling 5 μL from each suspended sample and interspersed throughout the run every 10 samples. The data was quality controlled for peak quality (poor chromatography), prefiltered with 20 % RSD cutoff of the pooled QC and noise. We identified metabolites that were differentially present within samples (Table S1).

Multi-omics integration

We performed multi-omics integration as previously described.[55] Briefly, we integrated bulk transcriptomics, proteomics, and metabolomics datasets derived from LS NPCs and control NPCs (*disease signature*), as well as transcriptomics and metabolomics

datasets from sildenafil-treated LS NPCs and untreated LS NPCs (*sildenafil signature*). For both cases, we used all significantly deregulated molecules (adjusted p-value ≤ 0.05) as input lists for the OmicsNet platform (v.2.0) and retrieved their interactions based on STRING (confidence score 0.7) and Recon3D databases. Molecular interactions were filtered with the Prize-Collecting Steiner Forest (PCSF) algorithm, retaining only the most informative nodes regarding network organization and functionality. The final network was analyzed for centrality measures using the CytoNCA plugin in Cytoscape (v.3.10.2) and enrichment analysis using the KEGG database (Release 112.0). For network visualization, we chose the Organic Layout from yFiles plugin in Cytoscape. To dissect the rescue mechanism of sildenafil, we searched for molecules with reversed expression in the disease signature and sildenafil signature datasets. Molecules were annotated in the REACTOME and GeneOntology databases for pathway and biological processes enrichment analyses, respectively, using the clusterProfiler package (v4.10.0).

To explore the regulatory effect of sildenafil in gene expression levels, we retrieved the drug's signatures from the L1000 FWD database. Genes that had a consistent pattern of re-regulation across all examined cell lines after sildenafil treatment were considered as literature-indicated drug targets. We evaluated these literature-indicated drug targets in our transcriptomics datasets by filtering those genes that had the same pattern of re-regulation in LS NPCs after sildenafil administration (LS + sildenafil vs. LS + DMSO). A final list of literature-indicated drug targets with a similar regulation pattern in treated LS NPCs was considered a cross-validated set of genes involved in the mechanism of action of sildenafil. To describe the mechanistic effect of sildenafil on *HOXA5*, we performed two parallel clustering analyses in LS + DMSO vs. controls + DMSO and in LS + sildenafil vs. LS + DMSO networks, respectively. Specifically, we implemented the GLay algorithm aiming to identify the densely connected clusters within each network. By isolating the clusters with *HOXA5* and comparing them using the Dynet plug-in in Cytoscape, we highlighted their common and/or condition-specific interactions. Each cluster's interactions were used as inputs for enrichment analysis of biological pathways and terms. Following this pipeline, we identified the modulated pathways of *HOXA5* due to sildenafil administration.

Calcium imaging in cortical brain organoid slices (cBOS)

cBOS were generated as previously described.[69,144] Briefly, 3 % low melting temperature agarose (Gibco) was diluted in Hank's Balanced Salt Solution (HBSS, Sigma-Aldrich), heated to 90 °C and slowly cooled down to 40 °C. Brain organoids were washed in HBSS, embedded in the agarose, and cooled on ice until the agarose was solid. For slicing, a Vibratome Microm HM 650 V (Thermo Fisher Scientific) was adjusted to the following settings: frequency of 60 Hz, amplitude of 1.0 mm, velocity of 33 mm/s, and slice thickness of 300 μm. The slices were directly transferred to a petri dish filled with HBSS, placed in a cell culture hood and washed four times. Finally, the slices were collected on Millicell-CM inserts (Millipore) and placed in a 6-well plate. 750 μl of cortical differentiation medium IV (CDMIV) were added in each well, so that the membrane was soaked but the top side of the slices was still exposed to air. cBOS were cultured at 36 °C and 5 % CO_2 for around 30-59 days before starting calcium imaging experiments.

For calcium imaging experiments,[69] membrane permeable Oregon Green 488 BAPTA-1 AM (OGB-1, Invitrogen) was first solved in 20 % pluronic and 80 % DMSO and diluted to 200 μM in HEPES-buffered saline, which was then injected into cBOS and incubated for 30 minutes. During the incubation and throughout the experiments, cBOS were perfused with artificial cerebrospinal fluid (ACSF), containing 138 mM NaCl, 2.5 mM KCl, 2 mM $CaCl_2$, 1 mM $MgCl_2$, 1.25 mM NaH_2PO_4, 18 $NaHCO_3$, and 10 glucose. The ACSF was bubbled with 95 % O_2 and 5 % CO_2, resulting in a pH of 7.4. OGB-1 was excited at 488 nm and signals were detected using the imaging software NIS-Elements and a variable scan digital imaging system (Nikon) attached to an upright microscope (Eclipse FN-1, Nikon). The microscope was equipped with a Fluor 40x/ 0.8 DIC M/N2 ∞ /0 WD 2.0 water immersion objective (Nikon) and an orca FLASH 4.0 LT camera (Hamamatsu Photonics). Images were routinely obtained at 1 Hz and emission was collected at >500 nm. Regions of interest (ROIs) representing cell somata were identified, and their signals were background-corrected. For calculating ΔF/F0, the traces were normalized to their initial baseline (first 30 s of measurement). Additionally, the fluorescence signals were corrected for bleaching and analysed with OriginPro Software (OriginLab Corporation). To probe for the cellular response to acute metabolic stress, ACSF was switched to glucose-free ACSF containing 5 mM sodium azide (Honeywell) and 2 mM 2-Deoxy-D-glucose (Apollo Scientific) for 2 min. Then, it was switched back to ACSF for 20-30 min until cellular calcium levels recovered to their original baseline. For each calcium signal, the area under the curve (AUC) and the peak amplitudes ΔF/F0 (in %) were analyzed.

Calcium imaging in NPCs

One day prior to imaging, LS NPCs (ATP6_2, ATP6_4, ATP6_5, ATP6_7) were seeded on FluoroDishes™ at a density of 1.5 million cells/dish and treated with either 10 μM sildenafil or DMSO for 16 h. On the day of recording, the cells were washed twice with Tyrode's solution (129 mM NaCl, 2 mM CaCl2, 1 mM MgCl2, 5 mM KCl, 30 mM D-glucose, 25 mM HEPES, pH 7.4) and incubated with 3 μM fura-2 acetoxymethyl ester (fura-2 AM) (Thermo Fischer Scientific) in Tyrode's solution with 0.01% (v/v) Pluronic F-127 (Sigma-Aldrich) for 20 min at RT in the dark. After washing with Tyrode's solution, the cells were incubated for 10 min at room temperature (RT) in Tyrode's solution to allow fura-2 de-esterification and equilibration. Next, the Tyrode's solution was replaced by a calcium-free Tyrode's solution (129 mM NaCl, 1 mM MgCl2, 5 mM KCl, 30 mM D-glucose, 25 mM HEPES, 0.5 mM EGTA, pH 7.4), and immediately placed in a temperature- and CO_2-controlled (37 °C, 5 % CO_2, and ~20 % O_2) sample holder attached to the stage of an Axio Observer 7 inverted microscope (Zeiss, Jena, Germany) equipped with a x 40 objective (F-Fluar M27; NA 1.3; oil immersion; Zeiss) and x 1 magnification changer (Tubelens Optovar; Zeiss). Fura-2 was alternatingly excited at 340 nm and 380 nm using a Sutter Lambda DG5 wavelength switcher (Sutter Instruments, Novato, CA, USA), FT 430 dichroic mirror, and BP525/50 emission filter. Fura-2 emission signals were captured in the dark using an Axiocam 702 camera (Zeiss), applying an exposure time of 20 ms and

image acquisition interval of 1 s. Microscopy hardware was controlled by Zen Pro software (version 3.2; Zeiss). During time lapse recordings, 1 μM thapsigargin (TG) (Thermo Fisher Scientific) was added to the extracellular medium by gentle pipetting. To achieve instantaneous mixing and a final concentration of 1 μM, 500 μl TG (prepared at 2 μM in calcium-free Tyrode's solution) was added to the FluoroDish™ containing 500 μl calcium-free Tyrode's solution. Numerical fluorescence intensity data was extracted from the fura-2 images using FIJI software (version 1.53q; https://fiji.sc/). ROIs were manually defined for each time lapse recording in the cytosol of individual cells and extracellular background. Next, in each image fura-2 emission signals were quantified for multiple cells at both excitation wavelengths. All cytosolic ROIs were of identical size and remained inside the cytosol during the full duration of the recording. Cytosolic fura-2 signals were first individually background-corrected for each excitation wavelength, after which the ratio value (340/380 nm) was calculated.

Neurite outgrowth quantification

We quantified neuronal outgrowth capacity in neurons treated for 8 days with 10 μM sildenafil or DMSO using our HCA-based protocol.[81] Briefly, neurons were split with 500 μl of Accutase at 37 °C for 10-15 min and were centrifuged for 5 min at 120 x g. All pipetting steps to dissociate the cells were performed slowly and gently to minimize damage to the more sensitive neurons. 10 μM ROCK inhibitor was added to the final media after splitting to promote neuron survival. Experiments and quantification were performed as previously described.[81] Neurons generated for neurite outgrowth quantification were treated with 10 μM sildenafil in 0.1 % DMSO or 0.1 % DMSO alone following media changes on days 8, 10, and 12. On day 14, the neurons were split and seeded onto black-wall, flat-clear-bottom 96-well plates (Greiner) at a density of 5,000 cells/well, and treated once more with Sildenafil or DMSO. Neurons were then cultured until day 16, when they were fixed with PFA, blocked, and stained for TUJ1 and Hoechst. Neurite images were then acquired using the Operetta CLS high content imaging system (Revvity) the TUJ1 and Hoechst signals at 20 x. Following acquisition, the neurite images were analyzed using CellProfiler (version 4.2.5). Briefly, the Hoechst signal was used to identify the nucleus as a primary object and the TUJ1 signal was used to identify the neurites as secondary objects. The nuclear objects were then expanded to serve as a proxy for the cell body and subtracted from the TUJ1 signal to leaving only the individual neurites. The results were exported as CSV for data analysis. Mean neurite length was calculated as the mean over the median per experiment.

For *PRKG1* knock-down (KD) in dopaminergic-enriched neuronal cultures, we used small interfering RNA (siRNA) against *PRKG1* using jetPRIME transfection (Polyplus) following the manufacturer's instruction. On day 12, neurons were transfected with 10 nM of *PRKG1* siRNA (Ambion) or scrambled siRNA (Ambion) by adding the transfection mix directly to the well. On day 14, after re-seeding the neurons onto the 96-well plates, neurons were transfected again with 10 nM of *PRKG1* siRNA or scramble siRNA. On day 16, *PRKG1* knock-down efficiency was evaluated by qPCR and neurite length was quantified with our HCA protocol.[81]

Experiments with *Ndufs4* KO mice

Sildenafil citrate (Sigma-Aldrich) was dissolved in DMSO, then diluted with tap water to obtain the final concentration of 400 mg/l drinking water and given *ad libitum*. Untreated mice (10 females, 8 males) were compared to sildenafil-treated *Ndufs4* KO mice (6 females, 6 males). Electrocardiography (ECG) recordings were recorded from conscious mice, using the INDUS Rodent Surgical Monitoring system without anesthesia. Transthoracic echocardiograms to measure ventricular size, wall thickness, and ejection fraction were performed on mice using the Vevo 2,700 VisualSonics System. Intraperitoneal injection with 0.1 mg midazolam was applied for anxiolytic muscle relaxant effects, without any anesthetic agent that may cause cardiac suppression. Standard 2D, M-mode, Doppler, Tissue Doppler images were obtained using a 30-MHz linear array transducer, including the parasternal short and long axis. All image analysis was performed by Vevo 2,100 analysis software (v.1.5) after rapid image collection. The diastolic function was measured using tissue Doppler imaging of the mitral annulus (E') and conventional mitral inflow (E wave). Metabolic chamber by Promethion (Sable Systems International) was applied to characterize the metabolism of whole-animal energy expenditure.[145] The 16-cage metabolic chamber system directly measures various parameters over a 72-hour period, such as heat production, oxygen consumption (VO_2), CO_2 production, and XY activity movement. The respiratory exchange ratio (RER) is calculated as the ratio of carbon dioxide production (VCO_2) to oxygen consumption. This parameter is useful to estimate the metabolic status. The xy axis detection of animal motion measure activity during day-time and night-time. The formula applied was Heat = $(1.232*VCO_2)+(3.815*VO_2)$.

Experiments with *SURF1* KO pigs

For generation of *SURF1* KO pigs, we followed a protocol for somatic cell nuclear transfer (SCNT) based on our previous method[11] with minor modifications. Briefly, ovaries from pubertal gilts of domestic pig, large white background were collected at a local abattoir and transported to the lab at 31-33 °C. Follicles larger than 3 mm were aspirated, and cumulus-oocyte complexes (COCs) were selected and matured in vitro at 38.5 °C under 5 % CO_2 for 42 h. One day before SCNT, donor cells were induced into quiescence via serum starvation (0.5 % FCS). On the day of SCNT, cells were trypsinized, washed, and resuspended in SOF-Hepes medium. Matured oocytes (with extruded polar body) were selected and zona pellucida was removed using 0.5 % pronase in DPBS. All manipulations were performed in SOF-Hepes with 10 % FCS. Oocytes were enucleated after a 5-min treatment with cytochalasin B (7.5 μg/ml) and Hoechst 33342 (5 μg/ml). Enucleated cytoplasts were exposed to phytohemagglutinin and fused with donor cells via double DC-pulse (1.2 kV/cm), then returned to maturation medium. As nuclear donor, we used a cell clone obtained by homologous direct recombination (HDR)[11] that harbors a 106 bp deletion on the left homology arm of exon 3 as well as a

puromycin-resistance cassette in both alleles of the *SURF1* gene. After ~48 h of maturation, embryos were activated with a second double DC-pulse and incubated for 2 h in maturation medium containing cytochalasin B (5 μg/ml) and cycloheximide (10 μg/ml). Embryos were cultured in modified mSOF medium with amino acids and 4 mg/ml BSA, using a modified Well-of-the-Well system. Sows were synchronized with 12 mg/day of altrenogest for 15 days. On day 13, they received 0.15 mg $PgF_2\alpha$, followed by 1000 IU hCG 96 h after the last altrenogest dose. On day 6 of SCNT embryo development (compacted morula to early blastocyst stage), embryos were surgically transferred via mid-ventral laparotomy, five days after standing estrus. Pregnancy was assessed via ultrasound on day 30 and confirmed on day 60 post-transfer. Farrowing was induced with $PgF_2\alpha$ on days 114-115 of gestation. All offspring were genotyped after birth. For body temperature detection we used a Thermal Imaging Camera (Dongguan Xintai Instrument Co., Ltd, China).

SURF1 KO male piglets were treated immediately after birth with sildenafil citrate (n=3 animals with 2.1 mg/kg/day, n=4 animals with 0.5 mg/kg/day). At birth, the animals were separated from the sow and transferred to an incubator kept at 35 °C. Sildenafil was always administered at the same time and dissolved in milk. The veterinarian ensured that the entire dose was consumed. For biochemical and immunoblot experiments, we isolated the basal ganglia of newborn male pigs: 3 *SURF1* KO, 3 *SURF1* KO treated with sildenafil (2.1 mg/kg/day), and 3 sex and age-matched WT. Spectrophotometric analyses of complex IV (CIV) and citrate synthase (CS) activities were carried out as previously described.[135] CIV activity was normalized to CS activity, an index of mitochondrial mass. For histological analysis, tissues were removed immediately after death, post-fixed in 4 % PFA at 4 °C for 48 h, cryoprotected in DPBS containing 30 % sucrose for 24 h at 4 °C, embedded in optimal cutting temperature (OCT) compound, and frozen on dry ice. Cryostat sections (10 μm thick) were then mounted on gelatin-coated glass slides. The sections were stained with hematoxylin and eosin (H&E). Images were acquired using a Nikon Eclipse E400 light microscope at 20 x or 40 x magnification.

Quantification of sildenafil concentration in patient plasma

The sildenafil plasma concentration was monitored in three treated LS patients. EDTA blood was drawn in the morning before the first dose (trough level) and one hour after oral sildenafil application (peak level). Depicted time points in Figure 6D were separated by more than 3 months for each patient. The quantification was performed by Liquid Chromatography-Tandem Mass Spectrometry (LC-MS/MS). The EDTA-blood sample was centrifuged at 3,000 x *g* for 10 min at 4 °C and the plasma was aliquoted and frozen at -80 °C until measurement. 100 μl sample was mixed with 400 μl of the internal standard d_3-sildenafil (10 nM in acetonitrile) (CDN Isotopes). Proteins were precipitated by vortexing for 1 min and subsequent storage for 60 min at -20 °C. Supernatants were obtained by centrifugation at 16,000 x *g* at 4 °C for 10 min and subjected to LC-MS/MS sildenafil quantification applying the multiple reaction monitoring (MRM) approach. Chromatographic separation was achieved on a 1290 Infinity II HPLC (Agilent Technologies) equipped with a Poroshell 120 EC-C18 column (3.0 x 150 mm, 2.7 μm; Agilent Technologies) guarded by a pre-column (3.0 x 5 mm, 2.7 μm) of identical material. Water (eluent A) and acetonitrile (eluent B), both acidified with 0.1 % formic acid, were pumped with 0.4 ml/min. Elution of sildenafil and its internal standard was achieved with a 10-min linear gradient from 5 % to 90 % eluent B. Total run-time was 17 min including re-equilibration of the LC system. MS/MS analyses were carried out using an Ultivo triple-quadrupole mass spectrometer (Agilent Technologies) operating in the positive electrospray ionization mode (ESI+). The following ion source parameters were set: sheath gas temperature, 400 °C; sheath gas flow, 12 l/min of nitrogen; nebulizer pressure, 20 psi; drying gas temperature, 100 °C; drying gas flow, 7 l/min of nitrogen; capillary voltage, 3.0 kV; nozzle voltage, 0 kV. The following mass transitions were recorded (fragmentor voltage [FV] and collision energies [CE] in parentheses): sildenafil: *m/z* 475.2 → 58.0 (FV: 220 V, CE: 68 eV, *quantifier*), *m/z* 475.2 → 100.0 (FV: 220 V, CE: 28 eV), *m/z* 475.2 → 283.1 (FV: 220 V, CE: 44 eV); d_3-sildenafil: *m/z* 478.2 → 60.9 (FV: 220 V, CE: 68 eV, *quantifier*), *m/z* 478.2 → 103.0 (FV: 220 V, CE: 28 eV), *m/z* 478.2 → 283.1 (FV: 220 V, CE: 44 eV). Peak areas were determined with MassHunter Software (Agilent Technologies) and sildenafil was directly quantified *via* its internal standard d_3-sildenafil that was concentrated to 8 nM in the samples.

Genotyping and heteroplasmy quantification

Heteroplasmy levels and mtDNA haplotypes in the whole exome sequencing (WES) datasets were determined using the software MToolBox v.1.[146,147] Results were visualized in the IGV viewer v2.16.[148] Heteroplasmy levels of the *MT-ATP6* mutations in fibroblasts, iPSCs, and NPCs were determined using polymerase chain reaction-restriction fragment length polymorphism (PCR-RFLP) analysis, as described before.[27] Genomic DNA was isolated using the Nucleo-Spin Tissue kit (Macherey-Nagel). We used restriction enzyme StuI (NEB, R0187, 10,000 units/ml) for the m.9185T>C mutation (wild-type: 24+90 pb, mutation: 114 pb), HpaII (NEB, R0171, 10,000 units/ml) for m.8993T>C and m.8993T>G (wild type: 25+155 bp; mutant: 180 bp), XbaI (NEB, R0145, 10,000 units/ml) for m.9176 T>G (wild type: 24+155 bp, mutant: 179 bp). The percentage of cleaved versus uncleaved fragments was determined by capillary electrophoresis and laser detection of the FAM-labelled RFLP-fragments using the 3,500 Series Genetic Analyzer (Applied Biosystems, RRID:SCR_021901) and normalized to a standard curve of known degrees of heteroplasmy.

Cranial magnetic resonance imaging (cMRI)

cMRI was performed for the six patients with LS carrying *MT-ATP6*. For Patient 1, imaging was carried out at 16.5 years of age and showed areas of increased T_2-signal intensity in the *Putamen* and *Nucleus caudatus* on both sides (Figure 6E) and at the perisylvian gray matter (Figure S12H). For patient 2, imaging was carried out at 2.2 years of age and showed lesional areas in the *Putamen* and *Nucleus caudatus* in both T_2-weighted images (Figure 6E) and Fluid Attenuated Inversion Recovery (FLAIR) images (Figure S12H). For patient 3, imaging was carried out at 5 years of age (Figure 6E) and at 14 years of age (Figure S12H). Areas with increased T_2-signal

intensity at 5 years of age (Figure 6E) had spontaneously resolved at 14 years of age (Figure S12H). In patient 4, FLAIR imaging was performed at 35 years of age and areas of increased signal intensity at the *Nuclei caudati* on both sides (Figure 6E) and enlargement of the internal and external liquor spaces due to diffused brain atrophy (Figure S12H). For patient 5, imaging was performed at 4.5 months of age and showed T_2-weighted images delayed myelination, enlarged external cerebral spinal fluid spaces, and a general frontal brain atrophy (Figure 6E). The T_2-signal intensity in the brain stem of patient 5 affected the *Fasciculus longitudinalis* and the *Substantia nigra* (Figure S12H). For patient 6, imaging was performed at 7.5 years of age and showed areas of increased T_2-signal intensity in the *Putamen, Pallidum*, and *Nucleus caudatus* on both sides (Figure 6E) and in the cortical gray matter (Figure S12H).

Toxicity assays

CellTiter-Glo assay (Promega) was used to determine cell viability based on cellular ATP concentration. NPCs were isolated using Accutase and seeded onto Geltrex-coated 96-well plates at a density of 1.5 x 10^5 cells/cm^2 and incubated in NPC medium overnight at 37 °C and 5 % CO_2. The day after, NPCs were treated with DMSO, FCCP+AA or sildenafil dilution series in 100 µl and incubated for 16 h at 37 °C and 5 % CO_2. One column contained an untreated reference. 50 µl Cell Titer-Glo reagent solution was added to each well and placed on a plate shaker (1 min, 100 rpm) and incubated at ambient temperature for 10 min to ensure cell lysis. 100 µl of the solution was transferred onto a new white wall, white bottom 96-well plate, and luminescence was measured using an EnSight multimode plate reader (Revvity).

For proliferation, NPCs were seeded in a coated 96-well plate (30,000 cells/well) and incubated at 37 °C and 5 % CO_2. Medium glucose concentration was either 21 mM or 4.5 mM, or glucose was substituted with galactose. With the first medium change, the medium was supplemented with 1 µM sildenafil, 10 µM sildenafil or DMSO (vehicle), respectively, or left without treatment. For toxicity analysis, the medium was additionally supplemented with Incuyte dye red (Sartorius) to indicate dead cells. Supplemented medium was changed every other day. Over the course of the experiment, the well plates were placed in the Cellcyte X (Cytena) microscope with a 10 x objective. Four pictures of each well were taken every three hours. Pipeline setup and analysis were done with the software CELLCYTE Studio (Cytena). Channels were "enhanced contour" for confluency and "red channel" (600 ms, 9 dB) for toxicity. Autofocus was set to "Classifier-based". Pictures taken with the "enhanced contour" channel were analyzed with the software-specific protocol "Cell Confluence" with the following settings: 58 a.u. contrast sensitivity, 2 a.u. smoothing, 200 μm^2 filled hole size, 100 μm^2 min object size. Pictures taken with "red channel" were analyzed with the software-specific protocol "object count" with the following settings: 30 a.u. contrast sensitivity, 50 a.u. separation sensitivity, 0 μm^2 filled hole size, 10 μm^2 min object size. Analysis results were exported to Excel and further processed with R studio.

Immunostaining

We fixed NPCs and neurons grown on Matrigel-coated coverslips with 4 % PFA (Thermo Fisher Scientific) in DPBS for 20 min at RT and washed two times with DPBS. For permeabilization, we incubated the fixed cells with a blocking solution containing 10 % normal donkey serum (DNS) (Merck Millipore) and 1% Triton X-100 (Sigma-Aldrich) in DPBS with 0.05 % Tween 20 (Sigma-Aldrich) for 1 h at RT. We diluted primary antibodies in blocking solution and incubated them overnight at 4 °C on a shaker. Next, the primary antibody was removed, and the wells were rinsed three times with DPBS. Corresponding secondary antibodies (all Alexa Fluor, 1:2,000, Thermo Fisher Scientific) together with 1:2,500 Hoechst 33342 (Thermo Fisher Scientific) were diluted in blocking solution and added to the wells for 1 h at RT on a shaker. Finally, the staining solution was removed, and the wells were rinsed with DPBS three times following mounting of the coverslips on microscopic slides. We acquired the images of 2D cultures using the fluorescence microscope ZEISS Axio Observer Apotome 3 (Zeiss) in combination with the ZEN Microscopy Software (Zeiss) and further processed with ImageJ.

For staining cortical brain organoids, we used 4 % PFA (Thermo Fisher Scientific) in DPBS for 1 h at RT and sliced them using the Vibratome Microm HM 650 V (Thermo Fisher Scientific). The samples were placed in a 3 % LB agar (Sigma-Aldrich) solution in DPBS and put in a cool place until the agar was solidified. The agar shape was freed from its mould and attached on the carrier plate of the vibratome and placed in cold DPBS. The cutting procedure was performed at an amplitude of 1.0 mm, a frequency of 60 Hz and a velocity of 13 mm/s. The organoids were sliced with a thickness of 100 µm and gently transferred to SuperFrost Plus glass slides (VWR) for staining. Blocking was carried out for 1 h at RT with a blocking solution containing 1 x DPBS, 10 % donkey serum (Sigma-Aldrich), 0.1 % Tween-20 (Sigma-Aldrich), and 1 % Triton-X (Merck). Primary antibodies were dissolved in blocking solution and applied on the slides and incubated at 4 °C overnight. The next day, the slides were rinsed three times for 10 min in 1 x DPBS and then exposed to secondary antibodies in blocking solution at a dilution of 1:300 counterstained with 1:2,500 Hoechst 3342 (Invitrogen). The slides were incubated for 1 h at RT protected from light and subsequently rinsed three times for 10 min with 1 x DPBS. Finally, coverslips were mounted using Pro-Long Glass Antifade Mountant (Invitrogen) on microscopic slides. Images of brain organoids were acquired using the Eclipse 90i upright widefield microscope (Nikon Microscope solutions) equipped with the imaging software NIS-Elements Advanced Research 3.2 (Nikon). Large images (7 x 7 stitches) were taken with a dry 20 x objective (Plan Apo VC 20 x / 0.75 air DIC N2 ∞/0.17 WD 1.0, Nikon Microscope Solutions) and three different filter channels (DAPI, FITC, TRITC). Specific structures of interest within the slices were imaged with the Confocal laser scanning microscope C1 (Nikon Microscope Solutions) and a dry 20 x objective (Plan Apo VC 20 x / 0.75 air DIC N2 ∞/0.17 WD 1.0, Nikon Microscope Solutions). Images were taken using the imaging software EZ-C1 Silver Version 3.91 at z-stack settings (1.1 µm step size, 10-30 steps).

Primary antibodies used for NPCs and organoids include rabbit anti-PAX-6 (BioLegend, 1:200), mouse anti-ß-Tubullin III (TUJ1, Sigma-Aldrich, 1:2000), mouse anti-Nestin (Merck/Sigma-Aldrich, 1:200). Secondary antibodies used include donkey anti-rabbit 488 (Invitrogen, 1:300), donkey anti-rabbit 647 (Invitrogen, 1:1000) and donkey anti-mouse Cy3 (Sigma-Aldrich, 1:300).

Tight junction proteins within BCECs were detected and visualized via immunofluorescence staining. For each step, 50 µl solution/insert was used. BCECs were fixed using 4% formaldehyde in DPBS for 10 min. After washing three times with DPBS, fixated cells were incubated in permeabilization solution (0.1% Triton X-100 in DPBS) for 15 min, washed twice with DPBS for 5 min each and subsequently, unspecific binding sites were blocked by incubation for at least 30 min in blocking solution (3% BSA in DPBS, 0.1% Tween 20). Primary antibodies were diluted in blocking solution and were applied to the inserts and incubated overnight at 4°C. Unbound antibodies were removed by washing twice for 5 min with DPBS. Next, cells were incubated with secondary antibodies, diluted in blocking solution, for 1 h at room temperature in the dark. After two additional washing steps, nuclear counterstaining was performed with 1 µg/ml Hoechst 33258 in DPBS. Cells were again washed twice with DPBS. Afterwards, the insert membranes were carefully cut out of the holder with a scalpel and transferred to the centre of glass slides, with the cell side facing upwards. These were then covered with approximately 5 µl mounting medium and a cover glass, which was framed with transparent nail varnish after drying. Glass slides were imaged using the Operetta CLS High Content Imaging System. Primary antibodies used: Occludin (mouse, Invitrogen 1:200) and ZO-1 (TJP1, Proteintech rabbit 1:100). Corresponding secondary antibodies used: Donkey anti-rabbit Alexa Fluor 488 (1:500, Thermo Fisher Scientific) and Goat anti-mouse Alexa Fluor 633 (1:500, Thermo Fisher Scientific).

Immunoblot analysis

Pellets of NPCs (at least 1.5 x 10^6 NPCs) or brain pig tissue (globus pallidus in the basal ganglia) were homogenized in 10 volumes of ice-cold 1x RIPA buffer (150 mM NaCl, 5 mM EDTA pH 8, 50 mM Tris pH 8, 1 % NP-40, 0.5 % sodium deoxycholate, 0.1 % sodium dodecyl sulfate) supplemented with protease and phosphatase inhibitors. Samples were incubated on ice for 30 min, followed by centrifugation at 14,000 rpm for 30 min at 4 °C. After three freeze-thaw cycles, protein concentration in the supernatants was determined using the Bradford assay (Bio-Rad). For SDS-PAGE, 30 µg of total proteins per sample were loaded onto 4-12% gradient polyacrylamide gels. Proteins were transferred to nitrocellulose membranes, which were then blocked for 1 h at RT with 5 % non-fat dry milk (Bio-Rad) or 5 % BSA (Sigma-Aldrich) in TBST (TBS + 0.1% Tween-20). Membranes were incubated overnight at 4 °C with primary antibodies diluted in blocking buffer. The following day, HRP-conjugated secondary antibodies (Sigma- Aldrich) were applied for 1 h at RT. Protein bands were visualized using either Clarity Western ECL substrate or Clarity Max from Bio-Rad. Images were acquired with the Azure Biosystems Aerogene 300Q imaging system. Densitometric quantification was performed using ImageJ software. After background subtraction, band intensities were normalized to the corresponding loading control β-ACTIN. Primary antibodies used were against PRKG1 (1:1000, Cell Signaling), anti-β-ACTIN (1:1000, Abcam), p-mTOR-Ser2448 (1:1,000, Cell Signaling), p-AMPKa-2270 Thr174 (1:1,000, Cell Signaling), p-PGC1a-Ser571 (1:1,000, Biotechne), p-4EBP-1 (1:1,000, Cell Signaling), PGC1a (1:1,000, Novus Bio), AMPKa (1:1,000, Cell Signaling), 4EBP-12272 (1:1,000, Cell Signaling), mTOR (1:1,000, Cell Signaling), anti-GAPDH (1:1,000, Abcam).

For MT-ATP6 immunoblotting, pooled NPCs (at least 1.5 x 10^6 NPCs) were homogenized in RIPA buffer and sonicated in an ultrasonic bath (Branson 1800-E) for 1 min, incubated in ice for 30 min and then centrifuged at 10,000 x g for 15 min at 4 °C. Protein concentration was determined with the Bicinchoninic Acid (BCA) protein assay kit (Thermo Fisher Scientific). 30 µg of proteins were run through a 4 % separating / 10 % resolving polyacrylamide gel with stain-free technology (Bio-Rad laboratories), to allow detection and quantification. Proteins were then electroblotted onto a PVDF membrane. After 1 h of blocking with 3 % BSA in TBS-Tween at RT, the membranes were incubated with the primary antibodies overnight at 4 °C and subsequently probed with HRP-conjugated secondary antibodies for 2 h at RT. Chemiluminescence-based immunostaining (SuperSignal West Pico PLUS Chemiluminescent Substrate, Thermo Fisher Scientific) was performed. Images were acquired with the ChemiDoc MP Imaging system. Data analysis and quantification was performed using Image Lab software, 6.1 (Bio-Rad Laboratories). The following primary antibody was used ATP6 (rabbit, 1:500, Immunological Science), with the appropriate secondary antibodies: anti-rabbit, HRP Conjugate (1:5000, Promega)

Mitochondrial complex assembly

For preparation of mitochondrial-enriched fractions for Blue Native PAGE, approximately 2 x 10^7 cells were resuspended in 400 µl of ice-cold Medium A (0.32 M sucrose, 10 mM Tris-HCl pH 7.4, 1 mM EDTA), homogenized in a glass/glass dounce homogenizer with a tight pestle by 10 strokes and centrifuged at 800 x g for 5 min at 4 °C to remove cell debris. Supernatants were collected and centrifuged at 9,000 x g for 10 min at 4 °C to obtain the enriched mitochondrial fractions and resuspended in 50 µl of cold Medium A to quantify the protein yield by Bicinchoninic Acid (BCA) protein assay Kit (Thermo Fisher Scientific). Samples were centrifuged again, resuspended in 1.5 M aminocaproic acid, 50 mM Bis-Tris/HCl pH 7, to a final protein concentration of 5 µg/µl, and solubilized with 1.6 µg of n-Dodecyl β-D-maltoside (DDM) per µg of protein, incubated on ice for 10 min and centrifuged at 16,000 x g for 30 min at 4 °C. Supernatants were collected, supplemented with 5 µl of Sample Buffer (750 mM aminocaproic acid, 50 mM Bis-Tris/HCl pH 7, 0.5 mM EDTA, and 5 % Serva Blue G-250) and stored at -80 °C until use.

For Blue Native Gel Electrophoresis (1D-BNGE) and 2D SDS-PAGE, about 40 µg of solubilized mitochondria were separated by pre-cast NativePAGE 3-12 % BisTris gels (Invitrogen) and run in a Mini Gel Tank (Thermo Fisher Scientific) at 4 °C. The upper buffer chamber was filled with Dark Blue Cathode buffer (50 mM Tricine, 15 mM Bis-Tris pH 7, 0.02 % Serva Blue G-250), and the lower buffer chamber with Anode buffer (50 mM Bis-Tris pH 7). Samples were run at 100 V for 30 min, then at 200 V. Dark Blue Cathode buffer was replaced with Light Blue Cathode Buffer (50 mM Tricine, 15 mM Bis-Tris pH 7, 0.002 % Serva Blue G-250) at half run.

Samples were then electroblotted onto a PVDF membrane and blocked for 1 h (3 % BSA in TBS-Tween) at RT before proceeding with the immunodetection. In 1D-BNGE, the antibody against ATP5B was used to visualize complex V holoenzyme and intermediate subassemblies; complex III (detected with antibody against UQCRFS1) was shown as loading control. Denaturing 2D-BNGE was used to confirm the presence of different subassemblies of complex V. For complex V and complex III visualization, we used antibodies against ATP5B (1:1,000, Sigma-Aldrich) and UQCRSF1 (1:1,000, Abcam). For 2D-PAGE, the gel strips of the 1D-BNGE were excised and covered with a denaturing solution (1 % SDS, 1 % β- Mercaptoethanol) for 1 h at RT. Each gel strip was run through a 4 % stacking / 10 % resolving polyacrylamide gel electrophoresis (Bio-Rad), electroblotted onto a PVDF membrane, and blocked for 1 h at RT with 3 % BSA in TBS-Tween. The following antibodies were used: ATP5B (1:1,000, Sigma-Aldrich), NDUFA9 (1:1,000, Invitrogen), and SDH-B (1:800, Abcam).

Quantitative polymerase chain reaction (qPCR)

Isolated total RNA was transcribed into complementary DNA (cDNA). Into a nuclease-free microcentrifuge tube, 1 μl of oligo $d(T)_{18}$ primers (Thermo Fisher Scientific), 1 μl of 10 mM dNTP mix (Thermo Fisher Scientific) and the respective volume of RNA solution that contained 1 μg RNA were filled up to 12 μl with RNase-free, distilled water. In the Mastercycler X50s (Eppendorf), the mixture was heated to 65 °C for 5 min and then quickly chilled on ice. 4 μl of 5 x First-Strand Buffer, 2 μl of 0.1M DTT and 1 μl of RNaseOUT (Invitrogen) were added to the tube, gently mixed and incubated at 37 °C for 2 min. 1 μl (200 units) of Moloney Murine Leukemia Virus Reverse Transcriptase (M-MLV RT) was added to the reaction tube and mixed. The reaction mixture was incubated for 50 min at 37 °C, and inactivated by heating at 70 °C for 15 min. For the qPCR reaction, the synthesized cDNA was mixed with 10 μM primer mix (primers designed with Integrated DNA technologies, Table S5) and SYBR™ Green PCR Master Mix (Applied Biosystems) diluted in water in a 96-well plate. The plate was transferred to CFX96™ Real-Time System qPCR machine (Bio-Rad) and the following program was started using CFX96 software: 2 min at 50 °C, 10 min at 95 °C, 39 x (15 s at 95 °C, 30 s at 62 °C, 30 s at 72 °C), 15 min at 95 °C, 5 s at 62 °C, and 50 s at 95 °C. To check the quality of the qPCR products, melting curves were assessed first. The obtained CT values were analyzed using the $2^{-\Delta\Delta CT}$ method. For this, the CT values of the genes of interest were subtracted from the CT values of the housekeeping genes Glyceraldehyde-3-phosphate dehydrogenase (*GAPDH*) and/or ornithine decarboxylase antizyme 1 (*OAZ1*). To investigate the differentiation ratio of brain organoids, we used SOX2/CTIP2 ratio. For this, the qPCR method was applied to RNA samples from each five pooled day 70 cortical brain organoids (CTRL_1, CTRL_2, ATP6_4, ATP6_7) with or without 10 μM sildenafil treatment for 24 hours.

Human blood-brain barrier (BBB) model

Control iPSCs (CTRL_8) and LS iPSCs (ATP6_2) were differentiated into brain capillary endothelial cells (BCECs) following previously described protocols.[149,150] Single cells were isolated using Accutase (Thermo Fisher Scientific) and seeded onto Matrigel-coated 6-well plates (Nunc™, Thermo Fisher Scientific) in 2 ml/well mTeSR™ Plus supplemented with 10 μM Y-27632 (STEMCELL Technologies). The starting cell number was optimized for both cell lines respectively. After 3 days, medium was changed to 2 ml/well unconditioned medium (UM) when the optimal cell density of 2 - 4 x 10^5 cells/cm^2 was reached (referred to as day 0). UM was composed of 78.5 % DMEM/F12 (Thermo Fisher Scientific), 20 % KnockOut serum replacement (Thermo Fisher Scientific), 1% MEM NEAA (Thermo Fisher Scientific), 0.5 % L-glutamine (Capricorn), and 0.1 mM β-mercaptoethanol (Thermo Fisher Scientific). UM was changed daily for the following five days to initiate co-differentiation of BCECs and neuronal cells. On day 6, medium was changed to 4 ml/well endothelial cell (EC) medium, composed of Human Endothelial-SFM (Thermo Fisher Scientific) and 0.5 % B27 Supplement (Thermo Fisher Scientific), supplemented with 20 ng/ml hFGF and 10 μM retinoic acid (RA) for BCEC expansion. On day 8, BCECs were dissociated using Accutase for 30 min and seeded at a cell density of 1 x 10^6 cell/cm^2 onto collagen IV/fibronectin-coated transwell membranes (0.4 μm pore size, 24-well format, Greiner) in EC medium supplemented with 20 ng/mL hFGF and 10 μM RA. BCECs were adapted to EC medium without hFGF and RA at day 9 for 24 h. We measured transendothelial electrical resistance (TEER) values using an electrode to evaluate the integrity of the in vitro BBB. Only BBBs with TEER values $\geq$ 1000 Ω*cm^2 at day 10 were included. To monitor monolayer integrity for both iPSC-derived BBB models, 10 μM sodium fluorescein (Sigma-Aldrich) was added to the apical compartment of two reference inserts for each BCEC differentiation. The intensity of the fluorescent tracer molecule was measured in pooled samples of both compartments respectively using a fluorescent plate reader (Infinite M1000 Pro, TECAN, excitation: 490 nm, emission: 525 nm). We applied 10 μM sildenafil, sildenafil citrate, or reference compounds in EC medium to the apical compartment of two inserts each and incubated the cells for 1 h at 37 °C, 5 % CO_2 on an orbital shaker (100 rpm). Diazepam and atenolol were used as internal controls given their known high and low BBB permeability, as previously demonstrated.[151,152] Media from both the apical (A) and basolateral (B) compartments were collected, pooled and stored at -80 °C until quantification. Peak areas were used to calculate the apparent permeability (*P*app) of each substance using equation:

$$Papp = \frac{\Delta Q}{\Delta t \times A\left(\frac{C_D + C_0}{2}\right) \times 10^6}$$

$$\Delta Q = Conc.\,receiver\,\Delta t$$

$$\Delta t = \textit{incubation time}$$

$$A = \textit{filter surface area}\left[\frac{cm^2}{well}\right]$$

$$C_D = \textit{Conc. donor}\,\Delta t$$

$$C_0 = \textit{Conc. donor}\ t_0$$

Quantification of sildenafil, diazepam and atenolol in apical and basolateral media samples was performed using LC-MS/MS. The settings were maintained except for minor adjustments. Chromatographic separation of atenolol (t_R = 3.5 min), sildenafil (t_R = 4.3 min) and diazepam (t_R = 5.5 min) was achieved with gradient elution within 10 min of total run-time. After positive electrospray ionization, the MS/MS detector recorded three mass transitions per drug compound (fragmentor voltage [FV] and collision energies [CE] in parentheses): Sildenafil: *m/z* 475.2 → 58.0 (FV: 220 V, CE: 68 eV, *quantifier*), *m/z* 475.2 → 100.0 (FV: 220 V, CE: 28 eV), *m/z* 475.2 → 283.1 (FV: 220 V, CE: 44 eV); Diazepam: *m/z* 285.1 → 154.1 (FV: 144 V, CE: 28 eV), *m/z* 285.1 → 193.1 (FV: 144 V, CE: 36 eV, *quantifier*), *m/z* 285.1 → 222.1 (FV: 144 V, CE: 28 eV) and Atenolol: *m/z* 267.2 → 56.0 (FV: 128 V, CE: 32 eV), *m/z* 267.2 → 74.1 (FV: 128 V, CE: 24 eV), *m/z* 267.2 → 144.9 (FV: 128 V, CE: 28 eV, *quantifier*). Peak areas were determined with MassHunter Quantitative Analysis software (version 10.1, Agilent Technologies) and the three drugs were quantified using matrix-matched external calibration in the concentration range of 0.001 to 10 μM.

iPSC-derived cardiomyocyte (iPSC-CMs)

iPSC-CMs lines were obtained through WNT signaling modulation followed by metabolic selection, as previously described.[153,154] The resulting iPSC-CMs were maintained under feeder-free, serum-free culture conditions until day 60 post-differentiation. Confirmation of iPSC-CM identity was performed by immunostaining against alpha-actinin (ACTN2) (Sigma-Aldrich) and mitochondria were visualized with MitoSpy (BioLegend).

To assess cell viability, 100,000 LS iPSC-CMs (ATP6_7) per well were seeded in 24-well plates. Following a seven-day period of recovery, sildenafil treatment (vehicle, 10 μM, 50 μM, 250 μM) was initiated and maintained for 24 h on alternate days by dilution in RPMI media. For imaging acquisition, the Calcein AM Viability Dye (Invitrogen) was dissolved in DMSO at 1 mg/ml, and applied at a final concentration of 1 μM in RPMI for 30 min at 37 °C. After incubation, cells were washed twice with 1 x DPBS. Propidium iodide (PI) (Invitrogen) was diluted in RPMI to 1.5 mM and administered at a final concentration of 500 nM. Imaging and analysis were performed using the Incucyte live-cell analysis system.

For Glycostress test, LS iPSC-CMs (ATP6_6 and ATP6_7) were seeded in 24-well Seahorse assay plates at a density of 100,000 cells/well ten days prior the experiment. A Glycostress test was used to evaluate glycolysis activity, following a previously established protocol.[155] One hour before assay initiation, the cell culture medium was replaced with glucose-free Agilent XF assay medium and iPSC-CMs were incubated for 20 min at 37 °C in the absence of CO_2. After three baseline acidification rate recordings, 10 mM of glucose was injected, followed by a sequential injection of 1 μM ATP synthase inhibitor oligomycin A, and 100 mM 2-deoxy-D-glucose. Measurements of extracellular acidification were obtained via a Seahorse XFe24 Analyzer. Total protein content served as normalization for oxygen consumption rate (OCR) in each well.

Computational modeling of calcium and bioenergetics

To determine the effect of impaired calcium signaling on mitochondrial function in LS, we applied a mathematical model that couples cytosolic calcium dynamics with mitochondrial function.[70] The cytosolic calcium equations were modified to incorporate calcium exchange between the cytoplasm and extracellular space through plasma membrane calcium ATPase (PMCA) and store-operated calcium channels (SOCC). In this model, both PMCA and sarcoplasmic/endoplasmic reticulum calcium ATPase (SERCA) fluxes depend on the ATP levels to capture the potential rise in cytosolic calcium due to reduced ATP levels in cells with *MT-ATP6* variants. Parameters used in the model are based on previous works[70,156–162] and listed in Table S2. We converted the calcium fluorescence traces from cBOS (Figure 4B) into corresponding cytosolic calcium concentration ($\left[Ca^{2+}\right]_c$) using the formula developed before.[163] That is,

$$\Delta\left[Ca^{2+}\right]_c = k_D\left(\frac{F_{max}}{F_0}\left(1-\frac{1}{R_F}\right)\frac{\Delta F}{(\Delta F_{max}-\Delta F)\Delta F_{max}}\right). \qquad \text{(Equation 1)}$$

Where $\Delta\left[Ca^{2+}\right]_c = \left[Ca^{2+}\right]_c - \left[Ca^{2+}\right]_0$ is the change in $\left[Ca^{2+}\right]_c$, $\left[Ca^{2+}\right]_0$ = 0.1 μM is the baseline cytosolic Ca^{2+} concentration, k_D = 0.2 mM in the dissociation constant for OBG-1 (used to label cytoplasmic calcium in cBOS), and $R_F = \frac{F_{max}}{F_{min}}$. F_{max} and F_{min} are the maximum and minimum fluorescent values in a trace, respectively. The instantaneous change in fluorescence is $\Delta F = F - F_0$, where F_0 = 0.01 is the baseline fluorescence. Finally, $\Delta F_{max} = F_{max} - F_0$ with F_{max} as the maximum fluorescence in the trace. To match the smaller timestep used in simulating mitochondrial bioenergetics, the time trace was interpolated. The resulting $\left[Ca^{2+}\right]_c$ traces were used for fitting the model to the observations in cells from MT-ATP6 and MT-ATP6 + Sil experiments. Rate equations for

$\left[Ca^{2+}\right]_c$, fraction of inactivated inositol 1,4,5-trisphsphate (IP_3) receptors (R_i), mitochondrial Ca^{2+} ($[Ca^{2+}]_m$), NADH ($[NADH]_m$), ADP ($[ADP]_m$), MMP ($[\Delta\psi]$), and cytosolic ADP ($[ADP]_c$) were adopted from Wacquier et al.[70] and Csordás et al.[164] The equation for $\left[Ca^{2+}\right]_c$ was modified to incorporate the effect of PMCA and SOCC entry from the extracellular space. These equations were solved in MATLAB 2023b using ode15s method, and are given as:

$$\frac{d\left[Ca^{2+}\right]_c}{dt} = f_c(\alpha J_{IP3} - J_{SERCA} - J_{PMCA} + J_{SOCC} + J_{SERCA} - \delta J_{MCU} - \delta J_{NCX} - \delta J_X) \quad \text{(Equation 2)}$$

$$\frac{dR_i}{dt} = k^+\left[Ca^{2+}\right]_c^{n_i}\left(\frac{1 - R_i}{1+\left(\frac{\left[Ca^{2+}\right]_c}{K_a}\right)^{n_a}}\right) - k^- R_i \quad \text{(Equation 3)}$$

$$\frac{d\left[Ca^{2+}\right]_m}{dt} = f_m(J_{MCU} - J_{NCX} + J_X), \quad \text{(Equation 4)}$$

$$\frac{d[NADH]_m}{dt} = J_{PDH} + J_{AGC} - J_o, \quad \text{(Equation 5)}$$

$$\frac{d[ADP]_m}{dt} = J_{ANT} - J_{F1F0}, \quad \text{(Equation 6)}$$

$$\frac{d[ADP]_c}{dt} = J_{HYD} - \delta J_{ANT}, \quad \text{(Equation 7)}$$

$$\frac{d\Delta\psi}{dt} = \frac{1}{c_{mito}}\left(b_1 J_O - b_2 J_{F1F0} - J_{ANT} - J_{H,LEAK} - J_{NCX} - 2J_{MCU} - 2J_X - J_{AGC}\right). \quad \text{(Equation 8)}$$

Where Ca^{2+} fluxes from the endoplasmic reticulum (ER) to the cytoplasm through IP_3 receptors (J_{IP3}), from the cytoplasm to the ER through SERCA (J_{SERCA}), from the cytoplasm to the extracellular space (ECS) through PMCA (J_{PMCA}), from the ECS to the cytoplasm through SOCC (J_{SOCC}), from the cytoplasm to mitochondria through mitochondrial calcium uniporter (MCU) (J_{MCU}), and from mitochondria to the cytoplasm through Na^+/Ca^{2+} exchangers (NCX) (J_{NCX}) are given as:

$$J_{IP3} = v_{IP3}(b_{IP3} + IR_a)\left(\left[Ca^{2+}\right]_{er} - \left[Ca^{2+}\right]_c\right), \quad \text{(Equation 9)}$$

$$IR_a = (1 - R_i)\left(\frac{IP_3^2}{K_i^2 + IP_3^2}\right)\left(\frac{\left[Ca^{2+}\right]_c^{na}}{K_a^{na} + \left[Ca^{2+}\right]_c^{na}}\right). \quad \text{(Equation 10)}$$

We modeled metabolic stress by a rise in IP_3 concentration through the phospholipase C (PLC) pathway due to the rise in glutamate during metabolic stress, which is formulated by equation (11). Metabolic stress also impairs the fluxes through PMCA and SERCA through a decrease in $[ATP]_c$, which is already incorporated in their respective equations. One can also model metabolic stress by decreasing the rate at which NADH is oxidized in the electron transport chain (ETC) (and/or decreasing the rate of glycolytic pathway and other complexes in ETC) by itself or in combination with a rise in IP_3 concentration. However, using this later approach does not change the conclusions from the model.

$$IP_3 = a_{01}\left(\frac{1}{e^{\frac{470-(t-t_{stim})}{10}}+1} + \frac{3.5}{e^{\frac{450-(t-300-t_{stim})}{40}}+1}\right)e^{\frac{-(t-t_{stim})}{100}}, \quad \text{(Equation 11)}$$

$$\left[Ca^{2+}\right]_{er} = \frac{f_{ER}}{\propto}\left(C_{tot} - \frac{\left[Ca^{2+}\right]_c}{f_c} - \frac{\delta\left[Ca^{2+}\right]_m}{f_m}\right), \quad \text{(Equation 12)}$$

$$J_{SERCA} = v_P \frac{\left[Ca^{2+}\right]_c^2}{K_P^2 + \left[Ca^{2+}\right]_c^2} \frac{[ATP]_c}{K_e + [ATP]_c}. \quad \text{(Equation 13)}$$

$$J_{PMCA} = v_{PMCA} \left(\frac{\left[Ca^{2+}\right]_c^2}{0.25 + \left[Ca^{2+}\right]_c^2} \right) \left(\frac{[ATP]_c}{300 + [ATP]_c} \right), \quad \text{(Equation 14)}$$

$$J_{SOCC} = v_{SOCC} \frac{K_{SOCC}^4}{K_{SOCC}^4 + \left[Ca^{2+}\right]_{ER}^4}, \quad \text{(Equation 15)}$$

$$J_{MCU} = v_{MCU} \frac{\frac{\left[Ca^{2+}\right]_c}{K_1} \left(1 + \frac{\left[Ca^{2+}\right]_c}{K_1}\right)^3}{\left(1 + \frac{\left[Ca^{2+}\right]_c}{K_1}\right)^4 + \frac{L}{\left(1 + \frac{\left[Ca^{2+}\right]_c}{K_2}\right)^{2.3}}} e^{p_1 \Delta\psi}, \quad \text{(Equation 16)}$$

$$J_{NCX} = v_{NCX} \left(\frac{\left[Ca^{2+}\right]_m}{\left[Ca^{2+}\right]_c} \right) e^{p_2 \Delta\psi} \quad \text{(Equation 17)}$$

The additional Ca^{2+} flux (J_x) was added to capture the many experimental results, and particularly the observations that mitochondrial Ca^{2+} does not drop to zero in MCU knocked-down cells.[70,164]

$$J_x = v_x \left(\left[Ca^{2+}\right]_c - \left[Ca^{2+}\right]_m \right) e^{p_3 \Delta\psi}. \quad \text{(Equation 18)}$$

The effects of pyruvate dehydrogenase (PDH)-catalyzed reaction, glycolytic pathway (v_{GLY}), and the TCA cycle (reduction of $[NAD^+]_m$ into NADH) is formulated as:

$$J_{PDH} = v_{GLY} \frac{1}{q_1 + \frac{[NADH]_m}{[NAD^+]_m}} \frac{\left[Ca^{2+}\right]_m}{q_2 + \left[Ca^{2+}\right]_m}, \quad \text{(Equation 19)}$$

The aspartate-glutamate carrier (AGC) is part of MAS NADH shuttle system defined as:

$$J_{AGC} = v_{AGC} \frac{\left[Ca^{2+}\right]_c}{K_{AGC} + \left[Ca^{2+}\right]_c} \frac{q_2}{q_2 + \left[Ca^{2+}\right]_m} e^{p_4 \Delta\psi}. \quad \text{(Equation 20)}$$

The rate at which NADH is oxidized in the ETC and the rate at which protons are extruded from the mitochondria are combined into one equation as:

$$J_O = v_O \frac{[NADH]_m}{q_3 + [NADH]_m} \left(1 + e^{\frac{\Delta\psi - q_4}{q_5}}\right)^{-1}. \quad \text{(Equation 21)}$$

The activity of adenine nucleotide translocator (ANT) in electrogenic exchange of ATP or ADP across the inner mitochondrial membrane is given by:

$$J_{ANT} = v_{ANT} \frac{1 - \left(\frac{\alpha_c}{\alpha_m}\right)\left(\frac{[ATP]_c}{[ADP]_c}\right)\left(\frac{[ADP]_m}{[ATP]_m}\right) e^{-\frac{F\Delta\psi}{RT}}}{\left(1 + \alpha_c \frac{[ATP]_c}{[ADP]_m} e^{-0.5\frac{F\Delta\psi}{RT}}\right)\left(1 + \frac{[ADP]_m}{\alpha_m [ATP]_m}\right)}, \quad \text{(Equation 22)}$$

where $\propto_c$ and $\propto_m$ denote the fact that only a fraction of nucleotides has access to the transporter. The dependence of the membrane potential is due to the negatively charged ADP and ATP. The rate of ATP synthesis by F_1F_0 ATPase is modeled as:

$$J_{F1F0} = v_{F1F0}\left(\frac{q_6}{q_6+[ATP]_m}\right)\left(1+e^{\frac{q_7-\Delta\psi}{q_8}}\right)^{-1}. \quad \text{(Equation 23)}$$

J_{HYD} represents the rate of ATP consumption (ATP hydrolysis) in the cytosol. The first term encodes the link between Ca^{2+} activity and ATP consumption in the cytosol whereas the second term captures ATP-consuming processes in the cytosol.

$$J_{HYD} = \frac{J_{SERCA}}{2}+\frac{J_{PMCA}}{2}+v_{HYD}\frac{[ATP]_c}{K_h+[ATP]_c}. \quad \text{(Equation 24)}$$

The Ohmic mitochondrial proton leak is given as:

$$J_{H,LEAK} = q_9\Delta\psi+q_{10}. \quad \text{(Equation 25)}$$

Finally, the total NADH, ADP, and ATP in the mitochondria and cytosol are given by conservation equations. That is:

$$[NADH]_m + [NAD^+]_m = [NAD]_m^{TOT}, \quad \text{(Equation 26)}$$

$$[ADP]_m + [ATP]_m = [A]_m^{TOT}, \quad \text{(Equation 27)}$$

$$[ADP]_c + [ATP]_c = [A]_c^{TOT}. \quad \text{(Equation 28)}$$

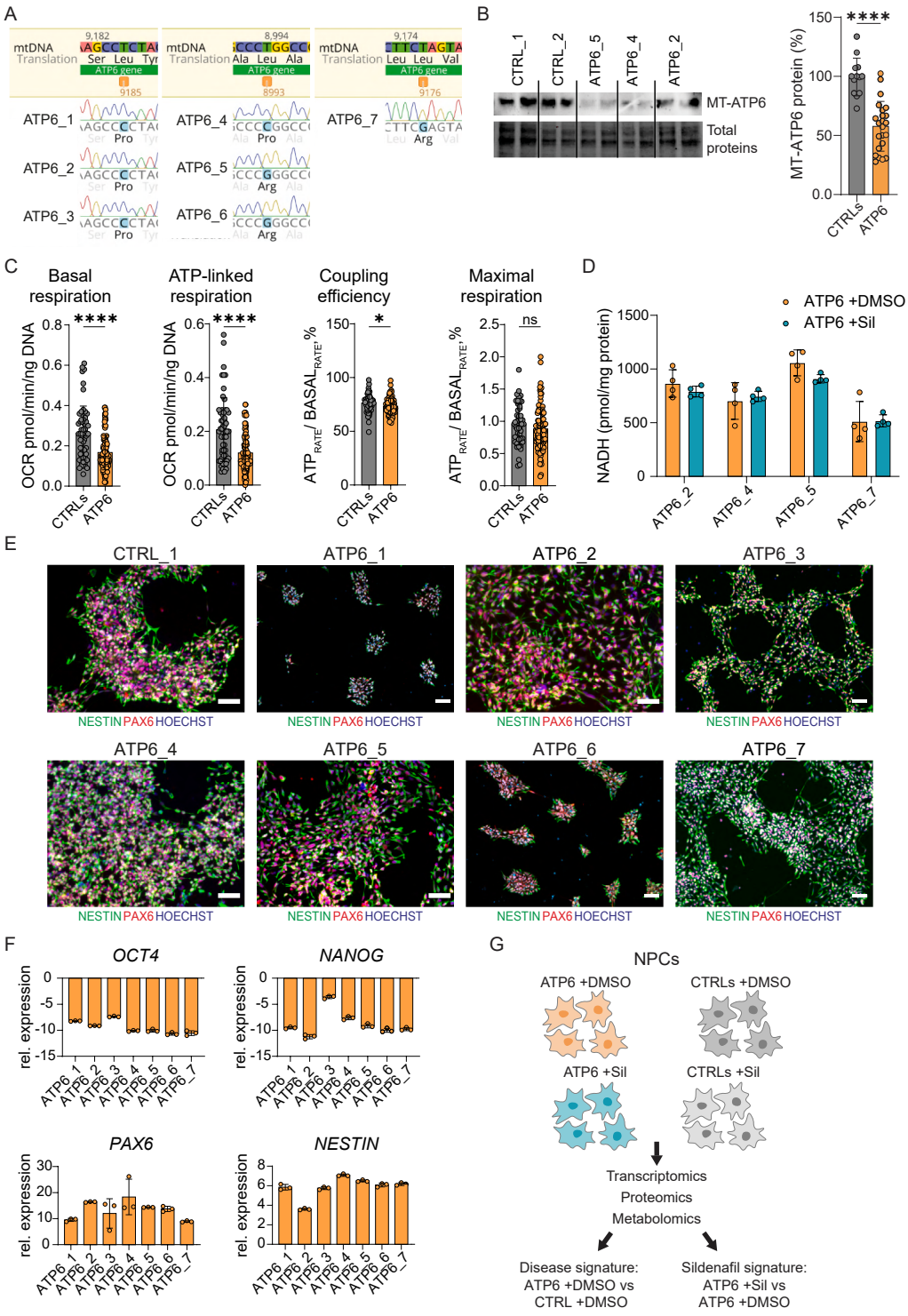
For global sensitivity analysis, we computed the first-order and total-order Sobol′ sensitivity indices following previous estimators[165,166] using Sobol-sequence sampling[167] including: resting value, amplitude value under metabolic stress (peak value – resting value), and full duration at half maximum (FDHM) value (the duration for which a variable is above (peak value – resting value) / 2). We modulated the key 8 parameters related to cytosolic calcium and mitochondrial bioenergetics: maximum rate of F_1F_0 ATPase activity (v_{F1F0}), glycolysis (v_{GLY}), adenine nucleotide translocator (v_{ANT}), NADH production via aspartate-glutamate carrier (v_{AGC}), NADH oxidation in ETC (v_O), plasma membrane calcium ATPase (v_{PMCA}), sarcoplasmic/endoplasmic reticulum calcium ATPase (v_{SERCA}), and of IP_3 receptors (v_{IP3R}). The model outputs were not very sensitive to other parameters and are therefore not presented. These 8 parameters were varied to analyze their effect on the 6 core variables: $[Ca^{2+}]_c$ (cytosolic calcium), $[Ca^{2+}]_c$ (mitochondrial calcium), $[NADH]_m$ (mitochondrial NADH), MMP, $[ATP]_m$ (mitochondrial ATP), $[ATP]_c$ (cytosolic ATP). In total, we delivered 18 model outputs from 81,920 model runs. In the generated graphs for the global sensitivity analysis (Figure S9A), the bullet size represents the significance of the effect of a parameter on a given model output (larger bullet means changing the parameter affects the output more) and the thickness of the edge indicates the significance of the interaction between the two parameters on the model output (thicker edge means changing the two parameters simultaneously affect the output more).

QUANTIFICATION AND STATISTICAL ANALYSIS

We analyzed the data using GraphPad-Prism software and employed the R environment for statistical computing. For all datasets, we tested the normality of the distribution using GraphPad-Prism (D'Agostino-Pearson test for large sample sizes and Shapiro-Wilk test for sample sizes under 50). After having performed outlier test analyses, we assessed statistical significance using parametric tests for normally distributed data (Student's *t* test, ANOVA) and non-parametric tests when normal distribution could not be verified (Mann-Whitney U and Kruskal-Wallis test). When possible, data are presented as scatter plots with individual data points showing all individual measurements. Unless otherwise indicated, we expressed the data as mean and standard deviation (mean ± SD). Experiments were repeated in independent biological experiments. Information on statistical details and number of replicates can be found in the respective figure legends. Figures were prepared with Adobe Illustrator.

CellPress
OPEN ACCESS

Supplemental figures



(legend on next page)

Figure S1. Generation of LS NPCs, related to Figures 1 and 2

(A) Genotyping of LS NPCs.

(B) Representative immunoblot and related quantification of MT-ATP6 protein expression in control NPCs and LS NPCs representing the four *MT-ATP6* variants (ATP6_2 for m.9176T>C, ATP6_4 for m.8993T>C, ATP6_5 for m.8993T>G, and ATP6_7 for m.9176T>G). $n = 3$ independent experiments. $^{****}p < 0.0001$; unpaired two-tailed *t* test.

(C) Seahorse-based bioenergetic profile of control NPCs (CTRL_1 and CTRL_2) and LS NPCs (ATP6_2, ATP6_4, ATP6_5, and ATP6_7). $n = 3$ independent experiments. Mean ± SD, $^{****}p < 0.0001$, $^{*}p < 0.05$; unpaired two-tailed *t* test.

(D) NADH quantification in LS NPCs treated with DMSO or 10 μM sildenafil for 16 h ($n = 3$ independent biological replicates per sample).

(E) Representative immunostaining of LS NPCs. Scale bar: 50 μm.

(F) qPCR analysis showing downregulation of iPSC markers *OCT4* and *NANOG*, and upregulation of NPC markers *NESTIN* and *PAX6* in LS NPCs compared with their respective LS iPSC lines. Mean $\log_2$ ratios (mean ± SD) in relation to control iPSCs (CTRL_1).

(G) Schematic of omics setup in control NPCs (CTRL_1, CTRL_2, CTRL_3, and CTRL_4) and LS NPCs (ATP6_2, ATP6_4, ATP6_5, and ATP6_7) to dissect the disease signature and sildenafil signature.

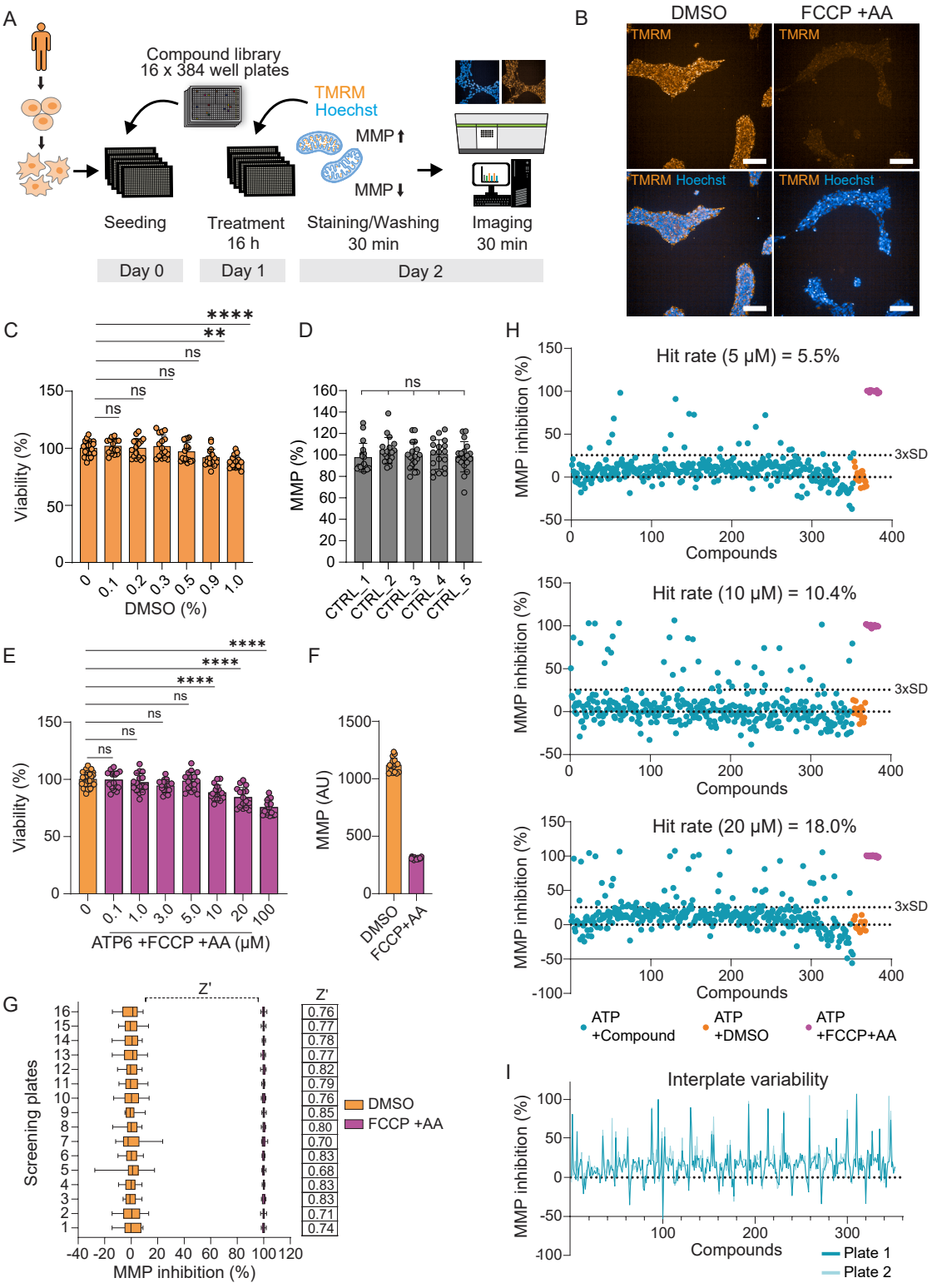


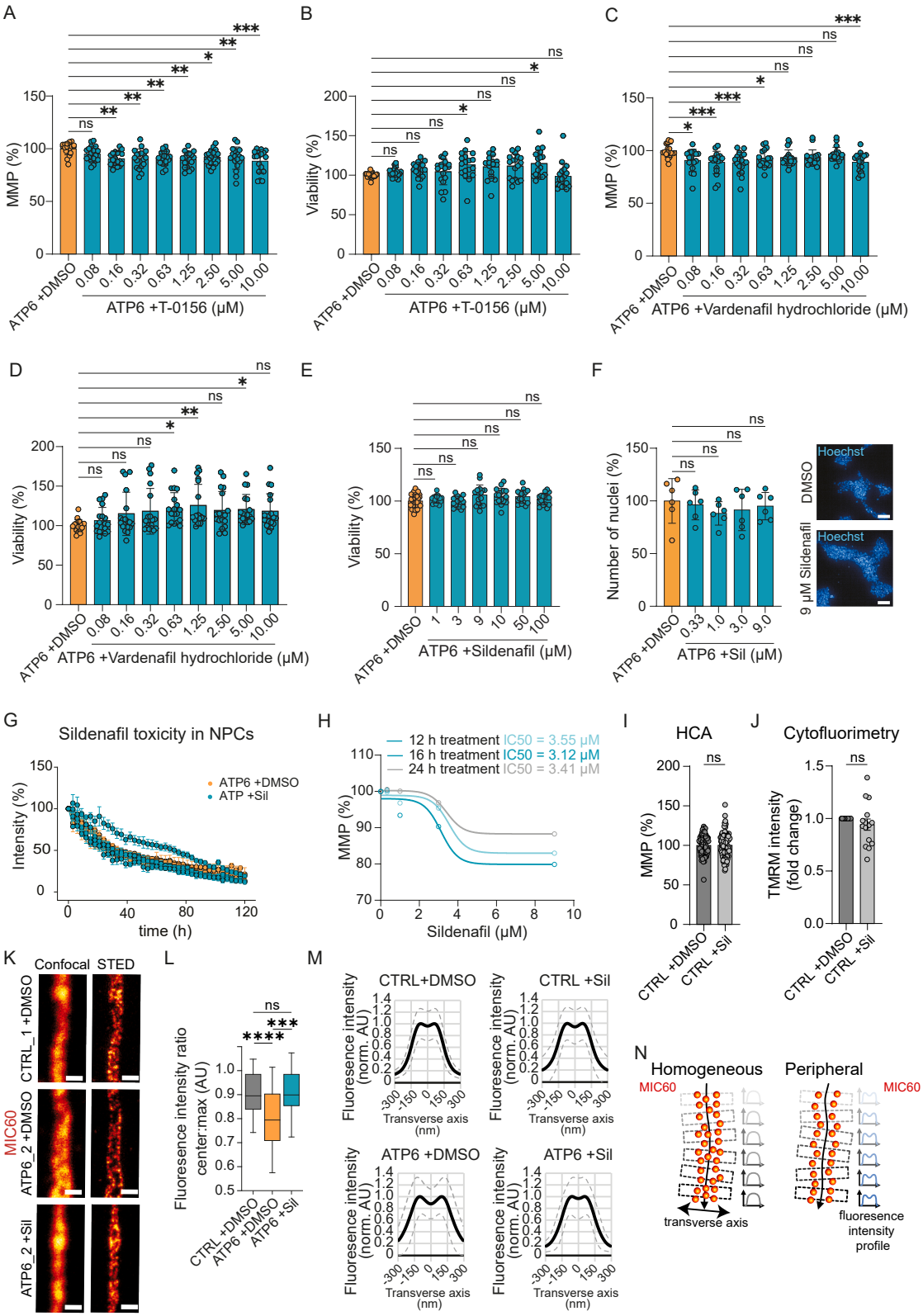
Figure S2. Compound screening in LS NPCs, related to Figure 1

(A) Compound screening workflow in LS NPCs.

(B) Representative images of LS NPCs (ATP6_2) treated with DMSO or 5 μM carbonyl cyanide-p-trifluoromethoxyphenylhydrazone (FCCP) and 5 μM antimycin A (AA) and live-cell stained with TMRM and Hoechst. Scale bar: 100 μm.

(legend continued on next page)

(C) Cell viability in LS NPCs (ATP6_2). Dots: mean value/well. $^{**}p < 0.01$, $^{****}p < 0.0001$; ordinary one-way ANOVA with Dunnett's multiple comparisons.
(D) HCA MMP in control NPC lines. Dots: mean value/well, $n = 3$ independent experiments; ordinary one-way ANOVA with Dunnett's multiple comparisons.
(E) Cell viability in LS NPCs (ATP6_2) after 16 h treatment with increasing FCCP + AA concentrations, normalized to DMSO (0 value). Dots: mean value/well. $^{****}p < 0.0001$; ordinary one-way ANOVA with Dunnett's multiple comparisons.
(F) HCA MMP in LS NPCs (ATP6_2) treated for 16 h with either 0.05% DMSO or 5 μM FCCP + AA. Dots: mean value/well.
(G) HCA MMP in LS NPCs (ATP6_2) in independent screening plates showing stability of Z′ factor.
(H) Screening tests with 16 h treatment of 352 compounds in LS NPCs (ATP6_2). Blue dots: compounds in DMSO; orange dots: DMSO only; purple dots: 5 μM FCCP + AA as positive controls. Upper dotted line: 3 × SD.
(I) HCA MMP in LS NPCs (ATP6_2) with 352 compounds (10 μM after 16 h) in different screening plates.



(legend on next page)

Figure S3. PDE5i compounds normalize MMP in LS NPCs, related to Figure 1

(A–D) HCA MMP and cell viability of LS NPCs (ATP6_2) treated with T-0156 or vardenafil hydrochloride compared with DMSO. Dots: mean value/well, $n = 3$ independent experiments. $^{*}p < 0.05$, $^{**}p < 0.01$, $^{***}p < 0.001$; ordinary one-way ANOVA with Dunnett's multiple comparisons.

(E) Cell viability of LS NPCs (ATP6_2) treated with sildenafil ($n = 16$ replicates) compared with DMSO ($n = 31$ replicates); ordinary one-way ANOVA with Dunnett's multiple comparisons.

(F) HCA Hoechst staining in LS NPCs (ATP6_2) treated with sildenafil. Dots: mean value/well; ordinary one-way ANOVA with Dunnett's multiple comparisons. Scale bar: 100 μm.

(G) Proliferation-based toxicity in LS NPCs (ATP6_2, ATP6_4, ATP6_5, and ATP6_7) treated with 0.1% DMSO (orange) or 10 μM sildenafil in 0.1% DMSO (cyan). Dots: individual signal for each line, $n = 3$ independent experiments.

(H) IC_{50} values in LS NPCs (ATP6_2) treated with sildenafil. Dots: mean value/well.

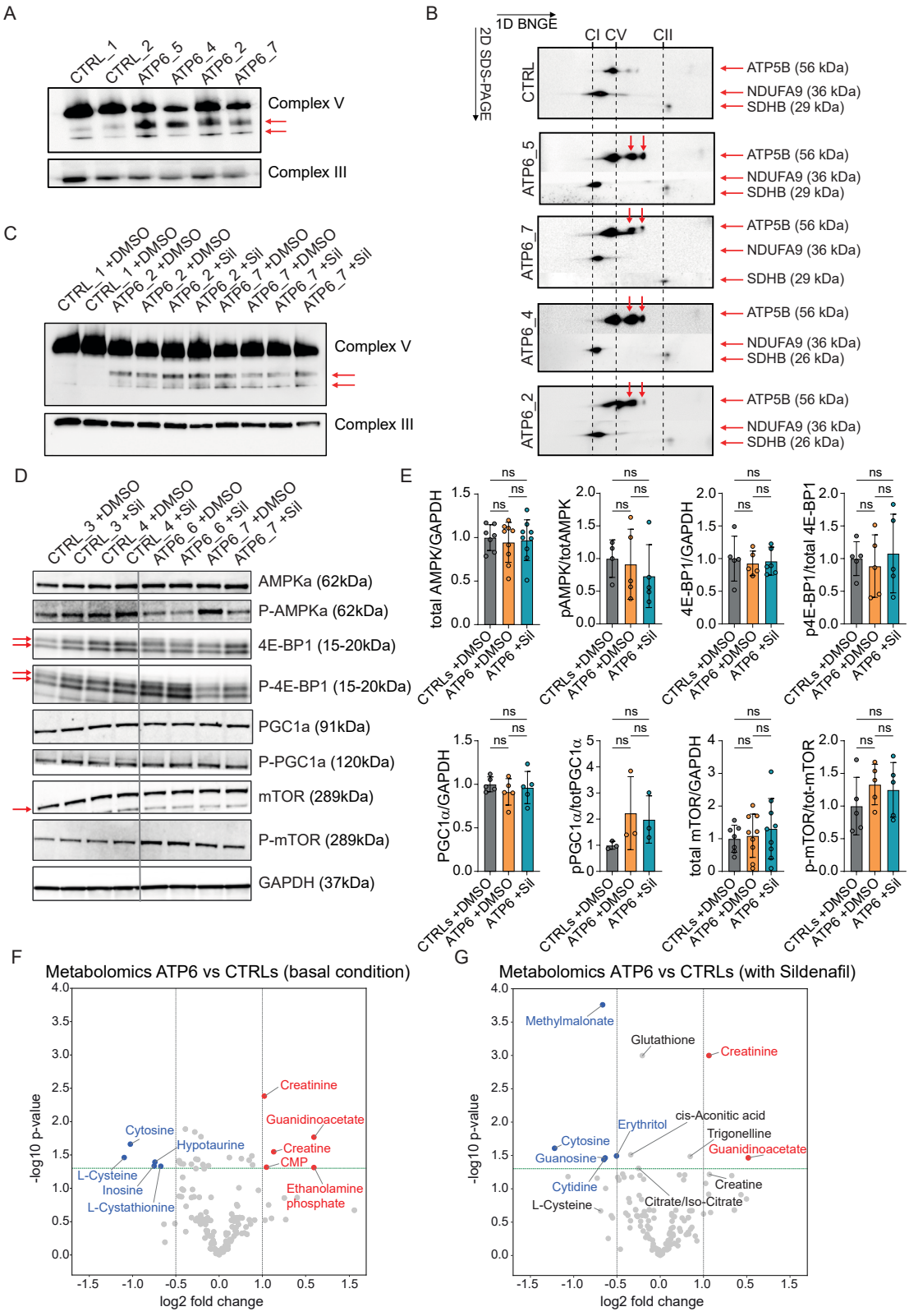
(I and J) HCA MMP and cytofluorimetry MMP in control NPCs (CTRL_1) treated with 10 μM sildenafil for 16 h.

(K) Representative images of MIC60 in control NPCs (CTRL_1) and LS NPCs (ATP6_2) treated with DMSO or 1 μM sildenafil for 24 h. Scale bar: 500 nm.

(L) MIC60 central fluorescence intensity over maximal intensity recorded with STED microscopy for the transversal profiles shown in (M). $^{***}p < 0.001$, $^{****}p < 0.0001$; ordinary one-way ANOVA with Dunnett's multiple comparisons.

(M) MIC60 average fluorescence intensity profiles (black lines) across the transverse axis of mitochondria recorded with STED microscopy in control NPCs (CTRL_1) and LS NPCs (ATP6_2) treated with DMSO or 1 μM sildenafil for 24 h. Dashed lines: SD.

(N) Distribution pattern of MIC60 in mitochondrial cristae in control NPCs and sildenafil-treated LS NPCs (homogeneous distribution) compared with DMSO-treated LS NPCs (peripheral distribution).



(legend on next page)

Figure S4. Effects of sildenafil on mitochondrial metabolism, related to Figures 1 and 2

(A) 1D-blue native gel electrophoresis (BNGE) images of n-dodecyl β-D-maltoside (DDM)-treated mitochondrial fraction of control NPCs and LS NPCs. ATP5B antibody: CV holoenzyme and intermediate subassemblies; UQCRFS1 antibody: complex III as loading control. *n* = at least 3 independent experiments.

(B) 2D-BNGE of samples in (A). Red arrows: subassembly forms. *n* = at least 3 independent experiments.

(C) 1D-BNGE images of DDM-treated mitochondrial fraction of control NPCs and LS NPCs treated with DMSO or 10 μM sildenafil for 16 h. ATP5B antibody: CV holoenzyme and intermediate subassemblies (red arrows).

(D) Representative immunoblot of control NPCs (CTRL_3 and CTRL_4) and LS NPCs (ATP6_6 and ATP6_7) treated with DMSO or 10 μM sildenafil for 16 h. UQCRFS1 antibody: complex III as loading control. *n* = at least 3 independent experiments.

(E) Quantification of immunoblot in (D), *n* = 3 independent experiments. Mean ± SD; one-way ANOVA with Tukey's multiple comparisons.

(F and G) Volcano plots of metabolomics depicting upregulated metabolites (red) and downregulated metabolites (blue) in LS NPCs (ATP6_2, ATP_4, ATP6_5, and ATP6_7), compared with control NPCs (CTRL_1, CTRL_2, CTRL_3, and CTRL_4), treated with DMSO or 10 μM sildenafil for 16 h.

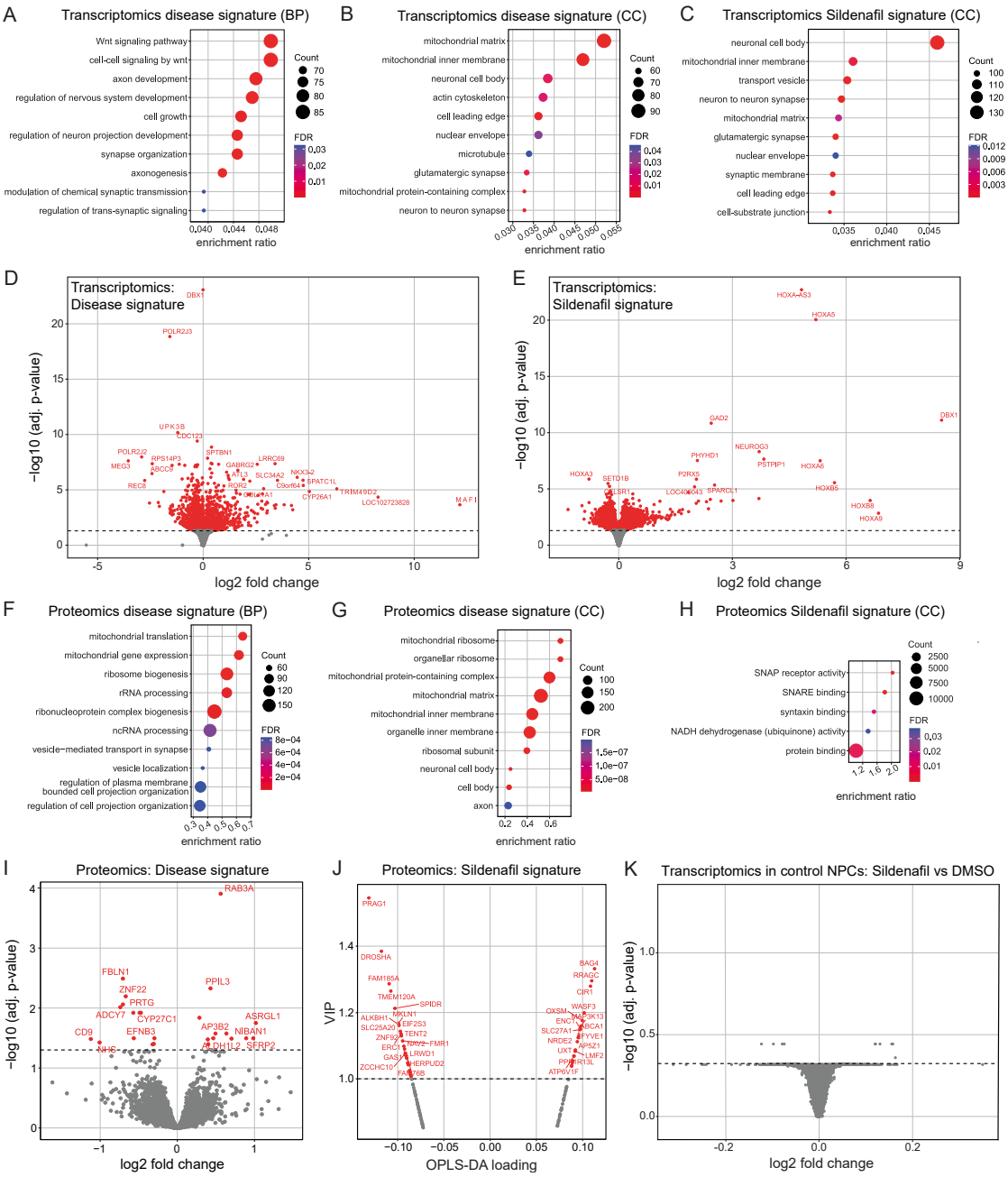


Figure S5. Disease signature and sildenafil signature revealed by multi-omics, related to Figure 2

(A and B) Top-ten Gene Ontology (GO) biological processes (BPs) and cellular components (CCs) in LS NPCs (ATP6_2, ATP_4, ATP6_5, and ATP6_7) compared with control NPCs (CTRL_1, CTRL_2, CTRL_3, and CTRL_4) based on transcriptomics.

(C) Top-ten GO CC in LS NPCs (ATP6_2, ATP_4, ATP6_5, and ATP6_7) treated with sildenafil for 16 h compared with DMSO based on transcriptomics.

(D and E) Differentially expressed genes (DEGs) (red dots) in LS NPCs (ATP6_2, ATP_4, ATP6_5, and ATP6_7) compared with control NPCs (CTRL_1, CTRL_2, CTRL_3, and CTRL_4) and in LS NPCs (ATP6_2, ATP_4, ATP6_5, and ATP6_7) treated with sildenafil compared with DMSO.

(F and G) Top-ten GO BP and GO CC in LS NPCs (ATP6_2, ATP_4, ATP6_5, and ATP6_7) compared with control NPCs (CTRL_1, CTRL_2, CTRL_3, and CTRL_4) based on proteomics.

(H) Top-ten enriched GO CC in LS NPCs (ATP6_2, ATP_4, ATP6_5, and ATP6_7) treated with sildenafil for 16 h compared with DMSO based on proteomics.

(I) Differentially expressed proteins (DEPs) (red dots) in LS NPCs (ATP6_2, ATP_4, ATP6_5, and ATP6_7) compared with control NPCs (CTRL_1, CTRL_2, CTRL_3, and CTRL_4).

(J) DEPs (red dots) in LS NPCs (ATP6_2, ATP_4, ATP6_5, and ATP6_7) treated with sildenafil compared with DMSO using the machine-learning classifier OPLS-DA.

(K) Bulk transcriptomics of control NPCs (CTRL_1, CTRL_2, CTRL_3, and CTRL_4) treated with sildenafil compared with DMSO.

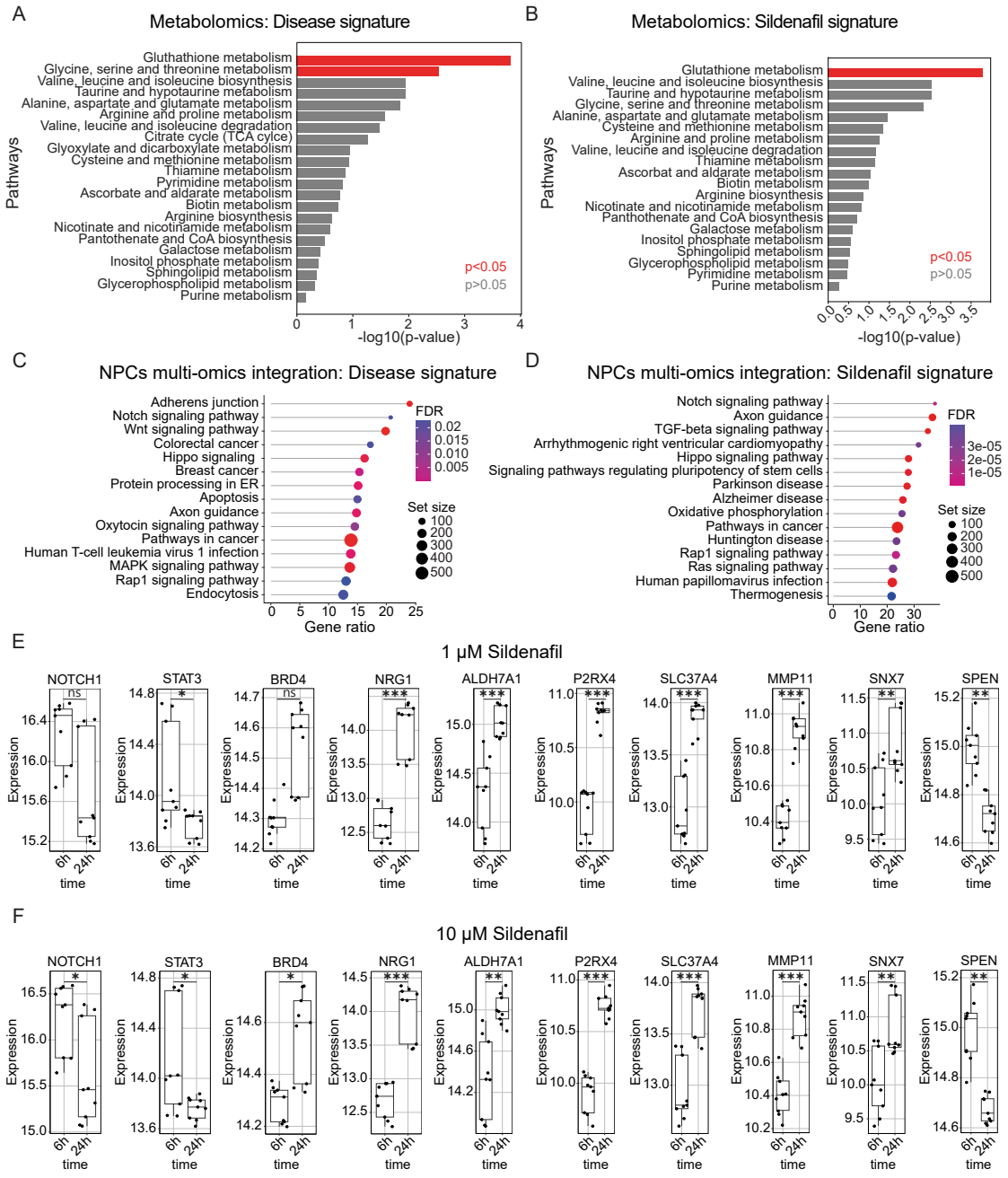


Figure S6. Metabolic signature of LS NPCs and multi-omics integration, related to Figure 2

(A and B) Altered metabolic pathways (red) and identified metabolic pathways (gray) in LS NPCs (ATP6_2, ATP_4, ATP6_5, and ATP6_7) compared with control NPCs (CTRL_1, CTRL_2, CTRL_3, and CTRL_4) (disease signature) and in LS NPCs treated with 10 μM sildenafil for 16 h compared with DMSO (sildenafil signature). One-way ANOVA with FDR adjustment for multiple comparisons ($p < 0.05$).

(C and D) Multi-omics integration: Kyoto Encyclopedia of Genes and Genomes (KEGG) pathways in LS NPCs compared with control NPCs (disease signature) or in LS NPCs treated with sildenafil compared with DMSO (sildenafil signature).

(E and F) Expression of putative sildenafil-responsive genes based on bulk transcriptomics of LS NPCs (ATP6_2, ATP6_4, ATP6_5, and ATP6_7) treated for 6 h or 24 h with 1 μM sildenafil (E) or with 10 μM sildenafil (F) compared with DMSO-treated LS NPCs. *y* axis: variance-stabilized counts obtained with DESeq2's vst() function; *p* values: computed with DESeq2 comparing expression levels at 24 h vs. 6 h, adjusted using Benjamini-Hochberg method.

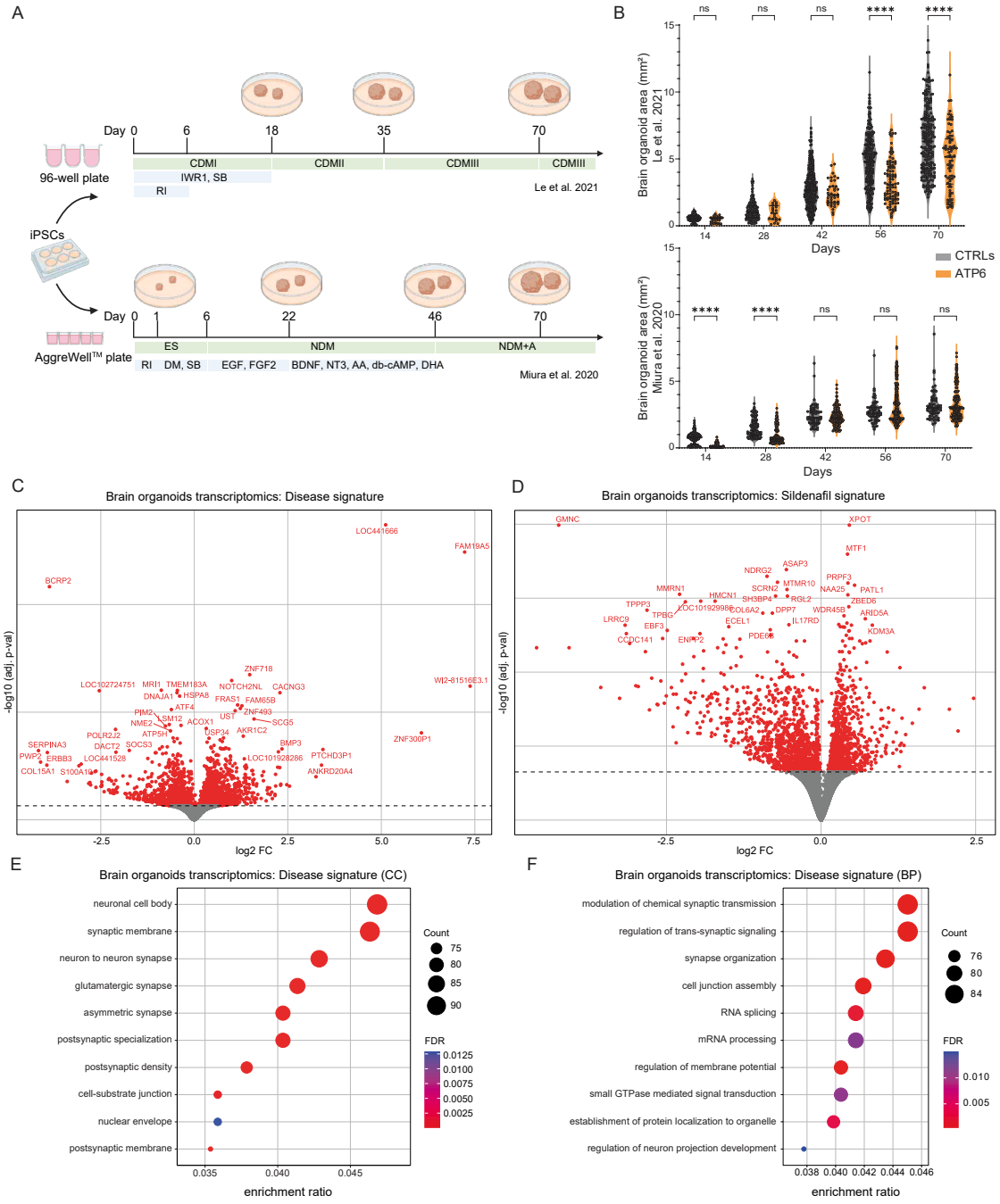


Figure S7. Brain organoid models of LS, related to Figure 3

(A) Schematic of the brain organoid protocols used: Le et al. with 96-well plates[62] or Miura et al. with AggreWells plates.[63]

(B) Size quantification of individual brain organoids grown following the two protocols until day 70. ****$p < 0.0001$; two-tailed Mann-Whitney U test.

(C and D) DEG (red dots) in day 70 LS brain organoids (ATP6_2 and ATP6_7) compared with control brain organoids (CTRL_1 and CTRL_2) and in day 70 LS brain organoids (ATP6_2 and ATP6_7) treated with 10 μM sildenafil for 24 h compared with DMSO.

(E and F) Top-ten GO BP and GO CC in day 70 LS brain organoids (ATP6_2 and ATP6_7) compared with control brain organoids (CTRL_1 and CTRL_2) based on bulk transcriptomics.

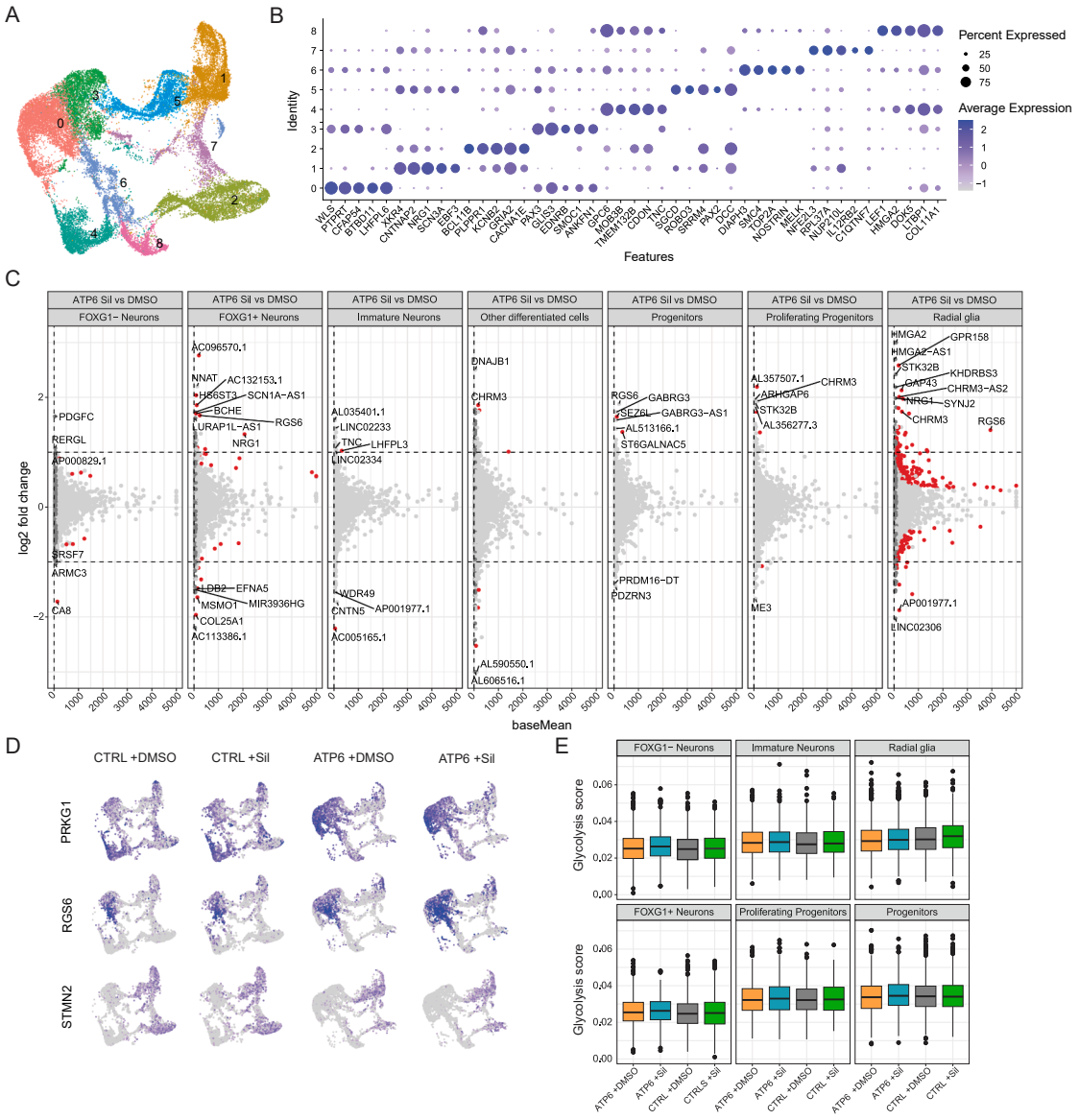


Figure S8. snRNA-seq of LS brain organoids, related to Figure 3

(A) Uniform manifold approximation and projection (UMAP) representation of 9 clusters in day 70 cortical brain organoids.

(B) Dot plot featuring five representative genes for each of the 9 clusters present in day 70 cortical brain organoids.

(C) DEG (red dots) in day 70 LS brain organoids (ATP6_7) treated with 10 μM sildenafil for 45 days compared with DMSO based on pseudo-bulk analysis of snRNA-seq.

(D) Expression distribution of *PRKG1*, *RGS6*, and *STMN2* in day 70 brain organoids from controls (CTRL_1) and LS (ATP6_7) treated with sildenafil or DMSO for 45 days.

(E) Molecular signatures database hallmark GLY score across the populations of day 70 brain organoids.

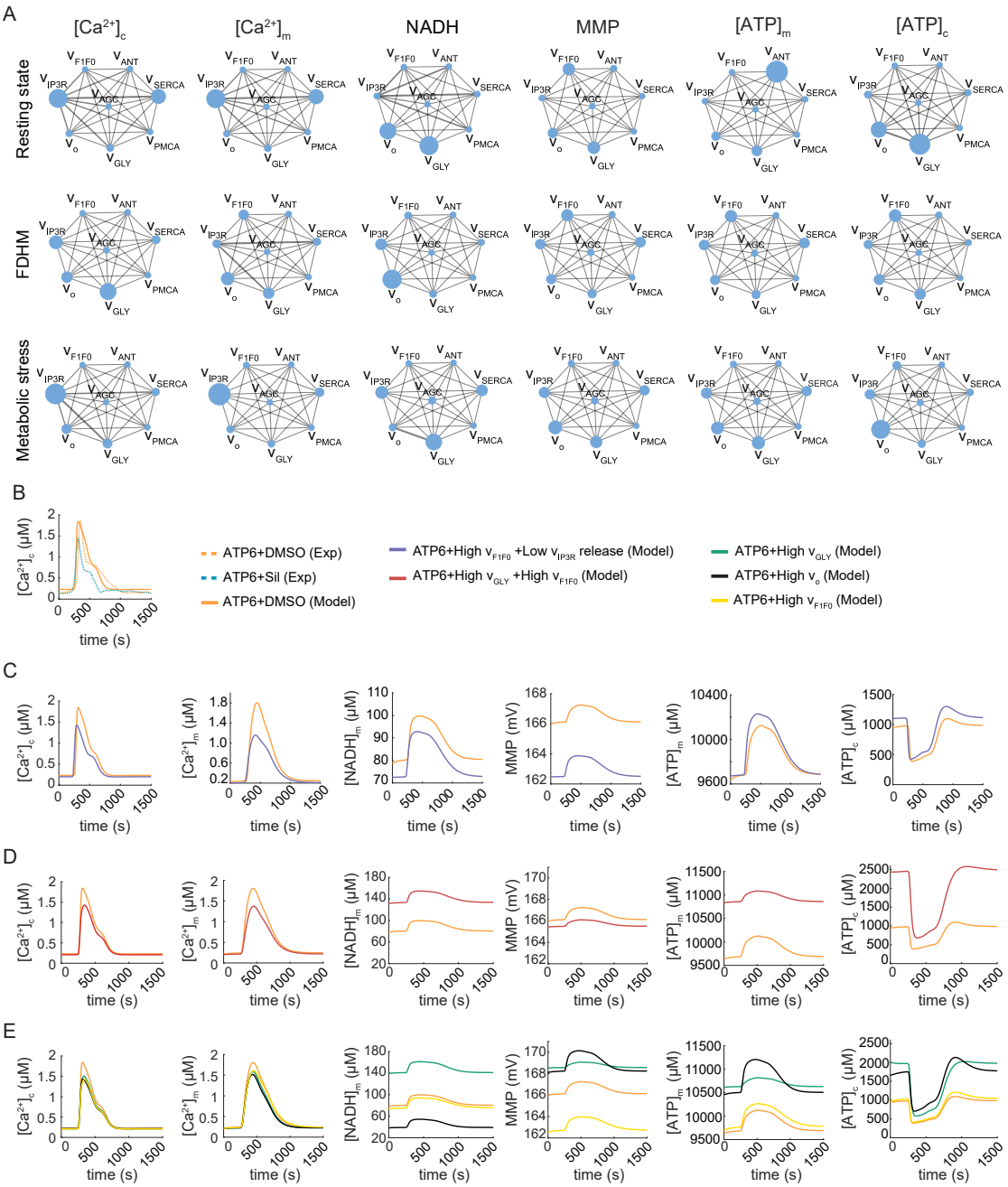


Figure S9. Computational model of calcium and bioenergetics, related to Figure 4

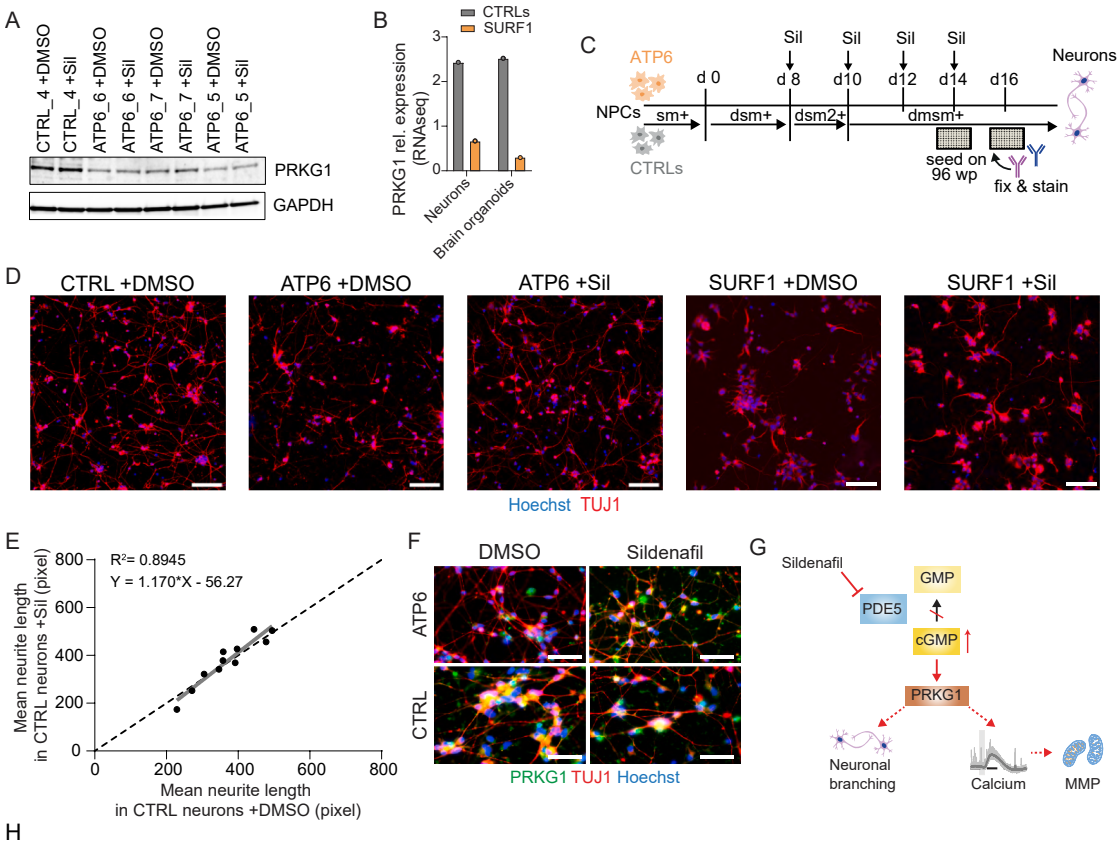
(A) Global sensitivity test for the mathematical model of calcium and bioenergetics. Values for resting state, full duration at half maximum (FDHM), and metabolic stress were computed for: $[Ca^{2+}]_c$ (cytosolic calcium), $[Ca^{2+}]_c$ (mitochondrial calcium), $[NADH]_m$ (mitochondrial NADH), MMP, $[ATP]_m$ (mitochondrial ATP), $[ATP]_c$ (cytosolic ATP) varying the key parameters: maximum rate of F_1F_0 ATPase activity (v_{F1F0}), GLY (v_{GLY}), ANT (v_{ANT}), NADH production via AGC (v_{AGC}), NADH oxidation in ETC (v_O), PMCA (v_{PMCA}), SERCA (v_{SERCA}), and of IP3Rs (v_{IP3R}). Bullet size: significance of the effect of a parameter; edge thickness: significance of the interaction between the two parameters.

(B) Comparison between experimental calcium traces obtained in LS cBOS and calcium traces computationally predicted by the mathematical model.

(C) Model prediction of the effects of *MT-ATP6* variants in basal conditions or in conditions with increased maximum rate of F1F0 (v_{F1F0}) together with decreased maximum rate of IP3R (v_{IP3R}).

(D) Model prediction of the effects of *MT-ATP6* variants in basal conditions or in conditions with increased maximum rate of GLY (v_{GLY}) together with increased maximum rate of F1F0 (v_{F1F0}).

(E) Model prediction of the effects of *MT-ATP6* variants in basal conditions or in conditions with increased maximum rate of either GLY (v_{GLY}), F1F0 (v_{F1F0}), or NADH oxidation in ETC (v_O).



H

Name	hPSCreg name	Alternative name	Sex	Age (years)	Variant	Heteroplasmy (Fibs)	Heteroplasmy (iPSCs)	Heteroplasmy (NPCs)	Publication of iPSC line (PMID)
CTRLs									
CTRL_1	HMGUi001-A	XM001	f	47	-	-	-	-	29396371
CTRL_2	HHUUKDi009-A	TFBJ	m	0	-	-	-	-	28132834
CTRL_3	CRMi003-A	NCRM1	f	0	-	-	-	-	36459969
CTRL_4	BIHi269-B	-	f	42	m.9176T>G	55.0%	1.0%	1.6%	36669241
CTRL_5	HVRDi004-B	PGP1	m	55	-	-	-	-	36459969
CTRL_6	IUFi004-A	iPS12-10	f	30	-	-	-	-	38217996
CTRL_7	BIHi266-A	-	f	31	m.8993T>G	0.0%	0.0%	0.0%	36669241
CTRL_8	WISCi004-B	-	f	0	-	-	-	-	18029452
CTRL_9	UMGi014-C	-	m	-	-	-	-	-	33905594
ATP6									
ATP6_1	HHUi001-A	TDA2	f	47	m.9185T>C	99.0%	100.0%	100.0%	28132834
ATP6_2	HHUi002-A	TDA3	f	20	m.9185T>C	100.0%	100.0%	100.0%	28132834
ATP6_3	HHUi003-C	A4_W1	m	4	m.9185T>C	93.5%	100.0%	100.0%	36137325
ATP6_4	MDCi008-A	8993 B12	m	9	m.8993T>C	96.8%	98.2%	97.9%	35279592
ATP6_5	MDCi009-A	8993 C11	f	2	m.8993T>G	97.8%	97.4%	96.2%	35279592
ATP6_6	MDCi010-A	8993 D7	m	3	m.8993T>G	98.1%	98.1%	97.9%	35279592
ATP6_7	BIHi267-B	-	m	17	m.9176T>G	98.0%	98.0%	98.0%	36669241
SURF1					**Variant**				
SURF1_1	HMGUi001-A-64	C1_mut2	f	47	Isogenic mutation (c.769G>A)				33771987
CTRL_1	HMGUi001-A	C1	f	47	Isogenic control				33771987
NDUFS4									
NDUFS4_1	HVRDi004-B-6	E9	m	55	Isogenic mutant (c.316C>T)				36741056
NDUFS4_2	HVRDi004-B-7	F3	m	55	Isogenic mutant (c.20C>G)				36741056
CTRL_5	HVRDi004-B	PGP1	m	55	Isogenic control				36741056

Figure S10. Functional validations in human neuronal models of LS, related to Figure 4

(A) Representative immunoblot of PRKG1 (78 kDa) and GAPDH (37 kDa) in control NPCs and LS NPCs treated with 10 μM sildenafil or DMSO for 16 h (quantification in Figure 4L).

(B) *PRKG1* gene expression in *SURF1* mutant neurons and brain organoids (SURF1_1) compared with isogenic controls (CTRL_1) based on published bulk RNA-seq.[25]

(C) Schematic of the differentiation into dopaminergic-enriched neuronal cultures.

(legend continued on next page)

(D) Representative images of neurons from controls (CTRL_1), *MT-ATP6* mutants (ATP6_7), and *SURF1* mutants treated with 10 μM sildenafil or DMSO for 8 days. Scale bar: 100 μm.

(E) Linear regression of the mean neurite length (mean over median) in control neurons (CTRL_1, $n = 4$; CTRL_2, $n = 3$; CTRL_3, $n = 1$; CTRL_5, $n = 3$) treated with sildenafil for 8 days over control neurons exposed to only DMSO (gray line). Dots: individual values per experiment. Black dotted line: hypothetical linear regression with no effect ($y = x$).

(F) Representative immunostaining for PRKG1 and TUJ1 in control neurons (CTRL_2) and LS neurons (ATP6_4) treated for 8 days with sildenafil or DMSO. Scale bar: 50 μm.

(G) Mode of action of sildenafil. Red arrows: known actions of sildenafil. Dashed arrows: suggested actions of sildenafil in LS neural cells.

(H) Details of the human iPSC lines used in this study. For lines carrying *MT-ATP6* variants, we quantified the heteroplasmy in the parental fibroblasts (Fibs) and in the respective iPSCs and NPCs.

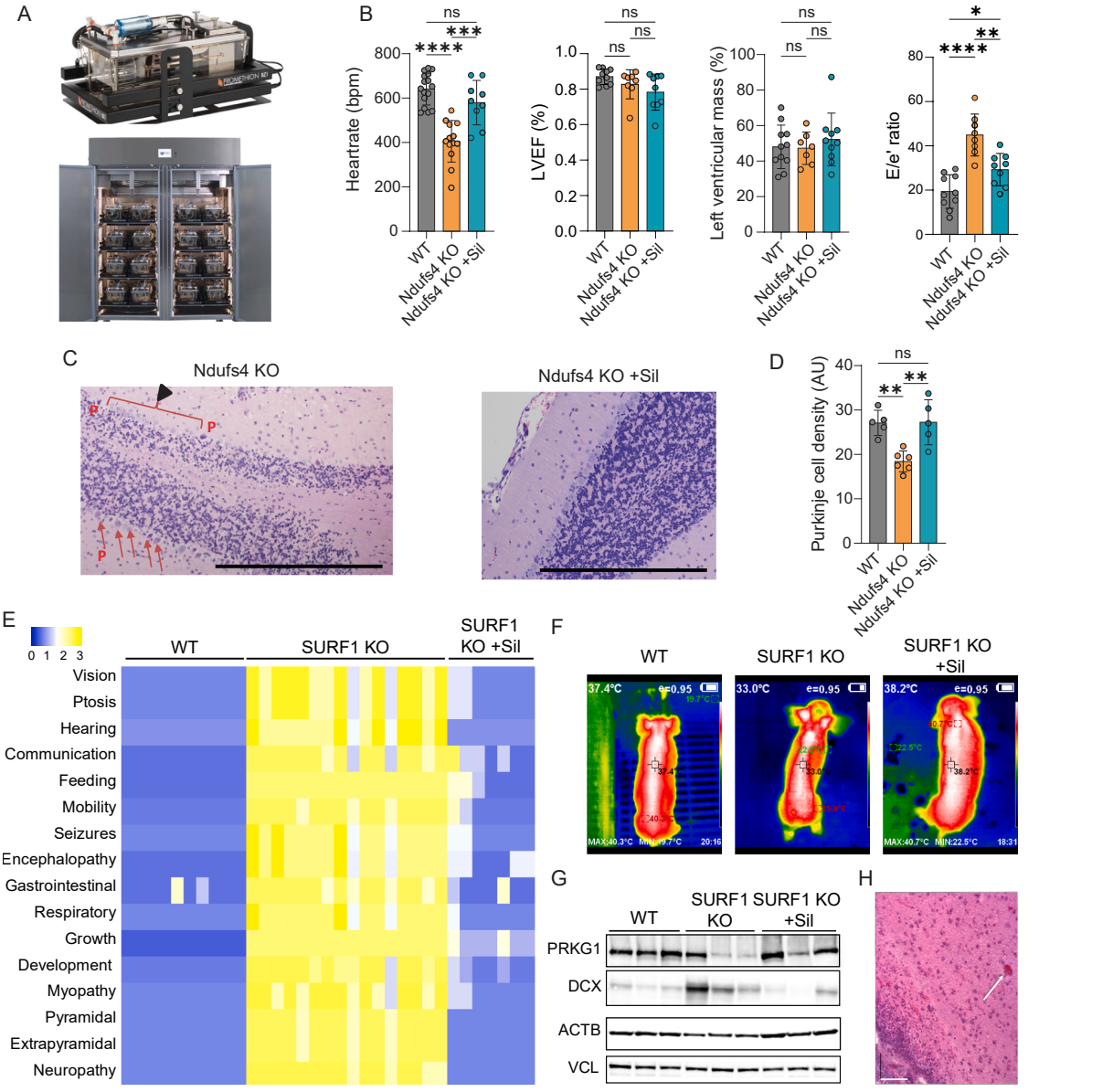


Figure S11. Sildenafil effects in LS animal models, related to Figure 5

(A) Metabolic chamber to assess metabolic fitness in *Ndufs4* KO mice.

(B) Cardiac effects of sildenafil in 42- to 45-day-old *Ndufs4* KO mice ($n = 8–10$): heart rate (bpm) and diastolic dysfunction measured by tissue Doppler imaging, left ventricular mass (%), left ventricular ejection fraction (LVEF, %), and ratio of the peak early mitral inflow velocity over the early diastolic mitral annular velocity (e′) measured by echocardiography. $^{*}p < 0.05$, $^{**}p < 0.01$, $^{***}p < 0.001$, $^{****}p < 0.001$; two-tailed Mann-Whitney U test.

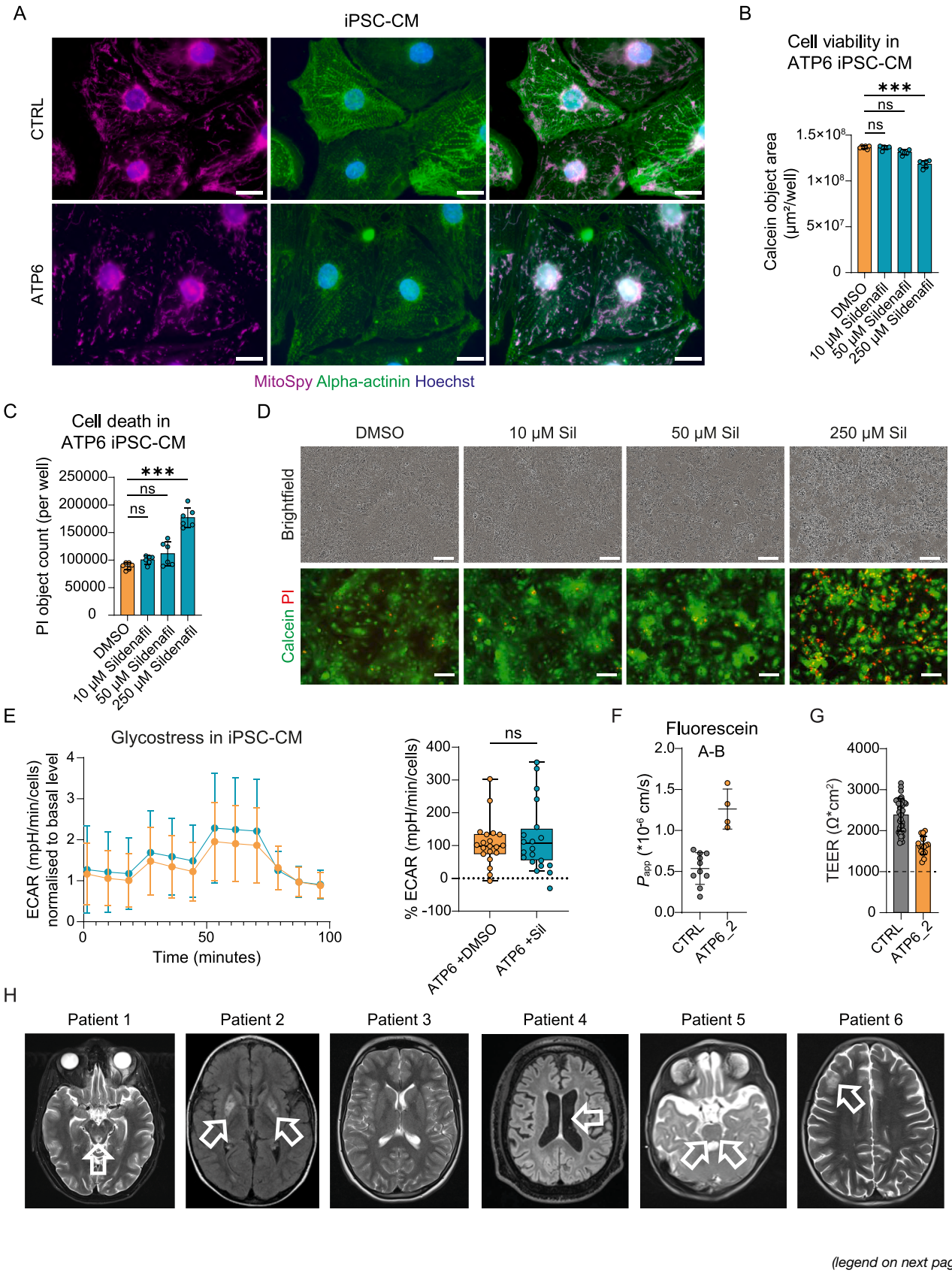
(C and D) Representative immunohistochemistry and related quantification of Purkinje cells (P) density in 42- to 45-day-old *Ndufs4* KO mice ($n = 5–6$). Arrows: loss of Purkinje cells. $^{**}p < 0.01$; ANOVA post hoc analysis. Scale bar: 500 μm.

(E) Clinical features of WT pigs ($n = 10$), untreated *SURF1* KO pigs ($n = 16$), and *SURF1* KO pigs treated with sildenafil ($n = 7$) based on the adaptation of the NPMDS scale.

(F) Representative thermal images of WT and *SURF1* KO pigs (quantification in Figure 5G).

(G) Representative immunoblot of PRKG1 and DCX in WT pigs ($n=3$), untreated *SURF1* KO pigs ($n = 3$), and *SURF1* KO pigs treated with sildenafil ($n = 3$). Vinculin (VCL) and actin beta (ACTB): loading controls (quantification in Figure 5J).

(H) Representative hematoxylin and eosin (H&E) staining of the brain of a *SURF1* KO pig receiving sildenafil 2.1 mg/kg/day who died after 4 days. White arrow: cerebral microhemorrhage. Scale bar: 100 μm.



(legend on next page)

Figure S12. Sildenafil impact on iPSC-CMs, BBB, and LS patients, related to Figure 6

(A) Representative immunostaining of iPSC-derived cardiomyocytes (iPSC-CMs) from LS (ATP6_7) and control (CTRL_9). Scale bar: 100 μm.

(B and C) Quantification and representative images for live-cell count via calcein and cell death count via propidium iodide (PI) in iPSC-CM from LS (ATP6_7) treated with sildenafil for 24 h. $n = 6$ from two independent experiments, $^{***}p < 0.005$; unpaired two-tailed *t* test. Scale bar: 100 μm.

(D and E) Representative images and related quantification of seahorse-based GLY stress test in iPSC-CM from LS (ATP6_6 and ATP6_7) treated with 10 μM sildenafil for 24 h. $n = 20$ from two independent experiments; unpaired two-tailed *t* test.

(F) Apparent permeability coefficient (*p*app, 10^{-6} * cm/s) from the apical to basolateral (A-B) compartment of fluorescein in control BCECs (CTRL_8) and LS BCECs (ATP6_2), $n = 3–5$ independent experiments.

(G) Transendothelial electrical resistance (TEER) measurement in BCECs from control (CTRL_8) and LS (ATP6_2), $n = 3–5$ independent experiments.

(H) Representative cMRI taken during the diagnosis of the six LS patients who were subsequently treated with sildenafil. Arrows indicate: T_2-signal increase in the perisylvian gray matter of the brain stem in Patient 1, FLAIR signal increase in the basal ganglia in Patient 2, spontaneous resolution of T_2-signal intensities at the age of 14 years in Patient 3 (see Figure 6E for comparison), FLAIR image with generalized brain atrophy and enlargement of the intracerebral fluid spaces in Patient 4, T_2-signal increase in the *Substantia nigra* and the *Fasciculus longitudinalis* of the brain stem in Patient 5, and T_2-signal increase in the cortical gray matter in Patient 6.

11. Appendix III

scientific reports

Check for updates

OPEN

Morphological profiling reveals neuroprotection via mitochondrial uncoupling in human dopaminergic neurons

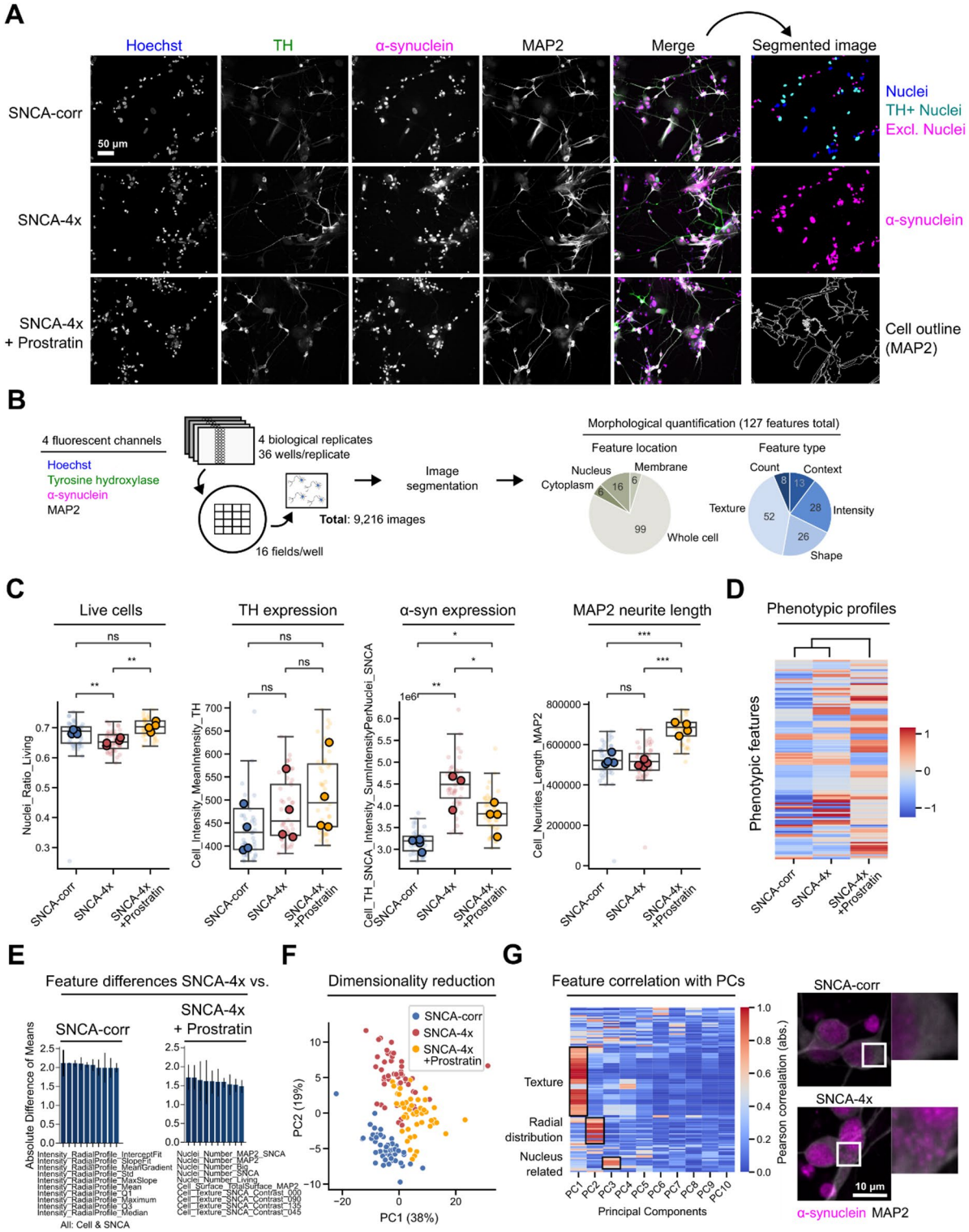
Vyron Gorgogietas[1,8], Amélie Weiss[2,8], Loïc Cousin[2], David Hoffmann[2], Karen Schmitt[2], Arnaud Ogier[2], Peter A. Barbuti[1,3,4], Bruno F. R. Santos[1,4], Ibrahim Boussaad[1], Annika Wittich[5], Andrea Zaliani[5], Ole Pless[5], Rejko Krüger[1,6,7], Peter Sommer[2] & Johannes H. Wilbertz[2]✉

Parkinson's disease (PD) involves multiple pathological processes in midbrain dopaminergic (mDA) neurons, including protein degradation defects, vesicular trafficking disruption, endolysosomal dysfunction, mitochondrial issues, and oxidative stress. Current PD models often lack complexity and focus on single phenotypes. We used patient-derived SNCA triplication (SNCA-4x) and isogenic control (SNCA-corr) mDA neurons, applying high-content imaging-based morphological profiling to identify and rescue multiple phenotypes. Screening 1,020 compounds, we identified top-scoring compounds that restored healthy profiles in SNCA-4x neurons, increasing Tyrosine hydroxylase (TH) and decreasing α-synuclein (αSyn) levels. Several hits were linked to mitochondrial biology. Tyrphostin A9, a mitochondrial uncoupler, and several of its structural analogues decreased ROS levels, normalized mitochondrial membrane potential, and increased respiration. Western blotting confirmed that Tyrphostin A9 reduces αSyn levels. Our study highlights the neuroprotective potential of mild mitochondrial uncoupling in mDA neurons.

Parkinson's disease (PD), with its diverse phenotypic, neuropathological, and genotypic manifestations, is increasingly acknowledged as a complex disorder rather than a singular disease entity[1–3]. While traditional models have been instrumental in devising symptomatic therapies to address PD's motor symptoms, they have been less successful in developing neuroprotective strategies[4]. Genetic stratification of patients into subgroups has emerged as a crucial approach[5,6]. Over the past 25 years, significant progress has been made in identifying genes associated with PD, including those responsible for rare monogenic forms of the disease[2]. These monogenic forms have proven invaluable for PD research, as patient-based cell models exhibit disease-specific cellular phenotypes that mirror those found in postmortem brain tissue[7–11]. This approach suggests that targets for pharmaceutical interventions might be identifiable based on rare but potent molecular signatures[12–14].

Point mutations, as well as duplications and triplications of the wild-type alpha-synuclein gene (*SNCA*), are responsible for causing autosomal dominantly inherited PD[15–18]. Patients with *SNCA* triplication (SNCA-4x) express α-synuclein protein (αSyn) from four alleles resulting in a roughly 2-fold increase of αSyn, and typically exhibit an early disease onset, accelerated disease progression, and significant dementia. In contrast, patients with SNCA duplications often display a more conventional late-onset PD phenotype. The severity of clinical trajectories in SNCA multiplication appears to correlate with gene dosage. Patient-derived induced pluripotent stem cells (iPSC) carrying the *SNCA* triplication have been successfully differentiated into midbrain dopaminergic (mDA) neurons and organoids[19–22]. Despite their young age, iPSC mDA neurons exhibit PD-relevant phenotypes. *SNCA* gene triplication leads to an increase in αSyn levels resulting in oligomeric αSyn pathology and elevated αSyn extracellular release[19,21,23,24]. Multiple pathophysiological defects correlate with increased αSyn protein expression, such as altered lysosomal and mitochondrial functions, dysregulated

[1]Luxembourg Centre for Systems Biomedicine (LCSB), Esch-sur-Alzette, Luxembourg. [2]Ksilink, Strasbourg, France. [3]Department of Neurology, Columbia University Irving Medical Center, New York, NY, USA. [4]Disease Modelling and Screening Platform, Esch-sur-Alzette, Luxembourg. [5]Fraunhofer Institute for Translational Medicine and Pharmacology ITMP, ScreeningPort, Hamburg, Germany. [6]Transversal Translational Medicine, Luxembourg Institute of Health (LIH), Strassen, Luxembourg. [7]Parkinson's Research Clinic, Centre Hospitalier de Luxembourg (CHL), Luxembourg, Luxembourg. [8]Vyron Gorgogietas and Amélie Weiss contributed equally to this work. ✉email: johannes.wilbertz@ksilink.com



autophagy increased endoplasmic reticulum stress, and heightened oxidative stress levels[20,22,24–28]. Due to the interconnection of many of the identified phenotypes, it is currently an open question whether a rescue of one key or multiple cellular PD hallmarks is necessary to achieve a significant neuroprotective effect. Imaging-based profiling is a strategy that transforms the rich data in biological images into multidimensional profiles of extracted features, which can be analyzed to reveal biological signatures, aiding in disease understanding and drug discovery, with advancements in machine learning and computational technologies enhancing its potential[29]. By capturing the observable characteristics of cells under different conditions, morphological profiling can provide valuable insights into the complex cellular mechanisms underlying PD[8,9,11].

In this study, we find that *SNCA* gene triplication results in a multidimensional alteration of the morphological profile in mDA neurons. We further identify multiple small molecular compounds correcting this altered profile to align with the phenotype of isogenic controls (SNCA-corr) mDA neurons. One of the identified compounds,

◀**Fig. 1**. SNCA-4x mDA neurons have a distinct but modulable morphological profile. (**A**) SNCA-4x and SNCA-corr mDA neurons were differentiated until D33, treated with 5 µM Prostratin or DMSO for 72 h and immunofluorescently stained. Image channels were segmented for morphological feature quantification. (**B**) Schematic overview of image data generation and morphological feature types. (**C**) Raw morphological feature values in control, and untreated and Prostratin treated SNCA-4x mDA neurons. Each datapoint represents technical replicate data from one 384-well plate well. Larger markers represent the medians each independent experiments. The boxplots show the median and the 2nd and 3rd quartiles of the data. Whiskers indicate 1.5X of the interquartile range. Welch's unequal variances t-test was performed using the medians of independent differentiation experiments. ns = not significant, * = $p < 0.05$, ** = $p < 0.01$, *** = $p < 0.001$. (**D**) Scaled well and replicate median feature values aggregated into morphological profiles. Cosine similarity was used for clustering. (**E**) Top ten absolute mean differences between features of SNCA-4x and Control or SNCA-4x neurons treated with Prostratin. Means with standard deviations are shown. (**F**) Two first principal components (PCs) explaining most variation in the dataset after Principal Component Analysis (PCA). Each data point represents mean data from one well. (**G**) Absolute Pearson correlation of all features with the first ten PCs after PCA. Representative images illustrate cellular αSyn staining patterns. All data in this figure was generated in four independent experiments each containing at least 12 technical replicates per condition.

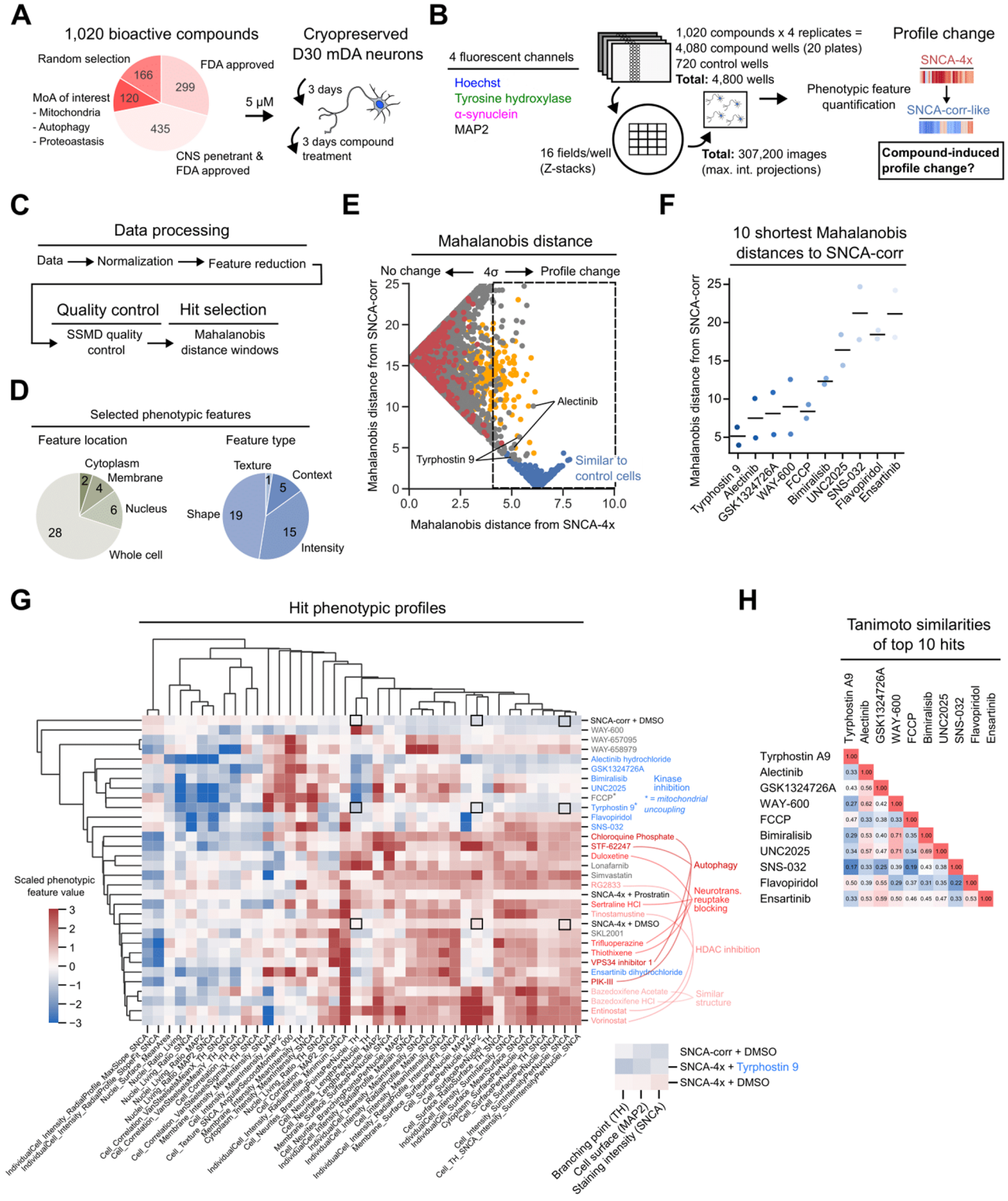
Tyrphostin A9, exerts its neuroprotective effect via mitochondrial uncoupling, which in turn reduces reactive oxygen species (ROS) and high molecular weight αSyn species. In summary, we show that screening small molecules in a PD-relevant human model system using a multi-phenotypical readout can identify modulators of not just a single, but multiple disease relevant phenotypes.

Results

SNCA-4x mDA neurons have a distinct but modulable morphological profile

We differentiated patient-derived SNCA gene triplication and isogenic control iPSCs into mDA neurons (SNCA-4x and SNCA-corr) for 30–37 days. These neurons showed the expected mDA neuron morphology and no *de novo* copy number variations. Both cell lines expressed neuro-typical markers β-tubulin III (90–94%), MAP2 (87–89%), and the dopaminergic neuron markers Tyrosine hydroxylase (TH) (84–88%) and FOXA2 (84–90% in TH positive cells) (Figure S1A-C). Western blotting revealed increased αSyn protein level and signs of αSyn aggregation in SNCA-4x mDA neurons after D70 (Figure S1D). A JC-1 dye assay indicated reduced mitochondrial membrane potential in D35 SNCA-4x mDA neurons (Figure S1E). For morphological profiling, mDA neurons were cultured until D36 in 384-well plates and stained with Hoechst, and antibodies against TH, αSyn, and MAP2 (Fig. 1A). Automated segmentation and feature quantification were used to overcome challenges in assessing subtle phenotypes. Image segmentation was performed on 16 fields per well and 127 morphological features were determined and expressed as means per well. Features were calculated for the whole cell, nucleus, cytoplasm or membrane and describe different aspects of the images (Fig. 1B, Table S4). Texture features capture the spatial distribution and arrangement of pixel intensities in an image. Context features provide information about the spatial relationship between signals, for example the correlation between image channels. Intensity features measure the fluorescence intensity and can provide insights into the expression levels of proteins. Count and area/shape features quantify the number, size and morphology of the cellular components. First, we examined basic morphological features of SNCA-4x and SNCA-corr mDA neurons. SNCA-4x neurons had fewer live cells and approximately 50% increased αSyn protein expression. In our study, we utilized Prostratin as a proof-of-concept molecule due to its proposed activity in degrading αSyn. Previous research has demonstrated that specific phorbol esters, such as PEP005 or Prostratin, can reduce αSyn through proteasomal degradation[7]. Based on these findings, we hypothesized that Prostratin's activity would lead to an altered morphological profile in our experimental model. Treatment with Prostratin indeed reduced dead cells and αSyn expression in SNCA-4x neurons to levels similar to SNCA-corr neurons (Fig. 1C). Neuronal morphological profiles before and after compound treatment were created by scaling feature values and calculating mean values across wells (Fig. 1D). We used the mean absolute difference to find the features that differed the most between profiles. Comparing SNCA-corr and SNCA-4x neurons, the radial αSyn intensity profile, which measures fluorescence intensity as a function of distance from a central point, differed most. Prostratin-treated and untreated SNCA-4x neurons also varied in number of nuclei, total MAP2 cellular surface, and αSyn staining contrast (Fig. 1E). These findings show that small molecular treatment can rescue morphological features in mDA neurons which can be measured by morphological profiling.

Next, we performed Principal Component Analysis (PCA) using the morphological profile data to visualize overall differences between compound-treated and untreated cells. The first two principal components (PCs) accounted for 57% of the variance and separated the tested cell lines and Prostratin-treated neurons, indicating significant differences between them (Fig. 1F). The remaining PCs each accounted for 11% or less of the variance, suggesting lesser contribution to the overall variance (Figure S1F). To understand which features were mainly responsible for distinguishing the experimental categories, we calculated the absolute Pearson's correlation between the first ten PCs and each morphological feature. PC1 correlated mostly with αSyn signal texture-related features, indicating a different αSyn subcellular distribution pattern in the neurons. PC2 and PC3 correlated with signal radial distribution and nucleus-related features, similar to the results we obtained when comparing experimental conditions pairwise using the mean absolute difference (Fig. 1G, Figure S1G). Manual inspection of images confirmed these findings, showing grainy αSyn localization outside the nucleus in SNCA-4x cells (Fig. 1G). This indicated that radial distribution and texture features indeed capture αSyn localization patterns. As a result, high-dimensional morphological profiling, by capturing a wide array of cellular characteristics,



allowed us to identify subtle differences between experimental conditions that may not be apparent through visual inspection alone.

Compound modulation shifts a SNCA-4x towards a control morphological profile

Based on our observation that small molecular compounds, such as Prostratin, can partially rescue SNCA-4x mDA neuron morphological profiles, we wondered whether more potent small molecules could be identified using a morphological profile screening approach. We assembled a 1,020 compound library which included 734 FDA-approved compounds, 435 of which can pass the blood-brain-barrier, 120 molecules targeting PD-relevant processes, and 166 diverse bioactive molecules (Fig. 2A, Table S3). Cryopreserved D30 mDA neurons were cultured in 384-well plates until D33, treated with 5 µM of each compound for 72 h and stained (Fig. 2B). Each compound was tested in 4 replicates across 20 384-well plates, with 36 control wells per plate. Control conditions

◀**Fig. 2**. Compound modulation shifts a SNCA-4x towards a control morphological profile. **(A)** Overview about screening library composition and neuron treatment scheme. **(B)** Schematic overview of image data generation. Morphological features were calculated from imaging data to measure compound-induced morphological profile changes from a SNCA-4x towards a SNCA-corr-like profile. **(C)** Schematic of morphological profile data processing workflow. **(D)** Overview of morphological feature types used for hit selection after removal of redundant features using a Pearson correlation threshold of 0.95. **(E)** Morphological profile Mahalanobis distances of compound treated mDA neurons relative to SNCA-4x and SNCA-corr morphological profiles. The black dashed line indicates the selection window based on 4σ from the SNCA-4x median. Each datapoint represents mean data from one well and for compounds the mean value of all four replicates is shown. **(F)** Compounds inducing morphological profiles with the 10 shortest mean Mahalanobis distances to the median SNCA-corr morphological profile. **(G)** Selected hits clustered by the Cosine similarity of their respective morphological profiles. Compounds are color coded by attributed biological activity. **(H)** Tanimoto similarities of top 10 selected compounds.

established baseline and maximum effect profiles (SNCA-4x + DMSO and SNCA-corr + DMSO, respectively). Morphological profiles were generated from 307,200 images and all data was aggregated per well (Fig. 2B).

We aimed to identify compounds shifting SNCA-4x profiles towards SNCA-corr-like phenotypes. Morphological profiles were Z-score normalized for comparability (Fig. 2C, Figure S2A). Pearson's correlation reduced the initial 127 features to 40 non-redundant ones, mostly describing cellular area, shape, and TH and αSyn staining intensities (Fig. 2D, Figure S2B). Plate quality was assessed using the Strictly Standardized Mean Difference (SSMD) of the Mahalanobis distances between treatment groups. All plates showed significant differences (Figure S2C). Linear Discriminant Analysis (LDA) was used to compare each compound profile with the reference profiles. LDA achieved a classification accuracy F1 score of 0.96 in a test data set and 0.93 ± 0.04 in a 10-fold cross-validation, indicating a high ability to correctly predict whether compound-induced morphological profiles resemble one of the reference classes (Figure S2D). Most compounds had no effect on the SNCA-4x profile, while some induced SNCA-corr-like profiles (Figure S2E).

We aimed to identify compounds that could shift SNCA-4x profiles towards SNCA-corr-like phenotypes. Morphological profiles were compared using the Mahalanobis distance, a metric that measures how different two profile vectors are. We identified 28 compounds with a mean distance of at least 4 to the SNCA-4x median profile (Fig. 2E, Table S1). Of these, the 10 compounds with the shortest distance to the SNCA-corr profile were considered to partially rescue the phenotype. Tyrphostin A9 and Alectinib were the most similar to the SNCA-corr profile (Fig. 2F). To validate our findings, we used Cosine similarity, a metric that measures whether two vectors (or morphological profiles) are pointing in the same direction. Nine out of the 10 compounds with the shortest Mahalanobis distance to SNCA-corr grouped in the same cluster as SNCA-corr, supporting a distance and directional similarity between their morphological profiles (Fig. 2F and G). Although the top hits' morphological profiles were highly similar among each other and compared to the SNCA-corr profile, their chemical structure-based Tanimoto similarities differed considerably (Fig. 2H). We validated the effect of the identified compounds on cellular phenotypes using data from the Joint Undertaking in Morphological Profiling (JUMP) consortium, an effort to create compound-induced morphological profiles in U2OS cells by CellPainting[30,31]. Also here, in a different cell type and using a different staining assay, we observed that compounds with similar mode of action induced similar morphological profiles (Figure S2F). This supports the notion that the identified compounds, while acting on different targets, might possibly acting on related pathways leading to a similar phenotypic outcome. Tyrphostin A9 was originally developed as an epidermal growth factor receptor (EGFR) inhibitor, but similar to other Tyrphostins has been linked to mitochondrial membrane fragmentation, reduced OXPHOS, and potentially neuroprotection via reduction of ROS[32–35]. Since mitochondrial defects play an important role in PD pathology, we decided to further characterize Tyrphostin A9's molecular mechanism in mDA neurons[3].

Tyrphostin A9 rescues the overall mDA neuron morphological profile in a dose dependent manner

To establish hit compound dose-response effects we focused on cell viability and αSyn level assessment as well as on morphological profiling using six different compound concentrations ranging from 0.25 to 20 µM and a treatment duration of 72 h (Figure S3, Figure S4). For Tyrphostin A9, we observed that higher compound concentrations in SNCA-4x neurons resulted in a higher resemblance to SNCA-corr neuron morphological features (Fig. 3A). To quantify this observation, we calculated the Cosine distance of the compound treated SNCA-4x morphological profile to the SNCA-4x + DMSO and SNCA-corr morphological profiles as a function of compound concentration. Cosine distance can be defined as 1 – Cosine similarity. The intuition behind this is that if two vectors are perfectly the same then the similarity is 1 (angle = 0) and thus, the distance is 0 (1–1 = 0). We found that increasing compound concentrations decreased the distance between SNCA-4x and SNCA-corr morphological profiles, therefore increasing their similarity (Fig. 3B). The opposite is true when SNCA-4x compound treated neurons were compared to SNCA-4x DMSO-treated morphological profiles. Here, the Cosine distance increased with increasing compound concentration, reflecting the change of phenotype towards the SNCA-corr profile. Next, we investigated the effect of increasing compound concentrations on three single morphological features: αSyn intensity, TH intensity and MAP2 neurite length (Fig. 3C). Tyrphostin A9 concentrations > 1 µM decreased the nuclear and cytoplasmic αSyn staining intensity. Tyrphostin A9 also positively impacted TH staining intensity. At higher concentrations we observed little effects on MAP2 neurite length, indicating no acute toxicity.

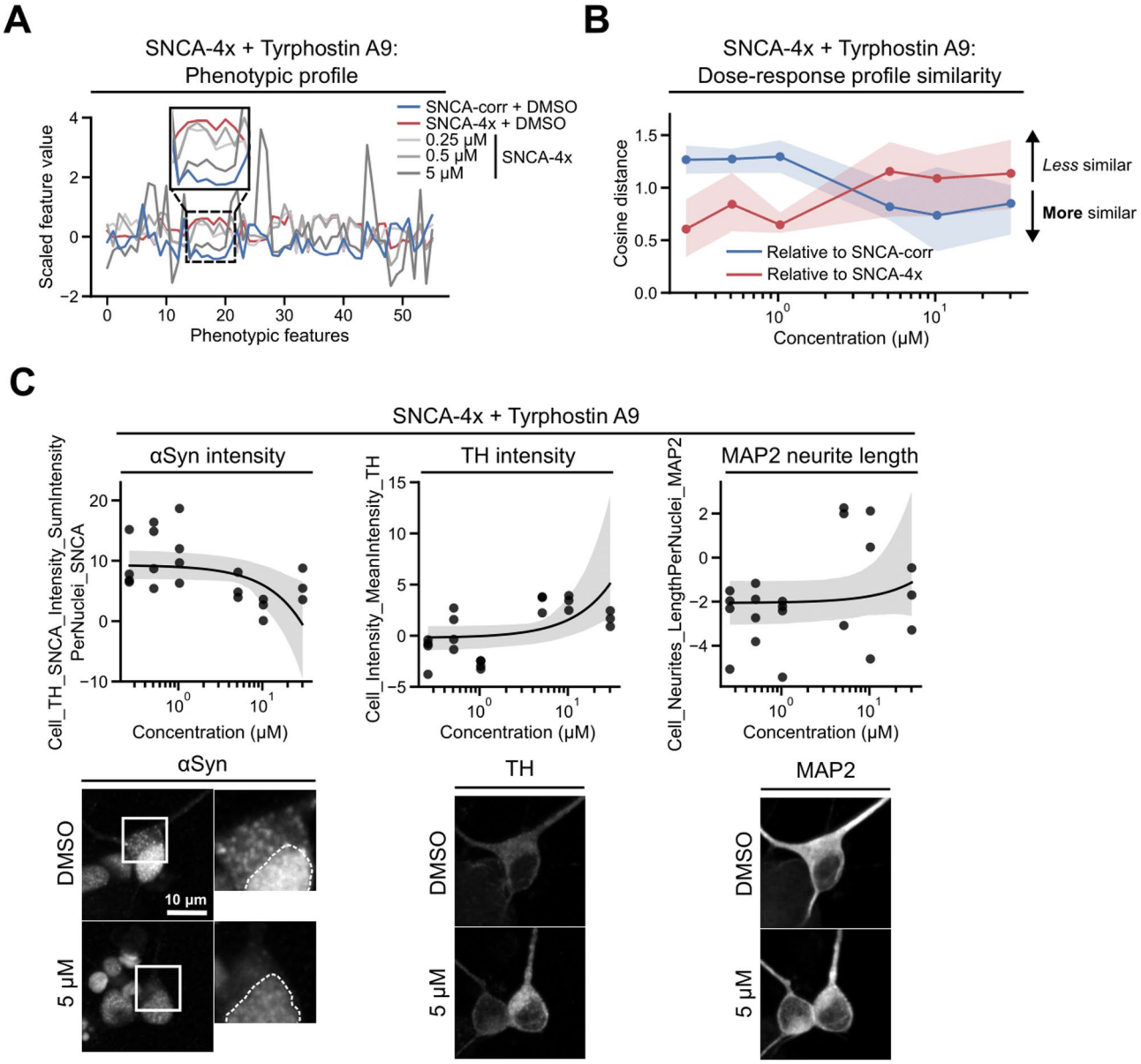


Fig. 3. Tyrphostin A9 rescues the overall morphological profile in a dose dependent manner. **(A)** Line plot representation of morphological profiles of Tyrphostin A9 treated and untreated mDA neurons. D33 neurons were treated with 0.25-20 µM compound for 72 h before fixation. All used 56 features are listed in Table S5. **(B)** Cosine distances of SNCA-4x neurons as a function of compound concentration relative to DMSO-treated SNCA-4x and SNCA-corr neurons. **(C)** Dose-response curves for the three selected morphological features αSyn intensity, TH intensity, and MAP neurite length. Representative images of the same cell in each fluorescent channel are shown for DMSO and 5 µM compound treatment. Each compound concentration was tested at least in triplicate. Mean and 95% confidence interval are shown.

Multiple identified hits induce mitochondrial uncoupling and ROS reduction

Tyrphostin A9 has been explored in vitro for its roles as neuroprotective agent, possibly functioning as an oxidative phosphorylation uncoupler reducing ROS[32,33,36]. Mitochondrial uncoupling involves the decrease of the mitochondrial proton gradient disrupting the coupling between the electron transport chain and ATP synthesis. Whether Tyrphostin A9 can exert these effects in mDA neurons is currently unclear. We first assessed Tyrphostin A9's ability to modulate the mitochondrial membrane potential using the JC-1 dye. We treated D33 mDA neurons for 72 h with increasing concentrations of Tyrphostin A9 (0.01 µM to 10 µM) and observed a decrease in red fluorescence for concentrations > 0.5 µM, indicating a concentration dependent decrease in mitochondrial membrane potential (Fig. 4A). Valinomycin was used as positive control inducing a very low membrane potential. While FCCP and Tyrphostin A9 lowered the mitochondrial membrane potential at the lowest doses, also other molecules with morphological profiles similar to Tyrphostin A9, such as Tinostamustine or VPS34 inhibitor 1, led to a decreased mitochondrial membrane potential (Figure S5). Since a reduction in

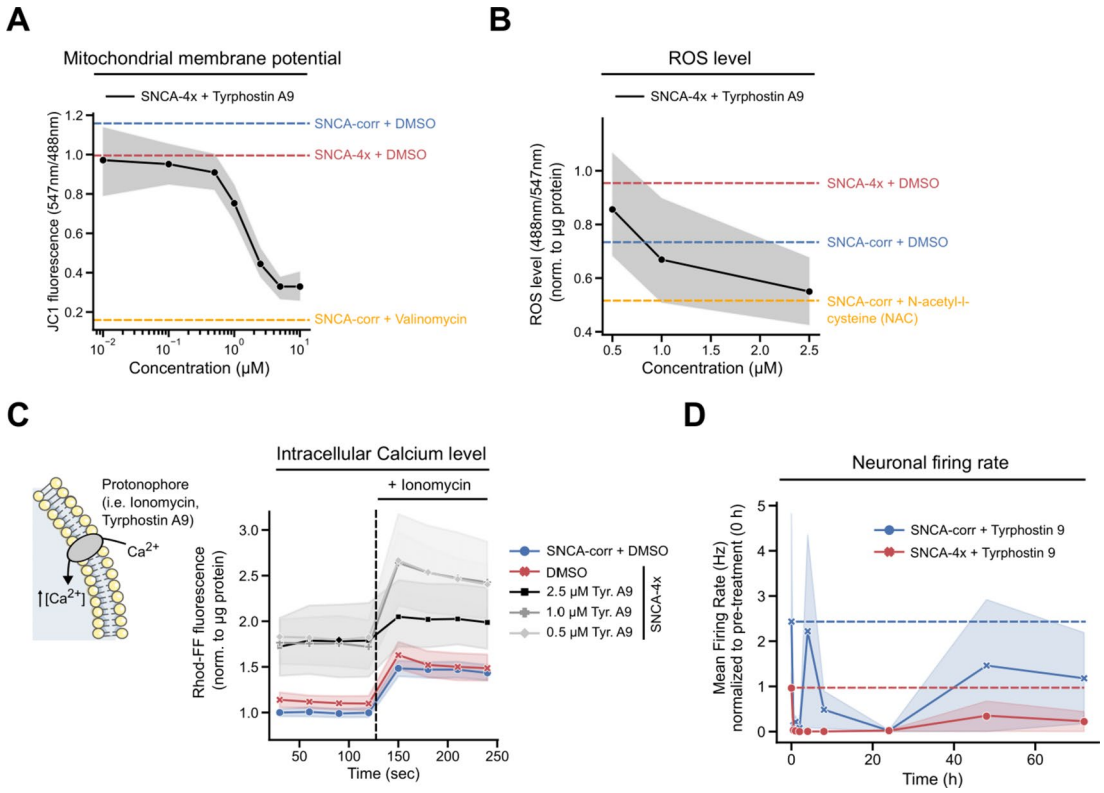
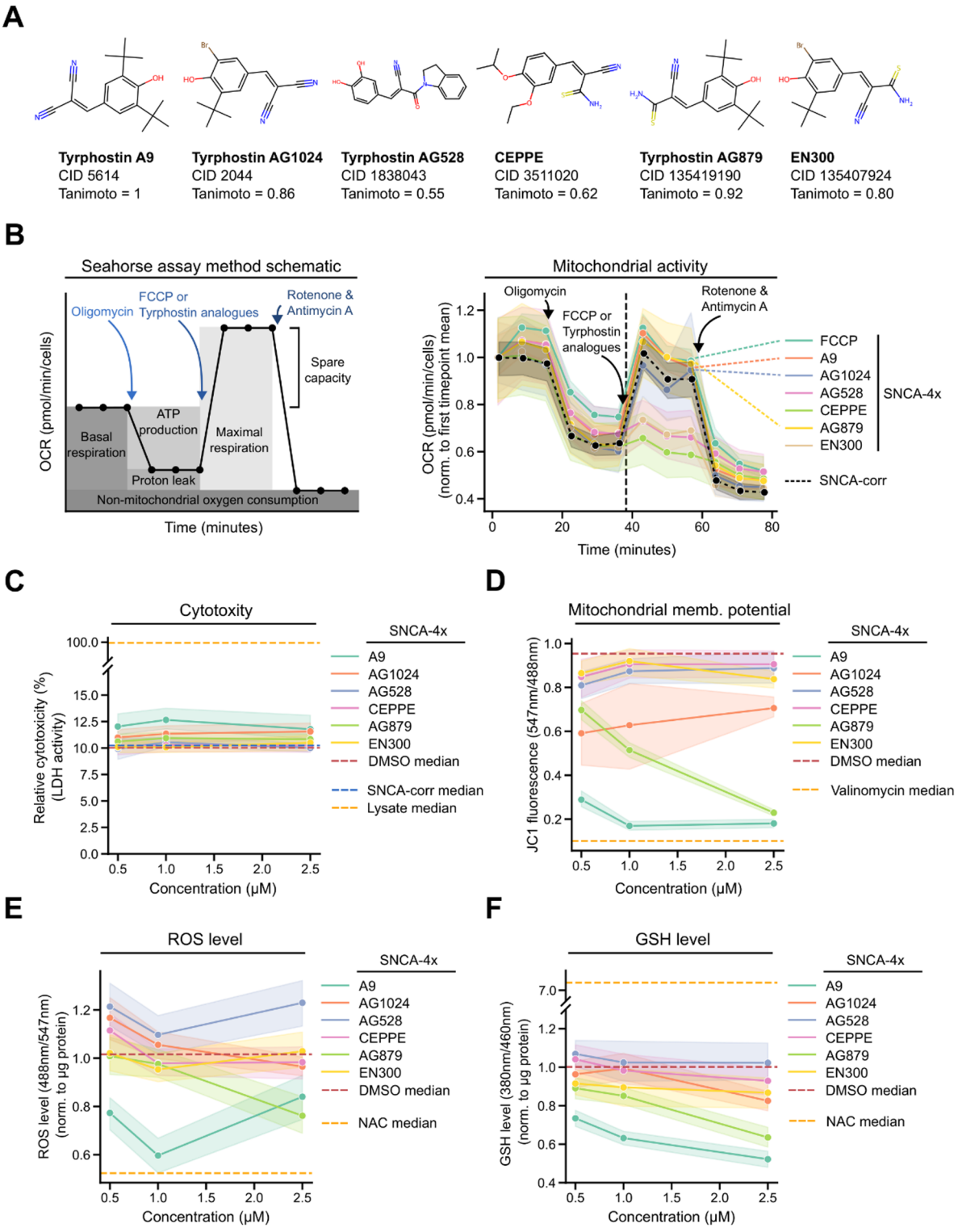


Fig. 4. Tyrphostin A9 acts as ROS-reducing mitochondrial uncoupler in mDA neurons. (**A**) mDA neurons were treated with 0.1–10 µM Tyrphostin A9 for 72 h and the mitochondrial membrane potential was measured using the JC1 dye. JC1 fluoresces red at high membrane potential and green at lower membrane potentials. Three independent experiments with at least three technical replicates each were performed. **(B)** mDA neurons were treated with 0.5, 1, and 2.5 µM Tyrphostin A9 for 72 h and the ROS level was determined using the CellROX dye. The obtained signal was normalized to total protein content. Three independent experiments with at least three technical replicates each were performed. **(C)***Left panel*: Scheme illustrating the protonophore mode of action. *Right panel*: mDA neurons were treated with 0.5, 1, and 2.5 µM Tyrphostin A9 for 72 h and the intracellular Calcium level was measured using the Rhod-FF dye for 250 s before and after the addition of Ionomycin. The obtained signal was normalized to total protein content. Two independent experiments with at least three technical replicates each were performed. **(D)** Neuronal activity was measured in ca. 60-day old mDA neurons using a microelectrode array (MEA). The neuronal firing rate was assessed before and up to 72 h after treatment with 2.5 µM Tyrphostin A9. Neuronal activity was measured in two independent experiments with at least three technical replicates each. For all data, the mean and 95% confidence interval is shown.

mitochondrial membrane potential is often associated with decreased ROS levels, we used a dye-based ROS assay to measure ROS levels in mDA neurons upon compound exposure. Tyrphostin A9 reduced ROS in a dose-dependent manner. At 2.5 µM Tyrphostin A9 reduced ROS down to the level of the positive control antioxidant N-acetyl-cysteine (NAC) (Fig. 4B). Interestingly, several other molecules that were pre-selected for inducing morphological profiles similar to the SNCA-corr phenotype, such as Simvastatin, Trifluoperazine, or WAY-600, also lowered neuronal ROS levels (Fig. 2G, Figure S6). We hypothesized that Tyrphostin A9 might lower mitochondrial membrane potential and ROS due to its function as protonophore facilitating proton transfer across membranes. We used a Rhod-FF assay which measures intracellular Ca^{2+} levels and found only small baseline differences between SNCA-corr and SNCA-4x mDA neurons, while the addition of Tyrphostin A9 to SNCA-4x mDA neurons increased intracellular Ca^{2+} levels by more than 70% (Fig. 4C). Addition of the known protonophore Ionomycin further increased intracellular Ca^{2+} levels demonstrating that Tyrphostin A9 likely uncouples the mitochondrial membrane potential via facilitating the entry of protons, thereby decreasing oxidative phosphorylation and ROS levels. In neurons protonophores are also expected to disrupt the neuronal membrane potential by decreasing the proton gradient, leading to a decrease in the driving force for the generation of action potentials, which might negatively impact neuronal firing. Using a microelectrode array (MEA) we measured the neuronal firing rate before and after Tyrphostin A9 treatment (Fig. 4D). Before treatment ca. 60-day old SNCA-corr mDA neurons showed approximately 2.5-fold higher firing rates than SNCA-4x neurons. When treating the mDA neurons for up to 72 h with 2.5 µM Tyrphostin A9 we observed a sharp drop in firing already 30 min after treatment. After > 24 h of treatment a slight recovery effect was observed and firing rates began to increase mildly. Taken together, our findings suggest that the identified compounds, although affecting



different targets, might be influencing related pathways, resulting in a similar phenotypic outcome such as mitochondrial membrane potential and ROS lowering.

The tyrphostin A9 structural analogue AG879 induces mitochondrial uncoupling

Tyrphostins represent a large family of small molecules with various attributed neuroprotective modes of action. Next to their role as mitochondrial uncouplers, Tyrphostins have been described as antioxidants or as having a positive effect on cellular glutathione levels[33]. We therefore compared a range of Tyrphostin A9 structural analogues using various biochemical assays to establish a Tyrphostin A9 structure-function relationship in mDA neurons (Fig. 5A). FCCP is a potent mitochondrial uncoupler used during oxygen consumption rate (OCR) measurements and facilitates proton transport across mitochondrial membranes. This action collapses the proton gradient and disrupts the mitochondrial membrane potential. As a result, the electron flow through the Electron

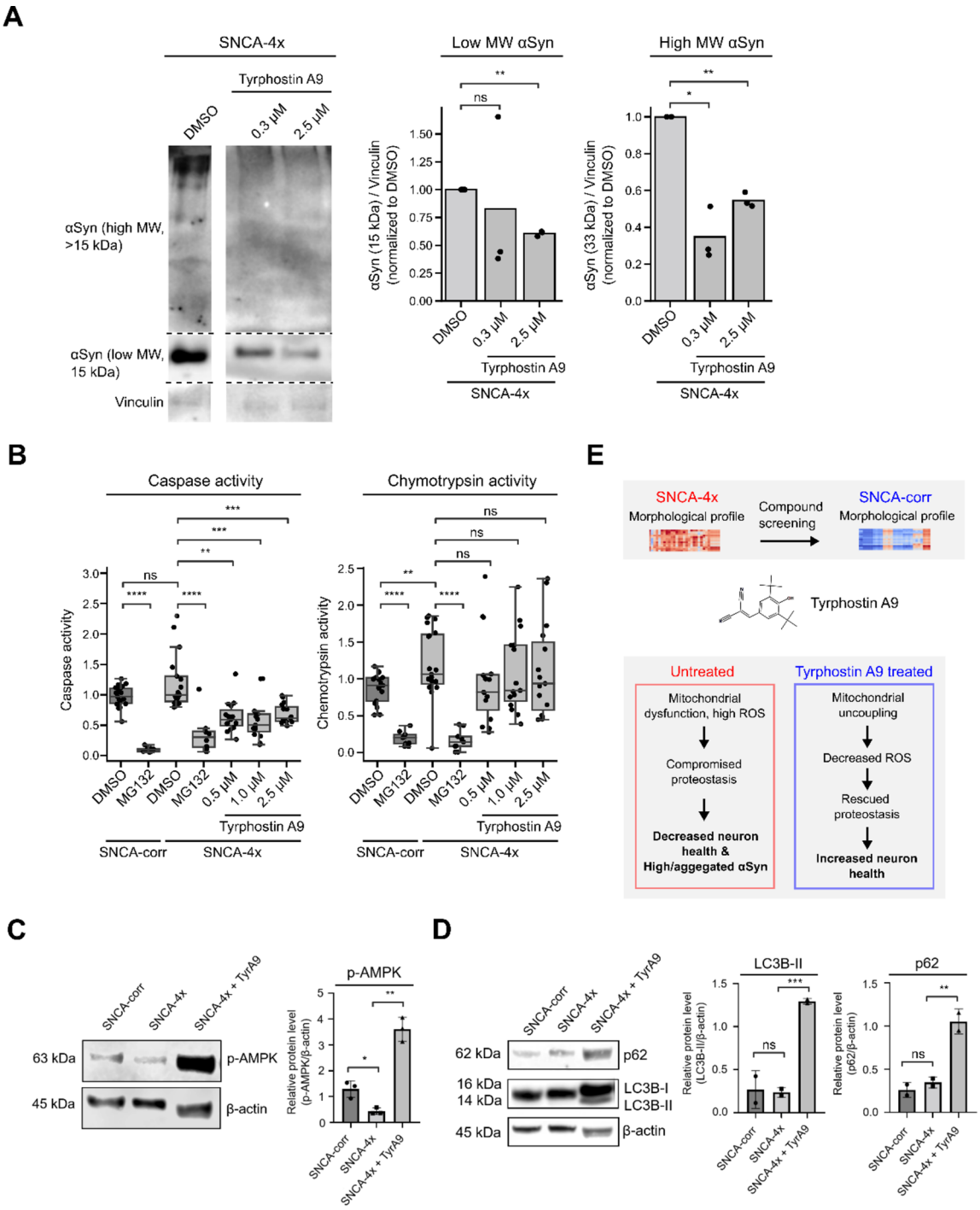
◀**Fig. 5**. Tyrphostin A9 structural analogues reduce mitochondrial membrane potential and ROS. **(A)** Molecular structures of Tyrphostin A9 and five selected structural analogues including their names, Compound ID (CID), and Tanimoto similarity coefficient relative to Tyrphostin A9. **(B)** Oxygen consumption rate (OCR), a proxy readout for mitochondrial respiration, was measured in D30 mDA neurons treated with 2.5 µM compound. (C-F) D33 mDA neurons were treated with 0.5–2.5 µM of each compound for 72 h. **(C)** Lactate dehydrogenase (LDH) activity was measured in the culture medium to determine relative cytotoxicity compared to cellular lysate (= 100%). **(D)** Mitochondrial membrane potential was measured using the JC-1 dye. **(E)** ROS level was determined using the ROS-ID detection kit and the obtained signal was normalized to total protein content. **(F)** Reduced glutathione (GSH) was measured using monochlorobimane (MCB) and the obtained signal was normalized to total protein content. Three independent experiments with at least three technical replicates were performed. The mean and 95% confidence interval are shown. Dashed lines indicate the median values of the respective controls.

Transport Chain (ETC) is uninhibited, allowing oxygen consumption by complex IV to reach its maximum. The resulting OCR increase is used as an estimation of the maximal respiratory capacity of the cell (Fig. 5B, left panel). Next to its use as a control compound, we also detected FCCP as one of the top hits during morphological profiling (Fig. 2F). We therefore compared Tyrphostin A9 and its structural analogues to FCCP using an OCR assay. We found that, similar to FCCP, Tyrphostin A9 and its closest structural analogues AG1024 and AG879 led to a strong increase in maximal respiratory capacity, highlighting their mitochondrial uncoupling activity (Fig. 5B, right panel). Next, we determined compound cytotoxicity by measuring Lactate dehydrogenase (LDH) in the culture medium. LDH is a stable enzyme, present in all cell types and rapidly released into the culture medium upon damage of the plasma membrane. None of the tested compounds induced significantly more cell death than the DMSO control when used at 0.5–2.5 µM for 72 h. Cell lysate was used as control corresponding to the maximum possible amount of released LDH (Fig. 5C). For Tyrphostin A9, we also tested concentrations ranging from 0.625 to 10 µM for 1–5 days and did not measure any increase of released LDH corresponding to low cytotoxicity (Figure S9). JC1 dye fluorescence was measured to determine the mitochondrial membrane potential. Tyrphostin A9 and its most closely related structural analogue Tyrphostin AG879 decreased the membrane potential as measured by the 547 nm/488nm fluorescence ratio from 0.95 to approximately 0.2. The second most similar analogue Tyrphostin AG1024 also decreased the membrane potential, although to a lesser extent (Fig. 5D). In line with the decreased membrane potential Tyrphostins A9 and AG879 also reduced ROS levels to ca. 80% of the DMSO baseline level (Fig. 5E). Next, we assessed glutathione levels. In healthy cells, both reduced glutathione (GSH) and its oxidized form (GSSG) are present, with the reduced form (GSH) making up the majority, while the oxidized form (GSSG) increases during oxidative stress. Although we expected an GSH increase due to ROS reduction, we observed that Tyrphostins A9, AG879 and AG1024 decreased GSH ratio, possibly due to lower overall glutathione synthesis after ROS decrease. Tyrphostin A9 lead to the strongest decrease of 48% at 2.5 µM (Fig. 5F). Mitochondrial uncoupling also strongly reduces cellular ATP production. We therefore tested the effects of all compounds on mDA neuron ATP level. We found that the compounds with the strongest uncoupling effects (Tyrphostins A9, AG1024, and AG879) reduced ATP levels the most (Figure S7A). mDA neuron treatment with the mitochondrial complex I inhibitor Rotenone led to similarly low ATP levels as Tyrphostin A9 treatment alone, indicating a near maximal Tyrphostin A9 uncoupling effect (Figure S7B). Since close Tyrphostin A9 structural analogues such as AG879 and AG1024 reproduce its cellular effects, the shared structural features may be critical for the molecule's function in mDA neurons.

Tyrphostin A9 induces αSyn Lowering

Our phenotypic compound screen revealed that mDA neuron αSyn levels were lowered by Tyrphostin A9 treatment (Fig. 3C). Since immunofluorescent staining is not sensitive enough to differentiate between αSyn monomers, oligomers, and larger structures such as fibrils, we performed Western blotting of Tyrphostin A9 treated and untreated > D50 mDA neuron lysates (Fig. 6A). We observed a 2-fold reduction of both low molecular weight αSyn (≈ 15 kDa) as well as higher molecular weight αSyn species. We observed a similar Tyrphostin A9-induced decrease of αSyn in an additional genetic Parkinson's disease model. mDA neurons carrying a Miro1 R272Q mutation showed a 70–80% decrease of 15 kDa and 33 kDa αSyn species (Figure S10)[37]. Most cellular proteins are selectively degraded by the proteasome via ubiquitination. Caspase and chymotrypsin are part of the proteasomal protein degradation machinery, contributing to the proteolytic activities of the proteasome. Using plate reader assays we therefore checked how caspase and chymotrypsin activities are impacted by Tyrphostin A9 in mDA neurons. Both enzymes' activities were not significantly different between SNCA-corr and SNCA-4x mDA neurons, while addition of Tyrphostin A9 rather decreased (≈ 50%) or did not impact caspase- or chymotrypsin-related proteasomal degradation, respectively (Fig. 6B). As expected, the known proteasome inhibitor MG132 strongly decreased both caspase and chymotrypsin activities in mDA neurons by > 70%.

Since Tyrphostin A9 did not positively impact proteasomal protein degradation in mDA neurons, the observed lower αSyn levels after compound treatment might result from a modulated alternative gene expression mechanism. To rule out transcriptional effects on α-synuclein (SNCA), we performed qPCR and found no significant change in SNCA mRNA levels following Tyrphostin A9 treatment (Figure S12). Next, we investigated the effect of Tyrphostin A9 on autophagy-related pathways in D38 mDA neurons. Cells were treated with 2.5 µM Tyrphostin A9 for 72 h, and protein levels were assessed by Western blotting. We observed increased phosphorylation of AMPK (p-AMPK) upon Tyrphostin A9 treatment, which is consistent with our findings that mitochondrial uncoupling by Tyrphostin A9 reduces cellular ATP levels, a known trigger for AMPK activation (Fig. 6C, Figure S7A). In line with this, we observed an increase in the levels of p62/SQSTM1, a selective



autophagy receptor, which is continuously synthesized during autophagy initiation (Fig. 6D). Additionally, LC3B levels were elevated, and two distinct bands corresponding to LC3-I and LC3-II were detected, suggesting altered autophagosome dynamics (Fig. 6D). The conversion from LC3-I (cytosolic form) to LC3-II (lipidated, membrane-bound form) reflects autophagosome formation[38].

Discussion

Here we used microscopy-based morphological profiling to characterize the effects of 1,020 FDA-approved or PD pathobiology-related small molecules on the overall morphological appearance of human iPSC-derived SNCA-4x mDA neurons. We observed that chemical compounds exist that impact two important hallmarks of PD pathophysiology: ROS reduction via mitochondrial uncoupling and αSyn reduction (Fig. 6C). We scored compounds based on their potential to induce a morphological profile resembling SNCA-corr mDA neurons (Fig. 2). Phenotypic or morphological profiling is increasingly used in iPSC-derived cells, primary cells or brain slice systems to study neuronal diversity and to complement single cell RNA sequencing data[39–42]. Previously, we established morphological profiling in LRRK2 G2019S mutated iPSC-derived mDA neurons and showed that multiple LRRK2 inhibitors can partially rescue the neuronal morphological profile[8]. Drug screens in mDA

◀**Fig. 6**. Tyrphostin A9 decreases αSyn protein expression. **(A)** Anti-αSyn Western blotting of mDA neuron lysates. Before lysis > D50 mDA neurons were treated with 0.3 or 2.5 µM Tyrphostin A9 for 72 h. Three independent neuronal differentiations were performed. Gel images are cropped. Full-length blots/gels are presented in Figure S8. **(B)** Caspase and Chemtrypsin activities were determined in approximately D30 mDA neurons treated with 1 or 2.5 µM Tyrphostin A9 or the proteasome inhibitor MG132 for 72 h. Three independent experiments with at least three technical replicates each were performed. The boxplots show the median and the 2nd and 3rd quartiles of the data. Whiskers indicate 1.5X of the interquartile range. **(C)** SNCA-4x mDA neurons were treated with 2.5 µM Tyrphostin A9 for 72 h and Western blotting was performed using antibodies against p-AMPK and β-actin. **(D)** SNCA-4x mDA neurons were treated with 2.5 µM Tyrphostin A9 for 72 h and Western blotting was performed using antibodies against p62, LC3B, and β-actin. Bar plots indicate the means of two or three independent differentiations. Welch's unequal variances t-test was performed using the (technical) replicates of all independent experiments. ns = not significant, * = $p < 0.05$, ** = $p < 0.01$, *** = $p < 0.001$. Uncropped Western blot images are shown in Figure S8 and Figure S11. **(E)** Scheme depicting the use of morphological profiling to identify compounds that produce a healthy control-like (SNCA-corr) profile in mutant (SNCA-4x) mDA neurons. The identified compound Tyrphostin A9 increases mitochondrial uncoupling and decreases ROS and αSyn levels which can explain the rescued morphological profile.

neuron model systems have been performed before, however either using only small screening libraries, non-human cell systems such as zebrafish, or very young mDA neuron progenitors (< 20 days of differentiation)[43–46]. This study combines detailed morphological profiling in human mDA neurons with a compound screen using a larger library (> 1,000 compounds). Although morphological profiling has the potential to identify completely novel targets, a limitation is that it typically provides little information about the actual potential compound targets, requiring detailed target and mode of action deconvolution studies.

In our study, we focused on mitochondrial uncoupling since two of our top scoring compounds (FCCP, Tyrphostin A9) are annotated as protonophores and mitochondrial uncouplers. Originally developed as an EGFR inhibitor, Tyrphostin A9 stood out due to its αSyn reducing and TH increasing effects in our morphological profiling assay as well as the molecule's previously described role in neuroprotection (Fig. 3)[33–35]. We found that the molecule promotes mitochondrial uncoupling and reduces ROS in mDA neurons in line with its previously described protonophore properties in other cell types (Fig. 4)[32,33,36]. In mDA neurons we made the observation that next to its mitochondrial uncoupling effect, Tyrphostin A9 also decreased neuronal activity which relies on charge-dependent action potentials (Fig. 4D). Tyrphostin A9 did not permanently damage the neurons, indicated by the gradual partial activity recovery over time, intact morphology, and low extracellular LDH levels (Fig. 3, Fig. 4D, Fig. 5C, Figure S9). Although the various Tyrphostins we tested were expected to increase GSH levels by reducing ROS, they instead decreased the GSH ratio. This might be due to reduced glutathione synthesis following ROS reduction, highlighting that the observed GSH depletion may reflect adaptive metabolic reprogramming and activation of protective pathways like Nrf2 signaling, rather than indicating toxicity[47–49].

A surprising observation we made is Tyrphostin A9's ability to reduce the low and high molecular weight αSyn levels in SNCA-4x and Miro1 R272Q mDA neurons by up to 80% (Figs. 3C and 6, Figure S10). We excluded a direct effect on caspase or chymotrypsin related proteasomal degradation mechanisms since Tyrphostin A9 either did not impact or even decreased these modes of protein degradation. Except for one study describing a role of Tyrphostin AG1024 in accelerating the degradation of Retinoblastoma Protein (pRb) likely involving the proteasome, Tyrphostins have not been directly linked to enhanced protein degradation[50]. Next to proteasomal protein degradation, the involvement of lysosomes in Parkinson's disease progression through two major autophagic pathways, chaperone-mediated autophagy and macroautophagy, and their central role in degrading αSyn is well documented[2]. In Tyrphostin A9 treated mDA neurons, we detected elevated levels of Thr172 phosoporylated AMPK, an activator of autophagy (Fig. 6C). AMPK typically becomes phosphorylated once ATP levels are low, an effect that we also attributed to Tyrphostin A9 due to its mitochondrial uncoupling activity (Figure S7A). We detected elevated levels of p62/SQSTM1, a selective autophagy receptor that is normally degraded during autophagic flux. LC3B levels were also increased, with Western blot analysis revealing two distinct bands corresponding to LC3-I and LC3-II, indicative of changes in autophagosome dynamics (Fig. 6D)[38]. While these findings are consistent with the initial activation phase of autophagy during which p62 transiently increases, the accumulation of p62 also raises the possibility of impaired autophagic clearance[51–53]. One study showed that Tyrphostin AG490, via JAK2 inhibition, prevented the hormone-receptor complex Epo-EpoR from targeting lysosomes in the UT-7 human cell line, highlighting a possible link between Tyrphostin action and lysosomal biology[54]. Taken together, the ROS-lowering effect of several Tyrphostins, likely due to mild mitochondrial uncoupling, may help prevent α-synuclein misfolding and facilitate its degradation through a lysosome-associated pathway. Autophagy might be further induced by Tyrphostins due to mitochondrial uncoupling, the resulting decreased ATP levels, and AMPK phosphorylation. However, the exact mechanism underlying the Tyrphostin-induced reduction in α-synuclein levels and associated morphological rescue remains to be clarified in future studies.

Tyrphostins have been described as mitochondrial uncouplers for almost half a century, while mitochondrial uncoupling as a neuroprotective strategy is more recent, but has faced several safety-related hurdles during pre-clinical drug development[55–58]. Recently the blocking of mitochondrial complex I in pro-inflammatory microglia has been shown to protect the central nervous system against neurotoxic damage in mice[59]. While our current study focuses on iPSC-derived neurons, future investigations into mitochondrial uncoupling as a neuroprotective strategy may benefit from exploring potential non-cell autonomous mechanisms. Such

mechanisms could be more effectively studied using advanced iPSC-derived co-culture systems or organoids that incorporate multiple central nervous system cell types, which are increasingly enabling the molecular characterization of complex cellular interactions[60–62]. Importantly, we do not propose Tyrphostin A9 itself as a therapeutic candidate for Parkinson's disease or other synucleinopathies. Rather, our study demonstrates that morphological profiling in a PD-relevant human model system can uncover compound classes with potentially underappreciated neuroprotective mechanisms. Tyrphostin A9 serves as a tool compound to explore such mechanisms, including mild mitochondrial uncoupling and enhanced lysosomal degradation of α-synuclein. Future research should investigate the long-term safety of mitochondrial uncoupling strategies, ideally in vivo, and further explore the link between Tyrphostin A9-induced lysosomal modulation and neuroprotection.

Materials and methods

Origin of iPSC lines and differentiation into mDA neurons

SNCA iPSC lines (originally named AST23 and AST23-2KO) were provided and generated by Dr. Tilo Kunath from The University of Edinburgh. The parental cell line AST23 was first described in Devine et al.[19]. The generation of the SNCA-corr cell line AST23-2KO is described in Chen et al.[63]. Both cell lines are deposited as EDi001-A and EDi001-A-5 in the hPSCreg repository, respectively (https://hpscreg.eu). The Miro1 R272Q and isogenic control cell lines originate from our laboratory and are described by Chemla et al.[37]. iPSCs were cultured on Geltrex-coated (Thermo Fisher Scientific) dishes in StemMACS iPS-Brew XF (Miltenyi Biotech). The medium was changed daily, and cells were passaged twice a week using 0.5 mM EDTA in PBS (Thermo Fisher Scientific). Mycoplasma testing was performed twice per month. mDA neurons were differentiated using a modified protocol based on Kriks et al.[64–66]. In summary, iPSCs were initially placed on Geltrex-coated six-well plates or T75 flasks at a density of 2×10^5 cells/cm2 in StemMACS iPS-Brew XF with 10 µM Y-27,632 (Hiss). The following day, the medium was changed to KnockOut DMEM medium with KnockOut serum replacement (both from Thermo Fisher Scientific), supplemented with 200 nM LDN19318 (Axon Medchem) and 10 µM SB431542 (Biozol) for dual SMAD-inhibition. On the second day, 100 ng/mL Shh C24II (Miltenyi Biotech), 2 µM Purmorphamine (Miltenyi Biotec), 100 ng/mL FGF8 (Peprotech), and 3 µM CHIR99021 (Miltenyi Biotec) were also added to the medium. After a period of 5 days, the medium was gradually transitioned to Neurobasal medium (Thermo Fisher Scientific), and SB431542 was removed from the medium. Starting from day 7, cells were cultivated only in the presence of LDN19318 and CHIR99021. On day 11, cells were transferred to Neurobasal/B27/L-glutamine medium with only CHIR99021. On day 13, cells were moved onto Geltrex-coated dishes in Neurobasal/B27/L-glutamine medium with supplements of 20 ng/mL BDNF, 20 ng/mL GDNF (both from Cell Guidance Sys.), 220 µM L-ascorbic-acid (Sigma-Aldrich), 10 µM DAPT (Axon Medchem), 1 ng/mL TGF-βIII (Peprotech), 0.5 mM dibutyryl-cAMP (Enzo Life Sciences), and 10 µM Y-27,632 (Hiss). Cells were kept in the same medium but without Y-27,632. Around days 23–25, cells were separated using StemPro Accutase (Thermo Fisher Scientific) and placed at a density of 1.4×10^5 cells/cm2 onto Geltrex-coated dishes. To remove non-neuronal cells, cultures were exposed to 1 µg/mL Mitomycin C for 2 h on day 26. On day 30, neuronal cultures were separated using StemPro Accutase with 10 µM Y-27,632 and singularized. Cells were counted and preserved at 2.5×10^6 cells/vial in CryoStor CS 10 tubes (Sigma-Aldrich).

Neuronal culture

30 days old mDA neurons were thawed and spun (400 g, 5 min, RT) in a basal medium (Table S2) supplemented with a ROCK inhibitor (Tocris #1254). The cell pellets were then reconstituted in a differentiation medium (Table S2) also supplemented with a ROCK inhibitor. 384-well plates (Perkin Elmer, Phenoplate poly-D-lysine-coated #6057500) were prepared with a coating of 10 µg/ml laminin at 4 °C overnight. Using trypan blue (Invitrogen, #T10282) and a Countess automated cell counter (Invitrogen), cells were seeded in the 384-well plates at a density of 10×10^3 cells/well. Edge wells were not used for seeding and were filled with PBS instead. Typically, the thawed cells were incubated at 37 °C and 5% CO2 for 6 days until they reached day 36, with changes in the differentiation medium occurring at D33. The processes of plate coating, cell seeding, and medium changes were automated using an Bravo Automated Liquid Handling Platform with 384ST head (Agilent) and a Multidrop Combi Dispenser (ThermoFischer Scientific).

Compound library and compound treatment

1,020 small molecules were selected from a bioactive compound library (Selleckchem), based on PD-relevant pathobiology, FDA approval status, and blood-brain-barrier penetrance (Table S3). *Prostratin treatment*: Neurons were cultured until D33, treated with 5 µM Prostratin (Biotechne) or DMSO for 72 h and immunofluorescently stained. *Primary screening*: Cryopreserved mDA D30 neurons were cultured in 384-well plates until D33, treated with each compound at a concentration of 5 µM for a duration of 72 h, and subsequently stained. Each compound underwent testing in four technical replicates. Compound wells were randomly assigned between technical replicates. 36 wells per plate were designated as control wells. The control conditions were used to establish the baseline and maximum effect profiles, specifically with SNCA-4x + DMSO serving as the baseline and SNCA-corr + DMSO as the maximum effect profile. Compounds and DMSO were dispensed using a Bravo Automated Liquid Handling Platform with 384ST head (Agilent). *Dose-response testing*: Identical to primary screening but with six different compound concentrations ranging from 0.25 to 20 µM. *Biochemical assays*: > D30 neurons were treated with 0.5–2.5 µM compound for 72 h. *Microelectrode array (MEA)*: Ca. D60-old mDA neurons were treated up to 72 h with 2.5 µM Tyrphostin A9. *Western blotting*: > D50 mDA neurons were treated with 0.3 and 2.5 µM Tyrphostin A9 for 5 days.

Immunofluorescent staining

Neurons were fixed using 4% PFA (EMS Euromedex, #15710) for a duration of 20 min, followed by three PBS washes (Gibco, #14190136). The cells were then permeabilized and blocked using a solution of 10% FBS (Sigma, #F7524) and 0.1% Triton X-100 (Sigma, #T9284) in PBS for an hour. Primary antibodies against TH, αSyn, and MAP2 (Table S2) were prepared in an antibody dilution buffer (PBS with 5% FBS and 0.1% Triton X-100) and left to incubate with the cells at 4 °C overnight. This was followed by three PBS washes. Secondary antibodies and Hoechst (Table S2) were added to the cells in the antibody dilution buffer and left for an hour at room temperature, followed by another three PBS washes. Immunofluorescent staining was automated using an EL406 plate washer and dispenser (Biotek).

Image acquisition and feature extraction

Imaging was performed on a Yokogawa CV7000 microscope in scanning confocal mode using a dual Nipkow disk and a cooled sCMOS camera with 2,560 × 2,160 pixels and a pixel size of 6.5 µm without pixel binning. The system's CellVoyager software (Yokogawa, version R1.17.05), the 405/488/561/640-nm solid laser lines, and a dry 40X objective were used to acquire 16 images in a 4 × 4 orientation from three 1 µm-separated Z-planes from the center of each well. Wells were visited in a row-wise "zigzag" fashion. Maximum intensity projections were performed. Image segmentation and feature extraction was performed with our in-house software PhenoLink (Ksilink, version 24.01.R0, https://github.com/Ksilink/PhenoLink). Image segmentation was performed on 4 × 4 stitched and illumination corrected images. Using intensity and size thresholds specific to each of the four imaging channels (Hoechst, TH, αSyn, and MAP2) we extracted a total of 124 morphological features, including count, texture, context, intensity and shape features (Table S4). We used location constraints to identify subcellular compartments. For example, by subtracting the segmented nucleus from the whole cell we obtained the cytoplasm or by calculating a 4 pixel-wide area around the outer edge of the cell we estimated the location of the cell membrane.

Data processing & morphological profile generation

All data manipulation and transformation processes were carried out using Python's Pandas package[67]. All plots were generated using the Seaborn package[68]. All data processing and plotting can be reproduced using the provided Python Jupyter Notebooks and accompanying raw data. Briefly, raw morphological profiles were created per well by using the information from all measured 127 morphological features (Table S4). First, per feature a mean feature value from all acquired 16 image fields per well was calculated. The feature values were subjected to a standard scaling process using the StandardScaler function from the sklearn.preprocessing module in Python, resulting in the creation of 127-feature raw morphological profiles per well[69]. To determine the most defining morphological features per treatment condition, the morphological profiles were grouped based on their experimental replicates and treatments. The absolute differences in the mean values of the grouped data were calculated and followed by the computation of the mean and standard deviation of these absolute differences. We employed Principal Component Analysis (PCA) to compare morphological feature profiles across biological conditions and treatments. PCA was performed with 10 components and the explained variance ratio for each of the principal components was calculated. To measure how each original feature contributed to the principal components, the correlation between the original features and the first 10 principal components was calculated.

Primary screening data processing and hit selection

The raw data was composed out of 307,200 images from 4,800 wells distributed over 20 384-well plates. For all fluorescent channel images (Hoechst, TH, αSyn, and MAP2) we performed image segmentation and feature extraction, giving rise to a raw 127-feature morphological profile. Per plate, extreme outlier features were eliminated using a robust standard deviation-based method. This involved calculating the absolute difference between each data point and the feature median, and retaining data that was within 4σ of the Median Absolute Deviation (MAD). Next, data was normalized to allow comparisons between plates. We applied a robust Z-score normalization, during which the original data was adjusted based on its deviation from the median of the DMSO control data and was scaled by the MAD of the DMSO control data. This method is robust to outliers as it uses median and MAD, which are less sensitive to extreme values. Feature reduction was performed in two separate steps. Since the morphological profile contains an overrepresentation of texture features, first the two most distinguishing texture features were selected by calculating the z-factors for each feature, sorting them in descending order, and picking the top two. In the second step, features with less than 95% pairwise Pearson correlation were retained. In total, 40 features remained (Figure S2B). Plate quality was assessed using the Strictly Standardized Mean Difference (SSMD) based on the 40-feature Mahalanobis distance of SNCA-4x + Prostratin-treated control wells to SNCA-4x + DMSO control wells. SSMD values for all 20 plates were <-1, indicating a good plate quality. We then calculated the 40-feature Mahalanobis distances of all SNCA-4x compound-treated wells to the SNCA-4x + DMSO and SNCA-corr + DMSO control wells. We applied a Mahalanobis distance threshold of >4 to identify compounds inducing morphological profiles different from SNCA-4x + DMSO control profiles. Additionally, we selected compounds based on close Mahalanobis distances to SNCA-corr + DMSO control profiles, thereby selecting compounds that induce morphological profiles similar to healthy control neurons. All data processing and hit selection steps can be reproduced by using the provided Python Jupyter Notebooks.

Evaluation of mitochondrial membrane potential

Mitochondrial membrane potential (Δψm) was estimated using the fluorescent probe JC-1 (ThermoFisher, T3168). Briefly, 60×10^3 mDA neurons were seeded per well in a Geltrex-coated black, clear-bottom 96-well cell culture plate and treated with selected compounds for three days. On neuronal maturation day 33, the neuronal medium was removed and cells were incubated with 100µL/well of fresh neuronal medium containing

10 µM of JC-1 dye for 30 min at 37 °C. After incubation, cells were washed three times with pre-warmed DPBS (ThermoFisher, #14190094). Fluorescence was measured using a Cytation 5 (Bio-Tek) fluorescence plate reader, with excitation at 560 nm and emission at 610 nm for the aggregated JC-1 and excitation at 500 nm and emission at 550 nm for the monomeric JC-1. Mitochondrial membrane potential was estimated by calculating the ratio of aggregated to monomeric JC-1 fluorescent signal. Statistical analyses were conducted on data from, at least, three independent biological replicates.

Measurement of intracellular ROS and glutathione levels

Intracellular ROS levels were measured using the ROS-ID Total ROS/Superoxide detection kit (Enzo, Enz-51010), following the manufacturer's instructions. Briefly, 60×10^3 mDA neurons were seeded per well in a Geltrex-coated black, clear bottom 96-well cell culture plate. Neurons were treated for three days with the selected compounds. On neuronal maturation day 33, the neuronal medium was removed and the cells were washed once with pre-warmed DPBS (ThermoFisher, #14190094). Cells were then incubated with 100 µL/well of ROS Detection Solution for 1 h at 37 °C. Finally, fluorescence is measured without removing the detection solution, using a Cytation 5 (Bio-Tek) fluorescence plate reader (bottom reading at Ex = 490 nm, Em = 520 nm). Fluorescence intensity was normalized to total cell protein levels, using the BCA Protein Detection Kit (ThermoFisher, #23227). Statistical analyses were conducted on data from three independent biological replicates. Simultaneously, intracellular GSH levels were measured using the monochlorobimane (MCB, AAT Bioquest, #76421-73-3) assay. In this procedure, 60×10^3 mDA neurons were seeded per well in a Geltrex-coated black, clear-bottom 96-well cell culture plate and treated with selected compounds for three days. On neuronal maturation day 33, the neuronal medium was removed, and the cells were washed once with pre-warmed DPBS (ThermoFisher, #14190094). The cells were then incubated with 100 µL per well of a detection solution containing 50 µM MCB for 1 h a, with excitation at 360 nm and emission at 480 nm t 37 °C. After incubation, fluorescence was measured directly without removing the detection solution using a Cytation 5 (Bio-Tek) fluorescence plate reader, with excitation at 360 nm and emission at 480 nm. The fluorescence intensity readings were normalized to total cell protein levels, which were determined using the BCA Protein Detection Kit (ThermoFisher, #23227). Statistical analyses were conducted on data from three independent biological replicates.

Evaluation of cytotoxicity

Cytotoxicity was estimated using the lactate dehydrogenase (LDH) assay (Canvax, CA0020), following the manufacturer's instructions. 60×10^3 mDA neurons were seeded per well in a Geltrex-coated black, clear bottom 96-well cell culture plate. Neurons were treated for three days with the selected compounds. On neuronal maturation day 33, 50 µL of media was obtained from each well and transferred to a 96-well cell culture plate, in order to evaluate the release of LDH into the cell culture media. It was added to an equal volume (50 µL) of mixed LSH assay buffer and dye solution and was incubated for 30 min, at room temperature, protected from light. Finally, 50 µL Stop Solution was added per well and the absorbance (OD) was measured using a Cytation 5 (Bio-Tek) plate reader (450 nm). LDH absorbance was normalized to total cell protein levels, using the BCA Protein Detection Kit (ThermoFisher, #23227). Statistical analyses were conducted on data from three independent biological replicates.

Measurement of intracellular ATP levels

Intracellular ATP levels were evaluated using the CellTiter-Glo 2.0 (Promega, G9241), according to the product's instructions. Briefly, 70×10^3 mDA neurons were seeded per well in a Geltrex-coated black, clear-bottom 96-well cell culture plate and treated with selected drugs or compounds for three days. On neuronal maturation day 33, the neuronal medium was removed, and cells were washed once pre-warmed DPBS (ThermoFisher, #14190094). Cells were incubated with 75 µL per well of HBSS and an equal volume of the CellTiter-Glo 2.0 mix was added in each well. The plates were shaken for 2 min in RT, followed by 10 min of incubation in RT. Luminescence was measured using a Cytation 5 (Bio-Tek) plate reader. Luminescence intensity was normalized to total cell protein levels, using the BCA Protein Detection Kit (ThermoFisher, #23227). Statistical analyses were conducted on data from three independent biological replicates.

Analysis of mitochondrial respiration

Oxygen consumption rates (OCRs) were measured using the Seahorse XFe96 FluxPak (Agilent, #102416-100) and the XF Cell Mito Stress Test Kit (Agilent, #103015-100), following the manufacturer's instructions. For this experiment, 70×10^3 mDA neurons were seeded per well in a Geltrex-coated 96-well Seahorse cell culture plate. On neuronal maturation day 33, the neuronal medium in each well was replaced with 175 µl of Seahorse XF DMEM Medium (pH 7.4, Agilent, #103575-100) containing 25 mM Glucose, 2 mM L-Glutamine, and 1 mM Sodium Pyruvate. The cells were incubated for 1 h at 37 °C without CO2. Meanwhile, the sensor cartridge, pre-equilibrated overnight in XF Calibrant solution at 37 °C without CO2, was prepared with standard mitochondrial inhibitors: Oligomycin (2.5 µM), FCCP or tyrphostin analogs (2.5 µM), and a mixture of Rotenone and Antimycin A (1 µM each). After a further 30-minute incubation at 37 °C without CO2, the sensor cartridge and the cell culture plate were loaded into the XFe96 Extracellular Flux Analyzer (Agilent). OCR was measured three times for basal respiration and after each injection of mitochondrial toxins. Post-assay, the cell culture medium was removed, and total protein content was determined using a BCA Protein Assay Kit (ThermoFisher, #23227). The OCR data were analyzed with XFe Wave Pro software (Agilent, version 10_3_0_515), normalized to total cell protein levels (based on the BCA assay), and exported using the Seahorse XF Cell Mito Stress Test Report Generator. Statistical analyses were conducted on data from three independent biological replicates. The study calculated various parameters related to oxidative phosphorylation, including basal respiration, proton leakage

across the inner mitochondrial membrane, ATP-coupled respiration, maximal respiration, and spare respiratory capacity.

Multi-electrode array (MEA)

Cryopreserved 30 days old neurons were thawed in a water bath and centrifuged (400 g, 5 min, RT) in basal medium (Table S2) supplemented with ROCK inhibitor (Tocris, #1254). Cell pellets were resuspended in differentiation medium (Table S2) supplemented with ROCK inhibitor. 48-well CytoView MEA plates (Axion Biosystems, #M768-tMEA-48 W) were coated with 15 µg/ml Polyethyleneimine solution (Sigma, #P3143) for 1 h at 37 °C followed by 10 µg/ml Laminin coating for 2 h at 37 °C. Using Tryphan Blue (Sigma, # T8154-20ML) and a Countess automated cell counter (Invitrogen), 80×10^3 cells/well were seeded in the CytoView plate. Cells were incubated at 37 °C and 5% CO_2 for 26–33 days with differentiation medium changes twice a week. Once a week, 1 µg/ml Laminin was added to the fresh media to maintain cell attachment. Neurons were then treated with compound for 72 h. The electrical activity was recorded on the Maestro Pro multiwell MEA (Axion Biosystems) using the AxIS Navigator software (version 3.5.1, Axion Biosystems). Electrical activity was recorded for 10 min at a 12.5 kHz sampling rate and a 5.5 standard deviation threshold level for action potential detection. Before plate loading the device was allowed to equilibrate for approximately 30 min to 37 °C and 5% CO2. Data analyses were performed using the Neural Metric Tool (version 3.1.7, Axion Biosystems). Activity is expressed as the mean firing rate across electrodes in a well.

SDS gel electrophoresis and Western blotting

1.5×10^6 mDA neurons were cultured for at least 50 days in Geltrex-coated 6-well plates with neuronal media and treated with compound for five days. At day 50, the neuronal media was removed and cells were washed with pre-warmed DPBS. For high resolution αSyn detection, the following steps were performed: DPBS was removed and cells were crosslinked by adding 1 mL pre-warmed PBSx1 supplemented with 2 mM disuccinimidyl glutarate (DSG, ThermoFisher, #20593) and protease inhibitors for 30 min at 37 °C. Crosslinking was terminated by adding 50 mM Tris-HCl, pH = 7.5 for 15 min at room temperature. Cells were collected and centrifuged for 10 min at 1000xg at room temperature. The supernatant was removed and the cell pellet was lysed using lysis buffer (100 mM NaCl, 5 mM EDTA, 50 mM Tris-Cl, pH 7.4, 50 mM NaF, containing 1% (v/v) Igepal CA-630 and supplemented with protease inhibitors). Cells were incubated for 30 min at 4 °C with the lysis buffer and sonicated three times. Total cellular protein was measured using the BCA Protein Detection Kit (ThermoFisher, #23227) and 25 µg of cell lysate were electrophoresed at 100 V constant on NuPAGE 4–12% Bis-Tris Midi gels (Invitrogen, NP0321BOX) with NuPage MES-SDS running buffer (Invitrogen, NP0002). After electrophoreses, gels were electroblotted in nitrocellulose membranes, using a wet-transfer approach. After electroblotting, the membranes were briefly rinsed in ultrapure water and incubated in 4% paraformaldehyde/PBS for 30 min at room temperature, followed by blocking for 1 h at room temperature in TBS-Tween 0.1% (v/v) supplemented with 5% (w/v) dry milk. To visualize other proteins and αSyn at lower size resolution, the following steps were performed: Cellular pellets were lysed using RIPA buffer, including phosphatase and protease inhibitors, and total protein was quantified using the Pierce BCA assay kit, according to the manufacturer's instructions. 30 mg of total exosomal extract was subjected to sodium dodecyl sulfate-polyacrylamide gel electrophoresis on 8–12% Bis-Tris gel (Thermo Fisher Scientific). The separated proteins were transferred onto a nitrocellulose membrane, followed by blocking with 5% non-fat milk powder (w/v) in Tris-buffered saline (10 mM Tris-HCl, pH 7.5, 100mM NaCl, 0.1% Tween 20) for 1 h at room temperature. After blocking, membranes were incubated with the primary antibodies listed in Table S2. The next day, membranes were washed 3 × 10 min in PBS-Tween 0.1% and incubated with the corresponding secondary antibodies (Table S2) at RT for 1 h in the dark. Membranes were rinsed in PBS-Tween 0.1%, washed at least 3 × 10 min in PBS-Tween 0.1%, incubated for 3 min with ECL western blotting substrate, and imaged on a LI-COR Odyssey XF imaging system.

Measurement of intracellular calcium levels

Intracellular calcium levels were evaluated using the cell-permeant calcium indicator Rhod-FF AM (Invitrogen, R23983). Briefly, 70×10^3 mDA neurons were seeded per well in a Geltrex-coated black, clear-bottom 96-well cell culture plate and treated with the selected compound for three days. On neuronal maturation day 33, the neuronal medium was removed, and cells were washed with the pre-warmed HBS buffer (145 mM NaCl, 5 mM KCl, 1 mM $CaCl_2$, 1 mM $MgCl_2$, 10 mM HEPES, 10mM glucose) and incubated for 1 h at room temperature, protected from light, with HBS buffer containing 0.1% (w/v) BSA and 5 µM Rhos-FF AM. After incubation, the cells were washed twice with 100µL per well HBS and were incubated for 20 min at room temperature, protected from light, for dye de-esterification. Fluorescence was measured 4 times, every 30 s, using a Cytation 5 (Bio-Tek) fluorescence plate reader, with excitation at 550 nm and emission at 580 nm, at 28 °C. After the first measurement, HBS buffer supplemented with 10 µM of Ionomycin (Sigma, #19657) was added to the cells, and the plate was measured again (8 times (8 times, every 30 s). Fluorescence intensity was normalized to total cell protein levels, using the BCA Protein Detection Kit (ThermoFisher, #23227).

Evaluation of proteasomal activity

The proteasomal activity was evaluated by measuring the chymotrypsin-like and caspase-like activity. The chymotrypsin-like activity was measured using the fluorogenic substrate Suc-Leu-Leu-Val-Tyr-AMC (Enzo, BML-PB02-0005) and the caspase-like activity was measured by using the fluorogenic substrate Z-Leu-Leu-Glu-AMC (Enzo, BML-ZW9345-0005). Briefly, 60×10^3 mDA neurons were seeded per well in a Geltrex-coated black, clear-bottom 96-well cell culture plate and treated with the selected compound for three days. On neuronal maturation day 33, the neuronal medium was removed and cells were washed with the pre-warmed assay buffer (20 mM Tris-HCl pH = 7.5, 5 mM $MgCl_2$, 0.1 mM EDTA, 1 mM DTT, 1 mM ATP, pH = 7.4). After washing,

cells are incubated for 30 min at 37 °C with 100 µL per well of assay buffer containing 100 µM of the respective fluorescent substrate. Finally, fluorescence was measured using a Cytation 5 (Bio-Tek) fluorescence plate reader, with excitation at 380 nm and emission at 460 nm, at 37 °C. Fluorescence intensity was normalized to total cell protein levels, using the BCA Protein Detection Kit (ThermoFisher, #23227). Statistical analyses were conducted on data from three independent biological replicates.

qPCR

Cellular pellets were used for RNA isolation using the RNeasy Plus Mini kit (Qiagen), following the manufacturer's instructions. The isolated RNA was converted to cDNA using the High-Capacity cDNA Reverse Transcription Kit (Applied Biosystems), following the manufacturer's instructions. Gene expression was assessed on a LightCycler 480 II (Roche Diagnostics), using the PowerTrack SYBR Green Mastermix (Thermo Fisher Scientific), following the manufacturer's instructions. The sets of primers that were used are shown in TableS2. SNCA fold changes were quantified relative to ACTB using the $\Delta\Delta C_t$ approach.

Structural analogues

Compounds were directly obtained from Selleckchem (CIDs: 5614, 2044, 1838043, 135419190), Enamine (CID: 135407924), or custom synthesized by SynHet (CID: 3511020). For compound CID 3511020, we chose the abbreviation CEPPE based on its IUPAC name 2-cyano-3-(3-ethoxy-4-propan-2-yloxyphenyl)prop-2-enethioamide. Chemical structures were plotted from their Simplified molecular-input line-entry system (SMILES) strings using Python. The rdkit package was used to create molecule objects from the SMILES strings and to compute 2D coordinates for these molecules. Tanimoto coefficients were calculated using their CID code via the PubChem Score Matrix service available at https://pubchem.ncbi.nlm.nih.gov/score_matrix/score_matrix.cgi.

Data availability

The datasets supporting the conclusions of this article are available in the GitHub repository, https://github.com/Ksilink/Notebooks/tree/main/Neuro/PD_MorphProfileScreening. Raw data is available as CSV files which can be processed using the provided Python-based Jupyter Notebooks.

Received: 4 February 2025; Accepted: 4 August 2025
Published online: 12 August 2025

References

1. Wüllner, U. et al. The heterogeneity of Parkinson's disease. *J. Neural Transm.* **130**, 827–838 (2023).
2. Poewe, W. et al. Parkinson disease. *Nat. Rev. Dis. Primer.* **3**, 17013 (2017).
3. Coukos, R. & Krainc, D. Key genes and convergent pathogenic mechanisms in Parkinson disease. *Nat. Rev. Neurosci.* **25**, 393–413 (2024).
4. Espay, A. J. et al. Biomarker-driven phenotyping in parkinson's disease: A translational missing link in disease-modifying clinical trials. *Mov. Disord.* **32**, 319–324 (2017).
5. Krüger, R. et al. Classification of advanced stages of parkinson's disease: translation into stratified treatments. *J. Neural Transm.* **124**, 1015–1027 (2017).
6. Prasuhn, J. & Brüggemann, N. Genotype-driven therapeutic developments in parkinson's disease. *Mol. Med.* **27**, 42 (2021).
7. Laperle, A. H. et al. iPSC modeling of young-onset parkinson's disease reveals a molecular signature of disease and novel therapeutic candidates. *Nat. Med.* **26**, 289–299 (2020).
8. Vuidel, A. et al. High-content phenotyping of parkinson's disease patient stem cell-derived midbrain dopaminergic neurons using machine learning classification. *Stem Cell. Rep.* **17**, 2349–2364 (2022).
9. D'Sa, K. et al. Prediction of mechanistic subtypes of parkinson's using patient-derived stem cell models. *Nat. Mach. Intell.* **5**, 933–946 (2023).
10. Bose, A., Petsko, G. A. & Studer, L. Induced pluripotent stem cells: a tool for modeling parkinson's disease. *Trends Neurosci.* **45**, 608–620 (2022).
11. Schiff, L. et al. Integrating deep learning and unbiased automated high-content screening to identify complex disease signatures in human fibroblasts. *Nat. Commun.* **13**, 1590 (2022).
12. Cholerton, B. et al. Precision medicine. *Am. J. Pathol.* **186**, 500–506 (2016).
13. Espay, A. J., Brundin, P. & Lang, A. E. Precision medicine for disease modification in Parkinson disease. *Nat. Rev. Neurol.* **13**, 119–126 (2017).
14. Haston, K. M. & Finkbeiner, S. Clinical trials in a dish: the potential of pluripotent stem cells to develop therapies for neurodegenerative diseases. *Annu. Rev. Pharmacol. Toxicol.* **56**, 489–510 (2016).
15. Polymeropoulos, M. H. et al. Mutation in the α-Synuclein gene identified in families with parkinson's disease. *Science* **276**, 2045–2047 (1997).
16. Krüger, R. et al. AlaSOPro mutation in the gene encoding α-synuclein in parkinson's disease. *Nat. Genet.* **18**, 106–108 (1998).
17. Singleton, A. B. et al. α-Synuclein locus triplication causes parkinson's disease. *Science* **302**, 841–841 (2003).
18. Chartier-Harlin, M. C. et al. α-synuclein locus duplication as a cause of Familial parkinson's disease. *Lancet* **364**, 1167–1169 (2004).
19. Devine, M. J. et al. Parkinson's disease induced pluripotent stem cells with triplication of the α-synuclein locus. *Nat. Commun.* **2**, 440 (2011).
20. Byers, B. et al. SNCA triplication parkinson's patient's iPSC-derived DA neurons accumulate α-Synuclein and are susceptible to oxidative stress. *PLoS ONE.* **6**, e26159 (2011).
21. Mohamed, N. V. et al. Midbrain organoids with an *SNCA* gene triplication model key features of synucleinopathy. *Brain Commun.* **3**, fcab223 (2021).
22. Iannielli, A. et al. Modeling native and seeded synuclein aggregation and related cellular dysfunctions in dopaminergic neurons derived by a new set of isogenic iPSC lines with SNCA multiplications. *Cell. Death Dis.* **13**, 881 (2022).
23. Oliveira, L. M. A. et al. Elevated α-synuclein caused by SNCA gene triplication impairs neuronal differentiation and maturation in parkinson's patient-derived induced pluripotent stem cells. *Cell. Death Dis.* **6**, e1994–e1994 (2015).
24. Zambon, F. et al. Cellular α-synuclein pathology is associated with bioenergetic dysfunction in parkinson's iPSC-derived dopamine neurons. *Hum. Mol. Genet.* **28**, 2001–2013 (2019).

25. Heman-Ackah, S. M. et al. Alpha-synuclein induces the unfolded protein response in parkinson's disease SNCA triplication iPSC-derived neurons. *Hum. Mol. Genet.* **26**, 4441–4450 (2017).
26. Burbulla, L. F. et al. Dopamine oxidation mediates mitochondrial and lysosomal dysfunction in parkinson's disease. *Science* **357**, 1255–1261 (2017).
27. Angelova, P. R. et al. Alpha synuclein aggregation drives ferroptosis: an interplay of iron, calcium and lipid peroxidation. *Cell. Death Differ.* **27**, 2781–2796 (2020).
28. Tanudjojo, B. et al. Phenotypic manifestation of α-synuclein strains derived from parkinson's disease and multiple system atrophy in human dopaminergic neurons. *Nat. Commun.* **12**, 3817 (2021).
29. Chandrasekaran, S. N., Ceulemans, H., Boyd, J. D. & Carpenter, A. E. Image-based profiling for drug discovery: due for a machine-learning upgrade? *Nat. Rev. Drug Discov.* **20**, 145–159 (2021).
30. Chandrasekaran, S. N. et al. *JUMP Cell Painting Dataset: Morphological Impact of 136,000 Chemical and Genetic Perturbations*. http://biorxiv.org/lookup/doi/10.1101/2023.03.23.534023. 10.1101/2023.03.23.534023 (2023).
31. Bray, M. A. et al. Cell painting, a high-content image-based assay for morphological profiling using multiplexed fluorescent dyes. *Nat. Protoc.* **11**, 1757–1774 (2016).
32. Park, S. J. et al. A receptor tyrosine kinase inhibitor, tyrphostin A9 induces cancer cell death through Drp1 dependent mitochondria fragmentation. *Biochem. Biophys. Res. Commun.* **408**, 465–470 (2011).
33. Sagara, Y., Ishige, K., Tsai, C. & Maher, P. Tyrphostins protect neuronal cells from oxidative stress. *J. Biol. Chem.* **277**, 36204–36215 (2002).
34. Ferreira, A. F. F. et al. Inhibition of TRPM2 by AG490 is neuroprotective in a parkinson's disease animal model. *Mol. Neurobiol.* **59**, 1543–1559 (2022).
35. Dai, X. et al. Tyrphostin A9 protects axons in experimental autoimmune encephalomyelitis through activation of ERKs. *Life Sci.* **294**, 120383 (2022).
36. Iaubasarova, I. R. et al. The mitochondria-targeted derivative of the classical uncoupler of oxidative phosphorylation carbonyl cyanide m-chlorophenylhydrazone is an effective mitochondrial recoupler. *PLOS ONE.* **15**, e0244499 (2020).
37. Chemla, A. et al. Generation of two induced pluripotent stem cell lines and the corresponding isogenic controls from parkinson's disease patients carrying the heterozygous mutations c.815G>A (p.R272Q) or c.1348C>T (p.R450C) in the RHOT1 gene encoding Miro1. *Stem Cell. Res.* **71**, 103145 (2023).
38. Mizushima, N. & Yoshimori, T. How to interpret LC3 Immunoblotting. *Autophagy* **3**, 542–545 (2007).
39. McDiarmid, A. H. et al. Morphological profiling in human neural progenitor cells classifies hits in a pilot drug screen for Alzheimer's disease. *Brain Commun.* **6**, fcae101 (2024).
40. Han, X. et al. Whole human-brain mapping of single cortical neurons for profiling morphological diversity and stereotypy. *Sci. Adv.* **9**, eadf3771 (2023).
41. Peng, H. et al. Morphological diversity of single neurons in molecularly defined cell types. *Nature* **598**, 174–181 (2021).
42. Kilfeather, P. et al. Single-cell Spatial transcriptomic and Translatomic profiling of dopaminergic neurons in health, aging, and disease. *Cell. Rep.* **43**, 113784 (2024).
43. Kim, G. H. J. et al. A zebrafish screen reveals Renin-angiotensin system inhibitors as neuroprotective via mitochondrial restoration in dopamine neurons. *eLife* **10**, e69795 (2021).
44. Cui, J., Carey, J. & Reijo Pera, R. A. Identification of DOT1L inhibitor in a screen for factors that promote dopaminergic neuron survival. *Front. Aging Neurosci.* **14**, 1026468 (2022).
45. Tabata, Y. et al. T-type calcium channels determine the vulnerability of dopaminergic neurons to mitochondrial stress in Familial Parkinson disease. *Stem Cell. Rep.* **11**, 1171–1184 (2018).
46. Yamaguchi, A. et al. Identifying therapeutic agents for amelioration of mitochondrial clearance disorder in neurons of Familial Parkinson disease. *Stem Cell. Rep.* **14**, 1060–1075 (2020).
47. Asantewaa, G. et al. Glutathione synthesis in the mouse liver supports lipid abundance through NRF2 repression. *Nat. Commun.* **15**, 6152 (2024).
48. Cvetko, F. et al. Nrf2 is activated by disruption of mitochondrial thiol homeostasis but not by enhanced mitochondrial superoxide production. *J. Biol. Chem.* **296**, 100169 (2021).
49. Harvey, C. J. et al. Nrf2-regulated glutathione recycling independent of biosynthesis is critical for cell survival during oxidative stress. *Free Radic Biol. Med.* **46**, 443–453 (2009).
50. von Willebrand, M., Zacksenhaus, E., Cheng, E., Glazer, P. & Halaban, R. The tyrphostin AG1024 accelerates the degradation of phosphorylated forms of retinoblastoma protein (pRb) and restores pRb tumor suppressive function in melanoma cells. *Cancer Res.* **63**, 1420–1429 (2003).
51. Shvets, E., Fass, E., Scherz-Shouval, R. & Elazar, Z. The N-terminus and Phe52 residue of LC3 recruit p62/SQSTM1 into autophagosomes. *J. Cell. Sci.* **121**, 2685–2695 (2008).
52. Shvets, E., Abada, A., Weidberg, H. & Elazar, Z. Dissecting the involvement of LC3B and GATE-16 in p62 recruitment into autophagosomes. *Autophagy* **7**, 683–688 (2011).
53. Bjørkøy, G., Lamark, T. & Johansen, T. p62/SQSTM1: A missing link between protein aggregates and the autophagy machinery. *Autophagy* **2**, 138–139 (2006).
54. Walrafen, P. et al. Both proteasomes and lysosomes degrade the activated erythropoietin receptor. *Blood* **105**, 600–608 (2005).
55. Terada, H. & Van Dam, K. On the, stoichiometry between uncouplers of oxidative phosphorylation and respiratory chains. The catalytic action of SF 6847 (3,5-di-tert-butyl-4-hydroxybenzylidenemalononitrile). *Biochim. Biophys. Acta BBA - Bioenerg.* **387**, 507–518 (1975).
56. Geisler, J. G., Marosi, K., Halpern, J. & Mattson, M. P. DNP, mitochondrial uncoupling, and neuroprotection: A little dab'll do Ya. *Alzheimers Dement.* **13**, 582–591 (2017).
57. Zorov, D. B. et al. Neuroprotective potential of mild uncoupling in mitochondria. Pros and cons. *Brain Sci.* **11**, 1050 (2021).
58. Terada, H., Fukui, Y., Shinohara, Y. & Ju-ichi, M. Unique action of a modified weakly acidic uncoupler without an acidic group, methylated SF 6847, as an inhibitor of oxidative phosphorylation with no uncoupling activity: possible identity of uncoupler binding protein. *Biochim. Biophys. Acta BBA - Bioenerg.* **933**, 193–199 (1988).
59. Peruzzotti-Jametti, L. et al. Mitochondrial complex I activity in microglia sustains neuroinflammation. *Nature* **628**, 195–203 (2024).
60. Gao, C., Jiang, J., Tan, Y. & Chen, S. Microglia in neurodegenerative diseases: mechanism and potential therapeutic targets. *Signal. Transduct. Target. Ther.* **8**, 359 (2023).
61. Park, D. S. et al. iPS-cell-derived microglia promote brain organoid maturation via cholesterol transfer. *Nature* **623**, 397–405 (2023).
62. Zhang, W. et al. Microglia-containing human brain organoids for the study of brain development and pathology. *Mol. Psychiatry.* **28**, 96–107 (2023).
63. Chen, Y. et al. Engineering synucleinopathy-resistant human dopaminergic neurons by CRISPR -mediated deletion of the *SNCA* gene. *Eur. J. Neurosci.* **49**, 510–524 (2019).
64. Kriks, S. et al. Dopamine neurons derived from human ES cells efficiently engraft in animal models of parkinson's disease. *Nature* **480**, 547–551 (2011).
65. Ryan, S. D. et al. Isogenic human iPSC parkinson's model shows nitrosative Stress-Induced dysfunction in MEF2-PGC1α transcription. *Cell* **155**, 1351–1364 (2013).

66. Weykopf, B. et al. Induced pluripotent stem cell-based modeling of mutant LRRK2-associated parkinson's disease. *Eur. J. Neurosci.* **49**, 561–589 (2019).
67. McKinney, W. Data structures for statistical computing in python. *Proc. 9th Python Sci. Conf.* **56-61** https://doi.org/10.25080/Majora-92bf1922-00a (2010).
68. Waskom, M. L. Seaborn: statistical data visualization. *J. Open. Source Softw.* **6**, 3021 (2021).
69. Pedregosa, F. et al. Scikit-learn: machine learning in python. *J. Mach. Learn. Res.* **12**, 2825–2830 (2011).

Acknowledgements

We thank Dr. Tilo Kunath (University of Edinburgh) for providing the AST23 and AST23-2KO iPSC lines. We are grateful for the constant discussions with various colleagues at Ksilink and the Luxembourg Centre for Systems Biomedicine (LCSB) which improved this work.

Author contributions

V.G. designed biochemical experiments, performed neuronal differentiation, biochemical assays, and data analysis; A.We. designed imaging experiments, performed neuronal culturing, imaging assay automation, and compound screening; L.C. developed and performed image analysis and data processing; D.H. performed MEA experiments; K.S. analyzed the MEA data; A.O. co-supervised data processing, P.A.B. co-initiated the study and contributed to grant writing; B.F.R.S. contributed to biochemical experiments; I.B. co-designed biochemical experiments; A.Wi., A.Z. and O.P. identified and provided Tyrphostin A9 structural analogues; R.K. co-initiated the study and supervised biochemical experiments; P.S. co-initiated the study and supported assay design; J.H.W. supervised the study, designed experiments, conceptualized and performed image analysis and data processing, and wrote the manuscript with input from all authors.

Declarations

Competing interests

A.We., L.C., D.H., K.S., A.O., P.S., and J.H.W. are or were employed by Ksilink. R.K. is receiving or has received research grants from the European Institute of Innovation and Technology (EIT Health), the Innovative Medicines Initiative (IMI) of the European Union and the European pharmaceutical industry, as well as personal speaker's honoraria and/or travel grants from Abbvie, Zambon and Medtronic; R.K. participated as PI or site-PI for industry sponsored clinical trials without receiving honoraria. All other authors declare no conflict of interest.

Additional information

Supplementary Information The online version contains supplementary material available at https://doi.org/10.1038/s41598-025-14735-0.

Correspondence and requests for materials should be addressed to J.H.W.

Reprints and permissions information is available at www.nature.com/reprints.

Publisher's note Springer Nature remains neutral with regard to jurisdictional claims in published maps and institutional affiliations.

Open Access This article is licensed under a Creative Commons Attribution-NonCommercial-NoDerivatives 4.0 International License, which permits any non-commercial use, sharing, distribution and reproduction in any medium or format, as long as you give appropriate credit to the original author(s) and the source, provide a link to the Creative Commons licence, and indicate if you modified the licensed material. You do not have permission under this licence to share adapted material derived from this article or parts of it. The images or other third party material in this article are included in the article's Creative Commons licence, unless indicated otherwise in a credit line to the material. If material is not included in the article's Creative Commons licence and your intended use is not permitted by statutory regulation or exceeds the permitted use, you will need to obtain permission directly from the copyright holder. To view a copy of this licence, visit http://creativecommons.org/licenses/by-nc-nd/4.0/.

© The Author(s) 2025

12. Appendix IV

Please cite this article in press as: Wittich et al., Human organoids: Fit for drug discovery?, Stem Cell Reports (2026), https://doi.org/10.1016/j.stemcr.2026.102898

STEM CELL REPORTS
Review
ISSCR
OPEN ACCESS

Human organoids: Fit for drug discovery?

Annika Wittich,[1] Kim Krieg,[1] Philip Gribbon,[1,2] Jakob J. Metzger,[3] Alessandro Prigione,[4] and Ole Pless[1,*]
[1]Fraunhofer Institute for Translational Medicine and Pharmacology ITMP, Discovery Research ScreeningPort, 22525 Hamburg, Germany
[2]EU-OPENSCREEN, Robert-Rössle-Street 10, 13125 Berlin, Germany
[3]Max Delbrück Center for Molecular Medicine (MDC), Quantitative Stem Cell Biology, 10115 Berlin, Germany
[4]Department of General Pediatrics, Neonatology and Pediatric Cardiology, Medical Faculty and University Hospital Düsseldorf, Heinrich Heine University Düsseldorf, Düsseldorf, Germany
*Correspondence: ole.pless@itmp.fraunhofer.de
https://doi.org/10.1016/j.stemcr.2026.102898

SUMMARY

Organoids are self-organizing three-dimensional (3D) *in vitro* tissues derived from pluripotent stem cells (PSCs) that recapitulate key structural and functional features of human organs. Their multicellular architecture and physiological relevance make them promising new approach methodologies (NAMs) for disease modeling, drug discovery, and toxicity testing. However, their reliability and scalability for compound screening remain under evaluation. This review summarizes current human PSC-derived organoid screening strategies, highlighting available readouts, related machine learning methods, and their potential advantages over traditional screening models. We also discuss major challenges, including assay robustness, throughput limitations, and the need for standardized protocols. Advancing validated and scalable approaches will be essential for integrating organoids into pharmaceutical development and improving the translational success of drug candidates.

INTRODUCTION

The first report of self-organized "organotypic" three-dimensional (3D) cortical tissue derived from mouse and human embryonic stem cells (ESCs) dates to 2008 (Eiraku et al., 2008). The term "organoid" was then introduced in 2009 to describe 3D intestinal structures derived from murine adult intestinal stem cells that can contain all the differentiated cell types of the epithelium and the architecture of intestinal crypts found in mammals (Sato et al., 2009). Organoids are 3D cellular models derived from self-organization processes and can recapitulate the cytoarchitecture and certain functional aspects of human organs (Lancaster et al., 2013; Sato et al., 2009). In contrast to two-dimensional (2D) cultures, this spatial confinement can recreate dynamic cell-cell interactions and mechanical properties of human tissues/organs (Anlaş and Nelson, 2018; Da Silva André and Labouesse, 2024). Whereas tissue stem cell-/adult stem cell-derived organoids can mimic organ regeneration and maintain their native tissue identity, the use of human pluripotent stem cells (PSCs) allows for following developmental trajectories through *in vitro* differentiation, thereby enabling the generation of diverse types of human organoids (Artegiani and Hendriks, 2025; Kim et al., 2020). To date, many differentiation protocols have been published, describing the generation of organoid models representing several human body tissues, including liver (Takebe et al., 2013), brain (Lancaster et al., 2013), kidney (Morizane et al., 2015; Takasato et al., 2015), lung (Dye et al., 2015), colon (Múnera et al., 2017; Spence et al., 2011), and heart (Drakhlis et al., 2021; Ho et al., 2022). Their applications in developmental studies, disease modeling, personalized medicine, and drug development have been extensively highlighted in the literature (Dutta et al., 2017; Vandana et al., 2023; Wang et al., 2025).

In this review, we will focus on human organoids derived from PSCs, either from induced PSCs (iPSCs) or ESCs. PSCs provide an unlimited source of derived cells and have the potential to differentiate into cell types of disease relevance (Figure 1). Due to their high proliferation rate, PSCs enable substantial cell yield for large-scale organoid production required for compound testing. By maintaining the genetic background of patients or healthy donors, they also allow addressing individualized compound responses in a defined diseased or healthy context. We here focus on the following organoid types, which have been applied successfully to answer questions related to drug discovery: colon, lung, airway, heart, kidney, liver, and various brain regions such as forebrain, midbrain, cortical brain organoids, and brain neuruloids.

With advancing technology, creating organoids that accurately model specific tissues in terms of cellular composition and function relevant for drug discovery approaches is becoming increasingly feasible. Brain organoids derived from human PSCs, for example, provide a promising platform for modeling neurological disease and testing therapeutic interventions, through the generation of accessible, self-organized neuronal cells that can mimic the (patho)physiology of the human brain (Birey et al., 2017; Lancaster et al., 2013). Given the brain's complexity, different models have been developed to focus on specific regions, thereby reducing heterogeneity (Cederquist et al., 2019). Forebrain organoids primarily model anterior brain regions such as the cerebral cortex and basal ganglia (Choe et al., 2025), midbrain organoids focus on regions rich in dopaminergic neurons

Published by Elsevier Inc. on behalf of International Society for Stem Cell Research.
This is an open access article under the CC BY license (http://creativecommons.org/licenses/by/4.0/).

Please cite this article in press as: Wittich et al., Human organoids: Fit for drug discovery?, Stem Cell Reports (2026), https://doi.org/10.1016/j.stemcr.2026.102898

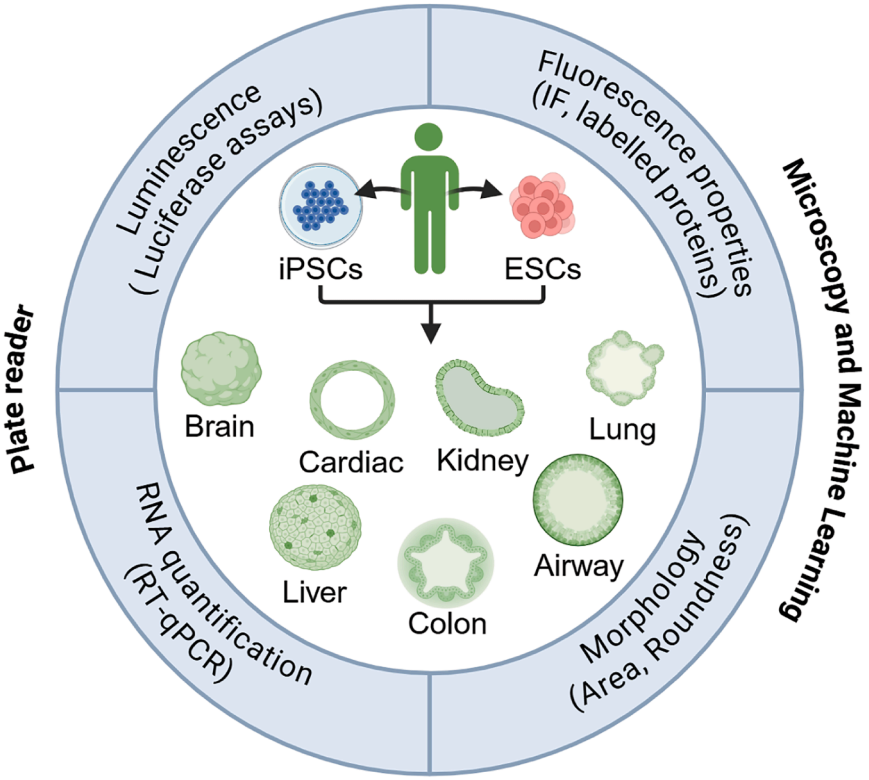


Figure 1. Readout methods in organoid applications for drug discovery

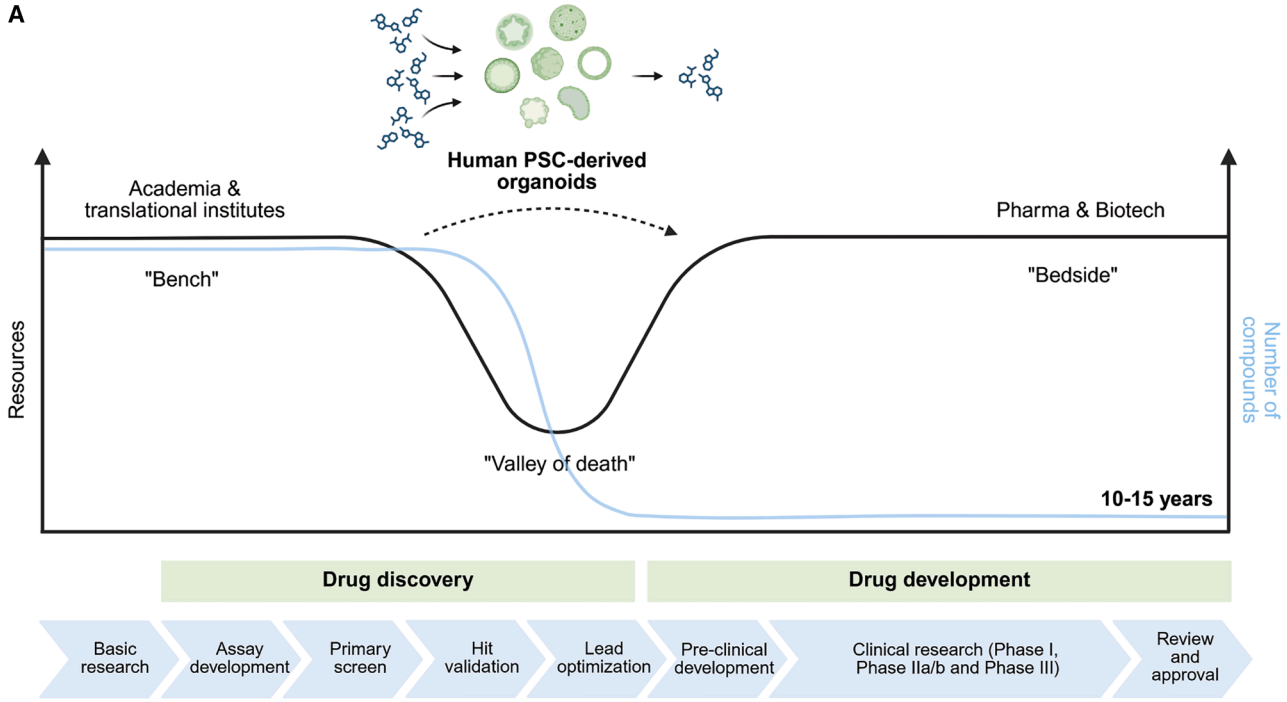
Schematic representation of human organoids, derived from either ESCs or iPSCs. ESCs are extracted from a blastocyst, whereas iPSCs are generated from somatic cells. Both ESCs and iPSCs are able to differentiate into the three germ layers (ectoderm, mesoderm, and endoderm) and can give rise to self-organizing 3D organoids. PSC-derived organoids can be used for compound screens, including the readouts and methodologies indicated on the border of the circle.

(Fiorenzano et al., 2021), and cortical organoids replicate the layered structure and cellular diversity of the cerebral cortex, responsible for higher cognition (Zhang et al., 2023). Importantly, brain organoids can contain electrophysiologically active neurons (Chung et al., 2022; Paşca et al., 2015). Neuruloids are organoids that simulate the entire ectodermal layer of the human embryo, including the neural, neural crest, placode, and epidermal tissues (Britton et al., 2019; Haremaki et al., 2019), enabling the study of human development and drug responses in otherwise inaccessible environments. Overall, human PSC-derived organoids show significant promise and advantages in physiological relevance compared to 2D models. However, they remain limited in their application to drug discovery compared to native tissues. Organoids often lack vascularization, neural and immune interactions, microbiomes, and full cellular diversity and functionality (Chang et al., 2021; Ouchi and Koike, 2023). Additionally, they lack consistent cellular composition and exhibit considerable variability in formation, morphology, and function, which often hampers their use in drug discovery due to variability in self-organization and cell fate decision (Hofer and Lutolf, 2021).

De novo drug development aiming to identify, develop, and market new therapeutics is a long and expensive process that usually takes 10–15 years with costs of up to 2 billion USD (Hinkson et al., 2020). This process can be divided into different stages: (1) basic research, where the underlying disease etiology and progression are studied; (2) drug discovery, which involves identification of disease modulating agents, for example small molecules or antibodies; (3) preclinical development, focusing on elucidating the mode of action of leads and drug candidates and efficacy and toxicity across various *in vitro* and *in vivo* models; (4) clinical research (phase I, phase IIa/b, and phase III studies) in humans; and (5) review and approval by regulatory bodies (e.g., Food and Drug Administration [FDA], European Medicines Agency [EMA], or others) (Singh et al., 2023) (Figure 2A).

Drug discovery is the first step in drug development, involving the process of identifying and validating new potential drugs for a specific intended use (Hughes et al., 2011; Zhou and Zhong, 2017). In the hit finding stages of drug discovery, complementary approaches can be applied, including target-based and phenotypic-based assays. With the advancing field of artificial intelligence (AI), AI-guided drug discovery has very recently emerged as a powerful tool, offering the potential to accelerate key aspects of hit finding and validation (Zhang et al., 2025a). Target-based screening aims to identify drugs that affect single genes or molecular mechanisms (the target) to specifically treat the deficit causing the disease (Samsdodd, 2005). In

Please cite this article in press as: Wittich et al., Human organoids: Fit for drug discovery?, Stem Cell Reports (2026), https://doi.org/10.1016/j.stemcr.2026.102898



B

Readouts and methods	Advantages	Limitations
• Cellular viability (luminescence)	• Robust, reliable in 3D, HT-compatible	• Bulk readout, no spatial or cell-type resolution, end-point assay
• Brightfield microscopy	• Live and rapid, good for morphology	• Limited molecular specificity
• Confocal microscopy	• Optical sectioning, 3D stacks/rendering	• High background, limited penetration, processing
• Light-sheet microscopy	• Deeper, informative 3D imaging	• Laborious preparation/processing, end-point assay
• Engineered fluorescent reporters	• Live monitoring of response/resistance	• Laborious engineering, overexpression artifacts
• Label-free confocal + ML	• Avoids fluorescent labeling complexity	• Needs ML models

Figure 2. Implementation of PSC-derived organoids in the drug discovery process

(A) The drug development process can be divided into different phases: basic research, drug discovery (assay development, primary screen, hit validation, and lead), pre-clinical development, clinical research (Phase I, Phase IIa/b, and Phase III studies), and review and approval. There is a high attrition rate of compounds during this process due to drug failure in early clinical development. Scalable and validated human PSC-derived organoids applied in drug screens can help bridge the drug development "valley of death" by providing meaningful readouts and increasing confidence in predictive value. Broader use can overcome academic resource limits and industry hesitancy, driving improvements in standardization, automation, and translational robustness.

(B) Available readouts and methods used in combination with human PSC-derived organoids for drug discovery, summarizing their respective advantages and current limitations. HT, high-throughput; ML, machine-learning.

contrast, phenotypic screening for hits and leads seeks to modulate a disease-specific trait (phenotype) with compounds tested in cells or organisms to determine whether a particular molecule exerts the desired effect, potentially in the absence of information about the underlying target (Horman, 2016; Inak et al., 2017; Khurana et al., 2015). Despite major progress in understanding biological systems through technological advances, a significant challenge in drug discovery remains the high attrition rate (Singh et al., 2023). The failure rate of drug candidates after entering clinical testing is approximately 90% (Sun et al., 2022). One reason for this low success rate is believed to be the limited predictive value of preclinical *in vivo* models (e.g., mice, zebrafish, or fruit flies) and more simplified *in vitro* models (e.g., 2D HeLa and A549 cells) of human disease, which may lead to reduced drug efficacy or unfavorable safety profiles (Harrison, 2016; Paul et al., 2010).

To effectively model human diseases, cellular systems must be designed to reflect the underlying molecular features seen in patients, such as the genetic background,

Please cite this article in press as: Wittich et al., Human organoids: Fit for drug discovery?, Stem Cell Reports (2026), https://doi.org/10.1016/j.stemcr.2026.102898

post-translational modifications, and pathway perturbations, as these factors represent the mechanistic drivers of pathology. Applying patient-derived cells helps ensure the model reflects not just superficial phenotypes but also the underlying biology that influences disease onset, progression, and treatment outcomes.

In contrast to PSC-derived 2D cellular models, PSC-derived organoids enable the assessment of multicellular responses and cell-cell interactions within a human genetic background, making them a valuable model for understanding the effectiveness and safety profiles of compounds that cannot be reliably predicted using non-human or 2D preclinical models (Hay et al., 2014; Kola and Landis, 2004; Paul et al., 2010; Seyhan, 2019). Importantly, organoids have the potential to decrease reliance on animal experimentation and support the 3Rs principles (replace, reduce, refine) (Russell and Burch, 1959). In recent years, significant efforts have been made to develop more predictive methods, based on human 2D and 3D *in vitro* models for phenotypic screening (Han, 2023; Zushin et al., 2023). In 2022, the FDA in the United States approved "alternatives to animal testing for purposes of drug and biological product applications," including cell-based or computational models (https://www.congress.gov/bill/117th-congress/senate-bill/5002). Recently, both the FDA and the EMA outlined a roadmap to reduce animal testing through new approach methodologies (NAMs), where the FDA is initially focusing on monoclonal antibodies to limit animal use in preclinical safety testing (https://www.fda.gov/news-events/press-announcements/fda-announces-plan-phase-out-animal-testing-requirement-monoclonal-antibodies-and-other-drugs) and the EMA decided to foster regulatory acceptance of NAMs (https://www.ema.europa.eu/en/documents/report/new-approach-methodologies-eu-horizon-scanning-report_en.pdf). NAMs include *in silico* (computer modeling), *in chemico* (chemical reactions), and *in vitro* (cell- and tissue-based) methods. Among *in vitro* systems, organoids and organ-on-a-chip (OoC) systems will play a key role in the future (Edwards et al., 2025; Park et al., 2024; Svendsen, 2025). Following extensive efforts to increase robustness and reliability, OoC are starting to be employed in regulatory toxicity tests (https://www.fda.gov/news-events/press-announcements/fda-announces-plan-phase-out-animal-testing-requirement-monoclonal-antibodies-and-other-drugs) (Leung et al., 2022). However, despite their great potential, organoid-based readouts are not yet routinely used in drug development, indicating that many critical challenges must still be addressed. A limitation of many current organoid models is the absence of functional vascular and immune components, which can restrict their ability to capture certain physiological responses to injury and disease. While not all organoid applications require these complex features, incorporating vascularization and immune elements may be important for specific disease contexts where higher levels of tissue complexity are needed (Huang et al., 2021). According to the new FDA guidelines, NAMs do not necessarily need to be fully validated but need to show that they are fit-for-purpose (https://www.fda.gov/media/191589/download). Hence, demonstrating that a specific NAM is appropriate in a defined context of use is a key goal for implementing NAMs into regulatory pipelines. Recent NAM-related breakthroughs include bioprinting and microfluidic technologies, such as OoC to improve vascularization, as well as adding immune cells to simulate tissue-specific immune responses (Chai et al., 2024; Du et al., 2024). Moreover, different organoids can be fused to obtain so-called assembloids, which can be functionally integrated to model interactions between cells of different lineages allowing increased physiological complexity (Onesto et al., 2024). This is the case, for example, of combining brain organoids with microglia or with endothelial organoids and mesenchymal cells to add immune aspects or achieve vascularization-like structures (Song et al., 2019). At the same time, the increased complexity of organoids requires thorough context-specific characterization before they can be applied in drug discovery and screening campaigns. In order to generate reliable physiological models and to interpret any screening outcome, cellular composition, growth behavior, location/cytoarchitecture, cellular trajectories, and levels of maturity need to be studied and must remain reproducible. Although there is significant progress toward developing more physiologically, well characterized organoid systems, their production remains very complex and is not yet fully reproducible and scalable.

In drug finding efforts, a substantial translational gap persists between early-stage discovery in academia and industry-driven development programs. Although many preclinical findings appear promising, a large proportion fail to progress to clinical success. Academic laboratories often lack the financial resources, infrastructure, and automation capabilities necessary for meaningful scale-up and industrial-grade validation. Conversely, industry stakeholders are frequently hesitant to adopt complex and costly model systems that have not yet demonstrated consistent predictive value at scale. The establishment of robust, well-validated organoid-based drug screening applications, along with meaningful readouts (the display of information produced by electronic equipment such as microscopes, sequencing machines, and plate readers), could help bridge this "valley of death," the gap where many promising preclinical results fail to translate into clinical application (Figure 2A). Broader implementation of organoids in screening campaigns would drive improvements in protocol standardization, automation, and upscaling.

Please cite this article in press as: Wittich et al., Human organoids: Fit for drug discovery?, Stem Cell Reports (2026), https://doi.org/10.1016/j.stemcr.2026.102898

Accumulated experience and shared knowledge are likely to further enhance robustness, efficiency, and translational impact.

Here, we provide an overview of case studies covering scaled and reproducible human PSC-derived organoid production, as well as automation systems enabling on 3D model implementation. We describe advanced assay readouts involving disease-relevant endpoints that enable higher-throughput screening, with a specific focus on organoids derived from human PSCs. Additionally, we highlight critical aspects that need to be addressed to enable the reliable integration of human PSC-derived organoids into the overall drug discovery process.

ORGANOID SPECIFICATIONS FOR THEIR USE IN DRUG DISCOVERY

In drug discovery, it is essential to consider both the biological and pharmacological relevance of a screening campaign. The screening model and potential modulators, such as compounds, peptides, or other biological effectors, should be carefully selected based on their physiology, quality, and feasibility. The general requirements for an assay suitable for high-throughput screening include: (1) relevance of the assay, (2) reproducibility, (3) costs, (4) desired (and non-desired) modulator effects, and (5) assay quality (Hughes et al., 2011). For each of these aspects, it is important to understand the potential added value of organoids. In the next section, we will focus on small molecule screening. However, many of the features are equally applicable for studies involving biological-based modulators.

Relevance of the assay

Several screening campaigns have identified active compounds that may be developed into promising drug candidates using 2D human PSC-based assays, which utilize their ability to differentiate into disease-relevant cell types (Kondo et al., 2017; Lee et al., 2012; Lorenz et al., 2017). Additionally, high-throughput screens were used for efficacy testing in nematodes, fruit flies, and zebrafish to mimic the effects of drugs in the human body and enhance the accuracy of drug screening (Chen et al., 2024). Some of these 2D human PSC-based assay campaigns, especially in the drug repurposing context, have led to active compounds that are progressing to clinical applications, such as retigabine (ezogabine) for amyotrophic lateral sclerosis (ALS), NCT02450552 (McNeish et al., 2015), or sildenafil for Leigh syndrome, NCT06967831 (Zink et al., 2026).

However, when compared to 2D systems, human 3D cellular models have the potential to emulate disease phenotypes more accurately and in a more physiologically relevant manner, as their cellular complexity and cell function are more closely aligned with disease-affected tissue (Kim et al., 2020; Lancaster et al., 2013). For example, qPCR data validated that podocytes derived from iPSC-derived kidney organoids showed enhanced podocyte-specific gene expression compared to 2D cultures, while also preserving polarized protein distribution, thereby demonstrating greater maturation than isolated podocytes or immortalized 2D lines (Hale et al., 2018). Importantly, organoids can maintain the dynamic, reciprocal biochemical, and biophysical interactions between their components, matrix mechanics, and the native niche of parenchymal tissues (Brafman, 2013; Gattazzo et al., 2014; Hofer and Lutolf, 2021), features that 2D PSC models mostly lack. When choosing a cell-based screening model, the assay should provide physiologically meaningful information to address the research question by displaying the disease-relevant phenotype. This means that organoids therefore have the opportunity to replace 2D disease models, when the phenotype cannot be recapitulated in 2D, and when their complexity is needed to answer research questions.

Reproducibility

A screening assay must be reproducible and replicable, meaning the results should remain consistent regardless of the screening day, assay plates, and stable across different labs, and, when using cells and organoids, independent of their cryopreserved stock or batch of differentiation (Hernández et al., 2022; Kelava and Lancaster, 2016; Phipson et al., 2019). In terms of pharmacology, general best practices for assay development indicate that a coefficient of variation (CV), reflecting the size of a standard deviation relative to its mean, $< 20\%$ is acceptable, and $CV < 10\%$ is an optimal quality criterion (Sui and Wu, 2007; Zhang et al., 1999; 2012). Moreover, reproducibility metrics such as the IC50 or EC50 shift, the variation in maximal responses, as well as the data of independent repeats, should be assessed and fall within the set CV.

As part of quality control, the intra- and inter-batch variability of parameters like organoid size or adenosine triphosphate (ATP) content should be analyzed and remain stable throughout and between experiments, as demonstrated by Nickels et al. (2020); Renner et al. (2020); Krieg et al. (2025). Some initial approaches have been made to simplify and optimize experimental steps, including reagents and liquid handling steps that substantially reduce variation and facilitate the (semi)-automation of multi-well plate compatible protocols (Boussaad et al., 2021; Brandenberg et al., 2020; Renner et al., 2020). Automated processes can provide superior control of liquid handling processes, such as medium exchanges and addition of detection reagents, ensuring consistency and potentially enhancing the quality of screening assays

Please cite this article in press as: Wittich et al., Human organoids: Fit for drug discovery?, Stem Cell Reports (2026), https://doi.org/10.1016/j.stemcr.2026.102898

using organoids. However, while automation can significantly improve throughput and standardization, it also introduces an additional layer of technical and logistical complexity. Automated workflows may give rise to new sources of variability, such as uneven extracellular matrix coating, non-uniform cellular distribution during seeding, or mechanical stress that can dislodge cells and compromise tissue integrity. Moreover, automated systems currently have limited ability to perform context-specific adaptations, as they typically execute protocols as defined sequences. This limitation is particularly relevant for complex assays running over multiple days, where unexpected deviations still require expert oversight. In addition, the implementation and maintenance of automated platforms are associated with substantial financial investment, specialized infrastructure requirements, and the need for technical expertise, all of which can represent significant practical hurdles, particularly for smaller laboratories.

Costs

When working with organoids, costs for production, maintenance, and data storage should be considered. Indeed, implementing organoid models is relatively expensive compared to 2D approaches, fly, yeast, or worm models (Kim et al., 2020). Additionally, drug screening is standardized for 384- and 1536-well plates, but some organoids grow too large to fit in these well formats and require larger volumes of medium provided by 96-well or 48-well plate formats (Giorgi et al., 2024), which results in higher costs per data point. Due to their complexity and 3D architecture, a large amount of data is generated (e.g., microscopic images and sequencing data), and costs for storage, computing power, and personnel can be high. Although initial expenses may be higher compared to other research models, a potential advantage is that organoids could ultimately lower overall costs by decreasing the need for downstream validation studies in expensive animal models. A typical 2D cell culture data point might cost on the order of several USD, whereas currently a PSC-derived organoid data point costs a multitude of this, reaching up to double or even triple digit USD, mainly due to specialized, expensive reagents, e.g., extracellular matrices (ECMs), growth factors (which are already needed for PSC maintenance), labor-intensive work, long culture times ranging from weeks to months (and thereby increased reagent consumption), and limited automation solutions resulting in lower throughput. These investments have to demonstrate added value in most organizations. Scale and automation represent critical inflection points in the cost curve. With continued automation, standardization, and miniaturization of assay formats, higher-throughput screens (> 1,000 compounds) using organoids could become more feasible (Kim et al., 2026).

Compound effect

Test compounds need to be soluble in the chosen medium, physically stable, and should not interfere with the assay readout, such as chemically modified proteins. For cell-based assays, compounds must be permeable when the target is located within the cell, non-toxic at screening concentrations, non-mutagenic, and, in order to be developed into an oral treatment, bioavailable (Zhang et al., 2012). Some organoids require hydrogels, which can affect compound diffusion and activity because of their physical barrier effect, increasing the risk of false-negative results in drug testing (Cameron et al., 2023; Mahdieh et al., 2022). Before testing a larger set of compounds, it is necessary to determine the appropriate concentration and incubation time that yields an acceptable hit rate using smaller pilot screens. Notably, the effect size achievable by compounds can differ between 2D and 3D systems. One study found that compounds that promoted iPSC-derived cardiomyocyte proliferation in a 2D format could not be confirmed in a 3D model of human cardiac organoids (Mills et al., 2019). Including a positive control targeting the specific mechanism of action, along with a negative control (often the solvent used for compounds, such as DMSO) on each assay plate enables for the statistical assessment of assay robustness. The plate layout should be evaluated beforehand, as edge effects can occur due to increased evaporation from outer wells during longer assay durations (Gribbon et al., 2005; Iversen et al., 2012; Mpindi et al., 2015).

Assay quality

Setting up a high-quality assay starts with selecting a reliable screening model. Currently, there are no consensus guidelines or acceptance criteria for organoid-based screening models, which makes it difficult to transition disease models into screening-ready assays. The screening model should undergo thorough validation before initiating the first steps of a screening campaign. This validation includes analyzing cell type composition using methods such as single-cell RNA sequencing (scRNA-seq) to reveal cell type heterogeneity and subpopulations, as well as immunostaining combined with fluorescent microscopy. Additionally, organoids should be evaluated for consistent, tissue-specific functionality. For example, neuronal activity can be measured using multi-electrode array (MEA) recordings or patch-clamp techniques. Cardiac tissue can be tested for contractile force, while liver organoids can be examined for albumin production using methods such as enzyme-linked immunosorbent assays (ELISA) (Tanimizu et al., 2021). Importantly, donor-derived

Please cite this article in press as: Wittich et al., Human organoids: Fit for drug discovery?, Stem Cell Reports (2026), https://doi.org/10.1016/j.stemcr.2026.102898

PSCs should be quality-controlled and cultivated according to the "standards for human stem cell use in research" of the International Society for Stem Cell Research (ISSCR) (https://www.isscr.org/basic-research-standards) to ensure high-quality starting material for organoid differentiation (Ludwig et al., 2023). This includes assessing the pluripotency state through quantitative measures of trilineage marker expression for PSC lines, alongside confirming the loss of markers indicating an undifferentiated state (Ludwig et al., 2023). Furthermore, genetic integrity should be verified through genomic analysis to monitor any cellular changes that could influence interpretation of the drug effects. For screening quality control, the Z′-factor is often used as an indicator for screening and as a parameter to assess assay suitability. It captures both the dynamic range and data variation related to signal measurements of both controls (Zhang et al., 1999). A $Z' > 0.5$ is generally considered acceptable, although a Z' of < 0.5 can be acceptable for cellular assays if the number of hits can be validated in follow-up tests (Bar and Zweifach, 2020). However, the implementation and feasibility of the Z′-factor in drug screening assays using complex model systems, such as organoids, is subject to debate in the literature (Bar and Zweifach, 2020; Booij et al., 2022). In particular, the selection of a threshold for Z' factor should be made in the context of the unmet need for the assay, e.g., < 0.5 (Francies et al., 2018). Decisions should therefore be made on a case-by-case basis. Additionally to the Z' factor, other assay parameters like signal-to-blank, signal-to-noise, dynamic range, coefficient of variation (CV), and the strictly standardized mean difference (SSMD) can be utilized for assessing the quality and performance of complex biological assays (An and Tolliday, 2010; Krieg et al., 2025; Zhang et al., 2007).

CURRENT APPLICATIONS AND BOTTLENECKS FOR 3D DRUG SCREENING

The development of cell-based assays requires a practical approach designed for the specific application. When moving from model systems to assay development, it is crucial to select a few interpretable measurements that reflect disease-relevant endpoints, and assays must be "fit for purpose" (Engle et al., 2018). Although there are an increasing number of protocols for generating PSC-derived organoids, covering nearly all tissue types, significant challenges remain in adapting 2D cellular assays to 3D models, because of their size and thickness, their inaccessibility to inner cells, and their heterogeneity.

Limitations in assay readout technologies continue to restrict the full potential of organoid systems and limit the amount of information that can be obtained (Hofer and Lutolf, 2021) (Figure 2B). For instance, a standard readout used in compound screening is cellular viability, estimated, for example, by the total ATP content of the cell mass, often quantified with luciferase-based assays. Assessing viability upon compound exposure to determine the window between efficacy and toxicity is crucial for drug discovery and the further development of hit compounds, as the cytotoxic concentration can vary depending on cell type and tissue. Cell viability assays, such as the ATP-based CellTiter-Glo (CTG) reagent, are reliable and robust for 3D models (Zanoni et al., 2016) and compatible with high-throughput screening (Han et al., 2021; Renner et al., 2020; Shinozawa et al., 2021). However, the bulk readouts lack spatial information and cannot distinguish cell-specific effects and morphological changes. To maximize the potential of 3D architectures, additional readouts should complement basic measurements like ATP content or size to provide a deeper understanding of biological processes following compound treatment (Lampart et al., 2023).

Imaging coupled with immunolabeling methods and cell compartment-specific dyes has been essential for revealing the cytoarchitecture of organoids and demonstrating that they faithfully reflect aspects of their *in vivo* counterparts (Rios and Clevers, 2018). Capturing reproducible, image-based differences in profiles between diseased and healthy samples forms the basis of a phenotypic assay used in drug screening. This imaging readout can be a single feature extracted from one image channel or a combination of parameters from multiple channels, which differentiates between diseased and healthy states (Chandrasekaran et al., 2021).

Imaging techniques for organoids include brightfield, confocal, and light-sheet microscopy, each with distinct advantages and limitations. Traditionally, thin section preparation combined with classical immunohistochemistry has been widely used to study tissue architecture in 2D and to observe the distribution of single or multiple markers in tissue (Rios and Clevers, 2018). However, full 3D microscopic visualization remains challenging and is not suitable for high-throughput. Live and rapid brightfield and fluorescence imaging in a few planes are preferred for high-throughput and longitudinal studies to monitor the onset of compound effects. Brightfield microscopy can reveal morphological features such as the size and shape of organoids, making it suitable for screening-compatible plate types. Additionally, confocal microscopy offers a non-invasive method for optical sectioning, producing relatively detailed images of organoids through stacked planes that enable rendering. Nonetheless, challenges remain, including high background noise, limited penetration depth, and the complexity of processing tiled images (Fei et al., 2022).

Please cite this article in press as: Wittich et al., Human organoids: Fit for drug discovery?, Stem Cell Reports (2026), https://doi.org/10.1016/j.stemcr.2026.102898

Additionally, automated imaging is complicated by the variable positioning of organoids along the *x*, *y*, and *z* axes. The use of engineered reporter cell lines, which intrinsically express a fluorescent protein, allows for live imaging and monitoring of drug responses, resistance, or relapse (Bury et al., 2024; Sarrafha et al., 2021). However, their application is limited by the labor-intensive process of fluorescent reporter engineering, the restricted number of fluorescence channels, and potential effects of protein overexpression (Jiang et al., 2008). Therefore, label-free confocal imaging methods utilizing machine learning (ML)-based algorithms can bypass the complexity of fluorescent labeling in PSC-derived organoids (Kok et al., 2025; Serafini et al., 2024).

To overcome the challenges of limited tissue penetration and high scattering, light-sheet microscopy offers a more effective and informative solution. However, it is less suitable for high-throughput applications due to the labor-intensive process of sample preparation and image analysis. Since organoids often exceed the microscopic field of view at the necessary magnification, reconstructing single images with 3D rendering software becomes essential. Even with light-sheet microscopy, segmenting and quantifying individual cells for downstream data analysis remains difficult. Tissue clearing is crucial for achieving the cellular resolution needed to apply segmentation and quantification algorithms effectively (Dekkers et al., 2019). Tissue clearing involves techniques that make biological samples transparent, allowing deep imaging of large tissue volumes (Richardson et al., 2021). While several clearing protocols are available, they are generally very time-consuming and often rely on toxic chemicals (Tian et al., 2021).

Furthermore, organoids often depend on animal-derived ECMs. While these support cell growth and differentiation, they are frequently chemically undefined and vary between batches, which hampers reproducibility. This reproducibility can be improved by evaluating multiple ECM batches, selecting the most consistent one, and securing a sufficient supply for long-term experiments. Additionally, physical properties such as temperature sensitivity and high viscosity pose significant challenges for integration into automated liquid handling systems used in scale-up screening applications (Renner et al., 2021).

ORGANOIDS FOR PRIMARY DRUG SCREENS

Primary screenings are the initial tests conducted in a screening campaign and are essential in the drug discovery process, as they reduce the number of test substances. The goal of the primary assay is to identify hits, which are substances that demonstrate the desired effect and may be biologically active chemical entities (EU-OPENSCREEN_HTS_QC_General_Guidelines200713.pdf) (Hughes et al., 2011).

In the following, we highlight studies using PSC-derived organoids within early-stage drug discovery and employing current screening-compatible readout formats. Some studies have already demonstrated the potential of their developed organoid models for compound testing by administering a single compound (Hale et al., 2018; Lane et al., 2020; Takasato et al., 2015; Winanto et al., 2020). Others confirmed that human PSC-derived organoid models enable a robust, reproducible, and scalable platform supporting drug discovery (Renner et al., 2020). Here, we provide examples of organoids in primary drug screening and hit validation assays, which ultimately overcame the bottlenecks associated with organoids (Table 1).

These studies adapted human PSC-derived organoids for compound screening in a disease-specific context affecting various tissues like airway (Duan et al., 2021), lung (Han et al., 2021), liver (Shinozawa et al., 2021), brain (Metzger et al., 2022), and kidney (Tran et al., 2022) to multi-well formats (96- or 384-well plates). Organoids were either plated intact (Metzger et al., 2022; Narazaki et al., 2025; Shinozawa et al., 2021; Tran et al., 2022) or dissociated (Duan et al., 2021; Han et al., 2021) into uniform cell suspensions to ensure consistent well-to-well readouts. This enabled screening libraries ranging from ~250 to > 1,300 compounds. Importantly, organoids retained key human cell types and gene-expression profiles that mirror adult tissues, e.g., $ACE2^{+}$ ciliated airway cells (Duan et al., 2021), AT2-like lung cells (Han et al., 2021), hepatocyte-like cells with bile transport (Shinozawa et al., 2021), early cortical progenitors (Metzger et al., 2022; Narazaki et al., 2025), or nephron-like kidney structures (Tran et al., 2022). This ensured that screening occurred in a context that recapitulates disease-relevant biology. Various readouts were applied assessing viral infection (Han et al., 2021), liver toxicity (Shinozawa et al., 2021), cyst formation (Tran et al., 2022), teratogenic risks (Narazaki et al., 2025) or neurodevelopmental phenotypes (Metzger et al., 2022) using high-content imaging and plate readers. Shinozawa et al., (2021) normalized the luminescence values for organoid size and number, and a deep-learning model was applied to classify phenotypes objectively, enabling unbiased, quantitative hit identification (Metzger et al., 2022). Overall, these studies demonstrate that organoids can function as first-line screening systems by uniting disease-relevant biology, along with scalable, quantitative workflows. Compared with 2D models, they capture tissue architecture, multicellular interactions, and disease phenotypes like viral tropism, bile transport, neurodevelopmental patterning, or cystogenesis, thereby improving the predictive power of primary drug discovery screens. The number of compounds screened to date, however, remains far

Please cite this article in press as: Wittich et al., Human organoids: Fit for drug discovery?, Stem Cell Reports (2026), https://doi.org/10.1016/j.stemcr.2026.102898

Table 1. Overview of human PSC-derived organoids utilized for primary compound screens and hit confirmation using a multi-well plate format and a screening-compatible readout

Screening type	Tissue	Organoid	Disease/application	Multi-well format	Compounds	Readout	Methodology	References
Primary screen	Airway	ESC-derived airway organoids	SARS-CoV-2	384-well	1,126 compounds at 10 μM; hit: GW6471	IF for SARS-CoV-2 N (infection rate)	Confocal microscopy	Duan et al. (2021)
	Liver	iPSC-derived liver organoids	Liver injury	384-well	238 compounds, 4 concentrations	Fluorescent intensity of bile acid CLF (uptake); luminescence CTG (viability); organoid size	Fluorescence imaging and brightfield microscopy; luminescence	Shinozawa et al. (2021)
	Lung	iPSC-derived lung organoids	SARS-CoV-2	384-well	∼1,300 compounds at 10 μM	Luciferase assay (activity) and CTG (viability)	Luminescence	Han et al. (2021)
	Brain	ESC-derived brain organoids	Huntington	96-well	1,065 compounds at 10 μM	IF for PAX6 (marker of NPCs) and Phalloidin (F-actin) and DAPI staining (Nuclei)	Confocal microscopy; classifier and autoencoder for analysis	Metzger et al. (2022)
	–	iPSC-derived cortical organoids	Teratogenic risk	24-well	298 compounds at 1 μM	Organoid size (area)	Bright-field live imaging	Narazaki et al., 2025
	Kidney	ESC CRSIPR-Cas9 edited kidney organoids	Autosomal dominant polycystic kidney disease (ADPKD)	96-well	247 compounds at 1 μM	Cyst outgrowth area	Brightfield live imaging	Tran et al. (2022)
Hit confirmation	Colon	iPSC-derived colonic organoids	Familial adenomatous polyposis (FAP) inherited colonic cancer	6-well	Geneticin, XAV939, and rapamycin	IF for CDX2 (posterior marker), CCND1, Ki67 (cell proliferation) in CDX2+ cells; quantification of RNA target genes	Confocal microscopy, RT-qPCR	Crespo et al. (2017)
	–	ESC-derived colonic organoids	SARS-CoV-2	24-well	GW6471	Quantification of viral RNA; IF for SARS-CoV-2 N (infection rate)	Confocal microscopy, qPCR	Duan et al. (2021)
	–	iPSC-derived colonic organoids	SARS-CoV-2	24-well	10 μM imatinib, 3 μM mycophenolic	IF for SARS-CoV-2 N and	Confocal microscopy, qPCR	Han et al. (2021)

(*Continued on next page*)

Please cite this article in press as: Wittich et al., Human organoids: Fit for drug discovery?, Stem Cell Reports (2026), https://doi.org/10.1016/j.stemcr.2026.102898

Table 1. *Continued*

Screening type	Tissue	Organoid	Disease/application	Multi-well format	Compounds	Readout	Methodology	References
					acid, 4.5 μM quinacrine dihydrochloride	RT-qPCR analysis for viral N transcripts		
	Cardiac	ESC-derived cardiac organoids	Cardiac disease	96-well	105 compounds in 3 concentrations	IF for Ki67 (pro-proliferative) and Hoechst 33342 staining (nuclei); force of contraction	Confocal microscopy, live imaging	Mills et al. (2019)
	Kidney	ESC CRSIPR-Cas9 edited kidney organoids	Autosomal dominant polycystic kidney disease (ADPKD)	96-well	9 hits in DRC (0.1, 1, and 10 μM)	Cyst outgrowth area	Brightfield live imaging	Tran et al. (2022)
	Brain	iPSC-derived cortical organoids	Brain metastasis	96-well	7 compounds at 10 μM	Fluorescent intensity of reporter-engineered melanoma cells; CTG (viability)	Fluorescence imaging and live brightfield microscopy; luminescence	Krieg et al. (2025)
	–	iPSC-derived midbrain organoids	Leigh syndrome	96-well	2 compounds (sertaconazole and talarozole)	IF of neuronal marker (MAP2, TH, SMI312; CTG (viability)	Fluorescence imaging; luminescence; absorbance	Menacho et al., 2026
	–	iPSC-derived forebrain organoids	Zika virus infection	96-well	Hippeastrine hydrobromide (HH), amodiaquine dihydrochloride dihydrate (AQ)	IF for ZIKV E (infection), Ki67 (cell proliferation) and DAPI staining (nuclei)	Widefield fluorescence imaging	Zhou et al. (2017)

ESC, embryonic stem cell; iPSC, induced pluripotent stem cell; IF, immunofluorescence; CTG, CellTiter-Glo; RT-qPCR, reverse transcription quantitative polymerase chain reaction.

Please cite this article in press as: Wittich et al., Human organoids: Fit for drug discovery?, Stem Cell Reports (2026), https://doi.org/10.1016/j.stemcr.2026.102898

below the throughput required to evaluate a chemically diverse library for the discovery of novel disease-associated targets or the identification of new chemical entities suitable for intellectual property protection. For organoid platforms to be competitive in primary screening campaigns, they must be scalable to enable screening of several thousand compounds in a robust, reproducible, and cost-effective manner.

ORGANOIDS FOR HIT VALIDATION

Following a primary screen, in which compounds are usually applied in singlicates, identified hits need to be confirmed and prioritized in a hit validation screen. Hit validation consists of a suite of assays designed to eliminate false positives and to confirm activity of identified hits in the primary assay, based on their mechanism of action, toxicity, or activity profile (Zhu et al., 2013). As each primary screening assay is unique, so is the follow-up strategy, and a systematic method of hit validation should ideally be in place before the primary screen is completed (Hevener et al., 2018).

On the one hand, organoids were utilized for hit validation following primary 2D drug screens, to confirm the effect in a 3D tissue-specific context (Krieg et al., 2025; Menacho et al., 2026; Mills et al., 2019; Zhou et al., 2017). On the other hand, they have been used for concentration-response testing and secondary assays within the same organoid model, also across diverse genetic backgrounds (e.g., *PKD1* and *PKD2* variants), ensuring that hits were robust and disease-relevant (Tran et al., 2022). Validation relied on whole-mount immunostaining, confocal or high-content imaging, fluorescence quantification, and plate-based assays (e.g., ATP, lactate) (Table 1). Readouts were normalized for organoid size (Menacho et al., 2026) and batch variability (Krieg et al., 2025), enabling reproducible, semi-high-throughput confirmation. Functional readouts included cardiomyocyte proliferation combined with contractile function for cardiac organoids (Mills et al., 2019), melanoma colonization and growth within cortical tissue (Krieg et al., 2025), neuromorphogenesis, and metabolic activity of midbrain organoids (Menacho et al., 2026). These readouts ensured that hits corrected pathological features, not just molecular markers. Some studies showed that compounds effective in 2D failed in organoids or caused unacceptable side effects. For example, compounds that induced proliferation in 2D cardiac cultures failed to do so in immature cardiac organoids, indicating a size effect of compounds in a more complex model (Mills et al., 2019). Moreover, amodiaquine showed anti-Zika virus activity in 2D but was toxic in brain organoids (Zhou et al., 2017). In the context of melanoma brain metastasis, organoids were able to distinguish compounds with anti-metastatic activity and low neurotoxicity (Krieg et al., 2025). Thus, organoids acted as a filter, reducing false positives and identifying the most potent drug candidates. In viral studies, hits from airway or lung screens were validated in colonic organoids, demonstrating efficacy across relevant tissues and strengthening biological conclusions (Duan et al., 2021; Han et al., 2021). This multi-organ approach ultimately increases translational confidence. Overall, human PSC-derived organoids enabled confirmation of therapeutic relevance, detection of tissue-specific toxicity, and assessment of complex phenotypes. Organoids served as physiologically grounded validation platforms that bridge the gap between high-throughput 2D screens and *in vivo* models, potentially reducing the reliance on animal models and increasing the accuracy of drug discovery.

However, examples of drug discovery campaigns using human PSC-derived organoids remain scarce, highlighting the complexity that come along with organoid research.

BRIDGING THE GAP: THE PROMISING ROLE OF ML

One of the most important aspects of organoid research is the analysis of the images generated by microscopy. Phenotypic screens in a high-throughput, 3D environment require significant technical infrastructure, such as computing power, data storage, and custom analysis pipelines, to extract meaningful insights from the data. Changes in organoid morphology, size, number, architecture, and function provide important information about organoid development and how they respond to changes after drug treatment, but manual image analysis is time-consuming, subjective, and often unable to capture the full 3D complexity of organoids (Bai et al., 2024; Shi et al., 2024).

A promising approach to maximize the potential of organoids in research and drug discovery is to analyze these complex biological models using ML, a subfield of AI that develops algorithms to learn patterns from data. ML-driven image analysis can identify and quantify various organoid features such as size, shape, and structural changes, which are essential for assessing organoid function and maturity. Moreover, ML can reveal image features or phenotypic patterns in screening data that are difficult to detect by manual inspection. By replacing labor-intensive manual scoring with automated algorithms, ML can reduce bias and errors, leading to more reliable and reproducible results in phenotypic assays (Bai et al., 2024). As an example, Lukonin et al. conducted a large-scale phenotypic compound screen in organoids from isolated crypts of mouse small intestine, combining high-content imaging with computational image analysis

Please cite this article in press as: Wittich et al., Human organoids: Fit for drug discovery?, Stem Cell Reports (2026), https://doi.org/10.1016/j.stemcr.2026.102898

Table 2. Image segmentation and feature extraction methods for phenotypic assessments of organoids

Software tool/model	Type	Application	References
Ilastik	Pixel-classifier	Class-based segmentation by assigning every pixel to a user-defined category	Berg et al. (2019)
Trainable Weka Segmentation	Pixel-classifier	Class-based segmentation by assigning every pixel to a user-defined category as part of the Fiji image processing distribution of ImageJ	Arganda-Carreras et al. (2017)
Cellpose	General-purpose segmentation model	Segments nuclei or whole organoids across diverse imaging conditions	Stringer et al. (2021)
MOrgAna	Pipeline/workflow	Segments organoids and quantifies morphological features	Gritti et al. (2021)
OrgaExtractor	Pipeline	Segments organoids of various sizes and track growth from brightfield images	Park et al. (2023)
Phindr3D	Segmentation-free feature learning	Extracts high-content voxel-based features from organoid images without explicit segmentation	Mergenthaler et al. (2021)
Cellos	Hybrid platform	Classical image processing to find organoid boundaries + 3D CNN (StarDist3D) to segment nuclei	Mukashyaka et al. (2023)
deepOrganoid	Deep-learning tool	Predicts cell viability directly from brightfield organoid images	Powell et al. (2022)
OrganoIDNet	Deep-learning model	Analyzes time-lapse microscopy of tumor organoids to detect treatment responses	Ferreira et al. (2025)
Digitalized organoids	Multi-level analysis platform	Multilevel 3D analysis of cellular morphology, cell-cell topology, and whole-organoid shape	Ong et al. (2025)

to quantify multivariate features. These measurements positioned each organoid within a high-dimensional phenotypic landscape, enabling clustering into discrete phenotypic classes that were subsequently consolidated into broader, biologically interpretable categories. By linking these phenotypic classes to specific compound exposures, the study generated a distinct phenotypic fingerprint for every compound, enabling systematic comparisons of phenotypic responses across large chemical libraries (Lukonin et al., 2020). However, this organoid screening was not based on human PSCs. Additional challenges, e.g., size, density, or cellular composition, might limit the transfer of this approach to human PSC-based organoids.

In image-based organoid analysis, ML can be applied at multiple stages of the image-analysis workflow. Features can be extracted using segmentation-based approaches, in which biologically meaningful structures such as nuclei, cells, or organoids are first detected and quantified, or through segmentation-free approaches, where models learn image representations directly from pixel or voxel data. These extracted features or learned embeddings can then be analyzed using ML methods such as supervised learning, for example, to classify phenotypes or predict treatment responses, or unsupervised learning to identify clusters or patterns in the data. While recent deep learning approaches can integrate feature extraction and prediction within a single model, their successful application to complex organoid systems often requires assay-specific training, careful validation, and large image datasets (Metzger et al., 2022). Consequently, although ML holds substantial promise for organoid screening, robust and generalizable analysis pipelines remain an active area of research.

Since organoid imaging faces limitations due to high data dimensionality, acquisition artifacts, low contrast, and bright-field noise, several image segmentation and feature extraction methods have been developed to overcome this specific bottleneck (Louey et al., 2021) (Table 2). General-purpose models like Cellpose (Stringer et al., 2021) and StarDist (Schmidt et al., 2018) are widely used for segmentation of cellular structures such as nuclei or entire cells across diverse imaging conditions. Additionally, there are pixel-classifiers that allow users to annotate pixels within a dataset. Here, ML algorithms learn from these annotations to classify pixels of the remaining dataset. Exemplary open-source tools are Ilastik (Berg et al., 2019) and Trainable Weka Segmentation

Please cite this article in press as: Wittich et al., Human organoids: Fit for drug discovery?, Stem Cell Reports (2026), https://doi.org/10.1016/j.stemcr.2026.102898

(Arganda-Carreras et al., 2017). Beyond these, specialized pipelines tailored to organoids have been developed, such as MOrgAna (Gritti et al., 2021), which provides a workflow to segment organoids and quantify their morphological features. Similarly, OrgaExtractor (Park et al., 2023) was developed to segment organoids of various sizes and to track their growth from brightfield images. In contrast, segmentation-free analyses, such as Phindr3D (Mergenthaler et al., 2021) use data-driven voxel-based feature learning to extract high-content features from organoid images. Another platform, Cellos (Mukashyaka et al., 2023), combines classical image processing with ML by using traditional algorithms to identify organoid boundaries and a 3D convolutional neural network (StarDist3D) to segment cell nuclei within organoids. The deep-learning tool deepOrganoid (Powell et al., 2022) predicts cell viability in organoids directly from brightfield images. In the context of drug screening, OrganoIDNet (Ferreira et al., 2025) analyzes time-lapse microscopy of patient-derived tumor organoids to detect treatment responses. These image-based phenotypes often require integrating information across spatial scales, from subcellular changes to whole-organoid structure. ML is particularly useful for such multi-scale integration, as demonstrated for example by the "digitalized organoids" platform, which introduced a multilevel 3D analysis pipeline to concurrently evaluate cellular morphology, cell-cell topology, and whole-organoid shape (Ong et al., 2025).

Despite these advances, several challenges remain to fully realize the potential of ML in organoid-based screens, with arguably the most important challenge being data variability and scale. The inherent heterogeneity of organoids can confound ML models. Large, diverse, and well-annotated image datasets are needed to train models that generalize across this heterogeneity. For example, OrganoIDNetData contains an open repository of annotated tumor organoid images. Similarly, the MultiOrg project (Bukas et al., 2024) collected a large database of organoid images, allowing for the quantification of annotation uncertainty by including multiple independent labels for organoid images.

Another notable gap is the interpretability of ML models. Complex deep learning algorithms often act as "black boxes," for which it is difficult to determine which image features drive a particular prediction. However, even when specific features can be identified and their contribution quantified, they do not necessarily translate into meaningful biological interpretation. Segmentation-free architectures face constraints in feature interpretability, because they are learned directly from raw pixels rather than from biologically grounded morphological structures. This makes it difficult to map model-derived features back to specific cellular or subcellular phenotypes (Mergenthaler et al., 2021). This lack of transparency can hinder biological insights and trust in AI-driven decisions. While ML and AI have been used in the context of drug discovery (Catacutan et al., 2024; Jiménez-Luna et al., 2020), this is a promising research direction that remains an emerging approach in organoid screening (Lukonin et al., 2020; Metzger et al., 2022).

CONCLUSION AND PERSPECTIVES

Despite several limitations of human PSC-derived organoids for drug discovery, including reproducibility, variability, upscaling challenges, batch-to-batch variations, and data analysis, 3D models present significant potential in drug discovery. The research field of organoids has extended the recapitulation of human tissue to study organ development, model diseases, and examine compound responses in a more physiological environment compared to 2D cellular models, aiming to accelerate drug discovery by making it more relevant and predictive. Developing standardized protocols, automating liquid handling systems, implementing ML strategies, and leveraging new technologies are now essential to overcoming the current limitations.

It is important to highlight that 3D models might not be suitable for all research purposes. Researchers need to carefully evaluate if a 3D model is the best option for their drug discovery study, asking whether it provides more robust evidence and physiologically relevant information compared to 2D models, and if the available analysis tools can extract meaningful data while meeting the quality requirements for primary high-throughput drug screening applications. Additionally, traditional gold-standard methods used in 2D cultures may not directly apply to 3D models, and current readouts often fail to fully capture the complexity of 3D architecture. Although we highlight exemplary studies that used human PSC-derived organoids for primary screens, the number of compounds and readout complexity used in these studies was still relatively low. Upscaled organoids may lack maturation and full functionality, while complex physiological organoids are time-consuming to produce and not yet suitable for screening thousands of compounds. A practical approach in modern drug discovery could be to use cellular models with enough complexity to match the assays to be performed. If 2D models provide sufficient physiologically relevant information, they can be used for large-scale screenings of compounds, with organoids then employed to validate a smaller list of hit compounds, potentially reducing the failure rate in drug development.

In the past years, OoC technology, defined as microfluidic devices, containing living engineered organ

Please cite this article in press as: Wittich et al., Human organoids: Fit for drug discovery?, Stem Cell Reports (2026), https://doi.org/10.1016/j.stemcr.2026.102898

substructures in a controlled microenvironment (Moruzzi et al., 2023), has supported drug screening, especially for toxicity assessment (Akarapipad et al., 2021; Schneider et al., 2021). Although a considerable variety of OoCs have been developed, the heart-, liver-, kidney-, and brain-on-a-chip are the most commonly investigated organs in the domain of drug screening, as they are the four major target organs of drug toxicity (Wang et al., 2023a). OoC mimic the microphysiological environment cells experience in a tissue, including the vasculature-like perfusion (Cipriano et al., 2022) but lacking the 3D structural architecture and cell-cell interactions. While OoC aims to replace animal toxicity studies, organoids may have a specific role in functional validations. The value of using organoids as physiologically relevant and complex NAMs in validation steps could possibly replace the use of extensive animal experimentations. However, organoids are still far from having the complexity, reproducibility, and functionality needed to completely replace animal studies before entering clinical phases. Currently, it is still crucial to assess whether findings from an organoid can be recapitulated in the more complex *in vivo* tissue (Taelman et al., 2022). At the same time, animal models may not be available for all possible disorders and could exhibit limitations in recapitulating specific human disease features. Hence, organoids may represent a complementary approach in drug development pipelines that may become increasingly used if it proves to demonstrate practical advantages.

Improving readout technologies is essential not only for drug discovery but also for organoid research overall. Despite progress in recent years, a gap remains between the complexity of organoid models and the analytical tools available. ML could potentially bridge this gap by providing individual downstream analysis tools to maximize the output and insights of phenotypic readouts, enabling strict classification of phenotypes and overcoming challenges associated with multicellular organoids and limited imaging techniques. Ongoing advancements in tissue clearing and high-resolution imaging (Huang et al., 2021) may enable multiparametric phenotypic screening like cell painting—a technique involving the simultaneous staining of various cellular features, capturing thousands of morphological features, including shape, texture, size, intensity, and spatial relationships among organelles to predict the mechanism of action of a perturbing substance (Bray et al., 2016; Pahl and Sievers, 2019; Seal et al., 2025) in the future. "Organoid painting" in combination with deep learning AI algorithms could potentially be a highly informative readout format. Moreover, AI models have the ability to preselect the compounds by predicting targets, pathways, or structures prior to *in vitro* screening. Using cutting-edge ML techniques like transformers, graph neural networks, and diffusion models, AI can forecast targets for future precision therapies and generate candidate compounds tailored to specific patient groups.

Diffusion models show promise in drug discovery to design novel molecular structures *de novo*, complementing traditional medicinal chemistry (Zhang et al., 2025b). Graph neural networks, which model molecules as atom-bond graphs, have improved molecular property prediction and binding affinity estimation (Wang et al., 2023b). Virtual screening, including methods based on AI-informed molecular dynamic simulations (Wang et al., 2024) is about to revolutionize drug screening by enabling the efficient identification of potential hits from extensive chemical repositories while still screening the minimum number of compounds (Gryniukova et al., 2023). AI informed *in vitro* screening workflows configured within tightly linked design/make/test/analyze (DMTA) cycles also enable testing fewer, curated sets of compounds directly in organoid models, reducing the overall number of compounds needed and thereby lowering costs and experimental workload, while maintaining screening success (Zhavoronkov et al., 2026). In a study by Menacho et al., the authors applied a deep-learning approach trained on a human database that did not include cancer cells to predict which gene-expression changes in progenitors would promote effective neural commitment in cells carrying pathogenic variants causative of Leigh syndrome, a currently incurable mitochondrial neurological disease. These gene expression changes were then used to predict repurposable compounds capable of inducing similar transcriptional signatures. This approach allowed the model to identify innovative treatment candidates that were subsequently validated in a focused hit confirmation screen using patient-derived midbrain organoids (Menacho et al., 2026).

To achieve successful employment of brain organoids as NAMs in drug development, appropriate guidelines on model validation, cell cultivation, image acquisition, and data analysis are necessary (Carragher et al., 2018). A thorough review of the legal framework surrounding organoids is still lacking, especially regarding their creation, legal status, and usage. Establishing an organoid data repository would be vital for comparing and assessing organoid quality and donor variability. Sharing data, protocols, and readout methods is essential to promote broader accessibility and collaboration within the research community, while also adhering to the FAIR principles (findability, accessibility, interoperability, and reusability) to improve the reuse of existing data (Wilkinson et al., 2016). To date, a comprehensive database (http://www.inbirg.com/organoid_db/) has been developed for multi-dimensional exploration of bulk and single-cell transcriptome profiles of organoids (Ma et al., 2023). Additionally, an Organoid Cell Atlas is under development within the Human

Cell Atlas (Regev et al., 2017), focusing on the single-cell characterization of organoids and complex *in vitro* systems (Bock et al., 2021; He et al., 2024).

In summary, finding the "sweet spot" when choosing a disease model with sufficient complexity while maintaining feasibility for compound screenings is crucial. The demonstration that organoids are fit-for-purpose within a defined context of use is essential to allow their implementation in regulatory settings. At the same time, the case studies presented here highlight the power of human PSC-derived organoid technology and its practical application in drug discovery. The limited number of examples, present to our knowledge, underscores the inherent difficulties associated with PSC-derived organoid systems. The scientific and technological progress in all the mentioned domains will support the transition of novel preclinical organoid models to more standardized applications for drug discovery.

ACKNOWLEDGMENTS

We acknowledge support from the Deutsche Forschungsgemeinschaft (DFG) (PR1527/6-1, PR1527/15-1, PR1527/14-1, PR1527/13-1 to A.P. and SFB TRR 305, 429280966 to O.P.), the European Joint Program on Rare Diseases (EJP RD) and Federal Ministry of Research, Technology and Space (BMFTR) (01GM2002A to A.P., 01GM2002B to O.P.), the European Commission's Horizon Europe Program (101080249 to A.P.), and AFM-Téléthon (28545 and 29044 to A.P.). Figures were created with BioRender.com.

AUTHOR CONTRIBUTIONS

Conceptualization, A.W., A.P., and O.P.; writing – original draft, A.W.; writing – review and editing, K.K., P.G., J.J.M., A.P., and O.P.; visualization, A.W.; funding acquisition, A.P. and O.P.

DECLARATION OF INTERESTS

The authors declare no competing financial or commercial interests. A.P. filed patent applications for the use of sildenafil, talarozole, and sertaconazole in mitochondrial diseases.

REFERENCES

Akarapipad, P., Kaarj, K., Liang, Y., and Yoon, J.-Y. (2021). Environmental Toxicology Assays Using Organ-on-Chip. Annu. Rev. Anal. Chem. *14*, 155–183. https://doi.org/10.1146/annurev-anchem-091620-091335.

An, W.F., and Tolliday, N. (2010). Cell-Based Assays for High-Throughput Screening. Mol. Biotechnol. *45*, 180–186. https://doi.org/10.1007/s12033-010-9251-z.

Anlaş, A.A., and Nelson, C.M. (2018). Tissue mechanics regulates form, function, and dysfunction. Curr. Opin. Cell Biol. *54*, 98–105. https://doi.org/10.1016/j.ceb.2018.05.012.

Arganda-Carreras, I., Kaynig, V., Rueden, C., Eliceiri, K.W., Schindelin, J., Cardona, A., and Sebastian Seung, H. (2017). Trainable Weka Segmentation: a machine learning tool for microscopy pixel classification. Bioinformatics *33*, 2424–2426. https://doi.org/10.1093/bioinformatics/btx180.

Artegiani, B., and Hendriks, D. (2025). Organoids from pluripotent stem cells and human tissues: When two cultures meet each other. Dev. Cell *60*, 493–511. https://doi.org/10.1016/j.devcel.2025.01.005.

Bai, L., Wu, Y., Li, G., Zhang, W., Zhang, H., and Su, J. (2024). AI-enabled organoids: Construction, analysis, and application. Bioact. Mater. *31*, 525–548. https://doi.org/10.1016/j.bioactmat.2023.09.005.

Bar, H., and Zweifach, A. (2020). Z' Does Not Need to Be > 0.5. SLAS Discov. *25*, 1000–1008. https://doi.org/10.1177/2472555220942764.

Berg, S., Kutra, D., Kroeger, T., Straehle, C.N., Kausler, B.X., Haubold, C., Schiegg, M., Ales, J., Beier, T., Rudy, M., et al. (2019). ilastik: interactive machine learning for (bio)image analysis. Nat. Methods *16*, 1226–1232. https://doi.org/10.1038/s41592-019-0582-9.

Birey, F., Andersen, J., Makinson, C.D., Islam, S., Wei, W., Huber, N., Fan, H.C., Metzler, K.R.C., Panagiotakos, G., Thom, N., et al. (2017). Assembly of functionally integrated human forebrain spheroids. Nature *545*, 54–59. https://doi.org/10.1038/nature22330.

Booij, T.H., Cattaneo, C.M., and Hirt, C.K. (2022). Tumor Organoids as a Research Tool: How to Exploit Them. Cells *11*, 3440. https://doi.org/10.3390/cells11213440.

Bock, C., Boutros, M., Camp, J.G., Clarke, L., Clevers, H., Knoblich, J.A., Liberali, P., Regev, A., Rios, A.C., et al. (2021). The Organoid Cell Atlas. Nat Biotechnol. *39*, 13–17. https://doi.org/10.1038/s41587-020-00762-x.

Boussaad, I., Cruciani, G., Bolognin, S., Antony, P., Dording, C.M., Kwon, Y.-J., Heutink, P., Fava, E., Schwamborn, J.C., and Krüger, R. (2021). Integrated, automated maintenance, expansion and differentiation of 2D and 3D patient-derived cellular models for high throughput drug screening. Sci. Rep. *11*, 1439. https://doi.org/10.1038/s41598-021-81129-3.

Brafman, D.A. (2013). Constructing stem cell microenvironments using bioengineering approaches. Physiol. Genomics *45*, 1123–1135. https://doi.org/10.1152/physiolgenomics.00099.2013.

Brandenberg, N., Hoehnel, S., Kuttler, F., Homicsko, K., Ceroni, C., Ringel, T., Gjorevski, N., Schwank, G., Coukos, G., Turcatti, G., and Lutolf, M.P. (2020). High-throughput automated organoid culture via stem-cell aggregation in microcavity arrays. Nat. Biomed. Eng. *4*, 863–874. https://doi.org/10.1038/s41551-020-0565-2.

Bray, M.-A., Singh, S., Han, H., Davis, C.T., Borgeson, B., Hartland, C., Kost-Alimova, M., Gustafsdottir, S.M., Gibson, C.C., and Carpenter, A.E. (2016). Cell Painting, a high-content image-based assay for morphological profiling using multiplexed fluorescent dyes. Nat. Protoc. *11*, 1757–1774. https://doi.org/10.1038/nprot.2016.105.

Britton, G., Heemskerk, I., Hodge, R., Qutub, A.A., and Warmflash, A. (2019). A novel self-organizing embryonic stem cell system reveals signaling logic underlying the patterning of human ectoderm. Development dev *146*, 179093. https://doi.org/10.1242/dev.179093.

Bukas, C., Subramanian, H., See, F., Steinchen, C., Ezhov, I., Boosarpu, G., Asgharpour, S., Burgstaller, G., Lehmann, M., Kofler, F.,

et al. (2024). MultiOrg: A Multi-rater Organoid-detection Dataset. https://doi.org/10.48550/arXiv.2410.14612.

Bury, L.A.D., Fu, S., and Wynshaw-Boris, A. (2024). Neuronal lineage tracing from progenitors in human cortical organoids reveals mechanisms of neuronal production, diversity, and disease. Cell Rep. *43*, 114862. https://doi.org/10.1016/j.celrep.2024.114862.

Cameron, A.P., Gao, S., Liu, Y., and Zhao, C.-X. (2023). Impact of hydrogel biophysical properties on tumor spheroid growth and drug response. Biomater. Adv. *149*, 213421. https://doi.org/10.1016/j.bioadv.2023.213421.

Carragher, N., Piccinini, F., Tesei, A., Trask, O.J., Jr., Bickle, M., and Horvath, P. (2018). Concerns, challenges and promises of high-content analysis of 3D cellular models. Nat. Rev. Drug Discov. *17*, 606. https://doi.org/10.1038/nrd.2018.99.

Catacutan, D.B., Alexander, J., Arnold, A., and Stokes, J.M. (2024). Machine learning in preclinical drug discovery. Nat. Chem. Biol. *20*, 960–973. https://doi.org/10.1038/s41589-024-01679-1.

Cederquist, G.Y., Asciolla, J.J., Tchieu, J., Walsh, R.M., Cornacchia, D., Resh, M.D., and Studer, L. (2019). Specification of positional identity in forebrain organoids. Nat. Biotechnol. *37*, 436–444. https://doi.org/10.1038/s41587-019-0085-3.

Chai, Y.C., To, S.K., Simorgh, S., Zaunz, S., Zhu, Y., Ahuja, K., Lemaitre, A., Ramezankhani, R., Van Der Veer, B.K., Wierda, K., et al. (2024). Spatially Self-Organized Three-Dimensional Neural Concentroid as a Novel Reductionist Humanized Model to Study Neurovascular Development. Adv. Sci. *11*, e2304421. https://doi.org/10.1002/advs.202304421.

Chandrasekaran, S.N., Ceulemans, H., Boyd, J.D., and Carpenter, A.E. (2021). Image-based profiling for drug discovery: due for a machine-learning upgrade? Nat. Rev. Drug Discov. *20*, 145–159. https://doi.org/10.1038/s41573-020-00117-w.

Chang, M., Bogacheva, M.S., and Lou, Y.-R. (2021). Challenges for the Applications of Human Pluripotent Stem Cell-Derived Liver Organoids. Front. Cell Dev. Biol. *9*, 748576. https://doi.org/10.3389/fcell.2021.748576.

Chen, S., Shen, C., Li, W., Fan, Y., Yang, D.-H., Wang, Y., Feng, R., Li, G., and Zhong, Z. (2024). Recent advances in bioactivity-guided drug screening strategies for pre-clinical and clinical drug discovery. TrAC Trends Anal. Chem. *181*, 118042. https://doi.org/10.1016/j.trac.2024.118042.

Choe, M.S., Lo, C., and Park, I.-H. (2025). Modeling forebrain regional development and connectivity by human brain organoids. Curr. Opin. Genet. Dev. *91*, 102324. https://doi.org/10.1016/j.gde.2025.102324.

Chung, W.G., Kim, E., Song, H., Lee, J., Lee, S., Lim, K., Jeong, I., and Park, J.-U. (2022). Recent Advances in Electrophysiological Recording Platforms for Brain and Heart Organoids. Adv. NanoBiomed Res. *2*, 2200081. https://doi.org/10.1002/anbr.202200081.

Cipriano, M., Schlünder, K., Probst, C., Linke, K., Weiss, M., Fischer, M.J., Mesch, L., Achberger, K., Liebau, S., Mesquida, M., et al. (2022). Human immunocompetent choroid-on-chip: a novel tool for studying ocular effects of biological drugs. Commun. Biol. *5*, 52. https://doi.org/10.1038/s42003-021-02977-3.

Crespo, M., Vilar, E., Tsai, S.-Y., Chang, K., Amin, S., Srinivasan, T., Zhang, T., Pipalia, N.H., Chen, H.J., Witherspoon, M., et al. (2017). Colonic organoids derived from human induced pluripotent stem cells for modeling colorectal cancer and drug testing. Nat. Med. *23*, 878–884. https://doi.org/10.1038/nm.4355.

Da Silva André, G., and Labouesse, C. (2024). Mechanobiology of 3D cell confinement and extracellular crowding. Biophys. Rev. *16*, 833–849. https://doi.org/10.1007/s12551-024-01244-z.

Dekkers, J.F., Alieva, M., Wellens, L.M., Ariese, H.C.R., Jamieson, P.R., Vonk, A.M., Amatngalim, G.D., Hu, H., Oost, K.C., Snippert, H.J.G., et al. (2019). High-resolution 3D imaging of fixed and cleared organoids. Nat. Protoc. *14*, 1756–1771. https://doi.org/10.1038/s41596-019-0160-8.

Drakhlis, L., Biswanath, S., Farr, C.-M., Lupanow, V., Teske, J., Ritzenhoff, K., Franke, A., Manstein, F., Bolesani, E., Kempf, H., et al. (2021). Human heart-forming organoids recapitulate early heart and foregut development. Nat. Biotechnol. *39*, 737–746. https://doi.org/10.1038/s41587-021-00815-9.

Du, Y., De Jong, I.E.M., Gupta, K., Waisbourd-Zinman, O., Har-Zahav, A., Soroka, C.J., Boyer, J.L., Llewellyn, J., Liu, C., Naji, A., et al. (2023). Human vascularized bile duct-on-a chip: a multi-cellular micro-physiological system for studying cholestatic liver disease. Biofabrication *16*, 15004. https://doi.org/10.1088/1758-5090/ad0261.

Duan, X., Tang, X., Nair, M.S., Zhang, T., Qiu, Y., Zhang, W., Wang, P., Huang, Y., Xiang, J., Wang, H., et al. (2021). An airway organoid-based screen identifies a role for the HIF1α-glycolysis axis in SARS-CoV-2 infection. Cell Rep. *37*, 109920. https://doi.org/10.1016/j.celrep.2021.109920.

Dutta, D., Heo, I., and Clevers, H. (2017). Disease Modeling in Stem Cell-Derived 3D Organoid Systems. Trends Mol. Med. *23*, 393–410. https://doi.org/10.1016/j.molmed.2017.02.007.

Dye, B.R., Hill, D.R., Ferguson, M.A.H., Tsai, Y.-H., Nagy, M.S., Dyal, R., Wells, J.M., Mayhew, C.N., Nattiv, R., Klein, O.D., et al. (2015). In vitro generation of human pluripotent stem cell derived lung organoids. eLife *4*, e05098. https://doi.org/10.7554/eLife.05098.

Edwards, M., Blanquie, O., and Ehmann, F. (2025). Insights into new approach methodology innovation: an EMA perspective. Nat. Rev. Drug Discov. *24*, 325–326. https://doi.org/10.1038/d41573-025-00052-8.

Eiraku, M., Watanabe, K., Matsuo-Takasaki, M., Kawada, M., Yonemura, S., Matsumura, M., Wataya, T., Nishiyama, A., Muguruma, K., and Sasai, Y. (2008). Self-Organized Formation of Polarized Cortical Tissues from ESCs and Its Active Manipulation by Extrinsic Signals. Cell Stem Cell *3*, 519–532. https://doi.org/10.1016/j.stem.2008.09.002.

Engle, S.J., Blaha, L., and Kleiman, R.J. (2018). Best Practices for Translational Disease Modeling Using Human iPSC-Derived Neurons. Neuron *100*, 783–797. https://doi.org/10.1016/j.neuron.2018.10.033.

Fei, K., Zhang, J., Yuan, J., and Xiao, P. (2022). Present Application and Perspectives of Organoid Imaging Technology. Bioengineering *9*, 121. https://doi.org/10.3390/bioengineering9030121.

Ferreira, N., Kulkarni, A., Agorku, D., Midelashvili, T., Hardt, O., Legler, T.J., Ströbel, P., Conradi, L.-C., Alves, F., Ramos-Gomes, F., et al.

(2025). OrganoIDNet: a deep learning tool for identification of therapeutic effects in PDAC organoid-PBMC co-cultures from time-resolved imaging data. Cell. Oncol. *48*, 101–122. https://doi.org/10.1007/s13402-024-00958-2.

Fiorenzano, A., Sozzi, E., Birtele, M., Kajtez, J., Giacomoni, J., Nilsson, F., Bruzelius, A., Sharma, Y., Zhang, Y., Mattsson, B., et al. (2021). Single-cell transcriptomics captures features of human midbrain development and dopamine neuron diversity in brain organoids. Nat. Commun. *12*, 7302. https://doi.org/10.1038/s41467-021-27464-5.

Francies, H.E., Barthorpe, A., McLaren-Douglas, A., Barendt, W.J., and Garnett, M.J. (2018). Erratum to: Drug Sensitivity Assays of Human Cancer Organoid Cultures. Methods Mol. Biol. *1576*, 339–351.

Gattazzo, F., Urciuolo, A., and Bonaldo, P. (2014). Extracellular matrix: A dynamic microenvironment for stem cell niche. Biochim. Biophys. Acta *1840*, 2506–2519. https://doi.org/10.1016/j.bbagen.2014.01.010.

Giorgi, C., Lombardozzi, G., Ammannito, F., Scenna, M.S., Maceroni, E., Quintiliani, M., d'Angelo, M., Cimini, A., and Castelli, V. (2024). Brain Organoids: A Game-Changer for Drug Testing. Pharmaceutics *16*, 443. https://doi.org/10.3390/pharmaceutics16040443.

Gribbon, P., Lyons, R., Laflin, P., Bradley, J., Chambers, C., Williams, B.S., Keighley, W., and Sewing, A. (2005). Evaluating Real-Life High-Throughput Screening Data. SLAS Discov *10*, 99–107. https://doi.org/10.1177/1087057104271957.

Gritti, N., Lim, J.L., Anlaş, K., Pandya, M., Aalderink, G., Martínez-Ara, G., and Trivedi, V. (2021). MOrgAna: accessible quantitative analysis of organoids with machine learning. Development *148*, dev199611. https://doi.org/10.1242/dev.199611.

Gryniukova, A., Kaiser, F., Myziuk, I., Alieksieieva, D., Leberecht, C., Heym, P.P., Tarkhanova, O.O., Moroz, Y.S., Borysko, P., and Haupt, V.J. (2023). AI-Powered Virtual Screening of Large Compound Libraries Leads to the Discovery of Novel Inhibitors of Sirtuin-1. J. Med. Chem. *66*, 10241–10251. https://doi.org/10.1021/acs.jmedchem.3c00128.

Hale, L.J., Howden, S.E., Phipson, B., Lonsdale, A., Er, P.X., Ghobrial, I., Hosawi, S., Wilson, S., Lawlor, K.T., Khan, S., et al. (2018). 3D organoid-derived human glomeruli for personalised podocyte disease modelling and drug screening. Nat. Commun. *9*, 5167. https://doi.org/10.1038/s41467-018-07594-z.

Han, J.J. (2023). FDA Modernization Act 2.0 allows for alternatives to animal testing. Artif. Organs *47*, 449–450. https://doi.org/10.1111/aor.14503.

Han, Y., Duan, X., Yang, L., Nilsson-Payant, B.E., Wang, P., Duan, F., Tang, X., Yaron, T.M., Zhang, T., Uhl, S., et al. (2021). Identification of SARS-CoV-2 inhibitors using lung and colonic organoids. Nature *589*, 270–275. https://doi.org/10.1038/s41586-020-2901-9.

Haremaki, T., Metzger, J.J., Rito, T., Ozair, M.Z., Etoc, F., and Brivanlou, A.H. (2019). Self-organizing neuruloids model developmental aspects of Huntington's disease in the ectodermal compartment. Nat. Biotechnol. *37*, 1198–1208. https://doi.org/10.1038/s41587-019-0237-5.

Harrison, R.K. (2016). Phase II and phase III failures: 2013–2015. Nat. Rev. Drug Discov. *15*, 817–818. https://doi.org/10.1038/nrd.2016.184.

Hay, M., Thomas, D.W., Craighead, J.L., Economides, C., and Rosenthal, J. (2014). Clinical development success rates for investigational drugs. Nat. Biotechnol. *32*, 40–51. https://doi.org/10.1038/nbt.2786.

He, Z., Dony, L., Fleck, J.S., Szałata, A., Li, K.X., Slišković, I., Lin, H.-C., Santel, M., Atamian, A., Quadrato, G., et al. (2024). An integrated transcriptomic cell atlas of human neural organoids. Nature *635*, 690–698. https://doi.org/10.1038/s41586-024-08172-8.

Hernández, D., Rooney, L.A., Daniszewski, M., Gulluyan, L., Liang, H.H., Cook, A.L., Hewitt, A.W., and Pébay, A. (2022). Culture Variabilities of Human iPSC-Derived Cerebral Organoids Are a Major Issue for the Modelling of Phenotypes Observed in Alzheimer's Disease. Stem Cell Rev. Rep. *18*, 718–731. https://doi.org/10.1007/s12015-021-10147-5.

Hinkson, I.V., Madej, B., and Stahlberg, E.A. (2020). Accelerating Therapeutics for Opportunities in Medicine: A Paradigm Shift in Drug Discovery. Front. Pharmacol. *11*, 770. https://doi.org/10.3389/fphar.2020.00770.

Ho, B.X., Pang, J.K.S., Chen, Y., Loh, Y.-H., An, O., Yang, H.H., Seshachalam, V.P., Koh, J.L.Y., Chan, W.-K., Ng, S.Y., et al. (2022). Robust generation of human-chambered cardiac organoids from pluripotent stem cells for improved modelling of cardiovascular diseases. Stem Cell Res. Ther. *13*, 529. https://doi.org/10.1186/s13287-022-03215-1.

Hofer, M., and Lutolf, M.P. (2021). Engineering organoids. Nat. Rev. Mater. *6*, 402–420. https://doi.org/10.1038/s41578-021-00279-y.

Horman, S.R. (2016). Complex High-Content Phenotypic Screening. In Special Topics in Drug Discovery, T. Chen and S.C. Chai, eds. (InTech).

Huang, Y., Huang, Z., Tang, Z., Chen, Y., Huang, M., Liu, H., Huang, W., Ye, Q., and Jia, B. (2021). Research Progress, Challenges, and Breakthroughs of Organoids as Disease Models. Front. Cell Dev. Biol. *9*, 740574. https://doi.org/10.3389/fcell.2021.740574.

Hughes, J.P., Rees, S., Kalindjian, S.B., and Philpott, K.L. (2011). Principles of early drug discovery. Br. J. Pharmacol. *162*, 1239–1249. https://doi.org/10.1111/j.1476-5381.2010.01127.x.

Inak, G., Lorenz, C., Lisowski, P., Zink, A., Mlody, B., and Prigione, A. (2017). Concise Review: Induced Pluripotent Stem Cell-Based Drug Discovery for Mitochondrial Disease. Stem Cell. *35*, 1655–1662. https://doi.org/10.1002/stem.2637.

Iversen, P.W., Beck, B., Chen, Y.-F., Dere, W., Devanarayan, V., Eastwood, B.J., Farmen, M.W., Iturria, S.J., Montrose, C., Moore, R.A., et al. (2012). HTS Assay Validation. In Assay Guidance Manual, S. Markossian, A. Grossman, H. Baskir, M. Arkin, D. Auld, C. Austin, J. Baell, K. Brimacombe, T.D.Y. Chung, and N.P. Coussens, et al., eds. (Bethesda (MD): Eli Lilly & Company and the National Center for Advancing Translational Sciences).

Jiang, T., Xing, B., and Rao, J. (2008). Recent Developments of Biological Reporter Technology for Detecting Gene Expression.

Biotechnol. Genet. Eng. Rev. *25*, 41–75. https://doi.org/10.5661/bger-25-41.

Jiménez-Luna, J., Grisoni, F., and Schneider, G. (2020). Drug discovery with explainable artificial intelligence. Nat. Mach. Intell. *2*, 573–584. https://doi.org/10.1038/s42256-020-00236-4.

Kelava, I., and Lancaster, M.A. (2016). Dishing out mini-brains: Current progress and future prospects in brain organoid research. Dev. Biol. *420*, 199–209. https://doi.org/10.1016/j.ydbio.2016.06.037.

Khurana, V., Tardiff, D.F., Chung, C.Y., and Lindquist, S. (2015). Toward stem cell-based phenotypic screens for neurodegenerative diseases. Nat. Rev. Neurol. *11*, 339–350. https://doi.org/10.1038/nrneurol.2015.79.

Kim, D., Youn, J., Kim, J., Lee, J., Yoon, J., and Kim, D.S. (2026). From organoid culture to manufacturing: technologies for reproducible and scalable organoid production. Npj Biomed. Innov. *3*, 12. https://doi.org/10.1038/s44385-025-00054-6.

Kim, J., Koo, B.-K., and Knoblich, J.A. (2020). Human organoids: model systems for human biology and medicine. Nat. Rev. Mol. Cell Biol. *21*, 571–584. https://doi.org/10.1038/s41580-020-0259-3.

Kok, R.N.U., Spoelstra, W.K., Betjes, M.A., Van Zon, J.S., and Tans, S.J. (2025). Label-free cell imaging and tracking in 3D organoids. Cell Rep. Phys. Sci. *6*, 102522. https://doi.org/10.1016/j.xcrp.2025.102522.

Kola, I., and Landis, J. (2004). Can the pharmaceutical industry reduce attrition rates? Nat. Rev. Drug Discov. *3*, 711–715. https://doi.org/10.1038/nrd1470.

Kondo, T., Imamura, K., Funayama, M., Tsukita, K., Miyake, M., Ohta, A., Woltjen, K., Nakagawa, M., Asada, T., Arai, T., et al. (2017). iPSC-Based Compound Screening and In Vitro Trials Identify a Synergistic Anti-amyloid β Combination for Alzheimer's Disease. Cell Rep. *21*, 2304–2312. https://doi.org/10.1016/j.celrep.2017.10.109.

Krieg, K., Materna-Reichelt, S., Naber, T., Rachad, F.-Z., Kauven, P., Weller, A., Haferkamp, U., Wittich, A., Zaliani, A., Woo, M.S., et al. (2025). Cortical organoid-derived models of the melanoma brain metastatic niche enable prioritization of cancer-targeting drugs. Cell Rep. Methods *5*, 101236. https://doi.org/10.1016/j.crmeth.2025.101236.

Lampart, F.L., Iber, D., and Doumpas, N. (2023). Organoids in high-throughput and high-content screenings. Front. Chem. Eng. *5*, 1120348. https://doi.org/10.3389/fceng.2023.1120348.

Lancaster, M.A., Renner, M., Martin, C.-A., Wenzel, D., Bicknell, L.S., Hurles, M.E., Homfray, T., Penninger, J.M., Jackson, A.P., and Knoblich, J.A. (2013). Cerebral organoids model human brain development and microcephaly. Nature *501*, 373–379. https://doi.org/10.1038/nature12517.

Lane, A., Jovanovic, K., Shortall, C., Ottaviani, D., Panes, A.B., Schwarz, N., Guarascio, R., Hayes, M.J., Palfi, A., Chadderton, N., et al. (2020). Modeling and Rescue of RP2 Retinitis Pigmentosa Using iPSC-Derived Retinal Organoids. Stem Cell Rep. *15*, 67–79. https://doi.org/10.1016/j.stemcr.2020.05.007.

Lee, G., Ramirez, C.N., Kim, H., Zeltner, N., Liu, B., Radu, C., Bhinder, B., Kim, Y.J., Choi, I.Y., Mukherjee-Clavin, B., et al. (2012). Large-scale screening using familial dysautonomia induced pluripotent stem cells identifies compounds that rescue IKBKAP expression. Nat. Biotechnol. *30*, 1244–1248. https://doi.org/10.1038/nbt.2435.

Leung, C.M., De Haan, P., Ronaldson-Bouchard, K., Kim, G.-A., Ko, J., Rho, H.S., Chen, Z., Habibovic, P., Jeon, N.L., Takayama, S., et al. (2022). A guide to the organ-on-a-chip. Nat. Rev. Methods Primers *2*, 33. https://doi.org/10.1038/s43586-022-00118-6.

Lorenz, C., Lesimple, P., Bukowiecki, R., Zink, A., Inak, G., Mlody, B., Singh, M., Semtner, M., Mah, N., Auré, K., et al. (2017). Human iPSC-Derived Neural Progenitors Are an Effective Drug Discovery Model for Neurological mtDNA Disorders. Cell Stem Cell *20*, 659–674.e9. https://doi.org/10.1016/j.stem.2016.12.013.

Louey, A., Hernández, D., Pébay, A., and Daniszewski, M. (2021). Automation of Organoid Cultures: Current Protocols and Applications. SLAS Discov. *26*, 1138–1147. https://doi.org/10.1177/24725552211024547.

Ludwig, T.E., Andrews, P.W., Barbaric, I., Benvenisty, N., Bhattacharyya, A., Crook, J.M., Daheron, L.M., Draper, J.S., Healy, L.E., Huch, M., et al. (2023). ISSCR standards for the use of human stem cells in basic research. Stem Cell Rep. *18*, 1744–1752. https://doi.org/10.1016/j.stemcr.2023.08.003.

Lukonin, I., Serra, D., Challet Meylan, L., Volkmann, K., Baaten, J., Zhao, R., Meeusen, S., Colman, K., Maurer, F., Stadler, M.B., et al. (2020). Phenotypic landscape of intestinal organoid regeneration. Nature *586*, 275–280. https://doi.org/10.1038/s41586-020-2776-9.

Ma, Q., Tao, H., Li, Q., Zhai, Z., Zhang, X., Lin, Z., Kuang, N., and Pan, J. (2023). OrganoidDB: a comprehensive organoid database for the multi-perspective exploration of bulk and single-cell transcriptomic profiles of organoids. Nucleic Acids Res. *51*, D1086–D1093. https://doi.org/10.1093/nar/gkac942.

Mahdieh, Z., Cherne, M.D., Fredrikson, J.P., Sidar, B., Sanchez, H.S., Chang, C.B., Bimczok, D., and Wilking, J.N. (2022). Granular Matrigel: restructuring a trusted extracellular matrix material for improved permeability. Biomed. Mater. *17*, 045020. https://doi.org/10.1088/1748-605X/ac7306.

McNeish, J., Gardner, J.P., Wainger, B.J., Woolf, C.J., and Eggan, K. (2015). From Dish to Bedside: Lessons Learned While Translating Findings from a Stem Cell Model of Disease to a Clinical Trial. Cell Stem Cell *17*, 8–10. https://doi.org/10.1016/j.stem.2015.06.013.

Menacho, C., Okawa, S., Álvarez-Merz, I., Wittich, A., Muñoz-Oreja, M., Lisowski, P., López Martín, M., Pentimalli, T.M., Zakin, S., Thevandavakkam, M., et al. (2026). Accelerating Leigh syndrome drug discovery through deep learning screening in brain organoids. Nat Commun *17*, 3570. https://doi.org/10.1038/s41467-026-71391-2.

Mergenthaler, P., Hariharan, S., Pemberton, J.M., Lourenco, C., Penn, L.Z., and Andrews, D.W. (2021). Rapid 3D phenotypic analysis of neurons and organoids using data-driven cell segmentation-free machine learning. PLoS Comput. Biol. *17*, e1008630. https://doi.org/10.1371/journal.pcbi.1008630.

Metzger, J.J., Pereda, C., Adhikari, A., Haremaki, T., Galgoczi, S., Siggia, E.D., Brivanlou, A.H., and Etoc, F. (2022). Deep-learning analysis of micropattern-based organoids enables high-throughput drug

screening of Huntington's disease models. Cell Rep. Methods *2*, 100297. https://doi.org/10.1016/j.crmeth.2022.100297.

Mills, R.J., Parker, B.L., Quaife-Ryan, G.A., Voges, H.K., Needham, E.J., Bornot, A., Ding, M., Andersson, H., Polla, M., Elliott, D.A., et al. (2019). Drug Screening in Human PSC-Cardiac Organoids Identifies Pro-proliferative Compounds Acting via the Mevalonate Pathway. Cell Stem Cell *24*, 895–907.e6. https://doi.org/10.1016/j.stem.2019.03.009.

Morizane, R., Lam, A.Q., Freedman, B.S., Kishi, S., Valerius, M.T., and Bonventre, J.V. (2015). Nephron organoids derived from human pluripotent stem cells model kidney development and injury. Nat. Biotechnol. *33*, 1193–1200. https://doi.org/10.1038/nbt.3392.

Moruzzi, A., Shroff, T., Keller, S., Loskill, P., and Cipriano, M. (2023). Training the Next Generation of Researchers in the Organ-on-Chip Field. Educ. Sci. *13*, 144. https://doi.org/10.3390/educsci13020144.

Mpindi, J.-P., Swapnil, P., Dmitrii, B., Jani, S., Saeed, K., Wennerberg, K., Aittokallio, T., Östling, P., and Kallioniemi, O. (2015). Impact of normalization methods on high-throughput screening data with high hit rates and drug testing with dose–response data. Bioinformatics *31*, 3815–3821. https://doi.org/10.1093/bioinformatics/btv455.

Mukashyaka, P., Kumar, P., Mellert, D.J., Nicholas, S., Noorbakhsh, J., Brugiolo, M., Courtois, E.T., Anczukow, O., Liu, E.T., and Chuang, J.H. (2023). High-throughput deconvolution of 3D organoid dynamics at cellular resolution for cancer pharmacology with Cellos. Nat. Commun. *14*, 8406. https://doi.org/10.1038/s41467-023-44162-6.

Múnera, J.O., Sundaram, N., Rankin, S.A., Hill, D., Watson, C., Mahe, M., Vallance, J.E., Shroyer, N.F., Sinagoga, K.L., Zarzoso-Lacoste, A., et al. (2017). Differentiation of Human Pluripotent Stem Cells into Colonic Organoids via Transient Activation of BMP Signaling. Cell Stem Cell *21*, 51–64.e6. https://doi.org/10.1016/j.stem.2017.05.020.

Narazaki, G., Miura, Y., Pavlov, S.D., Thete, M.V., Roth, J.G., Avar, M., Shin, S., Kim, J., Hudacova, Z., Heilshorn, S.C., et al. (2025). Scalable production of human cortical organoids using a biocompatible polymer. Nat. Biomed. Eng. *9*, 2115–2123. https://doi.org/10.1038/s41551-025-01427-3.

Nickels, S.L., Modamio, J., Mendes-Pinheiro, B., Monzel, A.S., Betsou, F., and Schwamborn, J.C. (2020). Reproducible generation of human midbrain organoids for in vitro modeling of Parkinson's disease. Stem Cell Res. *46*, 101870. https://doi.org/10.1016/j.scr.2020.101870.

Onesto, M.M., Kim, J.I., and Pasca, S.P. (2024). Assembloid models of cell-cell interaction to study tissue and disease biology. Cell Stem Cell *31*, 1563–1573. https://doi.org/10.1016/j.stem.2024.09.017.

Ong, H.T., Karatas, E., Poquillon, T., Grenci, G., Furlan, A., Dilasser, F., Mohamad Raffi, S.B., Blanc, D., Drimaracci, E., Mikec, D., et al. (2025). Digitalized organoids: integrated pipeline for high-speed 3D analysis of organoid structures using multilevel segmentation and cellular topology. Nat. Methods *22*, 1343–1354. https://doi.org/10.1038/s41592-025-02685-4.

Ouchi, R., and Koike, H. (2023). Modeling human liver organ development and diseases with pluripotent stem cell-derived organoids. Front. Cell Dev. Biol. *11*, 1133534. https://doi.org/10.3389/fcell.2023.1133534.

Pahl, A., and Sievers, S. (2019). The Cell Painting Assay as a Screening Tool for the Discovery of Bioactivities in New Chemical Matter. In Systems Chemical Biology, S. Ziegler and H. Waldmann, eds. (New York, NY: Springer New York), pp. 115–126.

Park, G., Rim, Y.A., Sohn, Y., Nam, Y., and Ju, J.H. (2024). Replacing Animal Testing with Stem Cell-Organoids : Advantages and Limitations. Stem Cell Rev. Rep. *20*, 1375–1386. https://doi.org/10.1007/s12015-024-10723-5.

Park, T., Kim, T.K., Han, Y.D., Kim, K.-A., Kim, H., and Kim, H.S. (2023). Development of a deep learning based image processing tool for enhanced organoid analysis. Sci. Rep. *13*, 19841. https://doi.org/10.1038/s41598-023-46485-2.

Paşca, A.M., Sloan, S.A., Clarke, L.E., Tian, Y., Makinson, C.D., Huber, N., Kim, C.H., Park, J.-Y., O'Rourke, N.A., Nguyen, K.D., et al. (2015). Functional cortical neurons and astrocytes from human pluripotent stem cells in 3D culture. Nat. Methods *12*, 671–678. https://doi.org/10.1038/nmeth.3415.

Paul, S.M., Mytelka, D.S., Dunwiddie, C.T., Persinger, C.C., Munos, B.H., Lindborg, S.R., and Schacht, A.L. (2010). How to improve R&D productivity: the pharmaceutical industry's grand challenge. Nat. Rev. Drug Discov. *9*, 203–214. https://doi.org/10.1038/nrd3078.

Phipson, B., Er, P.X., Combes, A.N., Forbes, T.A., Howden, S.E., Zappia, L., Yen, H.-J., Lawlor, K.T., Hale, L.J., Sun, J., et al. (2019). Evaluation of variability in human kidney organoids. Nat. Methods *16*, 79–87. https://doi.org/10.1038/s41592-018-0253-2.

Powell, R.T., Moussalli, M.J., Guo, L., Bae, G., Singh, P., Stephan, C., Shureiqi, I., and Davies, P.J. (2022). deepOrganoid: A brightfield cell viability model for screening matrix-embedded organoids. SLAS Discov. *27*, 175–184. https://doi.org/10.1016/j.slasd.2022.03.004.

Regev, A., Teichmann, S.A., Lander, E.S., Amit, I., Benoist, C., Birney, E., Bodenmiller, B., Campbell, P., Carninci, P., Clatworthy, M., et al. (2017). The Human Cell Atlas. eLife *6*, e27041. https://doi.org/10.7554/eLife.27041.

Renner, H., Grabos, M., Becker, K.J., Kagermeier, T.E., Wu, J., Otto, M., Peischard, S., Zeuschner, D., TsyTsyura, Y., Disse, P., et al. (2020). A fully automated high-throughput workflow for 3D-based chemical screening in human midbrain organoids. eLife *9*, e52904. https://doi.org/10.7554/eLife.52904.

Renner, H., Schöler, H.R., and Bruder, J.M. (2021). Combining Automated Organoid Workflows with Artificial Intelligence-Based Analyses: Opportunities to Build a New Generation of Interdisciplinary High-Throughput Screens for Parkinson's Disease and Beyond. Mov. Disord. *36*, 2745–2762. https://doi.org/10.1002/mds.28775.

Richardson, D.S., Guan, W., Matsumoto, K., Pan, C., Chung, K., Ertürk, A., Ueda, H.R., and Lichtman, J.W. (2021). Tissue clearing. Nat. Rev. Methods Primers *1*, 84. https://doi.org/10.1038/s43586-021-00080-9.

Rios, A.C., and Clevers, H. (2018). Imaging organoids: a bright future ahead. Nat. Methods *15*, 24–26. https://doi.org/10.1038/nmeth.4537.

Russell, W.M.S., and Burch, R.L. (1959). The Principles of Humane Experimental Technique (London, UK: Methuen).

Samsdodd, F. (2005). Target-based drug discovery: is something wrong? Drug Discov. Today *10*, 139–147. https://doi.org/10.1016/S1359-6446(04)03316-1.

Sarrafha, L., Parfitt, G.M., Reyes, R., Goldman, C., Coccia, E., Kareva, T., and Ahfeldt, T. (2021). High-throughput generation of midbrain dopaminergic neuron organoids from reporter human pluripotent stem cells. STAR Protoc. *2*, 100463. https://doi.org/10.1016/j.xpro.2021.100463.

Sato, T., Vries, R.G., Snippert, H.J., Van De Wetering, M., Barker, N., Stange, D.E., Van Es, J.H., Abo, A., Kujala, P., Peters, P.J., et al. (2009). Single Lgr5 stem cells build crypt-villus structures in vitro without a mesenchymal niche. Nature *459*, 262–265. https://doi.org/10.1038/nature07935.

Schmidt, U., Weigert, M., Broaddus, C., and Myers, G. (2018). Cell Detection with Star-Convex Polygons. In Medical Image Computing and Computer Assisted Intervention – MICCAI 2018, A.F. Frangi, J.A. Schnabel, C. Davatzikos, C. Alberola-López, and G. Fichtinger, eds. (Cham: Springer International Publishing), pp. 265–273.

Schneider, M.R., Oelgeschlaeger, M., Burgdorf, T., Van Meer, P., Theunissen, P., Kienhuis, A.S., Piersma, A.H., and Vandebriel, R.J. (2021). Applicability of organ-on-chip systems in toxicology and pharmacology. Crit. Rev. Toxicol. *51*, 540–554. https://doi.org/10.1080/10408444.2021.1953439.

Seal, S., Trapotsi, M.-A., Spjuth, O., Singh, S., Carreras-Puigvert, J., Greene, N., Bender, A., and Carpenter, A.E. (2025). Cell Painting: a decade of discovery and innovation in cellular imaging. Nat. Methods *22*, 254–268. https://doi.org/10.1038/s41592-024-02528-8.

Serafini, C.E., Charles, S., Casteleiro Costa, P., Niu, W., Cheng, B., Wen, Z., Lu, H., and Robles, F.E. (2024). Non-invasive label-free imaging analysis pipeline for in situ characterization of 3D brain organoids. Sci. Rep. *14*, 22331. https://doi.org/10.1038/s41598-024-72038-2.

Seyhan, A.A. (2019). Lost in translation: the valley of death across preclinical and clinical divide – identification of problems and overcoming obstacles. Transl. Med. Commun. *4*, 18. https://doi.org/10.1186/s41231-019-0050-7.

Shi, H., Kowalczewski, A., Vu, D., Liu, X., Salekin, A., Yang, H., and Ma, Z. (2024). Organoid intelligence: Integration of organoid technology and artificial intelligence in the new era of in vitro models. Med. Nov. Technol. Devices *21*, 100276. https://doi.org/10.1016/j.medntd.2023.100276.

Shinozawa, T., Kimura, M., Cai, Y., Saiki, N., Yoneyama, Y., Ouchi, R., Koike, H., Maezawa, M., Zhang, R.-R., Dunn, A., et al. (2021). High-Fidelity Drug-Induced Liver Injury Screen Using Human Pluripotent Stem Cell–Derived Organoids. Gastroenterology *160*, 831–846.e10. https://doi.org/10.1053/j.gastro.2020.10.002.

Singh, N., Vayer, P., Tanwar, S., Poyet, J.-L., Tsaioun, K., and Villoutreix, B.O. (2023). Drug discovery and development: introduction to the general public and patient groups. Front. Drug Discov. *3*, 1201419. https://doi.org/10.3389/fddsv.2023.1201419.

Song, L., Yuan, X., Jones, Z., Griffin, K., Zhou, Y., Ma, T., and Li, Y. (2019). Assembly of Human Stem Cell-Derived Cortical Spheroids and Vascular Spheroids to Model 3-D Brain-like Tissues. Sci. Rep. *9*, 5977. https://doi.org/10.1038/s41598-019-42439-9.

Spence, J.R., Mayhew, C.N., Rankin, S.A., Kuhar, M.F., Vallance, J.E., Tolle, K., Hoskins, E.E., Kalinichenko, V.V., Wells, S.I., Zorn, A.M., et al. (2011). Directed differentiation of human pluripotent stem cells into intestinal tissue in vitro. Nature *470*, 105–109. https://doi.org/10.1038/nature09691.

Stringer, C., Wang, T., Michaelos, M., and Pachitariu, M. (2021). Cellpose: a generalist algorithm for cellular segmentation. Nat. Methods *18*, 100–106. https://doi.org/10.1038/s41592-020-01018-x.

Sui, Y., and Wu, Z. (2007). Alternative Statistical Parameter for High-Throughput Screening Assay Quality Assessment. SLAS Discov. *12*, 229–234. https://doi.org/10.1177/1087057106296498.

Sun, D., Gao, W., Hu, H., and Zhou, S. (2022). Why 90% of clinical drug development fails and how to improve it? Acta Pharm. Sin. B *12*, 3049–3062. https://doi.org/10.1016/j.apsb.2022.02.002.

Svendsen, C.N. (2025). Adopting novel alternative methods (NAMs) for biomedical research—What is the right approach? Cell Stem Cell *32*, 1489–1490. https://doi.org/10.1016/j.stem.2025.08.014.

Taelman, J., Diaz, M., and Guiu, J. (2022). Human Intestinal Organoids: Promise and Challenge. Front. Cell Dev. Biol. *10*, 854740. https://doi.org/10.3389/fcell.2022.854740.

Takasato, M., Er, P.X., Chiu, H.S., Maier, B., Baillie, G.J., Ferguson, C., Parton, R.G., Wolvetang, E.J., Roost, M.S., Chuva De Sousa Lopes, S.M., and Little, M.H. (2015). Kidney organoids from human iPS cells contain multiple lineages and model human nephrogenesis. Nature *526*, 564–568. https://doi.org/10.1038/nature15695.

Takebe, T., Sekine, K., Enomura, M., Koike, H., Kimura, M., Ogaeri, T., Zhang, R.-R., Ueno, Y., Zheng, Y.-W., Koike, N., et al. (2013). Vascularized and functional human liver from an iPSC-derived organ bud transplant. Nature *499*, 481–484. https://doi.org/10.1038/nature12271.

Tanimizu, N., Ichinohe, N., Sasaki, Y., Itoh, T., Sudo, R., Yamaguchi, T., Katsuda, T., Ninomiya, T., Tokino, T., Ochiya, T., et al. (2021). Generation of functional liver organoids on combining hepatocytes and cholangiocytes with hepatobiliary connections ex vivo. Nat. Commun. *12*, 3390. https://doi.org/10.1038/s41467-021-23575-1.

Tian, T., Yang, Z., and Li, X. (2021). Tissue clearing technique: Recent progress and biomedical applications. J. Anat. *238*, 489–507. https://doi.org/10.1111/joa.13309.

Tran, T., Song, C.J., Nguyen, T., Cheng, S.-Y., McMahon, J.A., Yang, R., Guo, Q., Der, B., Lindström, N.O., Lin, D.C.-H., et al. (2022). A scalable organoid model of human autosomal dominant polycystic kidney disease for disease mechanism and drug discovery. Cell Stem Cell *29*, 1083–1101.e7. https://doi.org/10.1016/j.stem.2022.06.005.

Vandana, J.J., Manrique, C., Lacko, L.A., and Chen, S. (2023). Human pluripotent-stem-cell-derived organoids for drug discovery and evaluation. Cell Stem Cell *30*, 571–591. https://doi.org/10.1016/j.stem.2023.04.011.

Wang, D., Villenave, R., Stokar-Regenscheit, N., and Clevers, H. (2026). Human organoids as 3D in vitro platforms for drug discovery: opportunities and challenges. Nat. Rev. Drug Discov. *25*, 204–226. https://doi.org/10.1038/s41573-025-01317-y.

Wang, T., He, X., Li, M., Li, Y., Bi, R., Wang, Y., Cheng, C., Shen, X., Meng, J., Zhang, H., et al. (2024). Ab initio characterization of protein molecular dynamics with AI2BMD. Nature *635*, 1019–1027. https://doi.org/10.1038/s41586-024-08127-z.

Wang, Y., Gao, Y., Pan, Y., Zhou, D., Liu, Y., Yin, Y., Yang, J., Wang, Y., and Song, Y. (2023a). Emerging trends in organ-on-a-chip systems for drug screening. Acta Pharm. Sin. B *13*, 2483–2509. https://doi.org/10.1016/j.apsb.2023.02.006.

Wang, Y., Li, Z., and Barati Farimani, A. (2023b). Graph Neural Networks for Molecules. In Machine Learning in Molecular Sciences, C. Qu and H. Liu, eds. (Cham: Springer International Publishing), pp. 21–66.

Wilkinson, M.D., Dumontier, M., Aalbersberg, I.J., Appleton, G., Axton, M., Baak, A., Blomberg, N., Boiten, J.-W., Da Silva Santos, L.B., Bourne, P.E., et al. (2016). The FAIR Guiding Principles for scientific data management and stewardship. Sci. Data *3*, 160018. https://doi.org/10.1038/sdata.2016.18.

Winanto, Khong, Z.J., Soh, B.-S., Fan, Y., and Ng, S.-Y. (2020). Organoid cultures of MELAS neural cells reveal hyperactive Notch signaling that impacts neurodevelopment. Cell Death Dis. *11*, 182. https://doi.org/10.1038/s41419-020-2383-6.

Zanoni, M., Piccinini, F., Arienti, C., Zamagni, A., Santi, S., Polico, R., Bevilacqua, A., and Tesei, A. (2016). 3D tumor spheroid models for in vitro therapeutic screening: a systematic approach to enhance the biological relevance of data obtained. Sci. Rep. *6*, 19103. https://doi.org/10.1038/srep19103.

Zhang, J.-H., Chung, T., and Oldenburg, K.R. (1999). A Simple Statistical Parameter for Use in Evaluation and Validation of High Throughput Screening Assays. SLAS Discov *4*, 67–73. https://doi.org/10.1177/108705719900400206.

Zhang, K., Yang, X., Wang, Y., Yu, Y., Huang, N., Li, G., Li, X., Wu, J.C., and Yang, S. (2025a). Artificial intelligence in drug development. Nat. Med. *31*, 45–59. https://doi.org/10.1038/s41591-024-03434-4.

Zhang, P., Baker, D., Song, M., and Bi, J. (2025b). Unraveling the potential of diffusion models in small-molecule generation. Drug Discov. Today *30*, 104413. https://doi.org/10.1016/j.drudis.2025.104413.

Zhang, X.D., Ferrer, M., Espeseth, A.S., Marine, S.D., Stec, E.M., Crackower, M.A., Holder, D.J., Heyse, J.F., and Strulovici, B. (2007). The Use of Strictly Standardized Mean Difference for Hit Selection in Primary RNA Interference High-Throughput Screening Experiments. SLAS Discov *12*, 497–509. https://doi.org/10.1177/1087057107300646.

Zhang, X.-P., Wang, X.-Y., Wang, S.-N., and Miao, C.-Y. (2023). The generation and properties of human cortical organoids as a disease model for malformations of cortical development. Neural Regen. Res. *18*, 2119–2126. https://doi.org/10.4103/1673-5374.369100.

Zhang, Z., Guan, N., Li, T., Mais, D.E., and Wang, M. (2012). Quality control of cell-based high-throughput drug screening. Acta Pharm. Sin. B *2*, 429–438. https://doi.org/10.1016/j.apsb.2012.03.006.

Zhavoronkov, A., Gennert, D., and Shi, J. (2026). From Prompt to Drug: Toward Pharmaceutical Superintelligence. ACS Cent. Sci. *12*, 265–279. https://doi.org/10.1021/acscentsci.5c01473.

Zhou, S.-F., and Zhong, W.-Z. (2017). Drug Design and Discovery: Principles and Applications. Molecules *22*, 279. https://doi.org/10.3390/molecules22020279.

Zhou, T., Tan, L., Cederquist, G.Y., Fan, Y., Hartley, B.J., Mukherjee, S., Tomishima, M., Brennand, K.J., Zhang, Q., Schwartz, R.E., et al. (2017). High-Content Screening in hPSC-Neural Progenitors Identifies Drug Candidates that Inhibit Zika Virus Infection in Fetal-like Organoids and Adult Brain. Cell Stem Cell *21*, 274–283.e5. https://doi.org/10.1016/j.stem.2017.06.017.

Zhu, T., Cao, S., Su, P.-C., Patel, R., Shah, D., Chokshi, H.B., Szukala, R., Johnson, M.E., and Hevener, K.E. (2013). Hit Identification and Optimization in Virtual Screening: Practical Recommendations Based on a Critical Literature Analysis: Miniperspective. J. Med. Chem. *56*, 6560–6572. https://doi.org/10.1021/jm301916b.

Zink, A., Dai, D.-F., Wittich, A., Henke, M.-T., Pedrotti, G., Heiduschka, S., Santamaria, G., Pentimalli, T.M., Brueser, C., Notopoulou, S., et al. (2026). Pluripotent stem-cell-based screening uncovers sildenafil as a mitochondrial disease therapy. Cell *189*, 1656–1679.e42. https://doi.org/10.1016/j.cell.2026.02.008.

Zushin, P.-J.H., Mukherjee, S., and Wu, J.C. (2023). FDA Modernization Act 2.0: transitioning beyond animal models with human cells, organoids, and AI/ML-based approaches. J. Clin. Invest. *133*, e175824. https://doi.org/10.1172/JCI175824.

Hevener, K.E., Pesavento, R., Ren, J., Lee, H., Ratia, K., and Johnson, M.E. (2018). Hit-to-Lead: Hit Validation and Assessment. In Methods in Enzymology, C.A. Lesburg and In., eds. (Elsevier), pp. 265–309.

13. Appendix V

nature communications

Article

https://doi.org/10.1038/s41467-026-71391-2

Accelerating Leigh syndrome drug discovery through deep learning screening in brain organoids

Received: 7 August 2024

Accepted: 13 March 2026

Published online: 20 April 2026

Check for updates

Carmen Menacho[1,2,40], Satoshi Okawa[3,4,40], Iris Álvarez-Merz[5], Annika Wittich[6], Mikel Muñoz-Oreja[7], Pawel Lisowski[8,9,10,11], Mario López Martín[12], Tancredi Massimo Pentimalli[8,9,13], Shiri Zakin[14], Mathuravani Thevandavakkam[14], Caleb Jerred[1,2,15], Selene Lickfett[1,2], Laura Petersilie[5], Agnieszka Rybak-Wolf[8,9], Annette Seibt[1], Diran Herebian[1], Gizem Inak[8,38], Susanne Brodesser[16], Andrea Zaliani[6], Barbara Mlody[8,39], Justin Donnelly[13], Kasey Woleben[17], Francesc Xavier Soriano[18], Jose C. Fernandez-Checa[19,20,21,22], Natascia Ventura[15,23,24], Sidney Cambridge[25], Ertan Mayatepek[1], Antonella Spinazzola[26], Markus Schuelke[27,28], Nikolaus Rajewsky[8,9,28,29,30,31], Andrea Rossi[32], Alex Peralvarez-Marin[12], Felix Distelmaier[1], Ethan Perlstein[14], Ian J. Holt[7,33,34,35], Emma Puighermanal[36], Ole Pless[6], Christine R. Rose[5], Antonio Del Sol[3,33,37,41] ✉ & Alessandro Prigione[1,41] ✉

Leigh syndrome (Leigh) is an untreatable mitochondrial disorder characterized by lactic acidosis and basal ganglia and midbrain pathology, leading to psychomotor regression and early death. We previously uncovered impaired neuronal morphogenesis in Leigh cerebral organoids carrying *SURF1* gene variants. Leveraging this phenotype, we here develop a deep learning algorithm tailored for cell type-specific drug repurposing screening. In parallel, we perform a survival drug screen in a yeast model of Leigh. The two approaches independently converge on azole compounds, two of which - talarozole and sertaconazole - rescue neuronal morphogenesis in Leigh neurons and lower lactate release and improve growth rate in Leigh midbrain organoids. Mechanistically, these compounds modulate the retinoic acid pathway and membrane-associate lipid metabolism. The findings highlight azoles as promising candidates for Leigh and demonstrate the potential of combining in silico screens with human brain organoids as new approach methodologies (NAMs) to advance the discovery of therapeutics addressing rare neurodevelopmental disorders.

Leigh syndrome (Leigh) (OMIM #256000), also known as "infantile subacute necrotizing encephalomyelopathy", is a severe neurometabolic disorder affecting children[1]. Like other mitochondrial diseases, Leigh is caused by inherited gene variants in the nucleus or mitochondrial DNA (mtDNA) hampering the oxidative phosphorylation (OXPHOS) machinery that is responsible for cellular energy generation[2]. Hence, mitochondrial diseases typically impair tissues with high energy requirements such as nerves and muscles[3]. In

A full list of affiliations appears at the end of the paper. ✉e-mail: antonio.delsol@uni.lu; alessandro.prigione@hhu.de

particular, Leigh affects the central nervous system regions of basal ganglia and midbrain, leading to motor impairment, intellectual disability, lactic acidosis, and early mortality[4–8].

One of the most frequently mutated gene in Leigh is *SURF1* (surfeit locus protein 1, NM_003172.2), which encodes an assembly factor for cytochrome c oxidase (COX), the complex IV of the mitochondrial respiratory chain and terminal enzyme responsible for transferring electrons from cytochrome c to molecular oxygen that is then reduced to water[4,5]. The *SURF1* gene is highly conserved and ablation of the yeast homologue *SHY1* (ΔSHY) retards growth upon nutrient removal[6]. A *SURF1* knock-out piglet model displayed severe lethal neurodevelopmental phenotypes[7]. However, *Surf1* knock-out mice failed to develop Leigh-like phenotypes and instead exhibited prolonged lifespan[8,9], suggesting that mice possess compensatory mechanisms for COX deficiency that humans lack[9]. Due to the paucity of faithful mammalian models, it has been challenging to study Leigh caused by *SURF1* defects to identify possible interventions[10,11]. Indeed, Leigh is currently incurable[12] and there is a high need for effective strategies aiming at accelerating the drug discovery process.

To develop innovative models of Leigh[13,14] based on human-relevant new approach methodologies (NAMs), we previously combined patient-derived induced pluripotent stem cells (iPSCs) and CRISPR/Cas9 engineering to generate a brain organoid model of Leigh harboring *SURF1* variants[15]. Compared to isogenic controls, Leigh cerebral organoids (COs) exhibited aberrant progenitor organization, suggestive of defective neuronal morphogenesis[15]. Accordingly, Leigh iPSC-derived dopaminergic neurons showed impaired differentiation and branching capacity that resulted in defective firing[15]. The findings suggested that Leigh may interfere with neurodevelopment and particularly with the ability of neurons to form appropriate connections, leading to faulty wiring[16]. Cortical brain organoids of Leigh caused by other gene variants demonstrated a similar impairment in neurodevelopment[16,17]. Mitochondria might indeed play a central role in neural commitment[18–20], and differences in mitochondrial activity might underlie the species-specific temporality of brain development[21]. Pre-clinical and clinical studies revealed that signs of Leigh and other mitochondrial disorders may manifest before birth[22–25], potentially explaining the developmental delay seen in individuals with Leigh[26–28]. Collectively, these data suggest that Leigh impacts human brain development. Hence, approaches aiming at counteracting these defects and promoting neuronal morphogenesis might be of therapeutic value.

Here, we sought to exploit our brain organoid model of Leigh to uncover repurposable drugs. We recently showed that screening repurposable compounds in iPSC-derived neural cells led to the identification of sildenafil as a potential treatment of Leigh caused by *MT-ATP6* variants[29]. To further accelerate this process and allow the identification of repurposable candidates before performing time-consuming screens in cells, we establish here a deep learning (DL) algorithm for cell type-specific drug repurposing based on single-cell RNA-sequencing (scRNAseq) of Leigh COs. Concurrently, we screen a library of 2,250 FDA-approved drugs in ΔSHY yeasts. Both approaches independently identify azole compounds, two of which - sertaconazole and talarozole - effectively promote neural commitment in Leigh neural cells and rescue the aberrant growth rate and lactate release of Leigh midbrain organoids (MOs). In addition to modulating neuronal bioenergetics, sertaconazole and talarozole impact membrane-associated lipid metabolism and engage with the CYP26A enzyme activating the retinoic acid (RA) pathway. Taken together, we discover two drug candidates that could be repurposed for the treatment of individuals with Leigh. Our findings suggest that human neuronal morphogenesis may represent a therapeutic target for Leigh and underscore the power of combining in silico screens with brain organoid technology to develop human-based platforms for accelerating drug discovery of untreatable neurodevelopmental disorders.

Results

Deep learning-based framework for drug repurposing and yeast screen identify repurposable drugs for Leigh

To accelerate Leigh drug discovery, we employed deep learning (DL), a subset of machine learning that uses multi-layered artificial neural networks to learn from large amounts of data. We established a DL algorithm for cell type-specific drug repurposing based on scRNAseq of Leigh COs. We reanalyzed our published scRNAseq datasets of isogenic Leigh COs[15] to determine key affected populations. Uncommitted precursors showing markers of radial glia (RG) identity were present in both Leigh COs and control COs, while more committed intermediate progenitor cells (IPCs) and neurons were mostly absent in Leigh COs (Fig. 1a-b). Using pseudotime analysis[30] to reconstruct the continuous trajectory of cell development in COs, we confirmed that neuronal differentiation was following the directionality RG > IPCs > neurons (Fig. 1c-d, Supplementary Fig. 1a). Therefore, strategies capable of promoting neuronal fate in Leigh cells might represent innovative treatment interventions.

We developed a multi-stage, DL-based framework based on ChemPert, our recently developed database of perturbations in non-cancer cells[31]. The goal of the framework was to predict optimal drugs that drive a transcriptional state transition from an initial state (i.e. RG identity) to a desired target state (i.e. IPCs or neurons) (Fig. 1e). We first inferred protein-level perturbations as activation (1), inhibition (−1), or no perturbation (0). Unlike conventional drug-response tools, our framework learned the upstream interventions required to induce a specific downstream gene expression profile (Supplementary Fig. 1b-f). By decoupling protein-level perturbation prediction from the drugs used in training, this approach enabled prioritization of candidate drugs, including those not present in the training data, thereby making the framework suitable for non-cancer drug repurposing, where perturbation transcriptomics datasets are often limited in scope and coverage compared to oncology-focused resources. The framework operated over a curated molecular interaction graph comprising 20,455 protein nodes, assembled from integrated protein–protein interactions, signaling pathways, transcriptional regulation, and ligand–receptor relationships. We evaluated the framework using a strictly independent hold-out 47 test datasets associated with diverse cell conversion processes, including differentiation, metabolic shifts, and cell fate reprogramming (Supplementary Data 1, Supplementary Data 7). We compared our DL approach against gene set enrichment analysis (GSEA)-based methods and random ranking. Within the top 1st percentile of ranked drugs, our framework recalled 9.2% of known hits, outperforming GSEA (best case: 2.1%) and random ranking (1%). These results demonstrated that our DL framework added value beyond conventional pathway enrichment by enabling more accurate early prioritization of candidate drugs for experimental validation.

Given our perturbation input (transcriptomic profile of initial state and target state), the framework computed differentially expressed transcription factors (DETFs). We used this defined set of DETFs to uncover drugs capable of triggering cellular conversion from RG directly to neurons (DETF1) or from RG to IPCs and then to neurons (DETF2) (Fig. 1e, f). DETF influence was then propagated through the graph up to five hops, capturing both upstream and downstream effects. The framework also computed topological and functional attributes for each protein, such as shortest path lengths to DETFs, DETF reachability, and shared Reactome pathway counts, which were not part of the propagation step but were integrated as additional features. These features were then passed through a variational autoencoder (VAE) trained to denoise and regularize the unconstrained

https://doi.org/10.1038/s41467-026-71391-2

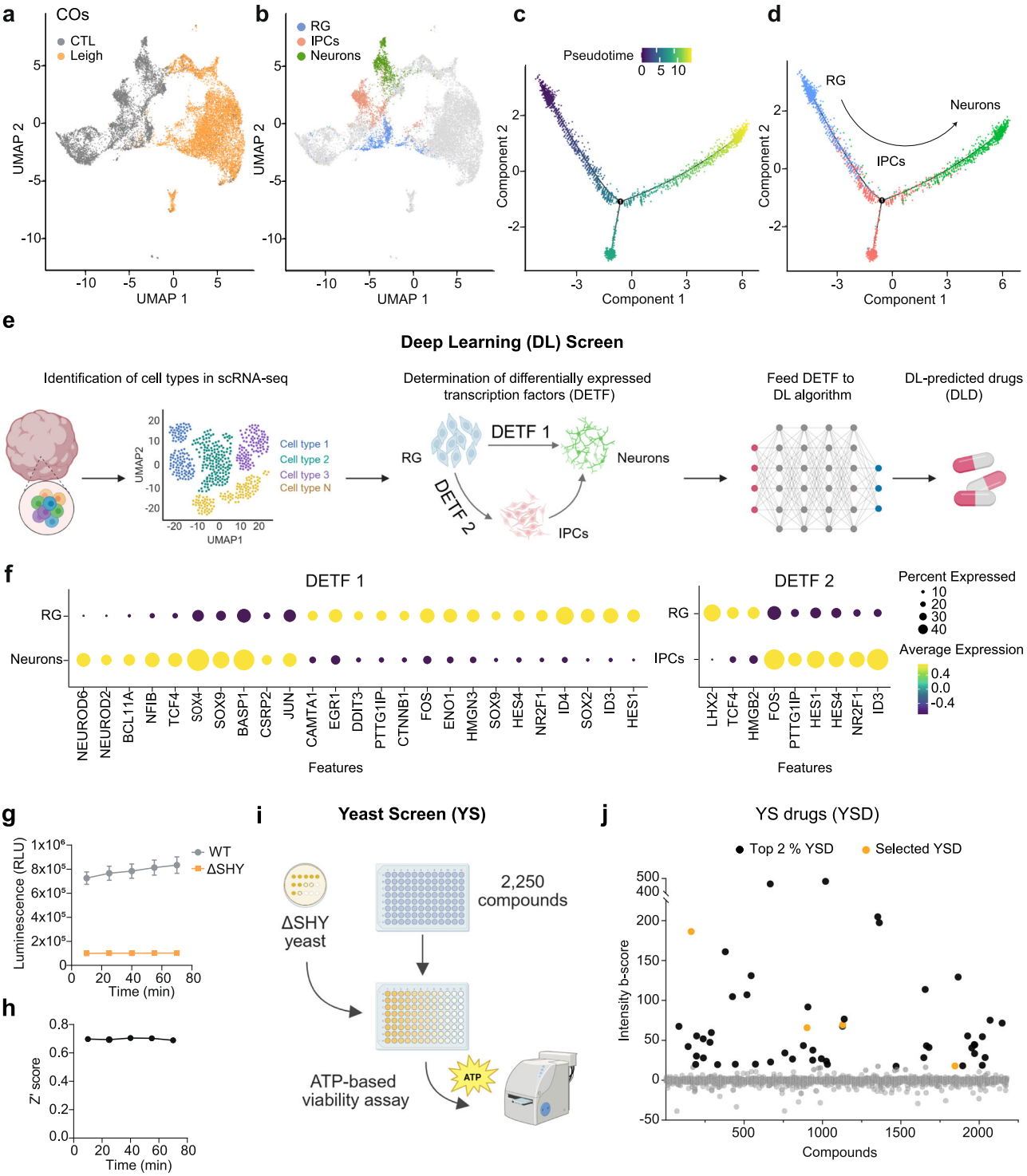


Fig. 1 | Deep learning and yeast screens to identify repurposable drugs for Leigh. a, **b** UMAP plots of scRNAseq of cerebral organoids (COs) from Leigh and isogenic control (CTL) showing uncommitted progenitors with radial glia (RG) identity and neural committed cells with identity of intermediate progenitor cells (IPCs) and mature neurons. **c**, **d** Pseudotime analysis reconstructing the developmental trajectory of the three populations following the directionality RG>IPCs>-Neurons. **e**, **f** Schematic of the deep learning (DL) algorithm to identify drugs promoting differentially expressed transcription factors (DETF)-specific cell fate conversion (created in BioRender. Menacho, C. (2026) https://BioRender.com/siziatp). **g**, **h** Survival assay in wild-type (WT) yeast and knock-out yeast for the *SURF1* homologue *SHY1* (ΔSHY). Dots in (**g**) show mean +/- SD of $n = 3$ independent experiments (**i**) Schematic representation of yeast screen (YS) strategy (created in BioRender. Menacho, C. (2026) https://BioRender.com/vaey7ea). **j** Screen of 2,250 FDA-approved repurposable compounds in ΔSHY yeast. Dots: individual drug responses to 20 μM treatment at 24 h; black dots: top 2% yeast screen drugs (YSDs); orange dots: YSDs selected for validation. Source data are provided as a Source Data file.

graph-based input (Supplementary Fig. 1b). The decoded output from the VAE, which preserved the original feature dimensionality, was then used as input to the classifier. The decoded input was processed by an ensemble of three independently trained feedforward neural networks (FNNs). Each model predicted one of three perturbation labels (1, −1 or 0) for every protein in the network. The ensemble output was determined by majority voting across the three FNN models (Supplementary Fig. 1b). The framework computed a Bayesian enrichment score (BES) for each drug. This score integrated: 1) hypergeometric enrichment between predicted perturbed proteins and known drug targets, 2) empirical robustness (p-value) calculated from randomized input feature matrices, and 3) normalized rank weighting (Supplementary Fig. 1c–f). The final BES reflected both statistical significance and model confidence. Drugs with no overlap (hypergeometric $p = 1.0$) received a BES of zero, and remaining drugs were ranked in descending BES order. To prioritize drug candidates from the prediction set, we selected drugs ranked within the top 2.5th percentile of the BES. This cutoff was chosen based on the test recall curve, which plateaued at 2.5% (Supplementary Fig. 1f-g), indicating diminishing returns for lower-ranked drugs. This cutoff resulted in 140 drugs for DETF1 and 143 drugs for DETF2, which we further prioritized based on annotation of metabolic function, given the central role of mitochondrial metabolism in Leigh pathophysiology and neural differentiation processes. This strategy highlighted a total of 34 DL-predicted drugs (DLDs). Among these, we selected 5 based on their safety profile in humans (DLD1, DLD3, DLD4, DLD5 from DETF1, and DLD2 from DETF2).

In parallel to the DL algorithm approach, we carried out a rescue screen in Leigh yeast cultures using a library of 2,250 repurposable drugs. The rescue assay was based on survival of wild-type (WT) and *SURF1* homologue *SHY1*[6] knock-out (ΔSHY) yeast strains upon nutrient removal (Fig. 1g–i, Supplementary Fig. 2a-b). Among the top 2% of rescuing yeast screen drugs (YSDs) (Fig. 1j, black dots), we selected 4 (YSD1, YSD2, YSD3, YSD4) that belonged to the class of azole-containing compounds, as this was among the most strongly affected classes of rescuer drugs (Fig. 1j, orange dots). Altogether, using the two screening strategies, we identified 9 candidate repurposable compounds.

Identified compounds sertaconazole and talarozole promote Leigh neuromorphogenesis

We previously demonstrated that Leigh variants impact the ability of neural progenitor cells (NPCs) to switch to OXPHOS and commit to neuronal fate[15]. Here, we used our high-content analysis (HCA) pipeline to quantify neuromorphogenesis[32] and investigate NPC commitment defects in Leigh. Through overexpression of the transcription factor Neurogenin 2 (*NGN2*)[33], we converted Leigh NPCs and isogenic control NPCs into induced neurons (iNs) in about 5-6 days (Supplementary Fig. 2c). In agreement with previous data obtained in Leigh midbrain dopaminergic neurons (mDANs)[15], the number of neurons was significantly reduced in Leigh iNs compared to control iNs (Fig. 2a, Supplementary Fig. 2d). The mean neurite length was slightly lower in Leigh iNs compared to control iNs, although the difference did not reach statistical significance (Supplementary Fig. 2e).

We next applied the HCA pipeline to assess the impact of the 9 candidate compounds (5 DLDs and 4 YSDs) on neuronal number and morphology. We treated Leigh iNs differentiating from NPCs with three different concentrations for compound (all dissolved in DMSO) and compared compound treated Leigh iNs to Leigh iNs exposed to DMSO only (Fig. 2b). We counterstained the plates with the nuclear dye Hoechst to monitor the effect of compounds on cellular viability.

Among DLDs, talarozole (DLD5) showed the most pronounced effect, increasing by two-fold the number of neurons in Leigh iNs in a Concentration-dependent manner for concentration of 1 μM and 10 μM (Fig. 2c, d). 10 μM talarozole also increased the mean neurite length in Leigh iNs (Supplementary Fig. 2g). Based on Hoechst signal, no neuronal toxicity was observed at 1 μM and 10 μM concentration, but 50 μM talarozole treatment led to 50% cell death (Supplementary Fig. 2f). Interestingly, talarozole showed one of the highest BES values in the DL screen (BES = 9.034277; 38th out of 5692 drugs, ~99.3rd percentile) (Supplementary Fig. 1h, i). We also assessed three non-predicted drugs (NPDs) that were outside the top 2.5% BES cutoff and found that they did not increase the number of neurons in Leigh iNs (Supplementary Fig. 2j, k).

Among YSDs, we identified sertaconazole (YSD4) as the most promising compound. 10 μM sertaconazole led to 1.5-fold increase in neuronal amount and to higher mean neurite length in Leigh iNs (Fig. 2e, f, Supplementary Fig. 2i). Similarly to talarozole, 50 μM sertaconazole proved to be toxic in Leigh iNs (Supplementary Fig. 2h). Therefore, we focused only on lower concentrations for further analyses with these two azole compounds.

Next, we assessed whether the two azoles could lead to a concentration-dependent rescue of ΔSHY yeast upon nutrient removal. Talarozole was effective in increasing by more than two-fold the survival of mutant yeast in a concentration-dependent manner both at 24 and 48 h of treatment (Fig. 2g). Sertaconazole also displayed a concentration-dependent rescue effect in mutant yeast up to almost two-fold at 24 and 48 h (Fig. 2h).

Overall, based on validations conducted in SURF1-mutant human Leigh neurons and mutant yeast, we concluded that the azoles sertaconazole and talarozole were promising drug candidates to be repositioned for Leigh.

Midbrain organoids as a 3D model of Leigh recapitulating disease features

We reasoned that the next step for assessing the potential effectiveness of the identified azoles would be to address their effect in a more complex human model. We previously employed whole-brain cerebral organoids (COs) to model Leigh[15]. However, since basal ganglia and midbrain regions are typically affected in Leigh[34–36], here we aimed to generate Leigh midbrain organoids (MOs) to assess the impact of compounds on this brain region under the condition of SURF1 deficiency.

In light of the defective neuronal generation of Leigh NPCs (Fig. 2a), we inferred that impaired neural commitment of NPCs contributes to the disease pathogenesis. Therefore, we generated MOs starting from NPCs[37] (Supplementary Fig. 3a) and used scRNAseq to benchmark our MOs with respect to previously published MOs derived from NPCs[38] (Supplementary Fig. 3b). The MOs that we generated contained a relatively high number of tyrosine hydroxylase (TH)-positive mDANs (31%) by day 35 (Supplementary Fig. 3c), indicating that our protocol led to the generation of functionally relevant cell types at this early time-point. We focused our analysis on MOs grown until day 30, when we could detect the expression of both progenitor cells (positive for SOX2 and NESTIN) and mature neurons (positive for MAP2 and for mDAN markers TH and NURR1) (Supplementary Fig. 3d).

To determine whether Leigh MOs could recapitulate neuromorphogenesis defects seen in Leigh COs (Fig. 1a-d), we carried out scRNAseq in Leigh MOs compared to isogenic control MOs (Fig. 3a). Unsupervised clustering identified eight main clusters in MOs (Supplementary Fig. 4a, Supplementary Data 2). Based on their gene expression, we assigned the clusters to the following categories: proliferative cells (cluster 0), aberrant neurons (cluster 1), aberrant undifferentiated cells (cluster 2), healthy neurons (cluster 3), RGs (clusters 4 and 6), other cell types (cluster 5), and IPCs (cluster 7) (Supplementary Fig. 4b, Supplementary Data 2). Dopaminergic markers were mainly expressed in the population of neurons and IPCs (Supplementary Fig. 4c). Based on this classification, we performed pseudotime analysis of RG, IPCs and healthy neurons (Fig. 3b-e, Supplementary Fig. 4e). Similar to the results obtained in COs, we obtained a directionality of differentiation from RG > IPCs > neurons (Fig. 3c-d).

https://doi.org/10.1038/s41467-026-71391-2

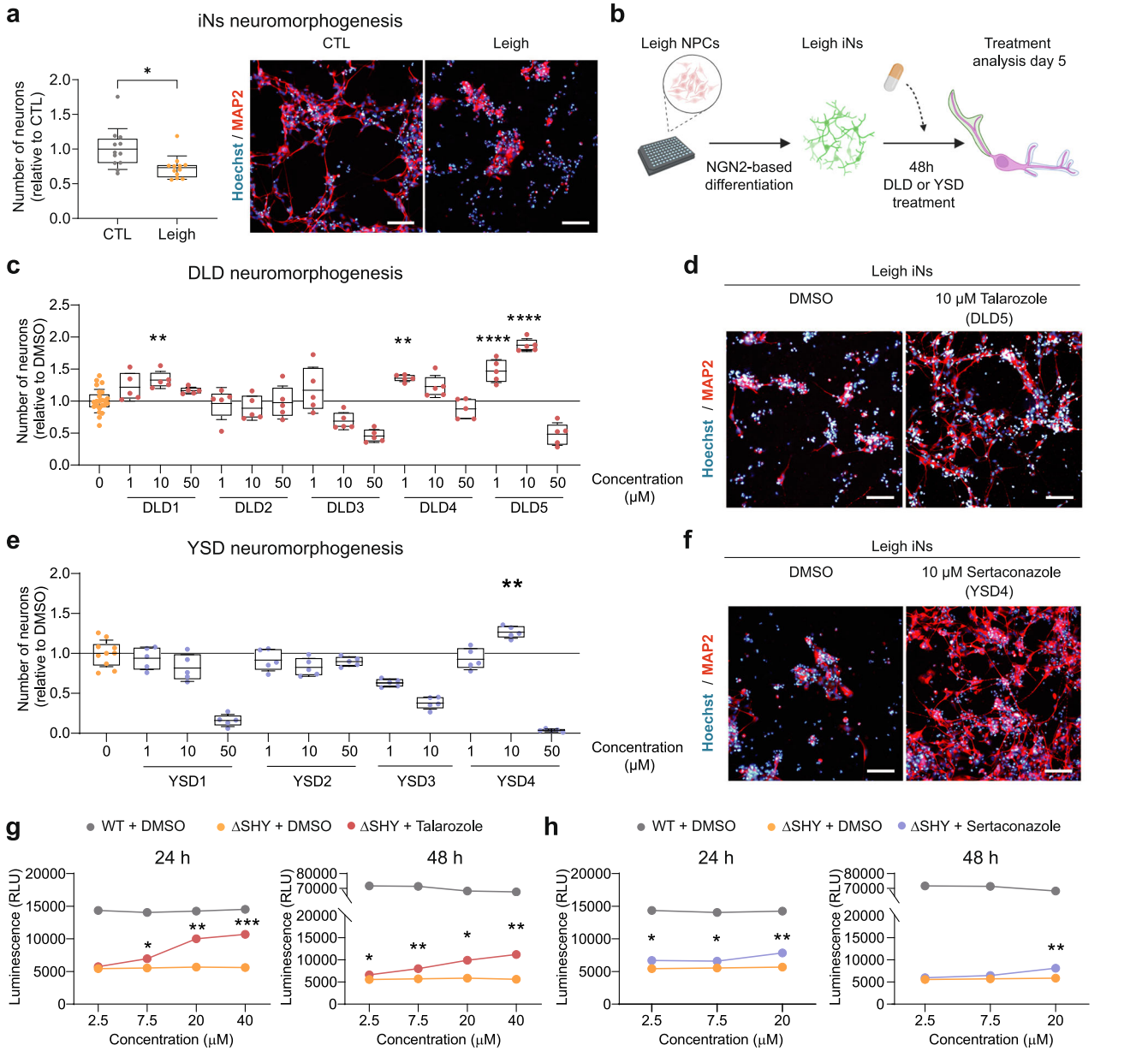
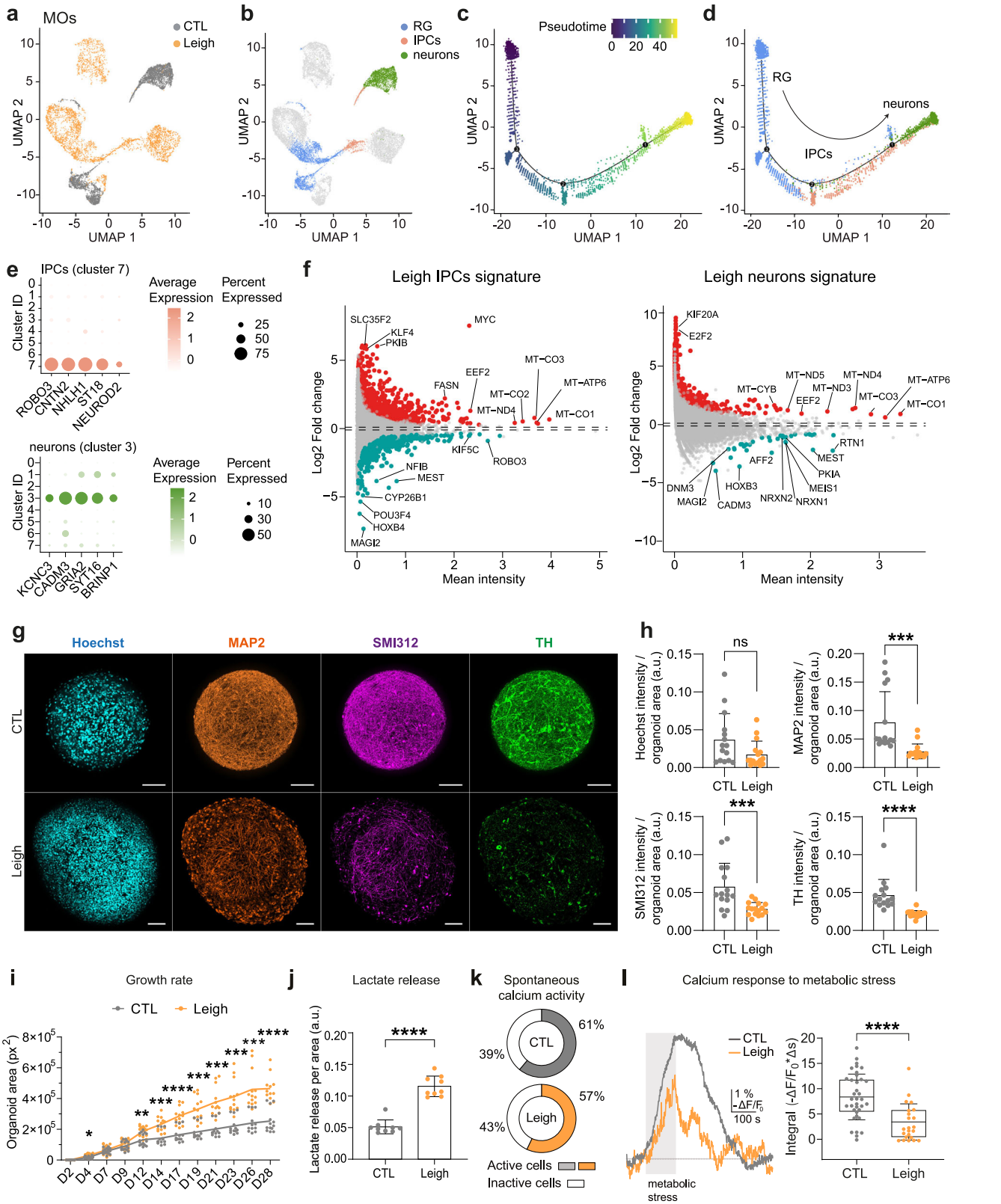


Fig. 2 | Neuromorphogenesis assay in Leigh iNs validate talarozole and sertaconazole. a Number of induced neurons (iNs) from Leigh NPCs and isogenic control (CTL) NPCs quantified with high-content analysis (HCA) based on neuronal dendritic marker MAP2 at day 5 of differentiation. Boxplots: mean (center), 25/75 percentiles (box), and 1x SD (whiskers). Individual dots: $n = 12$ biological replicates; $^{*}p < 0.05$, unpaired two-tailed t test. Scale bars: 100 μm. **b** Schematic of the 2D neuromorphogenesis screening in Leigh iNs using DL-predicted drugs (DLDs) and yeast screen drugs (YSDs) (created in BioRender. Menacho, C. (2026) https://BioRender.com/31a4745). **c**–**f** Quantification of Leigh iNs neurons after treatment with DMSO ("0") or with DLDs or YSDs and representative images for DLD5 (talarozole) and YSD4 (sertaconazole). Boxplots: mean (center), 25/75 percentiles (box), and 1x SD (whiskers). Individual dots: $n = 5$ biological replicates, related to DMSO-treated condition. Statistics are shown only for ameliorating compounds, $^{**}p < 0.01$, $^{***}p < 0.005$, $^{****}p < 0.001$, one-way ANOVA, compound-treated Leigh iNs vs DMSO-treated Leigh iNs. Scale bars: 100 μm. **g**, **h** Concentration-dependent validation of talarozole and sertaconazole on yeast survival after 24 h or 48 h of increasing concentrations. Dots: mean +/- SD; n = 3 replicates, $^{*}p < 0.05$, $^{**}p < 0.01$, $^{***}p < 0.001$, two-way ANOVA. Source data are provided as a Source Data file.

These results validated our Leigh MOs model and confirmed that it recapitulated key features seen in Leigh COs.

We next investigated the differential gene expression between Leigh and controls in the identified populations within MOs. The Leigh signature of the IPCs population highlighted the downregulation of genes associated with neuronal morphogenesis (*NFIB, ROBO3, MAGI2*), generation of mDANs (*MEST*), mitochondrial movements (*KIF5C*), and retinoic acid (RA) metabolism (*CYP26B1*) (Fig. 3f, Supplementary Data 3). Correspondingly, pathway enrichment analysis revealed downregulation of "nervous system development" and "generation of neurons" pathways in Leigh IPCs (Supplementary Fig. 5b). Upregulated genes in Leigh IPCs comprised genes regulating growth and proliferation (*SLC35F2, KLF4, PKIB, MYC, EEF2*), lipid metabolism (*FASN*), and mitochondrial respiratory chain genes (*MT-ATP6, MT-ND4*), including those belonging to central COX enzyme that is impaired by *SURF1* variants (*MT-CO1, MT-CO2, MT-CO3*) (Fig. 3f, Supplementary Data 3). Upregulated pathways in Leigh IPCs included "ribosome biogenesis", "cellular respiration", and "cholesterol biosynthetic process" (Supplementary Fig. 5a).

https://doi.org/10.1038/s41467-026-71391-2



In the neuronal population, the Leigh signature highlighted the downregulation of genes involved in neurogenesis (*CADM3, MAGI2, RTN1, AFF2*), mDANs development (*MEST*), and synaptic function (*DNM3, NRXN1, NRXN2*) (Fig. 3f, Supplementary Data 3), and the downregulation of pathways associated with "synapse assembly" (Supplementary Fig. 5d). Similarly to IPCs, Leigh neurons exhibited upregulation of genes related to cellular proliferation (*EEF2, KIF20A*) and mitochondrial respiration (*MT-ATP6, MT-ND5, MT-CO1, MT-CO2, MT-CO3*) (Fig. 3f, Supplementary Data 3). Upregulated pathways in Leigh neurons included "DNA metabolic process" and "regulation of cell cycle process" (Supplementary Fig. 5c).

RG appeared less impacted by Leigh pathology, as seen by the scRNAseq clustering of COs (Fig. 1a-b) and MOs (Fig. 3a, b). Nonetheless, the Leigh signature of RG still encompassed the

Fig. 3 | Midbrain organoids (MOs) recapitulate Leigh disease features. **a**, **b** UMAP plots of scRNAseq of Leigh MOs and CTL MOs showing uncommitted progenitors with RG identity and neural committed cells with identity of IPCs and mature neurons. **c**, **d** Pseudotime analysis of RG, IPCs, and neurons in MOs. **e** Dot plot highlighting top five genes enriched in IPCs (cluster 7) and neurons (cluster 3). **f** Pseudo-bulk analysis depicting the disease signature in the progenitor population (Leigh IPCs) and the neuronal population (Leigh Neurons) within Leigh MOs compared to CTL MOs. **g**, **h** Organization and quantification of MAP2-positive dendrites, SMI312-positive axons, and tyrosine hydroxylase (TH)-positive neurons in CTL MOs and Leigh MOs. Bar plots: mean +/- SD of signal intensity normalized to organoid area. Dots: individual MOs (CTL: 15 MOs, Leigh: 16 MOs); $^{**}p < 0.01$, unpaired two-tailed t test. Scale bars: 100 μm. **i** Growth rate of MOs relative to the initial size on day 2. Dots: individual MOs (CTL: 13-16 MOs; Leigh: 13-16 MOs); $n = 3$ independent experiments; $^{*}p < 0.05$, $^{**}p < 0.01$, $^{***}p < 0.005$, $^{****}p < 0.001$, two-way ANOVA. **j** Lactate release from MOs normalized to organoid area. Bar plots: mean +/- SD. Dots: individual MOs (CTL: 9 MOs; Leigh: 9 MOs); $^{****}p < 0.001$, two-tailed Mann-Whitney U test. **k** Active cells with spontaneous calcium activity: 25 out of 41 in 7 CTL MOs, 20 out of 35 in 6 Leigh MOs. Cells with calcium signals ≥ 2 x SD were considered as active. **l** Calcium response in MOs following metabolic stress (2 min of glucose-free medium + 2 mM 2-deoxyglucose + 5 mM sodium azide). Boxplots: mean (center), 25/75 percentiles (box), and 1x SD (whiskers). Dots: individual cells within MOs (CTL: 7 MOs; Leigh: 6 MOs); $^{****}p < 0.001$, two-tailed Mann-Whitney U test. Source data are provided as a Source Data file.

downregulation of neuronal genes (*RELN, TUBB3, MEST*) and the upregulation of genes related to mitochondrial respiration (*MT-ND4, MT-CO1, MT-CO2, MT-CO3*) and lipid metabolism (*FASN*) (Supplementary Fig. 4d, Supplementary Data 3).

In agreement with the transcriptional signature suggestive of defects in neuronal morphogenesis and mDANs generation, we detected significantly reduced expression of axonal marker SMI312, dendritic marker MAP2, and mDANs marker TH in Leigh MOs compared to isogenic control MOs (Fig. 3g, h). Leigh MOs were significantly larger than control MOs (Figs. 3g, i), in line with the observed increase in proliferation and cell cycle-related genes observed by transcriptomics.

Leigh MOs released more lactate in the media compared to control MOs (Fig. 3j). Elevated lactate in blood and cerebrospinal fluid represents a key diagnostic indicator of Leigh alongside specific brain abnormalities[39]. This feature is usually interpreted as a consequence of defective OXPHOS, which increases the reliance on glycolysis for ATP production, leading to a buildup of lactate[40–42]. The increase in lactate release was in agreement with the transcriptomics findings of Leigh MOs indicating a dysregulation of mitochondrial metabolism.

Lastly, we assessed the functionality of MOs by measuring calcium activity in whole organoids, as previously described[37]. Both Leigh MOs and control MOs were functionally active, with overall similar number of cells showing spontaneous calcium activity (Fig. 3k, Supplementary Fig. 5e–g). However, under condition of acute energy deprivation (2 min of glucose starvation with inhibition of glycolysis and OXPHOS), Leigh MOs displayed an aberrant response to metabolic stress, with a reduced ability to increase the calcium signal in comparison to control MOs (Fig. 3l, Supplementary Fig. 5h, i). This impaired response to metabolic stress could reflect a critical pathological feature of Leigh[1,43].

In summary, Leigh MOs showed transcriptional profiles reminiscent of those seen in Leigh COs and recapitulated key disease features including increased lactate release and aberrant response to metabolic stress. These findings suggest that Leigh MOs could serve as an effective model of Leigh on which to test treatment interventions.

Sertaconazole and talarozole rescue Leigh phenotypes in midbrain organoids

We next evaluated the effect of sertaconazole and talarozole on our MO model of Leigh (Fig. 4a). We established 0.1 μM sertaconazole or 1 μM talarozole as drug concentrations that could be used for long-term treatment of MOs with no apparent toxic effects in healthy control MOs (Supplementary Fig. 6a-b). At these concentrations, the two azoles significantly reduced the abnormal growth rate of Leigh MOs, although not to the levels seen in isogenic control MOs (Fig. 4b). Treatment of Leigh MOs with sertaconazole and talarozole decreased the amount of lactate in the media by 20% (Fig. 4c). Although the azoles did not significantly rescue neuronal generation or morphology in Leigh MOs (Supplementary Fig. 7a-b), talarozole treatment did increase the number of TH-positive neurons within MOs (Fig. 4d). Talarozole treatment also resulted in a higher number of active cells within Leigh MOs based on their calcium activity (Fig. 4e, Supplementary Fig. 6c) and increased by two-fold the calcium signal of Leigh MOs in response to metabolic stress (Fig. 4f, g, Supplementary Fig. 6d). These results indicate that while identified azoles did not fully revert the disease phenotypes of Leigh MOs, they led to significant rescue of key pathological aspects, with talarozole showing higher effectiveness than sertaconazole.

We then investigated the effects of the azole compounds on mitochondrial anchoring, which is crucial for neurite branching[44,45]. Indeed, the levels of mitochondrial anchoring-related genes were lower in Leigh mDANs and Leigh COs compared to controls (Supplementary Fig. 6e) and the anchoring gene *KIF5C* was downregulated in Leigh MOs (Fig. 3f, Supplementary Data 3). Concordantly, Leigh mDANs displayed abnormally increased mitochondrial motility with fewer mitochondria that were anchored or stationary (Supplementary Fig. 6f–h). These findings were not recapitulated by chemical inhibition of mitochondria using the uncoupling agent FCCP, which instead led to decreased mitochondrial motility (Supplementary Fig. 6g-h). Hence, the increase in mitochondrial motility seen in Leigh mDANs might not be due to simple mitochondrial impairment but rather to specific disease-related mechanisms, possibly linked to defective mitochondrial anchoring. Nonetheless, treating Leigh mDANs or Leigh MOs with sertaconazole or talarozole did not rescue the expression of anchoring proteins (Supplementary Fig. 6i-l).

To gain mechanistic insight into the action of the azoles, we performed scRNAseq of Leigh MOs treated for 30 days with sertaconazole or talarozole (Fig. 4a, Supplementary Fig. 7c, Supplementary Data 4). The azoles primarily affected the neuronal population of Leigh MOs. The sertaconazole signature in Leigh neurons included the upregulation of genes related to lipids and cholesterol (*STARD4, FABP3, MVD, SCD, HMGCR, HMGCS1*) and neuronal generation (*TUBB3, ELAVL3, MAP1B, DPYSL2*) (Fig. 4h), and the upregulation of pathways associated with cholesterol and lipid metabolism (Fig. 4i). Downregulated genes by sertaconazole in Leigh neurons included mitochondrial genes (*MT-ND3, MT-CO1, MT-CO2, MT-CO3)* and genes related to RA pathway (*CRABP1*) (Fig. 4h).

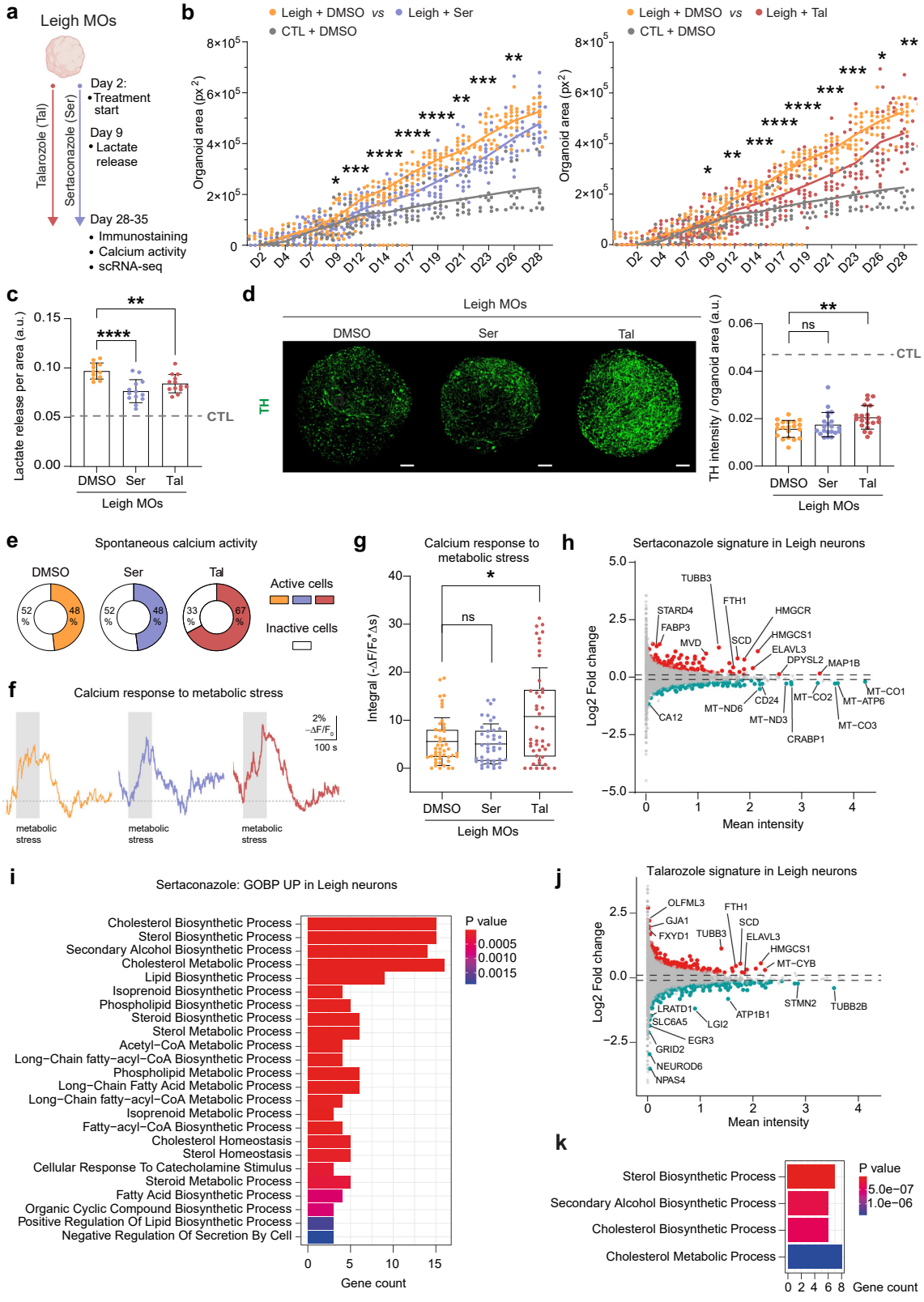
Talarozole similarly upregulated genes related to lipids and cholesterol (*SCD, HMGCS1*) and neuronal generation (*TUBB3, ELAVL3, FXYD1, GJA1*) in Leigh neurons (Fig. 4j), and upregulated pathways associated with cholesterol and lipid metabolism (Fig. 4k). It downregulated genes regulating cell morphology and embryonic growth (*LRATD1, EGR3*) (Fig. 4j). The effect of the two drugs on the IPCs population within Leigh MOs was less pronounced but still showed an upregulation of genes associated with neuronal generation and lipid metabolism (Supplementary Fig. 7d).

Thus, single-cell transcriptomics indicated that the two azoles shared an effect on lipid metabolism and neuronal generation. These findings suggest that the two compounds counteracted key transcriptional changes induced by Leigh in the neuronal population of midbrain organoids.

Sertaconazole and talarozole impact bioenergetics and lipid metabolism

To validate the transcriptomics results, we investigated the impact of the two azoles on energy metabolism and lipid metabolism in Leigh

https://doi.org/10.1038/s41467-026-71391-2



neural cells. Targeted metabolomics showed impaired AMP/ATP ratio by more than two-fold in Leigh NPCs compared to isogenic control NPCs (Fig. 5a, Supplementary Fig. 8a-b). The defective AMP/ATP ratio in Leigh NPCs was reversed by talarozole, while the recovery of AMP/ATP ratio by sertaconazole did not reach statistical significance (Fig. 5a, Supplementary Fig. 8a-b). Key glycolytic metabolites were defective in Leigh NPCs but were not rescued by the azoles (Supplementary Fig. 8a-b). Nonetheless, both sertaconazole and talarozole normalized the level of tricarboxylic acid cycle (TCA) intermediate succinyl-CoA (Fig. 5b, Supplementary Fig. 8c-d), and talarozole also normalized the levels of TCA intermediate oxaloacetate (Fig. 5c, Supplementary Fig. 8c-d).

Lipidomics highlighted the impact of the azoles on membrane-associated lipids in Leigh NPCs (Fig. 5d-e, Supplementary Data 5).

Fig. 4 | Sertaconazole and talarozole rescue key phenotypes in Leigh MOs. **a** Schematic of treatment in Leigh MOs (every other day starting from day 2) with 1 μM talarozole, 0.1 μM sertaconazole, or DMSO (created in BioRender. Menacho, C. (2026) https://BioRender.com/ewo91gu). **b** Growth rate of Leigh MOs treated with sertaconazole or talarozole compared to DMSO. Dots: individual MOs (DMSO: 20-25 MOs, Ser: 21-25 MOs, Tal: 21-25 MOs, CTL: 13-16 MOs); $n = 3$–4 independent experiments; $^{*}p < 0.05$, $^{**}p < 0.01$, $^{***}p < 0.005$, $^{****}p < 0.001$, two-way ANOVA. Growth rate of CTL MOs shown for reference. **c** Lactate release in treated Leigh MOs normalized to organoid area. Bar plots: mean +/- SD. Dots: individual MOs (DMSO: 12 MOs, Ser: 13 MOs, Tal: 13 MOs); $n = 3$ independent experiments; $^{**}p < 0.01$, $^{****}p < 0.001$, one-way ANOVA, compound-treated Leigh MOs vs DMSO-treated Leigh MOs. Dotted gray line: average of 9 CTL MOs for reference. **d** Organization and quantification of TH-positive neurons in treated Leigh MOs. Bar plots: mean +/- SD of signal intensity normalized to organoid area. Dots: individual MOs (DMSO: 20 MOs, Ser: 21 MOs, Tal: 20 MOs); $n = 6$ independent experiments; $^{*}p < 0.05$, $^{**}p < 0.01$, one-way ANOVA, compound-treated Leigh MOs vs DMSO-treated Leigh MOs. Scale bars: 100 μm. **e** Active cells within MOs: 27 out of 56 in 9 DMSO-treated Leigh MOs (48%), 39 out of 58 in 8 talarozole-treated Leigh MOs (67%), and 24 out of 50 in 8 sertaconazole-treated Leigh MOs (48%). **f** Representative calcium traces of Leigh MOs (average of 3 signals) upon metabolic stress (2 min of glucose-free medium + 2 mM 2-deoxyglucose + 5 mM sodium azide). **g** Calcium responses to metabolic stress. Boxplots: mean (center), 25/75 percentiles (box), and 1x SD (whiskers). Dots: individual cells within MOs (DMSO: 9 MOs; Ser: 7 MOs; Tal: 7 MOs); $n = 3$ independent experiments; $^{*}p < 0.05$, two-tailed Mann-Whitney U test. **h**–**k** Differentially expressed genes (DEG) and corresponding upregulated pathways in Leigh neurons based on pseudo-bulk analysis of scRNAseq of Leigh MOs treated with sertaconazole or talarozole. One-sided Fisher's exact test; Benjamini–Hochberg FDR-adjusted *P* values. Source data are provided as a Source Data file.

Among this lipid category, glycerophospholipids phosphatidylethanolamine (PE) and phosphatidylglycerol (PG) were mainly modulated by sertaconazole (Fig. 5d, Supplementary Fig. 7e). Sphingolipids, and particularly hexosylceramides (HexCer), showed a 50% reduction in Leigh NPCs, which was reverted by sertaconazole and not by talarozole (Fig. 5e, Supplementary Fig. 7f-g). In agreement with the transcriptomics results (Fig. 4i, k), cholesterol levels were significantly modulated by both azoles (Fig. 5f).

We next performed additional experiments to further assess the impact of membrane-associated lipids and cholesterol, given their importance for neuronal morphogenesis[46,47] and their potential disruption in mitochondrial diseases[48]. The levels of neutral lipids quantified with BODIPY staining showed a significant increase in Leigh NPCs treated with sertaconazole for 24 or 48 h (Fig. 5g-h). Using the cholesterol-specific probe perfringolysin O (PFO), we visualized and quantified membrane-bound cholesterol. The levels of membrane-bound cholesterol were significantly reduced in Leigh NPCs compared to control NPCs (Fig. 5i-j). Treatment with sertaconazole or talarozole for 48 h significantly increased membrane-bound cholesterol in Leigh NPCs, with sertaconazole leading to a more prominent effect (Fig. 5i-j).

Taken together, the two azoles impacted mitochondrial energy metabolism and membrane-associated lipids in Leigh neural cells, validating the findings indicated by scRNAseq of MOs. In particular, talarozole was effective in restoring mitochondrial bioenergetics, whereas sertaconazole principally affected lipid metabolism.

Sertaconazole and talarozole engage with RA and PPARγ pathways

To delve deeper into the mode of action of the two azoles, we analyzed their molecular structure to predict their pathway engagement.

We first employed the docking tool GOLD, which requires predefined binding regions for local docking[49]. We focused our search on cytochrome P450 26 (CYP26) enzymes, especifically CYP26A1 and CYP26B1, which represent the main protein targets of talarozole and belong to the retinoic acid (RA) pathway[50]. In fact, the transcriptomics of Leigh MOs showed downregulation of *CYP26B1* (Fig. 3f) and modulation of RA-associated genes by the azole compounds (Fig. 4h, Fig. 4j). Since the crystal structure of CYP26A1/B1 is not available, we performed the analysis on its homology model CYP120[51,52]. Sertaconazole and talarozole showed a bi-aromatic moiety close to the iron center of heme, with talarozole positioned in closer proximity to the center than sertaconazole (Fig. 6a). Thus, both azoles could bind CYP26A1/B1, although talarozole with higher affinity. Based on the structure of available azoles, we identified talarozole as the one with the highest binding affinity to the RA enzyme among the five azoles that we tested in iNs (DLD5, YSD1-4) (Fig. 2c-f, Supplementary Fig. 9a-b). In agreement with the effect of the azoles on the RA pathway in Leigh, Leigh mDANs exhibited upregulation of enzymes metabolizing RA (e.g. *CYP26A/B1*) and downregulation of RA receptors (e.g. *RORB*) (Fig. 6b), and the treatment with sertaconazole or talarozole repressed the elevated expression of *CYP26B1* in Leigh iNs (Fig. 6c).

To complement these results, we applied the machine learning docking algorithm DiffDock[53], which uses generative artificial intelligence (AI) to search the whole protein without the need of defining a binding site, thereby allowing unbiased global docking information based on a learned confidence score. To ensure physical plausibility, we refined the top poses determined by DiffDock using the docking tool SMINA[54], which applies a physics-based scoring function. This hybrid approach represents an efficient and scalable solution, allowing for the exploration of the molecular interactions of the azoles more broadly to obtain an unbiased search with physically accurate refinement. Using this pipeline, we confirmed that sertaconazole and talarozole could bind to CYP26A1 and CYP26B1 (Fig. 6d-e). Talarazole showed a stronger binding capacity as seen by lower SMINA score and tighter distribution (Fig. 6e). In agreement with the GOLD docking analysis, talarozole appeared as the azole with the highest affinity for the RA enzyme (Supplementary Fig. 10a).

Modulation of proliferator-activated receptor gamma (PPARγ) has been suggested as a possible mechanism of action of talarozole in osteoarthritis[55]. Moreover, PPARγ was recently identified as a therapeutic target for Leigh based on findings obtained in a mouse model of Leigh caused by depletion of the complex I gene *Ndufs4*[56]. Therefore, we applied the same docking pipeline to assess the potential engagement of the azoles on PPARγ. We used available crystal structure of PPARγ[57] and investigated the effects of azoles on the human ligand-binding domain based on three poses (2FVJ: PPARγ bound to PA-082[58], 3B1M: PPARγ bound to Cerco-A[59], and 6L8B: PPARγ ligand-free[60]). Both azoles showed potential binding affinity, with sertaconazole exhibiting increased affinity for the 3B1M pose and talarozole for 2DVJ (Fig. 6f-g). Indeed, among all azole compounds, sertaconazole and talarozole were the ones showing the greatest binding capacity for PPARγ (Supplementary Fig. 10b).

Lastly, we aimed to determine whether sertaconazole or talarozole could modulate RA or PPARγ activity in live Leigh neural cells. We used luciferase reporter assays in NPCs treated with the azoles (Fig. 6h). Since CYP26A1 is the most inducible gene by RA, we transfected NPCs with a luciferase-reporter under the control of the CYP26A1 promoter[61]. Quantification of luciferase signal demonstrated that Leigh NPCs have reduced CYP26A1 promoter activity compared to isogenic control NPCs at basal level (with DMSO treatment only) (Fig. 6h). Treatment with talarozole in Leigh NPCs was sufficient to restore CYP26A1 promoter activity, while sertaconazole appeared ineffective (Fig. 6h). The combination of the azoles also did not lead to enhanced RA gene expression activation (Fig. 6h).

For assessing PPARγ activity, we transfected NPCs with a PPRE (peroxisome proliferator-activated receptor response element) luciferase reporter[62]. This tool captures the activity of PPARγ, which binds

https://doi.org/10.1038/s41467-026-71391-2

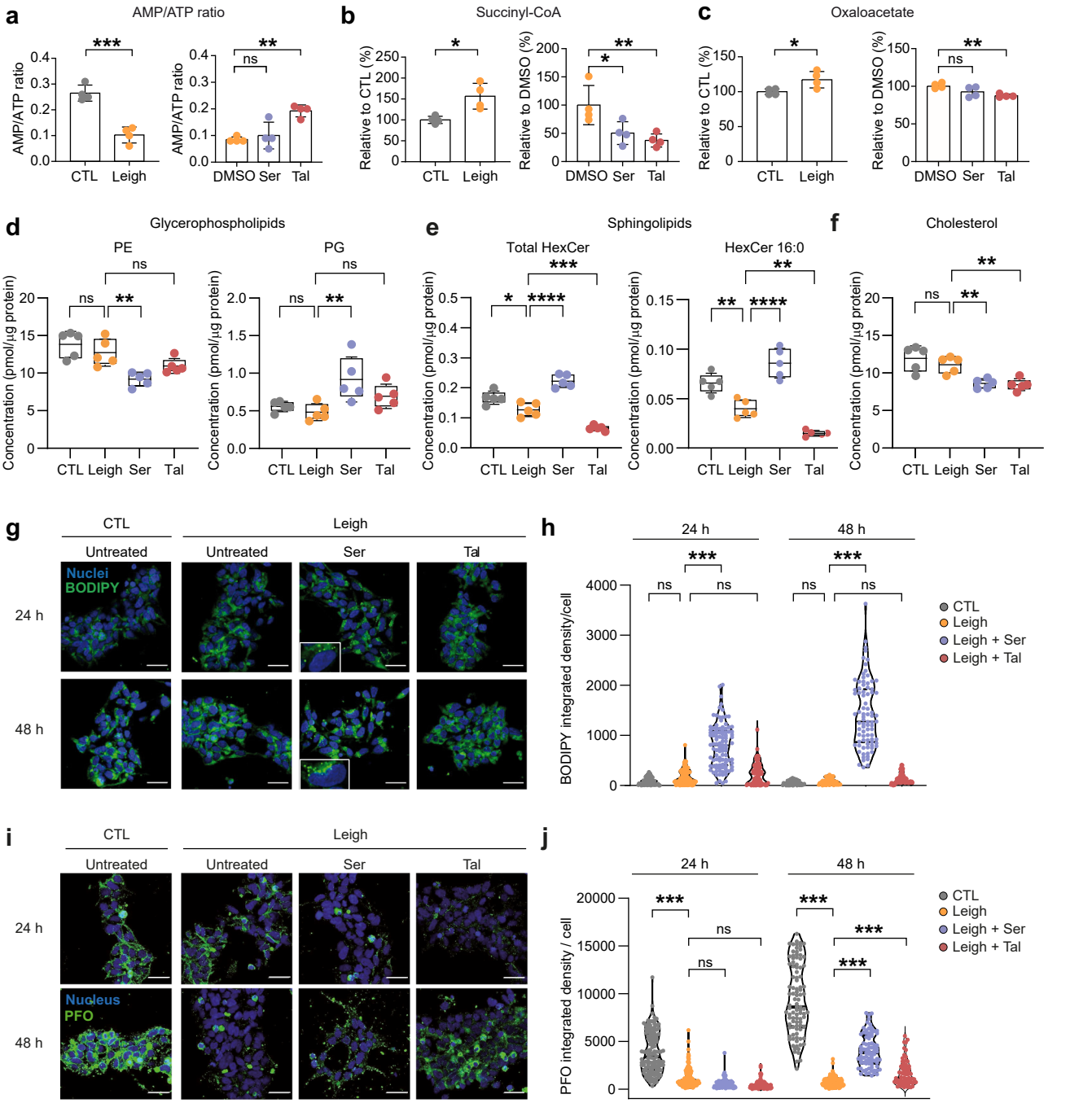
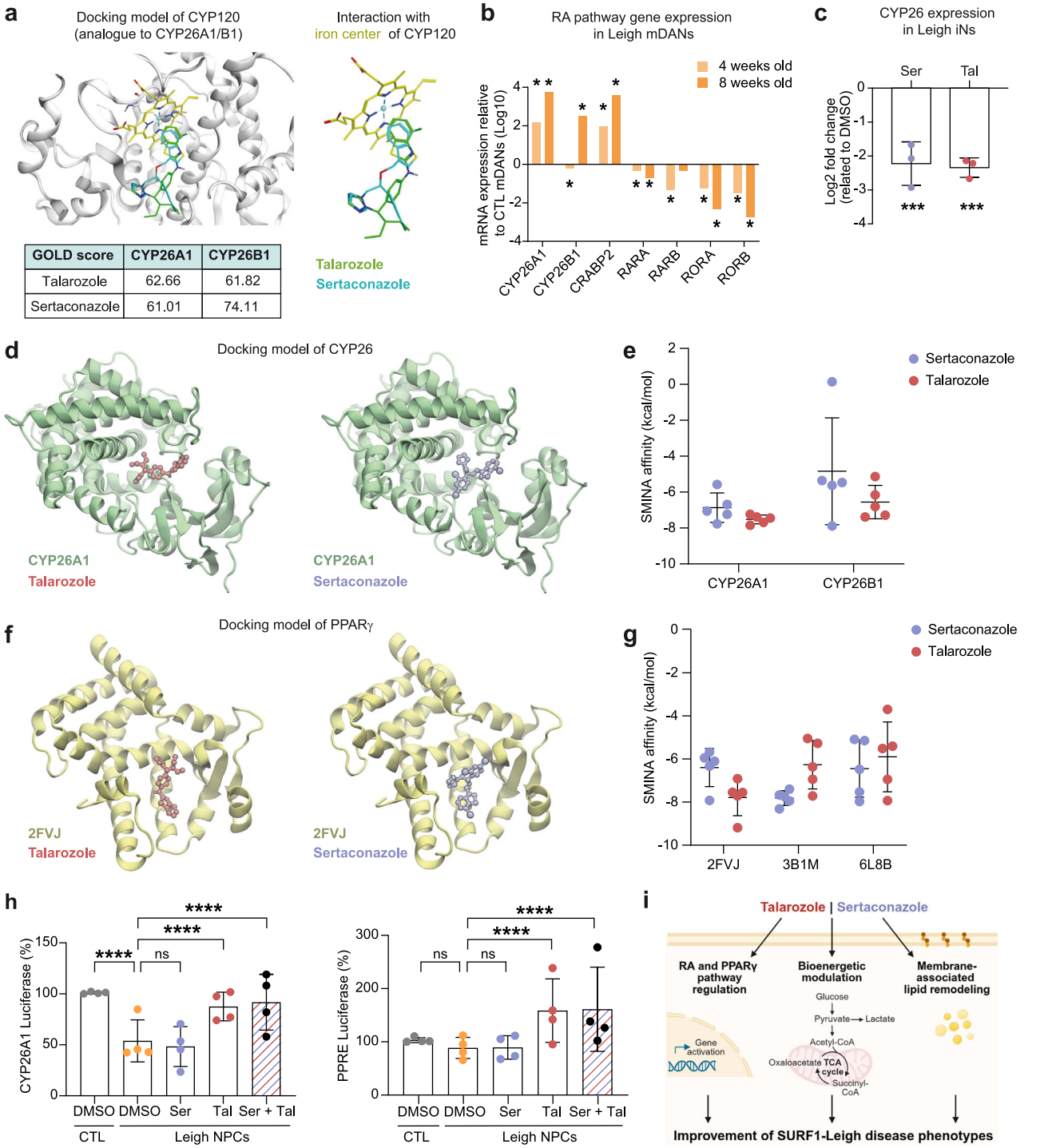


Fig. 5 | Sertaconazole and talarozole modulate bioenergetics and membrane-bound lipids in Leigh neural cells. a–c Targeted metabolomics in CTL NPCs and Leigh NPCs untreated, or treated with DMSO, 10 μM sertaconazole, or 10 μM talarozole for 24 h. Bar plots: mean +/- SD. Dots: biological replicates ($n = 4$) (dots); ns: not significant, *$p < 0.05$, **$p < 0.01$, ***$p < 0.005$; unpaired two-tailed t test for CTL vs Leigh and one-way ANOVA for treatments. **d–f** Targeted lipidomics in CTL NPCs and Leigh NPCs treated with DMSO, 10 μM sertaconazole, or 10 μM talarozole for 24 h, showing glycerophospholipids phosphatidylethanolamine (PE), phosphatidylglycerol (PG), hexosylceramides (HexCer), HexCer 16:0, and cholesterol. Boxplots: mean (center), 25/75 percentiles (box), and 1x SD (whiskers). Dots: biological replicates ($n = 5$); *p < 0.05, **$p < 0.01$, ***$p < 0.005$; one-way ANOVA. **g, h** Neutral lipids stained with BODIPY in CTL NPCs and Leigh NPCs treated with DMSO, 10 μM sertaconazole, or 10 μM talarozole for 24 h or 48 h. Violin plots: median and quartiles of integrated density/cell. Dots: values of individual NPCs; $n = 3$ independent experiments; ns, ***$p < 0.005$; one-way ANOVA Kruskal-Wallis test. Scale bars: 100 μm. **i–j** Membrane-bound cholesterol measured with PFO staining in CTL NPCs and Leigh NPCs treated with DMSO, 10 μM sertaconazole, or 10 μM talarozole for 24 h or 48 h. Violin plots: median and quartiles of the integrated density/cell. Dots: values of individual NPCs; $n = 3$ independent experiments; ns, ***$p < 0.005$; one-way ANOVA Kruskal-Wallis test. Scale bars: 100 μm. Source data are provided as a Source Data file.

to PPRE leading to its gene activation, and was used in *Ndusf4* KO mice to uncover PPARγ as a therapeutic target of Leigh[56]. However, unlike the *Ndusf4* KO mouse, Leigh NPCs showed only *a* ~10% decrease in PPRE activity that did not reach statistical significance (Fig. 6h). Nevertheless, talarozole treatment led to a significant 1.5-fold increase in PPARγ activity in Leigh NPCs (Fig. 6h). Sertaconazole treatment had no impact on PPARγ activity, and there was no combinatorial effect of sertaconazole and talarozole (Fig. 6h).

https://doi.org/10.1038/s41467-026-71391-2



GOLD score	CYP26A1	CYP26B1
Talarozole	62.66	61.82
Sertaconazole	61.01	74.11

Fig. 6 | Impact of sertaconazole and talarozole on RA and PPARγ in Leigh neural cells. a Predicted docking for sertaconazole and talarozole on the CYP120 pocket based on GOLD analysis. **b** Expression of retinoic acid (RA)-related genes in Leigh mDANs compared to CTL mDANs. Two-tailed Wald test with Benjamini-Hochberg correction for multiple comparisons (FDR < 0.05); *$p < 0.01$, fold change expression from bulk RNAseq dataset. **c** CYP26 mRNA expression in Leigh iNs treated with sertaconazole or talarozole compared to DMSO-treated Leigh iNs. Bar plots: mean +/- SD. Dots: biological replicates ($n = 3$); ***$p < 0.005$; unpaired two-tailed t test. **d** Molecular representation of CYP26A1 (green) with the best ranked pose of talarozole and sertaconazole. Residues 116 to 134 (CYP2A1) were removed for visualization. **e** Docking results of talarozole and sertaconazole in CYP26A1 and CYP26B1 using SMINA affinity scores. Dots: mean +/- SD of the top 5 Diffdock poses, re-docked, and energy-minimized with SMINA. (**f**) Molecular representation of PPARG 2FVJ (yellow) with the best ranked pose of talarozole and sertaconazole. Residues 260 to 305 (2FVJ) were removed for visualization. **g** Docking results of talarozole and sertaconazole in PPARG using SMINA affinity score. Dots: mean +/- SD of the top 5 Diffdock poses, re-docked, and energy-minimized with SMINA. **h** Luciferase activity in CTL NPCs and Leigh NPCs transfected with the reporter plasmid CYP26A1-Luc (left) or PPRE-Luc (right) and treated for 24 h with DMSO, 10 μM sertaconazole, 10 μM talarozole, or a combination of 5 μM sertaconazole and 5 μM talarozole. Bar plots: mean +/- SD. Dots: independent experiments ($n = 4$); data normalized to CTL + DMSO; ****p < 0.0001, two-way ANOVA. **i** Schematic of proposed mechanisms of action for sertaconazole and talarozole in Leigh neural cells (created in BioRender. Menacho, C. (2026) https://BioRender.com/t4fxyht). Source data are provided as a Source Data file.

In conclusion, talarozole appeared as the azole compound most effective in eliciting activity of the RA and PPARγ pathways. Sertaconazole might also be able to engage with these signaling pathways but with lower effectiveness. Other azoles showed even lower binding capacity for RA and PPARγ enzymes, which may potentially explain why they were not found capable of improving neuronal morphogenesis in Leigh iNs.

Discussion

Regulators are currently promoting drug discovery approaches based on non-animal models such as NAMs to possibly reduce or eliminate the need for validations in animals for drug approval[63,64]. In this context, complex human models such as 3D organoids are emerging as promising alternatives[65]. Nonetheless, despite the recent progress of NAMs in drug validation and toxicity, performing large-scale drug screening in iPSC-derived brain organoids remains challenging. In fact, most of the treatments assessed in iPSC models of Leigh and other mitochondrial diseases have been compounds already known from previous studies[14,66,67]. We recently screened repurposable compounds in iPSC-derived neural cells, leading to the identification of sildenafil as a potential treatment for Leigh caused by *MT-ATP6* variants[29]. However, innovative pipelines are needed to accelerate the screening process by reducing the number of potential drugs to be assessed in complex 3D human NAMs. In this work, we demonstrate that combining disease-specific brain organoids with computational drug discovery can lead to the identification of potential repurposable drugs for Leigh syndrome, an incurable neurological mitochondrial disease with highly unmet medical needs.

There is a growing interest in developing in silico approaches[68] to accelerate the drug discovery process, which is costly, time-consuming, and shows a high attrition rate[69]. Currently, widely used databases for predicting drugs, such as CMap[70], are, however, mainly comprised of transcriptional signatures of cancer cell lines. This feature may hinder the effectiveness of computational predictions for non-cancer diseases. Cancer cell lines exhibit particular signal transduction pathways and gene regulatory networks and unique metabolic features mainly relying on glycolysis[71,72]. In the context of neuronal diseases, these metabolic differences may play a relevant role, given that proper neuronal generation is accompanied by a switch from glycolysis to OXPHOS[73] and interventions based on modulation of mitochondrial metabolism may help tackle neurodegeneration[74]. Here, we developed a DL-based framework based on ChemPert, our recently developed database of perturbations in non-cancer cells[31]. We demonstrated that this approach delivered added value beyond conventional pathway enrichment by enabling more accurate early prioritization of candidate drugs for experimental validation. Since the feedforward artificial neural network (FNN) model was trained on non-cancer cells, we circumvented the issue of possible false positives due to predictions driven by cancer cells.

We applied this pipeline to a scRNAseq dataset that we previously obtained in Leigh COs carrying *SURF1* variants and isogenic control COs[40]. Our framework predicted first genes and then drugs in a cell-type specific manner, thereby allowing us to identify also drugs that were outside of training (as was the case for talarozole). In parallel, we conducted a survival screen in yeast deficient for *SHY1*, the yeast homologous gene of *SURF1*[6]. Yeast screens have been used before in the context of neurological and mitochondrial diseases[75,76], but their predictive power requires validation in more complex models[77]. By combining computational predictions and yeast screen with our human 2D and 3D models of Leigh, we were able to uncover sertaconazole and talarozole as repurposable drugs for Leigh (Supplementary Fig. 11). We also used healthy human brain organoids as NAMs to ensure that two compounds did not elicit toxic effects at the concentrations used to rescue the disease phenotypes (Supplementary Fig. 6a, b) and concluded that the compounds could ameliorate Leigh phenotypes at concentrations that appeared to be non-toxic in healthy cells.

The two azoles shared similarities in chemical structure that might enable them to interact similarly to specific targets, although with different effectiveness (Fig. 6i). Talarozole is a retinoic acid metabolism blocking agent (RAMBA) that inhibits cytochrome P450 CYP26A1/B1 thereby activating the RA pathway[78]. RA signaling plays a key role in regulating differentiation, organogenesis, and neuronal development[79–84]. Using two complementary docking strategies, we confirmed that talarozole was the azole with the highest binding affinity for CYP26A1/B1 among the ones we assessed (Supplementary Fig. 9b, Supplementary Fig. 10a). Accordingly, talarozole was more effective than sertaconazole in activating the RA pathway based on CYP26A1 promoter activation (Fig. 6h). Possibly because of this impact on RA, talarozole showed a stronger rescue than sertaconazole with respect to key disease phenotypes including neuronal generation and functionality in Leigh MOs (Fig. 4d-e), mitochondrial bioenergetics in Leigh NPCs (Fig. 5a-c), and survival in *SHY1* KO yeast (Fig. 2g). Talarozole also enhanced the calcium-mediated response of MOs to acute metabolic stress (Fig. 4f-g). This feature may potentially be of clinical value to Leigh individuals, who typically suffer from sudden metabolic decompensation triggered by events that place excessive demands on the body's energy production, such as infection or surgery[1,43].

Talarozole was initially developed for acne and psoriasis[85]. Although its use in these topical indications has been discontinued, talarozole is now being considered as a potential repurposed drug for osteoarthritis, where it showed benefits in vitro and in vivo related to a reduction of inflammation[86,87]. The anti-inflammatory effect of talarozole has been linked to a PPARγ-dependent mechanism[55]. Interestingly, PPARγ may represent a therapeutic target for Leigh, given that its modulation by cannabidiol (CBD) treatment extended the lifespan and improved disease comorbidities in a mouse model of Leigh due to KO of the Complex I gene *Ndufs4*[56]. Modulation of the PPARγ coactivator-1α (PGC-1α) have also been suggested as Leigh therapeutics[15,88]. Our docking results suggest that talarozole is indeed capable of binding to PPARγ, with higher affinity compared to the other azoles assessed (Supplementary Fig. 10b). Accordingly, talarozole treatment elicited PPARγ activity in Leigh NPCs (Fig. 6h). Therefore, some of the talarozole's beneficial effects seen in our Leigh models may be mediated trough PPARγ activation. At the same time, since our COs and MOs did not contain microglia and included only low numbers of astrocytes at these early stages of development, they may not represent the most suitable models to investigate inflammatory-related aspects. Future studies with more appropriate models should thus be performed to assess the in vivo impact of talarozole and further validate RA or PPARγ as putative interventional targets for Leigh.

Sertaconazole is currently used in topic anti-fungal medications, as it inhibits the synthesis of ergosterol, which is the orthologue of cholesterol and an essential component of fungal cell walls[89]. In agreement with this mode of action, we found that sertaconazole treatment in Leigh models led to modulation of membrane-bound lipids and cholesterol (Figs. 4h-i, 5d-j). Possibly due to structural similarities, talarozole treatment in Leigh models also affected lipid metabolism, although less effectively than sertaconazole (Figs. 4j-k, 5d-j). At the same time, sertaconazole rescued key Leigh phenotypes similarly to talarozole in Leigh MOs, including growth rate defects and abnormal lactate release (Fig. 4b-c). Modulation of lipid metabolism might have contributed to those rescue effects. Indeed, membrane-associated lipids and cholesterol play crucial roles in neuronal branching and morphogenesis[46,47] and their disruption is associated with mitochondrial diseases[48]. Future studies should therefore address the impact of modulating membrane-bound lipids as potential interventions for Leigh and other mitochondrial disorders. Sertaconazole also engaged with the RA and PPARγ pathways but with less effectiveness than talarozole (Fig. 6a-h, Supplementary Fig. 9a-b,

Supplementary Fig. 10a-b). The combinatorial treatment did not elicit an increased activity of those pathways. Further investigations are warranted to explore the potential synergistic effects of these drugs in Leigh or other conditions. In any case, the compounds likely exhibit polypharmacology and their action could be even more multifactorial than the ones suggested by our findings. Giving the rescue effect seen in yeast (Fig. 2g-h), it may also be possible to speculate that the azoles could act as COX stabilizers.

Our study also highlights how innovative complex NAMs based on computational screens in patient-specific brain organoids, can be combined with conventional screens in yeast, which are relatively rapid and cost-effective, to further accelerate drug discovery. This pipeline could represent a blueprint for rare neurodevelopmental disorders. Talarozole, our most effective candidate, had one of the highest BES values (Supplementary Fig. 1h-i), yet it was not recovered by GSEA-style enrichment, CMap-based signature reversal, or ChemPert-based similarity[31,70,90], suggesting that talarozole's prioritization by our DL framework was method-specific and not trivially recapitulated by existing approaches. At the same time, talarozole currently represents a single prospectively validated hit and should therefore be viewed as proof-of-concept example, with further testing of additional top-ranked candidates needed to generalize the framework's predictive performance. The clinical relevance of the drugs that we identified is underscored by the fact that other drugs belonging to the azole family are under consideration for neurological diseases[91,92]. In the context of Leigh, further studies are warranted to better understand the impact of these azoles on different brain regions besides the midbrain, for example, by using other region-specific brain organoids or assembloids generated by combining different region-specific organoids, possibly with included microglia[93]. Additional work is also necessary to evaluate whether the azoles might have positive effects in the context of other variants linked to Leigh, such as those in genes *MT-ATP6* or *NDUFS4*.

Lastly, our findings support a view of Leigh pathogenesis that involves not only early-onset neurodegeneration but also impaired neurodevelopment. Indeed, children affected by Leigh typically exhibit delays in reaching developmental milestones even prior to the onset of regressive phenotypes[26–28]. Antenatal manifestations are also observed in patients with Leigh or other mitochondrial diseases[23,24]. The underlying defects might possibly be related to the impact of mitochondria in neurodevelopment[18,21], potentially indicating that defective mitochondrial function interferes with this physiological neurogenesis[20,94]. Accordingly, defective embryonic development occurs in Leigh *Ndufs4* KO mice[22], which show specific defects in neural stem and progenitor cell proliferation, causing significant delays in neurogenesis and gliogenesis[25]. Brain organoid models of Leigh demonstrated a similar impairment of progenitor organization and defective corticogenesis[15,17]. Taken together, our data suggest that addressing neurodevelopmental aspects of mitochondrial diseases may lead to uncover innovative therapeutics for currently incurable diseases such as Leigh syndrome.

Methods

Ethics

iPSC lines were used in accordance with the ethical approval obtained by the Ethics Committee of the Medical Faculty of Heinrich Heine University (study number 2020-967_5).

Induced pluripotent stem cells (iPSCs)

Leigh iPSCs and isogenic control iPSCs were obtained before using Leigh patient-derived cells and CRISPR/Cas9 editing[15]. Leigh iPSCs carried the *SURF1* variant c.769 G > A (p.G257R) on both alleles in either a Leigh patient background or a healthy control background. The healthy iPSC line was obtained from Dr. Heiko Lickert (Helmholtz Center Munich) (HMGUi001-A)[95]. Isogenic control iPSCs carried no *SURF1* variants in either the patient background or the control background (HMGUi001-A-64)[15].

Neural progenitor cells (NPCs)

iPSC-derived Leigh NPCs and isogenic control NPCs used in this study were generated and characterized before[15]. All NPCs were cultured as described[96], with minor modifications. NPCs were grown in Matrigel-coated 6-well plates in sm+ medium, consisting of a base media 1:1 ratio of Neurobasal and DMEM-F12 supplemented with N2 (0.5×), B27 without vitamin A (0.5×), 2 mM glutamine, Myco-Zap-plus-CL (1×), 3 μM CHIR 99021, 0.5 μM purmorphamine, and 150 μM ascorbic acid. Media were exchanged every other day, and cells were passaged weekly at a ratio 1:6 to 1:10 using Accutase treatment. All NPCs were used in experiments between passages 10 and 25. All cells were routinely monitored to ensure lack of mycoplasma contamination.

Development of DL-based framework for drug repurposing

A multi-stage deep learning framework for predicting direct protein targets of drugs was developed using perturbation transcriptomics data (Supplementary Fig. 1b). Training data were retrieved from ChemPert[31], which provides transcriptomic profiles before and after drug treatment based on non-cancer cell types. We used 24,134 transcriptional signatures of 264 unique, diverse non-cancer cell types exposed to 2905 unique perturbagens (chemical and biological disruptive agents) for the model training (Supplementary Data 7). All drugs considered in this study, along with their known direct protein targets, were also retrieved from ChemPert; only drugs with annotated direct molecular targets were included, resulting in 5,686 total reference drugs. Signaling proteins and their molecular interaction data were compiled from multiple curated databases, including protein–protein interactions from iRefIndex[97], HIPPI[98], IID[99], signaling networks from OmniPath[100], ReactomeFI[101], KEGG[102], NicheNet[103], transcriprional regulatory interactions from TRRUST[104], CHEA[105], HOCOMOCO[106], TRANSFAC[107], as well as ligand–receptor interactions from a consolidated set of sources[103,108–119]. TFs were obtained from AnimalTFDB 3.0[119]. The resulting graph consisted of 20,455 protein nodes and 5,928,682 edges. The input features for model training included (1) differentially expressed TFs (DETFs) derived from the difference between initial and final transcriptomic states following perturbation, and (2) baseline gene expression levels of the initial cell state. Each of the 20,455 proteins was embedded in a network-aware feature space using precomputed graph metrics and local network topologies (Step 1). Consequently, each transcriptomic input yielded 20,455 independent training samples, one per protein, with the goal of classifying the optimal perturbation for that protein. These structured features were then denoised and regularized using a VAE (variational autoencoder), and the decoded output, preserving the same dimensionality as the original input, was used as input to a feedforward neural network (FNN) trained to predict direct protein targets of drugs (Step 3). Final drug rankings were generated based on predicted target enrichment using a Bayesian enrichment score (BSE) that incorporated hypergeometric overlap and empirical model robustness (Step 4).

Step 1: Graph-based feature embeddings. To capture topological and signaling context around each gene while avoiding memory-intensive full graph convolution, we used the Scalable Inception Graph Neural Network (SIGN) framework[120]. Each node (protein) in the graph was assigned two initial features: its raw expression value in the baseline (pre-treatment) cell state, and a DETF status label. DETF status was defined as follows: genes identified as differentially upregulated TFs were labeled as 1, downregulated TFs as −1, and all other genes as 0. When the number of DETFs exceeded 100 for a given perturbation, a maximum of 100 DETFs were randomly selected to serve as source nodes for propagation. This step was necessary to avoid oversaturation of the graph during message propagation, wherein too

many active source nodes diminish the ability to differentiate downstream nodes based on their signaling proximity. Although alternative strategies such as fold-change-based ranking were considered, fold change alone is not always a reliable indicator of regulatory importance and may overlook TFs with moderate expression changes but high centrality or signaling relevance. Moreover, fold-change thresholds can introduce bias toward cell type- or dataset-specific noise. Random selection avoids these pitfalls by preserving unbiased sampling across the DETF pool and improves overall generalizability across diverse perturbation contexts. Using this DETF labeling as node input, we applied SIGN-based message passing in both upstream and downstream directions through the network to compute graph convolution embeddings:

$$Z = Concat\left(X, \{A_{fwd}^{k}X\}_{k=1}^{K}, \{A_{rev}^{k}X\}_{k=1}^{K}\right), for\ k = 1, 2, \ldots, K \quad (1)$$

where $X \in \mathbb{R}^{nxd}$ is the input feature matrix where n is the number of proteins (nodes) and d is the number of input features per protein (e.g. expression + DETF label), $A \in \mathbb{R}^{nxn}$ is the adjacency matrix of the directed signaling graph (normalized), and K is the maximum number of message passing steps, which was set to 5 in this study. The propagated signals captured the multi-hop influence of DETFs on surrounding proteins and vice versa, generating a topological embedding for each protein that reflected its context in the perturbation-responsive network. The following statistics were also computed for each protein across the propagated feature dimensions: sum, mean, maximum, minimum, median, standard deviation, 25th, and 75th percentiles. To further enrich these embeddings with biologically relevant context, we appended the following network-derived features: the number of shared Reactome pathways between each protein and DETF, the minimum path length from each protein to all DETFs, and the percentage of DETFs reachable from each protein within the graph. Then, a second-degree polynomial expansion was applied using the PolynomialFeatures function from scikit-learn (degree=2, interaction_only=False). Following this expansion, any features that exhibited constant values across all samples were removed. This process produced a 20,455 by 1870 feature matrix per perturbation transcriptomics dataset. In preparation for supervised training, the drug' effects on their direct protein targets were labeled as follows: 1 for activation, −1 for inhibition, and 2 for unknown or ambiguous effects (either 1 or −1), and 0 for no effect. To reduce computational complexity without compromising representativeness, we applied MiniBatch KMeans clustering[121] with 50 clusters and sampled an equal number of examples from each cluster to construct a diverse and representative subsets. The resulting expanded feature matrix was then column-wise min-max normalized (i.e. normalized across samples (proteins) for each feature) by:

$$z_j = \frac{x_j - \min(x)}{\max(x) - \min(x)} \quad (2)$$

to ensure scale compatibility for downstream modeling, where x is each feature vector across all genes.

Step 2: Denoising and regularization with variational autoencoder (VAE). To enable robust training and mitigate variability introduced by heterogeneous transcriptomic data sources, including differences in experimental protocols, platforms (microarray, bulk RNA-seq, and scRNA-seq), and sample origins, we trained a VAE on the graph-based protein feature matrix. The VAE served to denoise and regularize the high-dimensional input space, producing a smoother and more consistent latent representation. The encoder consisted of five fully connected layers with progressively smaller sizes, starting from an initial hidden size of 1500 and halving at each layer down to a 100-dimensional latent space. The encoder used batch normalization and ReLU activations, without dropout. The decoder mirrored the encoder but omitted batch normalization to preserve the original data distribution during reconstruction. The latent space was parameterized by a mean and log-variance vector, and the reparameterization trick was applied to sample latent representations. Log-variance was clamped between −5 and 5 to avoid instability. To assess the quality of learned representations and guide hyperparameter selection, clustering performance was evaluated on both the VAE latent space and the decoded output space. Specifically, Mini-Batch KMeans clustering (with k = 3 clusters, corresponding to known target effect classes: 0 = no effect, 1 = activation, and -1 = inhibition. 2 = unknown effect was excluded from this analysis.) was applied to each representation. Optimal hyperparameters were selected based on the highest adjusted Rand index (ARI) and normalized mutual information (NMI) scores achieved across candidate configurations. A 1-fold validation strategy was used, with 10% of gene rows randomly held out as the validation set. Given the size and homogeneity of the resulting training pool, 5-fold cross-validation was not necessary and would provide limited additional benefit at significantly higher computational cost. The ARI and NMI for clustering in the VAE-decoded space were 0.2465 and 0.3457, respectively, nearly identical to those obtained from the raw input features (ARI = 0.2464, NMI = 0.3458). In contrast, clustering within the latent space yielded substantially lower ARI (0.1144) and NMI (0.2164). Although ARI and NMI do not directly assess training performance, these results indicate that the VAE preserved biologically meaningful structure while denoising and regularizing the input space. The absence of artificially inflated clustering performance suggests that the VAE did not introduce synthetic features or over-regularization, which could lead to overfitting or loss of generalizability to unseen samples. Based on these results, we used the VAE-decoded feature space for all downstream classification tasks. The final set of parameters was batch size of 1024, learning rate of 0.001, and $\beta = 0.001$ to weight the KL divergence term in the loss function.

Step 3: FNNs for drug target prediction. To predict direct protein targets of drugs from the VAE-decoded graph embedding features, we trained an FNN model with a decaying architecture implemented in PyTorch Lightning. The model consists of fully connected layers whose widths decrease exponentially by a decay factor from a user-defined initial hidden-layer size. This design helps compress and refine the high-dimensional input features into a more discriminative representation for classification. Each hidden layer includes batch normalization, LeakyReLU activation, and dropout, and the final layer outputs logits for three classes: 1 = activation, −1 = inhibition, and 0 = no effect, using integer-encoded labels (1, 2, and 0, respectively). Class 2 (ambiguous effect, either 1 or −1) was excluded from training due to its interpretational uncertainty to ensure that the model was trained only on high-confidence labels, enhancing prediction reliability. To reduce potential sources of training bias, the sample count for each class was adjusted to the mean of the original class sizes (451,476) via down-sampling and synthetic data generation using the VAE decoder from original protein feature inputs. Hyperparameters, including batch size, learning rate, dropout, initial layer size, number of layers, L1/L2 regularization, and weight decay, were tuned using a grid search based on performance on a randomly held-out 10% validation set. Given the large number of well-regularized training samples and the computational cost of k-fold cross-validation multiplied by the hyperparameter combinations, we used a 1-fold validation strategy. This approach provided stable and representative performance estimates, with marginal gain expected from further splits. Model performance was evaluated using the F1 score, false positive rate (FPR), and false negative rate (FNR). Following the optimization of hyperparameters, 21 best-performing models were selected, and ensemble model evaluation was conducted by testing all triplets of the 21 models to assess the robustness and potential performance gains from model aggregation.

In those ensemble models, final predictions were made via majority voting. To avoid ties, only individual models and triplets were included; pairs and four-model ensembles were excluded. The final ensemble model achieved a mean F1 score, FPR, and FNR of 0.700, 0.129, 0.305, respectively on the validation set (Supplementary Fig. 1c-e), and this model was used for subsequent applications. The final three model configurations are each using a learning rate of 0.005, a dropout rate of 0.0, an initial hidden layer size of 1500, and five hidden layers. The first configuration used a batch size of 1024 with no L1 or L2 regularization, the second configuration increased the batch size to 2048 and L1 and L2 regularization values of 0.2 and 0.1, respectively, and the third configuration also used a batch size of 2048 but did not include any regularization.

Step 4: Ranking drugs by Bayesian enrichment score (BES). The framework computes a one-sided hypergeometric p-value that quantifies whether the predicted targets are statistically enriched for each drug's known targets, i.e.,

$$p_{hypergeo} = \sum_{i=k}^{\min(n,N)} \frac{\binom{n}{i}\binom{M-n}{N-i}}{\binom{M}{N}} \tag{3}$$

where M is the total number of proteins (i.e. the size of the network), n is the number of known targets of the drug, N is the number of proteins predicted as targets, and k is the number of overlapping proteins between known and predicted targets. Next, to assess the robustness of drug predictions and control for potential false positives due to noise or uninformative features in input, we computed an empirical p-value (pemp) for each drug using a randomized null model. Specifically, the decoded input feature matrix, where each row corresponds to the feature vector of a protein, was randomly shuffled across rows, while preserving protein identities. Then, the FNN model was applied. The drug was considered "predicted" if at least one of its target proteins was among the predicted targets. This process was repeated 100 times and the pemp for that drug was defined as the fraction of the 100 randomized trials in which it was predicted. Drugs with low pemp values are thus considered robust predictions unlikely to occur under a random input distribution. We incorporated this empirical confidence into a posterior weight under a Bayesian prior belief that only 1% of the considered drugs are true positives, i.e. able to induce desired gene expression changes:

$$\pi_0 = 0.99 \Rightarrow posterior_i = 1 - \pi_0 \cdot pemp_i \tag{4}$$

where i denotes each drug. This posterior is then modulated to form a confidence weighting factor (CWF) by a soft exponential confidence weighting function, favouring drugs with highly confident predictions:

$$confidenceweightingfactor(CWF)_i = \exp\left[-\lambda \cdot (1 - pemp_i)\right] \tag{5}$$

with $-\lambda = 1.0$ by default. The Bayesian-weighted confidence score becomes:

$$confidenceweightingfactor(CWF)_i = \exp\left[-\lambda \cdot (1 - pemp_i)\right] \tag{6}$$

This sigmoid-like transformation ensures that enrichment near the top-ranked percentile is prioritized, reflecting the practical goal of selecting a small number of high-confidence candidates for downstream validation. The final BES for each drug is computed as a weighted sum of posterior confidence, statistical enrichment $\left(1 - p_{hypergeo}\right)$, and the normalized rank of the p-value:

$$BES_i = \omega_{posterior} \cdot s_{posterior,i} + \omega_{hypergeo} \cdot \left(1 - p_{hypergeo,i}\right) + \omega_{hypergeo_{rank}} \cdot r_{hypergeo,i} \tag{7}$$

where $r_{hypergeo,i}[0 \in 1]$ is the normalized rank (1 = best), $\omega_{posterior}, \omega_{hypergeo}, \omega_{hypergeorank}$ are tunable scalar weights. In our implementation, we used $\omega_{posterior} = 20, \omega_{hypergeo} = 1.0$, $\omega_{hypergeorank} = 1.0$, thereby placing greater emphasis on high-confidence model predictions while also rewarding statistical and rank-based enrichment. Drugs with hypergeometric p-value = 1.0 (i.e. no single drug target predicted) were automatically assigned a BES of 0. All non-zero BES values were then ranked in descending order, with ties resolved using the min method.

DL-based framework test performance and selection

To evaluate the generalizability of the DL-based framework, we assembled 47 independent test datasets centered on chemical drugs that induce cellular conversion processes, including differentiation, development, metabolic shift, reprogramming, and immune activation (Supplementary Data 1). Although some of the original datasets also included protein ligands or receptor-based agents, only small-molecule chemical drugs were considered in this evaluation, as the primary aim was to assess the tool's translational potential in small molecule drug discovery/repurposing. All gene expression datasets used in the test set were completely excluded from the training and validation phases, ensuring an unbiased performance assessment. To broaden the test set's scope, we allowed chemical perturbation knowledge (i.e. drugs known to promote specific cell-state transitions) and transcriptomic readouts to originate from different but mechanistically aligned studies. This design increased the diversity of test conditions while maintaining relevance between gene expression signatures and the biological actions of candidate drugs. During evaluation, we further filtered candidate drugs to remove those known to act on apoptotic pathways, as such agents are primarily relevant in cancer contexts and are not considered suitable for our cell conversion cases. Across the test set, the model achieved an F1 score, FPR, and FNR of 0.528, 0.167, and 0.472, respectively, in identifying drug target proteins (Supplementary Fig. 1c-e). Next, using the BES, we assessed whether the predicted protein targets overlapped significantly with known targets of each drug. Given the lack of well-defined positive and negative drug sets, we focused on early recall of true positives within top percentiles, a clinically relevant metric for downstream experimental validation. The DL-based framework achieved a 9.2% average recall of true positive hits within the top 1st percentile of ranked drugs (Supplementary Fig. 1f), outperforming gene set enrichment analysis (GSEA)-based methods, where the best-performing case reached only 2.1%, and random ranking yielded 1%, as expected. At the 2nd percentile cutoff, the DL-based framework achieved 16.3% recall, compared to 6.1% for the best GSEA result. This measure emphasizes the framework's ability to prioritize strong candidates from large pools. In the GSEA-based baseline, enriched pathways were identified from the input DETFs using Gene Ontology Biological Process (GOBP), Reactome, and KEGG via enrichR[122], applying adjusted p-value cutoffs of 0.05, 0.001, and 0.005 to each database. Differentially expressed genes (DEGs) within the enriched pathways were then used as predicted target proteins, which were subsequently used to rank drugs based on a BES. These results demonstrate that the DL-based framework offers improved early enrichment performance over GSEA-based methods, enabling more effective identification of candidate drugs.

To prioritize drug candidates from the prediction set, we selected drugs ranked within the top 2.5th percentile of the BES based on the test recall curve, which plateaued at 2.5% (Supplementary Fig. 1f-g). After

removing duplicates, this cutoff resulted in 140 drugs for DETF1 and 143 drugs for DETF2. We then prioritized the hits based on their postulated primary target or mode of action and selected those with known modulation of metabolism according to Chembl (https://www.ebi.ac.uk) and Drug Bank (https://go.drugbank.com/). This strategy resulted in a total of 34 DL-predicted drugs (DLDs) (20 for DETF1 and 14 for DETF2). Among these, we selected 5 based on their safety profile in humans (DLD1, DLD3, DLD4, DLD5 from DETF1, and DLD2 from DETF2).

Generation of midbrain organoids (MOs)

MOs were generated following a published protocol[37], with some modifications. To start the generation of MOs, NPCs were detached using Accutase to obtain a single cell suspension. NPCs were then counted using an automatic cell counter, with a gating size of 5–19 µm, and seeded onto low-attachment U-bottom 96-well plates at a density of 9000 cells/150 µl media per well. Seeding medium was composed of a basal medium containing 1:1 ratio DMEM-F12:Neurobasal, N2 (0.25×), B27 without vitamin A (0.25×), glutamax (1×), MycoZap-Plus-CL (1×), 0.4% (w/v) polyvinyl-alcohol (PVA) supplemented with the following small molecules: 0.5 µM Purmorphamine, 3 µM CHIR 99021 and 100 µM ascorbic acid. After 2 days, seeding medium was replaced with a basal medium supplemented with 100 µM ascorbic acid, 1 µM Purmorphamine, 1 ng/ml BDNF, and 1 ng/ml GDNF to induce ventral patterning. Four days later, the medium was exchanged to a maturation medium, composed of the basal medium supplemented with 100 µM ascorbic acid, 2 ng/ml BDNF, 2 ng/ml GDNF, 1 ng/ml TGF-β3, and 100 µM dibutyryl-cAMP. On day 6, a single concentration of 5 ng/ml activin A was added. From day 7 on, maturation medium (without activin A) was refreshed 3 times a week. For experiments with chronic treatment, MOs were treated from day 2 until the day of the assay (either until day 9 or day 28–35) with either 0.1 µM sertaconazole, 1 µM talarozole, or DMSO (vehicle). DMSO samples contained 0.1% (v/v) DMSO, which was equivalent to the amount of solvent in the samples that received compound treatment. Treatments were refreshed upon every media change every other day.

MO growth rate analysis, viability assay, and lactate release

To measure organoid size, pictures were taken every other day with a Nikon Eclipse TS2 inverted microscope using a 4× objective and ensuring good contrast between the background and the organoid. Organoid area and perimeter were measured using CellProfiler (v. 4.2.5). Color images were first converted into grayscale images using the modules "Color to gray" and "Invert for printing". Next, grayscale images were used as an input for the module "Identify Primary Objects" to identify a bright object (organoid) of a diameter ranging 300–1200 px on a dark background. The properties of identified objects could then be measured using the module "Measure Object Size Shape". Undesired identified objects (such as debris) were filtered out using the "Filter Objects" module, based on their compactness, with a maximum value of 4. After filtering, the module "Measure Object Size Shape" was again used to measure the properties of the filtered identified objects (organoid). The results of this module were exported to Excel files for analysis. The organoid area measured at day 2 was used as a reference starting point and was therefore subtracted from each individual value obtained. thereafter. At least 5 organoids per cell line for each time point from 3 independent experiments were analyzed. For the viability assay, control MOs were treated from day 2 to day 11 every second day with different concentrations (0.1 µM, 1 µM, 5 µM, 10 µM) of talarozole or sertaconazole. DMSO control samples contained 0.1% (v/v) DMSO, which is equivalent to the amount of solvent in the samples that received compound treatment. On day 9, organoid viability was measured using the CellTiter-Glo cell viability assay following a previously published protocol[37]. Briefly, the medium of each well was adjusted to 55 µl, and the plates with MOs together with the kit´s reagents were brought to room temperature (RT) for 30 min. Next, an equal volume of 55 µl of CellTiter-Glo reagent was added, and samples were shaken on a Thermomixer at 900 rpm for 5 min. Afterwards, plates were incubated for 25 min at RT protected from light. The contents of the plate were transferred to white/opaque 96-well plates with 2 technical replicates (20 µl each) per sample. Luminescence of each sample was recorded using a Tecan plate reader. Extracellular lactate released by MOs in the media was measured by collecting 100 µl of maturation medium at day 9 during MOs generation. Media from at least 5 individual MOs from 3 different batches were collected for analysis and stored at −20 °C until used. The manufacturer's instructions from the lactate assay commercial kit were followed for measuring the absorbance of each sample using a clear 96-well microplate assay and Tecan microplate to read the absorbance at 580 nm. The calculated amount of lactate per well was normalized to the respective organoid size and expressed as fold-change compared to control (when untreated) or to DMSO-treated sample (when treated with sertaconazole or talarozole) of their respective batch.

Single-cell RNA sequencing (scRNAseq) of untreated MOs

35 days-old MOs from control iPSCs were dissociated for scRNAseq using the papain dissociation system (Worthington). Papain was prepared by adding 5 ml of EBSS to one papain vial and incubated for 10 min at 37 °C. Additionally, 500 µl of EBSS was added to one DNAse vial and gently mixed. Half of the volume of DNAse in EBSS was then added to the papain vial, resulting in a final concentration of approximately 20 units/ml of papain and 0.005% DNase. About 48 individual MOs were collected onto a 6 well-plate, washed with PBS, and incubated with 2 ml of pre-warmed papain/DNase solution for 5–10 min at 37 °C in an orbital shaker. Using a 1 ml pipette, the organoids were gently triturated by mixing up and down and placed back into the incubator for another 5–10 min for further enzymatic digestion. The digested organoids were then collected in a 15 ml tube, and 5 ml of ovalbumin was added. Using a 225 mm polished glass pipette, the mixture was further triturated until mostly dissociated. The cell suspension was then filtered through a 30 µm cell strainer and transferred to a new 15 ml tube. The cell counts were determined, and cells were pelleted by centrifuging at 300 × *g* for 5 min. After removing the supernatant, the pellet was resuspended in 200 µl of ice-cold PBS and 800 µl of freezing-cold 100% methanol was added. The cell suspension was snap-frozen in liquid nitrogen and stored at −80 °C until library preparation. After rehydration of the samples, libraries were generated using 10x Chromium and sequenced with the Illumina NovaSeq 6000 platform. Samples were subjected to scRNAseq using 10× Genomics Chromium Single Cell 3' Gene Expression system with feature barcoding technology for cell multiplexing. Demultiplexed, raw paired-end scRNAseq data were processed using the Cell Ranger (v. 7.10) from 10x Genomics. Data were analyzed in three biological replicates, where each replicate was composed of 48 individual MOs. Sequencing was carried out in two separate batches. In the first batch, replicates 1 and 2 were processed, while replicate 3 was processed in the second batch. In this manner, we assessed reproducibility of the sequencing results across different independent runs. To compare our MOs to other MOs generated before, we employed scRNAseq datasets of MOs that were previously generated at different time points[38]. The datasets were obtained from GSE133894. Cell types were annotated following the approach described before[19], where eight cell types were determined based on the expression levels of their marker genes (endothelial cells, non-mDANs, mDANs, glia, NBs in vitro, NPCs, and pericytes). The percentage of each cell type with respect to the total cell counts was computed. Integration of the two datasets was performed using the *FindIntegrationAnchors()* function described before[71] with default parameters using the Seurat R package (v. 4.2.0)[123]. The scRNAseq data of MOs can be retrieved under accession code NCBI GEO: GSE271852. scRNAseq data of Leigh COs and isogenic control COs were carried out

as before[15] and can be retrieved under accession code NCBI GEO: GSE126360. Pseudotime analysis was performed on the RG, IPCs, and neurons populations in those scRNAseq data using Monocle3 R package[30]. Input genes were differentially expressed genes among the three populations with the adjusted p value cutoff <= 0.05. The DDRTree algorithm was used for the inference.

scRNAseq of compound-treated MOs

35-day-old MOs from isogenic CTL and from Leigh treated with either 0.1% DMSO (v/v), 0.1 μM sertaconazole, or 1 μM talarozole were dissociated for scRNAseq following the instructions of the Neural dissociation kit (Miltenyi) with a few modifications. Between 40-50 individual MOs were collected onto a 6 well-plate, washed with PBS, and incubated with 1 ml of Enzyme mix 1 for 5 min at 37 °C in an orbital shaker. Using a 1 ml pipette, the organoids were gently triturated by mixing up and down 10 times before adding Enzyme mix 2 for a second incubation. After 5 min incubation, the dissociation was stopped by adding 5 ml of stop solution. Cells were filtered through a 40 μm cell strainer and centrifuged at 300 × g for 5 min at 4 °C. After removing the supernatant, the pellet was resuspended in 4 ml of 0.04% BSA (bovine serum albumin) and further strained through a 70 μm cell strainer. The BSA solution was removed after a second centrifugation, and the obtained pellet was processed for fixation following the manufacturer's instructions (10X Genomics). The pellet was resuspended in 1 ml of fixation buffer for overnight incubation at 4 °C. The next day, samples were centrifuged at 850 × *g* for 5 min at RT, and the supernatant was removed. The obtained pellet was mixed 5 times in 500 μl of Quenching Buffer together with 50 μl pre-warmed Enhancer and glycerol (final concentration 10%). scRNAseq was carried out as described above. Unbiased clustering was performed using the *FindClusters()* function at a resolution of 0.3, followed by 2D visualization with the *RunUMAP()* function. Dot plots of selected marker genes for each cluster were generated using the *DotPlot()* function. Pseudotime analysis of selected cell clusters representing RG, IPCs, and neurons was carried out using the Monocle3 R package[30]. Input genes were differentially expressed genes among the three populations, filtered by an adjusted *p*-value ≤ 0.05. The DDRTree algorithm was used for trajectory inference. Gene set enrichment analysis (GSEA) was performed on differentially regulated genes in each cluster between LS and control organoids using the enrichR R package[122] with the "GO_Biological_Process_2021" database.

Immunostaining of MOs

Free-floating MOs were fixed with 4% PFA for 20 min at RT, followed by three 10 min washes with PBS. Organoids were blocked and permeabilized with a solution consisting of 3% BSA, 0.5% Triton-X-100 and 0.05% sodium azide in PBS, for 1 h at RT. Primary antibodies were diluted in blocking solution and incubated overnight at 4 °C. Afterwards, MOs were washed 3 times with PBS and incubated overnight at 4 °C with secondary antibodies at a 1:1000 dilution in blocking solution. Next, organoids were incubated for 1 h at RT with Hoechst 33342 (1:1000) and washed three times with PBS. Images were acquired using the ZEISS Axio Observer microscope with an apotome 3 as a z-stack, which were then deconvoluted using the Zeiss blue software default settings and z-projected with maximum intensity. Antibodies are reported in Supplementary Data 6. For quantification of image intensity of Hoechst, MAP2, SMI312 and TH within MOs, immunostained MOs z-projected images were analyzed using Columbus software (v. 2.9.0). Prior to analysis, images were downscaled using the greyscale function in Photoshop (v. 12.1 ×64) and resized from 300 to 72 pixels per inch. The images were converted from 8-bit to 16-bit channels to retain image information and saved as.tif files. An image analysis pipeline was established using different building blocks. MO objects were identified based on the stained channel using the "Find Image Region" block. The "Fill Region" and "Border" functions within the "Select Region" block were utilized to cover the entire organoid area. Within this defined area, the intensities of each channel were calculated using the "Calculate Intensity Properties" block and given as the average pixel intensity. Furthermore, morphological parameters such as area, width, length (all measured in μm), and roundness were assessed using the "Calculate Morphology Properties" block. For statistical comparison, we calculated the ratio of intensities of respective channels and the area of the individual MO.

Intracellular calcium imaging of MOs

28-37 -day-old MOs were stained with the membrane-permeable form of the calcium indicator Fura-2 (Fura-2 AM; 1 mM stock solution in 20% pluronic/DMSO; 15 μM final concentration) dissolved in artificial cerebrospinal fluid (ACSF), containing (in mM): 138 NaCl, 2.5 KCl, 2 $CaCl_2$, 1 $MgCl_2$, 1.25 NaH_2PO_4, 18 $NaHCO_3$, and 10 glucose (pH 7.4; osmolarity ~310 mOsm/l) at 37 °C in a humidified atmosphere with 95% O_2 and 5% CO_2 for 30 min, followed by additional 30 min in ACSF without dye. A single MO was placed onto an Omnipore membrane filter and stabilized by a grid in the recording chamber. MOs were continuously superfused (2–2.5 ml/min) with ACSF bubbled with 95% O_2 and 5% CO_2 and allowed to equilibrate for ~10 min before starting recordings. Experiments were carried out at 37 ± 1 °C. Wide-field calcium imaging was performed using an upright microscope equipped with a 40×/N.A. 0.8 water immersion objective. Fura-2 AM was alternately excited at 380 and 400 nm using a monochromator, and images were acquired at a frequency of 1 Hz with a complementary metal-oxide-semiconductor (CMOS) camera. Fura-2 AM emission was collected at 510 ± 40 nm from regions of interest (ROIs) manually drawn around individual cell bodies. Background correction was performed as previously described[124]. Spontaneous calcium activity was analyzed during a 5 min recording period, in which no other manipulation was performed. Cells with calcium signals ≥ 2x standard deviation (SD) were considered active. Metabolic stress was induced by perfusing preparations with a glucose-free ACSF containing 2 mM 2-deoxyglucose and 5 mM sodium azide for 2 min. Changes in fluorescence were normalized to the baseline and are expressed as percentage change.

Generation of iNs for neuromorphogenesis assay

To generate induced neurons (iNs), NGN2 lentiviruses were produced using HEK 293 cells seeded at a 70% confluence in a 150 cm^2 dish in DMEM medium[125]. Once attached, the medium was refreshed with DMEM supplemented with 25 μM chloroquine and cells were transfected with Lipofectamine 2000 according to the manufacturer´s protocol using the following plasmid mix: 8.1 μg pMD2.G, 12.2 μg pMDLg-pRRE, 5.4 μg pRSV-Rev, 5.4 μg FUW-M2-rtTA, 14.3 μg TetO-FUW-NGN2, 14.3 μg TetO-FUW-EGFP[126,127]. The next day, the medium was exchanged with DMEM-F12 containing 10 μM sodium butyrate. The supernatant containing viral particles was collected 24 and 48 h later. To concentrate the virus particles, the supernatant was first centrifuged at 500 × *g* for 10 min to remove cells and debris and then mixed with 1 volume of cold Lenti-X concentrator to every 3 volumes of lentivirus-containing supernatant. This mixture was kept overnight at 4 °C and further centrifuged at 1500 x *g* for 45 min at 4 °C. The obtained pellet containing the virus was diluted 1:100 in PBS. Virus aliquots were stored at −80 °C until further use. For neuronal morphogenesis screening, NPCs were seeded onto Matrigel-coated 96-well black Greiner-bio plates at a density of 40,000 cells/well in 100 μl of sm+ medium. The next day, the media were refreshed with sm+ supplemented with 4 μg/ml polybrene and 2.25×10^6 transducing units of NGN2 lentivirus. After overnight incubation, NPCs were washed 3 times with PBS and the media were refreshed with sm+ containing 2 μg/ml of doxycycline to start neuronal induction (day 0). On day 3, medium was exchanged to NGN2 medium, consisting of Neurobasal, B27 supplement with vitamin A (0.5×), NEAA (1×), 2 mM Glutamine, MycoZap-Plus-CL (1×), 10 ng/ml human NT-3, 10 ng/ml human BDNF

supplemented with 2 µg/ml doxycycline. On day 3, treatments with DLDs and YSDs were administered in the media using 3 different concentrations (1, 10, and 50 µM). Final concentration of DMSOs in the media were either 0.1% or 0.4% (for 50 µM treatment of DLD4 and DLD5), which was equivalent to the amount of solvent in the samples that received compound treatment. On day 5, after 48 h incubation with the compounds, iNs were fixed by adding equal volumes of 8% PFA to the medium. Cells were incubated in a final dilution of 4% PFA for 20 min and washed 3 times with PBS for 10 min/wash. For staining, iNs were blocked and permeabilized for 1 h at RT with blocking solution (3% BSA, Triton-X-100, 0.05% sodium azide in PBS). Primary antibody incubation with anti-MAP2 (1:1000) in blocking solution was carried out overnight at 4 °C. Afterwards, cells were washed 3 times with PBS and treated with Alexa Fluor anti-Guinea pig AF568 secondary antibody (1:1000) and Hoechst 33342 (1:2500) in blocking solution for 1 h at RT. Next, after 3 washes with PBS, wells were filled with 0.05% sodium azide in PBS and stored at 4 °C wrapped with parafilm until imaged. Antibodies are reported in Supplementary Data 6. iNs were imaged with the high-content microscope Operetta using the 0.4 NA 20x air objective. For each well, 20 areas across the well were selected for imaging. The areas remained constant for each plate analyzed. Images of Hoechst and MAP2 channels were then analyzed with CellProfiler[128] to analyze neuronal morphogenesis as previously described (https://zenodo.org/records/6642365)[18]. Data were summarized by calculating the mean per well. To compare different plates, numbers were compared to the mean of the DMSO-treated wells.

Yeast drug screen and concentration-dependent validation

Wild-type (WT) and SURF1-KO mutant (ΔSHY) strains were assessed for growth deficiency in a non-fermentable growth medium [YP medium (1% yeast extract, 2% bacto-peptone) plus 2% lactate] at 30 °C. A 384-well optimization assay was developed: 1) to identify the right starting density of cells that accentuates the growth difference phenotype and best assay time, 2) to establish that the assay has a good Z', which is a measure of assay quality and the likelihood of false positives and negatives in the screen[129]. In this assay, the Z' score was 0.7, indicating that the assay quality is excellent. Overnight cultures were diluted to an optical density (OD) of 0.025. 50 nl of 10 mM test compounds were added to columns 3-22 of 384-well plates to reach a final concentration of 20 µM, while 50 nl of DMSO was added to control columns 1–2 and 23–24, reaching a final concentration of 0.72 % (v/v). ΔSHY and WT cell suspensions were adjusted to an OD of 0.025, and 25 µl of mutant cells were added to columns 1-22, and WT cells to columns 23–24. The plates were spun at 250 × *g* for 1 min, sealed with a gas-permeable seal, and covered with a water-filled lid, then incubated at 30 °C for 24 h. After incubation, seals were removed and plates were equilibrated at RT for 15 min. 25 µl of Bactiter-glo solution was added to each well, plates were shaken for 2 min, incubated for 10 min, and luminescence was read using an Envision plate reader. Test compounds used in yeast drug screening belong to the UCSF Pharmakon library, including 1600 repurposable drugs that are FDA-approved with an existing safety record (Supplementary Table 1). A list of hits was generated, with the top 2% selected for further analysis. Concentration-dependent validations for sertaconazole and talarozole were carried out using the same procedures for either 24 h or 48 h.

Generation of midbrain dopaminergic neurons (mDANs)

The generation of mDANs from NPCs was performed following a previously published protocol[15,130]. To start differentiation, NPC media was switched to a mixture of 1:1 of Neurobasal:DMEM-F12, N2 (0.5×), B27 with vitamin A (0.5×), 2 mM glutamine and Mycozap-Plus-CL (1×) supplemented with 200 µM ascorbic acid, 100 ng/ml FGF8, and 0.5 µM purmorphamine for 7 days. The following two days, the concentration of ascorbic acid and purmorphamine was brought down to 100 µM and 0.25 µM, respectively. On day 9, cells were passaged with Accutase and seeded onto Matrigel-coated plates with 10 µM ROCK inhibitor in maturation media, made of a mixture 1:1 Neurobasal:DMEM-F12, N2 (0.5×), B27 with vitamin A (0.5×), 2 mM glutamine, Mycozap-Plus-CL (1×), with the addition of 200 µM ascorbic acid, 10 ng/ml BDNF, 10 ng/ml GDNF, 500 µM dibutyryl-cAMP, and 1 ng/ml of TGF-β3. The media was refreshed every other day, and the neurons were kept in culture for 4 and 8 weeks to reach different maturation stages.

Mitochondrial movements in mDANs

mDANs cultures were grown on 35 mm dishes with coated bottom and 1.5 coverslips. 25 nM MitoTrackerRed CMXRos was added for 10 min and then replaced with DA culture media. Live-cell imaging recordings were conducted using a spinning disk microscope with incubating conditions of 37 °C with 5% CO_2. Cells were imaged every 2 sec using a 40× oil objective. The raw image files were stored as 16-bit in ".nd2" format at 337 × 337 µm (1024 × 1024 pixel) at an interval of 2 sec and a total of 200 images per series (total time per series: 6:40 min). The image pre-processing was carried out with Fiji (ImageJ 1.52 h) adapted from a previous publication[131]. To compensate for photobleaching during the time series, the "Bleach Correction" tool was applied, followed by a top-hat spatial filter to increase gray values of mitochondrial objects. The total mitochondria count was calculated by creating a binary image where the minimum gray value (min) was set to min=Mean+StdDev and the maximum gray value (max) was set to max= Mean+StdDev+1, where "Mean" and "StdDev" were obtained by using the "Measure" tool. Next, the "watershed" tool was applied to break up large mitochondria networks. Total number of mitochondria was quantified using the "Analyze Particles" tool with standard settings and a size preference for 8–200 pixel. The moving mitochondria were defined by a particle size of at least 6 pixels that changed location over the time course of 4 frames (= 8 s). This was accomplished by subtracting the following 4th frame for each frame in the time series (on the top-hat filtered image). Afterward, the subtracted image series was converted into a binary image series. The number of moving mitochondria was similarly counted using the "Analyze Particles" tool with standard settings and a size preference for 6–200 pixel. Finally, the percentage of moving mitochondria per sample was calculated by dividing the average number of moving mitochondria by the average number of total mitochondria, multiplied by 100. The percentage of stationary mitochondria was obtained by the subtraction of moving mitochondria from 100.

Western blotting

For western blots, MOs were treated from day 2 until day 28-30 of differentiation with either DMSO (0.1% v/v), 0.1 µM sertaconazole or 1 µM talarozole. On day 28-30, 50 to 90 individual MOs per condition were collected in a 1.5 ml tube and washed 3 times with DPBS. MOs were then pelleted using a tabletop centrifuge at 8,000 rpm for 5 min. mDANs were treated with either DMSO (0.1% v/v), 0.1 µM sertaconazole or 1 µM talarozole every other day from day 8 until day 28–30 of differentiation. For each condition, one full 6-well plate of treated mDANs was washed 3 times with DPBS, collected with a cell scraper into a 1.5 ml tube and pelleted using a tabletop centrifuge at 8000 rpm for 5 min. Fresh pellets were weighed and resuspended in appropriate volume of RIPA Lysis Buffer supplemented with proteinase inhibitor and phosphatase inhibitor (1:100) cocktails. Samples were then transferred to tubes containing CK14 ceramic beads and processed using a tissue homogenizer. The suspension was incubated on ice for 30 min, followed by centrifugation for 10 min at 10,000 rcf at 4 °C. Protein levels in the supernatant were then quantified using the BCA protein assay reagent kit. Protein lysates (35 µg) were separated on 4–12% Bis–Tris gels, transferred to PVDF membranes, which were blocked with 3% skimmed milk powder in TBS-T and incubated with antibodies against SNPH, KIF5A and ACTB as a housekeeping protein. The details of all antibodies are reported in Supplementary Data 6. After overnight

incubation at 4 °C, membranes were washed and incubated with secondary antibodies, horseradish peroxidase-conjugated anti-rabbit or anti-mouse. Signals were visualized using ECL solutions and ChemiDoc Touch Imaging System and the intensity of the bands was quantified using Image Lab software (v. 6.1.0). The intensity of the bands of interest (SNPH and KIF5A) was normalized to that of ACTB in the samples. Values of treated MOs are expressed relative to DMSO-treated Leigh MOs.

Targeted metabolomics

NPCs were grown in Matrigel-coated 6-well plates until reaching 70% confluence. NPCs were either left untreated or were treated with 0.1% (v/v) DMSO, 10 μM sertaconazole, or 10 μM talarozole for 24 h. At this point, accutase was used to detach the cells from the plate. Cells were then centrifuged at 200 × *g* for 3 min and the obtained pellets were dissolved in PBS to allow for quantification of cells using an automatic cell counter. Using a gating size of 5–19 μm, 1 million NPCs/sample were pelleted for metabolomics and 4 million NPC/sample for lipidomics in a 1.5 ml tube using a tabletop centrifuge at 8,000 rpm for 5 min at 4 °C. The supernatant was discarded, and the pellet was snap-frozen in liquid nitrogen for subsequent measurement. Extraction of the targeted metabolites was performed by adding 300 μl methanol/H_2O (80/20; v/v) to the 1 ×10^6 cells, which were homogenized by ceramic beads CK14 using Precellys lysing kit. The corresponding isotopically labelled internal standards were added to the extraction solution. The targeted compounds were analyzed by UPLC-MS/MS. The system consists of a UPLC I-Class (Waters) coupled to a tandem mass spectrometer Xevo-TQ-XS (Waters). Electrospray ionization was performed in the negative ionization mode for the compounds fructose-1,6-bishphosphate, phosphoenolpyruvate (PEP) and 2/3-phosphoglycerate[132]. The TCA, energy metabolites (AMP, ADP and ATP) as well acetyl- and succinyl-CoA were measured in the positive ionization mode[133–135]. Mass spectrometric quantitation of the compounds was carried out in the multiple reaction monitoring (MRM) mode. MassLynx software (v. 4.2) was used for instrument's control and data acquisition. Quantitation analysis was performed by TageLynx XS software.

Targeted lipidomics

NPCs were prepared as explained for targeted metabolomics. Approximately 4 million cells were homogenized in 400 μl of Milli-Q water using a Precellys 24 Homogenisator (Peqlab) at 6.500 rpm for 30 sec. The protein content of the homogenate was routinely determined using bicinchoninic acid (Supplementary Data 5).

Glycerophospholipids and cholesterol: To 50 μl of cell homogenate, 450 μl Milli-Q water, 1.875 ml methanol/chloroform 2:1 (v/v) and internal standards (126 pmol PC 17:0-20:4, 138 pmol PE 17:0-20:4, 111 pmol PI 17:0-20:4, 118 pmol PS 17:0-20:4, 60 pmol PG 17:0-20:4, 50 pmol d7-PA 15:0-18:1, 1.3 nmol d7-cholesterol; Avanti Polar Lipids) were added. Lipids were extracted using the "One-Step Extraction" described before[136]. Glycerophospholipids (PC, PE, PI, PS; PG, PA) were analyzed by Nano-Electrospray Ionization Tandem Mass Spectrometry (Nano-ESI-MS/MS) with direct infusion of the lipid extract (*Shotgun Lipidomics*) as previously described[136,137]. Endogenous lipid species were quantified by referring their peak areas to those of the respective internal standard. The calculated lipid amounts were normalized to the protein content of the cell homogenate. Cholesterol levels in the lipid extract were determined by Liquid Chromatography coupled to Electrospray Ionization Tandem Mass Spectrometry (LC-ESI-MS/MS) as previously described[138].

Sphingolipids: To 50 μl of homogenate, 50 μl Milli-Q water, 500 μl methanol, 250 μl chloroform and internal standards (100 pmol d7-ceramide 15:0, 130 pmol glucosylceramide 12:0, 124 pmol sphingomyelin 12:0; Avanti Polar Lipids) were added. Lipid extraction, alkaline hydrolysis of glycerolipids and LC-ESI-MS/MS analysis of ceramides, hexosylceramides, and sphingomyelins were performed as previously described[139,140].

Cholesterol and lipids imaging

For cholesterol analysis, 40,000 NPCs per well were seeded onto a Matrigel-coated 96-well black Ibidi plates. The next day, NPCs were either fed with normal media (untreated condition) or treated with either 0.1% (v/v) DMSO, 10 μM sertaconazole, or 10 μM talarozole for 48 h. For the 24 h treatment, NPCs were treated with the above-mentioned conditions two days after. Both 24 h and 48 h treatment conditions were fixed on the same day using 4% PFA for 15 min at RT and washed 3 times for 10 min with PBS. For PFO-GST labelling of membrane-bound cholesterol, fixed NPCs were blocked and permeabilized with 10% goat serum in 0.1% Triton-X-100, PBS (0.1% PBST) for 1 h and incubated with 15 μg/ml recombinant PFO-GST for 3 h[141]. After washing the cells three times with 0.1% PBST, anti-GST (1:200) was applied in 10% goat serum 0.1% PBST, overnight at 4 °C. After three washes with 0.1% PBST, Alexa Fluor™ 488 goat anti-mouse IgG (H + L) secondary antibody was applied (1:500) for 1 h at RT. Lastly, wells were washed three times in PBS and cells were preserved in Mounting Medium with DAPI.

For neutral lipid labelling, fixed cells were incubated with 1 μg/ml BODIPY 493/503 in PBS for 20 min, followed by three washes of 5 min with PBS, and mounting medium with DAPI was added to the wells. Fluorescent images were acquired with a LSM 900 Zeiss confocal microscope. Laser power, gain, and offset parameters were kept constant for each experiment; any subsequent adjustments to contrast and brilliance were applied equally to all images. Image analysis and quantification were performed using Fiji ImageJ software using custom-made macros.

Molecular docking with GOLD

To test sertaconazole and talarozole binding to postulated targets, we performed in silico docking experiments using the docking tool GOLD[49]. We modeled docking to the protein targets of talarozole: cytochrome P450 26 (CYP26) enzymes, specifically CYP26A1 and CYP26B1. Since there is no experimental structure reported to date for CYP26A1/B1, we obtained CYP26A1/B1 from the AlphaFold[142] database based on PDB:2VE3 which reports the structure for retinoic acid bound to cyanobacterial CYP120A1. Overlap between the two protein structures enabled the localization of the iron-heme and the substrate structure within the cavity of CYP26A1/B1[143]. Removing the substrate and redocking it together with sertaconazole and talarozole revealed differences in poses and docking scores. CCDC Gold (v. 2022) was used for docking and CCG MOE (v. 2022.02) was used to visualize the results and generate images. Compound poses were analyzed using docking scores and by the minimal distance of any compound´s atom from the heme-iron reactive center for oxidation. The combination of distance from the iron atom and the relative energy needed to reach the ligand's position can suggest whether compounds act as substrate or as inhibitor, since inhibitors are usually closer to the iron-center, disturbing the oxygen recruitment from heme[144,145].

Molecular docking with DiffDock and SMINA

The docking protocol was performed using a combination of DiffDock[53] and SMINA[54]. The protein structures of human ligand-binding domain of the peroxisome proliferator-activated receptor gamma were obtained from PDB (2FVJ: PPARγ bound to PA-082[58], 3B1M: PPARγ bound to Cerco-A[59], and 6L8B: PPARγ ligand-free[60]). Residues not belonging to the receptor were removed, and the residues corresponding to missing loops were modelled using CHARMM-GUI[146]. The predicted structure of human cytochrome P450 26A1 and 26B1 was obtained from the AlphaFold Database (O43174 and Q9NR63, respectively)[142,147] and the transmembrane region was removed (residues 1-45 and 1-41, respectively). Each structure was then solvated in

explicit OPC water, adding counter ions to neutralize the system when necessary, and minimized with the Amber ff19sb force field[148] using the steepest descend algorithm in a two-step process: a first minimization with constraints on the heavy atoms of the protein backbone (400 kJ/mol) and side chains (40 kJ/mol), and a second unconstrained minimization. The DiffDock algorithm was used to perform a global, blind docking. Minimized structures were used as receptor input to dock each of the ligands, which were provided in SMILES format. A total of 40 poses per complex (receptor-ligand) were generated, with 20 inference steps each, ranked by confidence score. The top 5 poses were then refined with SMINA, using the pose to generate the searching box and adding 4 Å buffer space to allow ligand re-accommodation. Only a local search with an additional 200 steps of steepest descent energy minimization was performed. The lowest energy refined pose per complex was selected for analysis and plotting.

PCR and gene expression analyses

For quantitative real-time PCR (qPCR) analysis of CYP26B1 in iNs, 2 million NPCs were seeded onto Matrigel-coated 6 well-plates one day prior to NGN2 lentiviral transfection supplemented with 4 µg/ml polybrene. After overnight incubation with NGN2 lentiviruses, cells were washed 3 times with PBS and the media was refreshed with sm+ containing 2 µg/ml of doxycycline to start neuronal induction (day 0). Three days later, media was exchanged to iN media (see *Neuromorphogenesis analysis in iNs* for media formulation) with either DMSO (0.1% v/v), 10 µM sertaconazole, or 10 µM talarozole. On day 5, treatment was refreshed to incubate for another 6 h to observe changes in gene expression[149]. Afterwards, cells were collected using a cell scraper, pelleted using a tabletop centrifuge at 8,000 rpm for 5 min, and snap-frozen in liquid nitrogen. RNA extraction from pellets was performed with RNeasy kit. cDNA was generated from 2 µg RNA using the first strand cDNA synthesis kit. qPCR experiments were conducted for three technical replicates and three biological iNs replicates with the SYBR green Mastermix and CFX96 Real-Time System (Bio-Rad). After averaging the CT values of the three technical replicates, the $2^{-\Delta\Delta CT}$ method was used. The expression levels of the genes of interest were normalized relative to the average expression of housekeeping genes (*C1ORF43* and *YWHAZ*)[150] and relative to DMSO treatment. Primer sequences are reported in Supplementary Data 6. Expression of anchoring and RA pathway genes was obtained from our previously published bulk RNAseq datasets for Leigh mDANs and Leigh COs[15].

Statistical analysis

Data are expressed as mean and standard deviation (mean ± SD) where normality of the distribution could be verified, or as median and quartiles (median [1st; 4th quartiles]) otherwise. Significance was assessed using parametric tests (Welch's t-test, ANOVA) for normally distributed data and non-parametric tests (Mann-Whitney U test, Kruskal-Wallis) when normal distribution could not be verified. Unless otherwise indicated, data were analyzed and shown using GraphPad-Prism software (v. 10.2.2) (GraphPad Software, USA) or R (v. 4.10). Figures were prepared with Adobe Illustrator (v. 28.5). Schematic cartoons were made using Biorender.

Reporting summary

Further information on research design is available in the Nature Portfolio Reporting Summary linked to this article.

Data availability

There are restrictions to the availability of patient-derived iPSCs due to our ethical approval that does not support sharing with third parties without a specific amendment and does not allow performing genomic studies to respect the European privacy protection law.

Single-cell RNA sequencing (scRNAseq) data are deposited in the Sequence Read Archive (SRA) with bioproject number PRJNA1378526 and can be downloaded at: https://www.ncbi.nlm.nih.gov/bioproject/?term=PRJNA1378526.

Additional scRNAseq data used in this study have been previously deposited in the Gene Expression Omnibus (GEO) database: GSE152915, GSE126360, (https://www.ncbi.nlm.nih.gov/geo/query/acc.cgi?acc=GSE126360), GSE133894, GSE271852.

Lipidomics data are deposited in Metabolomics Workbench repository[151] with project number PR002944 and can be downloaded at: https://doi.org/10.21228/M84C4F. Source data are provided with this paper.

Code availability

The program code and input files are available at: https://github.com/OSB-codes/DL_drug_repurposing/tree/main.

References

1. Leigh, D. Subacute necrotizing encephalomyelopathy in an infant. *J. Neurol. Neurosurg. Psychiatry* **14**, 216–221 (1951).
2. McCormick, E. M. et al. Expert panel curation of 113 primary mitochondrial disease genes for the leigh syndrome spectrum. *Ann. Neurol.* **94**, 696–712 (2023).
3. Vafai, S. B. & Mootha, V. K. Mitochondrial disorders as windows into an ancient organelle. *Nature* **491**, 374–383 (2012).
4. Zhu, Z. et al. SURF1, encoding a factor involved in the biogenesis of cytochrome c oxidase, is mutated in Leigh syndrome. *Nat. Genet.* **20**, 337–343 (1998).
5. Wedatilake, Y. et al. SURF1 deficiency: a multi-centre natural history study. *Orphanet J. Rare Dis.* **8**, 96 (2013).
6. Mashkevich, G., Repetto, B., Glerum, D. M., Jin, C. & Tzagoloff, A. SHY1, the yeast homolog of the mammalian SURF-1 gene, encodes a mitochondrial protein required for respiration. *J. Biol. Chem.* **272**, 14356–14364 (1997).
7. Quadalti, C. et al. SURF1 knockout cloned pigs: Early onset of a severe lethal phenotype. *Biochim Biophys. Acta Mol. Basis Dis.* **1864**, 2131–2142 (2018).
8. Dell'agnello, C. et al. Increased longevity and refractoriness to Ca(2+)-dependent neurodegeneration in Surf1 knockout mice. *Hum. Mol. Genet.* **16**, 431–444 (2007).
9. Kovarova, N. et al. Tissue- and species-specific differences in cytochrome c oxidase assembly induced by SURF1 defects. *Biochim. Biophys. Acta* **1862**, 705–715 (2016).
10. Russell, O. M., Gorman, G. S., Lightowlers, R. N. & Turnbull, D. M. Mitochondrial diseases: hope for the future. *Cell* **181**, 168–188 (2020).
11. Weissig, V. Drug development for the therapy of mitochondrial diseases. *Trends Mol. Med.* https://doi.org/10.1016/j.molmed.2019.09.002 (2019).
12. Weissig, V. Drug development for the therapy of mitochondrial diseases. *Trends Mol. Med.* **26**, 40–57 (2020).
13. Tyynismaa, H. & Suomalainen, A. Mouse models of mitochondrial DNA defects and their relevance for human disease. *EMBO Rep.* **10**, 137–143 (2009).
14. Henke, M. T., Prigione, A. & Schuelke, M. Disease models of Leigh syndrome: from yeast to organoids. *J. Inherit. Metab. Dis.* **47**, 1292–1321 (2024).
15. Inak, G. et al. Defective metabolic programming impairs early neuronal morphogenesis in neural cultures and an organoid model of Leigh syndrome. *Nat. Commun.* **12**, 1929 (2021).
16. Zink, A. et al. Pluripotent stem cell-based drug discovery uncovers sildenafil as a treatment for mitochondrial disease. *medRxiv*, 2025.2005.2015.25325571. https://doi.org/10.1101/2025.05.15.25325571 (2025).

17. Romero-Morales, A. I. et al. Human iPSC-derived cerebral organoids model features of Leigh syndrome and reveal abnormal corticogenesis. *Development* **149**. https://doi.org/10.1242/dev.199914 (2022).
18. Iwata, R., Casimir, P. & Vanderhaeghen, P. Mitochondrial dynamics in postmitotic cells regulate neurogenesis. *Science* **369**, 858–862 (2020).
19. Baumann, N. et al. Regional differences in progenitor metabolism shape brain growth during development. *Cell* **188**, 3567–3582 e3520 (2025).
20. Khacho, M., Harris, R. & Slack, R. S. Mitochondria as central regulators of neural stem cell fate and cognitive function. *Nat. Rev. Neurosci.* **20**, 34–48 (2019).
21. Iwata, R. et al. Mitochondria metabolism sets the species-specific tempo of neuronal development. *Science* **379**, eabn4705 (2023).
22. Wang, M. et al. Mitochondrial complex I deficiency leads to the retardation of early embryonic development in Ndufs4 knockout mice. *PeerJ* **5**, e3339 (2017).
23. von Kleist-Retzow, J. C. et al. Antenatal manifestations of mitochondrial respiratory chain deficiency. *J. Pediatr.* **143**, 208–212 (2003).
24. Adelizzi, A. et al. Fetal and obstetrics manifestations of mitochondrial diseases. *J. Transl. Med.* **22**, 853 (2024).
25. Biswas, S. R. et al. Impaired Complex I dysregulates neural/glial precursors and corpus callosum development revealing postnatal defects in Leigh Syndrome mice. *bioRxiv*, 2025.2005.2016.654318. https://doi.org/10.1101/2025.05.16.654318 (2025).
26. Falk, M. J. Neurodevelopmental manifestations of mitochondrial disease. *J. Dev. Behav. Pediatr.* **31**, 610–621 (2010).
27. Tinker, R. J. et al. Early developmental delay in Leigh syndrome spectrum disorders is associated with poor clinical prognosis. *Mol. Genet. Metab.* **135**, 342–349 (2022).
28. Zilber, S. et al. Leigh syndrome global patient registry: uniting patients and researchers worldwide. *Orphanet J. Rare Dis.* **18**, 264 (2023).
29. Zink, A. et al. Pluripotent stem-cell-based screening uncovers sildenafil as a mitochondrial disease therapy. *Cell* **189**, 1656–1679.e42 (2026).
30. Qiu, X. et al. Reversed graph embedding resolves complex single-cell trajectories. *Nat. Methods* **14**, 979–982 (2017).
31. Zheng, M. et al. ChemPert: mapping between chemical perturbation and transcriptional response for non-cancer cells. *Nucleic Acids Res.* **51**, D877–D889 (2023).
32. Lickfett, S. et al. High-content analysis of neuronal morphology in human iPSC-derived neurons. *STAR Protoc.* **3**, 101567 (2022).
33. Zhang, Y. et al. Rapid single-step induction of functional neurons from human pluripotent stem cells. *Neuron* **78**, 785–798 (2013).
34. Rahman, S. et al. Leigh syndrome: clinical features and biochemical and DNA abnormalities. *Ann. Neurol.* **39**, 343–351 (1996).
35. Lake, N. J., Bird, M. J., Isohanni, P. & Paetau, A. Leigh syndrome: neuropathology and pathogenesis. *J. Neuropathol. Exp. Neurol.* **74**, 482–492 (2015).
36. Stenton, S. L. et al. Leigh syndrome: a study of 209 patients at the Beijing Children's Hospital. *Ann. Neurol.* **91**, 466–482 (2022).
37. Renner, H. et al. A fully automated high-throughput workflow for 3D-based chemical screening in human midbrain organoids. *Elife* **9** https://doi.org/10.7554/eLife.52904 (2020).
38. Zagare, A. et al. Midbrain organoids mimic early embryonic neurodevelopment and recapitulate LRRK2-p.Gly2019Ser-associated gene expression. *Am. J. Hum. Genet.* **109**, 311–327 (2022).
39. Magro, G., Laterza, V. & Tosto, F. Leigh syndrome: a comprehensive review of the disease and present and future treatments. *Biomedicines* **13**. https://doi.org/10.3390/biomedicines13030733 (2025)
40. Iannetti, E. F., Smeitink, J. A. M., Willems, P., Beyrath, J. & Koopman, W. J. H. Rescue from galactose-induced death of Leigh Syndrome patient cells by pyruvate and NAD. *Cell Death Dis.* **9**, 1135 (2018).
41. To, T. L. et al. A compendium of genetic modifiers of mitochondrial dysfunction reveals intra-organelle buffering. *Cell* **179**, 1222–1238 e1217 (2019).
42. Gerards, M., Sallevelt, S. C. & Smeets, H. J. Leigh syndrome: Resolving the clinical and genetic heterogeneity paves the way for treatment options. *Mol. Genet. Metab.* **117**, 300–312 (2016).
43. Baertling, F. et al. A guide to diagnosis and treatment of Leigh syndrome. *J. Neurol. Neurosurg. Psychiatry* **85**, 257–265 (2014).
44. Courchet, J. et al. Terminal axon branching is regulated by the LKB1-NUAK1 kinase pathway via presynaptic mitochondrial capture. *Cell* **153**, 1510–1525 (2013).
45. Sheng, Z. H. Mitochondrial trafficking and anchoring in neurons: new insight and implications. *J. Cell Biol.* **204**, 1087–1098 (2014).
46. Fan, Q. W. et al. Cholesterol-dependent modulation of dendrite outgrowth and microtubule stability in cultured neurons. *J. Neurochem* **80**, 178–190 (2002).
47. Park, D. S. et al. iPS-cell-derived microglia promote brain organoid maturation via cholesterol transfer. *Nature* **623**, 397–405 (2023).
48. Munoz-Oreja, M. et al. Elevated cholesterol in ATAD3 mutants is a compensatory mechanism that leads to membrane cholesterol aggregation. *Brain* **147**, 1899–1913 (2024).
49. Verdonk, M. L., Cole, J. C., Hartshorn, M. J., Murray, C. W. & Taylor, R. D. Improved protein-ligand docking using GOLD. *Proteins* **52**, 609–623 (2003).
50. Ross, A. C. & Zolfaghari, R. Cytochrome P450s in the regulation of cellular retinoic acid metabolism. *Annu Rev. Nutr.* **31**, 65–87 (2011).
51. Foti, R. S. et al. Identification of tazarotenic acid as the first×-enobiotic substrate of human retinoic acid hydroxylase CYP26A1 and CYP26B1. *J. Pharm. Exp. Ther.* **357**, 281–292 (2016).
52. Kuhnel, K. et al. Crystal structures of substrate-free and retinoic acid-bound cyanobacterial cytochrome P450 CYP120A1. *Biochemistry* **47**, 6552–6559 (2008).
53. DL, B. F. et al. Predicting molecular docking of per- and polyfluoroalkyl substances to blood protein using generative artificial intelligence algorithm DiffDock. *Biotechniques* **76**, 14–26 (2024).
54. Koes, D. R., Baumgartner, M. P. & Camacho, C. J. Lessons learned in empirical scoring with SMINA from the CSAR 2011 benchmarking exercise. *J. Chem. Inf. Model* **53**, 1893–1904 (2013).
55. Zhu, L. et al. Variants in ALDH1A2 reveal an anti-inflammatory role for retinoic acid and a new class of disease-modifying drugs in osteoarthritis. *Sci. Transl. Med.* **14**, eabm4054 (2022).
56. Puighermanal, E. et al. Cannabidiol ameliorates mitochondrial disease via PPARgamma activation in preclinical models. *Nat. Commun.* **15**, 7730 (2024).
57. Uppenberg, J. et al. Crystal structure of the ligand binding domain of the human nuclear receptor PPARgamma. *J. Biol. Chem.* **273**, 31108–31112 (1998).
58. Burgermeister, E. et al. A novel partial agonist of peroxisome proliferator-activated receptor-gamma (PPARgamma) recruits PPARgamma-coactivator-1alpha, prevents triglyceride accumulation, and potentiates insulin signaling in vitro. *Mol. Endocrinol.* **20**, 809–830 (2006).
59. Wakabayashi, K. et al. Pharmacology and in vitro profiling of a novel peroxisome proliferator-activated receptor gamma ligand, Cerco-A. *Biol. Pharm. Bull.* **34**, 1094–1104 (2011).
60. Ahn, S. et al. Cyclin-dependent kinase 5 inhibitor butyrolactone I elicits a partial agonist activity of peroxisome proliferator-activated receptor gamma. *Biomolecules* **10** https://doi.org/10.3390/biom10020275 (2020).
61. Zolfaghari, R. et al. CYP26A1 gene promoter is a useful tool for reporting RAR-mediated retinoid activity. *Anal. Biochem.* **577**, 98–109 (2019).

62. Tsai, F. Y., Cheng, Y. T. & Tsou, T. C. A recombinant PPRE-driven luciferase bioassay for identification of potential PPAR agonists. *Vitam. Horm.* **94**, 427–435 (2014).
63. Wadman, M. FDA no longer has to require animal testing for new drugs. *Science* **379**, 127–128 (2023).
64. Svendsen, C. N. Adopting novel alternative methods (NAMs) for biomedical research-What is the right approach?. *Cell Stem Cell* **32**, 1489–1490 (2025).
65. Zhou, L. et al. Organoids and organs-on-chips: Recent advances, applications in drug development, and regulatory challenges. *Med* **6**, 100667 (2025).
66. Tolle, I., Tiranti, V. & Prigione, A. Modeling mitochondrial DNA diseases: from base editing to pluripotent stem-cell-derived organoids. *EMBO Rep.* **24**, e55678 (2023).
67. McKnight, C. L., Low, Y. C., Elliott, D. A., Thorburn, D. R. & Frazier, A. E. Modelling mitochondrial disease in human pluripotent stem cells: What have we learned? *Int. J. Mol. Sci.* **22**. https://doi.org/10.3390/ijms22147730 (2021).
68. Sadybekov, A. V. & Katritch, V. Computational approaches streamlining drug discovery. *Nature* **616**, 673–685 (2023).
69. Waring, M. J. et al. An analysis of the attrition of drug candidates from four major pharmaceutical companies. *Nat. Rev. Drug Discov.* **14**, 475–486 (2015).
70. Lamb, J. et al. The Connectivity Map: using gene-expression signatures to connect small molecules, genes, and disease. *Science* **313**, 1929–1935 (2006).
71. Sharma, S. & Petsalaki, E. Large-scale datasets uncovering cell signalling networks in cancer: context matters. *Curr. Opin. Genet. Dev.* **54**, 118–124 (2019).
72. Amoedo, N. D., Valencia, J. P., Rodrigues, M. F., Galina, A. & Rumjanek, F. D. How does the metabolism of tumour cells differ from that of normal cells. *Biosci. Rep.* **33**. https://doi.org/10.1042/BSR20130066 (2013).
73. Zheng, X. et al. Metabolic reprogramming during neuronal differentiation from aerobic glycolysis to neuronal oxidative phosphorylation. *Elife* **5** https://doi.org/10.7554/eLife.13374 (2016).
74. Cunnane, S. C. et al. Brain energy rescue: an emerging therapeutic concept for neurodegenerative disorders of ageing. *Nat. Rev. Drug Discov.* **19**, 609–633 (2020).
75. Tardiff, D. F. et al. Yeast reveal a "druggable" Rsp5/Nedd4 network that ameliorates alpha-synuclein toxicity in neurons. *Science* **342**, 979–983 (2013).
76. Couplan, E. et al. A yeast-based assay identifies drugs active against human mitochondrial disorders. *Proc. Natl. Acad. Sci. USA* **108**, 11989–11994 (2011).
77. Chung, C. Y. et al. Identification and rescue of alpha-synuclein toxicity in Parkinson patient-derived neurons. *Science* **342**, 983–987 (2013).
78. Njar, V. C. et al. Retinoic acid metabolism blocking agents (RAMBAs) for treatment of cancer and dermatological diseases. *Bioorg. Med. Chem.* **14**, 4323–4340 (2006).
79. Cunningham, T. J. & Duester, G. Mechanisms of retinoic acid signalling and its roles in organ and limb development. *Nat. Rev. Mol. Cell Biol.* **16**, 110–123 (2015).
80. Gudas, L. J. & Wagner, J. A. Retinoids regulate stem cell differentiation. *J. Cell Physiol.* **226**, 322–330 (2011).
81. Diez del Corral, R. et al. Opposing FGF and retinoid pathways control ventral neural pattern, neuronal differentiation, and segmentation during body axis extension. *Neuron* **40**, 65–79 (2003).
82. Alekseenko, Z. et al. Robust derivation of transplantable dopamine neurons from human pluripotent stem cells by timed retinoic acid delivery. *Nat. Commun.* **13**, 3046 (2022).
83. Dmetrichuk, J. M., Carlone, R. L. & Spencer, G. E. Retinoic acid induces neurite outgrowth and growth cone turning in invertebrate neurons. *Dev. Biol.* **294**, 39–49 (2006).
84. Clagett-Dame, M., McNeill, E. M. & Muley, P. D. Role of all-trans retinoic acid in neurite outgrowth and axonal elongation. *J. Neurobiol.* **66**, 739–756 (2006).
85. Baert, D. S. Local skin pharmacokinetics of talarozole, a new retinoic acid metabolism-blocking agent. *Ski. Pharm. Physiol.* **24**, 151–159 (2011).
86. Iqbal, L., Zameer, U. & Iqbal Malick, M. Exploring Talarozole as a Novel Therapeutic Approach for Osteoarthritis: Insights From Experimental Studies. *Clin. Med Insights Arthritis Musculoskelet. Disord.* **17**, 11795441231222494 (2024).
87. Stevison, F., Jing, J., Tripathy, S. & Isoherranen, N. Role of retinoic acid-metabolizing cytochrome P450s, CYP26, in inflammation and cancer. *Adv. Pharm.* **74**, 373–412 (2015).
88. Steele, H. et al. Metabolic effects of bezafibrate in mitochondrial disease. *EMBO Mol. Med.* **12**, e11589 (2020).
89. Croxtall, J. D. & Plosker, G. L. Sertaconazole: a review of its use in the management of superficial mycoses in dermatology and gynaecology. *Drugs* **69**, 339–359 (2009).
90. Subramanian, A. et al. A next generation connectivity map: L1000 platform and the first 1,000,000 profiles. *Cell* **171**, 1437–1452 e1417 (2017).
91. Riancho, J. et al. Retinoids and motor neuron disease: Potential role in amyotrophic lateral sclerosis. *J. Neurol. Sci.* **360**, 115–120 (2016).
92. Suat Sari, S. Y., Merve Zengin, Monika Marcinkowska, Agata Siwek, Selma Saraç. Azoles display promising anticonvulsant effects through possible PPAR-α activation. *Neurosci. Lett.* **828** https://doi.org/10.1016/j.neulet.2024.137750 (2024).
93. Pasca, S. P. et al. A nomenclature consensus for nervous system organoids and assembloids. *Nature* **609**, 907–910 (2022).
94. Brunetti, D., Dyed graph embedding resolves cokstra, W., Le, S., Zink, A. & Prigione, A. Mitochondria in neurogenesis: Implications for mitochondrial diseases. *Stem Cells* https://doi.org/10.1002/stem.3425 (2021).
95. Wang, X. et al. Genome-wide analysis of PDX1 target genes in human pancreatic progenitors. *Mol. Metab.* **9**, 57–68 (2018). ×.
96. Zink, A., Lisowski, P. & Prigione, A. Generation of human iPSC-derived neural progenitor cells (NPCs) as drug discovery model for neurological and mitochondrial disorders. *Bio Protoc.* **11**, e3939 (2021).
97. Razick, S., Magklaras, G. & Donaldson, I. M. iRefIndex: a consolidated protein interaction database with provenance. *BMC Bioinforma.* **9**, 405 (2008).
98. Alanis-Lobato, G., Andrade-Navarro, M. A. & Schaefer, M. H. HIPPIE v2.0: enhancing meaningfulness and reliability of protein-protein interaction networks. *Nucleic Acids Res.* **45**, D408–D414 (2017).
99. Kotlyar, M., Pastrello, C., Sheahan, N. & Jurisica, I. Integrated interactions database: tissue-specific view of the human and model organism interactomes. *Nucleic Acids Res.* **44**, D536–D541 (2016).
100. Turei, D., Korcsmaros, T. & Saez-Rodriguez, J. OmniPath: guidelines and gateway for literature-curated signaling pathway resources. *Nat. Methods* **13**, 966–967 (2016).
101. Wu, G., Feng, X. & Stein, L. A human functional protein interaction network and its application to cancer data analysis. *Genome Biol.* **11**, R53 (2010).
102. Kanehisa, M. & Goto, S. KEGG: kyoto encyclopedia of genes and genomes. *Nucleic Acids Res.* **28**, 27–30 (2000).
103. Browaeys, R., Saelens, W. & Saeys, Y. NicheNet: modeling intercellular communication by linking ligands to target genes. *Nat. Methods* **17**, 159–162 (2020).
104. Han, H. et al. TRRUST: a reference database of human transcriptional regulatory interactions. *Sci. Rep.* **5**, 11432 (2015).
105. Lachmann, A. et al. ChEA: transcription factor regulation inferred from integrating genome-wide ChIP-X experiments. *Bioinformatics* **26**, 2438–2444 (2010).

106. Kulakovskiy, I. V. et al. HOCOMOCO: towards a complete collection of transcription factor binding models for human and mouse via large-scale ChIP-Seq analysis. *Nucleic Acids Res.* **46**, D252–D259 (2018).
107. Wingender, E. et al. TRANSFAC: an integrated system for gene expression regulation. *Nucleic Acids Res.* **28**, 316–319 (2000).
108. Hou, R., Denisenko, E., Ong, H. T., Ramilowski, J. A. & Forrest, A. R. R. Predicting cell-to-cell communication networks using NATMI. *Nat. Commun.* **11**, 5011 (2020).
109. Ximerakis, M. et al. Single-cell transcriptomic profiling of the aging mouse brain. *Nat. Neurosci.* **22**, 1696–1708 (2019).
110. Ramilowski, J. A. et al. A draft network of ligand-receptor-mediated multicellular signalling in human. *Nat. Commun.* **6**, 7866 (2015).
111. Shao, X. et al. CellTalkDB: a manually curated database of ligand-receptor interactions in humans and mice. *Brief Bioinform* **22**. https://doi.org/10.1093/bib/bbaa269 (2021).
112. Wang, J. et al. Ligand-triggered allosteric ADP release primes a plant NLR complex. *Science* **364** https://doi.org/10.1126/science.aav5868 (2019).
113. Jin, S. et al. Inference and analysis of cell-cell communication using CellChat. *Nat. Commun.* **12**, 1088 (2021).
114. Cabello-Aguilar, S. et al. SingleCellSignalR: inference of intercellular networks from single-cell transcriptomics. *Nucleic Acids Res.* **48**, e55 (2020).
115. Qiao, W. et al. Intercellular network structure and regulatory motifs in the human hematopoietic system. *Mol. Syst. Biol.* **10**, 741 (2014).
116. Vento-Tormo, R. et al. Single-cell reconstruction of the early maternal-fetal interface in humans. *Nature* **563**, 347–353 (2018).
117. Noel, F. et al. Dissection of intercellular communication using the transcriptome-based framework ICELLNET. *Nat. Commun.* **12**, 1089 (2021).
118. Pavlicev, M. et al. Single-cell transcriptomics of the human placenta: inferring the cell communication network of the maternal-fetal interface. *Genome Res.* **27**, 349–361 (2017).
119. Hu, H. et al. AnimalTFDB 3.0: a comprehensive resource for annotation and prediction of animal transcription factors. *Nucleic Acids Res.* **47**, D33–D38 (2019).
120. Fabrizio Frasca, E. R. et al. SIGN: Scalable Inception Graph Neural Networks. *arXiv* https://doi.org/10.48550/arXiv.2004.11198 (2020).
121. Sculley, D. Web-scale k-means clustering. *WWW '10: Proceedings of the 19th International Conference on World Wide Web* https://doi.org/10.1145/1772690.1772862 (2010).
122. Kuleshov, M. V. et al. Enrichr: a comprehensive gene set enrichment analysis web server 2016 update. *Nucleic Acids Res.* **44**, W90–W97 (2016).
123. Butler, A., Hoffman, P., Smibert, P., Papalexi, E. & Satija, R. Integrating single-cell transcriptomic data across different conditions, technologies, and species. *Nat. Biotechnol.* **36**, 411–420 (2018).
124. Langer, J. & Rose, C. R. Synaptically induced sodium signals in hippocampal astrocytes in situ. *J. Physiol.* **587**, 5859–5877 (2009).
125. Dull, T. et al. A third-generation lentivirus vector with a conditional packaging system. *J. Virol.* **72**, 8463–8471 (1998).
126. Busskamp, V. et al. Rapid neurogenesis through transcriptional activation in human stem cells. *Mol. Syst. Biol.* **10**, 760 (2014).
127. Vierbuchen, T. et al. Direct conversion of fibroblasts to functional neurons by defined factors. *Nature* **463**, 1035–1041 (2010).
128. Carpenter, A. E. et al. CellProfiler: image analysis software for identifying and quantifying cell phenotypes. *Genome Biol.* **7**, R100 (2006).
129. Zhang, J. H., Chung, T. D. & Oldenburg, K. R. A simple statistical parameter for use in evaluation and validation of high throughput screening assays. *J. Biomol. Screen* **4**, 67–73 (1999).
130. Reinhardt, P. et al. Derivation and expansion using only small molecules of human neural progenitors for neurodegenerative disease modeling. *PLoS One* **8**, e59252 (2013).
131. Iannetti, E. F., Smeitink, J. A., Beyrath, J., Willems, P. H. & Koopman, W. J. Multiplexed high-content analysis of mitochondrial morphofunction using live-cell microscopy. *Nat. Protoc.* **11**, 1693–1710 (2016).
132. Campos, C. G. et al. New Protocol Based on UHPLC-MS/MS for Quantitation of Metabolites in xylose-Fermenting Yeasts. *J. Am. Soc. Mass Spectrom.* **28**, 2646–2657 (2017).
133. Marquis, B. J., Louks, H. P., Bose, C., Wolfe, R. R. & Singh, S. P. A new derivatization reagent for HPLC-MS analysis of biological organic acids. *Chromatographia* **80**, 1723–1732 (2017).
134. Law, A. S., Hafen, P. S. & Brault, J. J. Liquid chromatography method for simultaneous quantification of ATP and its degradation products compatible with both UV-Vis and mass spectrometry. *J. Chromatogr. B Anal. Technol. Biomed. Life Sci.* **1206**, 123351 (2022).
135. Jones, A. E. et al. A single LC-MS/MS analysis to quantify CoA biosynthetic intermediates and short-chain acyl CoAs. *Metabolites* **11** https://doi.org/10.3390/metabo11080468 (2021).
136. Ozbalci, C., Sachsenheimer, T. & Brugger, B. Quantitative analysis of cellular lipids by nano-electrospray ionization mass spectrometry. *Methods Mol. Biol.* **1033**, 3–20 (2013).
137. Kumar, V. et al. A keratin scaffold regulates epidermal barrier formation, mitochondrial lipid composition, and activity. *J. Cell Biol.* **211**, 1057–1075 (2015).
138. Mourier, A. et al. Mitofusin 2 is required to maintain mitochondrial coenzyme Q levels. *J. Cell Biol.* **208**, 429–442 (2015).
139. Hammerschmidt, P. et al. CerS6-dependent ceramide synthesis in hypothalamic neurons promotes ER/mitochondrial stress and impairs glucose homeostasis in obese mice. *Nat. Commun.* **14**, 7824 (2023).
140. Shaner, R. L. et al. Quantitative analysis of sphingolipids for lipidomics using triple quadrupole and quadrupole linear ion trap mass spectrometers. *J. Lipid Res.* **50**, 1692–1707 (2009).
141. Goicoechea, L. et al. GST-Perfringolysin O production for the localization and quantification of membrane cholesterol in human and mouse brain and liver. *STAR Protoc.* **3**, 101068 (2022).
142. Jumper, J. et al. Highly accurate protein structure prediction with AlphaFold. *Nature* **596**, 583–589 (2021).
143. Jones, G., Willett, P., Glen, R. C., Leach, A. R. & Taylor, R. Development and validation of a genetic algorithm for flexible docking. *J. Mol. Biol.* **267**, 727–748 (1997).
144. Famulari, A. et al. Heme Spin Distribution in the Substrate-Free and Inhibited Novel CYP116B5hd: A Multifrequency Hyperfine Sublevel Correlation (HYSCORE) Study. *Molecules* **29** https://doi.org/10.3390/molecules29020518 (2024).
145. Xu, L. & Chen, L. Y. Molecular determinant of substrate binding and specificity of cytochrome P450 2J2. *Sci. Rep.* **10**, 22267 (2020).
146. Jo, S., Kim, T., Iyer, V. G. & Im, W. CHARMM-GUI: a web-based graphical user interface for CHARMM. *J. Comput Chem.* **29**, 1859–1865 (2008).
147. Varadi, M. et al. AlphaFold Protein Structure Database in 2024: providing structure coverage for over 214 million protein sequences. *Nucleic Acids Res.* **52**, D368–D375 (2024).
148. Tian, C. et al. ff19SB: amino-acid-specific protein backbone parameters trained against quantum mechanics energy surfaces in solution. *J. Chem. Theory Comput.* **16**, 528–552 (2020).
149. Stevison, F., Hogarth, C., Tripathy, S., Kent, T. & Isoherranen, N. Inhibition of the all-trans retinoic acid (atRA) hydroxylases CYP26A1 and CYP26B1 results in dynamic, tissue-specific changes in endogenous atRA signaling. *Drug Metab. Dispos.* **45**, 846–854 (2017).

150. Artyukhov, A. S. et al. New genes for accurate normalization of qRT-PCR results in study of iPS and iPS-derived cells. *Gene* **626**, 234–240 (2017).
151. Sud, M. et al. Metabolomics Workbench: an international repository for metabolomics data and metadata, metabolite standards, protocols, tutorials and training, and analysis tools. *Nucleic Acids Res.* **44**, D463–D470 (2016).

Acknowledgements

We thank Jens Schwamborn (Luxembourg University) and his group for providing their published MO datasets. We acknowledge support from the Deutsche Forschungsgemeinschaft (DFG) (PR1527/5-1, PR1527/6-1, PR1527/15-1, PR1527/14-1, and PR1527/13-1 to A.P.; RO5380/1-1 to A.R.; Ro2327/13-2 to C.R.R.; AL2956/1-1 to I.A-M.; VE366/12-1 to N.V.), the European Joint Programme on Rare Diseases (EJP RD) and Federal Ministry of Research, Technology and Space (BMFTR) (CureMILS #01GM2002A to A.P., #01GM2002B to O.P.), the Medical Faculty of Heinrich Heine University (FoKo grant to A.P. and S.C.), the European Commission's Horizon Europe Programme (SIMPATHIC #101080249 to A.P. and M.S.), AFM-Téléthon (SildeMITO #28545 to A.P. and M.S.; GenT-Leigh #29044 to A.P.), the United Mitochondrial Disease Foundation (UMDF) and the Leigh Syndrome International Consortium (LSIC) (to A.P.), People Against Leigh syndrome (PALS) (to A.P.), the Foundation Maladies Rare and Association (AMMi) (to A.P.), the patient organizations Mitocon, Cure Mito, Cure ATP6, Mito Foundation, and MitoHelp (to A.P.), and the Eva Luise Köhler Foundation (to A.P. and M.S.), the Studienstiftung des deutschen Volkes (to S.L.), the Agència de Gestió d'Ajuts Universitaris i de Recerca (AGUAR) Generalitat de Catalunya through the Indústria del Coneixement LLAVOR program (grant 2024 LLAV 00069 to E.Pu.), National Science Center OPUS (#2017/27/B/NZ1/02401 to P.L.), and funds from MICINN (PID2021-125079OA-I00 to E.Pu.). A.Sp. and I.J.H. receive research support from the UK Medical Research Council (MR/X002365/1), Muscular Dystrophy UK (17GRO-PG24-0184-1), and the CHAMP Foundation. A.Sp. is the recipient of a Miriam Marks Senior Fellowship, Brain Research UK (202021-26) and receives funds from the Lily Foundation. I.J.H. is supported by grants from the Instituto de Salud Carlos III PI20/00096, the Spanish Ministry of Science, PID2023-151649NB-I00, and the Basque Government Department of Health (Osasun Saila, Eusko Jaurlaritzako) (grants 2021111070; 2022333050; 2018111043; 2018222031). M.M.O. was partially supported by the Ikerbasque, Basque Foundation for Science IKUR strategy, Neurodegenprot project. S.L. was supported by the Studienstiftung des deutschen Volkes. J.F-C acknowledges support from the MICINN (PID2022-142956OB-100 and PID2025-173094OB-I00), the National Cancer Institute PO1 CA281819-O1A1 from the NIH, and the CIBEREHD and the European Horizon´s research and Innovation program HORIZON-HLTH-2022-STAYHLTH-02 under agreement #101095679). We are grateful to Anje Sporbert (Advanced Light Microscopy, MDC, Berlin) for help with the mitochondrial movement recordings and acknowledge the Center for Advanced Imaging (CAi) at Heinrich Heine University Düsseldorf for providing access to the PerkinElmer Operetta CLS (DFG grant # INST 208/760-1 FUGG) and Olympus FV3000 microscope.

Author contributions

Conceptualization, A.P., C.M., A.D.S.; Methodology, C.M., S.O., A.W., M.M-O., L.P., M.T., S.Z., D.H., A.Se., G.I., C.J., S.L., S.B., I.A-M.; Formal Analysis, S.O., T.M.P., C.M., A.Z., I.A-M., B.M., A.R-W., J.D., M.L.M.; Resources, E.M., A.P., A.D.S., P.L., A.Sp., E.Pe., F.D., A.R., N.R., K.W., F.X.S., J.F-C., N.V., S.C., M.S., E.Pu., C.R.R.; Writing – Original Draft, C.M., A.P.; Writing – Review & Editing, A.P., C.M., S.O., A.D.S., O.P., C.R.R., L.P., A.S., I.J.H., I.A-M., E.Pu.; Supervision, A.P., A.D.S., O.P., I.J.H., C.R.R., F.D., A.P-M.; Visualization, C.M., A.P.; Funding Acquisition, A.P., A.D.S., O.P.

Funding

Open Access funding enabled and organized by Projekt DEAL.

Competing interests

C.M., S.O., A.D.S., and A.P. filed a patent application for the use of talarozole in mitochondrial diseases. C.M., K.W., E.Pe, and A.P. filed a patent application for the use of sertaconazole in mitochondrial diseases. The remaining authors declare no competing interests.

Additional information

Supplementary information The online version contains supplementary material available at https://doi.org/10.1038/s41467-026-71391-2.

Correspondence and requests for materials should be addressed to Antonio Del Sol or Alessandro Prigione.

Peer review information *Nature Communications* thanks the anonymous reviewers for their contribution to the peer review of this work. A peer review file is available.

Reprints and permissions information is available at http://www.nature.com/reprints

Publisher's note Springer Nature remains neutral with regard to jurisdictional claims in published maps and institutional affiliations.

Open Access This article is licensed under a Creative Commons Attribution 4.0 International License, which permits use, sharing, adaptation, distribution and reproduction in any medium or format, as long as you give appropriate credit to the original author(s) and the source, provide a link to the Creative Commons licence, and indicate if changes were made. The images or other third party material in this article are included in the article's Creative Commons licence, unless indicated otherwise in a credit line to the material. If material is not included in the article's Creative Commons licence and your intended use is not permitted by statutory regulation or exceeds the permitted use, you will need to obtain permission directly from the copyright holder. To view a copy of this licence, visit http://creativecommons.org/licenses/by/4.0/.

© The Author(s) 2026

[1]Department of General Pediatrics, Neonatology and Pediatric Cardiology, Medical Faculty and University Hospital Düsseldorf, Heinrich Heine University Düsseldorf, Düsseldorf, Germany. [2]Faculty of Mathematics and Natural Sciences, Heinrich Heine University Düsseldorf, Düsseldorf, Germany. [3]Computational Biology Group, Luxembourg Centre for Systems Biomedicine, University of Luxembourg, Esch-sur-Alzette, Luxembourg. [4]University of Pittsburgh School of Medicine, Vascular Medicine Institute, Pittsburgh, PA, USA. [5]Institute of Neurobiology, Heinrich Heine University, Düsseldorf, Germany. [6]Fraunhofer Institute for Translational Medicine and Pharmacology ITMP, Discovery Research ScreeningPort, Hamburg, Germany. [7]Department of Neurosciences, Biogipuzkoa Health Research Institute, San Sebastian, Spain. [8]Max Delbrück Center for Molecular Medicine in the Helmholtz Association (MDC), Berlin, Germany. [9]Berlin Institute for Medical Systems Biology (BIMSB), Berlin, Germany. [10]Neuropsychiatry and Laboratory of Molecular Psychiatry, Department of Psychiatry and Neurosciences, Charité—Universitätsmedizin, Berlin, Germany. [11]Department of Molecular Biology, Institute of Genetics and Animal Biotechnology, Polish Academy of Sciences, Jastrzebiec n/Warsaw, Poland. [12]Unit of Biophysics, Department of Biochemistry and Molecular Biology Institute of Neurosciences,

Universitat Autònoma de Barcelona, Barcelona, Spain. [13]Charité—Universitätsmedizin, Berlin, Germany. [14]Perlara PBC, Vancouver, WA, USA. [15]Institute of Cell Biology, Heinrich Heine University, Düsseldorf, Germany. [16]Cluster of Excellence Cellular Stress Responses in Aging-associated Diseases (CECAD), Faculty of Medicine and University Hospital of Cologne, University of Cologne, Cologne, Germany. [17]Cure Mito Foundation, McKinney, TX, USA. [18]Celltec-UB, Departament de Biologia Cellular, Fisiologia i Immunologia, Institut de Neurociències, Universitat de Barcelona, Barcelona, Spain. [19]Department of Molecular and Cellular Biomedicine, Institute of Biomedical Research of Barcelona (IIBB), CSIC, Barcelona, Spain. [20]Liver Unit, Hospital Clinic i Provincial de Barcelona, Institut d'Investigacions Biomèdiques August Pi i Sunyer (IDIBAPS), Barcelona, Spain. [21]Centro de Investigación Biomédica en Red (CIBEREHD), Barcelona, Spain. [22]Department of Medicine, Keck School of Medicine, University of Southern California, Los Angeles, CA, USA. [23]IUF-Leibniz Research, Institute for Environmental Medicine, Düsseldorf, Germany. [24]Dept. for the Promotion of Human Science and Quality of Life, San Raffaele University of Rome, Rome, Italy. [25]Institute of Physiological Chemistry, University Medical Center of the Johannes Gutenberg University, Mainz, Germany. [26]Department of Clinical and Movement Neurosciences, UCL Queen Square Institute of Neurology, Royal Free Campus, London, UK. [27]Department of Neuropediatrics, Charité–Universitätsmedizin, Berlin, Germany. [28]NeuroCure Cluster of Excellence, Berlin, Germany. [29]German Center for Cardiovascular Research (DZHK), Berlin, Germany. [30]National Center for Tumor Diseases (NCT), German Cancer Consortium (DKTK), Berlin, Germany. [31]German Center for Neurodegenerative Diseases (DZNE), Berlin, Germany. [32]Genome Engineering and Model Development lab (GEMD), IUF-Leibniz Research, Institute for Environmental Medicine, Düsseldorf, Germany. [33]IKERBASQUE, Basque Foundation for Science, Bilbao, Spain. [34]University of the Basque Country-Bizkaia Campus, Bilbao, Spain. [35]CIBERNED (Center for Networked Biomedical Research on Neurodegenerative Diseases) Ministry of Economy and Competitiveness, Institute Carlos III), Madrid, Spain. [36]Neuroscience Institute, Department of Cell Biology, Physiology and Immunology, Autonomous University of Barcelona, Bellaterra, Spain. [37]CIC bioGUNE-BRTA (Basque Research and Technology Alliance), Bizkaia Technology Park, Derio, Spain. [38]Present address: Axol Bioscience Ltd, Berlin, Germany. [39]Present address: Centogene GmbH, Rostock, Germany. [40]These authors contributed equally: Carmen Menacho, Satoshi Okawa. [41]These authors jointly supervised this work: Antonio Del Sol, Alessandro Prigione. ✉e-mail: antonio.delsol@uni.lu; alessandro.prigione@hhu.de

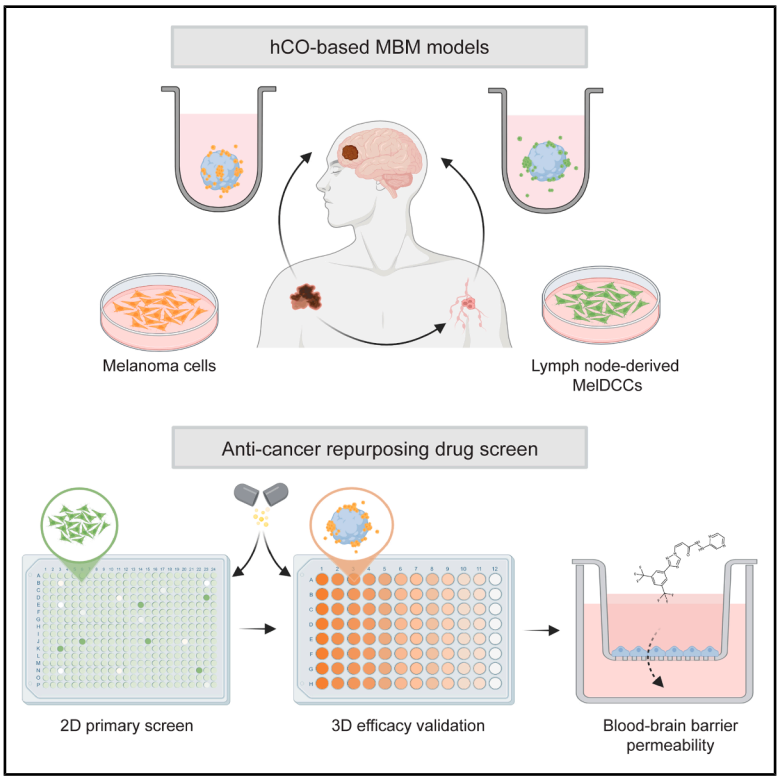
14. Appendix VI

Cell Reports
Methods

Article

Cortical organoid-derived models of the melanoma brain metastatic niche enable prioritization of cancer-targeting drugs

Graphical abstract



Highlights

- We develop melanoma brain metastasis (MBM) models using human cortical organoids
- MBM models can be applied to identify therapies targeting metastatic progression
- Compound screening with MBM models nominates selinexor as a therapeutic candidate

Authors

Kim Krieg, Silvia Materna-Reichelt, Tobias Naber, ..., Melanie Werner-Klein, Joachim Wegener, Ole Pless

Correspondence

ole.pless@itmp.fraunhofer.de

In brief

Krieg et al. develop melanoma brain metastasis models based on cortical brain organoids. They demonstrate the potential for therapeutic applications, screening a library of anti-cancer compounds and identifying the XPO1 inhibitor selinexor as a promising candidate that demonstrates effectiveness against cancer cells while maintaining low toxicity.

Krieg et al., 2025, Cell Reports Methods *5*, 101236
December 15, 2025 © 2025 The Author(s). Published by Elsevier Inc.
https://doi.org/10.1016/j.crmeth.2025.101236

CellPress

Please cite this article in press as: Krieg et al., Cortical organoid-derived models of the melanoma brain metastatic niche enable prioritization of cancer-targeting drugs, Cell Reports Methods (2025), https://doi.org/10.1016/j.crmeth.2025.101236

Cell Reports Methods

CellPress
OPEN ACCESS

Article

Cortical organoid-derived models of the melanoma brain metastatic niche enable prioritization of cancer-targeting drugs

Kim Krieg,[1] Silvia Materna-Reichelt,[2] Tobias Naber,[3,4] Fatima-Zahra Rachad,[1] Pia Kauven,[1] Arjen Weller,[1] Undine Haferkamp,[1] Annika Wittich,[1] Andrea Zaliani,[1] Marcel S. Woo,[5] Mark Walkenhorst,[5] Malte Siegmund,[6] Jann Harberts,[1,6] Robert Zierold,[6] Robert Blick,[6] Christian Conze,[7] Patricia Muschong,[8] Dominik Miltner,[8] Manuel A. Friese,[5] Mario Mezler,[8] Heiko Siegmund,[9] Katja Evert,[9] Susanne Krasemann,[10,11] Nataša Stojanović Gužvić,[2] Christoph A. Klein,[2,12] Melanie Werner-Klein,[12] Joachim Wegener,[3,4] and Ole Pless[1,13,*]

[1]Fraunhofer Institute for Translational Medicine and Pharmacology ITMP, Discovery Research ScreeningPort, 22525 Hamburg, Germany
[2]Fraunhofer Institute for Toxicology and Experimental Medicine ITEM-R, Division of Personalized Tumor Therapy, 93053 Regensburg, Germany
[3]Fraunhofer Institute for Electronic Microsystems and Solid-State Technologies EMFT, Cell-based Sensor Technology, 93053 Regensburg, Germany
[4]Institute for Analytical Chemistry, Chemo- & Biosensors, University of Regensburg, 93053 Regensburg, Germany
[5]Institute of Neuroimmunology and Multiple Sclerosis, University Medical Center Hamburg-Eppendorf, 20251 Hamburg, Germany
[6]Center for Hybrid Nanostructures, University of Hamburg, 22761 Hamburg, Germany
[7]Technology Platform Microscopy and Image Analysis (TP MIA), Leibniz Institute of Virology, 20251 Hamburg, Germany
[8]AbbVie Deutschland GmbH & Co. KG, 67061 Ludwigshafen, Germany
[9]Institute for Pathology, University of Regensburg, 93053 Regensburg, Germany
[10]Institute for Neuropathology, University Medical Center Hamburg-Eppendorf, 20246 Hamburg, Germany
[11]Experimental Pathology Core Facility, University Medical Center Hamburg-Eppendorf, 20246 Hamburg, Germany
[12]Experimental Medicine and Therapy Research, University of Regensburg, 93053 Regensburg, Germany
[13]Lead contact
*Correspondence: ole.pless@itmp.fraunhofer.de
https://doi.org/10.1016/j.crmeth.2025.101236

MOTIVATION There is a current lack of human models to identify effective therapies targeting brain metastases. In this work, we therefore sought to develop a robust method to study and target vulnerabilities of human metastases in the context of brain niche tissue. We aimed to integrate the high-throughput screening-compatible model into workflows for the identification of candidate therapeutics that counteract metastatic progression.

SUMMARY

Effective systemic therapies against brain metastases are severely limited. To understand and target vulnerabilities of human metastases in a brain niche context, we developed reproducible melanoma brain metastasis (MBM) models for metastasis-integrating drug screening. We co-cultured A375 melanoma cells or tumor regional lymph node-derived disseminated cancer cells (DCCs) in close proximity with human induced pluripotent stem cell-derived cortical organoids (hCOs). In these, RNA sequencing revealed an upregulation of metastasis-associated features. First, A375 cells and DCCs were screened against an anti-cancer library containing 315 compounds. Hits were ranked by neurotoxicity, central nervous system permeation, and anti-DCC efficacy. Only a minority of hits effectively targeted A375-MBMs, with the first-in-class XPO1 inhibitor selinexor emerging as top hit. Selinexor also demonstrated efficacy in DCC-MBM models and low toxicity on hCOs, suggesting a promising therapeutic window in clinically applied doses. Collectively, the MBM model provides a tool for identifying candidate therapies counteracting metastatic progression.

INTRODUCTION

Brain metastasis (BrM), the dissemination and growth of cancer cells to the central nervous system (CNS), occurs in at least 20% of cancer patients and imposes a significant clinical challenge.[1] Currently available treatment options include surgery, radiation therapy, and systemic therapies, primarily immune checkpoint inhibitors and targeted therapy, providing benefits to subgroups

This is an open access article under the CC BY license (http://creativecommons.org/licenses/by/4.0/).

Please cite this article in press as: Krieg et al., Cortical organoid-derived models of the melanoma brain metastatic niche enable prioritization of cancer-targeting drugs, Cell Reports Methods (2025), https://doi.org/10.1016/j.crmeth.2025.101236

of patients. However, systemic therapies are frequently associated with limited efficacy and fail to reliably prevent relapse and long-lasting disease progression.[2–5] Consequently, the use of predictive preclinical BrM models to target therapeutic vulnerabilities with anti-cancer agents could pave the way for prospective clinical trials that improve understanding of efficacy and CNS safety. Thus, several studies have developed *ex vivo* drug screening platforms utilizing mouse organotypic cultures, patient-derived and xenograft models.[6–8] In melanoma patients, the lifetime risk of developing BrM stays notably high up to approximately 40%.[9–11] During the early stages of metastasis, melanoma cells undergo phenotypic and molecular alteration and spread primarily to regional lymph nodes, which act as key exit routes for systemic dissemination via the bloodstream enabling melanoma cells to extravasate into the brain parenchyma or other distant organs.[12–16] Importantly, quantitative assessments of disseminated cancer cells (DCCs) in sentinel lymph node biopsies of melanoma patients allow for prediction of disease progression.[17,18] Thus, tumor regional lymph nodes represent reservoirs of the earliest metastatic seeds, providing an accessible and clinically relevant source of cells for preclinical drug testing (S.M.-R., M.W.-K., C.A.K., K. Weidele, C. Werno, and S. Treitschke, unpublished data). Metastatic organ colonization, the progression from solitary cancer cells to micrometastases, is considered the limiting step in the metastatic cascade.[19,20] During this critical phase, DCCs utilize phenotypic plasticity to adapt to and thrive within the foreign tumor microenvironment (TME) of the metastatic sites, making early colonization a pivotal therapeutic window. Bidirectional communication between invading DCCs and native cellular and non-cellular components has critical impact on metastatic growth, treatment response, and resistance.[21–25] This highlights the CNS microenvironment as an important component to consider in the development of novel therapeutic strategies targeting metastatic cancer cells in the brain. Human cortical organoids (hCOs) are self-organizing CNS-like structures derived from human induced pluripotent stem cells (hiPSCs). They contain neurons and astrocytes, which support neural function and can modulate inflammatory responses.[26,27] Such hCOs have been utilized as scaffolding host tissues for several primary tumor cells, such as small-cell lung cancer and breast cancer cells, to mimic BrM.[28–30] In this study, we implemented and validated a scalable platform of melanoma brain metastasis (MBM) models by using hCOs as a niche tissue for the colonization of melanoma cells and patient-derived DCCs. Based on this model, an anti-cancer drug repurposing library was evaluated with respect to metastasis regression *in situ*, enabling the identification and validation of biologically relevant drug candidates in a human brain niche-specific context.

RESULTS

Establishment of a scalable platform for cortical organoid and BrM model generation

To generate reproducible hCOs suitable for screening applications, we adapted a guided differentiation protocol[31] and established a standardized culture and compound treatment procedure (Figure 1A). hCOs generated from wild-type hiPSCs (WISCi004-B) were uniformly aggregated in microwells until day 6, after which they were individually transferred to 96-well round-bottom ultra-low attachment plates for further differentiation (Figures 1A; S1A). Throughout the culture period in 96-well plates, we monitored the organoid morphology of representative batch plates through bright-field imaging and spheroid detection analysis (Figure S1B). hCOs derived from hiPSC line WISCi004-B (Figure 1B), but also ZIPi013-B and HHUUKDi009-A (Figure S1C), exhibited progressive growth, reaching a similar area of approximately 2 mm^2 (1.970 ± 0.002 mm^2), with WISCi004-B demonstrating the lowest degree of intra-batch variability. Notably, these 50-day-old hCOs can be generated with consistent organoid areas and roundness both within individual batches and across batches, with a mean coefficient of variation of 11.56% ± 1.13% (area, Figure 1C) and 10.45% ± 0.41% (roundness, Figure S1D). Additionally, measurements of the partial oxygen pressure in randomly selected hCOs from different batches revealed similar profiles and adequate mean oxygenation above 45 torr, even within the central tissue core (Figures 1D and S1E).[32–35] These findings demonstrate the simultaneous production of reproducible and physiologically active batches of hundreds of hCOs. To initiate and visualize MBMs, we used the human melanoma cell line A375 stably transduced with a red fluorescent protein (RFP) tdTomato reporter (Figure S1F). A375 cells were added as a single-cell suspension to each 43-day-old hCO and co-cultured for 7 days (day 43 + 7, referred to as A375-MBMs), followed by characterization or compound treatment (Figure 1A). During this co-culture period, we selectively monitored the fluorescence intensity of cancer cells within the hCO area, representing colonized cancer cells (Figure S1G). The fluorescence intensity increased progressively over time, indicating significant adherence and proliferation of A375 cells in the hCO tissue (Figure 1E). Importantly, a comparative analysis between batches showed minimal intra- and inter-batch variability, with a mean coefficient of variation of 7.92% ± 1.95% (Figure 1F). These data indicate a robust assay window, in which potent drugs may reduce the fluorescence intensity as an indicator of A375-MBM viability to baseline. Light-sheet microscopy of a cleared A375-MBM sample, followed by three-dimensional rendering, revealed multiple RFP+ A375 colonies of various sizes and shapes distributed across the hCO, co-stained for the neuronal marker MAP2 (Figure 1G). These data suggest that the melanoma cells exhibit pronounced adhesion, infiltration into, and colonization of the neural parenchyma.

Characterization of brain parenchyma and melanoma BrM-like signatures

To investigate the hCO cytoarchitecture, samples from different batches were sectioned for histochemical analysis. By day 50, the majority of cells throughout the parenchyma had differentiated into neuronal cells and strongly expressed the marker MAP2 (Figure 2A). hCOs did not fully reach postmitotic stages, since we identified neural rosettes with a population of neural progenitor cells (NPCs) expressing PAX6 (Figure 2A). Following directed neural development, hCOs developed cortical-like structures with both ventricular zones (Figure S2A) and cortical plate, including superficial cortical neurons expressing SATB2 (Figure 2A). Additionally, we performed RT-qPCR analysis and

Please cite this article in press as: Krieg et al., Cortical organoid-derived models of the melanoma brain metastatic niche enable prioritization of cancer-targeting drugs, Cell Reports Methods (2025), https://doi.org/10.1016/j.crmeth.2025.101236

CellPress
OPEN ACCESS

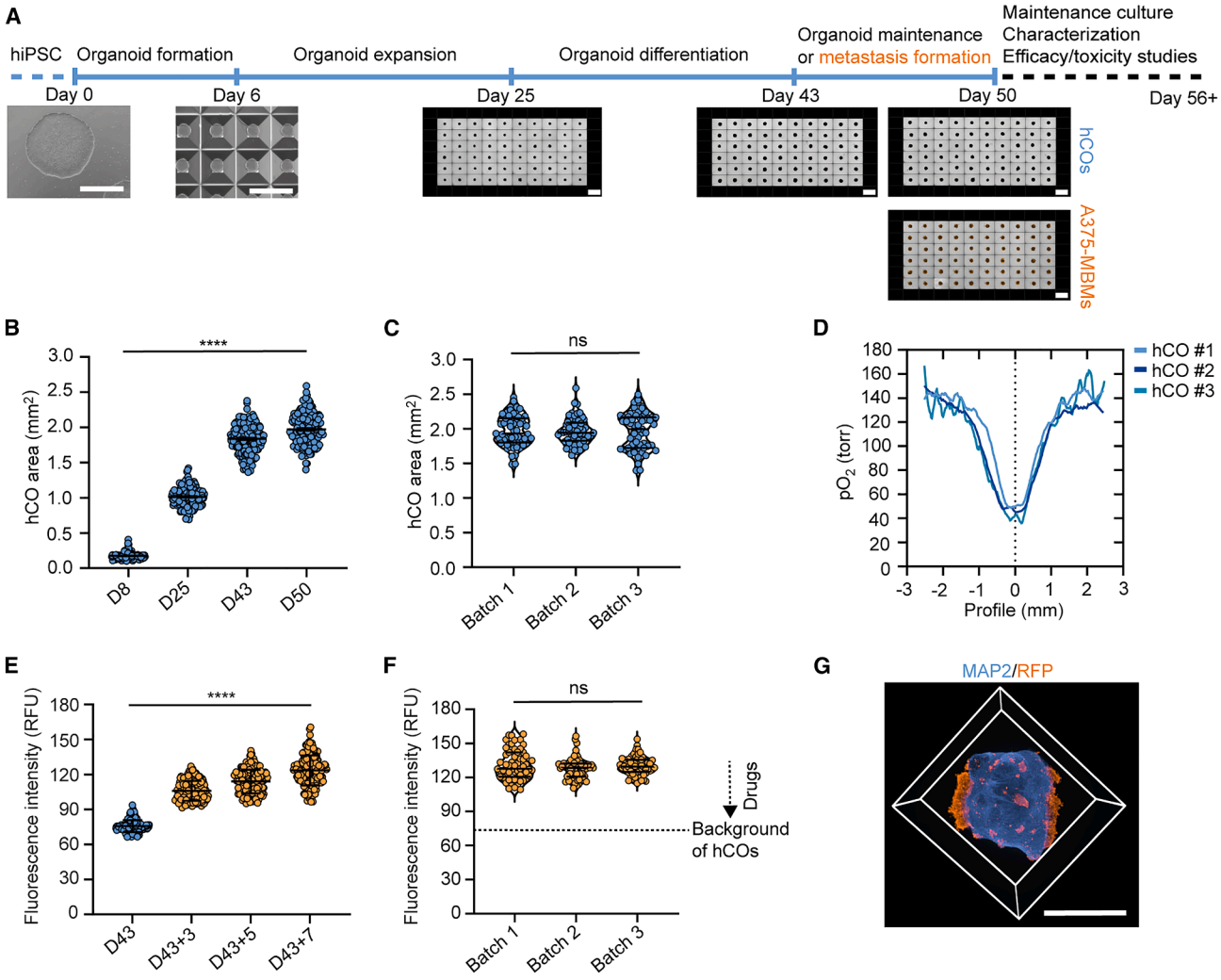


Figure 1. Robust generation of human cortical organoids and melanoma brain metastases in a screening-compatible format

(A) Schematic overview and microscopic images illustrating stages of hCO differentiation and metastasis formation using fluorescent labeled A375 melanoma cells (A375-MBMs) along the experimental timeline. Scale bars in both left images represent 1 mm; in 96-well plate overview the scale bars represent 2 mm.

(B) Increase of hCO area during differentiation ($n \geq 175$ hCOs from 3 independent batches per time point). Data are presented as mean ± SEM. Statistical analysis was performed using one-way ANOVA, followed by Tukey's multiple comparisons test. ****$p < 0.001$.

(C) Consistent mean hCO area at day 50 ($n \geq 58$ hCOs per batch). Data are presented as median and lower/upper quartile. Statistical analysis was performed using one-way ANOVA, followed by Tukey's multiple comparisons test. ns, not significant.

(D) Reproducible oxygen profiles through hCOs after 6 h of attachment to the sensor foil ($n = 3$ hCOs from independent batches). The dashed vertical line marks the center of hCOs.

(E) Time course analysis of A375-MBMs fluorescence intensity during 7 days of colonization ($n \geq 176$ hCOs from 3 independent batches). Data are presented as mean ± SEM. Statistical analysis was performed using one-way ANOVA, followed by Tukey's multiple comparisons test. ****$p < 0.001$.

(F) Consistent mean fluorescence intensity of A375-MBMs after 7 days ($n \geq 58$ per batch), offering a stable assay window to test drugs reducing viability of colonized A375 cells. Data are presented as median and lower/upper quartile. Statistical analysis was performed using one-way ANOVA, followed by Tukey's multiple comparisons test. ns, not significant.

(G) Three-dimensional rendering of A375-MBMs visualized by whole-mount staining and light-sheet microscopy for A375 cells (RFP) and neuronal tissue (MAP2). Scale bar represents 1 mm. See also Figure S1.

observed that the transcriptional identity of neural progenitors (*PAX6*) and neurons (*MAP2*), including glutamatergic neurons (*VGLUT1*) and synapses (*BSN*), was reproducible across differentiation batches (Figure 2B). Within the neural tissue (Figure S2B), we identified synapse-like structures (Figure S2C), and, for functional analysis, outgrowing neurons from post-seeded differentiated hCOs were accessible for patch-clamp techniques. Neurons exhibited passive membrane properties similar to published data of diverse hiPSC-based neuronal *in vitro* cultures (Figures S2D and S2E).[36,37] Functional neurons were found across different batches as demonstrated by their AP trains with distinct in- and outflow currents and defined AP

Please cite this article in press as: Krieg et al., Cortical organoid-derived models of the melanoma brain metastatic niche enable prioritization of cancer-targeting drugs, Cell Reports Methods (2025), https://doi.org/10.1016/j.crmeth.2025.101236

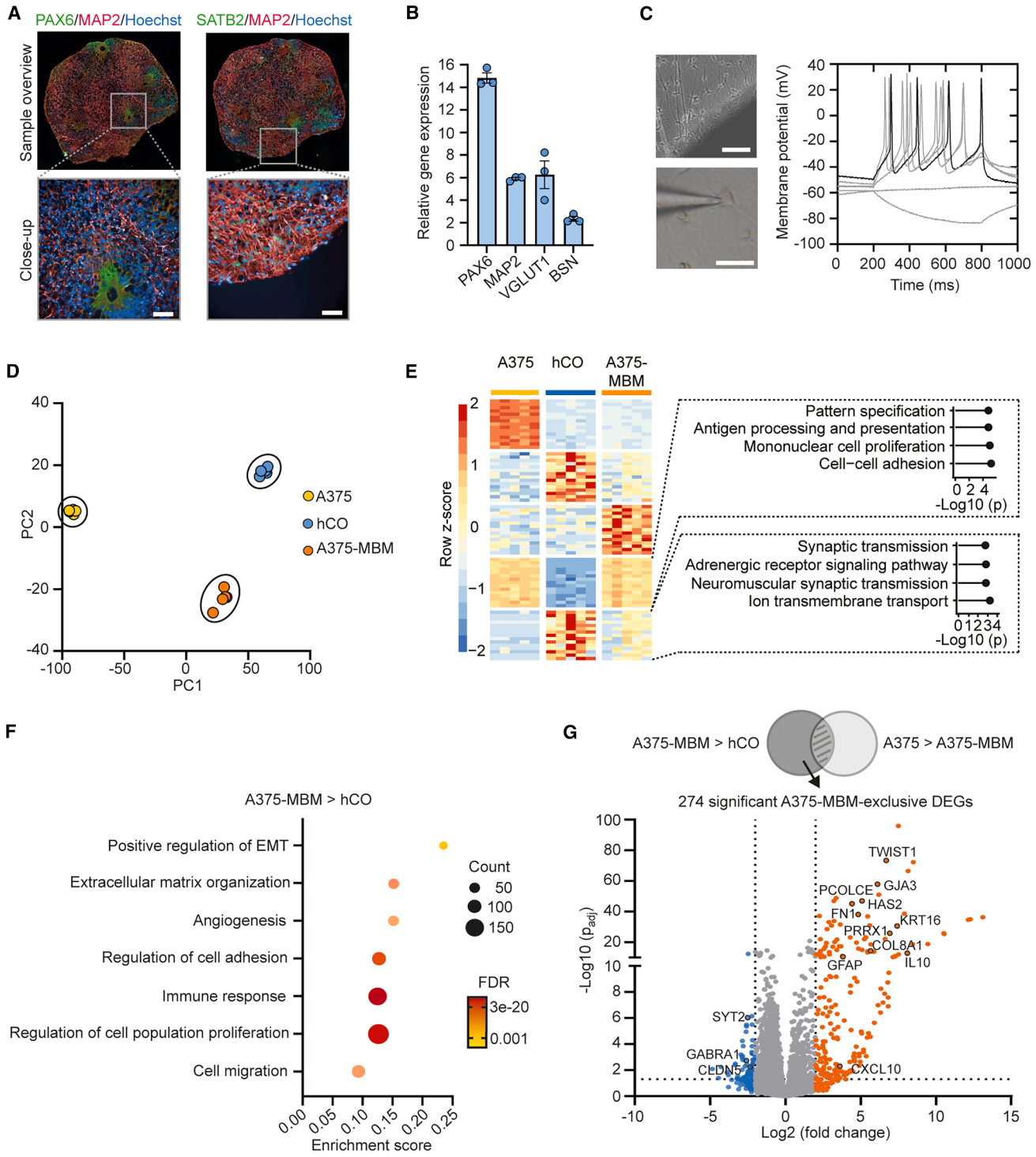


Figure 2. Characterization of cortical organoids and their co-culture with A375 cells

(A) Immunofluorescent confocal images of different hCO cell types stained for PAX6, MAP2, and SATB2. Images present sample overview or labeled sections with higher magnification. Scale bars represent 50 μm.

(B) hCO gene expression profile of *PAX6*, *MAP2*, *VGLUT1*, and *BSN* (n = 3 independent batches). Data are presented as mean ± SEM.

(C) Representative action potentials of outgrowing neurons from plated 50-day-old hCOs recorded during electrode polarization in current clamp mode. Black trace corresponds to rheobase value. Scale bar (upper) represents 100 μm, scale bar (lower) represents 20 μm.

(D) Principal-component analysis plot of mRNA-sequencing data of A375 cells, hCOs, and A375-MBMs (n = 5 samples per condition).

(legend continued on next page)

Please cite this article in press as: Krieg et al., Cortical organoid-derived models of the melanoma brain metastatic niche enable prioritization of cancer-targeting drugs, Cell Reports Methods (2025), https://doi.org/10.1016/j.crmeth.2025.101236

shapes (Figures 2C and S2F–S2I), i.e., type 5 neurons.[38] We investigated the molecular changes associated with A375 colonization and performed bulk mRNA sequencing of five samples each of A375 cells prior to colonization, hCOs alone, and A375-MBMs. Principal-component analysis (PCA) revealed a strong clustering of the samples within the different groups (Figure 2D). In accordance, we detected strong neuronal signatures in hCOs and A375-MBMs as well as transcriptional signatures related to proliferation and adhesion in A375 cells and A375-MBMs that were absent in hCOs (Figure 2E). Next, we aimed to identify genes that were differentially expressed by co-culturing the A375 cells and hCOs. Therefore, we focused on differentially expressed genes (DEGs) in A375-MBMs compared to hCOs. Gene ontology (GO) term analysis confirmed an enrichment of genes involved in metastasis-associated processes, including "immune response" (GO:0006955), "extracellular matrix organization" (GO:0030198), and "positive regulation of epithelial-to-mesenchymal transition (EMT)" (GO:0010718) (Figure 2F). To identify genes that were exclusively differentially expressed in A375-MBMs, we omitted candidates that were predominantly expressed in A375 cells prior to brain organoid colonization. This analysis identified a total number of 274 DEGs, including 199 upregulated and 75 downregulated genes (Figure 2G). Among the most significant DEGs, we identified *TWIST1*, a key transcription factor inducing EMT (−Log10 (padj) = 73.45). In summary, we identified significant transcriptional changes associated with EMT (*TWIST1* and *PRRX1*), extracellular matrix (ECM) (*PCOLCE*, *HAS2*, and *FN1*), and immune response (*GFAP*, *IL10*, and *CXCL10*) as a result of brain organoid colonization.

To assess the spatial relationship and distribution of metastatic A375 cells within the MBMs, we performed histological staining on paraffin-embedded samples. We observed a nested growth pattern, with RFP-expressing cancer cells forming nodule-like structures at the organoid surface, with more and bigger structures in prolonged A375-MBM cultures (day 43 + 13/56) (Figures 3A and 3B). A subpopulation of mostly single A375 cells penetrated the superficial organoid layers. Consistent with these data, ultrastructural analysis using transmission electron microscopy demonstrated direct contact sites between A375 and neuronal cells (Figure 3C). Notably, we detected besides the presence of Vimentin (Figure 3D) also a strong transcriptional and protein induction of the ECM component Fibronectin 1 (*FN1*; −Log10 (padj) = 37.97) and Collagen type VIII (COL8A1; −Log10 (padj) = 14.43) (Figures 2G and 3E), indicative of a mesenchymal phenotype of colonizing A375 cells. Furthermore, upregulation of GFAP (−Log10 (padj) = 10.66) suggests the presence of astrocyte-like cells (Figure 2F). In prolonged A375-MBM cultures (day 43 + 13/56), a population of astrocyte-like cells was observed in superficial layers, interspersed between melanoma cells and neurons, which were absent in the corresponding hCOs (Figure 3G). In addition, the expression of CXCL10, a chemokine associated with melanoma brain tropism,[39] was increased in supernatant of A375-MBM models in comparison to the corresponding hCOs (Figure 3G).

Drug repurposing strategy for MBMs

To identify clinically promising compounds targeting metastases with robust efficacy and established safety profiles, we conducted a drug repurposing screen using a focused library of 315 cancer-targeting compounds (all Food and Drug Administration approved or in clinical development; Figure 4A). We used GFP-labeled DCC lines derived from tumor regional lymph nodes of melanoma patients (MelDCC)[13] or primary tumor (A375), representing the diverse, previously described differentiation phenotypes[40] (Figures 4A and S3A). Normal human epidermal melanocytes (NHEMs) served as non-cancer controls. Given the importance of *BRAF* and *NRAS* driver mutations, we included BRAF-mutant (V600E: MelDCC3, MelDCC11, and A375) and NRAS-mutant (G12C: MelDCC8) lines. Differentiation phenotypes were confirmed by fluorescence-activated cell sorting analysis of Melan-A (melanocytic) and NGFR (neural-crest) expression (Figures 4B and S3B). While A375 and MelDCC11 represent undifferentiated and melanocytic phenotypes, respectively, MelDCC3 and MelDCC8 contain mixed phenotypes (melanocytic, neural crest-like, and undifferentiated). With this diverse melanoma panel at hand, the 315 compound anti-cancer library was screened at a concentration of 1 μM in 2D MelDCCs and A375 cells, recording viability values after 5 days of treatment (Figure 4C). Screening data of MelDCC11 and NHEMs were sourced from S.M.-R., M.W.-K., C.A.K., K. Weidele, C. Werno, and S. Treitschke (unpublished data) and re-analyzed. Using 10 μM bortezomib, a potent pan-proteasome inhibitor with high anti-cancer activity,[41] as a positive control and 0.1% DMSO as vehicle, we reached Z' scores $\geq$0.67 for each screening plate (Figure S3C), indicative of a high-quality screen,[42] with high correlation between replicates (Figure S3D). Compounds were ranked for their strongest impact on mean viability on all cell lines tested (Figure 4C). We observed varying sensitivities to compounds between cell lines. MelDCC3, MelDCC8, and A375, which exhibit a more dedifferentiated phenotype based on their Melan-A and NGFR expression, were generally more responsive than the differentiated, melanocytic MelDCC11 line or NHEM cells. For rational hit selection, we first eliminated candidates exhibiting general cellular toxicity, characterized by <80% viability in control NHEM cells (Figure 4D). Next, we excluded compounds with neurotoxicity (<80% viability) based on previously published screening data and a high-quality drug repurposing library[43] using hiPSC-derived NPCs.[44,45] Considering the significant dependency of drug efficacy on blood-brain barrier (BBB) permeation, we further included physico-chemical properties into the selection process. Selected compounds presented a topological polar

(E) Top 10 differentially expressed genes identified by mRNA sequencing in the following modules: only upregulated in A375, only upregulated in hCO, only upregulated in A375-MBM, upregulated in A375 and A375-MBM, and upregulated in hCO and A375-MBM. The heatmap shows row *Z* scores. Gene ontology (GO) term of the differentially expressed genes in A375 and A375-MBM and in hCO and A375-MBM is additionally shown.

(F) GO term analysis of differentially upregulated genes in A375-MBMs in comparison to hCOs. FDR, false discovery rate.

(G) Volcano plot representation of significantly up- and downregulated differentially expressed genes in A375-MBM in comparison to hCO, excluding genes that were differentially upregulated in A375 in comparison to A375-MBM, thereby predominantly expressed in A375 cells before hCO colonization. See also Figure S2.

Please cite this article in press as: Krieg et al., Cortical organoid-derived models of the melanoma brain metastatic niche enable prioritization of cancer-targeting drugs, Cell Reports Methods (2025), https://doi.org/10.1016/j.crmeth.2025.101236

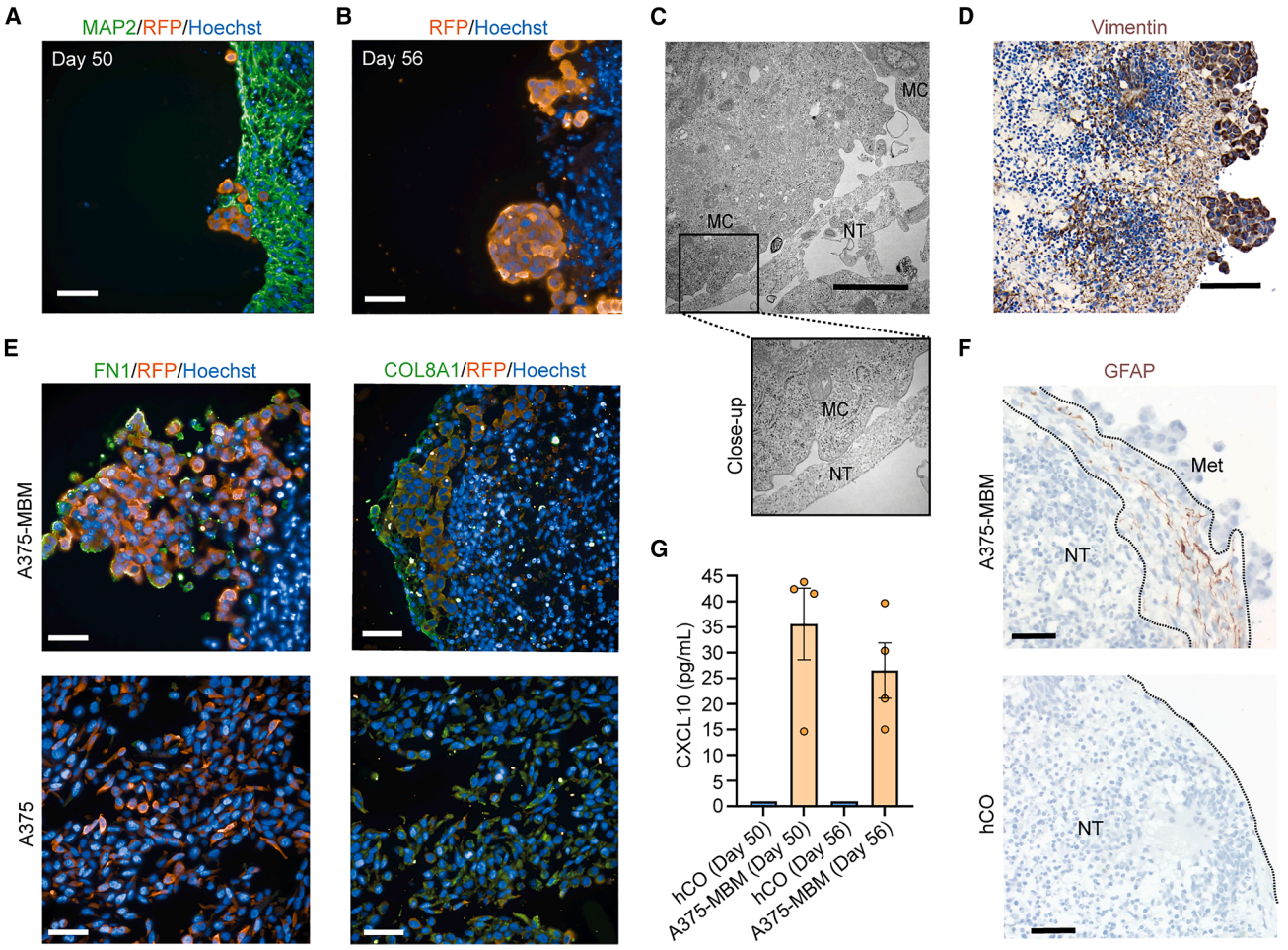


Figure 3. Validation of metastasis-like signatures in A375-MBMs

(A) Immunofluorescent confocal image of A375-MBMs on day 43 + 7 (day 50) stained for MAP2 and RFP indicates tumor colony formation. Scale bar represents 50 μm.

(B) Immunofluorescent confocal image of nodular metastasis outgrowth stained for RFP in prolonged A375-MBM cultures on day 43 + 13 (day 56). Scale bar represents 50 μm.

(C) Ultrastructural analysis of metastasis-like structures shows close proximity between melanoma cells (MCs) and neural tissue (NT) at day 43 + 7 (day 50). Scale bar represents 2 μm.

(D) Immunohistochemistry of A375-MBMs shows a strong Vimentin staining in the colonized melanoma cells at day 43 + 13 (day 56). Scale bar represents 100 μm.

(E) Immunofluorescent confocal images of A375 before and after colonization (A375-MBM) at day 43 + 13 (day 56) demonstrate staining of extracellular matrix components FN1 and COL8A1 in metastases. Scale bar represents 50 μm.

(F) GFAP-expressing cells in the interface of neural tissue (NT) and metastatic-like outgrowth (Met) in A375-MBMs and hCOs at day 43 + 13 (day 56) visualized by immunohistochemistry staining. Scale bar represents 50 μm.

(G) Elevated CXCL10 concentration in the supernatant of A375-MBM at day 43 + 7 (day 50) or day 43 + 13 (day 56) compared to hCOs ($n = 2$ samples of each, two independent differentiations). Data are presented as mean ± SEM. Values for hCOs are under the lower limit of detection and were set to 1.

surface area value below 118, assuming that the charged atomic space primarily influences the permeation through the BBB.[46] Finally, hits were characterized based on high efficacy (mean $E_{max} \geq 60\%$) to target the two most responsive MelDCC lines, MelDCC3 and MelDCC8. This process ultimately led to the nomination of seven compounds (Figure 4E): A MEK1/2 inhibitor (binimetinib), a XPO1 inhibitor (selinexor), a microtubule polymerization inhibitor (nocodazole), three HDAC inhibitors (pracinostat, vorinostat, and belinostat), and an antimetabolite (thioguanine). All candidates were confirmed in independent concentration-response titrations on MelDCC lines in 2D, but also 3D tumoroid culture, thereby increasing cancer tissue complexity (Figures 4F; S3E–S3J). To prioritize these validated hit compounds for their efficacy on BrM, we measured their cytotoxic effect in A375-MBM at a concentration of 10 μM for 72 h. We compared these results to a combination of BRAF and MEK1/2 inhibitors (encorafenib and binimetinib), one of the current standards of care in advanced melanoma[47] (Figure 4G). Notably, we identified selinexor as inducing the most significant decrease in fluorescence-based A375-MBM viability (26.6% ± 7.9% remaining viability). Consequently, selinexor was selected as the top candidate targeting BrM for further investigations.

Please cite this article in press as: Krieg et al., Cortical organoid-derived models of the melanoma brain metastatic niche enable prioritization of cancer-targeting drugs, Cell Reports Methods (2025), https://doi.org/10.1016/j.crmeth.2025.101236

CellPress
OPEN ACCESS

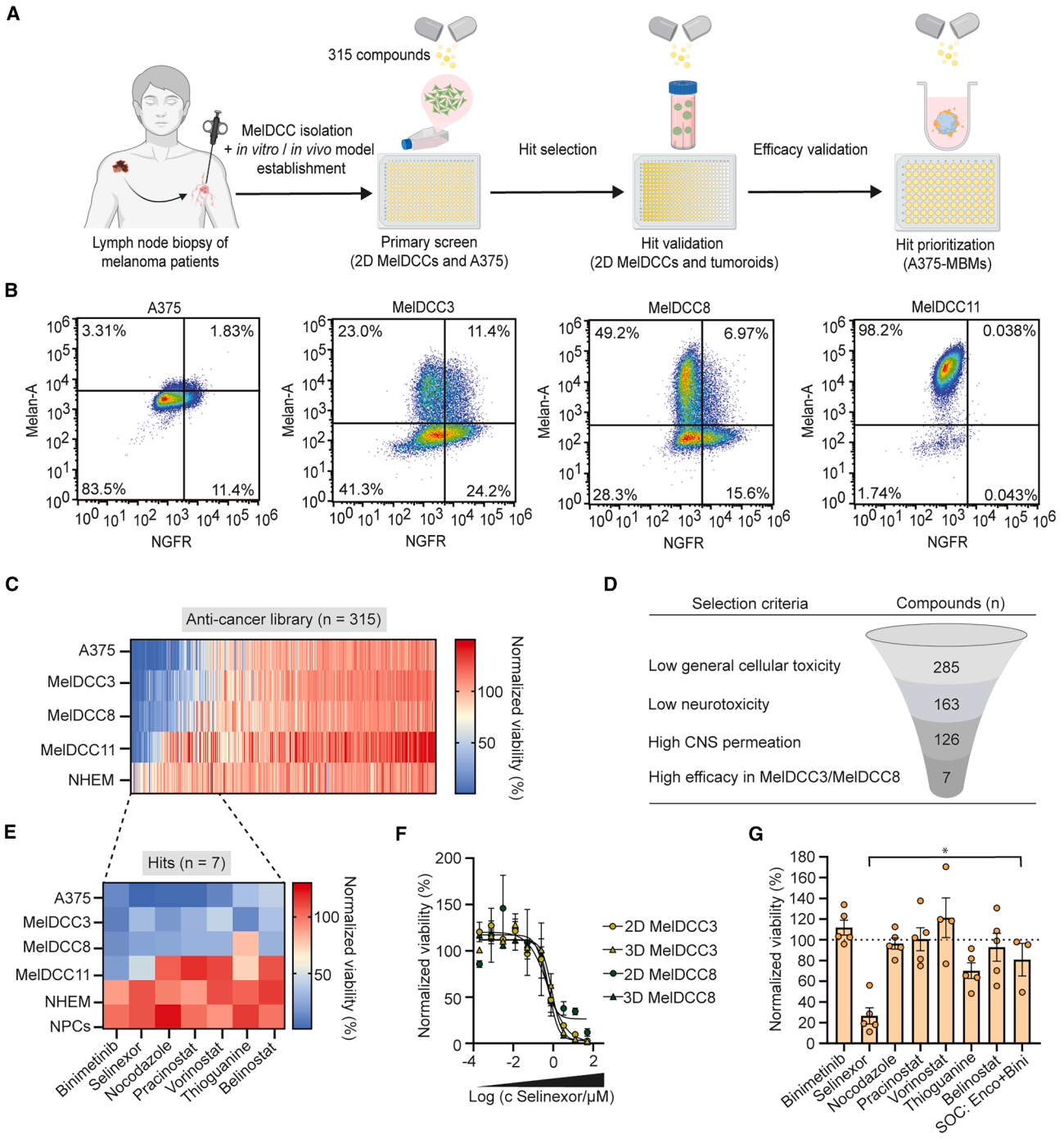


Figure 4. Anti-cancer drug screen and MBM validation strategy

(A) Schematic overview of the drug repurposing screening strategy starting with the primary screen using 2D A375 cells and MelDCCs from patient's lymph node specimen.

(B) Flow cytometry analysis of MelDCC and A375 cells stained for Melan-A and NGFR receptor.

(C) Heatmap of ATP-based cellular viability of A375, MelDCC3, MelDCC8, and MelDCC11 cells and NHEM control cell line after 5-day exposure to 315 anti-cancer drugs screened at 1 μM. Viability values are ranked from left to right based on their impact on the mean viability of all cell lines. Each data point is represented by one individual colored line.

(D) Workflow outlining the criteria and steps for rational hit selection starting from 2D screening data.

(E) Close-up of heatmap showing the sensitivity of the cell panel including neural progenitor cells (NPCs) toward selected compound hits.

(legend continued on next page)

Please cite this article in press as: Krieg et al., Cortical organoid-derived models of the melanoma brain metastatic niche enable prioritization of cancer-targeting drugs, Cell Reports Methods (2025), https://doi.org/10.1016/j.crmeth.2025.101236

The MBM platform confirms selinexor's selective effect on metastasis regression through inhibition of nuclear export

Due to recent efforts in preclinical and clinical trials to repurpose selinexor for glioblastoma patients,[48,49] we investigated in depth its efficacy and toxicity aspects with the MBM platform. As a reference compound, we selected the HSP90 inhibitor DEBIO-0932, due to its previously established efficacy against BrMs and good BBB permeability.[8,50] In our experiments, DEBIO-0932 exhibited a defined concentration-dependent toxicity in 2D and 3D tumoroid MelDCC8 cultures (Figure 5A). In addition, fluorescence-based monitoring of A375-MBMs demonstrated DEBIO-0932's potent anti-metastatic activity, with viability decreasing significantly to 19.7 ± 5.5% at 10 μM (IC_{50} of 0.25 μM) in a concentration-dependent manner over 6 days with daily compound replenishment (Figure 5B). Next, we investigated the selinexor response of A375-MBMs across a concentration range of 0.04–10 μM, spanning the maximal plasma concentrations of 0.65 μM detected in patients after oral administration.[48,51–53] In comparison to DEBIO-0932, selinexor exhibited a faster onset and more potent reduction of A375-MBM (3.7% ± 1.6% at 10 μM; IC_{50} of 0.13 μM) (Figure 5C). Exposure of hCOs to selinexor resulted in a strong shift in maximum efficacy on metastases ($E_{max} \approx 90\%$) compared to neuronal tissue ($E_{max} \approx 46\%$) (Figure 5D). Importantly, hCO viability remained high, despite potential compound accumulation in the tissue, demonstrating favorable selectivity against metastatic cancer cells. Caspase-3/7 was activated in a concentration-dependent manner, indicative of selinexor-induced apoptosis in A375-MBMs (Figure 5E) resulting in a concomitant reduction in Ki-67-positive metastases (Figure 5F). To determine if the metastatic regression correlated with nuclear export inhibition, we analyzed selinexor-treated A375-MBMs for a functional alteration of XPO1, the molecular target of selinexor. In the remaining cancer cells, treatment had induced a nuclear accumulation of TP53, a key XPO1 cargo,[51] suggesting target engagement (Figure 5F). For a clinically relevant validation, we expanded the platform to patient-derived MelDCC lines. Over 7 days of co-culture with hCOs, we monitored a similar metastasis growth profile of MelDCC3- and MelDCC8-MBMs compared to A375-MBMs, although the overall fluorescence intensity differed (Figure 5G). Notably, colonized cancer cells were found in very close proximity to neuronal cells at the surface of each MBM model (Figure 5H). Additionally, we validated the MBM generation and assay workflow using male MelDCC8 cells and the sex-matched hiPSC line HHUUKDi009-A, reaching a similar assay window during colonization than the female models (A375-MBM based on hCOs derived from WISCi004-B or ZIPi013-B hiPSCs) or any of the mixed-sex models (Figures S4A and S4B). Following the previously optimized parameters for compound exposure, we then treated MBMs with 0.25 and 0.5 μM selinexor. Data revealed a concentration-dependent anti-metastatic activity in a clinically promising concentration range in both MBM models (Figure 5I). We observed a distinct sensitivity in A375- and MelDCC8-MBMs with a residual viability indicating a refractory subpopulation of cancer cells.

Confirmation of selinexor's BBB permeability

Although the penetration of DCCs into the brain parenchyma may remodel the BBB into a blood-tumor barrier (BTB), it does not exclude the possibility of a selective barrier for systemically administered drugs.[54] Since our hiPSC-derived MBM models do not incorporate aspects of BBB permeability, we tested the permeation of selinexor and DEBIO-0932 in a human iPSC-derived *in vitro* assay. We differentiated wild-type hiPSCs (WISCi004-B) into brain capillary endothelial cells (BCECs), as previously reported.[55–58] To assess the transport of compounds across the BBB-like structure, we seeded BCECs differentiated for 8 days onto insert membranes (Figure 6A). We continuously measured transendothelial electrical resistance (TEER) values exceeding 1,000 Ω *cm^2 over a 60-h period, along with capacitance values ranging from 1 to 2 μF/cm^2, indicative of the formation of a tight BCEC monolayer[59] (Figure 6B). We chose 48 h post-seeding as the treatment time point for 1 h exposure to 10 μM selinexor or DEBIO-0932. We assessed flux in both directions (apical to basolateral [A-B] and basolateral to apical [B-A]) and compared permeability values to reference compounds (carbamazepine [quick permeation], verapamil [medium permeation], and atenolol [slow permeation]). Sodium fluorescein solution was administered together with the test compounds and confirmed limited passive diffusion and maintenance of barrier integrity during the treatment period (Figure 6C). Mass spectrometry analysis revealed good permeability for both selinexor and DEBIO-0932, similar to Verapamil. We detected higher apparent permeability coefficients (P_{app}) for selinexor in apical-to-basolateral permeation and relatively low efflux ratios, suggesting additional active uptake of these drugs from vessels to brain parenchyma, beyond passive permeation (Figures 6D and 6E). These data further indicate a good permeation with low efflux transport at the BBB, essential for achieving therapeutic selinexor concentrations and minimizing dosage requirements.

DISCUSSION

Improving the clinical management of BrM requires the availability of preclinical model systems that reproducibly capture key features of human disease, particularly in screening-compatible assay formats. It is already widely acknowledged that two-dimensional (melanoma) cell lines often fail to exhibit critical molecular and phenotypic alterations of metastatic cells and lack key structural and functional interactions with the metastatic niche.[60] Since early metastatic colonization is the rate-limiting step in the metastatic cascade, adjuvant therapeutic targeting of the early metastatic seed, the DCCs, is key to prevent the onset of difficult to cure BrM. Our scalable and reproducible human MBM platform proposed here, combining hiPSC-derived

(F) Concentration-response titration of selinexor on ATP-based cellular viability of 2D and tumoroid (3D) cell cultures (n = 2–3 experiments per condition). Data are presented as mean ± SEM. IC_{50}(2D MelDCC3): 0.83 μM; IC_{50}(3D MelDCC3): 0.54 μM; IC_{50}(2D MelDCC8): 0.6 μM; IC_{50}(3D MelDCC8): 0.4 μM.
(G) Fluorescence-based cellular viability of A375-MBMs treated with hit compounds at 10 μM for 72 h (n = 3–5 experiments). Data are presented as mean ± SEM. Statistical analysis was performed using one-way ANOVA, followed by Tukey's multiple comparisons test. *p = 0.0179. See also Figure S3.

Please cite this article in press as: Krieg et al., Cortical organoid-derived models of the melanoma brain metastatic niche enable prioritization of cancer-targeting drugs, Cell Reports Methods (2025), https://doi.org/10.1016/j.crmeth.2025.101236

CellPress
OPEN ACCESS

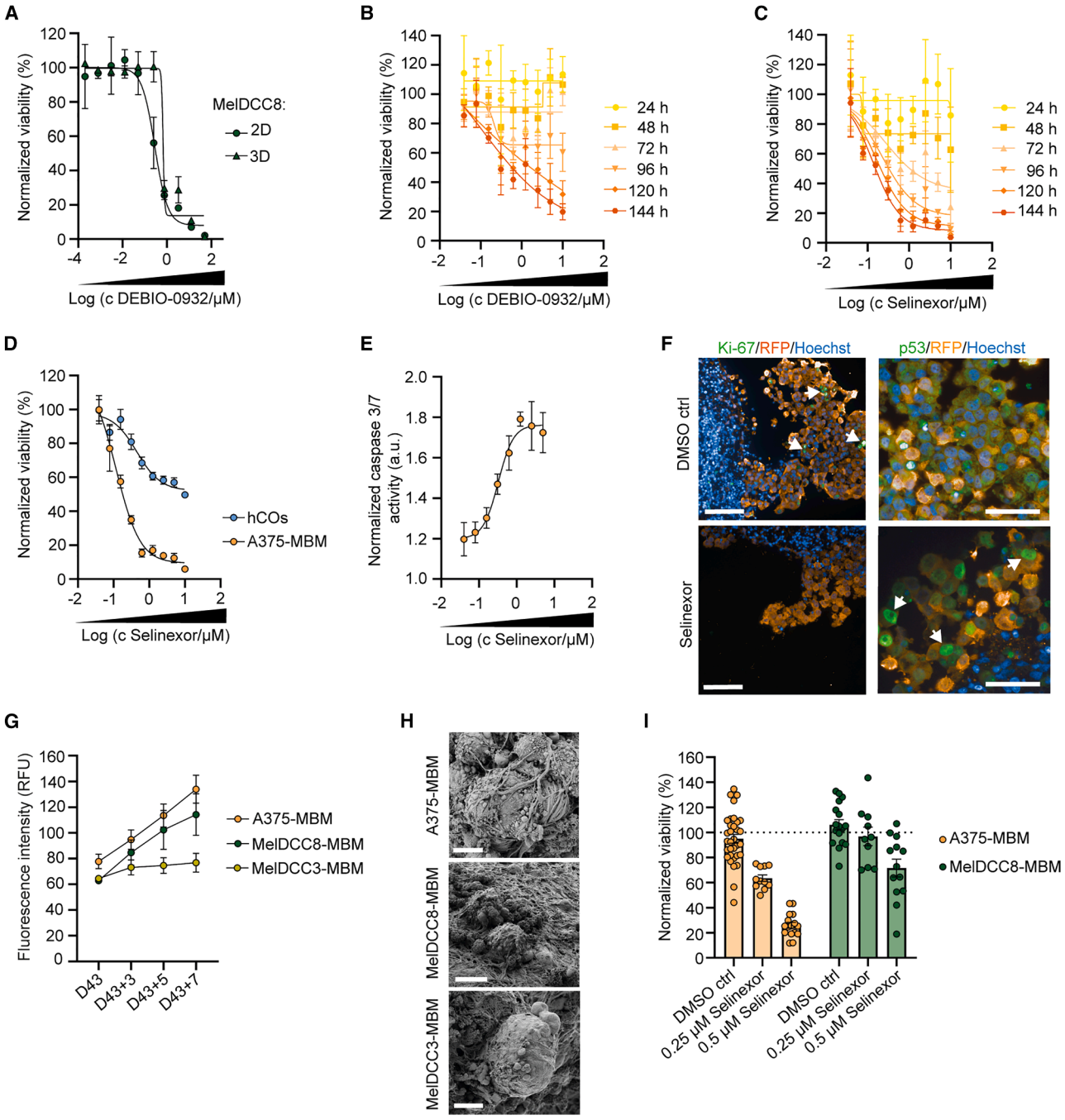


Figure 5. Selinexor selectively causes metastasis regression in A375- and MelDCC8-MBMs

(A) Dose-dependent effect of DEBIO-0932 on ATP-based cellular viability of 2D and tumoroid (3D) MelDCC8 cell cultures after 5 days (n = 2 experiments per condition). Data are presented as mean ± SEM. IC_{50}(2D): 0.65 µM; IC_{50}(3D): 0.23 µM.

(B) Dose- and time-dependent effect of DEBIO-0932 on fluorescence-based cellular viability of A375-MBMs (n = 3 technical replicates per condition). Data are presented as mean ± SD. IC_{50}: 0.25 µM.

(C) Dose- and time-dependent effect of selinexor on fluorescence-based cellular viability of A375-MBMs (n = 3 technical replicates per condition). Data are presented as mean ± SD. IC_{50}: 0.13 µM.

(D) Concentration response of selinexor in A375-MBMs and hCOs. Viability is assessed based on the fluorescence intensity or ATP-based 3D CellTiter-Glo assay after 6 days of treatment (n = 2 experiments per condition). Data are presented as mean ± SEM.

(E) Concentration-dependent caspase-3/7 activity in A375-MBM after 6 days of selinexor exposure (n = 2 experiments). Data are presented as mean ± SEM.

(F) Immunohistochemical confocal images of A375-MBMs treated with 0.25 µM for 72 h of cancer cells (RFP), proliferation marker Ki-67, and XPO1 target TP53. Scale bars represent 50 µm.

(legend continued on next page)

Please cite this article in press as: Krieg et al., Cortical organoid-derived models of the melanoma brain metastatic niche enable prioritization of cancer-targeting drugs, Cell Reports Methods (2025), https://doi.org/10.1016/j.crmeth.2025.101236

hCOs with early metastatic cancer cells in a robust screening assay format, addresses a previously unmet need for improved preclinical studies. The model recapitulates key features of metastatic colonization, capturing the dynamic transition from DCCs to micrometastases within the brain TME. Notably, our model shows a strong metastasis-like signature, a pronounced EMT phenotype, and demonstrates intimate cancer cell interactions with both neuronal and astroglia-like cells, aligning with contemporary concepts of neurooncology.[61]

We have here demonstrated that we can profile anti-cancer drugs in screening mode across diverse melanoma cell types, including tumor-derived (A375) or patient-derived DCCs, representing varied melanoma differentiation phenotypes, genetic backgrounds, and biological sexes. Critically, the MBM platform's utility extends beyond testing of therapeutics in early preclinical or clinical stages of drug development. It also provides a clinically relevant context to evaluate therapies for patients with established BrMs, addressing a key unmet need. Patients with BrM are often excluded from clinical trials, also due to the limited information on the ability of drugs to cross the BBB or BTB, hindering the development of new therapeutic opportunities targeting BrM.[8] In addition to assessing sensitivity to targeted molecular therapies, this model also allows for the interrogation of unwanted side effects in the brain parenchyma, as shown here for the BBB-permeating XPO1 inhibitor selinexor. Our study aims to emphasize the differences in drug sensitivity of model systems, i.e., metastatic cancer cells in 2D or 3D, with or without niche tissue, and holds the potential to identify potent compounds that initiate MBM regression. The MBM platform may therefore provide a means to offer a relevant tissue context in which drugs, not previously tested for BrMs, could be easily evaluated and prioritized. This triaging strategy for metastasis drug screening, from less complex 2D models to a multicellular metastasis model system, could enable a rational, cost- and time-effective hit selection for further *in vivo* validation.

Prediction of treatment responses using *ex vivo* systems may pave the way to personalized medicine. Our proposed co-culture and drug screening workflow aligns with clinically relevant timelines, including postoperative recovery and histological analysis of biopsies. Given the regular availability of hCO and patient specimens, this platform could serve as an additional tool for exploring candidate therapies *ex vivo*, either as monotherapy or in combination with the standard of care. It could also support treatment decisions for individual (high-risk) BrM patients and/or certain subgroups. We implemented the colonization procedure with patient-derived specimens, which can also be potentially expanded to DCC lines from patients with different diagnoses, such as breast cancer. We are confident that the MBM platform will support optimal patient stratification and improve clinical trial design, thus promoting the impact of personalized medicine in oncology.

Limitations of the study

We acknowledge that our approach to an experimental drug-screening platform targeting metastasis has limitations. The MBM model does not fully recapitulate the metastatic cascade due to missing vascularization of the hCOs. Therefore, we investigated compound permeability with an additional hiPSC-derived BBB model. The colonization in our model cannot fully recapitulate the *in vivo* situation due to a lack of peripheral immune cells and an incomplete ECM. Limits of the platform include availability of patient tissue, particularly on reporter-transduced DCC lines, which is a time-critical factor. All data shown here were derived from one melanoma cell line and three patients and may not fully represent the generalizability of the approach. Also, we cannot exclude any lack of sensitivity of DCC-derived MBMs due to prior exposure of patients to different treatment therapies.

RESOURCE AVAILABILITY

Lead contact

Requests for further information and resources should be directed to and will be fulfilled by the lead contact, Dr. Ole Pless (ole.pless@itmp.fraunhofer.de).

Materials availability

The A375-tdTomato cell line generated in this study will be made available on request but will require a completed materials transfer agreement. There are restrictions to the availability of MelDCC cell lines owing to hospital's ethical regulations.

Data and code availability

- mRNA sequencing data reported in this paper have been deposited at GEO: GSE293348 and are publicly available. Microscopy data reported in this paper will be shared by the lead contact upon request.
- This study does not report original code.
- Any additional information required to re-analyze the data reported in this study is available from the lead contact upon request.

ACKNOWLEDGMENTS

This work was supported by the German Research Foundation (Deutsche Forschungsgemeinschaft [DFG], SFB TRR 305, project number 429280966 [to K.E., M.W.-K., C.A.K., J.W., and O.P.]), by the Bundesministerium für Bildung und Forschung (BMBF) Clusters4Future project "BioDEL" to M.M. (03ZU1109GD) and O.P. (03ZU1109GB), by the Else-Kröner-Fresenius Foundation (2023_EKMS.03 to M.S.W.), by the Corona foundation (S0199/10110/2025 to M.S.W.), and by a short-term scientific mission grant from COST Action CA20140 "CorEuStem" (to K.K.). We thank the EMBL mesoscopic imaging facility Barcelona (head: Dr. James Swoger), the tissue engineering unit (head: Dr. Laura Batlle Morera) of the Centre for Genomic Regulation (CRG) Barcelona, and Kristin Hartmann (Experimental Pathology Core Facility, University Medical Center Hamburg-Eppendorf) for providing their support in sample preparation and image acquisition. In addition, we thank nanoAnalytics GmbH (Münster) and PreSens Precision Sensing GmbH (Regensburg) for resource and technical support and Norbert Garbow (Revvity) for support with the customized spheroid detection analysis. We thank Dr. Julian Kött and Dr. Falk Klose (University Medical Center Hamburg-Eppendorf, Department of Dermatology and Venerology) for critical reading and discussion of

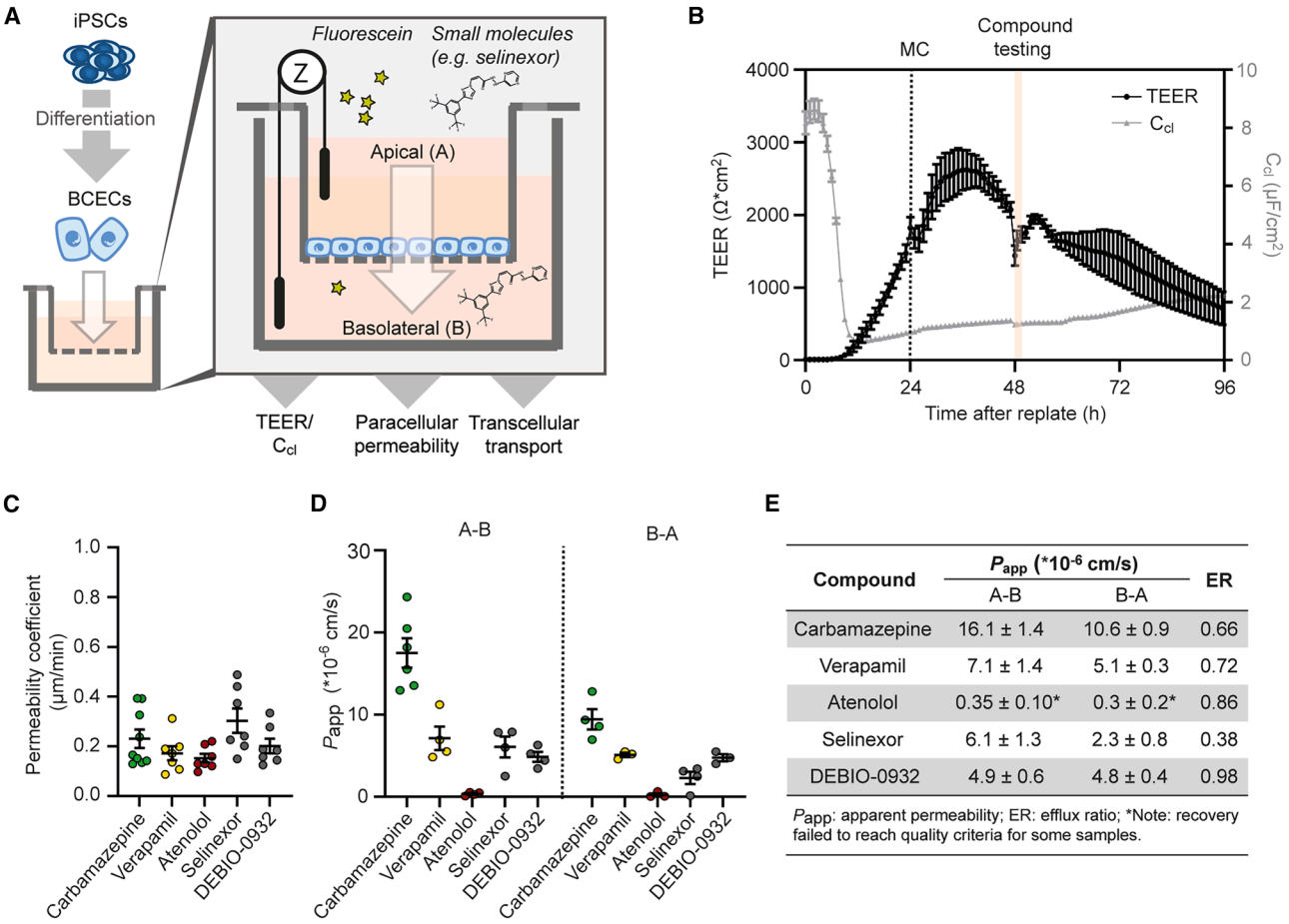
(G) Time-course analysis of MelDCC3- and MelDCC8-MBMs compared to A375-MBMs during 7 days of colonization ($n = 6$ independent batches each). Data are presented as mean ± SEM.

(H) Ultrastructural analysis of A375-, MelDCC8-, MelDCC3-MBMs demonstrates close proximity of colonized cancer and neuronal cells. Scale bars represent 10 μm.

(I) Fluorescence-based cellular viability readout of MBMs treated with 0.25 and 0.5 μM selinexor for 144 h ($n = 10–33$ from at least 2 independent experiments). Data are presented as mean ± SEM. See also Figure S4.

Please cite this article in press as: Krieg et al., Cortical organoid-derived models of the melanoma brain metastatic niche enable prioritization of cancer-targeting drugs, Cell Reports Methods (2025), https://doi.org/10.1016/j.crmeth.2025.101236

CellPress
OPEN ACCESS



E

Compound	P_{app} (*10^{-6} cm/s)		ER
	A-B	B-A	
Carbamazepine	16.1 ± 1.4	10.6 ± 0.9	0.66
Verapamil	7.1 ± 1.4	5.1 ± 0.3	0.72
Atenolol	0.35 ± 0.10*	0.3 ± 0.2*	0.86
Selinexor	6.1 ± 1.3	2.3 ± 0.8	0.38
DEBIO-0932	4.9 ± 0.6	4.8 ± 0.4	0.98

P_{app}: apparent permeability; ER: efflux ratio; *Note: recovery failed to reach quality criteria for some samples.

Figure 6. Blood-brain barrier permeation of selinexor and DEBIO-0932 tested in an hiPSC-derived brain capillary endothelial cell model

(A) Schematic overview of small-molecule permeation and transport assay between apical (A) and basolateral (B) compartment using hiPSC-derived brain capillary endothelial cells (BCECs). Impedance (Z)-based measurements of transendothelial electrical resistance (TEER) and capacitance (C_{cl}) as well as fluorescein permeability underlining blood-brain barrier (BBB) integrity.

(B) Monitoring of TEER (left axis) and C_{cl} (right axis) to analyze BBB integrity over time after replating onto insert membranes (n = 3 independent differentiations). Data are presented as mean ± SEM. Labels indicate the time point of medium change (MC) and 1 h window for compound testing.

(C) Analysis of fluorescein permeability coefficient during compound administration (n = 6–9 independent experiments). Data are presented as mean ± SEM. Carbamazepine (quick), verapamil (medium), and atenolol (slow permeation) serve as reference compounds.

(D) Apparent permeability coefficient (P_{app}) in both directions (apical to basolateral [A-B] and basolateral to apical [B-A]) after 1 h of selinexor or DEBIO-0932 exposure in comparison to reference compounds carbamazepine (quick), verapamil (medium), and atenolol (slow permeation) analyzed by mass spectrometry (n = 3–6 experiments). Data are presented as mean ± SEM.

(E) Overview of calculated P_{app} values and efflux ratios (ERs) of selinexor, DEBIO-0932, and reference compounds.

the manuscript. We are grateful to all patients for the donation of cancer cell specimen, which enabled the studies described here. Some figures were created with BioRender.

AUTHOR CONTRIBUTIONS

Conceptualization, K.K. and O.P.; data curation, K.K., S.M.-R., T.N., F.-Z.R., U.H., A.Z., M.S.W., M.S., P.M., H.S., K.E., and S.K.; formal analysis, K.K., S.M.-R., T.N., F.-Z.R., P.K., U.H., A. Wittich, A.Z., M.S.W., M.W., M.S., J.H., and P.M.; funding acquisition, K.K., M.S.W., M.A.F., M.M., K.E., N.S.G., C.A.K., M.W.-K., J.W., and O.P.; investigation, K.K., S.M.-R., T.N., F.-Z.R., P.K., A. Weller, A. Wittich, M.S., J.H., P.M., D.M., H.S., and S.K.; methodology, K.K., S.M.-R., T.N., U.H., and J.W.; project administration, K.K., M.M., K.E., N.S.G., C.A.K., M.W.-K., J.W., and O.P.; resources, R.B., C.C., M.M., K.E., S.K., C.A.K., M.W.-K., J.W., and O.P.; software, A.Z. and M.S.W.; supervision, R.Z., R.B., M.A.F., M.M., K.E., N.S.G., C.A.K., M.W.-K., J.W., and O.P.; validation: K.K., S.M.-R., T.N., F.-Z.R., P.K., A. Weller, U.H., M.S., P.M., D.M., H.S., K.E., S.K., and M.W.-K.; visualization, K.K., U.H., M.S.W., M.W., M.S., H.S., K.E., and S.K.; writing – original draft, K.K. and O.P.; writing – review & editing, K.K., U.H., C.A.K., M.W.-K., J.W., and O.P. All co-authors contributed to the editing and discussion of the manuscript and approved the final version.

DECLARATION OF INTERESTS

The authors declare no competing interests.

STAR★METHODS

Detailed methods are provided in the online version of this paper and include the following:

- KEY RESOURCES TABLE

Please cite this article in press as: Krieg et al., Cortical organoid-derived models of the melanoma brain metastatic niche enable prioritization of cancer-targeting drugs, Cell Reports Methods (2025), https://doi.org/10.1016/j.crmeth.2025.101236

- EXPERIMENTAL MODEL AND STUDY PARTICIPANT DETAILS
- METHOD DETAILS
  - Cultivation of human hiPSCs
  - Differentiation of hiPSC-derived cortical organoids
  - Differentiation of hiPSC-derived BCECs for *in vitro* BBB models
  - 2D cultivation of melanoma cells
  - Lentiviral transduction of melanoma cells
  - Melanoma brain metastases models
  - MelDCC tumoroid propagation using semi-solid culture
  - Live imaging
  - Oxygen measurements
  - Whole-mount imaging
  - Immunohistochemistry
  - Quantitative reverse-transcription PCR analysis
  - Patch clamp analysis
  - Bulk RNA sequencing
  - Transmission electron microscopy
  - Scanning electron microscopy
  - CXCL10 ELISA
  - Flow cytometry
  - Anti-cancer approved library drug screen
  - Drug sensitivity assay in 3D MBM models
  - Drug sensitivity assay in hCOs
  - Impedance measurements
  - *In vitro* blood-brain barrier permeability assay
  - LC-MS/MS sample preparation and analysis
- QUANTIFICATION AND STATISTICAL ANALYSIS

SUPPLEMENTAL INFORMATION

Supplemental information can be found online at https://doi.org/10.1016/j.crmeth.2025.101236.

Received: June 2, 2025
Revised: September 10, 2025
Accepted: October 15, 2025

REFERENCES

1. Achrol, A.S., Rennert, R.C., Anders, C., Soffietti, R., Ahluwalia, M.S., Nayak, L., Peters, S., Arvold, N.D., Harsh, G.R., Steeg, P.S., and Chang, S.D. (2019). Brain metastases. Nat. Rev. Dis. Primers *5*, 5. https://doi.org/10.1038/s41572-018-0055-y.
2. Czogalla, M., Stöhr, J., Gleim, N., Papsdorf, K., Klagges, S., Hambsch, P., Kuhnt, T., Nägler, F., Barrantes-Freer, A., Wach, J., et al. (2025). Short-term survivors with brain metastases have modest benefits from focal and systemic therapies and remain frequent despite improving treatment landscape. Clin. Transl. Radiat. Oncol. *51*, 100919. https://doi.org/10.1016/j.ctro.2025.100919.
3. Moravan, M.J., Fecci, P.E., Anders, C.K., Clarke, J.M., Salama, A.K.S., Adamson, J.D., Floyd, S.R., Torok, J.A., Salama, J.K., Sampson, J.H., et al. (2020). Current multidisciplinary management of brain metastases. Cancer *126*, 1390–1406. https://doi.org/10.1002/cncr.32714.
4. Suh, J.H., Kotecha, R., Chao, S.T., Ahluwalia, M.S., Sahgal, A., and Chang, E.L. (2020). Current approaches to the management of brain metastases. Nat. Rev. Clin. Oncol. *17*, 279–299. https://doi.org/10.1038/s41571-019-0320-3.
5. Valiente, M., Ahluwalia, M.S., Boire, A., Brastianos, P.K., Goldberg, S.B., Lee, E.Q., Le Rhun, E., Preusser, M., Winkler, F., and Soffietti, R. (2018). The Evolving Landscape of Brain Metastasis. Trends Cancer *4*, 176–196. https://doi.org/10.1016/j.trecan.2018.01.003.
6. Jeising, S., Nickel, A.C., Trübel, J., Felsberg, J., Picard, D., Leprivier, G., Wolter, M., Huynh, M.K., Olivera, M.B., Kaulich, K., et al. (2024). A clinically compatible in vitro drug-screening platform identifies therapeutic vulnerabilities in primary cultures of brain metastases. J. Neuro Oncol. *169*, 613–623. https://doi.org/10.1007/s11060-024-04763-7.
7. Lee, S., Weiss, T., Bühler, M., Mena, J., Lottenbach, Z., Wegmann, R., Sun, M., Bihl, M., Augustynek, B., Baumann, S.P., et al. (2024). High-throughput identification of repurposable neuroactive drugs with potent anti-glioblastoma activity. Nat. Med. *30*, 3196–3208. https://doi.org/10.1038/s41591-024-03224-y.
8. Zhu, L., Retana, D., García-Gómez, P., Álvaro-Espinosa, L., Priego, N., Masmudi-Martín, M., Yebra, N., Miarka, L., Hernández-Encinas, E., Blanco-Aparicio, C., et al. (2022). A clinically compatible drug-screening platform based on organotypic cultures identifies vulnerabilities to prevent and treat brain metastasis. EMBO Mol. Med. *14*, e14552. https://doi.org/10.15252/emmm.202114552.
9. Cagney, D.N., Martin, A.M., Catalano, P.J., Redig, A.J., Lin, N.U., Lee, E.Q., Wen, P.Y., Dunn, I.F., Bi, W.L., Weiss, S.E., et al. (2017). Incidence and prognosis of patients with brain metastases at diagnosis of systemic malignancy: a population-based study. Neuro Oncol. *19*, 1511–1521. https://doi.org/10.1093/neuonc/nox077.
10. Fager, A., Samuelsson, M., Olofsson Bagge, R., Pivodic, A., Bjursten, S., Levin, M., Jespersen, H., and Ny, L. (2025). Immune checkpoint inhibitor therapy is associated with a decreased risk of developing melanoma brain metastases. BJC Rep. *3*, 22. https://doi.org/10.1038/s44276-025-00137-2.
11. Sandhu, M.R.S., Chiang, V.L., Tran, T., Yu, J.B., Weiss, S.A., Goldberg, S.B., Aboian, M.S., Kluger, H.M., and Mahajan, A. (2021). Incidence and characteristics of metastatic intracranial lesions in stage III and IV melanoma: a single institute retrospective analysis. J. Neuro Oncol. *154*, 197–203. https://doi.org/10.1007/s11060-021-03813-8.
12. Brown, M., Assen, F.P., Leithner, A., Abe, J., Schachner, H., Asfour, G., Bago-Horvath, Z., Stein, J.V., Uhrin, P., Sixt, M., and Kerjaschki, D. (2018). Lymph node blood vessels provide exit routes for metastatic tumor cell dissemination in mice. Science *359*, 1408–1411. https://doi.org/10.1126/science.aal3662.
13. Guetter, S., König, C., Koerkel-Qu, H., Markiewicz, A., Scheitler, S., Katzer, M., Berneburg, M., Renner, P., Cucuruz, B., Guttenberger, L., et al. (2025). MCSP(+) metastasis founder cells activate immunosuppression early in human melanoma metastatic colonization. Nat. Cancer *6*, 1017–1034. https://doi.org/10.1038/s43018-025-00963-w.
14. Joyce, J.A., and Pollard, J.W. (2009). Microenvironmental regulation of metastasis. Nat. Rev. Cancer *9*, 239–252. https://doi.org/10.1038/nrc2618.
15. Pereira, E.R., Kedrin, D., Seano, G., Gautier, O., Meijer, E.F.J., Jones, D., Chin, S.M., Kitahara, S., Bouta, E.M., Chang, J., et al. (2018). Lymph node metastases can invade local blood vessels, exit the node, and colonize distant organs in mice. Science *359*, 1403–1407. https://doi.org/10.1126/science.aal3622.
16. Werner-Klein, M., Scheitler, S., Hoffmann, M., Hodak, I., Dietz, K., Lehnert, P., Naimer, V., Polzer, B., Treitschke, S., Werno, C., et al. (2018). Genetic alterations driving metastatic colony formation are acquired outside of the primary tumour in melanoma. Nat. Commun. *9*, 595. https://doi.org/10.1038/s41467-017-02674-y.
17. Ulmer, A., Dietz, K., Hodak, I., Polzer, B., Scheitler, S., Yildiz, M., Czyz, Z., Lehnert, P., Fehm, T., Hafner, C., et al. (2014). Quantitative measurement of melanoma spread in sentinel lymph nodes and survival. PLoS Med. *11*, e1001604. https://doi.org/10.1371/journal.pmed.1001604.
18. Ulmer, A., Pfefferle, V., Walter, V., Granai, M., Keim, U., Fend, F., Sulyok, M., and Bösmüller, H. (2022). Reporting of melanoma cell densities in the sentinel node refines outcome prediction. Eur. J. Cancer *174*, 121–130. https://doi.org/10.1016/j.ejca.2022.06.054.
19. Klein, C.A. (2020). Cancer progression and the invisible phase of metastatic colonization. Nat. Rev. Cancer *20*, 681–694. https://doi.org/10.1038/s41568-020-00300-6.

Please cite this article in press as: Krieg et al., Cortical organoid-derived models of the melanoma brain metastatic niche enable prioritization of cancer-targeting drugs, Cell Reports Methods (2025), https://doi.org/10.1016/j.crmeth.2025.101236

20. Luzzi, K.J., MacDonald, I.C., Schmidt, E.E., Kerkvliet, N., Morris, V.L., Chambers, A.F., and Groom, A.C. (1998). Multistep nature of metastatic inefficiency: dormancy of solitary cells after successful extravasation and limited survival of early micrometastases. Am. J. Pathol. *153*, 865–873. https://doi.org/10.1016/S0002-9440(10)65628-3.

21. Dai, J., Cimino, P.J., Gouin, K.H., Grzelak, C.A., Barrett, A., Lim, A.R., Long, A., Weaver, S., Saldin, L.T., Uzamere, A., et al. (2022). Astrocytic laminin-211 drives disseminated breast tumor cell dormancy in brain. Nat. Cancer *3*, 25–42. https://doi.org/10.1038/s43018-021-00297-3.

22. Hurst, R.E., Bastian, A., Bailey-Downs, L., and Ihnat, M.A. (2016). Targeting dormant micrometastases: rationale, evidence to date and clinical implications. Ther. Adv. Med. Oncol. *8*, 126–137. https://doi.org/10.1177/1758834015624277.

23. Massague, J., and Obenauf, A.C. (2016). Metastatic colonization by circulating tumour cells. Nature *529*, 298–306. https://doi.org/10.1038/nature17038.

24. Schwartz, H., Blacher, E., Amer, M., Livneh, N., Abramovitz, L., Klein, A., Ben-Shushan, D., Soffer, S., Blazquez, R., Barrantes-Freer, A., et al. (2016). Incipient Melanoma Brain Metastases Instigate Astrogliosis and Neuroinflammation. Cancer Res. *76*, 4359–4371. https://doi.org/10.1158/0008-5472.CAN-16-0485.

25. Srinivasan, E.S., Deshpande, K., Neman, J., Winkler, F., and Khasraw, M. (2021). The microenvironment of brain metastases from solid tumors. Neurooncol. Adv. *3*, v121–v132. https://doi.org/10.1093/noajnl/vdab121.

26. Lancaster, M.A., Renner, M., Martin, C.A., Wenzel, D., Bicknell, L.S., Hurles, M.E., Homfray, T., Penninger, J.M., Jackson, A.P., and Knoblich, J.A. (2013). Cerebral organoids model human brain development and microcephaly. Nature *501*, 373–379. https://doi.org/10.1038/nature12517.

27. Pasca, A.M., Sloan, S.A., Clarke, L.E., Tian, Y., Makinson, C.D., Huber, N., Kim, C.H., Park, J.Y., O'Rourke, N.A., Nguyen, K.D., et al. (2015). Functional cortical neurons and astrocytes from human pluripotent stem cells in 3D culture. Nat. Methods *12*, 671–678. https://doi.org/10.1038/nmeth.3415.

28. Peng, T., Ma, X., Hua, W., Wang, C., Chu, Y., Sun, M., Fermi, V., Hamelmann, S., Lindner, K., Shao, C., et al. (2025). Individualized patient tumor organoids faithfully preserve human brain tumor ecosystems and predict patient response to therapy. Cell Stem Cell *32*, 652–669.e11. https://doi.org/10.1016/j.stem.2025.01.002.

29. Quaranta, V., and Linkous, A. (2022). Organoids as a Systems Platform for SCLC Brain Metastasis. Front. Oncol. *12*, 881989. https://doi.org/10.3389/fonc.2022.881989.

30. Wang, C., Nagayach, A., Patel, H., Dao, L., Zhu, H., Wasylishen, A.R., Fan, Y., Kendler, A., and Guo, Z. (2024). Utilizing human cerebral organoids to model breast cancer brain metastasis in culture. Breast Cancer Res. *26*, 108. https://doi.org/10.1186/s13058-024-01865-y.

31. Birey, F., Andersen, J., Makinson, C.D., Islam, S., Wei, W., Huber, N., Fan, H.C., Metzler, K.R.C., Panagiotakos, G., Thom, N., et al. (2017). Assembly of functionally integrated human forebrain spheroids. Nature *545*, 54–59. https://doi.org/10.1038/nature22330.

32. Dings, J., Meixensberger, J., Jäger, A., and Roosen, K. (1998). Clinical experience with 118 brain tissue oxygen partial pressure catheter probes. Neurosurgery *43*, 1082–1095. https://doi.org/10.1097/00006123-199811000-00045.

33. Forcione, M., Ganau, M., Prisco, L., Chiarelli, A.M., Bellelli, A., Belli, A., and Davies, D.J. (2021). Mismatch between Tissue Partial Oxygen Pressure and Near-Infrared Spectroscopy Neuromonitoring of Tissue Respiration in Acute Brain Trauma: The Rationale for Implementing a Multimodal Monitoring Strategy. Int. J. Mol. Sci. *22*, 1122. https://doi.org/10.3390/ijms22031122.

34. Grimes, D.R., Kelly, C., Bloch, K., and Partridge, M. (2014). A method for estimating the oxygen consumption rate in multicellular tumour spheroids. J. R. Soc. Interface *11*, 20131124. https://doi.org/10.1098/rsif.2013.1124.

35. Lee, C.W., and Stantz, K.M. (2016). Development of a mathematical model to estimate intra-tumor oxygen concentrations through multi-parametric imaging. Biomed. Eng. Online *15*, 114. https://doi.org/10.1186/s12938-016-0235-5.

36. Harberts, J., Haferkamp, U., Haugg, S., Fendler, C., Lam, D., Zierold, R., Pless, O., and Blick, R.H. (2020). Interfacing human induced pluripotent stem cell-derived neurons with designed nanowire arrays as a future platform for medical applications. Biomater. Sci. *8*, 2434–2446. https://doi.org/10.1039/d0bm00182a.

37. Rosa, F., Dhingra, A., Uysal, B., Mendis, G.D.C., Loeffler, H., Elsen, G., Mueller, S., Schwarz, N., Castillo-Lizardo, M., Cuddy, C., et al. (2020). In Vitro Differentiated Human Stem Cell-Derived Neurons Reproduce Synaptic Synchronicity Arising during Neurodevelopment. Stem Cell Rep. *15*, 22–37. https://doi.org/10.1016/j.stemcr.2020.05.015.

38. Bardy, C., van den Hurk, M., Kakaradov, B., Erwin, J.A., Jaeger, B.N., Hernandez, R.V., Eames, T., Paucar, A.A., Gorris, M., Marchand, C., et al. (2016). Predicting the functional states of human iPSC-derived neurons with single-cell RNA-seq and electrophysiology. Mol. Psychiatry *21*, 1573–1588. https://doi.org/10.1038/mp.2016.158.

39. Doron, H., Amer, M., Ershaid, N., Blazquez, R., Shani, O., Lahav, T.G., Cohen, N., Adler, O., Hakim, Z., Pozzi, S., et al. (2019). Inflammatory Activation of Astrocytes Facilitates Melanoma Brain Tropism via the CXCL10-CXCR3 Signaling Axis. Cell Rep. *28*, 1785–1798.e6. https://doi.org/10.1016/j.celrep.2019.07.033.

40. Tsoi, J., Robert, L., Paraiso, K., Galvan, C., Sheu, K.M., Lay, J., Wong, D.J.L., Atefi, M., Shirazi, R., Wang, X., et al. (2018). Multi-stage Differentiation Defines Melanoma Subtypes with Differential Vulnerability to Drug-Induced Iron-Dependent Oxidative Stress. Cancer Cell *33*, 890–904.e5. https://doi.org/10.1016/j.ccell.2018.03.017.

41. Chen, D., Frezza, M., Schmitt, S., Kanwar, J., and Dou, Q.P. (2011). Bortezomib as the first proteasome inhibitor anticancer drug: current status and future perspectives. Curr. Cancer Drug Targets *11*, 239–253. https://doi.org/10.2174/156800911794519752.

42. Zhang, J.H., Chung, T.D., and Oldenburg, K.R. (1999). A Simple Statistical Parameter for Use in Evaluation and Validation of High Throughput Screening Assays. J. Biomol. Screen *4*, 67–73. https://doi.org/10.1177/108705719900400206.

43. Corsello, S.M., Bittker, J.A., Liu, Z., Gould, J., McCarren, P., Hirschman, J.E., Johnston, S.E., Vrcic, A., Wong, B., Khan, M., et al. (2017). The Drug Repurposing Hub: a next-generation drug library and information resource. Nat. Med. *23*, 405–408. https://doi.org/10.1038/nm.4306.

44. Zink, A., Dai, D.-F., Wittich, A., Henke, M.-T., Pedrotti, G., Heiduschka, S., Aguilar, G.S., Pentimalli, T.M., Brueser, C., Notopoulou, S., et al. (2025). Pluripotent stem cell-based drug discovery uncovers sildenafil as a treatment for mitochondrial disease. Preprint at medRxiv. https://doi.org/10.1101/2025.05.15.25325571.

45. Zink, A., Haferkamp, U., Wittich, A., Beller, M., Pless, O., and Prigione, A. (2022). High-content screening of mitochondrial polarization in neural cells derived from human pluripotent stem cells. STAR Protoc. *3*, 101602. https://doi.org/10.1016/j.xpro.2022.101602.

46. Cornelissen, F.M.G., Markert, G., Deutsch, G., Antonara, M., Faaij, N., Bartelink, I., Noske, D., Vandertop, W.P., Bender, A., and Westerman, B.A. (2023). Explaining Blood-Brain Barrier Permeability of Small Molecules by Integrated Analysis of Different Transport Mechanisms. J. Med. Chem. *66*, 7253–7267. https://doi.org/10.1021/acs.jmedchem.2c01824.

47. Schadendorf, D., Dummer, R., Flaherty, K.T., Robert, C., Arance, A., de Groot, J.W.B., Garbe, C., Gogas, H.J., Gutzmer, R., Krajsová, I., et al. (2024). COLUMBUS 7-year update: A randomized, open-label, phase III trial of encorafenib plus binimetinib versus vemurafenib or encorafenib in patients with BRAF V600E/K-mutant melanoma. Eur. J. Cancer *204*, 114073. https://doi.org/10.1016/j.ejca.2024.114073.

48. Lassman, A.B., Wen, P.Y., van den Bent, M.J., Plotkin, S.R., Walenkamp, A.M.E., Green, A.L., Li, K., Walker, C.J., Chang, H., Tamir, S., et al. (2022). A Phase II Study of the Efficacy and Safety of Oral Selinexor in Recurrent

Glioblastoma. Clin. Cancer Res. *28*, 452–460. https://doi.org/10.1158/1078-0432.CCR-21-2225.

49. Tang, Y., Sprinzen, L., Terada, Y., Kiang, K.M., Li, C., Zeng, Y., Liu, F., Zhou, H., Liang, X., Zhang, J., et al. (2025). Autophagy Modulates Glioblastoma Cell Sensitivity to Selinexor-mediated XPO1 inhibition. Neuro Oncol. *27*, 1210–1226. https://doi.org/10.1093/neuonc/noae280.

50. Bao, R., Lai, C.J., Qu, H., Wang, D., Yin, L., Zifcak, B., Atoyan, R., Wang, J., Samson, M., Forrester, J., et al. (2009). CUDC-305, a novel synthetic HSP90 inhibitor with unique pharmacologic properties for cancer therapy. Clin. Cancer Res. *15*, 4046–4057. https://doi.org/10.1158/1078-0432.CCR-09-0152.

51. Abdul Razak, A.R., Mau-Soerensen, M., Gabrail, N.Y., Gerecitano, J.F., Shields, A.F., Unger, T.J., Saint-Martin, J.R., Carlson, R., Landesman, Y., McCauley, D., et al. (2016). First-in-Class, First-in-Human Phase I Study of Selinexor, a Selective Inhibitor of Nuclear Export, in Patients With Advanced Solid Tumors. J. Clin. Oncol. *34*, 4142–4150. https://doi.org/10.1200/JCO.2015.65.3949.

52. Alexander, T.B., Lacayo, N.J., Choi, J.K., Ribeiro, R.C., Pui, C.H., and Rubnitz, J.E. (2016). Phase I Study of Selinexor, a Selective Inhibitor of Nuclear Export, in Combination With Fludarabine and Cytarabine, in Pediatric Relapsed or Refractory Acute Leukemia. J. Clin. Oncol. *34*, 4094–4101. https://doi.org/10.1200/JCO.2016.67.5066.

53. Gounder, M.M., Zer, A., Tap, W.D., Salah, S., Dickson, M.A., Gupta, A.A., Keohan, M.L., Loong, H.H., D'Angelo, S.P., Baker, S., et al. (2016). Phase IB Study of Selinexor, a First-in-Class Inhibitor of Nuclear Export, in Patients With Advanced Refractory Bone or Soft Tissue Sarcoma. J. Clin. Oncol. *34*, 3166–3174. https://doi.org/10.1200/JCO.2016.67.6346.

54. Arvanitis, C.D., Ferraro, G.B., and Jain, R.K. (2020). The blood-brain barrier and blood-tumour barrier in brain tumours and metastases. Nat. Rev. Cancer *20*, 26–41. https://doi.org/10.1038/s41568-019-0205-x.

55. Appelt-Menzel, A., Cubukova, A., Günther, K., Edenhofer, F., Piontek, J., Krause, G., Stüber, T., Walles, H., Neuhaus, W., and Metzger, M. (2017). Establishment of a Human Blood-Brain Barrier Co-culture Model Mimicking the Neurovascular Unit Using Induced Pluri- and Multipotent Stem Cells. Stem Cell Rep. *8*, 894–906. https://doi.org/10.1016/j.stemcr.2017.02.021.

56. Krasemann, S., Haferkamp, U., Pfefferle, S., Woo, M.S., Heinrich, F., Schweizer, M., Appelt-Menzel, A., Cubukova, A., Barenberg, J., Leu, J., et al. (2022). The blood-brain barrier is dysregulated in COVID-19 and serves as a CNS entry route for SARS-CoV-2. Stem Cell Rep. *17*, 307–320. https://doi.org/10.1016/j.stemcr.2021.12.011.

57. Lippmann, E.S., Al-Ahmad, A., Azarin, S.M., Palecek, S.P., and Shusta, E.V. (2014). A retinoic acid-enhanced, multicellular human blood-brain barrier model derived from stem cell sources. Sci. Rep. *4*, 4160. https://doi.org/10.1038/srep04160.

58. Neal, E.H., Marinelli, N.A., Shi, Y., McClatchey, P.M., Balotin, K.M., Gullett, D.R., Hagerla, K.A., Bowman, A.B., Ess, K.C., Wikswo, J.P., and Lippmann, E.S. (2019). A Simplified, Fully Defined Differentiation Scheme for Producing Blood-Brain Barrier Endothelial Cells from Human iPSCs. Stem Cell Rep. *12*, 1380–1388. https://doi.org/10.1016/j.stemcr.2019.05.008.

59. Wegener, J., Abrams, D., Willenbrink, W., Galla, H.J., and Janshoff, A. (2004). Automated multi-well device to measure transepithelial electrical resistances under physiological conditions. Biotechniques *37*, 590–597. https://doi.org/10.2144/04374ST03.

60. Gregg, R.K. (2021). Model Systems for the Study of Malignant Melanoma. Methods Mol. Biol. *2265*, 1–21. https://doi.org/10.1007/978-1-0716-1205-7_1.

61. Venkataramani, V., Yang, Y., Ille, S., Suchorska, B., Loges, S., Tost, H., Sahm, F., Pfister, S.M., Trumpp, A., Krieg, S.M., et al. (2025). Cancer Neuroscience of Brain Tumors: From Multicellular Networks to Neuroscience-Instructed Cancer Therapies. Cancer Discov. *15*, 39–51. https://doi.org/10.1158/2159-8290.CD-24-0194.

62. Tandon, R., Brändl, B., Baryshnikova, N., Landshammer, A., Steenpaß, L., Keminer, O., Pless, O., and Müller, F.J. (2018). Generation of two human isogenic iPSC lines from fetal dermal fibroblasts. Stem Cell Res. *33*, 120–124. https://doi.org/10.1016/j.scr.2018.10.004.

63. Lorenz, C., Lesimple, P., Bukowiecki, R., Zink, A., Inak, G., Mlody, B., Singh, M., Semtner, M., Mah, N., Auré, K., et al. (2017). Human iPSC-Derived Neural Progenitors Are an Effective Drug Discovery Model for Neurological mtDNA Disorders. Cell Stem Cell *20*, 659–674.e9. https://doi.org/10.1016/j.stem.2016.12.013.

64. Dobin, A., Davis, C.A., Schlesinger, F., Drenkow, J., Zaleski, C., Jha, S., Batut, P., Chaisson, M., and Gingeras, T.R. (2013). STAR: ultrafast universal RNA-seq aligner. Bioinformatics *29*, 15–21. https://doi.org/10.1093/bioinformatics/bts635.

65. Liao, Y., Smyth, G.K., and Shi, W. (2014). featureCounts: an efficient general purpose program for assigning sequence reads to genomic features. Bioinformatics *30*, 923–930. https://doi.org/10.1093/bioinformatics/btt656.

66. Love, M.I., Huber, W., and Anders, S. (2014). Moderated estimation of fold change and dispersion for RNA-seq data with DESeq2. Genome Biol. *15*, 550. https://doi.org/10.1186/s13059-014-0550-8.

67. Durinck, S., Spellman, P.T., Birney, E., and Huber, W. (2009). Mapping identifiers for the integration of genomic datasets with the R/Bioconductor package biomaRt. Nat. Protoc. *4*, 1184–1191. https://doi.org/10.1038/nprot.2009.97.

68. Yu, G., Wang, L.G., Han, Y., and He, Q.Y. (2012). clusterProfiler: an R package for comparing biological themes among gene clusters. OMICS *16*, 284–287. https://doi.org/10.1089/omi.2011.0118.

69. Haferkamp, U., Hartmann, C., Abid, C.L., Brachner, A., Höchner, A., Gerhartl, A., Harwardt, B., Leckzik, S., Leu, J., Metzger, M., et al. (2023). Human isogenic cells of the neurovascular unit exert transcriptomic cell type-specific effects on a blood-brain barrier in vitro model of late-onset Alzheimer disease. Fluids Barriers CNS *20*, 78. https://doi.org/10.1186/s12987-023-00471-y.

70. Sharpe, J., Ahlgren, U., Perry, P., Hill, B., Ross, A., Hecksher-Sørensen, J., Baldock, R., and Davidson, D. (2002). Optical projection tomography as a tool for 3D microscopy and gene expression studies. Science *296*, 541–545. https://doi.org/10.1126/science.1068206.

71. Harberts, J., Fendler, C., Teuber, J., Siegmund, M., Silva, A., Rieck, N., Wolpert, M., Zierold, R., and Blick, R.H. (2020). Toward Brain-on-a-Chip: Human Induced Pluripotent Stem Cell-Derived Guided Neuronal Networks in Tailor-Made 3D Nanoprinted Microscaffolds. ACS Nano *14*, 13091–13102. https://doi.org/10.1021/acsnano.0c04640.

72. Teksin, Z.S., Seo, P.R., and Polli, J.E. (2010). Comparison of drug permeabilities and BCS classification: three lipid-component PAMPA system method versus Caco-2 monolayers. AAPS J. *12*, 238–241. https://doi.org/10.1208/s12248-010-9176-2.

73. Neuhaus, W., Plattner, V.E., Wirth, M., Germann, B., Lachmann, B., Gabor, F., and Noe, C.R. (2008). Validation of in vitro cell culture models of the blood-brain barrier: tightness characterization of two promising cell lines. J. Pharm. Sci. *97*, 5158–5175. https://doi.org/10.1002/jps.21371.

74. Muschong, P., Awwad, K., Price, E., Mezler, M., and Weinheimer, M. (2024). Conquering the beyond Rule of Five Space with an Optimized High-Throughput Caco-2 Assay to Close Gaps in Absorption Prediction. Pharmaceutics *16*, 846. https://doi.org/10.3390/pharmaceutics16070846.

Please cite this article in press as: Krieg et al., Cortical organoid-derived models of the melanoma brain metastatic niche enable prioritization of cancer-targeting drugs, Cell Reports Methods (2025), https://doi.org/10.1016/j.crmeth.2025.101236

CellPress
OPEN ACCESS

STAR★METHODS

KEY RESOURCES TABLE

REAGENT or RESOURCE	SOURCE	IDENTIFIER
Antibodies		
Mouse monoclonal anti-MAP2 (Clone: M13)	Invitrogen	Cat#13–1500; RRID: AB_2533001
Rabbit polyclonal anti-PAX6	Abcam	Cat# ab5790; RRID: AB_305110
Rabbit polyclonal anti-SATB2	Abcam	Cat# ab34735; RRID: AB_2301417
Rabbit polyclonal anti-RFP	Antibodies-Online	Cat# ABIN129578; RRID: AB_10781500
Mouse monoclonal anti-RFP	Invitrogen	Cat# MA5-15257; RRID: AB_10999796
Chicken polyclonal anti-RFP (mScarlet)	Synaptic Systems	Cat# 409 006; RRID: AB_2725776
Mouse monoclonal anti-Fibronectin (Clone: 1G10F9)	Proteintech	Cat# 66042-1-Ig; RRID: AB_11182385
Rabbit polyclonal anti-COL8A1	Proteintech	Cat# 17251-1-AP; RRID: AB_10696173
Mouse monoclonal anti-Vimentin	Novocastra	Cat# NCL-L-VIM-V9; RRID: AB_564055
Rabbit monoclonal anti-GFAP	Synaptic Systems	Cat# 173 008; RRID: AB_2864794
Rabbit monoclonal anti-GFAP	Synaptic Systems	Cat# 173 208; RRID: AB_2864795
Mouse monoclonal anti-p53 (Clone: DO-1)	Invitrogen	Cat# MA5-12571; RRID: AB_10986581
Rabbit polyclonal anti-Ki-67	Abcam	Cat# ab15580; RRID: AB_443209
Goat anti-rabbit AF635	Invitrogen	Cat# A-31576; RRID: AB_10374303
Donkey anti-rabbit AF488	Invitrogen	Cat# A-21206; RRID: AB_2535792
Goat anti-mouse AF633	Invitrogen	Cat# A-21050; RRID: AB_2535718
Goat anti-mouse AF488	Invitrogen	Cat# A-11001; RRID: AB_2534069
Goat anti-chicken AF488	Invitrogen	Cat# A-11039; RRID: AB_2534096
Mouse anti-CD271 (NGFR) Pacific Blue	BioLegend	Cat# 345131; RRID: AB_2894480
Mouse anti-Melan-A AF647	Santa Cruz Biotechnology	Cat# sc-20032 AF647; RRID: AB_3106925
Pacific Blue mouse IgG1, κ isotype control	BioLegend	Cat# 400131; RRID: AB_2923473
Alexa Fluor 647 mouse IgG1, κ isotype control	BioLegend	Cat# 400155; RRID: AB_2832978
Chemicals, peptides, and recombinant proteins		
Gentle Cell Dissociation Reagent	STEMCELL Technologies	Cat# 100-0485
Matrigel	Corning	Cat# 356231
Y-27632 (Dihydrochloride)	STEMCELL Technologies	Cat# 72304
Anti-adherence rinsing solution	STEMCELL Technologies	Cat# 07010
Penicillin-streptomycin	Capricorn Scientific	Cat# PS-B
Penicillin-streptomycin	PAN-Biotech	Cat# P06-07100
DMEM/F-12	Gibco	Cat# 21331046
KnockOut serum replacement	Gibco	Cat# 10828028
L-glutamine	Capricorn Scientific	Cat# GLN-B
MEM Non-Essential Amino Acids Solution	Gibco	Cat# 11140050
β-Mercaptoethanol	Gibco	Cat# 31350010
Human Endothelial Serum-Free Medium	Gibco	Cat# 11111044
B-27	Gibco	Cat# 17504044
FGF	PeproTech	Cat# 100-18b
Retinoic acid	STEMCELL Technologies	Cat# 72262
Collagen type IV	Sigma-Aldrich	Cat# C5533
Fibronectin	Gibco	Cat# 33016015
RPMI 1640	PAN-Biotech	Cat# P04-17500
FBS good	PAN-Biotech	Cat# P40-37500

(*Continued on next page*)

Please cite this article in press as: Krieg et al., Cortical organoid-derived models of the melanoma brain metastatic niche enable prioritization of cancer-targeting drugs, Cell Reports Methods (2025), https://doi.org/10.1016/j.crmeth.2025.101236

Continued

REAGENT or RESOURCE	SOURCE	IDENTIFIER
FBS advanced	Capricorn Scientific	Cat# 10-FBS-11F
GlutaMAX Supplement	Thermo Fisher Scientific	Cat# 35050038
TrypLE Express Enzyme	Gibco	Cat# 12604013
Trypsin-EDTA	PAN-Biotech	Cat# P10-024100
Puromycin-dihydrochloride	Gibco	Cat# A1113803
Geltrex	Gibco	Cat# A1413202
Formaldehyde	Carl Roth	Cat# 6742.5
Tween 20	Sigma-Aldrich	Cat# P7949
Methanol	VWR International	Cat# 20846.292
Dimethyl sulfoxide (DMSO)	Sigma-Aldrich	Cat# D5879
Hydrogen peroxide solution	Sigma-Aldrich	Cat# H1009
Triton X-100	Carl Roth	Cat# 3051.3
Low melt agarose	Bio-Rad Laboratories	Cat# 1613111
Benzyl 4-hydroxybenzoate	Sigma-Aldrich	Cat# 07389
Benzyl alcohol	Sigma-Aldrich	Cat# 108006
Poly-L-Ornithine	Sigma-Aldrich	Cat# P4957
Laminin	Sigma-Aldrich	Cat# L2020
Universal R buffer	Aptum Biologics	Cat# AP0530-500
Bovines Serum Albumin (BSA)	Carl Roth	Cat# 8076.4
Hoechst 33342	Invitrogen	Cat# H3570
TrueBlack	Biotium	Cat# 23007
ProLong Diamond Antifade Mounting Medium	Invitrogen	Cat# P36965
Hematoxylin	Ventana Roche	Cat# 760-2021
Bluing Reagent	Ventana Roche	Cat# 760-2037
qPCR Master Mix	Applied Biosystems	Cat# 4369016
Sodium chloride	Carl Roth	Cat# 0601
Potassium chloride	Sigma-Aldrich	Cat# P9541
Magnesium chloride	Carl Roth	Cat# KK36
Calcium chloride	Sigma-Aldrich	Cat# C1016
HEPES	Sigma-Aldrich	Cat# H3375
D-glucose	Sigma-Aldrich	Cat# X997
Potassium D-gluconate	Sigma-Aldrich	Cat# G4500
EGTA	Carl Roth	Cat# 3054
ATP magnesium	Sigma-Aldrich	Cat# A9187
Formaldehyde	Sigma-Aldrich	Cat# 252549
Glutaraldehyde	EMS	Cat# 16400
Paraformaldehyde	EMS	Cat# 19200
Cacodylic Acid-Sodium Salt	EMS	Cat# 12310
Sucrose	EMS	Cat# 21600
Osmium tetroxide	EMS	Cat# 19110
Ethanol	Sigma-Aldrich	Cat# 32221-M
Embed 812	EMS	Cat# 14900
D.D.S.A.	EMS	Cat# 13710
NMA	EMS	Cat# 19000
DMP-30	EMS	Cat# 13600
Uranyl acetate	Fluka	Cat# 94260
Ultrostain 2	Leica Biosystems	Cat# 16707235
Dulbecco's Phosphate Buffered Saline (D-PBS)	Sigma-Aldrich	Cat# D8537

(*Continued on next page*)

Please cite this article in press as: Krieg et al., Cortical organoid-derived models of the melanoma brain metastatic niche enable prioritization of cancer-targeting drugs, Cell Reports Methods (2025), https://doi.org/10.1016/j.crmeth.2025.101236

Continued

REAGENT or RESOURCE	SOURCE	IDENTIFIER
Ethanol	VWR International	Cat# 85651
BD Cytofix/Cytoperm Fixation and Permeabilization Solution	BD Biosciences	Cat# 554722
FluoroFix Buffer	BioLegend	Cat# 422101
Intracellular Staining Permeabilization Wash Buffer	BioLegend	Cat# 421002
Anti-cancer approved drug library	Hölzel Diagnostika Handels GmbH	Cat# L2110-1-TM
Temsirolimus	Biomol	Cat# TGM-T2145
GSK343	Biomol	Cat# TGM-T6059
Bortezomib	Hölzel Diagnostika Handels GmbH	Cat# TMO-T2399
GrowDex-T	Revvity	Cat# 200103002
Selinexor	Selleckchem	Cat# S7252
DEBIO-0932	MedChemExpress	Cat# HY-13469
Carbamazepine	Sigma-Aldrich	Cat# C4024
Atenolol	Sigma-Aldrich	Cat# A7655
Verapamil hydrochloride	Sigma-Aldrich	Cat# V4629
Fluorescein sodium salt	Sigma-Aldrich	Cat# F6377
Carbutamid	AbbVie	In-house synthesis
Water with 0.1% (v/v) formic acid	VWR International	Cat# 84867.290
Acetonitrile	VWR International	Cat# 83640.290
Ammonium bicarbonate	Sigma-Aldrich	Cat# 5.33005
Ammonium hydroxide	Honeywell International	Cat# 30501-1L
Critical commercial kits		
mTeSR Plus	STEMCELL Technologies	Cat# 100-0276
Venor GeM Sample Preparation Kit	Minerva Biolabs	Cat# 56-1050
Venor GeM OneStep Kit	Minerva Biolabs	Cat# 11-8100
STEMdiff Dorsal Forebrain Organoid Differentiation Kit	STEMCELL Technologies	Cat# 08620
STEMdiff Neural Organoid Maintenance Kit	STEMCELL Technologies	Cat# 100-0120
UltraView Universal DAB Detection Kit	Roche	Cat# 760-500
QIAshredder	QIAGEN	Cat# 79656
RNeasy Micro Kit	QIAGEN	Cat# 74004
RevertAid H Minus First Strand cDNA Synthesis Kit	Thermo Fisher Scientific	Cat# K1632
TaqMan Primer Assay TBP	Thermo Fisher Scientific	TaqMan Assay ID: Hs00427620_m1
TaqMan Primer Assay MAP2	Thermo Fisher Scientific	TaqMan Assay ID: Hs00258900_m1
TaqMan Primer Assay PAX6	Thermo Fisher Scientific	TaqMan Assay ID: Hs01088114_m1
TaqMan Primer Assay VGLUT1	Thermo Fisher Scientific	TaqMan Assay ID: Hs00220404_m1
TaqMan Primer Assay BSN	Thermo Fisher Scientific	TaqMan Assay ID: Hs01109152_m1
SYLGARD 184 Silicone Elastomer Kit	Dow	N/A
ATPlite 1step Luminescence Assay System	Revvity	Cat# 6016736
Caspase-Glo® 3/7 3D Assay	Promega	Cat# G8981
CellTiter-Glo 3D Cell Viability Assay	Promega	Cat# G9682
Human CXCL10/IP-10 ELISA Kit - Quantikine	Bio-Techne	Cat# DIP100
Deposited data		
Bulk RNA seq dataset	This paper	GEO: GSE293348
Experimental models: Cell lines		
Human iPSC line: WISCi004-B	WiCell Research Institute	RRID: CVCL_C437

(*Continued on next page*)

Please cite this article in press as: Krieg et al., Cortical organoid-derived models of the melanoma brain metastatic niche enable prioritization of cancer-targeting drugs, Cell Reports Methods (2025), https://doi.org/10.1016/j.crmeth.2025.101236

Continued

REAGENT or RESOURCE	SOURCE	IDENTIFIER
Human iPSC line: ZIPi013-B	ZIP gGmbH; Tandon et al.[62]	RRID: CVCL_UF44
Human iPSC line: HHUUKDi009-A	HHU Düsseldorf; Lorenz et al.[63]	RRID: CVCL_B3T9
Human melanoma cell line: A375	ATCC	Cat# CRL-1619; RRID: CVCL_0132
Human melanoma cell line: MelDCC3	University of Regensburg/ Fraunhofer ITEM-R	N/A
Human melanoma cell line: MelDCC8	University of Regensburg/ Fraunhofer ITEM-R	N/A
Human melanoma cell line: MelDCC11	University of Regensburg/ Fraunhofer ITEM-R	N/A
Recombinant DNA		
pRRL-CMV-GFP-puro	Swiss Institute of Cancer Research	N/A
LeGO-T2	University Medical Center Hamburg-Eppendorf	Addgene, Cat#27342; RRID: Addgene_27342
Software and algorithm		
Kaleido software	Revvity	N/A
VisiSens scientifical software	PreSens	https://www.presens.de/de/produkte/detail/visisens-scientifical-software
ImageJ 1.54	NIH	https://imagej.net; RRID: SCR_003070
Imaris 10.0.0	Oxford Instruments	http://www.bitplane.com/imaris/imaris; RRID: SCR_007370
Harmony	Revvity	https://www.perkinelmer.com/product/harmony-5-1-office-hh17000012; RRID: SCR_023543
Patch Master V2x80	HEKA Elektronik	https://www.heka.com/downloads/downloads_main.html#down_patchmaster
Origin Pro	OriginLab	http://www.originlab.com/index.aspx?go=PRODUCTS/Origin; RRID: SCR_014212
STAR v.2.4	Dobin et al.[64]	http://code.google.com/p/rna-star/; RRID: SCR_004463
featureCounts v.1.5.1	Liao et al.[65]	http://bioinf.wehi.edu.au/featureCounts/; RRID: SCR_012919
DESeq2 v.3.12	Love et al.[66]	https://bioconductor.org/packages/release/bioc/html/DESeq2.html; RRID: SCR_015687
biomaRt v.4.0	Durinck et al.[67]	https://bioconductor.org/packages/biomaRt/; RRID: SCR_019214
clusterProfiler	Yu et al.[68]	http://bioconductor.org/packages/release/bioc/html/clusterProfiler.html; RRID: SCR_016884
STRING	Global Biodata Coalition and ELIXIR	http://string.embl.de/; RRID: SCR_005223
FlowJo	BD Biosciences	https://www.flowjo.com/solutions/flowjo; RRID: SCR_008520
Analyst 1.7.2	Sciex	https://sciex.com/products/software/analyst-software
GraphPad Prism 10	GraphPad	http://www.graphpad.com/; RRID: SCR_002798
Other		
6-well plates	Greiner Bio-One	Cat# 657-160
AggreWell 800	STEMCELL Technologies	Cat# 34815
96-well ultra-low attachment plates	Corning	Cat# 7007

(*Continued on next page*)

Please cite this article in press as: Krieg et al., Cortical organoid-derived models of the melanoma brain metastatic niche enable prioritization of cancer-targeting drugs, Cell Reports Methods (2025), https://doi.org/10.1016/j.crmeth.2025.101236

Continued

REAGENT or RESOURCE	SOURCE	IDENTIFIER
Nunc 6-well plates	Thermo Scientific	Cat# 140675
ThinCert cell culture inserts	Greiner Bio-One	Cat# 662-641
Corning mini bioreactor	Sigma-Aldrich	Cat# CLS431720
24-well plates	Greiner Bio-One	Cat# 662160
35 mm Petri dish	Thermo Scientific	Cat# 130180
Echo Qualified 384-well plates	Labcyte	Cat# 001-16128
384-well plates	Greiner Bio-One	Cat# 781091
96-well cell culture microplate, CELLSTAR, black	Greiner Bio-One	Cat# 655090
96-well cell culture microplate, CELLSTAR, white	Greiner Bio-One	Cat# 655083
Breathseal sealer	Greiner Bio-One	Cat# 676050
Multi-channel micropipettes	Brand	N/A
Cell culture warming plate	Labotect	N/A
EnSight multimode plate reader	Revvity	N/A
Oxygen-sensor foils	PreSens	Cat# SF-RPSu4
VisiSens TD	PreSens	N/A
CS-Mount Lens	ArduCam	Cat# CS2325ZM01
Silicon glue	RS Components	N/A
Muvi SPIM	Bruker	N/A
ASP300S tissue processor	Leica biosystems	N/A
Antigen Retriever 2100	Aptum	N/A
Operetta CLS High Content Imaging System	Revvity	N/A
Ventana BenchMark XT autostainer	Ventana	N/A
Zeiss Axioscope 5 microscope	Zeiss	N/A
Axiocam 208 color camera	Zeiss	N/A
NanoDrop 1000 spectrophotometer	Thermo Fisher Scientific	N/A
QuantStudio 6 Flex Real-Time-PCR-System	Applied Biosystems	N/A
EPC 10 USB System with Red Star Headstage	Warner Instruments	Cat# 89-5273
Eclipse FN1 microscope	Nikon	N/A
LYNX microscopy tissue processor	Reichert-Jung	N/A
Side-mounted 2kx2k camera	TRS TRÖNDLE Restlichtverstärkersysteme	N/A
LEO 912AB electron-microscope	ZEISS	N/A
Ultracut S Microtome	Reichert-Jung	N/A
Diamond knives	DiATOME	N/A
Autosamdri-815	Tousimi	N/A
Goldpalladium	Leica Microsystems	Cat# EM ACE 200
Crossbeam 550	Zeiss	N/A
FACSymphony A3	BD Biosciences	N/A
Gallios 10C 3L Flow Cytometer	Beckmann Coulter	N/A
Echo 550 liquid handler	Labcyte	N/A
MultiDrop	Thermo Fisher Scientific	N/A
Standard Tube Cassettes	Steinle Labtechnology	N/A
EnVision Multimode Plate Reader	Revvity	N/A
cellZscope	nanoAnalytics	N/A
Infinite M1000 Pro	TECAN	N/A
MTS4 microtiter shaker	IKA	N/A

(*Continued on next page*)

Please cite this article in press as: Krieg et al., Cortical organoid-derived models of the melanoma brain metastatic niche enable prioritization of cancer-targeting drugs, Cell Reports Methods (2025), https://doi.org/10.1016/j.crmeth.2025.101236

Continued

REAGENT or RESOURCE	SOURCE	IDENTIFIER
Acquity UPLC	Waters	N/A
Sciex 6500+	Sciex	N/A
BEH C18 column	Waters	Cat# 186002349

EXPERIMENTAL MODEL AND STUDY PARTICIPANT DETAILS

All experiments involving cells originated from patient biopsies and were approved by the medical ethics committee of the University of Regensburg. MelDCC lines were derived from lymph node biopsies of melanoma patients after tumor resection and were propagated directly *in vitro* or in xenografts as described previously[16] and S.M.-R., M.W.-K., C.A.K., K. Weidele, C. Werno, and S. Treitschke (unpublished data).

METHOD DETAILS

Cultivation of human hiPSCs

Human wild-type iPSCs (WISCi004-B, WiCell), ZIPi013-B,[62] and HHUUKDi009-A[63] were maintained on Matrigel (Corning, 356231)-coated 6-well plates (Greiner Bio-One, 657-160) in mTeSR Plus medium (STEMCELL Technologies, 100–0276). Passaging was performed approximately every five days at 50–70% confluency, using Gentle Cell Dissociation Reagent (STEMCELL Technologies, 100–0485), and medium was refreshed every other day. To routinely confirm the absence of mycoplasma contamination, the Venor GeM Sample Preparation Kit (Minerva Biolabs, 56–1050) and Venor GeM OneStep Kit (Minerva Biolabs, 11–8100) were utilized according to the manufacturer's instructions. All cell cultures were conducted at 37°C and 5% CO_2 in humidified incubators, unless otherwise stated.

Differentiation of hiPSC-derived cortical organoids

Differentiation of hiPSCs into hCO was performed as previously described[27,31] using the STEMdiff Dorsal Forebrain Organoid Differentiation Kit (STEMCELL Technologies, 08620) with some adaptations. First, hiPSCs at a confluency of 60–80% were detached using Gentle Cell Dissociation Reagent (STEMCELL Technologies, 100–0485) and 3×10^6 cells transferred to each well of an AggreWell 800 microwell culture plate (STEMCELL Technologies, 34815) in forebrain organoid formation medium supplemented with 10 μM Y-27632 (STEMCELL Technologies, 72304). The medium was changed daily using forebrain organoid formation medium without Y-27632. On day 6, embryoid bodies were individually transferred to 96-well clear round bottom ultra-low attachment microplates (Corning, 7007) on a cell culture warming plate (Labotect) using sterilized wide-bore tips (prepared in-house) coated with anti-adherence rinsing solution (STEMCELL Technologies, 07010). To prevent evaporation and minimize plate effects, border wells were filled with D-PBS. Until day 25, hCOs were cultured in organoid expansion medium (200 μL/well), followed by organoid differentiation medium (200 μL/well). From day 43, hCOs were maintained in organoid maintenance medium (200 μL/well) using the STEMdiff Neural Organoid Maintenance Kit (STEMCELL Technologies, 100–0120). All medium changes were carefully performed as partial medium changes (50–75% of the volume) using multi-channel micropipettes (Brand) three times a week. Organoid media used in microplates were supplemented with 0.5% penicillin-streptomycin (Capricorn Scientific, PS-B). Each batch contained a maximum of 240 hCOs distributed across four 96-well plates.

Differentiation of hiPSC-derived BCECs for *in vitro* BBB models

The brain capillary endothelial cell (BCEC) differentiation was performed as reported previously[56,69]. Differentiation of hiPSCs (WISCi004-B), cultured in mTeSR Plus (STEMCELL Technologies, 100–0276) on Matrigel (Corning, 356231)-coated Nunc 6-well plates (Thermo Scientific, 140675), was initiated three days post-seeding. At an optimal cell density of $2–4 \times 10^3$ cells/cm^2, the medium was changed to unconditioned medium containing 78.5% DMEM/F-12 (without Glutamine; Gibco, 21331046), 20% KnockOut serum replacement (Gibco, 10828028), 1 mM L-glutamine (Capricorn Scientific, GLN-B), 1% non-essential amino acids (Gibco, 11140050), and 0.1 mM β-mercaptoethanol (Gibco, 31350010). At day 6, medium was switched to endothelial cell (EC) medium containing 99.5% Human Endothelial Serum-Free Medium (Gibco, 11111044) and 0.5% B-27 (Gibco, 17504044), supplemented with 20 ng/mL hFGF (PeproTech, 100-18b) and 10 μM retinoic acid (RA) (STEMCELL Technologies, 72262). By day 8 of differentiation, 1×10^6 cells/cm^2 were seeded onto Collagen IV (Sigma-Aldrich, C5533)/Fibronectin (Gibco, 33016015)-coated inserts (0.4 μm pore size, transparent, 24-well format; Greiner Bio-One, 662-641). The next day, BCECs were adapted to EC medium without hFGF and RA. We monitored transendothelial electrical resistance (TEER) to assess the integrity of the established *in vitro* BBB, including only inserts with values $\geq$1000 Ω*cm^2 for subsequent permeability studies.

2D cultivation of melanoma cells

MelDCC lines were derived from DCC xenografts or directly propagated *in vitro* as described previously[16] and S.M.-R., M.W.-K., C.A.K., K. Weidele, C. Werno, and S. Treitschke (unpublished data). Patient origin was verified by STR analysis (Cell-ID, Promega),

Please cite this article in press as: Krieg et al., Cortical organoid-derived models of the melanoma brain metastatic niche enable prioritization of cancer-targeting drugs, Cell Reports Methods (2025), https://doi.org/10.1016/j.crmeth.2025.101236

melanoma origin by a surgical pathologist, and genotype by copy number alterations. MelDCCs were cultured in complete MelDCC medium containing RPMI 1640 (without L-Glutamine, with 2.0 g/L $NaHCO_3$; PAN-Biotech, P04-17500) with 10% FBS good (PAN-Biotech, P40-37500), 1% penicillin-streptomycin (PAN-Biotech, P06-07100), and 1% GlutaMAX Supplement (Thermo Fisher Scientific, 35050038). Depending on the growth rate, cells were passaged every three to five days using TrypLE Express Enzyme (Gibco, 12604013) in ratios between 1:2 and 1:10. A375 (CRL-1619) cell line was obtained from ATCC. Cells were maintained in complete A375 medium containing DMEM/F-12 (without Glutamine; Thermo Fisher Scientific, 21331046) with 10% FBS advanced (Capricorn Scientific, 10-FBS-11F), 1% penicillin-streptomycin (Capricorn Scientific, PS-B) and 2 mM L-Glutamine (Capricorn Scientific, GLN-B) and regularly passaged every three to four days using 0.05% Trypsin/0.02% EDTA (PAN Biotech, P10-024100). All cells were regularly tested for mycoplasma contamination.

Lentiviral transduction of melanoma cells

To induce and restrict fluorescence reporter protein expression to cancer cells only, we produced stable lines prior to co-cultivation. MelDCCs were transduced using the lentiviral vector pRRL-CMV-GFP-puro (kindly provided by Stephan Duss, ISREC, Swiss Institute of Cancer Research, Lausanne). A375-tdTomato reporter cell line was generated by lentiviral transduction using the LeGO-T2-Puro vector (kindly provided by Kristoffer Riecken, University Medical Center Hamburg-Eppendorf). Antibiotic selection was performed using puromycin-dihydrochloride (Gibco, A1113803), and tdTomato and GFP expressing cells were cryopreserved for follow-up experiments.

Melanoma brain metastases models

43-day-old hCOs with visible integrity were co-cultured with fluorescence-labeled melanoma cells for seven days. Therefore, melanoma cells from 2D maintenance cultures were detached as described before at a confluency of 60–90% and 1×10^4 cells were applied by performing a regular medium change to each hCO followed by centrifugation for 3 min at 100 g. Co-culture formation was done at 37°C for 48 h in organoid maintenance medium. All medium changes were carried out with organoid maintenance medium supplemented with 0.5% penicillin-streptomycin (Capricorn Scientific, PS-B). They were carefully performed as partial medium changes (50–75% of the volume) using multi-channel micropipettes (Brand) three times a week. At day 50 (day 43 + 7), MBM models were used for downstream analysis as well as efficacy and safety studies.

MelDCC tumoroid propagation using semi-solid culture

Tumoroids were grown in Corning mini bioreactor centrifuge tubes with vented caps (Sigma-Aldrich, CLS431720). 3.5×10^5 single cells from 2D cultures were transferred into each bioreactor and cultured in 5 mL semi-solid culture medium containing complete MelDCC medium supplemented with 5% Geltrex LDEV-Free Reduced Growth Factor Basement Membrane Matrix (Gibco, A1413202). Every three to four days, 2.5 mL of the semi-solid culture medium was added, and the suspension was mixed by pipetting up and down approximately 10 times using a 1 mL pipette tip. Tumoroids were harvested on day 10 for drug screening.

Live imaging

Brightfield and fluorescence imaging of hCOs and MBMs at different stages were conducted using the EnSight multimode plate reader (Revvity). Live imaging allowed monitoring of morphological parameters (organoid area and roundness) as well as the fluorescence intensity of MBMs with or without compound exposure, and did not exceed 15 min imaging time per plate. Single images were processed as z-stacks (seven images spanning 1800 μm) for a representative image and plate overviews. Images were analyzed by spheroid detection using Kaleido software (Revvity) with object detection settings (tuning of brightness limit: 0.6, flatfield correction scale of brightfield: 0, minimum object size: 100,000 μm^2, minimum contrast requirements: very relaxed, ring-shaped objects: yes, largest objective, only: yes) and well detection settings (channel: automatic, exclude well margin 400 px, mode: small well, well dimensions: automatic, well shape: round, well diameter: 6.3 mm). Analyzed fluorescence data exclusively accounted for the fluorescence intensity of cancer cells within the detected organoid region. For MBM values, the fluorescence background of hCOs in organoid maintenance medium was subtracted.

Oxygen measurements

Oxygen levels were monitored using VisiSens TD (PreSens) at 37°C and 5% CO_2 in a dry incubator. VisiSens TD was customized with a CS-Mount Lens (CS2325ZM01, ArduCam), providing the necessary field of view and magnification to monitor the organoids with sufficient lateral resolution. The oxygen-sensitive sensor foil was glued to the bottom of a standard 24- well cell-culture plate (Greiner Bio-One, 662160) using a biocompatible silicon glue (RS Components). Before use, the sensor plates were treated with argon plasma for 1 min hCOs at day 43 were transferred to Poly-L-Ornithine/Laminin (Sigma-Aldrich, P4957, L2020) coated oxygen-sensor foils (PreSens, SF-RPSu4) and cultured in organoid maintenance medium (STEMCELL Technologies). Oxygen imaging was started directly after organoid transfer. An image was taken every 5 min over the time course of 12 h. Data was analyzed using the VisiSens Scientifical software (PreSens) and ImageJ 1.54 (NIH). Sensors were calibrated via a 2-point calibration at 0% and 100% air saturation. A solution of sodium sulfite in medium served as 0% calibration solution.

Whole-mount imaging

Staining, clearing, and imaging procedures were based on previous reports.[70] A375-MBMs were transferred to a 4% formaldehyde (Carl Roth, 6742.5) solution for 24 h. Samples were then incubated in 0.1% Tween 20 (Sigma-Aldrich, P7949) in D-PBS, followed by methanol (VWR, 20846.292) dehydration series, each 20 min. Samples can be stored in 100% methanol at −20°C. Incubation in methanol/DMSO/H_2O_2 solution (VWR International, 20846.292; Sigma-Aldrich, D5879; Sigma-Aldrich, H1009) in a ratio of 2:1:3 was conducted at 4°C overnight, followed by a methanol rehydration series, each for 20 min, and washing in 0.1% Tween 20 in D-PBS. Permeabilization and blocking were subsequently achieved using 0.1% Triton X-100 (Carl Roth, 3051.3) and 10% BSA (Carl Roth, 8076.4) in D-PBS overnight. Primary antibodies MAP2 (Invitrogen, 13–1500) and RFP (Antibodies-Online, ABIN129578) were incubated in a dilution of 1:100 in permeabilization and blocking solution supplemented with 5% DMSO (Sigma-Aldrich, D5879) on an orbital shaker for three days at room temperature. After washing in 0.1% Triton X-100 in D-PBS for 1 day, samples were incubated in secondary antibodies listed in the key resources table 1:500 for three days, washed, and embedded in 1% low melt agarose (Bio-Rad Laboratories, 1613111). Embedded samples were incubated in 100% methanol followed by optical clearing in BABB solution (1:2 Benzylalcohol:Benzylbenzoate; Sigma-Aldrich) for 24 h each. Samples were imaged using the light-sheet microscope Muvi SPIM (Bruker) with a 10× objective in BABB clearing solution. 3D data stacks were reconstructed using Imaris software 10.0.0 (Oxford Instruments). Alpha blending was applied to the images to adjust transparency and improve detail perception.

Immunohistochemistry

2D cell cultures of A375 cells were fixed in a 4% formaldehyde solution for 20 min, scratched, and pelleted before paraffin embedding. Whole hCOs and A375-MBMs were fixed in 4% formaldehyde for 24 h, protected in 3% agarose prior to embedding, dehydrated using an ASP300S tissue processor (Leica Biosystems), and embedded in paraffin. Sections were cut at 3 μm, followed by deparaffination, rehydration, and antigen retrieval by pressure boiling in Universal R buffer (Aptum Biologics, AP0530-500) for 20 min using an Antigen Retriever (Aptum, 2100). For histological assessment, sections were stained with hematoxylin and eosin (H&E) according to standard procedures. For immunohistochemical staining, sections were permeabilized in 0.2% Triton X-100 (Carl Roth, 2051), blocked in 3% BSA (Carl Roth, 8076.4) and 0.1% Tween 20 (Sigma-Aldrich, P7949) in D-PBS and primary antibodies MAP2 (1:500, Invitrogen, 13–1500), PAX6 (1:200, Abcam, ab5790), SATB2 (1:500, Abcam, ab34735), RFP (1:1000, Antibodies-Online, ABIN129578), RFP (1:500, Invitrogen, MA5-15257), RFP (1:100, Synaptic Systems, 409006), Fibronectin (1:300, Proteintech, 66042-1-Ig), COL8A1 (1:50, Proteintech, 17251-1-AP), GFAP (1:2000, Synaptic Systems, 173008 and 1:200, Synaptic Systems, 173208), Ki-67 (1:500, Abcam, ab15580) and p53 (1:50, Invitrogen, MA5-12571) incubated over night at 4°C. The next day, sections were thoroughly washed in 0.1% Tween 20 in D-PBS and cold tap water, incubated with secondary antibodies listed in the key resources table in a dilution of 1:500 for 1 h, and thoroughly washed again. Nuclei were stained using 1 μg/μL Hoechst 33342 (Invitrogen, H3570). TrueBlack (Biotium, 23007) was shortly applied to mask autofluorescence before sections were mounted in ProLong. Diamond Antifade Mounting Medium (Invitrogen, P36965) with glass coverslips. We used the Operetta CLS High Content Imaging System (Revvity) with a 40× objective and confocal mode to image tissue sections on slide holders. Images covering full samples were acquired with 20% overlap and reconstructed using the Harmony software (Revvity). For comparative analysis of immunostaining, the samples were processed in parallel and imaged using the same settings.

GFAP-DAB and Vimentin (1:750, Novocastra, NCL-L-VIM-V9) staining was performed using the Ventana BenchMark XT autostainer (Ventana/Roche). After dewaxing and inactivation of endogenous peroxidases (3% hydrogen peroxide), sections were blocked and afterward incubated with the primary antibody (see above). For detection of specific binding and DAB staining, the UltraView Universal DAB Detection Kit (Roche, 760-500) was used, which contains both anti-mouse and anti-rabbit secondary antibodies. Counterstaining and bluing were performed with Hematoxylin (Ventana/Roche, 760–2021) and Bluing Reagent (Ventana/Roche, 760–2037) for 4 min. Subsequently, stained sections were mounted in mounting medium. Representative pictures were taken with a Zeiss Axioscope 5 microscope (Zeiss) and an Axiocam 208 color camera (Zeiss).

Quantitative reverse-transcription PCR analysis

Total RNA was extracted from pooled hCOs ($n = 3$ per batch) and corresponding hiPSC cultures using QIAshredder (QIAGEN, 79656) and the RNeasy Micro Kit (QIAGEN, 74004). RNA concentration was measured by NanoDrop 1000 spectrophotometer (Thermo Fisher Scientific), followed by cDNA synthesis using RevertAid H Minus First Strand cDNA Synthesis Kit (Thermo Fisher Scientific, K1632). cDNA synthesis was carried out using the following protocol: 5 min at 25°C, 60 min at 42°C, and 5 min at 70°C, followed by cooling to 4°C. cDNA was diluted to reach a 10 ng/μL concentration for the PCR reaction. Gene expression analysis for *TBP*, *MAP2*, *PAX6*, *VGLUT1*, and *BSN* was performed using qPCR Master Mix (Applied Biosystems, 4369016), with TaqMan primers listed in the key resources table. We used the QuantStudio 6 Flex Real-Time-PCR-System (Applied Biosystems) with the following protocol: 2 min at 50°C, 10 min at 95°C, 15 s at 95°C (for 40 cycles), and 1 min at 60°C. All measurements were performed in triplicate. hCO CT values were analyzed using the $2^{-\Delta\Delta CT}$ method, normalized to the reference gene TBP and to the corresponding hiPSC control, and reported as Log2 fold change.

Patch clamp analysis

50-day-old hCOs were seeded on Poly-L-Ornithine/Laminin (Sigma-Aldrich, P4957, L2020) coated glass coverslips in organoid maintenance medium supplemented with 10 μM Y-27632 (STEMCELL Technologies, 72304). The next day, the medium was

replaced with fresh organoid maintenance medium. Electrophysiology measurements were performed two to three days post-seeding as previously described with a few modifications.[71] Coverslips were transferred to a 35 mm Petri dish (Thermo Scientific, 130180), washed three times and submerged in bath solution (140 mM NaCl (Carl Roth, 0601), 2.4 mM KCl (Sigma-Aldrich, P9541), 1.3 mM $MgCl_2$ (Carl Roth, KK36), 2.5 mM $CaCl_2$ (Sigma-Aldrich, C1016), 10 mM HEPES (Sigma-Aldrich, H3375), 10 mM D-glucose (Sigma-Aldrich, X997), pH 7.4) at room temperature. Pipettes were filled with pipette solution consisting of 125 mM potassium gluconate (Sigma-Aldrich, G4500), 10 mM NaCl (Carl Roth,0601), 1 mM EGTA (Carl Roth, 3054), 4 mM magnesium ATP (Sigma-Aldrich, A9187), 10 mM HEPES (Sigma-Aldrich, H3375), 10 mM D-glucose (Sigma-Aldrich, X997), pH 7.4, at room temperature. For data recording, a HEKA EPC 10 USB patch-clamp amplifier with a Red Star Headstage (Warner Instruments, 89–5273) and the Patch Master V2x80 software (HEKA Elektronik) were employed. A Bessel low-pass filter was set to 2.9 kHz, and capacitance and series resistance were automatically compensated. The set-up was mounted to an upright Nikon Eclipse FN1 microscope with a Nikon CFI TU Plan EPI ELWD 50x N.A. 0.60/W.D. 11.00 mm objective.

Outgrowing neurons from organoids on coverslips were patched, and three batches were analyzed. Their electrophysiology was assessed by their response to a current step function in current clamp mode from −5 to 40 pA in 5 pA steps. Currents were applied for 600 ms. Solely, neurons exhibiting action potential (AP) trains ($n_{AP} \geq 3$) were further analyzed, i.e., $n = 8$ cells per batch. For AP characterization, the first AP of an AP train at rheobase current was examined. AP threshold was defined as the membrane potential where the second derivative became different from zero, AP height as the threshold to peak, and AP duration as the full-width half-maximum of the AP. The resting membrane potential was determined in current-clamp mode at a current set to zero, the membrane capacitance by the Patch Master software. Inward and outward currents were recorded in whole-cell mode by a voltage step function from −70 to +30 mV in 10 mV steps. Currents were applied for 100 ms. Maximum inward and outward currents were plotted against the applied voltage. Data interpretation was conducted with Origin Pro (OriginLab), and the second derivative was derived with Savitzky−Golay smooth (polynomial order 3, points of window: 30).

Bulk RNA sequencing

Total RNA was isolated from single hCOs, A375-MBMs, and 2D A375 cells ($n = 5$ per condition) using QIAshredder (QIAGEN, 79656) and the RNeasy Micro Kit (QIAGEN, 74004). RNA concentration was measured by the NanoDrop 1000 spectrophotometer (Thermo Fisher Scientific). RNA sequencing was performed at CeGAT GmbH with the library preparation kit TruSeq Stranded mRNA (Illumina) and NovaSeq 6000, 2x101bp. The reads were aligned to the Ensembl human reference genome (GRCh38) using STAR v.2.4 with default parameters.[64] The overlap with annotated gene loci was counted with featureCounts v.1.5.1.[65] Differential expression analysis was performed with DESeq2 (v.3.12)[66] calling differentially expressed genes with a minimal 2-fold change and false discovery rate (FDR)-adjusted $p < 0.05$. Top regulated genes were identified using the Wald-statistic that is used by DESeq2. Gene lists were annotated using biomaRt (v.4.0).[67] Gene set enrichment analysis (GSEA) was performed using the clusterProfiler package and STRING.[68] Principal component analysis was performed using the top 500 regulated genes estimated by Wald-statistics.

Transmission electron microscopy

hCOs and A375-MBMs for ultrastructural analysis were first fixed in Karnovsky fixative (2.5% glutaraldehyde (EMS, 16400), 2% paraformaldehyde (EMS, 19200), 0.1 M sodium-cacodylate buffer (EMS,12310), 1% sucrose (EMS, 21600)) and afterward embedded (post-fixation with osmium tetroxide (EMS,19110), dehydration with graded ethanol (Sigma-Aldrich, 32221-M), infiltration with EPON (90 g (EMbed812) (EMS, 14900), 60 g DDSA (EMS, 13710), 40 g NMA (EMS, 19000), 3 g DMP-30 (EMS, 13600)) in the LYNX microscopy tissue processor (Reichert-Jung). The EPON blocks were polymerized for two days at 60°C. Semi-thin sections (0.75 μm) for the selection of relevant areas and ultra-thin sections (80 nm) were cut with an Ultracut S Microtome (Reichert-Jung) with diamond knives (DiATOME). The ultra-thin sections were contrasted with aqueous 2% uranyl acetate (Fluka, 94260) and 2% lead-citrate solution (Ultrostain 2) (Leica Biosystems, 16707235) for 10 min each. For the sample documentation, the side-mounted 2kx2k camera (TRS TRÖNDLE Restlichtverstärkersysteme) of a LEO 912AB electron-microscope (Zeiss) was used with the imageSP-software (TRS TRÖNDLE Restlichtverstärkersysteme).

Scanning electron microscopy

For high-resolution scanning electron microscopy, MBM models were fixed overnight at room temperature by the addition of equal volumes of 8% formaldehyde in D-PBS (Sigma-Aldrich, 252549, D8537) to the culture medium and washed three times with D-PBS. Fixed MBM models were transferred in a small droplet onto a 1 cm thick piece of PDMS (Dow, SYLGARD 184 Elastomer Kit) and lanced with a 150 μm thick stainless-steel needle (Golrisen). Subsequently, MBM models were dehydrated by a stepwise ethanol exchange, i.e., incubation in 25% ethanol in PBS, 50% EtOH in deionized (DI) water, 75% ethanol in DI water, and 100% ethanol (VWR International, 85651) for 10 min at room temperature each. Critical point drying was conducted using an Autosamdri-815 (Tousimi). Factory presets were used, purge time was 15 min. Dried MBM models were sputtered with 5 nm gold palladium (Leica Microsystems, EM ACE 200) from top and bottom, and stored at room temperature until imaging with a Crossbeam 550 (Zeiss).

CXCL10 ELISA

Cell supernatant was collected from hCOs and A375-MBM cultures at day 50 or day 56, and stored at −20°C. Chemokine concentration was determined using the Human CXCL10/IP10 Quantikine enzyme-linked immunosorbent assay (ELISA) kit (Bio-Techne,

Please cite this article in press as: Krieg et al., Cortical organoid-derived models of the melanoma brain metastatic niche enable prioritization of cancer-targeting drugs, Cell Reports Methods (2025), https://doi.org/10.1016/j.crmeth.2025.101236

DIP100) according to the manufacturer's instructions. The optical density was measured using the EnVision Multimode Plate Reader (Revvity). All measurements were performed in duplicates.

Flow cytometry

For tdTomato expression analysis, cells were fixed in BD Cytofix Fixation Buffer (BD Biosciences, 554722) for 20 min at room temperature and analyzed using FACSymphony A3. To confirm GFP expression, cells were fixed in FluoroFix Fixation Buffer (BioLegend, Cat# 422101) for 20 min and analyzed using Gallios 10C 3L Flow Cytometer (Beckmann Coulter). For phenotyping, cells were stained for NGFR (1:20, BioLegend, Cat# 345131) or isotype control (1:33, BioLegend, 400131) for 20 min at room temperature, fixed in FluoroFix Fixation Buffer (BioLegend, Cat# 422101) for 20 min, and subsequently washed with 1 × Permeabilization Wash Buffer (BioLegend, Cat# 421002). Intracellular marker Melan-A (1:40, Santa Cruz Biotechnology, Sc-20032) or isotype control (1:20, BioLegend, 400155) was stained for 30 min at room temperature. Labeled cells were recorded in FACS Buffer (2% FCS in D-PBS) using Gallios 10C 3L Flow Cytometer (Beckmann Coulter). Data were analyzed using the FlowJo software (BD Biosciences).

Anti-cancer approved library drug screen

Anti-cancer approved drug library (L2110-1-TM) was acquired from Hölzel Diagnostika Handels GmbH containing 313 compounds at a concentration of 10 mM in DMSO. We further included temsirolimus (Biomol, TGM-T2145) and GSK343 (Biomol, TGM-T6059) in the library. From drug library source plates, dilution plates containing 1 mM, 0.1 mM, or 0.001 mM compound concentration were prepared, and 8 μL of compound was transferred into Echo Qualified 384-Well Low Dead Volume Microplates. Library plates (Labcyte, 001–16128) were stored at −80°C. Final assay-ready plates (Greiner Bio-One,781091) were prepared using the Echo 550 liquid handler (Labcyte) to obtain a final compound concentration of 1 μM for single-point drug screening. 10 μM bortezomib (Hölzel Diagnostika Handels GmbH, TMO-T2399) was used as a positive control and 0.1% DMSO as a negative control on each plate. For drug validation, assay-ready plates with 10-point dose-response titration in 1:4 dilution steps starting from 50 μM were prepared. For 2D drug screen, single cell suspensions (300–2500 cells/well, depending on growth rate) of A375, MelDCC3, and MelDCC8 were seeded in 40 μL complete medium in assay-ready plates using MultiDrop Combi reagent dispenser (Thermo Fisher Scientific) and Standard Tube Cassettes (Steinle Labtechnology). For 3D drug screening, tumoroids were counted by live imaging using the Operetta Imaging System (Revvity) based on GFP signal in 96-well plates (Greiner Bio-One, 655090) with 10× objectives, non-confocal mode, 5% overlap, and analyzed using a building block-based algorithm in Harmony software (Revvity). 200 tumoroids per well were plated in assay-ready plates in 40 μL complete medium containing 0.005% GrowDex-T (Revvity, 200103002). Plates were sealed with Breathseal sealer (Greiner Bio-One, 676050) and incubated for 120 h. Sensitivity of 2D cultures toward compounds was assessed by ATPlite 1step Luminescence Assay System (Revvity, 6016736) following manufacturer's instructions. MelDCC tumoroid viability was measured using CellTiter-Glo 3D Cell Viability Assay (Promega, G9682) according to the manufacturer's instructions. Luminescence signals were measured with EnVision Multimode Plate Reader (Revvity). Values were normalized to corresponding DMSO controls. As a quality criterion, we calculated Z′ values for each assay plate. Data for the MelDCC11 cell line and immortalized melanocytes (NHEM) were included from S.M.-R., M.W.-K., C.A.K., K. Weidele, C. Werno, and S. Treitschke (unpublished data).

Drug sensitivity assay in 3D MBM models

For the validation of the primary drug screen, hit compounds were screened using 50-day-old A375-MBMs at 10 μM concentration for 72 h in comparison to the combination therapy of encorafenib and binimetinib. Compounds were selected from an in-house drug repurposing library based on.[43] For dosing experiments of selinexor (Selleckchem, S7252) and DEBIO-0932 (MedChemExpress, HY-13469) in MBM models, either dose-response titration in 1:2 dilution steps starting from 10 μM or single compound concentrations were refreshed daily during six consecutive days. Control wells were treated with 0.1% DMSO. Compounds and concentrations were tested in duplicates or triplicates. All experiments were performed by full medium changes of organoid maintenance medium supplemented with compounds (100 μL/well) in final the dilution using multichannel pipettes. The viability of MBMs was measured by brightfield and fluorescence live imaging as described before. To measure caspase activation, we performed the Caspase-Glo 3/7 3D Assay (Promega, G8981) according to the manufacturer's instructions. Caspase-Glo reagent was added in equal amounts, mixed on a shaker (30 s, 60 rpm), and incubated for 30 min at room temperature. Luminescence was recorded using the EnSight multimode plate reader (Revvity). Viability values were normalized to corresponding DMSO controls. Samples referred to as prolonged A375-MBM cultures correspond to the DMSO control samples at day 56.

Drug sensitivity assay in hCOs

hCOs were treated with compounds as described above in parallel to corresponding A375-MBMs. For the assessment of hCO viability, we performed CellTiter-Glo 3D Cell Viability Assay (Promega, G9682) according to the manufacturer's instructions. For this, the CellTiter-Glo reagent was added in equal amounts, and cell lysis was induced by repetitive pipetting and repetitive shaking (5 min, 60 rpm). Lysates were transferred in a ratio of 1:10 to D-PBS in white-bottom microplates (Greiner Bio-One, 655083) and additionally incubated with equal amount of the CellTiter-Glo reagent, first on a shaker (5 min, 60 rpm) and then for another 25 min at room temperature. Luminescence was recorded using the EnSight multimode plate reader (Revvity). Viability values were normalized to corresponding DMSO controls.

Please cite this article in press as: Krieg et al., Cortical organoid-derived models of the melanoma brain metastatic niche enable prioritization of cancer-targeting drugs, Cell Reports Methods (2025), https://doi.org/10.1016/j.crmeth.2025.101236

Impedance measurements

To monitor the integrity of the *in vitro* BBB over time, we used impedance spectroscopy, enabling simultaneous measurement of transendothelial electrical resistance (TEER) and cell layer capacitance (C_{cl}). hiPSC-derived BCECs were seeded onto inserts and placed in a 24-well cell module of a cellZscope device (nanoAnalytics) inside an incubator at 37°C with 5% CO_2. TEER and C_{cl} values were extracted from the impedance spectra using equivalent circuit modeling as implemented in the cellZscope software. Both values were assessed every hour for a duration of 96 h.

In vitro blood-brain barrier permeability assay

At day 10 of differentiation, hiPSC-derived BCECs were used to investigate the BBB permeation of selinexor and DEBIO-0932. We compared their transport properties to reference substances with varying BBB permeation: Carbamazepine (quick permeation; Sigma-Aldrich, C4024), atenolol (slow permeation; Sigma-Aldrich, A7655), and verapamil (considered medium permeation, as its classification varies by study and model used; Sigma-Aldrich, V4629).[72] Compounds were diluted in EC medium to a concentration of 10 μM and applied to the donor compartment, which is the apical (A) compartment for A-to-B transport or the basolateral (B) compartment for B-to-A transport. After incubating the BCECs with compounds for 1 h at 37°C on an orbital shaker set to 100 rpm, medium samples from both apical and basolateral compartments were collected for downstream analysis. To monitor monolayer integrity during the experiment, 10 μM fluorescein solution (Sigma-Aldrich, F6377) was added together with the test compounds in each apical compartment at a concentration of 10 μM. The concentration of the fluorescent tracer molecule was measured using a fluorescent plate reader (excitation: 490 nm, emission: 525 nm; Infinite M1000 Pro, TECAN), and its permeability coefficient was calculated according to the clearance principle, as described previously,[73] to confirm the integrity of the BBB during compound treatment. The samples for liquid chromatography with tandem mass spectrometry (LC-MS/MS) measurement were stored at −80°C until analysis. Apparent permeability (P_{app}) values were calculated from peak areas using the following equation, as previously described[74]:

$$P_{app} = \frac{\Delta Q}{\Delta t} \times \frac{1}{A \times \left(\frac{C_D + C_0}{2}\right)}$$

Where ΔQ is the amount of the compound permeated into the acceptor compartment as determined by the response (= peak area) of compound in the acceptor compartment at the end of the incubation time. A is the surface area of the insert membrane (0.34 cm^2), C_0 is the initial nominal compound concentration, C_D is the response in the donor compartment at the end of the incubation time, and t the incubation time.

The efflux ratio (ER) is calculated as follows, with ER > 2 indicating active efflux:

$$ER = \frac{P_{app}(BA)}{P_{app}(AB)}$$

Where P_{app} (A-B) refers to the permeability in the direction of apical to basolateral, and P_{app} (B-A) refers to the permeability in the direction of basolateral and apical.

Unless stated otherwise, only assays with recovery rates (mass balance) between 65% and 135% were considered. Recovery was determined with the following equation:

$$Recovery\ (\%) = \frac{C_A + C_D}{C_0}\ x\ 100$$

Where C_A and C_D are the responses of the compound determined in the acceptor and donor compartments at the end of the incubation time, respectively. C_0 is the initial nominal compound concentration.

LC-MS/MS sample preparation and analysis

For LC-MS/MS analysis, the samples from the BBB permeability assays were thawed and thoroughly mixed for 5 min at 600 rpm on an orbital microtiter plate shaker (IKA MTS 4) and 5x up- and down pipetting. Donor samples were diluted 1:5 with assay buffer (EC medium), and all samples were mixed with 100% ethanol containing 25 nM Carbutamid (AbbVie, in-house synthesis) as internal LC-MS/MS process control. The samples were centrifuged at 3000 x *g* for 30 min, and the supernatants were taken for measurement.

LC-MS/MS analysis was performed using an Acquity UPLC (Waters) coupled with a tandem mass spectrometer Sciex 6500+ (Sciex) operating in multiple reaction monitoring (MRM). Samples were separated with the BEH C18 column (30 mm × 2.1 mm, 1.7 μm; Waters, 186002349) at 50°C using a two-step gradient elution with water (mobile phase A, VWR International, 84867.290) and acetonitrile (mobile phase B, VWR International, 83640.290), both acidified with 0.1% formic acid. The run time of chromatographic separation was a linear 1.1 min gradient, starting with 95% mobile phase A and peaking with 95% mobile phase B. In the case of selinexor, mobile phase A was replaced with 25 mM ammonium bicarbonate (Sigma-Aldrich, 5.33005) supplemented with 25 mM ammonium hydroxide (Honeywell International, 30501-1L). The mass spectrometer was operating in positive electrospray ionization (ESI) mode. Data acquisition and analysis were performed using Analyst 1.7.2 (Sciex). Results were reported and further used for calculation as peak area (response).

Please cite this article in press as: Krieg et al., Cortical organoid-derived models of the melanoma brain metastatic niche enable prioritization of cancer-targeting drugs, Cell Reports Methods (2025), https://doi.org/10.1016/j.crmeth.2025.101236

QUANTIFICATION AND STATISTICAL ANALYSIS

Statistical analysis was performed with GraphPad Prism 10.2.2 Software. Unless otherwise indicated, data are presented as mean with the standard error of the mean and individual data points plotted. Replicates were selected by random sampling of each hCO or MBM batch. Asterisks represent the significance as follows: ***: $p < 0.001$, **: $p < 0.01$, *: $p < 0.05$ and ns: $p \geq 0.05$. Information on statistical analysis and number of replicates is stated in the respective figure legend. Dose-response curves and IC_{50} values were calculated and plotted based on a sigmoidal dose-response equation. As maximum efficacy (E_{max}), we calculated the differences between the highest and lowest points of the curve. GraphPad Prism was used to perform Pearson correlation analysis to compare screening plates and coefficient of variation analyses to determine intra-batch variability.

15. Appendix VII

High-throughput drug repurposing screen identifies candidates targeting Multiple sulfatase deficiency

Annika Wittich[1], Alisa DeGrave[2], Jeanette Reinshagen[1], Lina Schmidt[2,3], Ole Pless[1,*,§] and Lars Schlotawa[2,3,*,§]

[1]Fraunhofer Institute for Translational Medicine and Pharmacology ITMP, Discovery Research ScreeningPort, 22525 Hamburg, Germany

[2]Fraunhofer Institute for Translational Medicine and Pharmacology ITMP, Translationale Neuroinflammation und Automatisierte Mikroskopie TNM, 37075 Göttingen, Germany

[3]Department of Pediatrics and Adolescent Medicine, University Medical Center Göttingen (UMG), 37075 Göttingen, Germany

*Corresponding authors

[§]Both authors contributed equally.

Correspondence: ole.pless@itmp.fraunhofer.de and lars.schlotawa@med.uni-goettingen.de

SUMMARY

Multiple sulfatase deficiency (MSD, MIM #272200) is an ultra-rare lysosomal storage disorder. It is caused by mutations in the *SUMF1* gene, which encodes the formylglycine-generating enzyme (FGE). FGE's function is essential for the post-translational activation of all 17 cellular human sulfatases, most of which are localized in the lysosome. Their dysfunction leads to the accumulation of glycosaminoglycans and sulfatides, resulting in lysosomal storage and, consequently, cell pathology, progressive organ failure, and death. No curative treatment options are currently available for MSD. We developed a high-throughput assay using patient-derived fibroblasts to identify therapeutic agent candidates that restore arylsulfatase A (ARSA) activity, one of the most important sulfatases affected in MSD. We screened a highly annotated small-molecule repurposing library containing 5,632 compounds, including (pre-)clinical candidates, marketed, and withdrawn drugs. We identified 80 compounds that significantly increased ARSA activity and confirmed their potency in 56 of these compounds through concentration-response titration experiments in the primary assay. Based on this, six top candidates were selected and ranked according to potency, toxicity, predicted target classes, and blood-brain barrier permeability. Our findings highlight repurposable compounds harbouring the potential to restore sulfatase activity and paving the way for the fast-track development of targeted treatments for this devastating disorder.

INTRODUCTION

Multiple sulfatase deficiency (MSD) is a rare neurological disorder and is caused by pathogenic variants in the *sulfatase-modifying factor 1* (*SUMF1*) gene, which encodes the formylglycine-generating enzyme (FGE) (Cosma et al., 2003; Dierks et al., 2003). FGE posttranslationally activates sulfatases (Dierks et al., 1998; Appel and Bertozzi, 2014). Variants in the *SUMF1* gene lead to reduced activity of FGE, potentially caused by inhibition of either the FGE's active side or protein instability (Cosma et al., 2003; Dierks et al., 2003, 2005; Schlotawa et al., 2011). This, in turn, results in incomplete post-translational activation of all 17 human sulfatases, a group of enzymes that degrade or remodel sulfate esters (Mashima and Nakanishi, 2022). FGE is located in the endoplasmic reticulum and activates sulfatases by the oxidation of an active-site cysteine to Cα-formylglycine (Schmidt *et al.*, 1995), which is activated by Cu (I) with two cysteine residues (Appel *et al.*,

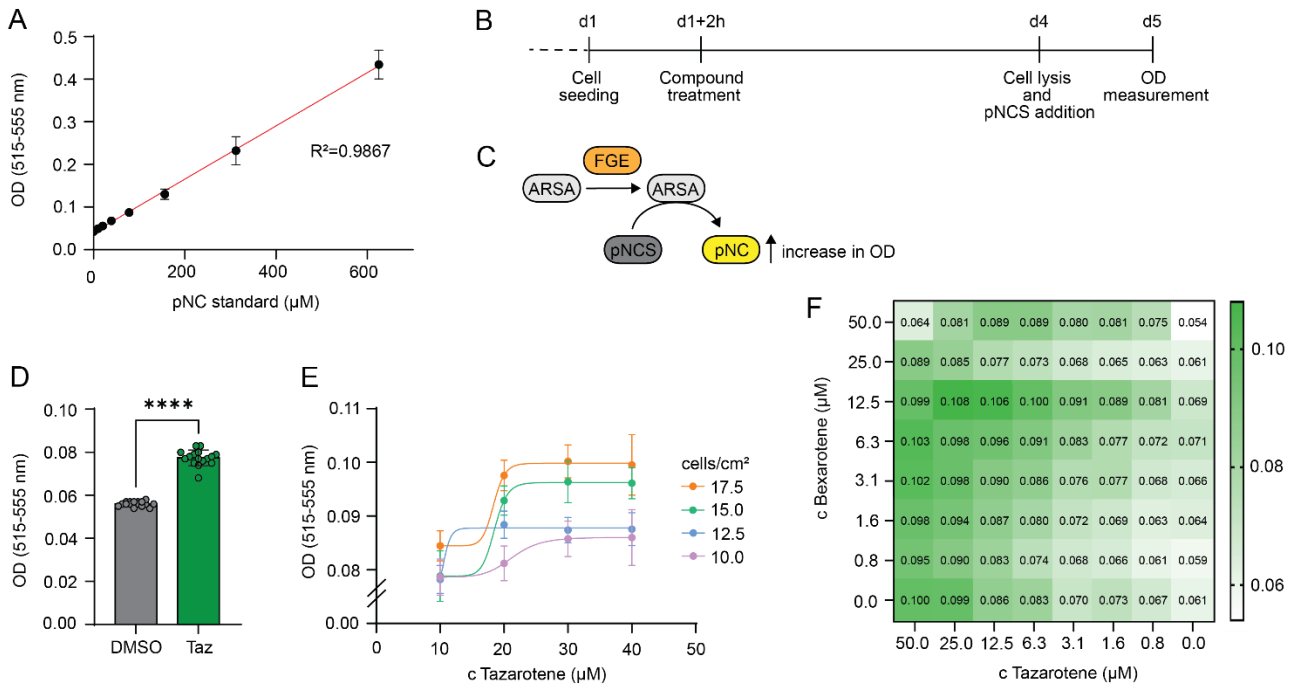


Figure 1: Assay Development of ARSA high-throughput screen. **(A)** Concentration-dependent increase in optical density (OD) of pNC standard at 515-555 nm wavelength. **(B)** Schematic workflow of screening procedure. **(C)** Scheme of ARSA activity assay. ARSA is activated by FGE and cleaves the sulfate residue of pNCS, resulting in an increase in OD at wavelengths of 515-555 nm. **(D)** Treatment of patient-derived immortalized fibroblasts (MSDi (GM3245i) - G3026/03) with 10 µM Tazarotene for 72 h results in an increased ARSA activity (measured by OD) compared to DMSO control. Each dot represents one well of a 384 well plate. ****p<0.0001, unpaired two-tailed t-test. **(E)** Cell number-dependent increase of ARSA activity after treatment with different concentrations of Tazarotene for 72 h. Data are represented as mean and standard deviation out of 16 technical replicates. **(F)** Dose-response titration experiments of Tazarotene in combination with Bexarotene. A combination of 25 µM Tazarotene and 12.5 µM Bexarotene resulted in the highest ARSA activity. Values represent the mean OD of two biological replicates, each consisting of three technical replicates.

2019). Sulfatases are enzymes that catalyze the removal of a sulfate residue from biological substances with a high substrate specificity, e.g, sulfatide for ARSA (Mashima and Nakanishi, 2022). The majority of sulfatases are located in the lysosome, and therefore, the loss of their activity results in the accumulation of substrates like glycosaminoglycans (GAGs) and sulfatides in the lysosome. Others are located in the ER, Golgi, or on the cell surface (Schlotawa, Adang, *et al.*, 2020). MSD is inherited in an autosomal recessive manner. To date, 85 pathological variants of *SUMF1* have been identified (Henrie *et al.*, 2018), while the most frequently reported variants are p.Gly247Arg, p.Ser155Pro, p.Arg349Trp, p.Ala279Val, p.Arg345Cys, and p.Gly263Val (Schlotawa *et al.*, 2019). Although clinical symptoms are multisystemic and widely variable, common symptoms are neurologic deterioration, cardiac disease, hearing loss, and airway compromise (Schlotawa *et al.*, 2019). Affected individuals often exhibit normal development in early childhood followed by a progressive decline in cognitive and motor functions. Disease severity is classified by cases based on age of onset and disease progression. Subtypes have been historically distinguished in neonatal, late infantile and juvenile MSD (Eto *et al.*, 1987) but recently re-classified in severe and attenuated forms of MSD (Adang et al. 2020; Schlotawa, Preiskorn et al. 2020). The mean survival of MSD patients is 13 years (95% CI 9.8-16.2 years) (Schlotawa, Preiskorn, *et al.*,

2020). Currently, there are only symptomatic treatment options available, but no curative therapy for MSD exists. In a smaller-scale drug screen, the FDA-approved retinoids Tazarotene and Bexarotene were found to synergistically ameliorate MSD pathophysiology (Schlotawa *et al.*,

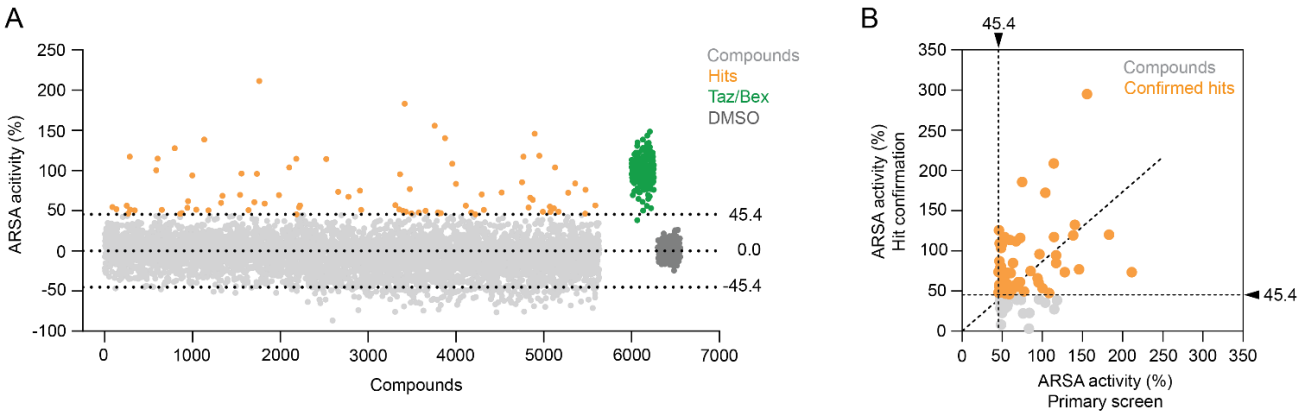


Figure 2: Primary screening data and hit confirmation. **(A)** Screening of the repurposing compound library, consisting of 5,632 compounds, using the ARSA assay identified 80 hits (shown in orange) that were able to increase ARSA activity by at least 45.4% (5 × SD of DMSO) compared to controls. DMSO (dark grey) was used as a negative control (0%) and a combination of 25 µM Tazarotene and 12.5 µM Bexarotene (green) was used as a positive control (100%). Each dot represents one well of a 384 well plate. n=1 **(B)** 80 hits of the primary screen against data of the hit confirmation assay. 56 hits out of 80 could be confirmed using the same assay and the same threshold. Confirmed hits are shown in orange, compounds that did not reach 45.4% activity are shown in grey. The data represent the mean value of four technical replicates for the Hit confirmation and one replicate for the primary screen.

2023). However, both compounds are primarily used for the topical treatment of psoriasis (Chandraratna, 1996). Although Bexarotene has been approved for oral treatment of cutaneous T-cell lymphoma in 1999 (U.S. Food and Drug Administration, 1999), their chronic oral administration has not yet been approved for pediatric use. Additionally, side effects for retinoids have been described, including ophthalmologic, gastrointestinal, neuromuscular, psychiatric, rheumatologic, and laboratory abnormalities (Ellis and Krach, 2001; Sekula-Gibbs, Uptmore and Otillar, 2004).
We aimed to identify new lead compounds from a repurposing compound collection that could enhance FGE function and potentially serve as an alternative treatment option for MSD patients. This well-annotated compound collection was compiled by the Broad Institute and included approved and marketed drugs, as well as drugs that reached phases 1–3 in clinical development for various targets and indications (Corsello *et al.*, 2017). This approach of drug repurposing, which involves applying an existing therapeutic to a new disease indication, holds promise, especially for rare diseases, at a lower cost and timeline than *de novo* drug development (Roessler *et al.*, 2021). Based on previously conducted high-throughput screening (HTS) assays that measure Arylsulfatase A (ARSA) activity in SV40 large T antigen (SV40t) immortalized fibroblasts from patients (Geng *et al.*, 2011; Schlotawa *et al.*, 2023), we developed an HTS-compatible assay using MSD patient-derived cells carrying a frequent *SUMF1* variant (c.463C>T, Ser155Pro). By using the colorimetric ARSA substrate paranitrocatechol sulfate (pNCS), ARSA activity could be quantified as a result of increased FGE activity. We identified, confirmed, and profiled six repurposable compounds that increased ARSA activity in a dose-dependent manner, more effectively than Tazarotene and Bexarotene, and even more when combined with Tazarotene, without observing toxicity.

RESULTS

Development and miniaturization of the ARSA assay

To identify alternative therapeutic candidates to Tazarotene and Bexarotene, we used patient-derived immortalized fibroblasts carrying the SUMF1 variant c.463C > T (Ser155Pro), leading to a severe clinical presentation and a remaining FGE activity of 1.6% (Schlotawa et al., 2011). ARSA is one of the 17 human sulfatases that FGE activates and can hydrolyze the chromogenic salt pNCS. Desulfation by ARSA produces paranitrocatechol (pNC) as a product, resulting in an increased OD (**Figure 1C**), which is proportional to ARSA activity (Baum, Dodgson and Spencer, 1959). Therefore, we first evaluated whether we could reliably measure pNC at 515-555 nm wavelength by titrating different concentrations of the pNC product in the assay plates. We observed an increase in optical density (OD) that correlated with the amount of pNC product (**Figure 1A**). To assess ARSA activity, cells were seeded at a density of 17.5 cells/cm². After 2 hours, cells were treated with compounds or an equivalent of DMSO (the solvent for each compound) for 72 hours before being lysed and ARSA substrate pNCS was added in respective pNCS buffer. After 17 hours NaOH was added to each well, to deprotonate the phenolic groups of pNC in order to change OD and OD was measured immediately (**Figure 1B**). To optimize assay conditions for the positive control Tazarotene, we tested different cell densities from 10 to 17.5 cells/cm² for cell seeding in a 384 well format, and found optimal conditions using 17.5 cells/cm², resulting in an increased pNCS turnover after treatment with the same concentrations of Tazarotene (**Figure 1E**). Treatment with Tazarotene resulted in a significant increase in ARSA activity, as demonstrated previously (Schlotawa et al., 2023) (**Figure 1D**). It was also previously demonstrated that the retinoids Tazarotene and Bexarotene work synergistically (Schlotawa et al., 2023). We systematically evaluated the concentrations of both retinoids and found that 25 µM Tazarotene, in combination with 12.5 µM Bexarotene, produced the highest ARSA activity (**Figure 1F**). These combined concentrations were used in the following as the positive control for the primary screen, as well as for hit confirmation and hit profiling.

Table 1: Six nominated hit compounds and their annotation. We prioritized hits based on EC50, topological surface area (TPSA), molecular weight (MW), number of rotatable bonds (RB), ARSA activity (mean of n=2), viability (mean of n=2), reported targets, and clinical phase of testing.

Compound #	EC50 (µM)	TPSA (<90)	MW (<500)	RB (<8)	Mean ARSA activity (%) at 50 µM	Mean viability (%) at 50 µM	Reported targets	Clinical Phase
19	1.31	43.70	295.38	3	104.21	90.18	Dopamine receptor 1	Preclinical
21	9.19	80.62	247.28	2	120.41	93.12	Protein kinase B (Akt)	Preclinical
45	7.20	30.87	312.44	0	110.51	90.93	Dopamine and serotonin receptor	Launched
55	12.07	83.79	399.43	5	74.66	60.05	Activin receptor type 1B, TGFBR1	Phase 2
22	20.29	70.83	349.48	7	143.53	79.09	CCR5, CXCR4	Phase 3
40	108.10	39.19	249.27	2	157.65	91.95	unspecified	Phase 2

Small molecule repurposing screen identifies activators of ARSA

For the HTS, we used a well-annotated compound library consisting of 5,632 repurposable compounds. We screened the compounds at single points, meaning each well of a 384 well plate contained one compound. For controls, one entire column (16 wells) was designated for the positive control (a combination of Tazarotene and Bexarotene) and the negative control (DMSO, used as a solvent for all compounds) on each assay plate. We set the hit threshold at five times the standard deviation of the negative control and identified 80 compounds that increased ARSA activity by at least 45.4% compared to controls (**Figure 2A**). These 80 compounds were then validated in a hit confirmation assay using the previously described primary assay (n=4 technical

replicates). Out of the initial 80 hits, 56 were confirmed using the same threshold, resulting in a 70% hit confirmation rate (**Figure 2B**). For hit profiling, we tested the 56 compounds at 10 different concentrations (50 µM to 0.1 µM, in a 1:2 serial dilution). We observed concentration-dependent effects for many compounds, although with varying effect sizes **(Supplementary Figure 1)**. In parallel, we assessed the toxicity of the compounds using an ATP-based cell viability assay (CellTiter-Glo). We identified some compounds with mild toxicity at higher doses, but overall low toxicity for all compounds **(Supplementary Figure 1)**. To further reduce the number of compounds, we mined compound annotations from public repositories. We extracted reported targets, clinical stage of testing, and physicochemical characteristics, including molecular weight (MW), topological surface area (TPSA), and the number of rotatable bonds (RB). Those characteristics are of high interest when predicting the likelihood of crossing the blood-brain barrier (BBB) (Geldenhuys *et al.*, 2015; Gupta *et al.*, 2019). Given the strong neurological involvement in MSD, therapeutics need to cross the BBB to reach the central nervous system in sufficient amounts. Reduced molecular flexibility, as measured by the number of RB, and low TPSA, favors BBB penetration (Hitchcock and Pennington, 2006). Larger molecules rarely cross the BBB without active transport mechanisms (Alo and Lamers, 2025). Therefore, compounds with TPSA values below 90, molecular weight below 500, and less than eight RBs, are considered more likely to cross the BBB (Pajouhesh and Lenz, 2005; Hitchcock and Pennington, 2006; Reichel, 2015; Gupta *et al.*, 2019). Based on EC50, toxicity, physicochemical properties, and predicted targets, we prioritized six compounds for follow-up studies **(Figure 3; Table 1)**.

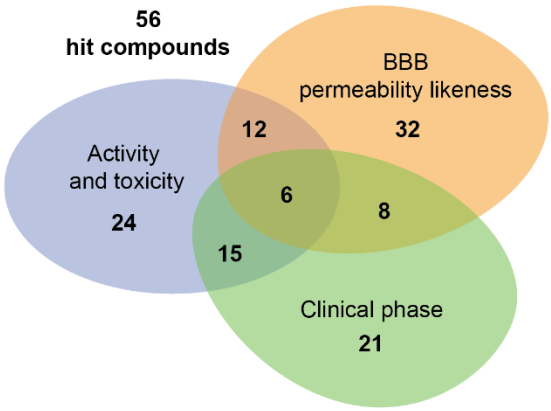


Figure 3: Priorization of confirmed hit compounds. 56 compounds were classified with respect to ARSA activity and toxicity at 50 µM compound concentration, as well as EC50 values, the likelihood of penetrating the blood-brain barrier (BBB), and the maximal phase of drug development for each respective compound. Six compounds were identified that matched all criteria.

Combining six hit compounds with Tazarotene enhances ARSA activity

The combination of Tazarotene and Bexarotene in a 1:2 ratio has been shown to boost ARSA activity more effectively than Tazarotene alone in a time- and dose-dependent manner (Schlotawa et al., 2023). Combining two drugs can potentially lower the required doses for each medication, reducing side effects while enhancing benefits. For example, combining the chemotherapeutic agents Cisplatin and Gemcitabine is highly effective in treating metastatic breast cancer (Jassem *et al.*, 2002; Chew *et al.*, 2009). We therefore investigated whether the six compounds work synergistically with Tazarotene to explore a potential combination therapy. Eight different concentrations of each compound were tested, including a fixed concentration for each, resulting in 49 distinct concentration combinations. We observed increased ARSA activity across all compound combinations, with certain concentrations producing the highest activity (**Figure 4**). Data analysis was performed using Synergy Finder (Zheng et al., 2022). The zero interaction potency (ZIP)

model (Yadav et al., 2015) indicated a synergistic effect for all combinations, with ZIP scores greater than ten (>10) suggesting likely synergy between two drugs (Ianevski, Giri and Aittokallio, 2022) (**Supplementary Table 1**). However, it is important to interpret these results with caution, as the EC50 values of Tazarotene vary across different combinations (**Supplementary Table 1**).

Notably, for compounds 22 and 40, the highest doses at 50 µM decreased ARSA activity, potentially due to toxicity (**Figure 4**). Despite this, combining specific doses of these hit compounds with Tazarotene appears to enhance ARSA activity more than either agent alone, indicating at least an additive effect of the compounds.

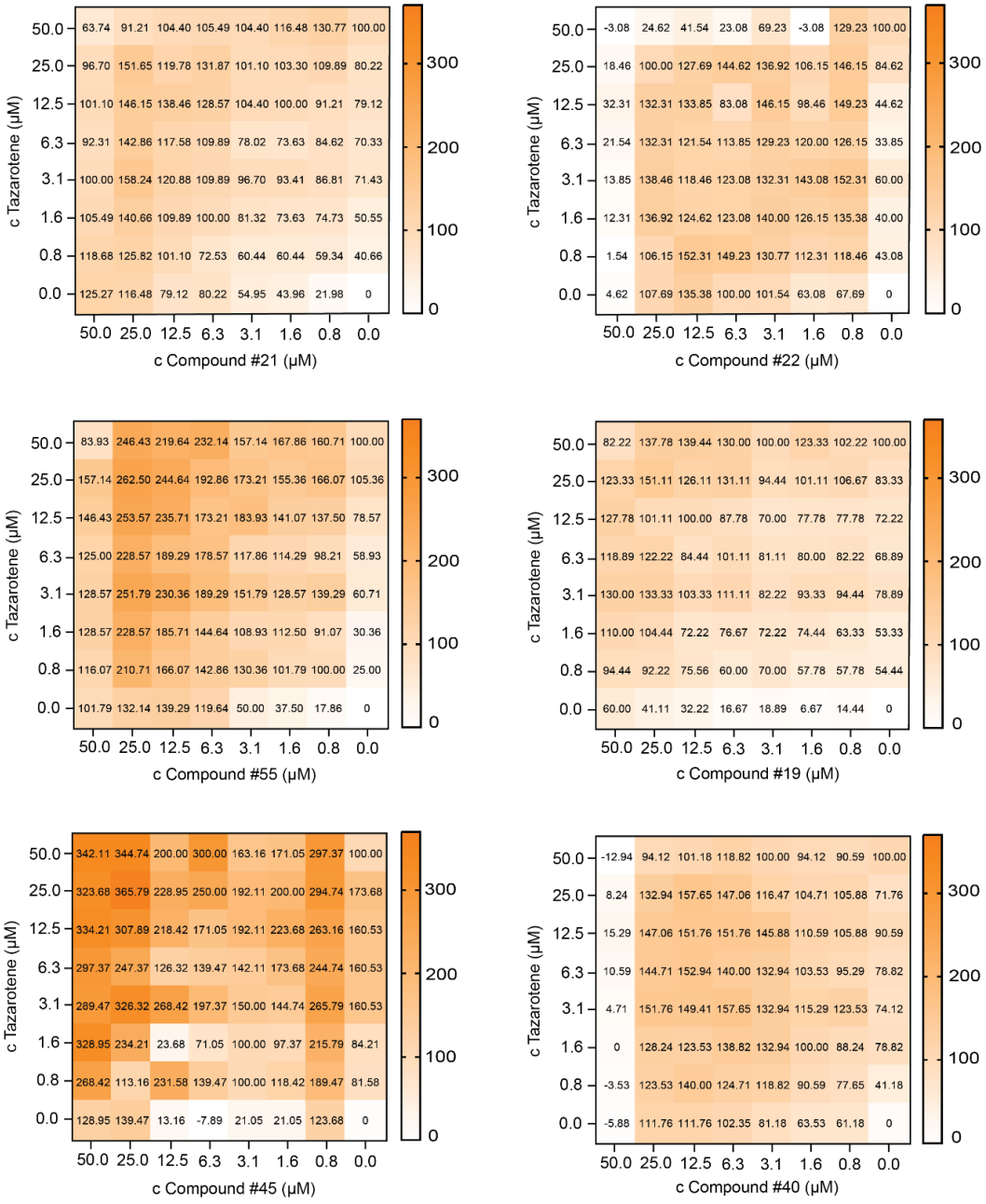


Figure 4: Combination of six nominated hit compounds with Tazarotene. ARSA activity of six nominated and validated hit compounds in combination with Tazarotene using different concentrations (50 µM to 0 µM in 1:2 serial dilution). Value represents the mean value out of three technical replicates. Data is normalized to DMSO (0%) and 50 µM Tazarotene (100%).

DISCUSSION

Currently, there is no cure for MSD, and treatment focuses on managing and alleviating the multisystemic symptoms (Ahrens-Nicklas et al., 2018). Since MSD results from insufficient functional FGE protein, strategies that enhance FGE activity present a cell-type-independent therapeutic approach. Gene replacement therapy is a promising opportunity to treat MSD. Several trials are ongoing for related single sulfatase disorders, including Mucopolysaccharidosis (MPS) II (NCT04571970, NCT03566043), MPS III (NCT02716246), MLD (NCT01801709), and MPS VI (NCT03173521). Recently, a study showed the successful use of an scAAV9/SUMF1 vector in a *Sumf1* knockout (*Sumf1*−/−) mouse model of MSD (Presa et al., 2025). The *Sumf1*−/− mouse model exhibits nearly absent sulfatase activity and mimics many of the phenotypic features seen in MSD patients (Settembre et al., 2007). scAAV9/SUMF1 gene therapy prevented death, restored sulfatase activity, and improved neurological, visual, and cardiac symptoms in the MSD mouse model (Presa et al., 2025). A Phase I/II clinical trial for AAV9 *SUMF1* gene therapy is planned (NCT03047369). Similarly, *ex vivo SUMF1* lentiviral gene therapy combined with hematopoietic stem cell transplantation improved sulfatase activity and decreased glycosaminoglycan accumulation in MSD patient-derived cells and treated mice (Pham et al., 2024). These results emphasize the strong potential of gene replacement approaches for MSD, although safety concerns, especially regarding immune responses and toxicity, remain (Cring and Sheffield, 2022). However, gene replacement therapies are costly, and it's uncertain whether they can offer a complete cure. Therefore, alternative therapies, using small molecules, can provide an inexpensive way to bridge the current lack of therapeutic options for MSD. Tazarotene and Bexarotene were recently identified as activators of FGE function through a small-scale drug repurposing screen (Schlotawa et al., 2023), offering an alternative potential therapy. Currently, Tazarotene is only approved for topical use in psoriasis and acne, and approval for oral use in MSD patients will require proven safety and efficacy. In fact, Tazarotene is progressing toward clinical testing for MSD within the EU-funded REMEDi4ALL project (Grant number: 101057442), which is a significant milestone towards drug repurposing of Tazarotene. Our newly identified compounds could offer a non-retinoid therapeutic avenue by targeting FGE and potentially enhancing its enzymatic activity directly or by stabilizing the protein. Combining our hit compounds with Tazarotene further increased ARSA activity, suggesting the potential for a combination therapy to reduce the needed retinoid dose by improving efficacy. More systematic testing, such as safety and efficacy towards different sulfatases in primary fibroblasts with various *SUMF1* variants, is necessary to determine if these combinations would benefit MSD patients. However, understanding the mechanism of action is crucial, and preclinical studies using mice or advanced disease models, such as induced pluripotent stem cell (iPSC) models, are essential to evaluate safety and efficacy prior to clinical testing and application.

In summary, we have developed a strong HTS drug discovery pipeline using patient-derived fibroblasts to identify and confirm therapeutic candidates for MSD. Our results add-on new non-retinoid compounds with the ability to restore sulfatase activity, opening the door for the development of treatments for MSD patients.

MATERIAL AND METHODS

Cell lines

The cell line MSDi (GM03245i) - G3026/03 used in this work is a fibroblast cell line from a male MSD patient, immortalized with SV40 large T Antigen. *SUMF1* variant c.463C > T, (p.Ser155Pro) Corriell Institute for Medical Research (Cosma *et al.*, 2003).

Maintenance and cryopreservation of fibroblast cultures

Human immortalized fibroblasts were grown in cell culture medium (DMEM/F12 (Gibco, 21969-035) with 10% FBS (Capricorn, FBS-11A), 1% Glutamine (Capricorn, GLN-B) and 1% Penicillin/Streptomycin (Gibco, 15070063)) in T75 tissue culture flasks (Sarstedt, 83.3911.002) at 37 °C with 5% CO2. Cells were passaged at 90-100% confluency via incubation with 4 ml Trypsin/EDTA (Capricorn, TRY-1B) for 5 min at 37 °C. The enzymatic reaction was stopped by adding 8 ml of DMEM/F12 (Gibco, 21969-035) to the flask.

Complete cell suspension was collected in a 15 ml tube (Greiner, 188271-N) and centrifuged at 300 × g for 5 min (Thermo Scientific, Heraeus Megafuge 16R). The supernatant was aspirated, and the cell pellet was gently resuspended in 1 ml fresh cell culture medium and seeded at a 1:5-1:10 ratio onto new T75 flasks with a final volume of 12 ml. Medium was changed every three to four days.

For cryopreservation, cells were detached from cell culture flasks as described above. Cell pellet was resuspended in 1 ml cold (2-8 °C) Fetal Bovine Serum (FBS) (Capricorn, FBS-11A) with 10% DMSO (Carl Roth, HN47.1), counted using the CytoSMART cell counter (Corning, 6749) and 3.0×10^6 cells/ml/tube were transferred to a CryoPure tube (Sarstedt, 72.379) and placed in a freezing container (Corning® CoolCell™ LX, 432005). The freezing container was stored at -80 °C overnight and subsequently transferred to a -150 °C freezer for long-term storage. For thawing, cryopreserved cells were removed from -150 °C storage and directly placed into a 37 °C water bath until ¾ of the cell suspension was thawed. The cell suspension was transferred into a 15 ml tube containing 5 ml DMEM/F12 and centrifuged at 300 × g for 5 min. The supernatant was aspirated and the cell pellet was gently resuspended with medium and seeded onto a T75 flask.

High-throughput screening assay

The primary screen was performed in two weeks using the same cell passage number (p15). Cells were seeded using a Multidrop (ThermoFisher, 5840300) standard tube cassette (Thermo, 24072670), which was rinsed with RBS35 (Carl Roth, 9238.1), 70% Ethanol and ddH2O and calibrated before usage. Cells were collected as described above and seeded with a density of 17.5×10^4 cells/cm^2 in 25 µl cell culture medium onto 384 well SpectraPlates (Revvity, 6007650). The plate lid was changed to a MicroClime Environmental Lid (Beckman Coulter, 001-5719) that was previously filled with ddH_2O to prevent evaporation effects. Two hours after cell seeding, compounds were transferred using the Echo650 (Beckman Coulter) onto the assay plates with a final concentration of 20 µM as well as controls. 0.2% DMSO served as a negative control (column 24), and 25 µM Tazarotene (Selleckchem, S1569) in combination with 12.5 µM Bexarotene (Selleckchem, S2098) were used as a positive control (column 24). One plate was treated with DMSO only and served as a control plate for each screening week, respectively. After 72 h incubation time, medium was aspirated and cells were washed twice with DPBS (Gibco, 14190144) using the Janus MDT (PerkinElmer). Therefore, 384 well pipette tips (Axygen, PK-384-R) were initially washed with ddH_2O. One reservoir (Thermo, 1064-15-7) was used for fresh DPBS and one served as a waste container. Afterwards, cells were lysed using 10 µl/well CellLytic M Cell Lysis Reagent (Sigma, C2978), including protease inhibitor (Roche, 04693116001) for 2 h at 4 °C. To avoid evaporation, plates were sealed with aluminum foil (Excel Scientific, XTR-FOIL-100). 10 µl/well of 25 mM p-nitrocatechol sulfate (pNCS) (Sigma, N7251) dissolved in pNCS buffer (0.5 M sodium acetate (Supelco, 1062681000) (pH 5.0), 0.5 mM sodium pyrophosphate (Sigma, P8010-500G), 1.7 M (10%) sodium chloride (Carl Roth, 3957.1)) was added to each well and plates were again sealed with aluminum foil. Plates were shaken at 37 °C and 170 rpm for 30 minutes and then stored at 37 °C, 5% CO2 in a rotating incubator (Thermo Scientific, Cytomat 10). After 17 h incubation, 30 µl 1 N NaOH (Sigma, 72068) solution was added to each well using the Janus MDT. Afterwards, plates were centrifuged at 1,200 × g for 15 min to pellet cell debris (Thermo Scientific, Heraeus Megafuge 16R). 30 µl of each well was transferred into a fresh 384 well SpectraPlate using the Janus MDT. Air bubbles were removed using a cannula. Optical density (OD) was measured using the EnVision (Revvity, 2103 Multilabel Reader) and the filter Resonfine/Amplex Red FP 535 (124) (Measurement height 6.5 mm, Excitation 60%, Number of Flashes: 200). For the hit confirmation and hit profiling, cells were seeded manually onto 384 well plates. The hit confirmation assay was performed in quadruplicate on one day using one 384 well plate. Hit profiling was performed in duplicates.

Cell viability assay (CellTiter-Glo)

CellTiter-Glo assay (Promega, #G7572) was used to determine viability based on cellular ATP concentrations and was performed in duplicates. Cells were isolated and seeded manually onto 384 well plates in 25 µl medium as described previously. Additionally, 10% DMSO (v/v) served as

a positive control for the toxicity assessment and was added to column 22 manually. After 72 h incubation with the 56 nominated compounds in 10 different doses (serial dilution from 50 µM to 0.1 µM), 12.5 µl CellTiter-Glo reagent was added to each well using the Janus MDT and plates were incubated for 10 min at room temperature. 30 µl/well were transferred to a white 384 well plate (Greiner, 781073) using the Janus MDT. Afterwards, the plates were centrifuged for 1 min at 1,000 rpm, and Bioluminescence was measured using the EnSight (Revvity, 1410231).

Data analysis

Data was analyzed using GraphPad-Prism software and for statistical computing (v.10.4.1). Statistical significance was assessed using parametric tests for normally-distributed data (Student's t-test, ANOVA). When possible, data are presented as scatter plots with individual data points showing all individual measurements. Unless otherwise indicated, we expressed the data as mean and standard deviation (mean ± SD). Experiments were repeated in independent biological experiments. Information on statistical details and the number of replicates can be found in the respective figure legends. Screening data was analyzed using Abase (v.7.4.4) and KNIME (v.7.3). For Synergy analysis and ZIP scoring, the open-source application SynergyFinder+ (https://synergyfinder.org/#!/) was used (Yadav *et al.*, 2015; Zheng *et al.*, 2022).

References

1. Alo, B., Lamers, C., 2025. Crossing Barriers: Advancements in Macromolecular Therapeutics for Neurodegenerative Diseases and Strategies to Overcome the Blood–Brain Barrier. ACS Pharmacol. Transl. Sci. 8, 2353–2383. https://doi.org/10.1021/acsptsci.5c00153
2. Appel, M.J., Meier, K.K., Lafrance-Vanasse, J., Lim, H., Tsai, C.-L., Hedman, B., Hodgson, K.O., Tainer, J.A., Solomon, E.I., Bertozzi, C.R., 2019. Formylglycine-generating enzyme binds substrate directly at a mononuclear Cu(I) center to initiate O_2 activation. Proc. Natl. Acad. Sci. 116, 5370–5375. https://doi.org/10.1073/pnas.1818274116
3. Baum, H., Dodgson, K.S., Spencer, B., 1959. The assay of arylsulphatases A and B in human urine. Clin. Chim. Acta 4, 453–455. https://doi.org/10.1016/0009-8981(59)90119-6
4. Chandraratna, R.A.S., 1996. Tazarotene-first of a new generation of receptor-selective retinoids. Br. J. Dermatol. 135, 18–25. https://doi.org/10.1111/j.13652133.1996.tb15662.x
5. Chew, H.K., Doroshow, J.H., Frankel, P., Margolin, K.A., Somlo, G., Lenz, H.-J., Gordon, M., Zhang, W., Yang, D., Russell, C., Spicer, D., Synold, T., Bayer, R., Hantel, A., Stiff, P.J., Tetef, M.L., Gandara, D.R., Albain, K.S., 2009. Phase II Studies of Gemcitabine and Cisplatin in Heavily and Minimally Pretreated Metastatic Breast Cancer. J. Clin. Oncol. 27, 2163–2169. https://doi.org/10.1200/JCO.2008.17.4839
6. Corsello, S.M., Bittker, J.A., Liu, Z., Gould, J., McCarren, P., Hirschman, J.E., Johnston, S.E., Vrcic, A., Wong, B., Khan, M., Asiedu, J., Narayan, R., Mader, C.C., Subramanian, A., Golub, T.R., 2017. The Drug Repurposing Hub: a next-generation drug library and information resource. Nat. Med. 23, 405–408. https://doi.org/10.1038/nm.4306
7. Ellis, C.N., Krach, K.J., 2001. Uses and complications of isotretinoin therapy. J. Am. Acad. Dermatol. 45, S150–S157. https://doi.org/10.1067/mjd.2001.113717
8. Eto, Y., Gomibuchi, I., Umezawa, F., Tsuda, T., 1987. Pathochemistry, Pathogenesis and Enzyme Replacement in Multiple-Sulfatase Deficiency. Enzyme 38, 273–279. https://doi.org/10.1159/000469216
9. Geldenhuys, W.J., Mohammad, A.S., Adkins, C.E., Lockman, P.R., 2015. Molecular Determinants of blood–brain Barrier Permeation. Ther. Deliv. 6, 961–971. https://doi.org/10.4155/tde.15.32
10. Geng, H., Whiteley, G., Ribbens, J., Zheng, W., Southall, N., Hu, X., Marugan, J.J., Ferrer, M., Maegawa, G.H.B., 2011. Novel Patient Cell-Based HTS Assay for Identification of Small Molecules for a Lysosomal Storage Disease. PLoS ONE 6, e29504. https://doi.org/10.1371/jounal.pone.0029504
11. Gupta, M., Lee, H.J., Barden, C.J., Weaver, D.F., 2019. The Blood–Brain Barrier (BBB) Score. J. Med. Chem. 62, 9824–9836. https://doi.org/10.1021/acs.jmedchem.9b01220
12. Henrie, A., Hemphill, S.E., Ruiz-Schultz, N., Cushman, B., DiStefano, M.T., Azzariti, D., Harrison, S.M., Rehm, H.L., Eilbeck, K., 2018. ClinVar Miner: Demonstrating utility of a Web-based tool for viewing and filtering ClinVar data. Hum. Mutat. 39, 1051–1060. https://doi.org/10.1002/humu.23555

13. Hitchcock, S.A., Pennington, L.D., 2006. Structure−Brain Exposure Relationships. J. Med. Chem. 49, 7559–7583. https://doi.org/10.1021/jm060642i

14. Jassem, J., Krzakowski, M., Roszkowski, K., Ramlau, R., Marek Słomiński, J., Szczęsna, A., Krawczyk, K., Możejko-Pastewka, B., Lis, J., Miracki, K., 2002. A phase II study of gemcitabine plus cisplatin in patients with advanced non-small cell lung cancer: clinical outcomes and quality of life. Lung Cancer 35, 73–79. https://doi.org/10.1016/S0169-5002(01)00286-0

15. Mashima, R., Nakanishi, M., 2022. Mammalian Sulfatases: Biochemistry, Disease Manifestation, and Therapy. Int. J. Mol. Sci. 23, 8153. https://doi.org/10.3390/ijms23158153

16. Pajouhesh, H., Lenz, G.R., 2005. Medicinal chemical properties of successful central nervous system drugs. NeuroRX 2, 541–553. https://doi.org/10.1602/neurorx.2.4.541

17. Reichel, A., 2015. Pharmacokinetics of CNS Penetration, in: Di, L., Kerns, E.H. (Eds.), Blood-Brain Barrier in Drug Discovery. Wiley, pp. 5–41. https://doi.org/10.1002/9781118788523.ch2

18. Roessler, H.I., Knoers, N.V.A.M., Van Haelst, M.M., Van Haaften, G., 2021. Drug Repurposing for Rare Diseases. Trends Pharmacol. Sci. 42, 255–267. https://doi.org/10.1016/j.tips.2021.01.003

19. Schlotawa, L., Adang, L., De Castro, M., Ahrens-Nicklas, R., 2019. Multiple Sulfatase Deficiency, in: Adam, M.P., Feldman, J., Mirzaa, G.M., Pagon, R.A., Wallace, S.E., Amemiya, A. (Eds.), GeneReviews®. University of Washington, Seattle, Seattle (WA). https://pubmed.ncbi.nlm.nih.gov/30896912

20. Schlotawa, L., Adang, L.A., Radhakrishnan, K., Ahrens-Nicklas, R.C., 2020a. Multiple Sulfatase Deficiency: A Disease Comprising Mucopolysaccharidosis, Sphingolipidosis, and More Caused by a Defect in Posttranslational Modification. Int. J. Mol. Sci. 21, 3448. https://doi.org/10.3390/ijms21103448

21. Schlotawa, L., Preiskorn, J., Ahrens-Nicklas, R., Schiller, S., Adang, L.A., Gärtner, J., Friede, T., 2020b. A systematic review and meta-analysis of published cases reveals the natural disease history in multiple sulfatase deficiency. J. Inherit. Metab. Dis. 43, 1288–1297. https://doi.org/10.1002/jimd.12282

22. Schlotawa, L., Tyka, K., Kettwig, M., Ahrens-Nicklas, R.C., Baud, M., Berulava, T., Brunetti-Pierri, N., Gagne, A., Herbst, Z.M., Maguire, J.A., Monfregola, J., Pena, T., Radhakrishnan, K., Schröder, S., Waxman, E.A., Ballabio, A., Dierks, T., Fischer, A., French, D.L., Gelb, M.H., Gärtner, J., 2023. Drug screening identifies tazarotene and bexarotene as therapeutic agents in multiple sulfatase deficiency. EMBO Mol. Med. 15, e14837. https://doi.org/10.15252/emmm.202114837

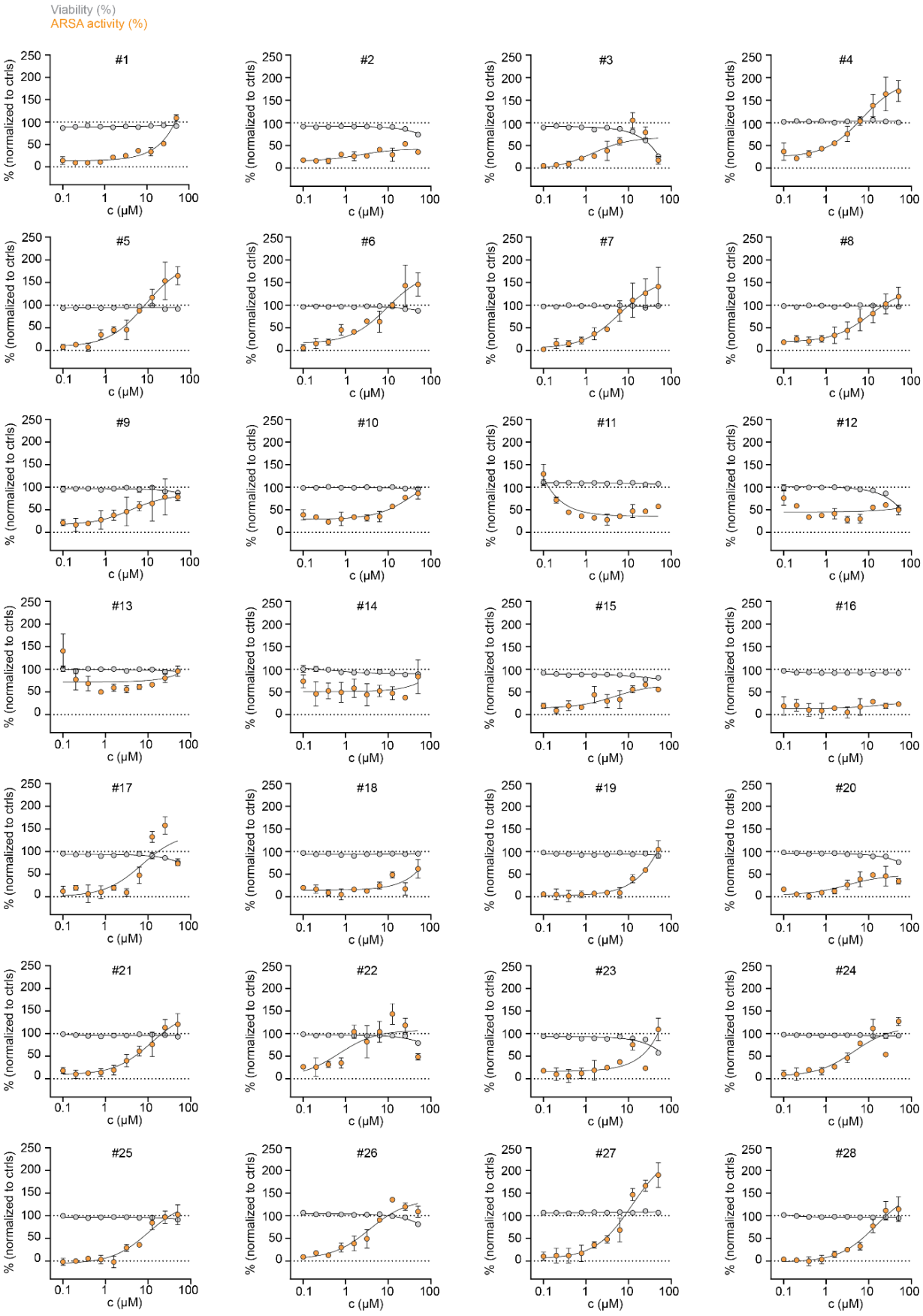
23. Schmidt, B., Selmer, T., Ingendoh, A., Figurat, K.V., 1995. A novel amino acid modification in sulfatases that is defective in multiple sulfatase deficiency. Cell 82, 271–278. https://doi.org/10.1016/0092-8674(95)90314-3

24. Sekula-Gibbs, S., Uptmore, D., Otillar, L., 2004. Retinoids. J. Am. Acad. Dermatol. 50, 405–415. https://doi.org/10.1016/j.jaad.2003.08.001

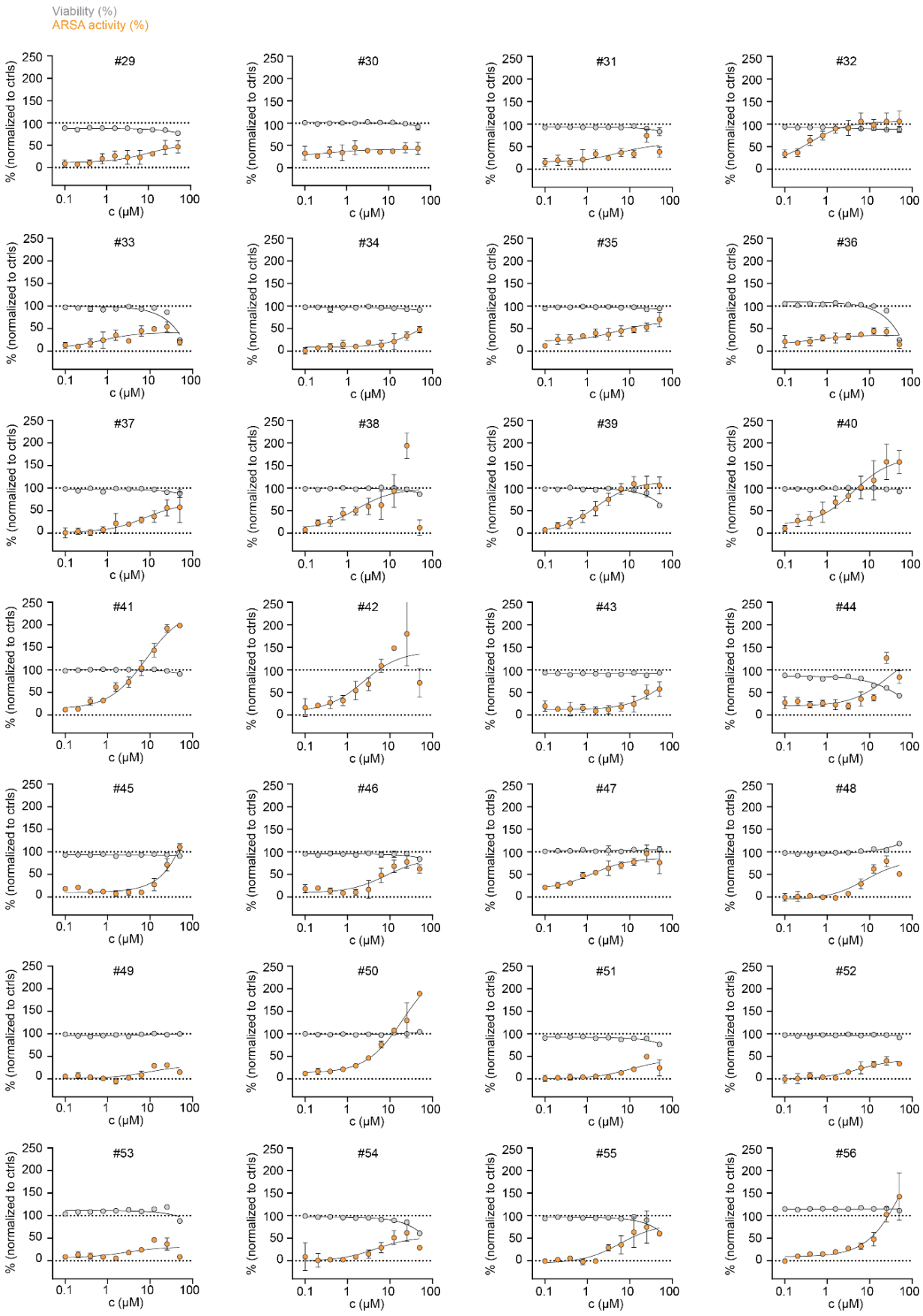
25. U.S. Food and Drug Administration, 1999. U.S. Food and Drug Administration, Center for Drug Evaluation and Research. Bexarotene NDA 21-055 approval letter, December 29, 1999. Retrieved October 06, 2025, from https://www.accessdata.fda.gov/drugsatfda_docs/nda/99/21055_Targretin_Approv.pdf.

26. Yadav, B., Wennerberg, K., Aittokallio, T., Tang, J., 2015. Searching for Drug Synergy in Complex Dose–Response Landscapes Using an Interaction Potency Model. Comput. Struct. Biotechnol. J. 13, 504–513. https://doi.org/10.1016/j.csbj.2015.09.001

27. Zheng, S., Wang, W., Aldahdooh, J., Malyutina, A., Shadbahr, T., Tanoli, Z., Pessia, A., Tang, J., 2022. SynergyFinder Plus: Toward Better Interpretation and Annotation of Drug Combination Screening Datasets. Genomics Proteomics Bioinformatics 20, 587–596. https://doi.org/10.1016/j.gpb.2022.01.004



Supplementary Figure 1: Dose-response profiles of 56 confirmed hits. Figure legend on the next page.



Supplementary Figure 1: Dose-response profiles of 56 confirmed hits. Figure legend on the next page.

Supplementary Figure 1: Dose-response profiles of 56 confirmed hits. Ten different concentrations were tested in duplicates in the ARSA activity assay (orange dots) and the CellTiter-Glo viability assay (grey dots). Value represents the mean value with standard deviation. Data is normalized to DMSO (0%) and 12.5 µM Bexarotene in combination with 25 µM Tazarotene (100%) for ARSA activity readout. For the Viability assay (CellTiter-Glo), 10% (v/v) DMSO served as a positive control (0%), and 0.2% DMSO (100%) was used as a negative control, equivalent to the DMSO percentage used for compound treatment. Note: For compound #42, viability data is missing because of the limited amount of compound material.

Supplementary Table 1: Summary of combination treatments of hit compounds with Tazarotene. Compound concentrations (c) for hit compounds and for Tazarotene that resulted in the maximal ARSA activity response are highlighted. Synergy testing using the zero-interaction potency (ZIP) model (Yadav *et al.*, 2015) revealed synergistic effects for all combinations (above 10). EC50 values for Tazarotene in the respective combination experiments are shown in the last column.

Compound #	Compound c (µM)	Tazarotene c (µM)	max. response (%)	ZIP score	EC50 Tazarotene (µM)
19	25.0	25.0	151.11	16.89	0.69
21	25.0	3.13	158.24	11.35	1.32
45	25.0	25.0	365.79	101.39	0.52
55	25.0	25.0	262.50	70.79	2.80
22	0.78	3.13	152.31	16.34	3.39
40	6.25	3.13	157.65	13.37	0.63